Sensitivity to anomalous VVH couplings induced by dimension-6 operators at the ILC

小川　智久

博士（理学）

総合研究大学院大学
高エネルギー加速器科学研究科
素粒子原子核専攻

平成３０（２０１８）年度

Ph.D dissertation

Sensitivity to anomalous VVH couplings induced by dimension-6 operators at the ILC

次元 6 演算子により導入される異常 VVH 結合の ILC 実験における感度

Tomohisa Ogawa

The Graduate University for Advanced Studies

School of High Energy Accelerator Science

Department of Particle and Nuclear Physics

June 8, 2018

Abstract

The Standard Model (SM), which is comprised of the Glashow-Weinberg-Salam theory describing electro-weak interactions based on $SU(2) \times U(1)$ gauge symmetry, quantum chromodynamics representing strong interactions based on $SU(3)$ gauge symmetry, where the Higgs mechanism has a critical role for giving rise to mass to matter and gauge particles, has successfully interpreted phenomena which are observed in reality in the field of elementary particle physics. However, several phenomena which have not been included in the SM yet are known such as dark matter, neutrino mass and so on. Therefore, the SM must be expanded to explain more observation, which is called beyond the SM (BSM). In 2012 the SM-like Higgs boson was discovered at the Large Hadron Collider (LHC) and the SM was completed through verifications afterwards. At the same time, we entered a new phase where we do not have a clear map like the SM to lead us to the BSM, and we expect that one of the hints exists in the discovered Higgs boson.

A lot of BSM models, such as a general extension of the SM and a super symmetry model, predict that Higgs couplings to the SM particles would be shifted because of mixing and corrections originating from a new heavier particle and such variation will appear with a specific pattern from the SM expectations, or these models require new Lorentz structures for describing new interactions between the Higgs boson and the SM particles. Therefore, the most important task for elementary particle physicists is to explore and verify the structures relevant to the Higgs boson and those couplings. One theoretical framework for exploring the Lorentz structures, which is rather physics driven, is to employ an Effective Field Theory (EFT) where it is possible to introduce higher dimension field operators which satisfy the gauge invariance and are restrained with inverse power of a new physics scale. The EFT can verify the structures more model-independently compared to the traditional κ-framework. Furthermore, measurements which are not related to the Higgs boson can also effectively contribute to constraining the Higgs related Lorentz structures in the EFT.

In this thesis, we focus on the couplings and the structures between the Higgs boson and the vector bosons, γ, Z, and W, which are critical parts in the Higgs sector of the SM, especially responsibility for the mass generation. By introducing relevant dimension-6 field operators to the VVH (V=γ, Z, and W) couplings under the EFT, an effective Lagrangian is given, which naturally includes anomalous VVH couplings after imposing the symmetry breaking. Effects coming from these anomalous VVH couplings will appear in cross-sections of corresponding processes and kinematical shape distributions as deviations from the SM expectations. We expect that the future International Linear Collider (ILC) can perform measurements for these anomalous VVH couplings very precisely.

To evaluate the reachable sensitivity to these anomalous VVH couplings at the ILC, full detector simulation was performed at both operation energies of $\sqrt{s} = 250$ and 500 GeV using the International Large Detector (ILD) model, which is one of the detector concepts of the ILC. The evaluation was done by analyzing all Higgs production processes such as Higgs-strahlung, ZZ-fusion, and WW-fusion, and also the decay channel of $H \to WW$, where all SM backgrounds are considered as well. To evaluate the variation of the kinematical shape distributions, detector response functions are considered, which can describe smearing effects derived from detector resolution and physical effects. The response functions can apply to any generated distributions to transfer the distribution to the detector-level distribution. The beam polarization, which is one strong point of the linear collider, can also give impact on disentanglement of γ and Z by exploiting the physics that the gauge fields B and W^3 differ in their interactions, and give the sensitivities to both of the anomalous ZZH and γZH couplings.

It turned out, as our results, that the reachable sensitivities to the anomalous VVH couplings, assuming a certain ILC full operation program, are 0.55 %, 0.17 %, and 0.27 % for the anomalous ZZH couplings of η_Z, ζ_{ZZ}, and $\tilde{\zeta}_{ZZ}$, and also the sensitivities to the anomalous γZH couplings are less than 0.10 % for both ζ_{AZ} and $\tilde{\zeta}_{AZ}$. The reachable sensitivities to the anomalous WWH couplings are respectively 0.45 %–0.80 %, 0.88 %–1.72 %, and 4.40 % for η_W, ζ_{WW}, and $\tilde{\zeta}_{WW}$. These sensitivities to VVH at the ILC are better more than tenfold compared to the LHC, and the VVH structures will be completely revealed.

Contents

1 Introduction

In the elementary particle physics, a theory which can most accurately describe states and behaviors of elementary particles at the present is the Standard Model (SM): Sheldon Glashow in 1961 gave an idea for unifying quantum electrodynamics and weak interaction based on SU(2)×U(1) gauge symmetry [1], in 1964 François Englert and Peter Higgs devised a mechanism that brings spontaneous symmetry breaking of the gauge symmetry and gives rise to mass terms for the gauge fields [2,3], and finally Steven Weinberg and Abdus Salam completed its theory in 1967 by applying the Higgs mechanism to the SU(2)×U(1) gauge symmetry [4].

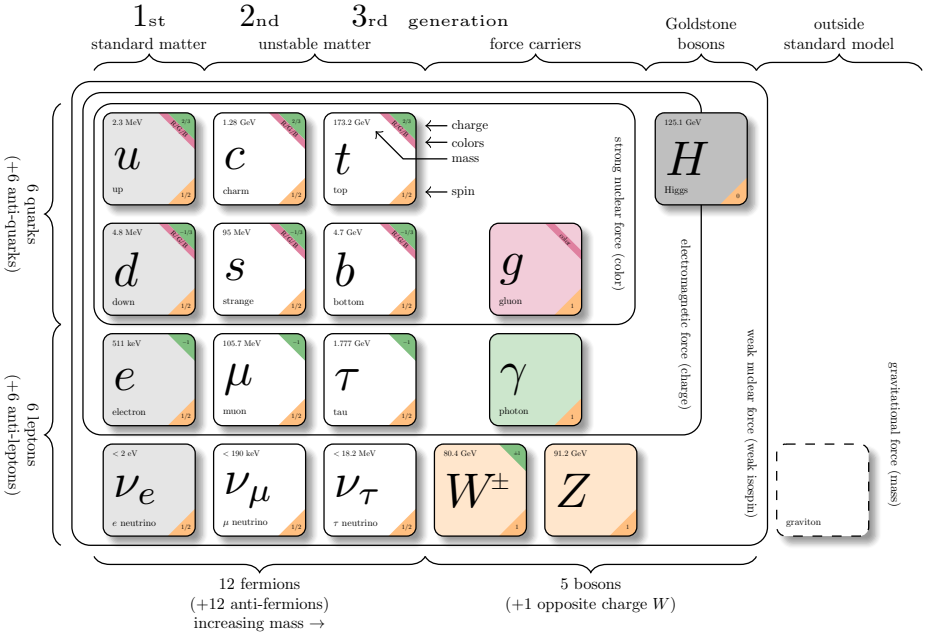

Figure 1: The elementary particles composing the universe. The plot is referred from [5].

The SM is composed of several elementary particles: fermions and bosons, which are shown in Fig. 1. The fermions are constituents of matter and the bosons are mediators of forces or interactions between the elementary particles. Currently, it is considered that nature is consist of these particles. At the 4th of July in 2012, both experimental groups, ATLAS [6,7] and CMS [8], announced that a Higgs-like particle, which was a last missing piece of the SM, was discovered with the mass of about 125 GeV [9,10] at the Large Hadron Collider (LHC) [11] in CERN, which are shown in Fig. 2 and Fig. 3. At this moment the SM was established completely.

The SM has been explained well about many experimental results and behaviors. It is also true, however, that there are several phenomena that we can not describe with the SM such as identity of the dark matter in the universe, existence of neutrino mass which has been already proven by the neutrino oscillation experiments, asymmetry between matter and anti-matter, and so on. Therefore, it is obvious that the SM must be expanded so that it can explain these phenomena, which is called beyond the SM (BSM). A tons of BSM theories have been proposed to give answers to these phenomena being not to be understood yet, and theses theories very often require variations in properties and coupling strengths between the SM particles. Thus, any deviations of the properties from the SM expectations must be connected to the BSM. To get these clues, it is necessary to measure the properties of the discovered Higgs boson thoroughly such as spin, CP (-mixture), and its couplings to the other SM particles. And in fact, such properties of the Higgs boson have been measured at LHC since the discovery. However, it is still the Higgs boson of the SM introduced in 1964 so far.

The International Linear Collider (ILC), which is a future project with linearly accelerated elementary particles: electron and positron, will provide ideal environment for performing precision measurements of the properties of the Higgs boson, where well-defined initial state information and background-less condition are given while the LHC can not get it because of enormous background

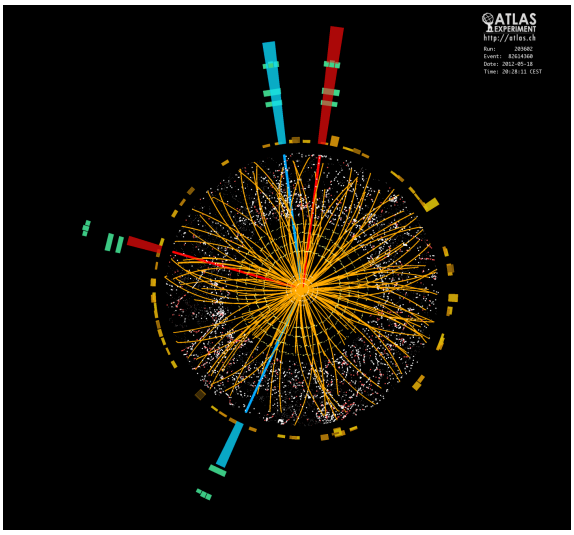

Figure 2: A candidate reaction of $h \to 4e$ recorded on 18-May-2012, 20:28:11 CEST. The plot is referred from [12].

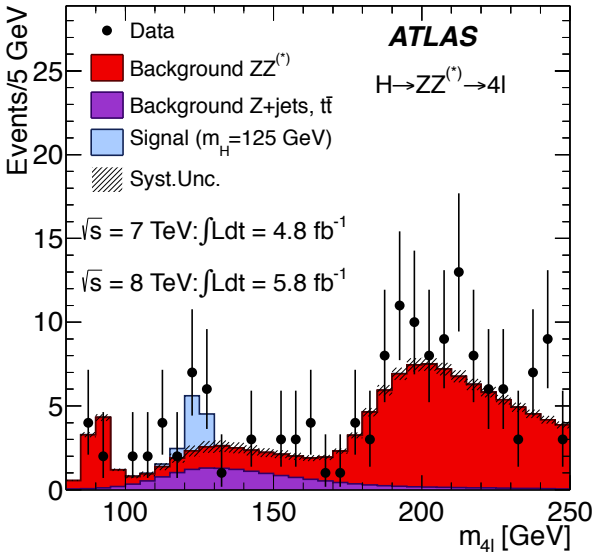

Figure 3: The distribution of four-lepton invariant mass using data taken in 2011 and 2012. The plot is referred from [9].

reactions coming from strong interactions.

One of the most important measurements related to the Higgs boson is Lorentz structures between the Higgs boson and the SM particles, especially vector bosons such as γ, Z and W bosons, which are critical particles to understand the spontaneous symmetry breaking and the mechanism giving rise masses to the matter and gauge particles. If there exists new physics in higher energy scales, it is expected that these effects appear in the couplings between the Higgs boson and the vector bosons: because of the uncertainty principle it might be possible that heavier particles temporary exist in the couplings between the Higgs boson and vector bosons, or new particles might take states mixing with the Higgs boson. These effects must definitely vary the couplings from the SM expectations as reflections from the BSM.

The ATLAS and CMS groups have reported that the measurement precision of these structures are possible to attain in 5–10 % level after including data-accumulation of high luminosity operation [13]. However, it is clear that 5–10 % sensitivities are not sufficient to verify BSM models and determine a correct direction. In contrast, the ILC will be possible to achieve the precision in a few % level.

This thesis is organized as follows.

- Chapter 2
  This chapter gives introduction of the Standard Model which is constructed from the $SU(2)_L \otimes U(1)_Y$ gauge theory and the Higgs mechanism. In addition, κ-framework, which is generally used by ATLAS and CMS groups to verify deviations of the Higgs couplings to the other SM particles from the SM expectations, is explained although it can not introduce any new Lorentz structures, which, in fact, does not satisfy model-independence of estimation. In the end of the section, effective Lagrangian defined based on the Effective Field Theory is described, where new Lorentz structures are possible to introduce as anomalous couplings (anomalies) which can describe new kinematics and interactions.

- Chapter 3
  This chapter gives rough descriptions of the ILC and performance of ILD that is one of the detector concepts for the ILC.

- Chapter 4
  This chapter shows main observables which are useful to verify the anomalous VVH cou-

plings. The illustration of the observables with different anomalous couplings is given for all Higgs production processes and one decay process $H \to W^+W^-$. A strategy for testing the anomalous couplings and evaluating the sensitivities to the new Lorentz structures is also discussed.

- Chapter 5
  General analysis tools which are necessary to study ILC related physics topics are given in this chapter. Analysis shown in this thesis is also based on these tools.

- Chapter 6 and 7
  These chapters show the analysis for evaluating the sensitivities to the anomalous couplings of ZZH (Chapter 6) and WWH (Chapter 7). Because the general analysis strategy is relatively similar for every channel, a few processes at center-of-mass energy of $\sqrt{s} = 250$ GeV are picked up as an example for illustrating the analysis for both anomalous ZZH and WWH couplings. Results of the sensitivities to both of the anomalous ZZH and WWH couplings will be shown assuming both of benchmark and ILC-full operation conditions.

- Chapter 8 and 9
  These chapters give discussions on the results and conclusion on the analysis of the anomalous VVH couplings. In addition, one prospect toward improvement of the sensitivities to the VVH couplings will be shortly illustrated.

- Appendix A and B
  In these section the remaining analysis for ZZH and WWH are shown, which are not discussed in the chapter 6 and 7 but used to evaluate the sensitivities to anomalous couplings.

2 A theoretical framework

A theoretical framework is always necessary to give predictions, describe behaviors, and explain mechanisms and observations. Corrections of the framework are also sometimes necessary for more accurate descriptions of subjects. The SM had been also established in such a way. And now The SM might need to be modified in this way.

2.1 The gauge symmetry and invariance

Following descriptions of theoretical frameworks are referred to several textbooks of elementary particle physics [14, 15] and thesises whose subjects relate to the LEP experiment [16–18].

2.1.1 $U(1)$ gauge symmetry and quantum electrodynamics

Any physical laws must be described as an invariant form for any transformations. In the particle physics, the Poincare invariance completely prescribes symmetry of a field of an elementary particle: translational invariance of spacetime of the field (translational symmetry) and Lorentz invariance of spacetime, which satisfies symmetry of changing of orientation (Rotation) and velocity (Boost). When requiring these invariances of a certain field under a local transformation, for instance, assuming a Dirac field which describes a fermion ψ, interactions between a gauge boson is naturally introduced. The phase transformation given in locally is described as

$$\psi(x) \to \psi'(x) = e^{-iQ\chi(x)}\psi(x),$$

where $\chi(x)$ gives a coordinate in the spacetime, and Q denotes charge of U(1) symmetry. When considering the Dirac Lagrangian with a free fermion including mass m_f, the Lagrangian to which the local transformation is applied is given as

$$\begin{aligned} \mathcal{L} = \bar{\psi}(i\gamma^\mu\partial_\mu - m_f)\psi \quad &\to \quad \bar{\psi}'(i\gamma^\mu\partial_\mu - m_f)\psi' \\ &= \quad \bar{\psi}(i\gamma^\mu\partial_\mu + Q\partial_\mu\chi(x) - m_f)\psi \neq \mathcal{L} \end{aligned}$$

where the Lagrangian is not already invariant. To make the Lagrangian retain the invariance, a covariant derivative is introduced and replaced with the partial derivative ∂_μ, which is defined as

$$\partial_\mu \to D_\mu \equiv \partial_\mu + iQA_\mu(x),$$

where $A_\mu(x)$ is a new field for making the Lagrangian invariant. The field $A_\mu(x)$ also transforms simultaneously under the local transformation as

$$A_\mu(x) \to A'_\mu(x) = A_\mu(x) + \partial_\mu\chi(x).$$

The given new Lagrangian, which is

$$\mathcal{L} = \bar{\psi}(i\gamma^\mu D_\mu - m_f)\psi,$$

can keep the invariance under the local transformation. A notable thing is that the requirement of the local gauge invariance required the introduction of a vector particle, which is the γ described with the field $A_\mu(x)$, and its form of the interactions is automatically given. When adding a kinematic term of the γ to the above Lagrangian, the Lagrangian which can describe quantum electrodynamics is established:

$$\mathcal{L}_{QED} = \bar{\psi}(i\gamma^\mu\partial_\mu - m_f)\psi - QA^\mu\bar{\psi}\gamma_\mu\psi - \frac{1}{4}F^{\mu\nu}F_{\mu\nu}$$

where $F^{\mu\nu}$ represents a field strength tensor defined as $F^{\mu\nu} = \partial^\mu A^\nu - \partial^\nu A^\mu$. Naively thinking, it might seem that the field A_μ can take mass as a coefficient of a quadratic term of the field like $m_A^2 A_\mu A^\mu$. However, it can not retain the invariance under the local transformation: $m_A^2 A_\mu A^\mu \to$

$m_A^2(A_\mu(x)+\partial_\mu\chi(x))(A^\mu(x)+\partial^\mu\chi(x)) \neq m_A^2 A_\mu A^\mu$. Therefore, the mass of the A_μ must be 0 here. This is consistent with the γ.

2.1.2 $SU(2)$ gauge symmetry and weak interaction

Again, let's assume that the Dirac Lagrangian and Dirac spinor Ψ are give. Because we consider internal space symmetry of a fermion, the Dirac spinor is also considered as a doublet being composed of two-component of Dirac fields ν_e and e, which is suitable to handle behaviors of a pair of fermions. An arbitrary 2×2 matrix of $SU(2)$ is given with three real parameters $\vec{\alpha}$ and the Pauli matrices $\boldsymbol{\tau}$, which give a basis of the 2×2 matrix when adding an identity matrix in addition:

$$\vec{\alpha}\cdot\boldsymbol{\tau} \;=\; \alpha_1\begin{pmatrix}0 & 1\\ 1 & 0\end{pmatrix} + \;\alpha_2\begin{pmatrix}0 & -i\\ i & 0\end{pmatrix} + \;\alpha_3\begin{pmatrix}1 & 0\\ 0 & -1\end{pmatrix}$$

In the same manner as the $U(1)$ local gauge transformation, $SU(2)$ transformation is applied to the Dirac field Ψ as

$$\Psi \rightarrow \Psi' = e^{-i\vec{\alpha}(x)\cdot\boldsymbol{\tau}}\Psi,$$

where α is assumed to have spacetime dependence. The invariance of the Dirac Lagrangian for a massless fermion is

$$\begin{aligned}\mathcal{L} = \bar{\Psi}(i\gamma^\mu\partial_\mu)\Psi \;\rightarrow\; \bar{\Psi}'(i\gamma^\mu\partial_\mu)\Psi' \;&\simeq\; (1+i\vec{\alpha}(x)\cdot\boldsymbol{\tau})\;\bar{\Psi}(i\gamma^\mu\partial_\mu)\;(1-\vec{\alpha}(x)\cdot\boldsymbol{\tau})\;\Psi\\ &=\; \bar{\Psi}(i\gamma^\mu\partial_\mu+\gamma^\mu\partial_\mu\vec{\alpha}(x)\cdot\boldsymbol{\tau})\Psi\\ &\neq\; \mathcal{L},\end{aligned}$$

To retain the $SU(2)$ gauge invariance for above Lagrangian, vector fields $\boldsymbol{W}_\mu$, which is defined as $\boldsymbol{W}_\mu(x) \equiv \vec{W}_\mu(x)\cdot\boldsymbol{\tau}$, must be introduced into the Lagrangian. The vector fields, here, are corresponding to the derivatives of the phases induced by the three generators $\boldsymbol{\tau}$ of the $SU(2)$ transformation. In addition, ∂_μ is also replaced with the covariant derivative, which is given as

$$\partial_\mu \rightarrow D_\mu \equiv \partial_\mu + \frac{ig_2}{2}\boldsymbol{W}_\mu(x),$$

where a coupling parameter g_2 of the $SU(2)$ is introduced, and three kinds of the fields $\boldsymbol{W}(x)$ are also given for the generators $\boldsymbol{\tau}$. The gauge transformation of the vector fields $\boldsymbol{W}_\mu(x)$ under the $SU(2)$ local transformation must be also defined, which would be

$$\boldsymbol{W}_\mu(x) \rightarrow \boldsymbol{W}'_\mu(x) = \boldsymbol{U}(x)\boldsymbol{W}(x)\boldsymbol{U}^\dagger(x) + \frac{2i}{g_2}\left(\partial_\mu\boldsymbol{U}(x)\right)\boldsymbol{U}^\dagger(x),$$

where $\boldsymbol{U}(x)$ denotes the $SU(2)$ transformation,

which is given as $\boldsymbol{U}(x) = e^{-i\vec{\alpha}(x)\cdot\boldsymbol{\tau}}$

The Lagrangian being invariant for the $SU(2)$ transformation can be given as

$$\mathcal{L}_{SU(2)} = \bar{\Psi}(i\gamma^\mu\partial_\mu)\Psi - ig_2\boldsymbol{W}_\mu(x)\bar{\Psi}\gamma^\mu\Psi.$$

2.2 The Standard Model and the Higgs mechanism

2.2.1 The Standard Model based on the $SU(2)\times U(1)$ gauge theory

The Standard Model is a non-Abelian theory based on the $SU(2)\times U(1)$ gauge transformation where the electromagnetic interaction and the weak interaction are represented as different components of one gauge theory. Based on the fact that a left-handed particle (or a right-handed

anti-particle) can contribute reactions in the weak interaction which can vary a charge, also the fact that there exists only left-handed neutrino and no right-handed neutrino, the left-handed fermions and the right-handed fermions are grouped in different weak isospin multiplets: respectively in doublets $\boldsymbol{L}$ and singlets e_R (three generations). The transformation of both doublets and singlets under the both $U(2)$ and $U(1)$ transformation are given as

$$
\begin{aligned}
U(1) \quad & \begin{cases} \boldsymbol{L} \ \to \boldsymbol{L}' = e^{-\frac{i}{2}\beta(x)Y}\boldsymbol{L} \\ e_R \to e'_R = e^{-\frac{i}{2}\beta(x)Y} e_R \end{cases}, \\
SU(2) \quad & \begin{cases} \boldsymbol{L} \ \to \boldsymbol{L}' = e^{-\frac{i}{2}\vec{\alpha}(x)\cdot\boldsymbol{\tau}}\boldsymbol{L} \\ e_R \to e'_R = e_R \end{cases}, \\
SU(2)\times U(1) \quad & \begin{cases} \boldsymbol{L} \ \to \boldsymbol{L}' = (1 - \frac{i}{2}\beta(x)Y - \frac{i}{2}\vec{\alpha}(x)\cdot\boldsymbol{\tau})\boldsymbol{L} \\ e_R \to e'_R = (1 - \frac{i}{2}\beta(x)Y) e_R \end{cases},
\end{aligned}
$$

where Y denotes weak hyper charge which is a generator of $U(1)$, and $\frac{\boldsymbol{\tau}}{2}$ are 2-dimensional representations of generators $\vec{I}$ of $SU(2)$. The weak hyper charge and the weak isospin being a third component of $SU(2)$ generator are related to electromagnetic charge Q as follows

$$
Q = I^3 + \frac{Y}{2}.
$$

In response to the $SU(2) \times U(1)$ transformation, let's introduce two gauge fields B_μ and $\boldsymbol{W}_\mu$, where the covariant derivatives for both doublets and singlets are respectively given as

$$
\begin{aligned}
\boldsymbol{L}: \quad \partial_\mu \ &\to \ D_\mu = \partial_\mu + \frac{ig_1}{2}B_\mu Y + \frac{ig_2}{2}\boldsymbol{W}_\mu \\
e_R: \quad \partial_\mu \ &\to \ D_\mu = \partial_\mu + \frac{ig_1}{2}B_\mu Y
\end{aligned}
$$

The given gauge fields are also transformed correspondingly as with the previous section, where the $U(1)$ local transformation is also described with the matrix. Therefore,

$$
\begin{aligned}
B_\mu(x) \ &\to \ B'_\mu(x) = B_\mu(x) + \frac{1}{g_1}\partial_\mu\beta(x) \\
\boldsymbol{W}_\mu(x) \ &\to \ \boldsymbol{W}'_\mu(x) = \boldsymbol{U}(x)\boldsymbol{W}(x)\boldsymbol{U}^\dagger(x) + \frac{2i}{g_2}\left(\partial_\mu \boldsymbol{U}(x)\right)\boldsymbol{U}^\dagger(x)
\end{aligned}
$$

where $\boldsymbol{U}(x) = e^{-i\vec{\alpha}(x)\cdot\boldsymbol{\tau}}$. Adding the kinematic terms of the B_μ and $\boldsymbol{W}_\mu$ and self-interaction between the $\boldsymbol{W}_\mu$ fields in addition, the $SU(2) \times U(1)$ gauge invariant Lagrangian, which can describe the Dirac fields for left- and right-handed massless fermions and their interactions with the gauge fields, is given as

$$
\begin{aligned}
\mathcal{L}_{SU(2)\times U(1)} \ = \ & \boldsymbol{L}^\dagger i\gamma^\mu\left(\partial_\mu + \frac{ig_1}{2}B_\mu Y + \frac{ig_2}{2}\boldsymbol{W}_\mu\right)\boldsymbol{L} + e_R^\dagger i\gamma^\mu\left(\partial_\mu + \frac{ig_1}{2}B_\mu Y\right)e_R \\
& -\frac{1}{4}B_{\mu\nu}B^{\mu\nu} - \sum_i^3 \frac{1}{4}W^i_{\mu\nu}W^{i\mu\nu},
\end{aligned}
$$

where field strength tensors for $W_{\mu\nu}$ are defined as

$$
W_{\mu\nu} = \partial_\mu W_{\nu i} - \partial_\nu W_{\mu i} - \sum_{jk}\epsilon_{ijk}W_{\mu j}W_{\nu k}
$$

The second term of above field strength tensor gives self-interaction between the $\boldsymbol{W}$ fields, which originate from a feature of $SU(2)$ group that the generators do not commute each other. The $W^\pm$

bosons are defined by the two fields: $W^{\pm}_{\mu} \equiv \frac{1}{\sqrt{2}}(W^1_{\mu} \mp iW^2_{\mu})$. In the next section the two gauge fields B_μ and W^3_μ are mixed after the spontaneous symmetry breaking, and fields of the γ and the Z bosons, respectively A_μ and Z_μ, are defined as linear combinations with an mixing angle:

$$A_\mu = B_\mu \cos\theta_W + W^3_\mu \sin\theta_W \quad (1)$$

$$Z_\mu = -B_\mu \sin\theta_W + W^3_\mu \cos\theta_W \quad (2)$$

where an angle θ_W is known as the weak mixing angle (Weinberg angle), which is depending on the both couplings g_1 and g_2 as

$$\sin\theta_W = \frac{g_1}{\sqrt{g_1^2 + g_2^2}} \text{ , and } \cos\theta_W = \frac{g_2}{\sqrt{g_1^2 + g_2^2}} \text{ .} \quad (3)$$

As shown in the previous subsection, the introduction of mass terms by hands breaks the $SU(2) \times U(1)$ gauge invariance of the given Lagrangian. Therefore, the mass for each boson must be introduced naturally without breaking the gauge symmetry, which is possible by introducing the Higgs mechanism.

2.2.2 The Higgs mechanism

In the Standard Model the gauge invariance under the local transformation strictly forbid the vector bosons to have the masse terms, and it does not match the reality. However, the Higgs mechanism can naturally give the masse terms for the vector bosons, the $W^{\pm}$ and the Z bosons, through the spontaneous symmetry breaking without violating the $SU(2) \times U(1)$ gauge invariance under the local transformation.

Let's start from a one doublet Φ which is composed of two complex scalar fields ϕ_1 and ϕ_2, and simple potential $V(\Phi^\dagger\Phi)$ like

$$\Phi = \begin{pmatrix} \phi_1 \\ \phi_2 \end{pmatrix}, \text{ and } V(\Phi^\dagger\Phi) = \mu^2(\Phi^\dagger\Phi) + \lambda(\Phi^\dagger\Phi)^2$$

where μ^2 and λ are arbitrary parameters. The potential has symmetry around (0, 0) in the Re(Φ)–Im(Φ) plane. When taking a condition of $\mu^2 > 0$, a shape of the potential becomes parabolic and its minimum is always in (0, 0). However, taking the condition of $\mu^2 < 0$ and $\lambda > 0$, the symmetry spontaneously breaks and a minimum point appear at $|\Phi|^2 = -\mu^2/2\lambda = v^2/2$ in which the ground state (vacuum state) is shifted from 0 and denoted with v.

In order to consider behaviors of the ground state (vacuum expectation value: v), let's assume that it is excited from the ground state, gets small perturbations and Φ is expanded around there (ϕ should have two components in a real-imaginary plane). The complex field Φ could be rewritten using scalar fields as

$$\begin{aligned} \Phi &= e^{-i\vec{\theta}(x)\cdot\boldsymbol{\tau}} \frac{1}{\sqrt{2}} \begin{pmatrix} 0 \\ v + h(x) \end{pmatrix} \simeq \frac{1}{\sqrt{2}} \begin{pmatrix} 1 + i\theta_3 & i(\theta_1 - i\theta_2) \\ i(\theta_1 - i\theta_2) & 1 - i\theta_3 \end{pmatrix} \begin{pmatrix} 0 \\ v + h(x) \end{pmatrix} \\ &\simeq \frac{1}{\sqrt{2}} \begin{pmatrix} v\theta_2(x) + iv\theta_1(x) \\ v + h(x) - iv\theta_3(x) \end{pmatrix} \\ V(\Phi^\dagger\Phi) &= \lambda v^2 h^2(x) + \lambda v h^3(x) + \frac{1}{4}\lambda h^4(x) - \frac{1}{4}\lambda v^4. \end{aligned}$$

Here, θs are set to be 0 by selecting a condition that Φ' becomes real number after the $SU(2)$ gauge transformation (unitary gage). The quadratic term of $h^2(x)$ is describing mass of the field $h(x)$ like $m_h = v\sqrt{\lambda}$, and the other terms are giving self-interactions between the fields.

2.2.3 Generating masses for vector bosons

When assuming that the complex scalar fields ϕ_1 and ϕ_2 constitute a $SU(2)$ doublet, it must receive the $SU(2) \times U(1)$ gauge transformation which is similar with that of the doublet $\boldsymbol{L}$ composed of the left-handed fermions, where the derivative ∂_μ must be also replaced by the covariant derivative of D_μ, and recalling the Lagrangian of the scalar field, it would be

$$\begin{aligned} D^\mu\Phi &= \frac{1}{\sqrt{2}}\begin{pmatrix} 0 \\ \partial^\mu h(x) \end{pmatrix} + \frac{ig_1}{2\sqrt{2}}\begin{pmatrix} 0 \\ B^\mu(x)(v+h(x)) \end{pmatrix} + \frac{ig_2}{2\sqrt{2}}\begin{pmatrix} W^{1\mu} - iW^{2\mu}(v+h(x)) \\ -W^{3\mu} \quad (v+h(x)) \end{pmatrix} \\ \mathcal{L}_\Phi &= (D_\mu\Phi)^\dagger(D^\mu\Phi) - V(\Phi^\dagger\Phi) \\ &= \frac{1}{2}\partial_\mu h(x)\partial^\mu h(x) - V(h(x)) \\ &\quad + \frac{g_2^2}{4}W_\mu^- W^{+\mu}(v+h(x))^2 + \frac{1}{2}\left(\frac{1}{2}\right)^2 (g_1 B_\mu - g_2 W^{3\mu})^2 (v+h(x))^2 \end{aligned}$$

Replacing the vector filds B_μ and W_μ with the mixing vector fields A_μ and Z_μ, the Lagrangian $\mathcal{L}_\Phi$ would be

$$\begin{aligned} \mathcal{L}_\Phi = &\frac{1}{2}\partial_\mu h(x)\partial^\mu h(x) - V(h(x)) \\ &+ \frac{g_2^2}{4}W_\mu^- W^{+\mu}(v+h(x))^2 + \frac{1}{2}\frac{(g_1^2+g_2^2)}{4}Z_\mu Z^\mu (v+h(x))^2. \end{aligned} \tag{4}$$

The masses of the vector bosons are described as coefficients of the quadratic terms of the fields. Thus, the masses are given like

$$\begin{aligned} \frac{g_2^2}{4}v^2 W_\mu^- W^{+\mu} &: M_W = v\frac{g_2}{2} \\ \frac{(g_1^2+g_2^2)}{4}v^2 Z_\mu Z^\mu &: M_Z = v\frac{\sqrt{g_1^2+g_2^2}}{2} \end{aligned}$$

Since a term of $A_\mu A^\mu$ does not appear, mass of the field A retains $m_\gamma = 0$.

2.2.4 Generating masses for fermions

The fermion masses are given by making the Higgs field interact with the fermion fields (left- and right-). The Lagrangian giving the masses to fermions is written, using the lepton $\boldsymbol{L}$ and the scalar Φ doublet, as

$$\mathcal{L}_{Yukawa} = -g_l\left[(\boldsymbol{L}^\dagger\Phi)e_R + e_R^\dagger(\Phi^\dagger\boldsymbol{L})\right] ,$$

Applying the spontaneous symmetry breaking, it could be

$$\mathcal{L}_{Yukawa} = -\frac{vg_l}{\sqrt{2}}(e_L^\dagger e_R + e_R^\dagger e_L) - \frac{g_l}{\sqrt{2}}(e_L^\dagger e_R + e_R^\dagger e_L)h(x)$$

The masses of the leptons are given as $m_l = vg_l$ whereas the mass terms for the neutrinos do not appear in the description of the Lagrangian. The masses for quarks are also given in the same

way.

Before the symmetry breaking the Lagrangian is given as :

$$\begin{aligned}\mathcal{L}^{SM} = \boldsymbol{L}^\dagger i\gamma^\mu D_\mu \boldsymbol{L} + e_R^\dagger i\gamma^\mu D_\mu e_R - \frac{1}{4}B_{\mu\nu}B^{\mu\nu} - \sum_i^3 \frac{1}{4}W^i_{\mu\nu}W^{i\mu\nu} \\ + (D_\mu\Phi)^\dagger(D^\mu\Phi) - V(\Phi^\dagger\Phi) - g_l\left[(\boldsymbol{L}^\dagger\Phi)e_R + e_R^\dagger(\Phi^\dagger\boldsymbol{L})\right],\end{aligned} \tag{5}$$

After the symmetry breaking the Lagrangian would be described as :

$$\begin{aligned}
\mathcal{L}^{SM}_{EWSB} &= e_L^\dagger i\gamma^\mu\partial_\mu e_L + \nu_L^\dagger i\gamma^\mu\partial_\mu\nu_L + e_R^\dagger i\gamma^\mu\partial_\mu e_R && \text{the kinetic terms for fermions}\\
&+ e_L^\dagger\gamma^\mu e A_\mu e_L + e_R^\dagger\gamma^\mu e A_\mu e_R && \text{the interaction with the } A \text{ field}\\
&- \frac{1}{2}\frac{g_2}{\cos\theta_w}\left(\nu_L^\dagger\gamma^\mu Z_\mu\nu_L - e_L^\dagger\gamma^\mu\cos 2\theta_w Z_\mu e_L\right) && \text{the interaction with the } Z \text{ field}\\
&- \frac{g_2}{\cos\theta_w}e_R^\dagger\gamma^\mu\sin^2\theta_w Z_\mu e_R && \text{the interaction with the } Z \text{ field}\\
&- \frac{g_2}{\sqrt{2}}(\nu_L^\dagger\gamma^\mu W_\mu^+ e_L + e_L^\dagger\gamma^\mu W_\mu^-\nu_L) && \text{the interactions with the } W \text{ field}\\
&- \frac{v g_l}{\sqrt{2}}(e_L^\dagger e_R + e_R^\dagger e_L) - \frac{g_l}{\sqrt{2}}(e_L^\dagger e_R + e_R^\dagger e_L)h(x) && \text{the fermion mass and Yukawa couplings}\\
&- \frac{1}{4}B_{\mu\nu}B^{\mu\nu} - \frac{1}{4}W^3_{\mu\nu}W^{3\,\mu\nu} - \frac{1}{2}W^-_{\mu\nu}W^{+\,\mu\nu} && \text{the interaction between the vector fields}\\
&+ \frac{1}{2}\partial_\mu h(x)\partial^\mu h(x) - V(h(x)) && \text{the Higgs kinetic term and its potential}\\
&+ \frac{1}{2}\frac{(g_1^2+g_2^2)}{4}Z_\mu Z^\mu(v+h(x))^2 && \text{the } Z \text{ mass and the interactions with the Higgs field}\\
&+ \frac{g_2^2}{4}W_\mu^- W^{+\mu}(v+h(x))^2 && \text{the } W \text{ mass and the interactions with the Higgs field}
\end{aligned}$$

where values of -1 and -2 are respectively substituted in the hyper charge Y of left- and right-handed fermions, and $g_1\cos\theta_w$ is given as e (elementary charge) assuming the coupling between an electron and a photon.

2.3 Measurements of Higgs boson and beyond the Standard Model

The SM had completely established as an effective theory which can describe a low energy region being less than $O(100)$ GeV. There exist, however, several phenomena that can not be explained with the framework of the SM: masses of neutrinos, dark matter and so on. Therefore, theories for describing such phenomena are clearly required. One of the possible ways to establish such theories is to explore precisely and elucidate the Higgs sector, which includes the mechanism of the mass generation, $\mathcal{L}_{\Phi}$, $\mathcal{L}_{Yukawa}$, and new Lorentz structures induced by higher order field operators composed of the Higgs boson and the SM particles, at least with the lowest dimension-6 operators[1] $\mathcal{L}_{eff}(1/\Lambda^2)$.

The Higgs sector is still unknown and any deviations from the SM expectations will connect to physics beyond the SM. Especially, the coupling strengths between the Higgs boson and the other SM particles, which is proportional to the masses of the particles coupled with the Higgs boson, and also the Higgs potential which is really unique for the SM. Thus, verification of both two things is extremely critical for the exploration of the BSM physics. Furthermore, it is known that a pattern in deviations from the SM expectations for the familiar particles is possible to give us suggestions how the Higgs sector should be extended: a SUSY model, a composite model, and other models [20]. It is also predicted that those deviations are small [21, 22]. Therefore, precise measurements for the Higgs properties are necessary .

Modifications of the Higgs boson couplings due to expansions :

One of the simplest SUSY extended models is called the minimal supersymmetric standard model (MSSM) that is like one of the general expansion of the Higgs sector of the SM by introducing two Higgs doublets. This general expansion is called the type-II two Higgs doublet model where five different Higgs bosons are appeared. In the case that one of the Higgs boson mass, CP-odd Higgs with the mass M_A, is heavy, a feature called decoupling limit [23] appears where the heavier Higgs bosons become almost degenerate in mass $\sim M_A$ and the lightest CP-even Higgs boson, h_0, has very identical properties with the Higgs boson, h_{SM}, in the SM. Therefore, to distinguish h_{SM} from h_0 seems a formidable challenge. Fortunately, it also has been understood that radiative corrections derived from two angles of the supersymmetric structure, the eigenstate mixing angle α and the vacuum mixing angle β can modify and will enhance the SM expectations. Several theoretical studies have been performed on the general expectation of the variation of the Higgs couplings to the SM particles with decoupling limit [22, 24]. According to the studies, the Higgs couplings will respectively change for the vector bosons, up-type, and down-type fermions with the moderate parameter choice like

$$\begin{aligned}
\frac{g_{hVV}}{g_{hVV}^{SM}} &\sim 1 - 0.3\ \% \left(\frac{200\ \text{GeV}}{M_A}\right)^4 \\
\frac{g_{htt}}{g_{htt}^{SM}} &\sim 1 - 1.7\ \% \left(\frac{200\ \text{GeV}}{M_A}\right)^2 \\
\frac{g_{hbb}}{g_{hbb}^{SM}} = \frac{g_{h\tau\tau}}{g_{h\tau\tau}^{SM}} &\sim 1 + 1.7\ \% \left(\frac{1\ \text{TeV}}{M_A}\right)^2
\end{aligned}$$

It is understood that the Higgs couplings to the vector bosons and up-type are quickly reach their SM values, and the couplings to the down-type will be luckily observed. In fact other theoretical models are also predicting possible deviations of the Higgs coupling from the SM expectations,

[1] In the real lowest order dimension-5 operator $(1/\Lambda)\mathcal{O}^{(5)}$, there exists only one combination: $\mathcal{O}^{(5)} = (\boldsymbol{L}^{\mathrm{T}} C\epsilon\Phi)(\Phi^{\mathrm{T}}\epsilon\boldsymbol{L})$, where $\boldsymbol{L}$, Φ are the lepton and scalar doublets, C is a charge conjugation operator, and ϵ is a 2-dimension Levi-civita matrix. This operator is famous as Weinberg operator [19], which generates Majonara neutrino mass and violates lepton number conservation. This does not relate to our interest in the thesis, so it is ignored

which are given under the composite Higgs models in [22] for the vector bosons and fermions.

$$\begin{aligned}
\frac{g_{hVV}}{g_{hVV}^{SM}} &\sim 1-3\ \% \left(\frac{1\ \text{TeV}}{f}\right)^2 \\
\frac{g_{hff}}{g_{hff}^{SM}} &\sim 1-3\ \% \left(\frac{1\ \text{TeV}}{f}\right)^2 \quad \text{refer to [25]} \\
\frac{g_{hff}}{g_{hff}^{SM}} &\sim 1-9\ \% \left(\frac{1\ \text{TeV}}{f}\right)^2 \quad \text{refer to [26]}
\end{aligned}$$

where f is the compositeness scale and takes typically a few TeV. In any case it is obvious that 1 % precision for each Higgs coupling to the SM particles is definitely necessary to distinguish between h_{SM} and h_0 or the extended models.

2.3.1 The κ-framework

In the early stage when the LHC had not been constructed yet, researchers had established an interim framework to verify the deviations of the properties of the Higgs boson from the SM expectations, which is so-called κ-framework introduced in references [27, 28]. The Higgs couplings in the framework are described with the SM expectations and scaling factors κ, which are generally defined using the same scaling factor for both Higgs production and Higgs decay which are originating from the same particle A as

$$\kappa_{AA} \equiv \frac{\sigma_{AA}}{\sigma_{AA}^{SM}}, \quad \text{and} \quad \kappa_{AA} \equiv \frac{\Gamma_{AA}}{\Gamma_{AA}^{SM}}.$$

In the early studies under the LHC environment [29] and recent many studies using real data, the κ-framework is often used to verify the Higgs couplings. However, an application of the κ-framework actually brings problems which relate to, for instance, model-independence of estimation of the Higgs couplings as referred in page-4 of a reference [27]:

"Only modifications of couplings strengths, i.e. of absolute values of couplings, are taken into account, while the tensor structure of the couplings is assumed to be the same as in the SM prediction". This point will be discussed in the latter part of this section.

A measurable observable for certain signal process related to the Higgs boson is $\sigma \times \text{BR}$, where σ is production cross-section and BR denotes a branching ratio of the Higgs boson. Under the narrow-width approximation[2], this observable can be decomposed as

$$\sigma_{ii\to h} \times \text{BR}_{h\to jj} = |\mathcal{M}(ii \to h)|^2 \frac{\Gamma_{h\to jj}}{\Gamma_h} \simeq \frac{g_{ii} \cdot g_{jj}}{\Gamma_h}$$

where a process is assumed to be $ii \to h \to ff$. σ_{ii} denotes the production cross-section, and Γ_{jj} and Γ_h are respectively the partial decay width into jj and the total decay width of the Higgs boson. In the application of the κ-framework all couplings are assumed to be expected values of the SM, in which higher order QCD and EW corrections are possible to include in the parameter evaluation. The possible deviations of the couplings from the SM are pushed on the scaling factor

[2] In the limit of $\Gamma/M \to 0$, we can approximate the Breit-Wigner distribution by a delta function, for instance [30].

$$\lim_{\Gamma\to 0} \frac{1}{(s-M_h^2)^2 + M_h^2\Gamma_h^2} \simeq \frac{\pi}{M_h\Gamma_h}\delta(s-M_h^2)$$

In the case of the SM Higgs boson Γ_h/M_h is very small. Thus, the observable is completely decomposed.

κ, which are given as,

$$\frac{g_{ii}\cdot g_{jj}}{\Gamma_h} \rightarrow \frac{g_{ii}\cdot g_{jj}}{\Gamma_h}\cdot\frac{\kappa_{ii}^2\cdot\kappa_{jj}^2}{\kappa_h^2},$$

where κ_{ii}^2, κ_{jj}^2, and κ_h^2 are defined as

$$\frac{\sigma_{ii\rightarrow h}}{\sigma_{ii\rightarrow h}^{SM}}=\kappa_{ii}^2,\quad \frac{\Gamma_{h\rightarrow jj}}{\Gamma_{h\rightarrow jj}^{SM}}=\kappa_{jj}^2,\quad \text{and}\quad \frac{\Gamma_h}{\Gamma_h^{SM}}=\kappa_h^2\quad .$$

Every definitions of the scaling parameters κ_i are given in [27, 28]. To determine the scaling parameters, global fitting is performed using all Higgs related data which are measurable in the LHC. Because the total width of the Higgs boson Γ_H can not be measured directly in the LHC environment, only ratios of the scale factors κ_i are measurable at the LHC. If the total width of the Higgs boson varies, this simultaneous variation by the common factor κ_h^2 propagate to the other κ_i factors and this feature can not be actually distinguished. Therefore, several assumptions are considered, which are also mentioned in [27,28]. Possible sensitivities to each κ_i parameter at the LHC and the ILC are given in Fig. 4. Ii is clear that the capability of the LHC towards the Higgs couplings does not reach to the required precision of less than 1 % level to test the BSM models. In contrast, it is clearly shown that the ILC has the sufficient capability for exploring the Higgs couplings. Fig. 5 gives examples of deviation patterns predicted by each theory and the precision of the Higgs couplings that the ILC can reach after full physics program including the 500 GeV operation.

Problems and internal inconsistency in the κ-framework :

The κ-framework has several problems which relate to the coupling measurements.

- The κ-framework does not consider the $SU(2)\times U(1)$ gauge symmetry although the symmetry breaking is imposed with the assumption of the $SU(2)\times U(1)$ gauge symmetry. Therefore, the scaling factors κ for vector bosons should have some relations, but it is completely independent in the κ-framework.
- Once staring to consider higher order radiative (loop) corrections, the κ-framework will brings serious inconsistencies for the coupling evaluations. All contributions due to the radiative corrections derived from the SM particles are regarded as one single κ factor although it is actually composed of several κ factors.
- Once assuming new (next leading order) tensor structures which describe new dynamics or kinematics and introducing them into the Lagrangian, the κ-framework misses internal consistency. Because the coupling strengths of certain production process ($ii\rightarrow h$) and a corresponding decay process ($h\rightarrow ii$) do not match each other in terms of the scaling due to the new structures (which have usually momentum dependence). Therefore, the same scaling factors κ as shown in Fig. 6 are not usable to describe both scaling.

Because of these reasons the application of the κ-framework is possible only for the leading order consideration and not actually suitable for precise evaluation and exploration of the new physics.

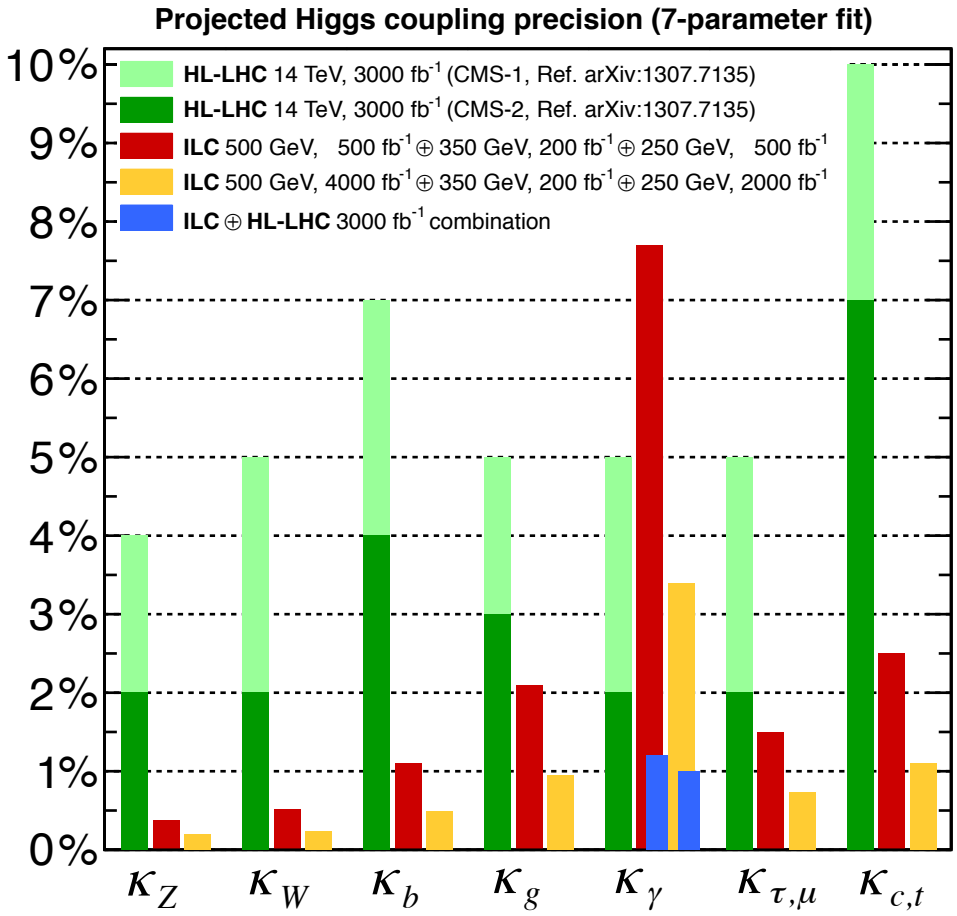

Figure 4: Expected relative precisions on the Higgs couplings between the SM particles under constrained 7-parameter fit assuming no BSM production or decay modes. The red and yellow bands show the expected errors from the initial phase and full operation of the ILC. The blue bands for κ_γ show the effect of combined analysis using high luminosity LHC and the ILC data. The plot is referred from [31].

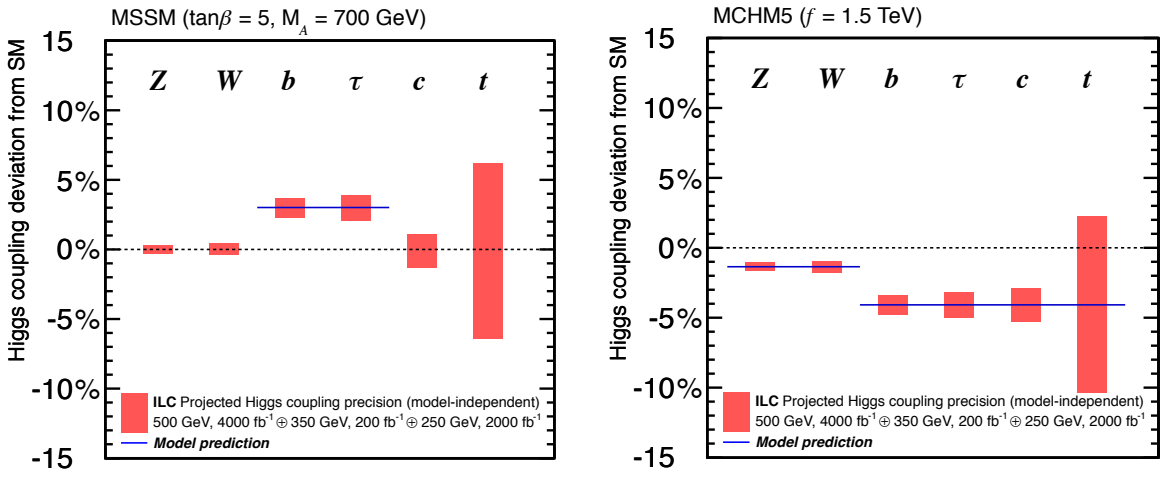

Figure 5: Examples show new physics effects in deviation patterns of the Higgs couplings. (Left) A supersymmetric model. (Right) A model with Higgs boson compositeness. The error bars indicate the uncertainties. The plots is referred from [20, 32].

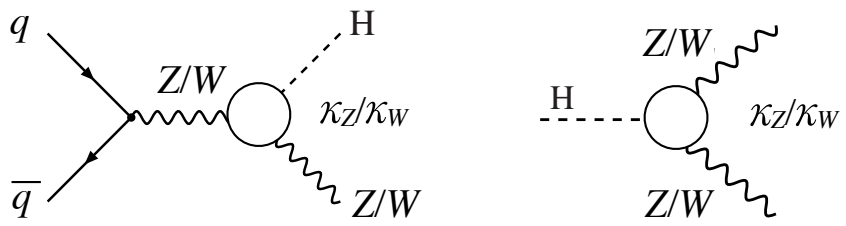

Figure 6: If new Lorentz structures are introduced, for instance $\mathcal{L}_{ZZh} = \frac{M_z^2}{v} Z_\mu Z^\mu h + \frac{b}{\Lambda} Z_{\mu\nu} Z^{\mu\nu} h$ where first one is the one of the SM and the second one is the new one, the same scaling factor κ_Z is not already proper. Because the new term is composed of the field strengths of the Z fields, it has momentum dependence. Thus, the effect varies between the production and the decay process depending on the momenta of the Z bosons, and the relation: $\kappa_Z \propto \sigma_{ZH} \propto \Gamma_{ZZ}$ does not hold any more.

2.3.2 The effective field theory

To describe the Effective Field Theory (EFT) here, several papers which are related to EFT studies are referred. The SM is the succeeded theory which explain low-energy behaviors of the elementary particles, However, when regarding it as an effective low-energy theory, other new interaction terms induced by higher dimension operators could appear in the Lagrangian, which is so-called an effective Lagrangian. A first study based on the effective Lagrangian in the EFT was given by Buchmuller and Wyler [33] where dimension-5 and dimension-6 operators are listed, which are constructed with combinations of scalar, vector, and fermion fields in the SM.

Fermi's theory on 4-point interaction :

Enrico Fermi in 1933 tried to describe the beta decay by introducing a 4-fermion interaction at a single point, which was a beginning of application of the effective field theory. At sufficiently higher energy in which a energy scale that the fermions relate to is the mass of the W boson, a propagator of the W boson $1/(M_W^2 - q^2)$ plays central roles in the interaction among the fermions. In contrast, the propagator is approximated as $1/M_W^2$ in the sufficiently low energy scale compared to the mass of the W boson ($E \ll M_W$), that means existence of a heavy particle induces renormalization of a coupling constant and new Lorentz structures which are suppressed by powers of the mass scale of the new heavy particle.

General requirements as a field theory :

An effective Lagrangian expanded from the SM-Lagrangian must satisfy several features as the effective field theory:

- The effective Lagrangian must satisfy the Lorentz invariance and the $SU(2) \times U(1)$ gauge symmetry under the local transformation as the SM-Lagrangian does.
- The Lagrangian has mass dimension of four. Thus, higher dimension operators appear with a coefficient of inverse power of new energy scale of Λ and the operators are suppressed when the energy scale is sufficiently large compared to possible experimental energies. Usually, the scale Λ is assumed to be around TeV to the Planck scale.
- The effective Lagrangian should recover the SM in the low-energy scale of $\mathcal{O}(100)$ GeV.

Construction of dimension-n operators :

The effective Lagrangian is given with a general description, which was originally introduced in [33]

as

$$\mathcal{L}_{eff} \;=\; \mathcal{L}^{(4)}_{SM} + \sum_i \frac{C^{(5)}_i}{\Lambda^1}\mathcal{O}^{(5)}_i + \sum_i \frac{C^{(6)}_i}{\Lambda^2}\mathcal{O}^{(6)}_i + \cdots .$$

where $\mathcal{L}^{(4)}_{SM}$ denotes the general Lagrangian of the SM. $\mathcal{O}^{(5)}_i$ and $\mathcal{O}^{(6)}_i$ show energy dimension-5 and -6 field operators and Λ is a coefficient for reducing the field operators to the mass dimension of four. $c^{(5)}_i$ and $c^{(6)}_i$ are dimensionless coupling constants, which are usually called Wilson coefficients, for each operator in each dimension. The Lagrangian must be hermitian. Thus, each linear term $\mathcal{O}_i$ must be composed of combination of the non-hermitian operator and the hermitian conjugate operator.

Dimension-5 field operators :

When considering the dimension-5 operators with fermion fields and scalar fields (and derivatives), and considering the fermion fields and the scalar fields are doublets, a possible operator which can satisfy the gauge invariance is only a combination of $\Phi, \Phi^\dagger, \Psi, \Psi^\dagger$. To retain $SU(2)$ invariant, it must not be $\Phi^\dagger\Phi$ and two Ψ must be doublets which is the left-handed $\boldsymbol{L}$. To make Lorentz scalar, a possible connection would be $(\boldsymbol{L}^{\mathrm{T}} C\epsilon\Phi)(\Phi^{\mathrm{T}}\epsilon\boldsymbol{L})$ only. After the symmetry breaking this structure gives mass of $\sim (v^2/\Lambda)\nu^\dagger_L\nu_L$ to neutrinos, which is known as the Majorana mass. Therefore, since this structure violates lepton number and generates the Majorana mass which would happen in the GUT scale of $\Lambda = 10^{23}$ GeV when assuming $m_\nu \sim 1$ eV, the dimension-5 operator is set to be out of interest.

X^3		φ^6 and $\varphi^4 D^2$		$\psi^2\varphi^3$	
Q_G	$f^{ABC}G^{A\nu}_\mu G^{B\rho}_\nu G^{C\mu}_\rho$	Q_φ	$(\varphi^\dagger\varphi)^3$	$Q_{e\varphi}$	$(\varphi^\dagger\varphi)(\bar{l}_p e_r\varphi)$
$Q_{\widetilde{G}}$	$f^{ABC}\widetilde{G}^{A\nu}_\mu G^{B\rho}_\nu G^{C\mu}_\rho$	$Q_{\varphi\Box}$	$(\varphi^\dagger\varphi)\Box(\varphi^\dagger\varphi)$	$Q_{u\varphi}$	$(\varphi^\dagger\varphi)(\bar{q}_p u_r\widetilde{\varphi})$
Q_W	$\varepsilon^{IJK}W^{I\nu}_\mu W^{J\rho}_\nu W^{K\mu}_\rho$	$Q_{\varphi D}$	$\left(\varphi^\dagger D^\mu\varphi\right)^\star\left(\varphi^\dagger D_\mu\varphi\right)$	$Q_{d\varphi}$	$(\varphi^\dagger\varphi)(\bar{q}_p d_r\varphi)$
$Q_{\widetilde{W}}$	$\varepsilon^{IJK}\widetilde{W}^{I\nu}_\mu W^{J\rho}_\nu W^{K\mu}_\rho$				
$X^2\varphi^2$		$\psi^2 X\varphi$		$\psi^2\varphi^2 D$	
$Q_{\varphi G}$	$\varphi^\dagger\varphi\, G^A_{\mu\nu}G^{A\mu\nu}$	Q_{eW}	$(\bar{l}_p\sigma^{\mu\nu}e_r)\tau^I\varphi W^I_{\mu\nu}$	$Q^{(1)}_{\varphi l}$	$(\varphi^\dagger i\overleftrightarrow{D}_\mu\varphi)(\bar{l}_p\gamma^\mu l_r)$
$Q_{\varphi\widetilde{G}}$	$\varphi^\dagger\varphi\,\widetilde{G}^A_{\mu\nu}G^{A\mu\nu}$	Q_{eB}	$(\bar{l}_p\sigma^{\mu\nu}e_r)\varphi B_{\mu\nu}$	$Q^{(3)}_{\varphi l}$	$(\varphi^\dagger i\overleftrightarrow{D}^I_\mu\varphi)(\bar{l}_p\tau^I\gamma^\mu l_r)$
$Q_{\varphi W}$	$\varphi^\dagger\varphi\, W^I_{\mu\nu}W^{I\mu\nu}$	Q_{uG}	$(\bar{q}_p\sigma^{\mu\nu}T^A u_r)\widetilde{\varphi}\, G^A_{\mu\nu}$	$Q_{\varphi e}$	$(\varphi^\dagger i\overleftrightarrow{D}_\mu\varphi)(\bar{e}_p\gamma^\mu e_r)$
$Q_{\varphi\widetilde{W}}$	$\varphi^\dagger\varphi\,\widetilde{W}^I_{\mu\nu}W^{I\mu\nu}$	Q_{uW}	$(\bar{q}_p\sigma^{\mu\nu}u_r)\tau^I\widetilde{\varphi}\, W^I_{\mu\nu}$	$Q^{(1)}_{\varphi q}$	$(\varphi^\dagger i\overleftrightarrow{D}_\mu\varphi)(\bar{q}_p\gamma^\mu q_r)$
$Q_{\varphi B}$	$\varphi^\dagger\varphi\, B_{\mu\nu}B^{\mu\nu}$	Q_{uB}	$(\bar{q}_p\sigma^{\mu\nu}u_r)\widetilde{\varphi}\, B_{\mu\nu}$	$Q^{(3)}_{\varphi q}$	$(\varphi^\dagger i\overleftrightarrow{D}^I_\mu\varphi)(\bar{q}_p\tau^I\gamma^\mu q_r)$
$Q_{\varphi\widetilde{B}}$	$\varphi^\dagger\varphi\,\widetilde{B}_{\mu\nu}B^{\mu\nu}$	Q_{dG}	$(\bar{q}_p\sigma^{\mu\nu}T^A d_r)\varphi\, G^A_{\mu\nu}$	$Q_{\varphi u}$	$(\varphi^\dagger i\overleftrightarrow{D}_\mu\varphi)(\bar{u}_p\gamma^\mu u_r)$
$Q_{\varphi WB}$	$\varphi^\dagger\tau^I\varphi\, W^I_{\mu\nu}B^{\mu\nu}$	Q_{dW}	$(\bar{q}_p\sigma^{\mu\nu}d_r)\tau^I\varphi\, W^I_{\mu\nu}$	$Q_{\varphi d}$	$(\varphi^\dagger i\overleftrightarrow{D}_\mu\varphi)(\bar{d}_p\gamma^\mu d_r)$
$Q_{\varphi\widetilde{W}B}$	$\varphi^\dagger\tau^I\varphi\,\widetilde{W}^I_{\mu\nu}B^{\mu\nu}$	Q_{dB}	$(\bar{q}_p\sigma^{\mu\nu}d_r)\varphi\, B_{\mu\nu}$	$Q_{\varphi ud}$	$i(\widetilde{\varphi}^\dagger D_\mu\varphi)(\bar{u}_p\gamma^\mu d_r)$

Figure 7: The table is referred from [34]. The dimension-6 field operators constructed with a scaler (Higgs) field, here φ, except 4-fermion combination.

Dimension-6 field operators :

It is possible to construct many dimension-6 field operators with imposition of the gauge invariance. A set of dimension-6 operators was firstly classified in 1986 [33]. After that, a complete non-redundant set of the field operators are written down based on specific basis in 2010 [34], which is called Warsaw basis and includes 59 different operators as shown in Fig. 7. In LHC EFT studies, Higgs Basis [34], which is proposed by the LHC Higgs group, has been used. All bases are generally equivalent, and selected based on convenience of applications.

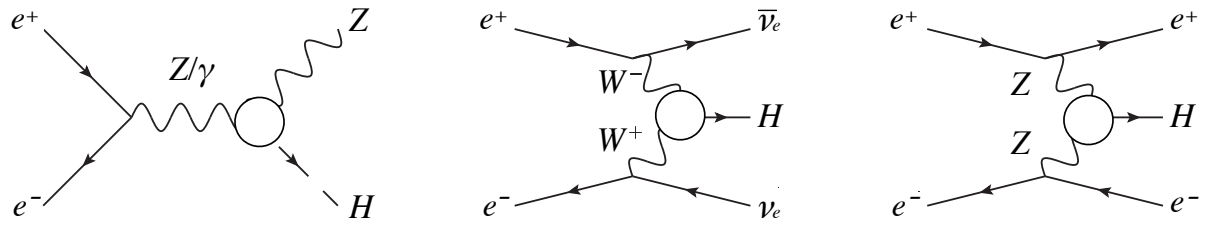

Figure 8: Diagrams of Higgs production processes in the ILC: (left) Higgs-strahlung, (middle) WW-fusion, and (right) ZZ-fusion.

Dimension-7 and 8 field operators :

Much higher dimension field operators are just sub-leading of the dimension-6 operators. Thus, it is possible to ignore them when considering current reachable energy we can provide. Furthermore, dimensions-7 or -odd operators are generally violating the $B-L$ symmetry (a difference between the Baryon number and the Lepton number) which is strongly suppressed in the SM. However, one thing we have to notice is that each experimental observable are given with squared of the amplitude, which means that interference terms between the SM terms and dimension-8 terms can induce several dimension-6 terms which must be considered in the future for precise evaluation.

$$\text{Observables} \propto \left(\text{SM} + \frac{C_i^{(6)}}{\Lambda^2} + \frac{C_i^{(8)}}{\Lambda^4}\right)^2$$

2.3.3 Description of the effective Lagrangian $\mathcal{L}_{eff}^{(6)}$ with the dimension-6 operators

Since the theme of this thesis is anomalous couplings between the Higgs boson and vector bosons such as Z, γ, and W, possible production diagrams are shown in Fig. 7. When picking up relevant operators which are composed of the Higgs field or gauge-boson fields based on the table from Fig. 8, the Lagrangian involving such operators would be constructed with 9 dimension-6 field operators, which is as follows,

$$\begin{aligned}\mathcal{L}_{eff}^{(6)} =& \frac{C_{\Phi\Box}}{\Lambda^2}\partial_\mu(\Phi^\dagger\Phi)\partial^\mu(\Phi^\dagger\Phi) + \frac{C_{\Phi D}}{\Lambda^2}(\Phi^\dagger \overleftrightarrow{D}^\mu \Phi)(\Phi^\dagger \overleftrightarrow{D}_\mu \Phi) + \frac{c_\Phi}{\Lambda^2}(\Phi^\dagger\Phi)^3 \\ &+ \frac{C_{\Phi B}}{\Lambda^2}\Phi^\dagger\Phi B_{\mu\nu}B^{\mu\nu} + \frac{C_{\Phi W}}{\Lambda^2}\Phi^\dagger\Phi W^a_{\mu\nu}W^{a\mu\nu} + \frac{C_{\Phi WB}}{\Lambda^2}\Phi^\dagger\tau^a\Phi W^a_{\mu\nu}B^{\mu\nu} \\ &+ \frac{C_{\Phi\tilde{B}}}{\Lambda^2}\Phi^\dagger\Phi B_{\mu\nu}\tilde{B}^{\mu\nu} + \frac{C_{\Phi\tilde{W}}}{\Lambda^2}\Phi^\dagger\Phi W^a_{\mu\nu}\tilde{W}^{a\mu\nu} + \frac{C_{\Phi\tilde{W}B}}{\Lambda^2}\Phi^\dagger\tau^a\Phi\tilde{W}^a_{\mu\nu}B^{\mu\nu}\ .\end{aligned} \tag{6}$$

Coefficients for each field operator C_{xx} are dimensionless and show coupling constants of those corresponding structures. $W^a_{\mu\nu}$ and $B_{\mu\nu}$ are the Yang-Mills field-strength tensors for the $SU(2)$ and $U(1)$ symmetry, which is $V_{\mu\nu} = \partial_\mu V_\nu - \partial_\nu V_\mu$, and D_μ is the covariant derivative for retaining the gauge invariance of $SU(2)\times U(1)$ symmetry. τ^a shows the $SU(2)$ generators, which are defined

with Pauli matrices ($\tau^a = \sigma^a/2$). $\Phi^\dagger \overset{\leftrightarrow\mu}{D} \Phi$, and the dual field strength tensors $\tilde{B}^{\mu\nu}$ and $\tilde{W}^{a\mu\nu}$ are respectively given as

$$\begin{aligned} \Phi^\dagger \overset{\leftrightarrow\mu}{D} \Phi &= \Phi^\dagger (D_\mu \Phi) - (D_\mu \Phi)^\dagger \Phi \ , \\ \tilde{B}_{\mu\nu} &= \frac{1}{2} \epsilon_{\mu\nu\rho\sigma} B^{\rho\sigma} \ , \\ \tilde{W}^a_{\mu\nu} &= \frac{1}{2} \epsilon_{\mu\nu\rho\sigma} B^{\rho\sigma} \ . \end{aligned}$$

Let's apply the spontaneous symmetry breaking (SSB) and consider the first term in the effective Lagrangian with the Higgs doublet $\Phi = \frac{1}{\sqrt{2}} \begin{pmatrix} 0 \\ v + h(x) \end{pmatrix}$,

$$\begin{aligned} \frac{C_{\Phi\Box}}{\Lambda^2} \partial_\mu (\Phi^\dagger \Phi) \partial^\mu (\Phi^\dagger \Phi) &= \frac{C_{\Phi\Box}}{\Lambda^2} \Big((\partial_\mu \Phi^\dagger)\Phi) + \Phi^\dagger (\partial_\mu \Phi) \Big) \Big((\partial^\mu \Phi^\dagger)\Phi) + \Phi^\dagger (\partial^\mu \Phi) \Big) \\ &= \frac{C_{\Phi\Box}}{\Lambda^2} \Big(v^2 (\partial_\mu h)(\partial^\mu h) + 2v (\partial_\mu h)(\partial^\mu h) h + (\partial_\mu h)(\partial^\mu h) h^2 \Big) \end{aligned}$$

In the equation here, a new kinetic term of the Higgs boson appears in the first term, which will affect all SM couplings between the Higgs boson as well as the Higgs potential. Thus, when the SSB is imposed for the Lagrangian $\mathcal{L}^{(6)}_{eff}$, it is necessary to add the modification of the Higgs field due to the new kinetic term and renormalize those effects which modify the SM couplings. When going back to the the Lagrangian $\mathcal{L}^{SM}_\Phi$ in Eq. (4) which gives the couplings between the vector bosons, the Higgs wave function in the Lagrangian will be redefined to negate the modification due to the higher operator, which is

$$h \to \Big(1 - \frac{C_{\Phi\Box} v^2}{\Lambda^2} \Big) h \ .$$

Under the this definition the SM Lagrangian will be also modified as

$$\begin{aligned} \mathcal{L}^{SM}_\Phi &= \frac{1}{2} \Big(1 - \frac{C_{\Phi\Box} v^2}{\Lambda^2} \Big)^2 \partial_\mu h \partial^\mu h \\ &\quad + \frac{g_2^2}{4} W^-_\mu W^{+\mu} \Big(v + \big(1 - \frac{C_{\Phi\Box} v^2}{\Lambda^2} \big) h \Big)^2 + \frac{1}{2} \frac{(g_1^2 + g_2^2)}{4} Z_\mu Z^\mu \Big(v + \Big(1 - \frac{C_{\Phi\Box} v^2}{\Lambda^2} \Big) h \Big)^2 \ . \end{aligned}$$

where the Higgs potential is completely ignored since the Higgs triple and quartic couplings are not discussed in this thesis. As shown in the Lagrangian, firstly the new contribution coming from the Higgs kinetic term due to the higher operator is canceled out because of the modification of the Higgs wave function here, and secondary, the mass terms of the vector bosons are not affected by the higher operator. These mass terms are not discussed anymore, here. When expanding the interaction terms between the Higgs and the vector bosons in the Lagrangian with ignorance of the quadratic term, the modified couplings of the Lagrangian derived from the first higher operator are respectively

$$\Big(\frac{1}{v^2} - \frac{C_{\Phi\Box}}{\Lambda^2} \Big) \frac{M_Z^2}{2} 2v Z_\mu Z^\mu h + \Big(\frac{1}{v^2} - 2 \frac{C_{\Phi\Box}}{\Lambda^2} \Big) \frac{M_Z^2}{2} Z_\mu Z^\mu h^2 \ , \tag{7}$$

$$\Big(\frac{1}{v^2} - \frac{C_{\Phi\Box}}{\Lambda^2} \Big) M_W^2 2v W^-_\mu W^{+\mu} h + \Big(\frac{1}{v^2} - 2 \frac{C_{\Phi\Box}}{\Lambda^2} \Big) M_W^2 W^-_\mu W^{+\mu} h^2 \ . \tag{8}$$

When considering the covariant derivative of the $SU(2)\times U(1)$ gauge: $D_\mu \equiv \partial_\mu + i\frac{g_1}{2}B_\mu + i\frac{g_2}{2}\mathbf{W}_\mu$, the second term can be decomposed as

$$\begin{aligned}\frac{C_{\Phi D}}{\Lambda^2}(\Phi^\dagger \overset{\leftrightarrow}{D}^\mu \Phi)(\Phi^\dagger \overset{\leftrightarrow}{D}_\mu \Phi) &= \frac{C_{\Phi D}}{\Lambda^2}\Big(\Phi^\dagger(D^\mu\Phi) - (D^\mu\Phi)^\dagger\Phi\Big)\Big(\Phi^\dagger(D_\mu\Phi) - (D_\mu\Phi)^\dagger\Phi\Big) \\ &= \frac{C_{\Phi D}}{\Lambda^2}\frac{i^2}{4}\left[g_1 B^\mu - g_2 W^{3\mu}\right]\left[g_1 B_\mu - g_2 W^3_\mu\right](v+h)^4 \\ &= -\frac{C_{\Phi D}}{\Lambda^2}\frac{(g_1^2+g_2^2)}{4}Z_\mu Z^\mu (v+h)^4 \ ,\end{aligned}$$

where Eq. (3) is used to reach the last line. When ignoring the higher order Higgs terms, the modification because of the second higher operator appears for the couplings between the Higgs boson and the Z boson only in the end, which is

$$-\frac{C_{\Phi D}}{\Lambda^2}M_Z^2 Z_\mu Z^\mu (v^2 + 4vh + 6h^2) \ . \tag{9}$$

In fact the mass terms of the Z boson is also modified, but it is ignored in this thesis. The third term will shift the Higgs potential only like

$$\frac{c_\Phi}{\Lambda^2}(\Phi^\dagger\Phi)^3 = \frac{c_\Phi}{\Lambda^2}\frac{1}{8}(v+h)^6 \ .$$

Since we do not handle the Higgs potential here, we ignore this term. The second line in the effective Lagrangian in Eq. (6) are composed of combinations with the Higgs fields and the vector boson fields, which are respectively decomposed as follows. Unless otherwise noted, $\sin\theta_w$ and $\cos\theta_w$ are simplified as s_w and c_w.

$$\begin{aligned}\frac{C_{\Phi B}}{\Lambda^2}\Phi^\dagger\Phi B_{\mu\nu}B^{\mu\nu} &= \frac{C_{\Phi B}}{\Lambda^2}\frac{1}{2}(v+h)^2\big[(c_w A_{\mu\nu} - s_w Z_{\mu\nu})(c_w A^{\mu\nu} - s_w Z^{\mu\nu})\big] \\ &= \frac{C_{\Phi B}}{\Lambda^2}\frac{1}{2}(v+h)^2\left(c_w^2 A_{\mu\nu}A^{\mu\nu} - 2s_w c_w A_{\mu\nu}Z^{\mu\nu} + s_w^2 Z_{\mu\nu}Z^{\mu\nu}\right)\end{aligned}$$

where the field strength tensor $B_{\mu\nu}$ is defined here[3].
The next term would be

$$\begin{aligned}\frac{C_{\Phi W}}{\Lambda^2}\Phi^\dagger\Phi W^a_{\mu\nu}W^{a\mu\nu} &= \frac{C_{\Phi W}}{\Lambda^2}\frac{1}{2}(v+h)^2(W^3_{\mu\nu}W^{3\mu\nu} + 2W^-_{\mu\nu}W^{+\mu\nu}) \\ &= \frac{C_{\Phi W}}{\Lambda^2}\frac{1}{2}(v+h)^2\Big(s_w^2 A_{\mu\nu}A^{\mu\nu} + 2s_w c_w A_{\mu\nu}Z^{\mu\nu} + c_w^2 Z_{\mu\nu}Z^{\mu\nu} \\ &\quad -2ig_2(W^{-\mu}W^{+\nu} - W^{-\nu}W^{+\mu})(s_w A_{\mu\nu} + c_w Z_{\mu\nu}) \\ &\quad +i^2 g_2^2(W^-_\mu W^+_\nu - W^-_\nu W^-_\mu)(W^{-\mu}W^{+\nu} - W^{-\nu}W^{+\mu}) + 2W^-_{\mu\nu}W^{+\mu\nu}\Big) \\ &= \frac{C_{\Phi W}}{\Lambda^2}\frac{1}{2}(v+h)^2\Big(s_w^2 A_{\mu\nu}A^{\mu\nu} + 2s_w c_w A_{\mu\nu}Z^{\mu\nu} + c_w^2 Z_{\mu\nu}Z^{\mu\nu} + 2W^-_{\mu\nu}W^{+\mu\nu}\Big)\end{aligned}$$

[3]Each field strength tensor $B_{\mu\nu}$ and $W^3_{\mu\nu}$ are respectively defined in any text books.

$$\begin{aligned}B_{\mu\nu} &= c_w A_{\mu\nu} - s_w Z_{\mu\nu} \\ W^3_{\mu\nu} &= s_w A_{\mu\nu} + c_w Z_{\mu\nu} - ig_2(W^-_\mu W^+_\nu - W^-_\nu W^+_\mu)\end{aligned}$$

where the imaginary parts disappear[4]. Then, the sixth term would be

$$\begin{aligned}
\frac{C_{\Phi WB}}{\Lambda^2}\Phi^\dagger\tau^a\Phi W^a_{\mu\nu}B^{\mu\nu} &= -\frac{C_{\Phi WB}}{\Lambda^2}\frac{1}{2}\frac{1}{2}(v+h)^2 W^3_{\mu\nu}B^{\mu\nu} \\
&= -\frac{C_{\Phi WB}}{\Lambda^2}\frac{1}{2}\frac{1}{2}(v+h)^2 \\
&\qquad \Big[s_w A_{\mu\nu} + c_w Z_{\mu\nu} - ig_2(W^-_\mu W^+_\nu - W^-_\nu W^+_\mu)\Big](c_w A^{\mu\nu} - s_w Z^{\mu\nu}) \\
&= -\frac{C_{\Phi WB}}{\Lambda^2}\frac{1}{2}\frac{1}{2}(v+h)^2\Big(s_w c_w A_{\mu\nu}A^{\mu\nu} - (s_w^2 - c_w^2)A_{\mu\nu}Z^{\mu\nu} - s_w c_w Z_{\mu\nu}Z^{\mu\nu} \\
&\qquad +ig_2(W^-_\mu W^+_\nu - W^-_\nu W^+_\mu)(s_w Z^{\mu\nu} - c_w A^{\mu\nu})\Big) \\
&= -\frac{C_{\Phi WB}}{\Lambda^2}\frac{1}{2}\frac{1}{2}(v+h)^2\Big(s_w c_w A_{\mu\nu}A^{\mu\nu} - (s_w^2 - c_w^2)A_{\mu\nu}Z^{\mu\nu} - s_w c_w Z_{\mu\nu}Z^{\mu\nu}\Big)
\end{aligned}$$

where the imaginary parts also disappear[5]. Up to here, new structure induced by the dimension-6 field operators placed in the second line of the Eq. (6) are shown. In the similar manner, new structures induced by the third line of the Eq. (6) are given, which are CP violating terms. Defining general parameters to simplify the equation and listing up the terms being relevant to the Higgs

[4]Using the description of the fields A_μ and Z_μ which are given in Eq. (2), the imaginary part would be,

$$\begin{aligned}
&-2ig_2(W^{-\mu}W^{+\nu} - W^{-\nu}W^{+\mu})(s_w A_{\mu\nu} + c_w Z_{\mu\nu}) \\
&= -2ig_2(W^{-\mu}W^{+\nu} - W^{-\nu}W^{+\mu})\Big[s_w(\partial_\mu A_\nu - \partial_\nu A_\mu) + c_w(\partial_\mu Z_\nu - \partial_\nu Z_\mu)\Big] \\
&= -2ig_2(W^{-\mu}W^{+\nu} - W^{-\nu}W^{+\mu}) \\
&\quad \Big[s_w\Big(\partial_\mu(s_w W^3_\nu + c_w B_\nu) - \partial_\nu(s_w W^3_\mu + c_w B_\mu)\Big) + c_w\Big(\partial_\mu(c_w W^3_\nu - s_w B_\nu) - \partial_\nu(c_w W^3_\mu - s_w B_\mu)\Big)\Big] \\
&= -2ig_2(W^{-\mu}W^{+\nu} - W^{-\nu}W^{+\mu})(\partial_\mu(s_w^2 W^3_\nu + c_w^2 W^3_\nu) - \partial_\nu(s_w^2 W^3_\mu + c_w^2 W^3_\mu)) \\
&= -2ig_2(W^{-\mu}W^{+\nu} - W^{-\nu}W^{+\mu})(\partial_\mu W^3_\nu - \partial_\nu W^3_\mu) \\
&= 0
\end{aligned}$$

[5]Similary, using the description of the fields A_μ and Z_μ,

$$\begin{aligned}
&ig_2(W^-_\mu W^+_\nu - W^-_\nu W^+_\mu)(s_w Z^{\mu\nu} - c_w A^{\mu\nu}) \\
&= ig_2(W^{-\mu}W^{+\nu} - W^{-\nu}W^{+\mu}) \\
&\quad \Big[s_w\Big(\partial^\mu(c_w W^{3\nu} - s_w B^\nu) - \partial^\nu(c_w W^{3\mu} - s_w B^\mu)\Big) - c_w\Big(\partial^\mu(s_w W^{3\nu} + c_w B^\nu) - \partial^\nu(s_w W^{3\mu} + c_w B^\mu)\Big)\Big] \\
&= ig_2(W^-_\mu W^+_\nu - W^-_\nu W^+_\mu)(\partial^\mu(s_w c_w W^{3\nu} - \partial^\nu(s_w c_w W^{3\mu} - \partial^\mu(s_w c_w W^{3\nu} + \partial^\nu(s_w c_w W^{3\mu}) \\
&= 0
\end{aligned}$$

and the vector boson couplings, these are as follows,

$$\begin{cases} \zeta_{ZZ} &= C_{\Phi B}s_w^2 + C_{\Phi W}c_w^2 + \frac{1}{2}C_{\Phi WB}s_w c_w \\ \zeta_{AA} &= C_{\Phi B}c_w^2 + C_{\Phi W}s_w^2 - \frac{1}{2}C_{\Phi WB}s_w c_w \\ \zeta_{AZ} &= -2C_{\Phi B}c_w s_w + 2C_{\Phi W}s_w c_w + \frac{1}{2}C_{\Phi WB}(s_w^2 - c_w^2) \\ \zeta_{WW} &= C_{\Phi W} \end{cases}$$

$$\begin{aligned} ZZ: &\quad \zeta_{ZZ}Z_{\mu\nu}Z^{\mu\nu}\left(\frac{v}{\Lambda^2}h + \frac{1}{2\Lambda^2}h^2\right) + \tilde{\zeta}_{ZZ}Z_{\mu\nu}\tilde{Z}^{\mu\nu}\left(\frac{v}{\Lambda^2}h + \frac{1}{2\Lambda^2}h^2\right) \\ AA: &\quad \zeta_{AA}A_{\mu\nu}A^{\mu\nu}\left(\frac{v}{\Lambda^2}h + \frac{1}{2\Lambda^2}h^2\right) + \tilde{\zeta}_{AA}A_{\mu\nu}\tilde{A}^{\mu\nu}\left(\frac{v}{\Lambda^2}h + \frac{1}{2\Lambda^2}h^2\right) \\ AZ: &\quad \zeta_{AZ}A_{\mu\nu}Z^{\mu\nu}\left(\frac{v}{\Lambda^2}h + \frac{1}{2\Lambda^2}h^2\right) + \tilde{\zeta}_{AZ}A_{\mu\nu}\tilde{Z}^{\mu\nu}\left(\frac{v}{\Lambda^2}h + \frac{1}{2\Lambda^2}h^2\right) \\ W^-W^+: &\quad \zeta_{WW}W^-_{\mu\nu}W^{+\mu\nu}\left(2\frac{v}{\Lambda^2}h + \frac{1}{\Lambda^2}h^2\right) + \tilde{\zeta}_{WW}W^-_{\mu\nu}\tilde{W}^{+\mu\nu}\left(2\frac{v}{\Lambda^2}h + \frac{1}{\Lambda^2}h^2\right) \end{aligned}$$

Most of the structures being relevant to the structures between the Higgs and the vector bosons induced by the dimension-6 field operators after the SSB are all presented. When compiling the coefficients of the SM structures with η_Z and η_W like,

$$\begin{cases} \eta_Z = -C_{\Phi\Box} - 4C_{\Phi D} \\ \eta_{ZZ} = -2C_{\Phi\Box} - 12C_{\Phi D} \\ \eta_W = -C_{\Phi\Box} \\ \eta_{WW} = -2C_{\Phi\Box} \end{cases},$$

the general Lagrangian composed of these structures based on the Warsaw bases is given as follows, where the contribution and the modification of the Higgs potential are ignored,

$$\begin{aligned} \mathcal{L}_{SM} + \mathcal{L}^{(6)}_{eff} = &\frac{1}{2}\partial_\mu h \partial^\mu h \\ &+ \frac{M_Z^2}{v}\left(1+\eta_Z\right)Z_\mu Z^\mu h + \frac{M_Z^2}{2v^2}\left(1+\eta_{ZZ}\right)Z_\mu Z^\mu h^2 \\ &+ \frac{2M_W^2}{v}\left(1+\eta_W\right)W^-_\mu W^{+\mu} h + \frac{M_W^2}{v^2}\left(1+\eta_{WW}\right)W^-_\mu W^{+\mu} h^2 \\ &+ \zeta_{ZZ}Z_{\mu\nu}Z^{\mu\nu}\left(\frac{h}{v} + \frac{h^2}{2v^2}\right) + \tilde{\zeta}_{ZZ}Z_{\mu\nu}\tilde{Z}^{\mu\nu}\left(\frac{h}{v} + \frac{h^2}{2v^2}\right) \\ &+ \zeta_{AA}A_{\mu\nu}A^{\mu\nu}\left(\frac{h}{v} + \frac{h^2}{2v^2}\right) + \tilde{\zeta}_{AA}A_{\mu\nu}\tilde{A}^{\mu\nu}\left(\frac{h}{v} + \frac{h^2}{2v^2}\right) \\ &+ \zeta_{AZ}A_{\mu\nu}Z^{\mu\nu}\left(\frac{h}{v} + \frac{h^2}{2v^2}\right) + \tilde{\zeta}_{AZ}A_{\mu\nu}\tilde{Z}^{\mu\nu}\left(\frac{h}{v} + \frac{h^2}{2v^2}\right) \\ &+ \zeta_{WW}W^-_{\mu\nu}W^{+\mu\nu}\left(2\frac{h}{v} + \frac{h^2}{v^2}\right) + \tilde{\zeta}_{WW}W^-_{\mu\nu}\tilde{W}^{+\mu\nu}\left(2\frac{h}{v} + \frac{h^2}{v^2}\right), \end{aligned} \tag{10}$$

where the normalization of Λ is replaced with the convenient notation of $v/\Lambda^2 = 1/v$ to match it to the literature [35]. In addition the original Lagrangian in Eq. (6) given by the Warsaw bases is actually modified in the the literature [35] to make it comfortable notation for e^+e^- study as the

ILC-EFT convention[6]

In order to fit the given effective Lagrangian to the effective Lagrangian based on the ILC-EFT, the convention is connected to the one of the ILC-EFT. The coefficients of the operators are replaces like,

$$\begin{cases} C_{\Phi\Box} &= \frac{1}{2}C_H \\ C_{\Phi D} &= \frac{1}{2}C_T C_{\Phi W} \;= 4C_{WW} \\ C_{\Phi B} &= 4C_{BB}\frac{s_w^2}{c_w^2} \\ C_{\Phi WB} &= 16C_{WB}\frac{s_w}{c_w} \end{cases} .$$

Under this notation the effective Lagrangian relevant to the VVH ($ZZH, \gamma ZH$, and WWH) structures would be

$$\begin{aligned} \mathcal{L}_{VVH} \;=\; & M_Z^2 \frac{1}{v}\left(1+\eta_Z\right) Z_\mu Z^\mu h + 2M_W^2 \frac{1}{v}\left(1+\eta_W\right) W_\mu^- W^{+\mu} h \\ & + \frac{\zeta_{ZZ}}{2v} Z_{\mu\nu} Z^{\mu\nu} h + \frac{\zeta_{AA}}{2v} A_{\mu\nu} A^{\mu\nu} h + \frac{\zeta_{AZ}}{v} A_{\mu\nu} Z^{\mu\nu} h + \frac{\zeta_{WW}}{v} W_{\mu\nu}^- W^{+\mu\nu} h \\ & + \frac{\tilde{\zeta}_{ZZ}}{2v} Z_{\mu\nu} \tilde{Z}^{\mu\nu} h + \frac{\tilde{\zeta}_{AA}}{2v} A_{\mu\nu} \tilde{A}^{\mu\nu} h + \frac{\tilde{\zeta}_{AZ}}{v} A_{\mu\nu} \tilde{Z}^{\mu\nu} h + \frac{\tilde{\zeta}_{WW}}{v} W_{\mu\nu}^- \tilde{W}^{+\mu\nu} h \quad . \end{aligned} \tag{11}$$

where each coefficients are respectively described as

$$\begin{cases} \eta_Z = -\frac{1}{2}C_H - C_T \\ \eta_W = -\frac{1}{2}C_H \\ \zeta_{ZZ} \;= 2(4C_{BB}\frac{s_w^4}{c_w^2} + 4C_{WW}c_w^2 + 8C_{WB}s_w^2) \\ \zeta_{AA} \;= 2(4C_{BB}s_w^2 + 4C_{WW}s_w^2 - 8C_{WB}s_w^2) \\ \zeta_{AZ} \;= s_w c_w \left(-8C_{BB}\frac{s_w^2}{c_w^2} + 8C_{WW} + 8C_{WB}\left(\frac{s_w^2}{c_w^2} - 1\right)\right) \\ \zeta_{WW} = 8C_{WW} \end{cases}$$

[6]For instance, the $C_{\Phi\Box}$ term in the Warsaw basis is replaced by a C_H term in the ILC-EFT. This is because the $C_{\Phi\Box}$ term can induce contact interactions like C_{HL}/C'_{HL} terms. The effect by C_H terms is probably more simply represented, for just redefinition of the Higgs wave function. Please refer the literature [35].

3 International Linear Collider and International Large Detector

In this section overviews on both International Linear Collider (ILC) and International Large Detector (ILD) are given. A few official reports, Technical Design Report (TDR) [36, 37] and Detailed Baseline Document (DBD) [38], which describe the detail designs for both of the ILC and ILD were already published. Thus, the overviews of the ILC and ILD given here are briefly summaries since information are referred to those official reports.

3.1 An overview of the ILC design

The ILC shown in Fig. 9 is a future electron-positron collider based on superconducting acceleration technology, in which electrons and positrons are linearly accelerated. An accessible range of centre-of-mass-energy is currently from 250 to 500 GeV. However, there exists technological capability that the energy is extended up to 1 TeV. Two main 11 km linacs are planned to build, where superconducting cavities operating at average gradient of 31.5 MV/m will be installed.

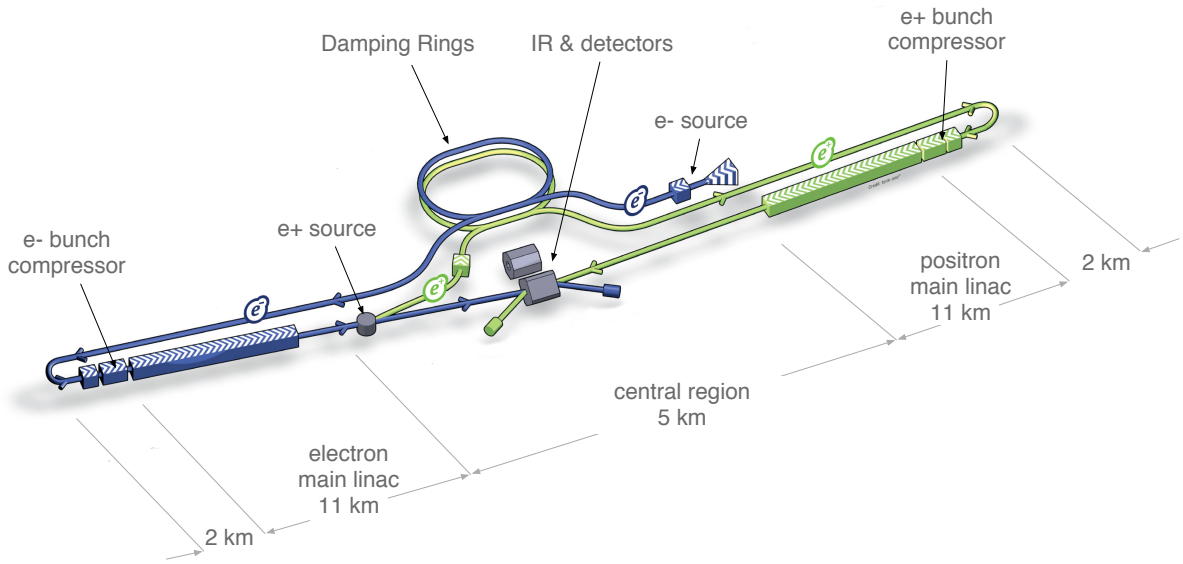

Figure 9: The picture is referred from [36]. A schematic view of the ILC design.

Advantages of the linear collider and the electron-positron :

Naively thinking, to explore minimum structures of material or go back to early universe where everything probably were unified, we need to use higher energy particle (Matter wave) or create higher energy environment. Thus, particles must be accelerated as much as possible. When making a particle accelerate with a circular accelerator, one concern is that the particle radiates photons (synchrotron radiations) during the acceleration and lose own energy, which can be described as $\Delta E \propto (E/m)^4 \, 1/R$ where E, m, and R are respectively energy, mass of the particle, and radius of the circular accelerator. Therefore, the circular accelerator is suitable to accelerate massive particles, or it's necessary to build bigger accelerator to achieve higher energy. However, when assuming a linear accelerator, it's not necessary to consider it.

In the LHC protons are accelerated. Since the proton is composed of quarks (uud) and a part of quarks is involved in interactions of a reaction, the initial information of the reaction is not clearly defined. In addition, a tons of processes which relate to quantum chromodynamics (QCD) become huge backgrounds, and it contaminates interesting reactions we want to observe. Thus, the LHC is not sufficient for precise measurements of interactions between particles. In contrast, the ILC where an electron and a positron are used can provide extremely clean environment for the precise measurements: well-defined initial information and very low backgrounds. The ILC has, in addition, one more large benefit that it can make both particles polarize for left- and

right-handed state up to ±80% and ±30% for the electron and positron, which allows us to access specific physics studies such as the weak interactions and the chiral structures of particles. Making the electron and positron polarize is impossible in the circular accelerator because of synchrotron radiation and depolarization effect derived from magnets.

One of the important considerations on collider physics is to consider how many events one can generate and whether there exist sufficient number of events to argue that something exist if something exist. This can be described as

$$N\ [\mathrm{sec}^{-1}] = L\ [\mathrm{cm}^{-2}\mathrm{sec}^{-1}] \times \sigma\ [\mathrm{cm}^{2}]$$

where N, L, and σ are respectively the number of events, luminosity, and production cross-section of certain process. Thus, we have to make luminosity L increase as much as possible. The formula is also understood as

$$L = \frac{kN_eN_pf}{4\pi\sigma_x\sigma_y}$$

where k, N_e, N_p, and f are respectively the number of bunches in per beam train, the number of electrons and positrons per bunch, and revolution frequency of an accelerator. σ_x and σ_y are beam sizes at a collision point. Since the ILC can not increase f, it is necessary to make both electron and positron beam squeeze and condense. Basic designed parameters of the ILC are listed in Fig. 10.

			Baseline 500 GeV Machine			1st Stage	L Upgrade
Centre-of-mass energy	E_{CM}	GeV	250	350	500	250	500
Collision rate	f_{rep}	Hz	5	5	5	5	5
Electron linac rate	f_{linac}	Hz	10	5	5	10	5
Number of bunches	n_{b}		1312	1312	1312	1312	2625
Bunch population	N	$\times 10^{10}$	2.0	2.0	2.0	2.0	2.0
Bunch separation	Δt_{b}	ns	554	554	554	554	366
Pulse current	I_{beam}	mA	5.8	5.8	5.8	5.8	8.8
Main linac average gradient	G_{a}	MV m^{-1}	14.7	21.4	31.5	31.5	31.5
Average total beam power	P_{beam}	MW	5.9	7.3	10.5	5.9	21.0
Estimated AC power	P_{AC}	MW	122	121	163	129	204
RMS bunch length	σ_{z}	mm	0.3	0.3	0.3	0.3	0.3
Electron RMS energy spread	$\Delta p/p$	%	0.190	0.158	0.124	0.190	0.124
Positron RMS energy spread	$\Delta p/p$	%	0.152	0.100	0.070	0.152	0.070
Electron polarisation	P_-	%	80	80	80	80	80
Positron polarisation	P_+	%	30	30	30	30	30
Horizontal emittance	$\gamma\epsilon_{\mathrm{x}}$	µm	10	10	10	10	10
Vertical emittance	$\gamma\epsilon_{\mathrm{y}}$	nm	35	35	35	35	35
IP horizontal beta function	β^*_{x}	mm	13.0	16.0	11.0	13.0	11.0
IP vertical beta function	β^*_{y}	mm	0.41	0.34	0.48	0.41	0.48
IP RMS horizontal beam size	σ^*_{x}	nm	729.0	683.5	474	729	474
IP RMS veritcal beam size	σ^*_{y}	nm	7.7	5.9	5.9	7.7	5.9
Luminosity	L	$\times 10^{34}$ cm^{-2}s^{-1}	0.75	1.0	1.8	0.75	3.6
Fraction of luminosity in top 1%	$L_{0.01}/L$		87.1%	77.4%	58.3%	87.1%	58.3%
Average energy loss	δ_{BS}		0.97%	1.9%	4.5%	0.97%	4.5%
Number of pairs per bunch crossing	N_{pairs}	$\times 10^3$	62.4	93.6	139.0	62.4	139.0
Total pair energy per bunch crossing	E_{pairs}	TeV	46.5	115.0	344.1	46.5	344.1

Figure 10: The table is referred from [36]. A summary table of the baseline ILC parameters for $\sqrt{s}$ =250–500 GeV, upgraded luminosity and energy parameters are also shown.

3.2 An overview of the ILD design

The design of the ILD detector shown in Fig. 11 is based on a concept of particle flow analysis [39, 40] where all particles, charged and neutral ones generated through a reaction, are individually tried to identify, and momentum and energy of those particles are measured by using the most suitable sub-detectors. Thus, the sub-detectors are required to achieve extremely great spatial resolution to separate them, which have approximately one-order magnitude better performance compared to current and past utilized detectors of the high energy collider physics.

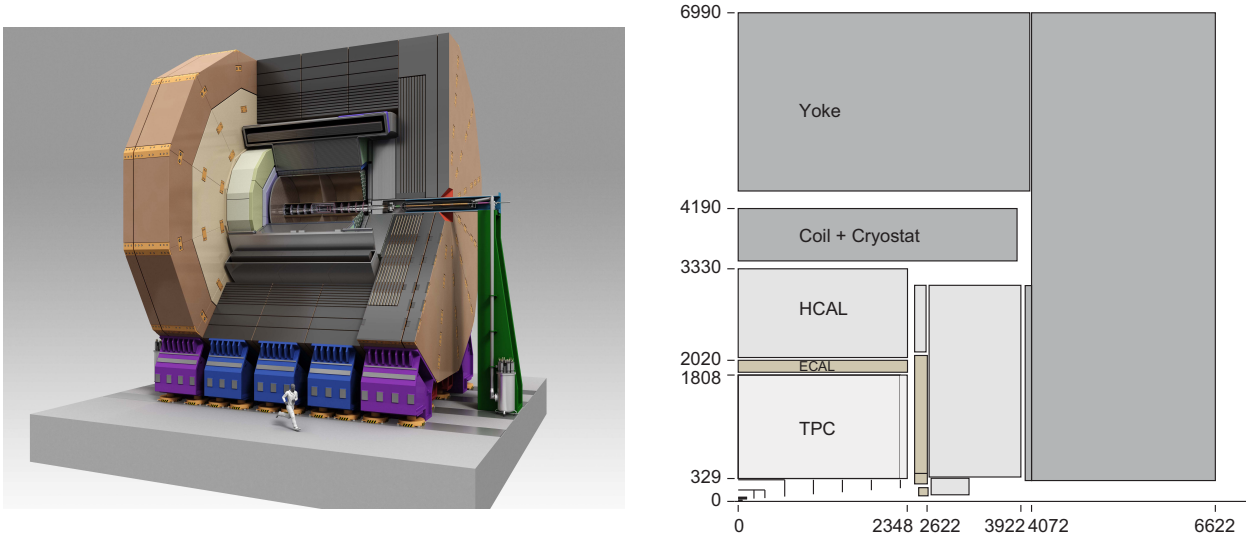

Figure 11: The pictures are taken from [37] (left) and [41] (right). A schematic view of the ILD design and its quadrant cross-section where the unit is milimeter.

In the physics program covers by the ILC, identification of heavy quarks like c and b, and τ leptons is necessary. To reconstruct such short lived particles, decay vertices must be correctly identified, which requires that the performance of impact parameter resolution must be sufficiently good. The required impact parameter resolution is $\sigma_{r\phi} < 5 \oplus 10/p \sin^{3/2}\theta \ \ [\mu m]$. One of the flag ship measurements of the Higgs boson is performed by recoil mass technique using $e^+e^- \rightarrow ZH \rightarrow l^+l^-H$ process where it is possible to measure the Higgs boson without looking at the Higgs boson at all, and the necessity is to measure momentum of a lepton pair. In terms of the precision measurements the required momentum resolution is $\sigma_{1/p_T} \sim 2 \times 10^{-5} \ \ [\mathrm{GeV}^{-1}]$ with a combination of a central tracker and enveloped silicon trackers. The ILD performance for both of the impact parameter and the momentum resolution are shown in the left of Fig. 12.

Particle Flow Analysis (PFA) :

In many processes in which we have interested in the ILC condition or we do not, hadronic jets appear, which are often from W and Z bosons, such as $e^+e^- \rightarrow t\bar{t} \rightarrow W^+bW^-\bar{b}$. Therefore, given that both bosons are well reconstructed, it's possible to separate a signal process from background processes by exploiting the information of invariant mass of a di-jet which will correspond to the mass of the W and Z bosons. Ultimately, the invariant mass resolution against the widths of the gauge bosons is a goal which the ILD targets at, namely $\Gamma_W/m_W \simeq \Gamma_Z/m_Z \simeq \sigma_m/m = 2.7$ %. The mass resolution can be translated into jet energy resolution in the di-jet system like[7]: $\sigma_m/m \simeq \sigma_E/E$, and also the jet energy resolution is typically described with a form of $\sigma_E/E = (\alpha/\sqrt{E}+\beta)$, where the first and second respectively called a stochastic and a constant term. Thus,

[7]Mass is described as

$$m_{ij} = 2E_iE_j(1 - \cot\theta_{ij})$$

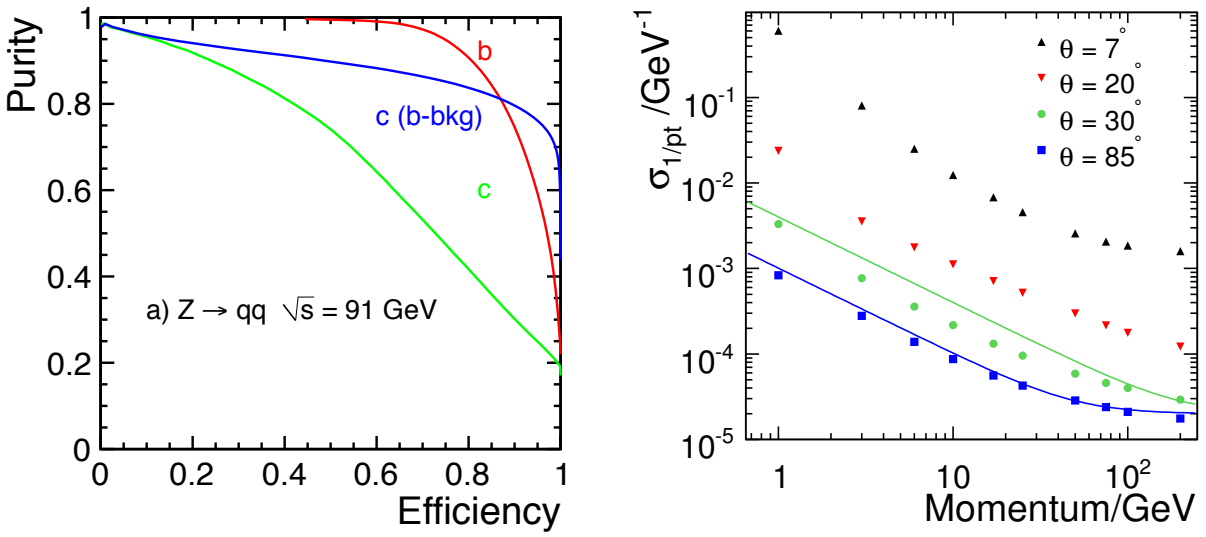

Figure 12: The plots are referred from [37, 42]. (Left) the performance of the heavy flavor tag, (Right) the momentum resolution for several angles

the requirement of the jet energy resolution for the ILD is $\sigma_m/m = \alpha/\sqrt{E} = 2.7$ %, which means the stochastic term in a possible energy range of 150–350 GeV in the ILC is $< 30\ \%/\sqrt{E\ (\mathrm{GeV})}$.

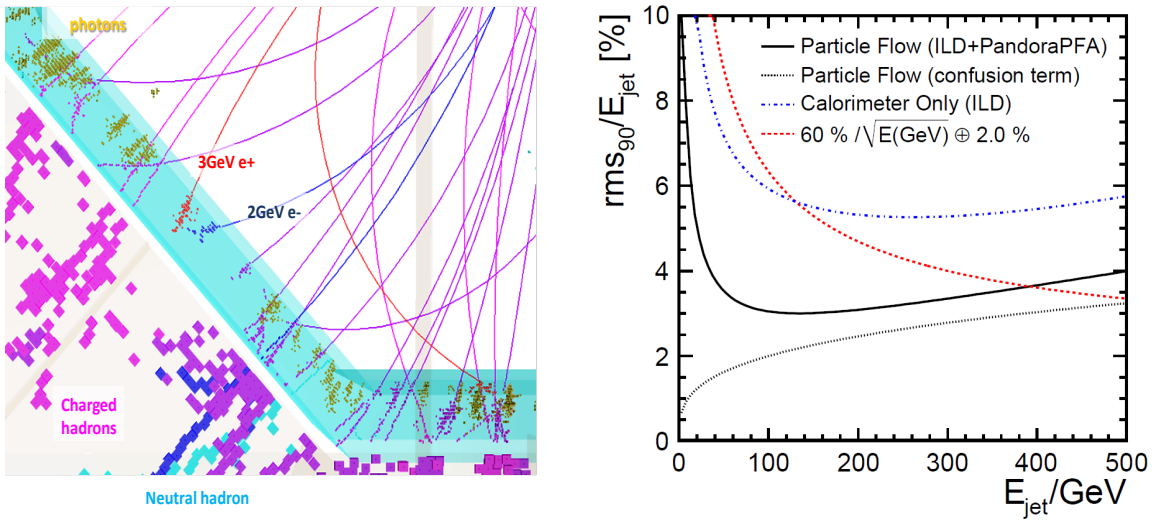

Figure 13: The plots are referred from [37, 43]. (Left) the schematic view of Particle Flow Objects based on Particle Flow Analysis and (Right) the jet energy resolution for different radius of electromagnetic calorimeters.

Particle composition inside a hadron jet had been studied in detail in the past collider experiments such as LEP and LEP2 [44]. Among particles observed in a detector, roughly 62 % is by a charged particle which is mainly a hadron, 10 % is by a neutral hadron, 27 % is by a photon,

Therefore, the mass resolution is given by

$$\frac{\sigma_M}{M} = \frac{1}{2}\left(\left(\frac{\sigma_{E_1}}{E_1}\right)^2 + \left(\frac{\sigma_{E_2}}{E_2}\right)^2 + \left(\frac{\sigma_\theta}{\tan\frac{\theta}{2}}\right)^2\right)^{\frac{1}{2}}$$

usually the angular resolution can be measured well compared to the jet energy resolution.

and remaining is by a neutrino. Because an electro magnetic interaction can be well measured, the energy resolution is 15 $\%/\sqrt{E\ (\mathrm{GeV})}$. In contrast, development of a hadronic shower is more complicated and its energy resolution is worse, which is typically 55 $\%/\sqrt{E\ (\mathrm{GeV})}$. In the traditional way the sum of the energies deposited in the ECAL and HCAL had been used to measure the jet energy, whose jet energy resolution is typically 60 $\%/\sqrt{E\ (\mathrm{GeV})}$ due to the composition of hadronic particles of 72 %. To achieve $< 30\ \%/\sqrt{E\ (\mathrm{GeV})}$ for the jet energy resolution, it is necessary to perform the measurement that energy of all particles, except neutral hadrons, composing jet are measured with the tracker and the ECAL, and remaining neutral hadrons are measured with the HCAL. For this purpose it is also necessary that the detector has sufficient granularity to separate each particle well.

4 Observables and analysis strategies for anomalous coupling measurements

The general effective Lagrangian which includes relevant structures to VVH couplings is given in Eq. (11). Because beam polarization effects are not assumed in the effective Lagrangian, we slightly change the parametrization by replacing the general parameters to a_V, b_V, and $\tilde{b}_V$ to consider left- and right-handed beam polarization states. And the new physics scale parameter Λ is also made back to the effective Lagrangian for our convenience. The given effective Lagrangians for the ZZH and WWH anomalous couplings are individually as follows,

$$\mathcal{L}_{ZZH} = M_Z^2\Big(\frac{1}{v}+\frac{a_Z}{\Lambda}\Big)Z_\mu Z^\mu h + \frac{b_Z}{2\Lambda}Z_{\mu\nu}Z^{\mu\nu}h + \frac{\tilde{b}_Z}{2\Lambda}Z_{\mu\nu}\tilde{Z}^{\mu\nu}h \ , \tag{12}$$

$$\mathcal{L}_{WWH} = 2M_W^2\Big(\frac{1}{v}+\frac{a_W}{\Lambda}\Big)W_\mu^- W^{+\mu}h + \frac{b_W}{\Lambda}W_{\mu\nu}^- W^{+\mu\nu}h + \frac{\tilde{b}_W}{\Lambda}W_{\mu\nu}^-\tilde{W}^{+\mu\nu}h \ . \tag{13}$$

Illustrations of kinematical distributions which are plotted from the next subsection are assumed to be $\Lambda = 1$ TeV in any case.

4.1 Observables for anomalous ZZH couplings

The two kinds of tensor structures appeared in the effective Lagrangian in Eq. (12), $Z_{\mu\nu}Z^{\mu\nu}$ and $Z_{\mu\nu}\tilde{Z}^{\mu\nu}$, can bring not only different production cross-sections for the Higgs-strahlung and ZZ-fusion processes but also kinematical distributions which are different from SM predictions.

In the moment the Z bosons generate and decay, weak isospin or weak hyper-charge when a interaction with γ is considered, flow along relevant fermions which are production and decay particles of the Z bosons. In the same moment, one like an electroweak magnetic field should be generated because of running of the weak charge, that can be imagined based on an analogous dynamics of electromagnetism. Let me result in the electromagnetism to illustrate behaviors derived from the new tensor structures. A structure of an electromagnetic field tensor $F^{\mu\nu}$, which describes an electromagnetic field, is given as follows,

$$F^{\mu\nu} = \begin{bmatrix} 0 & -E_1 & -E_2 & -E_3 \\ E_1 & 0 & B_3 & -B_2 \\ E_2 & -B_3 & 0 & B_1 \\ E_3 & B_2 & -B_1 & 0 \end{bmatrix} \ .$$

where $\boldsymbol{E}$ and $\boldsymbol{B}$ show an electric field and a magnetic field which are composed of three space components. The phenomena led by the new tensor structures should be understood, using the Higgs-strahlung process in the Higgs rest-frame.

When the Higgs boson is generated through a (virtual) Z boson and decays into a Z boson which also decay into a pair of fermions, charges of each pair of fermions can individually imitate a state of an electric dipole as illustrated in Fig. 14. Because it's possible to consider the state that an electric current is running, a magnetic field can be also generated consequently. Inner products of the electromagnetic tensors with the electric and the magnetic field can be easily given as follows,

$$\begin{aligned} \hat{F}_{\mu\nu}\hat{F}^{\mu\nu} &\propto \boldsymbol{B}_1\cdot\boldsymbol{B}_2 - \boldsymbol{E}_1\cdot\boldsymbol{E}_2 \\ \hat{F}_{\mu\nu}\widetilde{\hat{F}}^{\mu\nu} &\propto \boldsymbol{E}_1\cdot\boldsymbol{B}_2 \end{aligned}$$

where the indexes 1 and 2 mean each of the fermion pairs originating from each of the Z bosons. The existence of the new tensor structures $Z_{\mu\nu}Z^{\mu\nu}$ and $Z_{\mu\nu}\tilde{Z}^{\mu\nu}$ would give peculiar kinematical distributions which are clearly different form the SM expectations. One of the observables being sensitive these structures is $\Delta\Phi$ that is an angle between production planes made up from the initial and final state fermions, where the Z boson which is a parent of the final state fermions is

necessary to define an axis for both planes. The existence of the structure of $Z_{\mu\nu}Z^{\mu\nu}$ makes both planes tend to take a parallel state, whereas the structure of $Z_{\mu\nu}\tilde{Z}^{\mu\nu}$ makes both planes tend to take a perpendicular state.

4.1.1 The Higgs-strahlung $e^+e^- \to Zh \to l^+l^-h$ at $\sqrt{s}$ =250 and 500 GeV

Variation of kinematics caused by the new structures can be also understandable based on the given effective Lagrangian itself. In general, a boson wave-function is defined with a product of a four-polarization vector and a wave function as $Z_\mu = \epsilon_\mu e^{-iqx}$. Let's focusing on the second structure $Z_{\mu\nu}Z^{\mu\nu}$ in Eq. (12). When assuming the Higgs-strahlung process in Fig. 14 and assuming two Z bosons that are Z_1 and Z_2 to be $Z_1(q_1, \epsilon_1)$ and $Z_2(q_2, \epsilon_2)$, where q_i and ϵ_i denote four-momentum and a polarization four-vector on an i-th particle ($i = 1, 2$), its matrix element can be calculated as

$$\begin{aligned}
\mathcal{M}_{a_Z}^{Zh} &= Z_{1\mu}Z_2^{\mu} = \epsilon_{1\mu}{\epsilon_2}^{\mu} \\
\mathcal{M}_{b_Z}^{Zh} &= Z_{1\mu\nu}{Z_2}^{\mu\nu} = (\partial_{1\mu}Z_{1\nu} - \partial_{1\nu}Z_{1\mu})(\partial_2{}^{\mu}Z_2{}^{\nu} - \partial_2{}^{\nu}Z_2{}^{\mu}) \\
&= i^2(q_{1\mu}\epsilon_{1\nu} - q_{1\nu}\epsilon_{1\mu})(q_2{}^{\mu}\epsilon_2{}^{\nu} - q_2{}^{\nu}\epsilon_2{}^{\mu}) \\
&= -2\big[(q_1q_2)(\epsilon_1\epsilon_2) - (q_1\epsilon_2)(q_2\epsilon_1)\big]
\end{aligned}$$

where momentum (operator) q can be translated through the canonical quantization ($q = -i\partial$). In the case of the Higgs-strahlung Zh process, the Z_1 boson assuming to be a virtual Z as an intermediate state gives $q_1(\sqrt{s}, \mathbf{0})$ and the polarization vector gives $\epsilon_1(0, \boldsymbol{\epsilon}_1)$ by considering the Lorentz condition for maintaining the gauge invariance: $q_1\epsilon_1 = 0$. When another outgoing Z_2 boson is assumed to fly along the beam axis like $q_2(E_2, 0, 0, p_{2Z})$, that means it is actually transversely polarized according to the Lorentz condition, the polarization vector gives $\epsilon_2(0, \boldsymbol{\epsilon}_2)$. Thus both invariant amplitudes can be calculated with consideration that the Z_2 boson is outgoing particle ($q_2 \to -q_2$), which should be

$$\mathcal{M}_{a_Z}^{Zh} = \epsilon_{1\mu}\epsilon_2^{\mu} = 0 - (\boldsymbol{\epsilon}_1 \cdot \boldsymbol{\epsilon}_2) \tag{14}$$

$$\mathcal{M}_{b_Z}^{Zh} = -2\big[- E_2\sqrt{s}(-\boldsymbol{\epsilon}_1 \cdot \boldsymbol{\epsilon}_2) - 0 \big] = -2E_2\sqrt{s}(\boldsymbol{\epsilon}_1 \cdot \boldsymbol{\epsilon}_2) \tag{15}$$

This formula implies that, firstly E_2 must be affected, consequently absolute momentum of the Z_2 boson will vary, secondly $\boldsymbol{\epsilon}_2$ must be also affected, thus a production angle of the Z_2 boson will vary. Therefore, angular and momentum information are essential to identify the anomalous couplings between the Higgs boson and the Z boson. Secondary decay products from the Z boson must also preserve the information of the couplings on the ZZH vertex.

To verify the anomalous ZZH couplings in leptonic $Zh \to l^+l^-h$ process of the Higgs-strahlung process, several observables are defined. The defined observables are explained below, and these illustrations are given in Fig. 16 and Fig. 17 as examples. Since the field strength tensors have momentum dependence of corresponding particles, the variation of shape of kinematical distributions quickly gets larger at $\sqrt{s}$ =500 GeV compared to $\sqrt{s}$ =250 GeV. Such behaviors can be seen in Fig. 18 and Fig. 19.

- A momentum distribution of the outgoing Z boson interacting with the Higgs boson must vary depending on the parameter b_Z and $\tilde{b}_Z$.
- A production(polar) angle of the outgoing Z boson must vary depending on the parameter b_Z and $\tilde{b}_Z$. A daughter fermion in the final state which is derived from the Z boson would also vary since the daughter fermions run away with the polarization information of the Z boson.
- A helicity angle of the daughter fermion coming from the Z boson, which represents projection of a spin of particle, is also an important observable and must vary due to the parameters. The helicity angle is defined an angle between a momentum direction of the Z

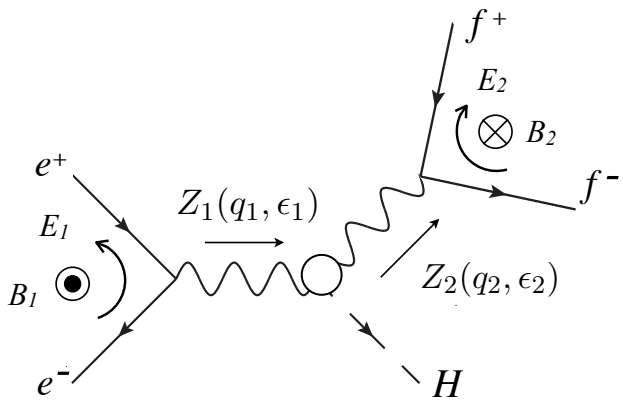

Figure 14: A schematic view of generation of an electroweak and an electroweak magnetic fields as an analogues of the electromagnetism, which is illustrated with the Higgs-strahlung in the Higgs rest-frame.

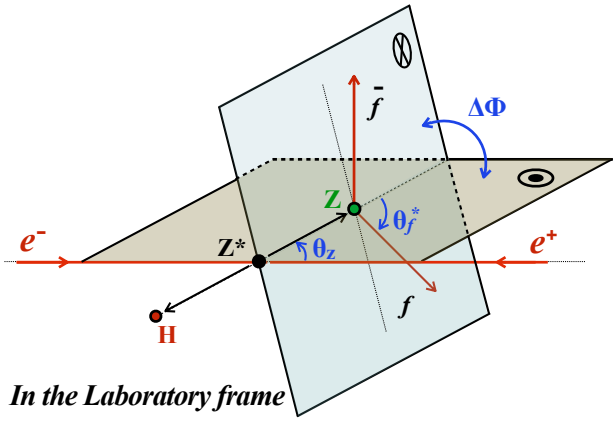

Figure 15: A schematic view of the Higgs-strahlung process $e^+e^- \to ZH \to f\bar{f}H$. θ_Z, θ_f^*, and $\Delta\Phi_{f\bar{f}}$ show the production angle of the Z boson, the helicity angle of the fermion derived from the Z boson, and the angle between two production planes.

boson and a momentum direction of its daughter fermion boosted in the Z rest-frame. The distribution of the helicity angle with the SM prediction gives a quadratic distribution since the spin of the Z boson is 1 in the SM. Because the spin is preserved to the daughters, the helicity angle would receive effects from the Z boson.

- An angle between production planes, which is constructed by momentum directions of the initial state electron and the final state anti-fermion and a momentum direction of the Z boson as a plane axis in the Higgs rest-frame/Laboratory-frame, is an useful observable , which is calculated as,

$$
\begin{aligned}
\Delta\Phi(f\bar{f};V) \quad & [0 \leq \Delta\Phi \leq 2\pi] \\
&= \begin{cases} (\cos\xi \leq 0), & \arctan(\tan\xi) \\ (\cos\xi \geq 0), & \arctan(\tan\xi) + \pi \cdot \mathrm{sgn}(\sin\xi) \end{cases} \\
\cos\xi &= \frac{(\hat{\boldsymbol{P}}_V \times \hat{\boldsymbol{P}}_f) \times (\hat{\boldsymbol{P}}_V \times \hat{\boldsymbol{P}}_{\bar{f}})}{|\hat{\boldsymbol{P}}_V \times \hat{\boldsymbol{P}}_f||\hat{\boldsymbol{P}}_V \times \hat{\boldsymbol{P}}_{\bar{f}}|} \\
\sin\xi &= \frac{\hat{\boldsymbol{P}}_V \cdot [(\hat{\boldsymbol{P}}_V \times \hat{\boldsymbol{P}}_f) \times (\hat{\boldsymbol{P}}_V \times \hat{\boldsymbol{P}}_{\bar{f}})]}{|\hat{\boldsymbol{P}}_V \times \hat{\boldsymbol{P}}_f||\hat{\boldsymbol{P}}_V \times \hat{\boldsymbol{P}}_{\bar{f}}|}
\end{aligned}
$$

where $\hat{\boldsymbol{P}}$ denotes a unit vector of momentum vector of each particle. In the case of the Higgs-strahlung process, $\boldsymbol{P}_V$ and $\boldsymbol{P}_f$ are the Z boson and the initial state electron, which are respectively denoted with $\boldsymbol{P}_Z$ and $\boldsymbol{P}_e$. $\cos\xi$ gives an angle calculated by directions of each plane which are constructed with momenta vectors of both fermions and the Z boson while $\sin\xi$ decides the direction of the planes against the direction of the Z boson, which is -1 or 1. The description of the behavior is given in the previous subsection.

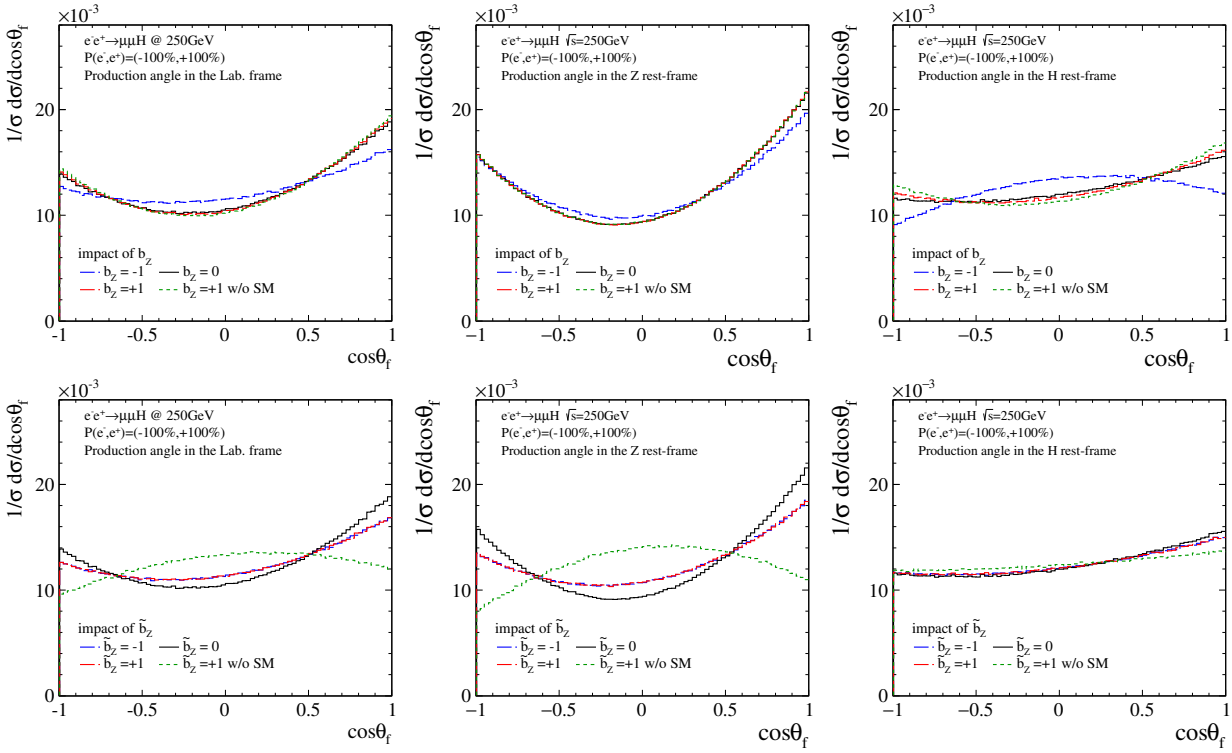

Figure 16: Distributions of polar angles of the final state lepton-minus in the Higgs-strahlung $e^+e^- \to ZH \to llH$ process at $\sqrt{s} = 250$ GeV with the complete beam polarization state of P(e^-, e^+)= (-100%,+100%). The calculation is done in the laboratory frame, the Z rest-frame, and the Higgs rest-frame. The difference of upper and lower row correspond to input parameters of b_Z and $\tilde{b}_Z$. Black and green lines show the exactly SM Higgs boson and completely the pseudo-scalar state, and blue and red lines are mixed states corresponding to $b_Z = \pm 1$ and $\tilde{b}_Z = \pm 1$.

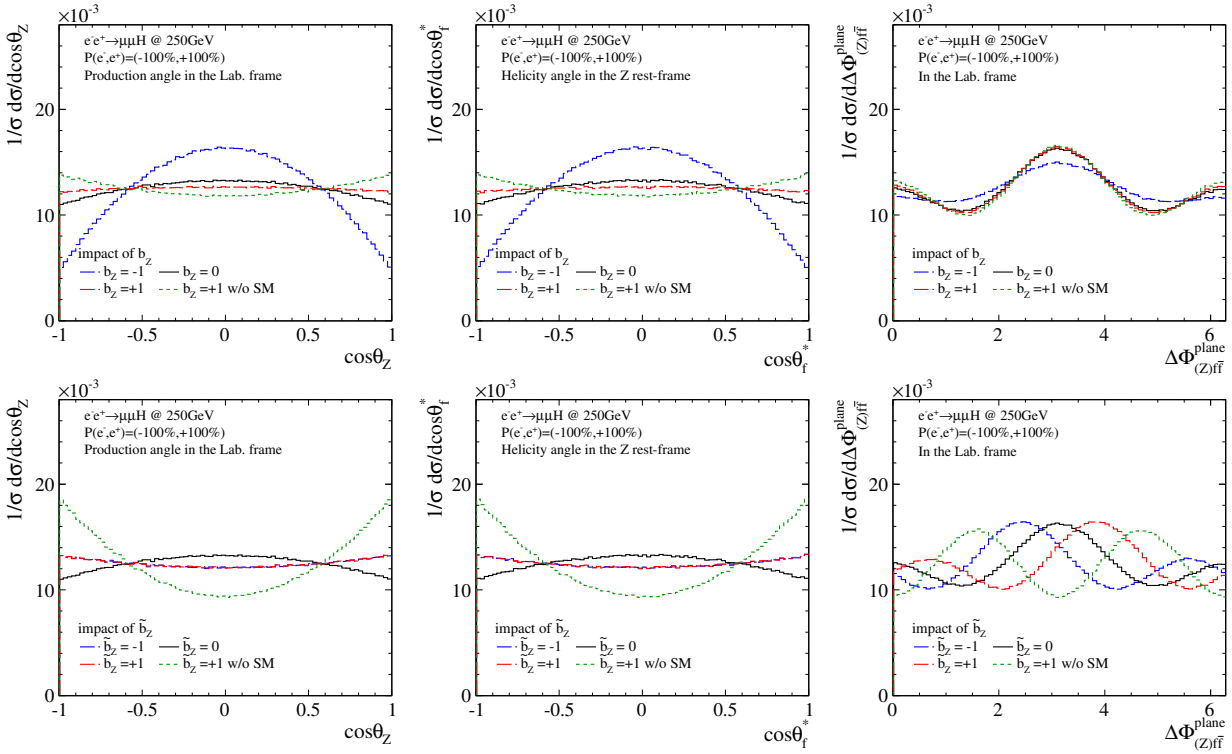

Figure 17: Distributions of polar angle of the Z boson in the laboratory frame ($\cos\theta_Z$), the helicity angle of the daughter fermion of the Z boson in the Z rest-frame ($\cos\theta^*_f$), and the angle between production planes $\Delta\Phi$ in the laboratory frame in the Higgs-strahlung $e^+e^- \to ZH \to llH$ process at $\sqrt{s} = 250$ GeV. The other explanations are same as the above.

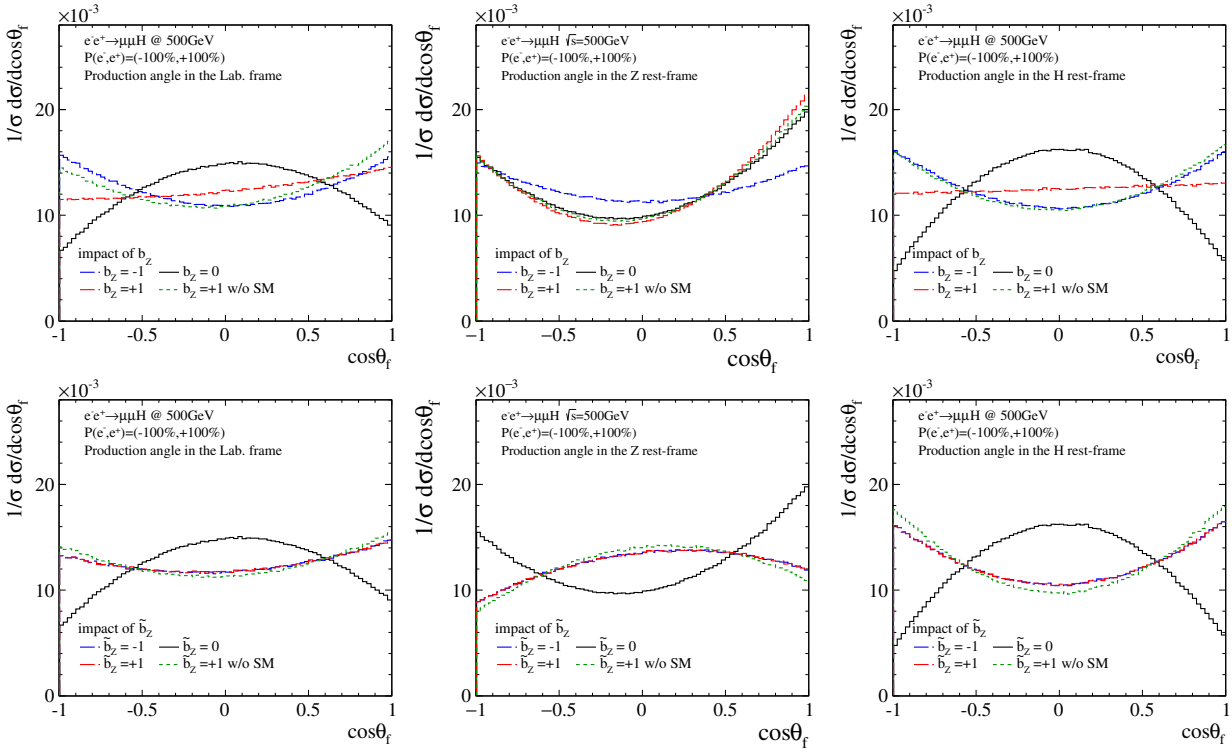

Figure 18: Distributions of polar angles of the final state lepton-minus in the Higgs-strahlung $e^+e^- \to ZH \to llH$ process at $\sqrt{s} = 500$ GeV with the complete beam polarization state of P(e^-, e^+)= (-100%,+100%). The calculation is done in the laboratory frame, the Z rest-frame, and the Higgs rest-frame. The difference of upper and lower row correspond to input parameters of b_Z and $\tilde{b}_Z$. Black and green lines show the exactly SM Higgs boson and completely the pseudo-scalar state, and blue and red lines are mixed states corresponding to $b_Z = \pm 1$ and $\tilde{b}_Z = \pm 1$.

Figure 19: Distributions of polar angle of the Z boson in the laboratory frame ($\cos\theta_Z$), the helicity angle of the daughter fermion of the Z boson in the Z rest-frame ($\cos\theta^*_f$), and the angle between production planes $\Delta\Phi$ in the laboratory frame in the Higgs-strahlung $e^+e^- \to ZH \to llH$ process at $\sqrt{s} = 500$ GeV. The other explanations are same as the above.

4.1.2 The Higgs-strahlung $e^+e^- \to Zh \to q\bar{q}H$ at $\sqrt{s}$ =250 and 500 GeV

In the case of a hadronic decay reaction of the $Zh \to q\bar{q}H$ channel, the angle $\Delta\Phi$ will not be able to fully reconstructed with the range of [0–2π] if any jet charge identification is not implemented in the reconstruction chain, which is illustrated in Fig. 20. Therefore, the sensitivity that $\Delta\Phi$ has becomes half [0–π] by folding the $\Delta\Phi$ distribution with $\Delta\Phi - \pi$ when $\Delta\Phi$ exceeds π.

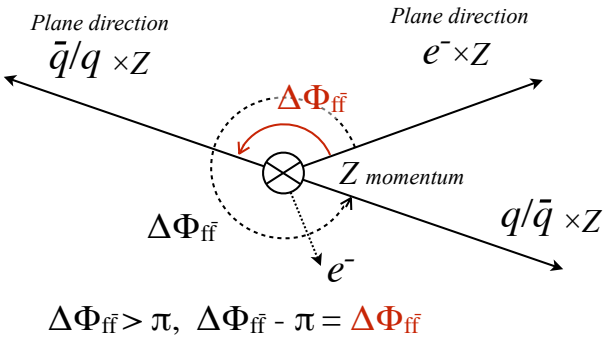

Figure 20: A illustration of $\Delta\Phi$ in the $Zh \to q\bar{q}H$ channel. $\Delta\Phi$ can be reconstructed within the range of [0–π] if no jet charge identification is imposed.

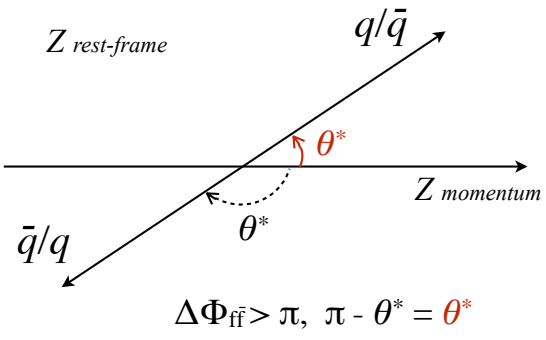

Figure 21: A illustration of the helicity angle θ^*_f in the $Zh \to q\bar{q}H$ channel. The angle can be given with the range of [0–π] when folding it together with $\Delta\Phi$.

When calculating the helicity angle of a daughter fermion coming from the outgoing Z boson $\cos\theta^*_f$, it is necessary to identify the charge to distinguish the fermion from the anti-fermion. However, a hemisphere is already distinguished by folding the information of $\Delta\Phi$. Therefore, the helicity angle $\cos\theta^*_f$ can be identified with a full range of [0–π] by folding θ^*_f with $\theta^*_f - \pi$ together with $\Delta\Phi$ when $\Delta\Phi$ is folded with $\Delta\Phi - \pi$. Such situation can be seen in Fig. 21.

Since the neutral current interaction through a Z boson has the V-A structure: $(c_V - c_A\gamma^5)$, the formula of coupling between a quark and the Z boson is different from the one of a lepton case[8]. Therefore, the kinematics and consequently degree of variation must be different. Fig. 22 and Fig. 23 show one-dimensional distributions as illustrations in the hadronic $Zh \to q\bar{q}H$ channel of the Higgs-strahlung process at $\sqrt{s}$ =250 GeV. Fig. 24 and Fig. 25 show the variations depending on the parameters at $\sqrt{s}$ =500 GeV.

[8]The Lagrangian describing interaction of eeZ is given as

$$\mathcal{L}_{eeZ} = \frac{g_2}{\cos\theta_w}\bar{\psi}\gamma^\mu\frac{c_V - c_A\gamma^5}{2}\psi Z_\mu$$

The differential decay rate can be calculated as

$$\begin{aligned} d\Gamma &= \frac{1}{2M_Z}\sum_{\text{spin}}|\mathcal{M}|^2 d\Phi_2 \ , \\ \frac{d\Gamma}{d\cos\theta} &= \frac{1}{32\pi M_Z}\left[\left(\frac{c_V^2 - c_A^2}{2}\right)^2(1+\cos\theta)^2 + \left(\frac{c_V^2 + c_A^2}{2}\right)^2(1-\cos\theta)^2\right] \\ \frac{d\Gamma}{d\cos\theta} &= \frac{1}{32\pi M_Z}\left[g_Z^2 Q\sin^4\theta_w(1+\cos\theta)^2 + \frac{1}{4}g_Z^2(I_3 - Q\sin^2\theta_w)^2(1-\cos\theta)^2\right] \end{aligned}$$

where c_V and c_A are respectively given as $-g_Z/2(I_3 - 2Q\sin^2\theta_w)$ and $-g_Z/2(I_3)$. Depending on charge and weak-isospin of fermions, the shapes must vary.

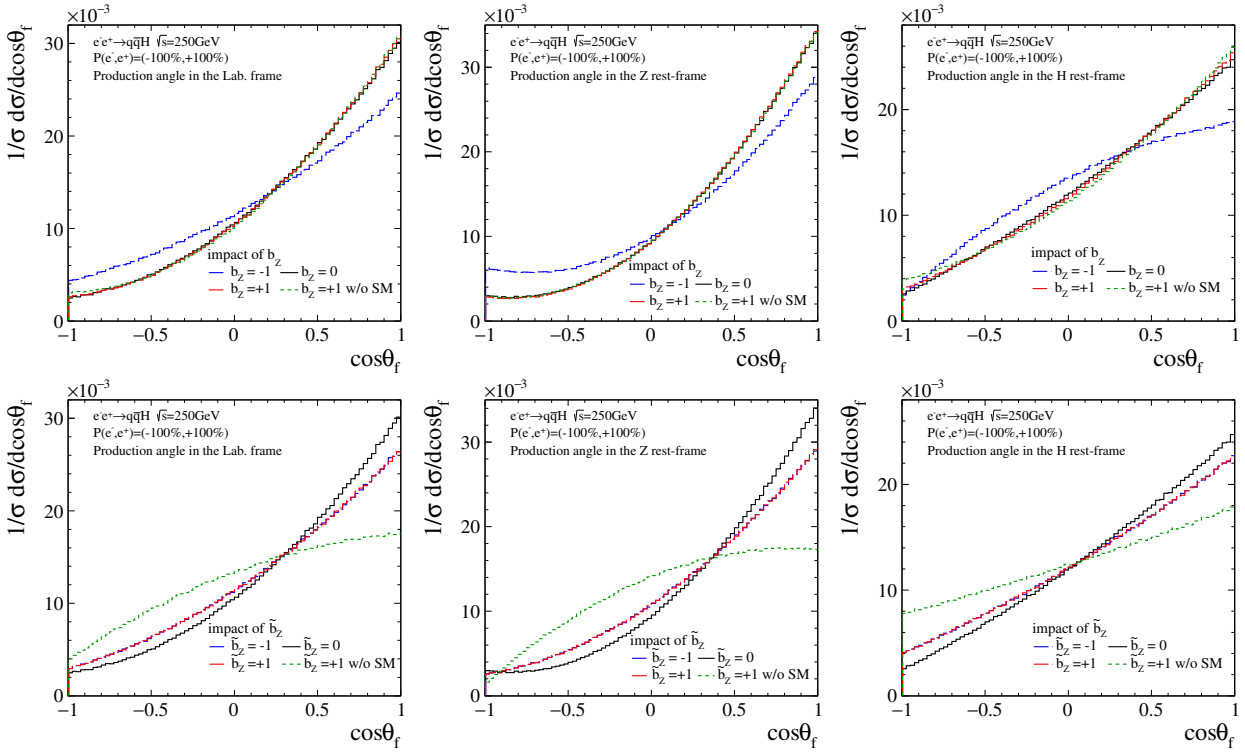

Figure 22: Distributions of polar angles of the final state fermion in the Higgs-strahlung $e^+e^- \to ZH \to q\bar{q}H$ process at $\sqrt{s} = 250$ GeV with the complete beam polarization state of P(e^-, e^+)= (-100%,+100%). The calculation is done in the laboratory frame, the Z rest-frame, and the Higgs rest-frame. The difference of upper and lower row correspond to input parameters of b_Z and $\tilde{b}_Z$. Black and green lines show the exactly SM Higgs boson and completely the pseudo-scalar state, and blue and red lines are mixed states corresponding to $b_Z = \pm 1$ and $\tilde{b}_Z = \pm 1$.

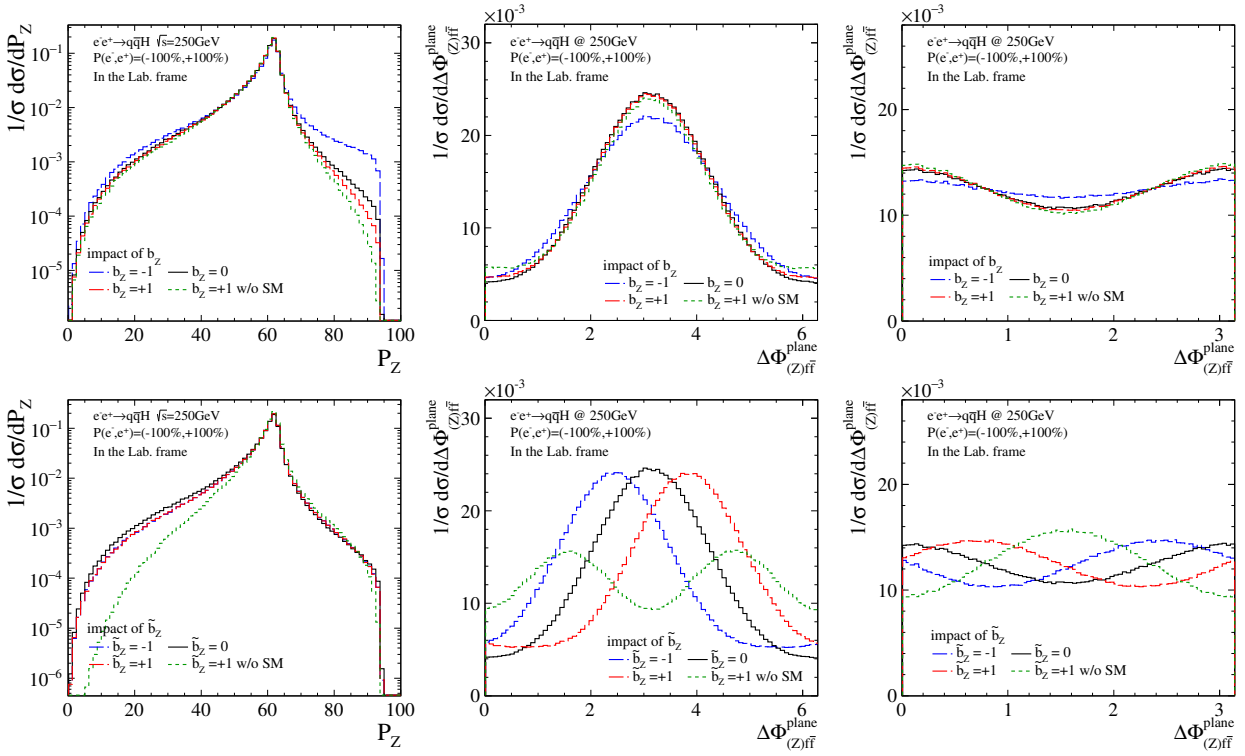

Figure 23: Distributions of momentum of the Z boson in the laboratory frame (P_Z), (middle) the full angle between production planes $\Delta\Phi$ in the laboratory frame in the Higgs-strahlung $e^+e^- \to ZH \to q\bar{q}H$ process at $\sqrt{s} = 250$ GeV, and (right) the folded angle with $\Delta\Phi - \pi$ if $\Delta\Phi$ exceeds π. The other explanations are same as the others.

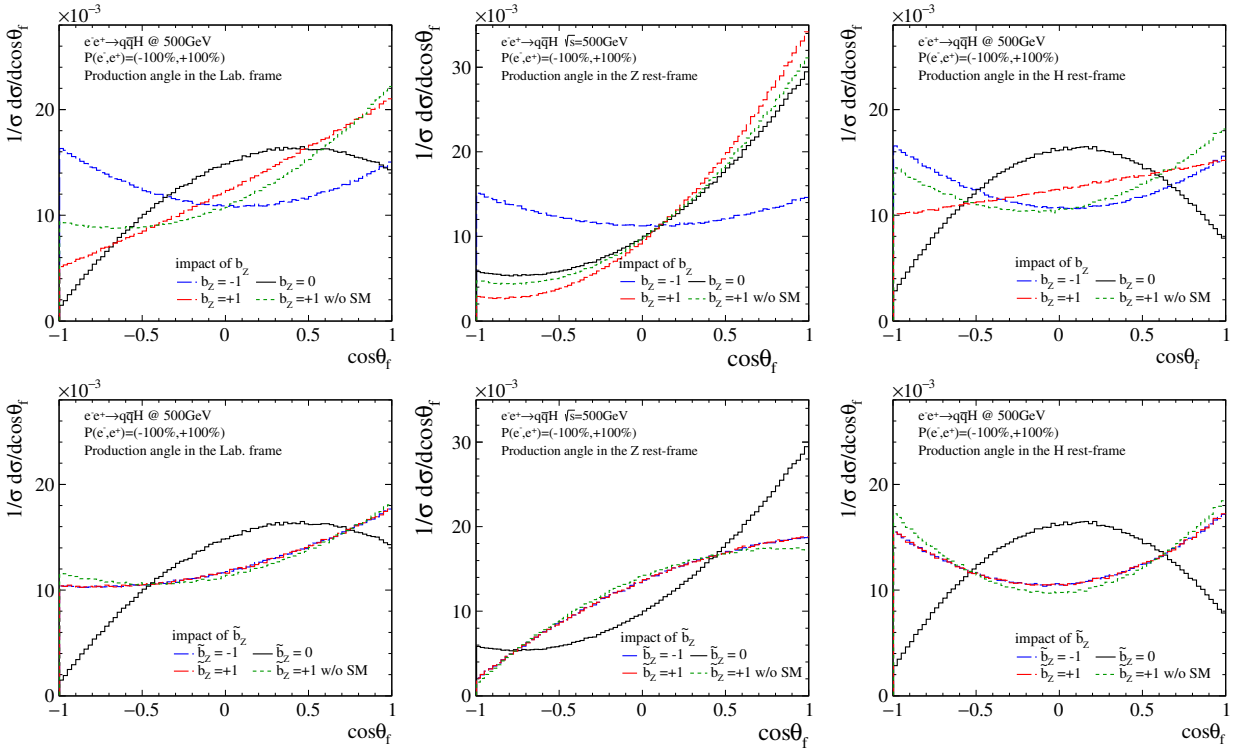

Figure 24: Distributions of polar angles of the final state fermion in the Higgs-strahlung $e^+e^- \to ZH \to q\bar{q}H$ process at $\sqrt{s} = 500$ GeV with the complete beam polarization state of P(e^-, e^+)= (-100%,+100%). The calculation is done in the laboratory frame, the Z rest-frame, and the Higgs rest-frame. The difference of upper and lower row correspond to input parameters of b_Z and $\tilde{b}_Z$. Black and green lines show the exactly SM Higgs boson and completely the pseudo-scalar state, and blue and red lines are mixed states corresponding to $b_Z = \pm 1$ and $\tilde{b}_Z = \pm 1$.

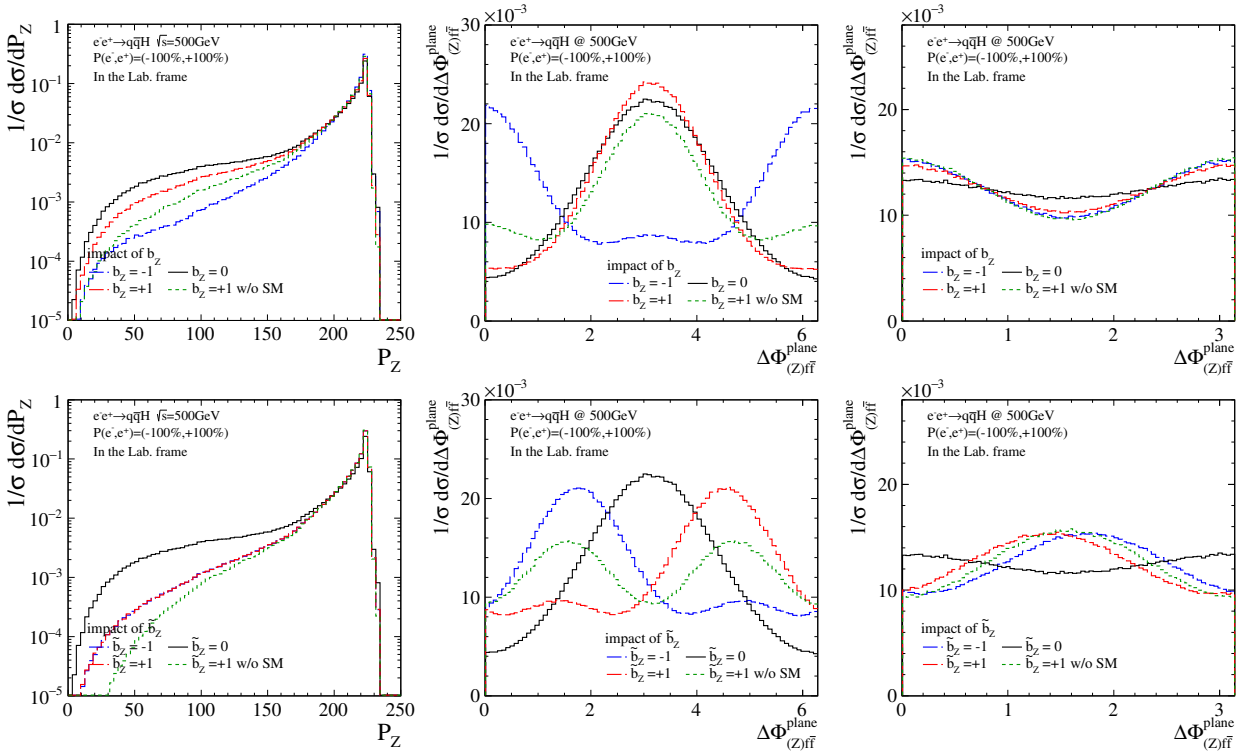

Figure 25: Distributions of momentum of the Z boson in the laboratory frame (P_Z), (middle) the full angle between production planes $\Delta\Phi$ in the laboratory frame in the Higgs-strahlung $e^+e^- \to ZH \to q\bar{q}H$ process at $\sqrt{s} = 500$ GeV, and (right) the folded angle with $\Delta\Phi - \pi$ if $\Delta\Phi$ exceeds π. The other explanations are same as the others.

4.1.3 The ZZ-fusion $e^+e^- \to e^+e^-H$ at $\sqrt{s}$ =250 and 500 GeV

The ZZ-fusion process will be also able to provide a clear signature on the $\Delta\Phi$ distribution which is given in Fig. 27 if the anomalous ZZH couplings exist. When focusing on the b_Z term in Eq. (12) and defining four-vectors for both of the virtual Z bosons as $Z_1(q_1, \epsilon_1)$ and $Z_2(q_2, \epsilon_2)$ as illustrated in Fig. 26, the structure of the matrix element can be described as

$$\mathcal{M}^{ZZf}_{a_Z} = \epsilon_{1\mu}\epsilon_2^{\mu} = -(\boldsymbol{\epsilon}_1 \cdot \boldsymbol{\epsilon}_2) \tag{16}$$

$$\begin{aligned}\mathcal{M}^{ZZf}_{b_Z} &= -2\big[(q_1q_2)(\epsilon_1\epsilon_2) - (q_1\epsilon_2)(q_2\epsilon_1)\big] \\ &= -2\Big[\Big(\frac{1}{2}(q_1+q_2)^2 - q_1^2 - q_2^2\Big)(-\boldsymbol{\epsilon}_1 \cdot \boldsymbol{\epsilon}_2) - (\boldsymbol{q}_1 \cdot \boldsymbol{\epsilon}_2)(\boldsymbol{q}_2 \cdot \boldsymbol{\epsilon}_1)\Big] \\ &= (q_h^2 - 2q_1^2 - 2q_2^2)(\boldsymbol{\epsilon}_1 \cdot \boldsymbol{\epsilon}_2) + 2(\boldsymbol{q}_1 \cdot \boldsymbol{\epsilon}_2)(\boldsymbol{q}_2 \cdot \boldsymbol{\epsilon}_1)\end{aligned} \tag{17}$$

where q_h denotes four-momentum of the Higgs boson. The structure implies that the polarization of both Z_1 and Z_2 are affected by the four-momenta of the Higgs boson and the virtual Z bosons, which will propagate to angular distributions of final state particles such as an electron, a positron, and the Higgs boson. In addition the he structure indicate that the energy-momentum of the Higgs boson will vary depending on the parameters. These behaviors according to the parameters b_Z and $\tilde{b}_Z$ can be seen in Fig. 28, Fig. 29 and Fig. 30, Fig. 31, which are respectively $\sqrt{s}$ =250 GeV and 500 GeV.

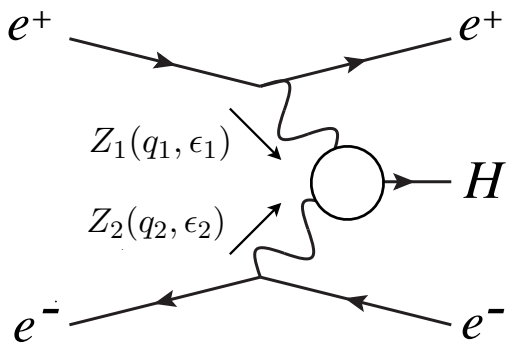

Figure 26: A diagram showing the ZZ-fusion process, and definition of virtual Z bosons: Z_1 and Z_2 .

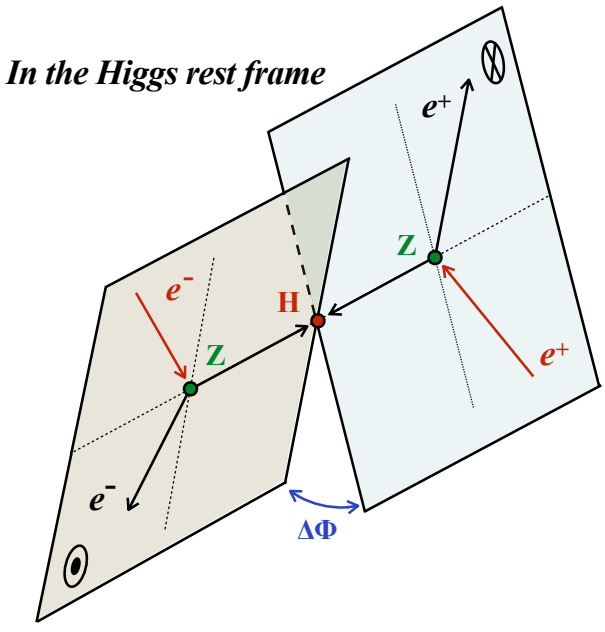

Figure 27: A schematic view of the ZZ-fusion process. $\Delta\Phi_{f\bar{f}}$ is defined as the angle between two production planes.

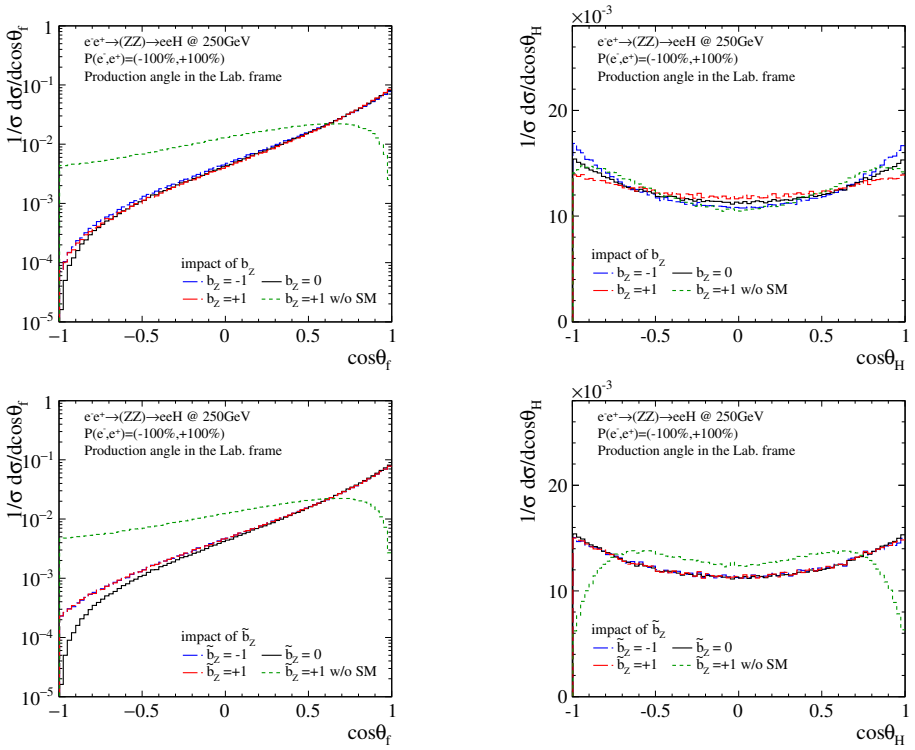

Figure 28: Distributions of the polar angle of the final state electron and the polar angle of the Higgs boson in the laboratory frame in the ZZ-fusion $e^+e^- \to ZZ \to e^+e^-H$ process at $\sqrt{s} = 250$ GeV with the complete beam polarization state of P(e^-, e^+)= (-100%,+100%). The difference of upper and lower row correspond to input parameters of b_Z and $\tilde{b}_Z$. Black and green lines show the exactly SM Higgs boson and completely the pseudo-scalar state, and blue and red lines are mixed states corresponding to $b_Z = \pm 1$ and $\tilde{b}_Z = \pm 1$.

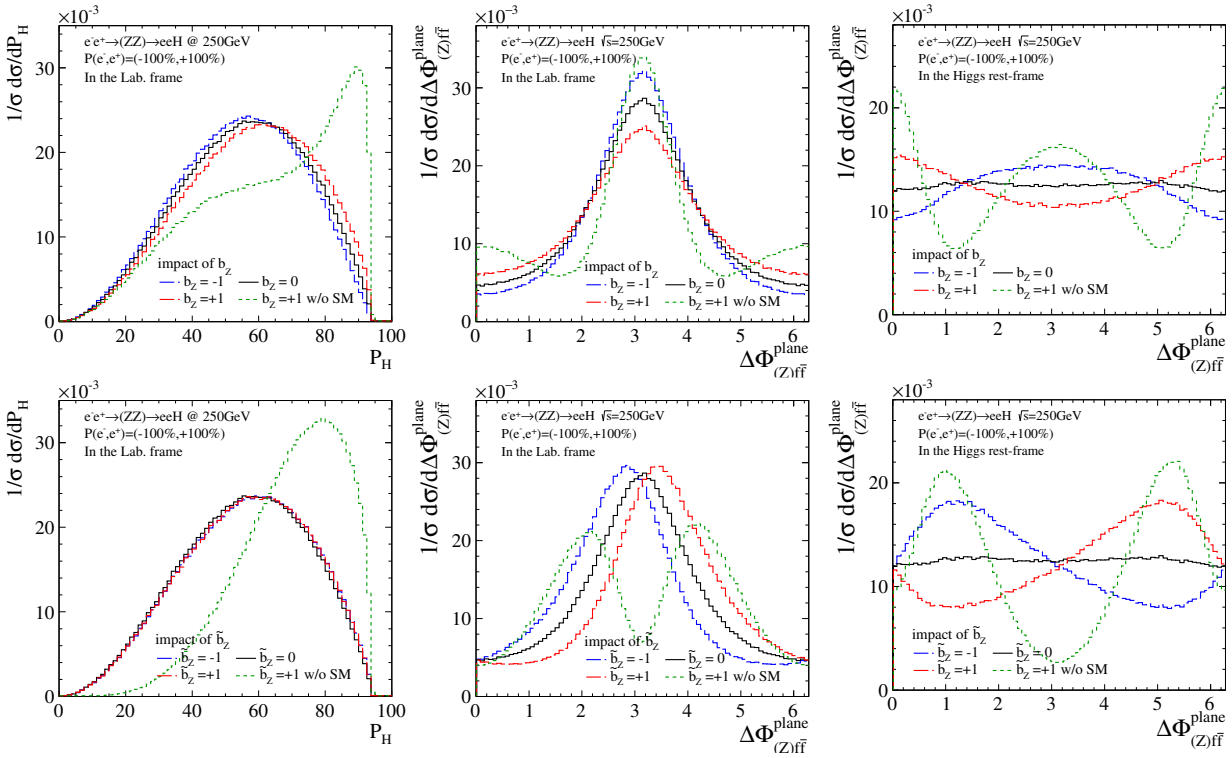

Figure 29: Distributions of the momentum of the Higgs boson and the angle between production planes $\Delta\Phi$ in the laboratory frame and the Higgs rest-frame in the ZZ-fusion $e^+e^- \to ZZ \to e^+e^-H$ process at $\sqrt{s} = 250$ GeV. The other explanations are same as the above.

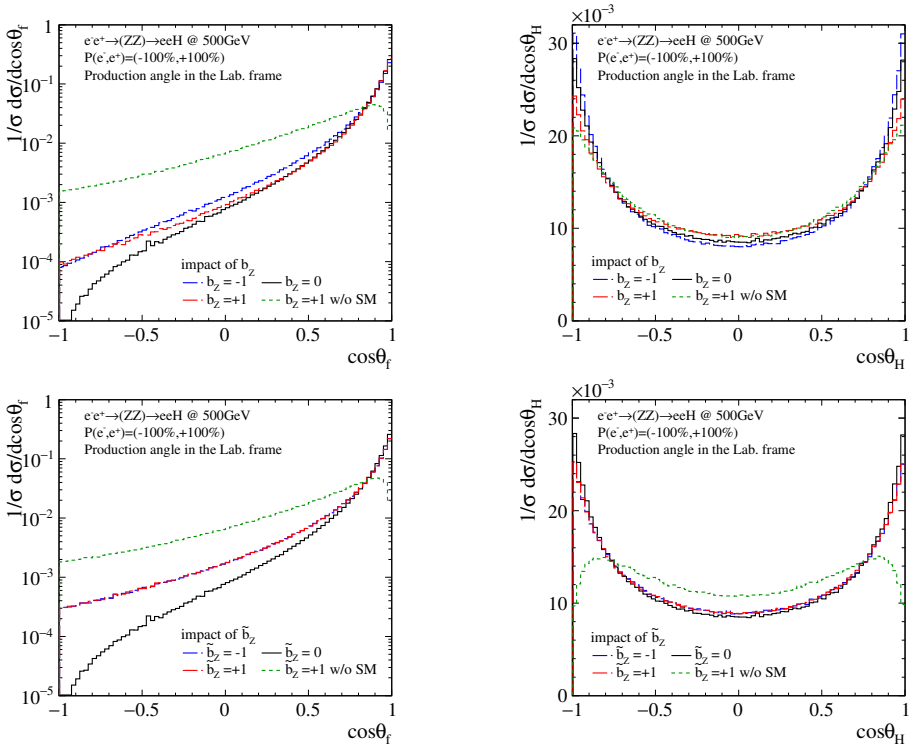

Figure 30: Distributions of the polar angle of the final state electron and the polar angle of the Higgs boson in the laboratory frame in the ZZ-fusion $e^+e^- \to ZZ \to e^+e^-H$ process at $\sqrt{s} = 500$ GeV with the complete beam polarization state of P(e^-, e^+)= (-100%,+100%). The difference of upper and lower row correspond to input parameters of b_Z and $\tilde{b}_Z$. Black and green lines show the exactly SM Higgs boson and completely the pseudo-scalar state, and blue and red lines are mixed states corresponding to $b_Z = \pm 1$ and $\tilde{b}_Z = \pm 1$.

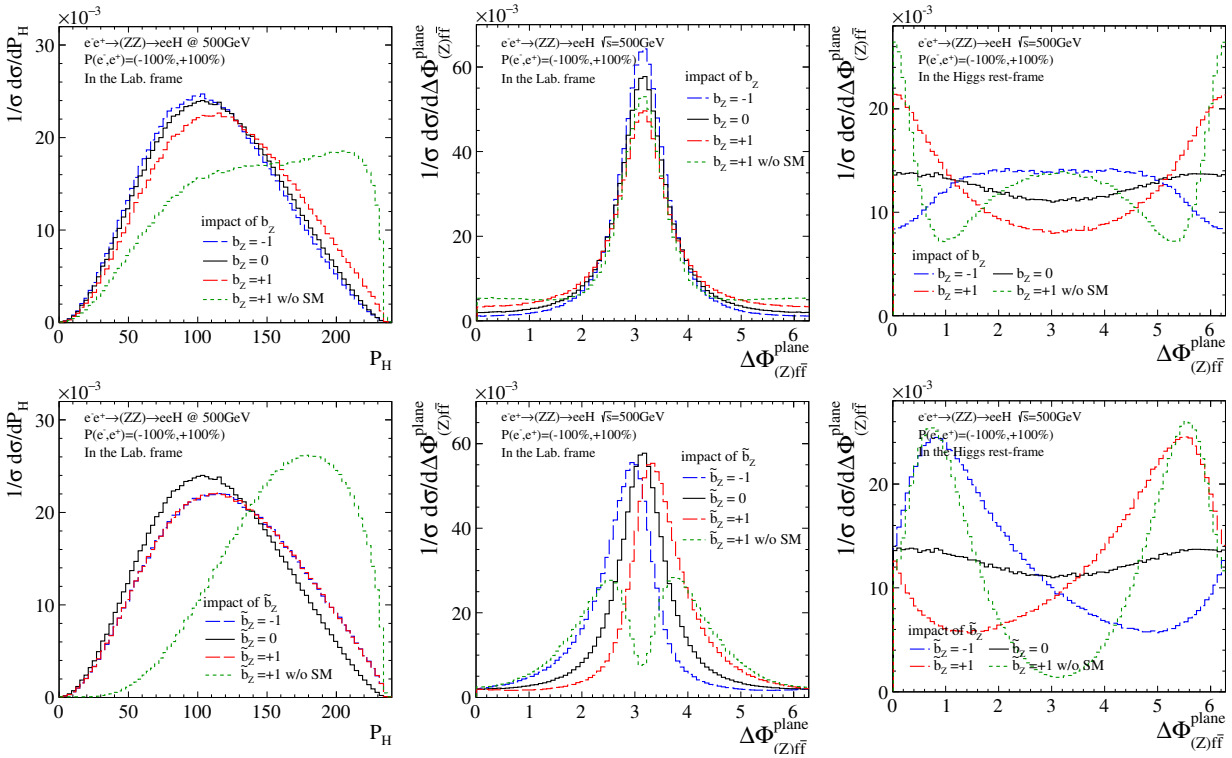

Figure 31: Distributions of the momentum of the Higgs boson and the angle between production planes $\Delta\Phi$ in the laboratory frame and the Higgs rest-frame in the ZZ-fusion $e^+e^- \to ZZ \to e^+e^-H$ process at $\sqrt{s} = 500$ GeV. The other explanations are same as the above.

4.2 Observables for anomlaous WWH couplings

4.2.1 The WW-fusion $e^+e^- \to \nu_e\bar{\nu}_e h$ at $\sqrt{s}$ =250 and 500 GeV

In the WW-fusion process the observables for identifying the anomalous couplings are same with ones of the ZZ-fusion process except $\Delta\Phi$ due to missing neutrinos in the final state. Fig. 32 and Fig. 33 illustrate the variation of the distribution of the observables at $\sqrt{s}$ =250 GeV and 500 GeV where the parameters set to be ± 2.

4.2.2 The Higgs decay $H \to WW^*$

The $H \to WW^*$ decay process can also give sizable information for testing the anomalous WWH couplings. Focusing on the b_W term in Eq. (13) and defining the four-vectors as $W_1(q_1, \epsilon_1)$ and $W_2(q_2, \epsilon_2)$ like Fig. 34 assuming the Higgs rest-frame in which the momenta of both W_1 and W_2 are given with back-to-back, the structure can be calculated as

$$\begin{aligned}
\mathcal{M}_{b_Z}^{WWd} &= -2\big[(q_1q_2)(\epsilon_1\epsilon_2) - (q_1\epsilon_2)(q_2\epsilon_1)\big] \\
&= -2\Big[\Big(\frac{1}{2}(q_1+q_2)^2 - q_1^2 - q_2^2\Big)(-\boldsymbol{\epsilon}_1\cdot\boldsymbol{\epsilon}_2) - (\boldsymbol{q}_1\cdot\boldsymbol{\epsilon}_2)(-\boldsymbol{q}_1\cdot\boldsymbol{\epsilon}_1)\Big] \\
&= (m_h^2 - 2q_1^2 - 2q_2^2)(\boldsymbol{\epsilon}_1\cdot\boldsymbol{\epsilon}_2)
\end{aligned}$$

where the second term in the second line would be 0 by considering $\boldsymbol{q}_1 = -\boldsymbol{q}_2$ and the Lorentz condition $q\epsilon = 0$. This structure will affect polarization of the W bosons and helicity angle of the decay products and the four-momenta of related particles as well. As discusses in the first

[10] In the plot "Azimuth angle" is written, but it is actually opening angle between X-axis and momentum direction of the Higgs boson, which partially includes polar angle of the Higgs boson.

[0] By the definition of the field strength tensor $F_{\mu\nu}$, the anomalous structure $F_{\mu\nu}F^{\mu\nu}$ in the effective Lagrangian can be decomposed into,

$$\begin{aligned}
F_{\mu\nu}F^{\mu\nu} &= (\partial_{1\mu}A_{1\nu} - \partial_{1\nu}A_{1\mu})(\partial_2{}^{\mu}A_2{}^{\nu} - \partial_2{}^{\nu}A_2{}^{\mu}) \\
&= (\partial_1\partial_2)(A_1A_2) - (\partial_1A_2)(A_1\partial_2) - (\partial_1A_2)(A_1\partial_2) + (\partial_1\partial_2)(A_1A_2) \\
&= 2\ [\ (\partial_1\partial_2)(A_1A_2) - (\partial_1A_2)(A_1\partial_2)\ ] \\
(F_{\mu\nu}F^{\mu\nu})^2 &= 4\ [\ (\partial_1\partial_2)(A_1A_2) - (\partial_1A_2)(A_1\partial_2)\ ]^2 \\
&= 4\ [\ i^2(q_1q_2)(\epsilon_1\epsilon_2) - i^2(q_1\epsilon_2)(\epsilon_1q_2)\ ]^2 \to \text{ several terms with different signs.}
\end{aligned}$$

where the square of the structure is taken since the contribution of amplitude can be given with the square of the structure. Derivatives and field potentials are translated into four-momenta (quantization) and four-polarization vectors in going to the last line. In contrast, the structure $F_{\mu\nu}\tilde{F}^{\mu\nu}$ can be,

$$\begin{aligned}
F_{\mu\nu}\tilde{F}^{\mu\nu} &= \frac{1}{2}\epsilon^{\mu\nu\rho\sigma}F_{\mu\nu}F_{\rho\sigma} \\
&= \frac{1}{2}\epsilon^{\mu\nu\rho\sigma}(\partial_{1\mu}A_{1\nu} - \partial_{1\nu}A_{1\mu})(\partial_{2\rho}A_{2\sigma} - \partial_{2\sigma}A_{2\rho}) \\
&= \frac{1}{2}\epsilon^{\mu\nu\rho\sigma}[(\partial_{1\mu}A_{1\nu})(\partial_{2\rho}A_{2\sigma}) - (\partial_{1\mu}A_{1\nu})(\partial_{2\sigma}A_{2\rho}) - (\partial_{1\nu}A_{1\mu})(\partial_{2\rho}A_{2\sigma}) + (\partial_{1\nu}A_{1\mu})(\partial_{2\sigma}A_{2\rho})] \\
&= \frac{1}{2}\epsilon^{\mu\nu\rho\sigma}4(\partial_{1\mu}A_{1\nu})(\partial_{2\rho}A_{2\sigma}) \\
(F_{\mu\nu}\tilde{F}^{\mu\nu})^2 &= 4\epsilon^{\mu\nu\rho\sigma}\epsilon^{abcd}(\partial_{1\mu}A_{1\nu})(\partial_{2\rho}A_{2\sigma})(\partial_{1a}A_{1b})(\partial_{2c}A_{2d}) \\
&= 4g^{\mu\zeta}g^{\nu\eta}g^{\rho\theta}g^{\sigma\gamma}\delta^{abcd}_{\zeta\eta\theta\gamma}(\partial_{1\mu}A_{1\nu})(\partial_{2\rho}A_{2\sigma})(\partial_{1a}A_{1b})(\partial_{2c}A_{2d}) \\
&= 4(\partial_1{}^{\zeta}A_1{}^{\eta})(\partial_2{}^{\theta}A_2{}^{\gamma})\delta^{abcd}_{\zeta\eta\theta\gamma}(\partial_{1a}A_{1b})(\partial_{2c}A_{2d}) \qquad (18) \\
&= 4(\partial_1\partial_1)(A_1A_1)(\partial_2\partial_2)(A_2A_2) \\
&= 4\ i^2q_1^2\epsilon_1^2\ i^2q_2^2\epsilon_2^2 \quad \to \text{ one term with positive sign.}
\end{aligned}$$

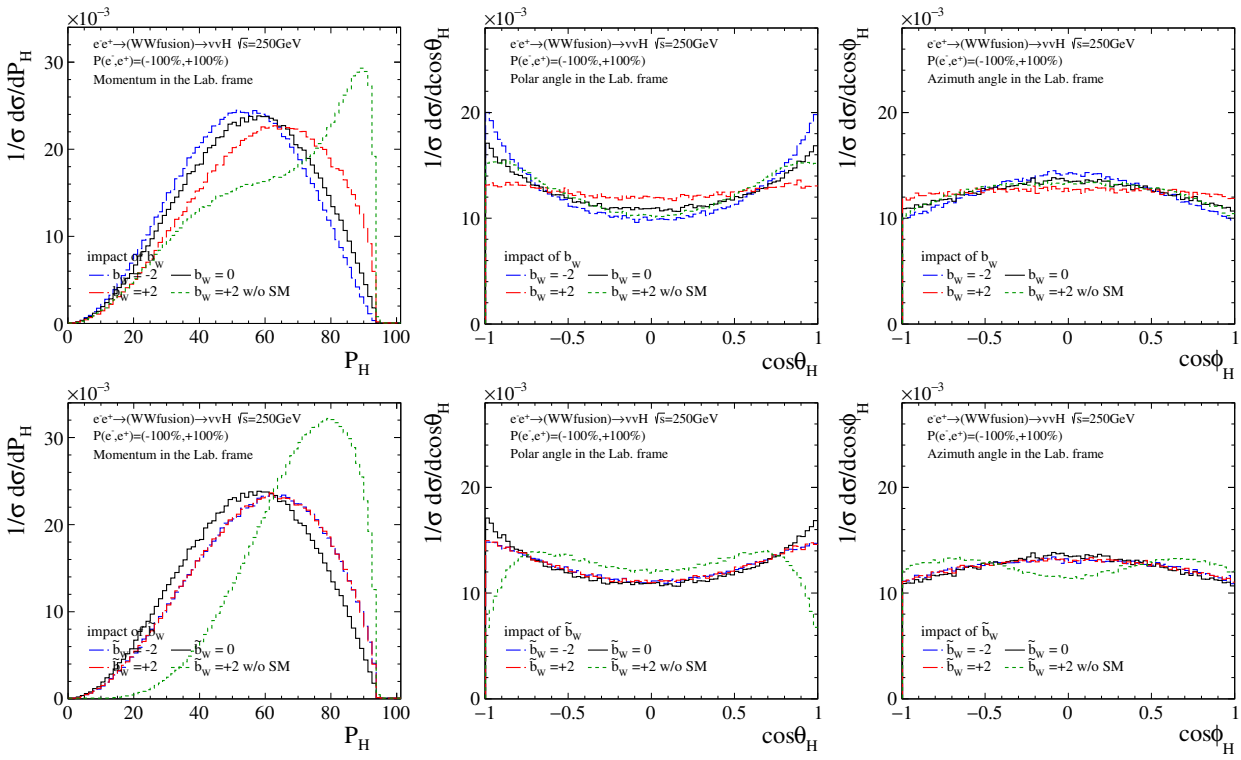

Figure 32: Distributions of the momentum, polar angle of the Higgs boson, and angle between X-axis and momentum direction of the Higgs boson[10]in the laboratory frame of the WW-fusion $e^+e^- \to WW \to \nu\bar{\nu}H$ process at $\sqrt{s} = 250$ GeV. The difference of upper and lower rows are input parameters of b_W and $\tilde{b}_W$. Black and green lines show the exactly SM Higgs boson and completely the pseudo-scalar state, and blue and red lines are mixed states corresponding to $b_W = \pm 2$ and $\tilde{b}_W = \pm 2$.

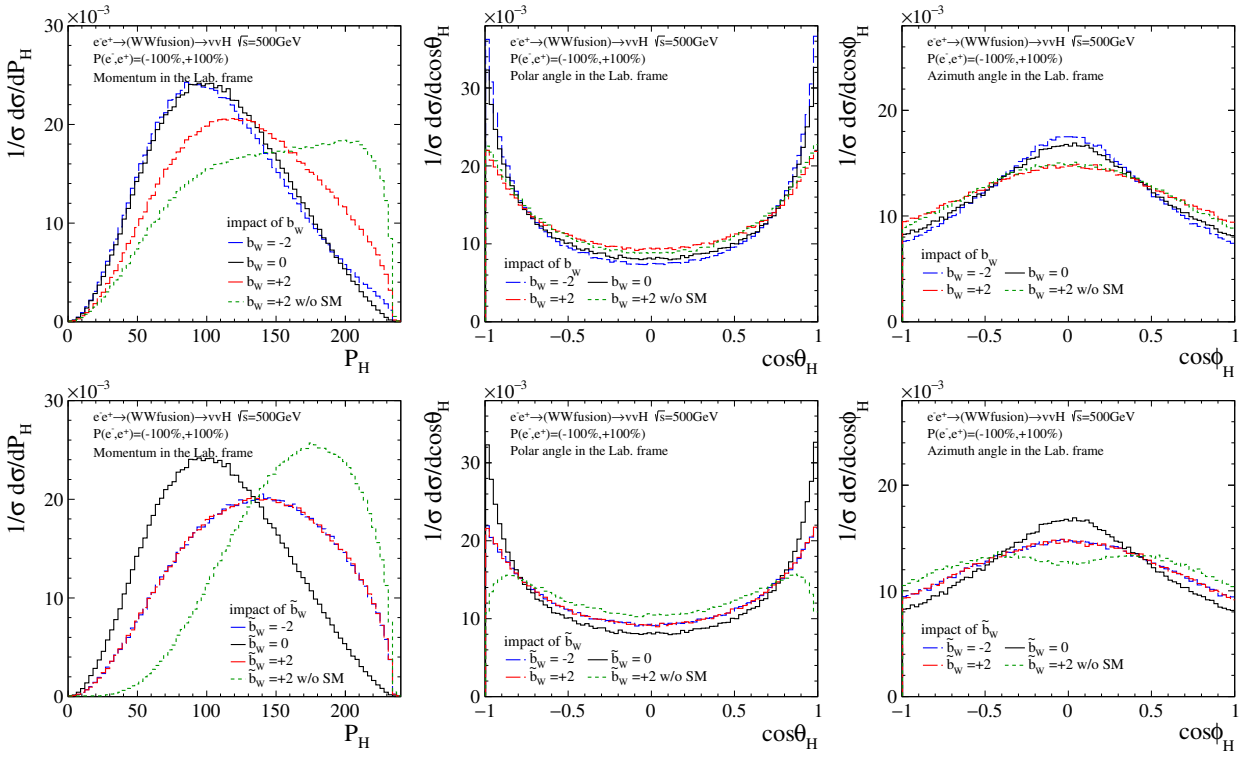

Figure 33: Kinematical distributions of the WW-fusion $e^+e^- \to WW \to \nu\bar{\nu}H$ process at $\sqrt{s} = 500$ GeV. The explanations are given in the above caption.

subsection the $\Delta\Phi$ distribution is one of the strong observable for testing the couplings, which is illustrated in Fig. 35.

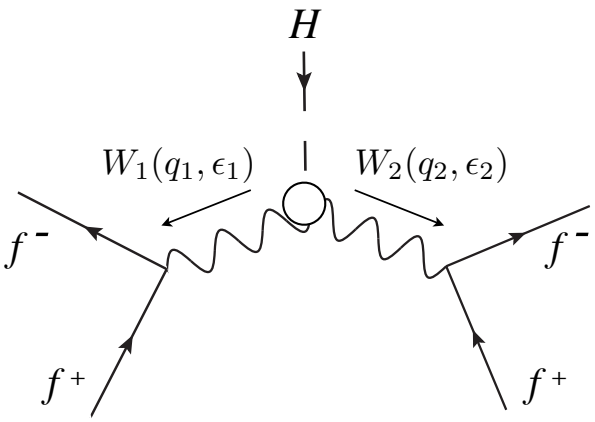

Figure 34: A diagram showing the $H \to WW$ decay process, and definition of W_1 and W_2.

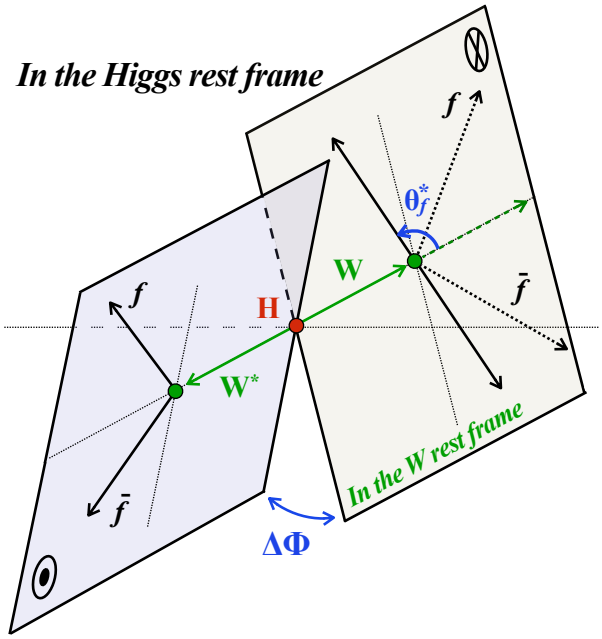

Figure 35: A schematic view to define angles in the $H \to WW$ decay process. Assuming the Higgs rest-frame, a helicity angle of a daughter fermion of the W boson which is θ_f^* and an angle constructed with decay planes which is $\Delta\Phi$ are defined.

Several useful kinematical information for testing the anomalous WWH couplings are listed below, and those one-dimensional distributions are illustrated in Fig. 36 and Fig. 37.

- A momentum distribution of the W boson in the Higgs rest-frame decaying from the Higgs boson must vary depending on the parameters.
- Since the polarization of the W bosons are affected by the parameters, a helicity angle distribution of a daughter fermion decaying from the W bosons, which is defined an angle between a momentum direction of the W boson in the Higgs rest-frame and a momentum direction of its daughter fermion boosted in the W rest-frame, must also change. If no algorithm identifying jet charged is implemented, the helicity angle must be folded.
- The angle between decay planes, which is denoted with $\Delta\Phi$ and constructed by a fermion from one W and an anti-fermion from another W with a momentum direction of one W as a plane axis in the Higgs rest-frame, must vary. In the case that jet charges and flavors are not identified, the sensitivity of $\Delta\Phi$ becomes minimum angle with the range of [0–$\pi/2$] by folding it: if $\Delta\Phi$ exceeds π, $\Delta\Phi$ must be folded with $\Delta\Phi - \pi$, and, if it still exceeds $\pi/2$, it must additionally be folded with $\pi - \Delta\Phi$, which is the minimum angle constructed with two jets from each W.
  When the final state is the $WW \to qql^+\nu$ process, a final state lepton can be identified as a fermion or an anti-fermion. In such a case, $\Delta\Phi$ must be folded with $\Delta\Phi = \Delta\Phi - \pi$ if $\Delta\Phi$ exceeds π. Similarly, in the case that the final state has two heavy flavor quarks in a decay $WW \to c\bar{q}q\bar{c}$, it is not clear to distinguish which one is a fermion or an anti-fermion. In such a case, $\Delta\Phi$ must be folded with $\Delta\Phi = 2\pi - \Delta\Phi$ when $\Delta\Phi$ exceeds π.

These are illustrated in Fig. 38 and Fig. 39. Fig. 40 and Fig. 41 show variation of the $\Delta\Phi$ distributions after folding it.

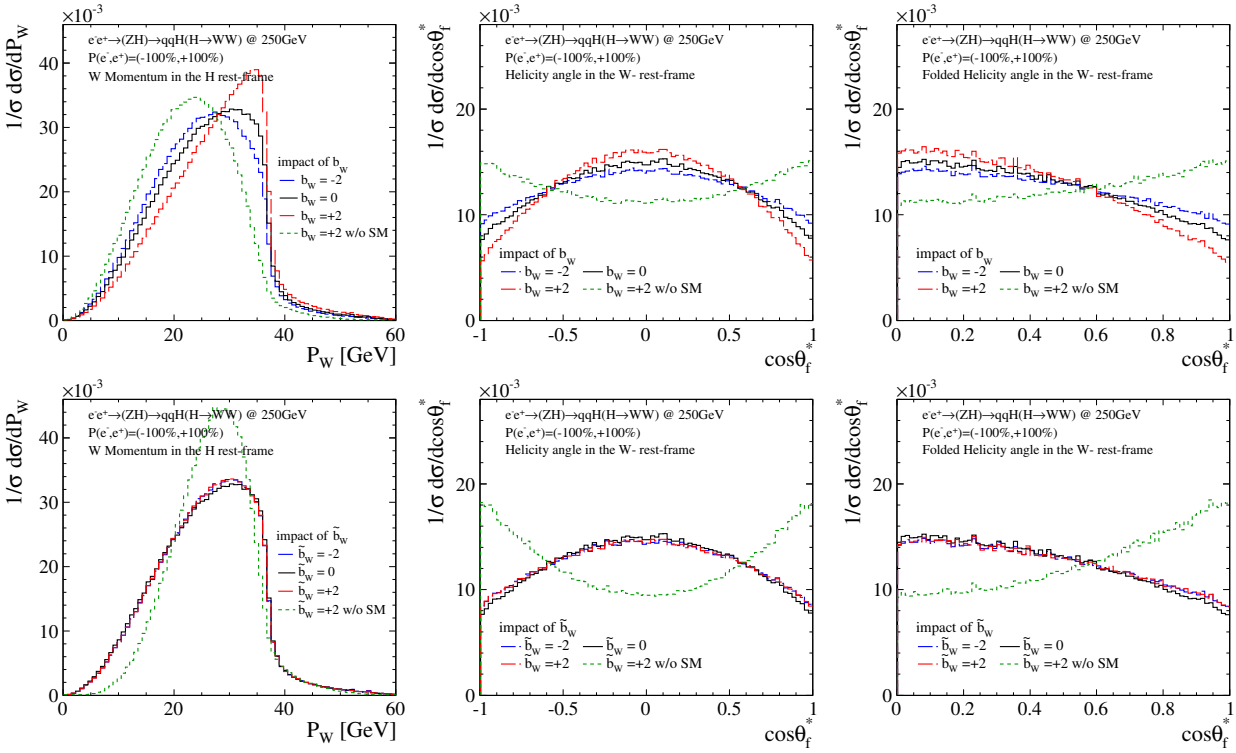

Figure 36: Distributions of the momentum of the W boson in the Higgs rest-frame P_W, the helicity angle of the daughter fermion of the W boson, and the folded helicity angle in the W rest-frame in the Higgs decay $H \to WW$ process. The difference of upper and lower row correspond to input parameters of b_W and $\tilde{b}_W$. Black and green lines show the exactly SM Higgs boson and completely the pseudo-scalar state, and blue and red lines are mixed states corresponding to $b_W = \pm 2$ and $\tilde{b}_W = \pm 2$.

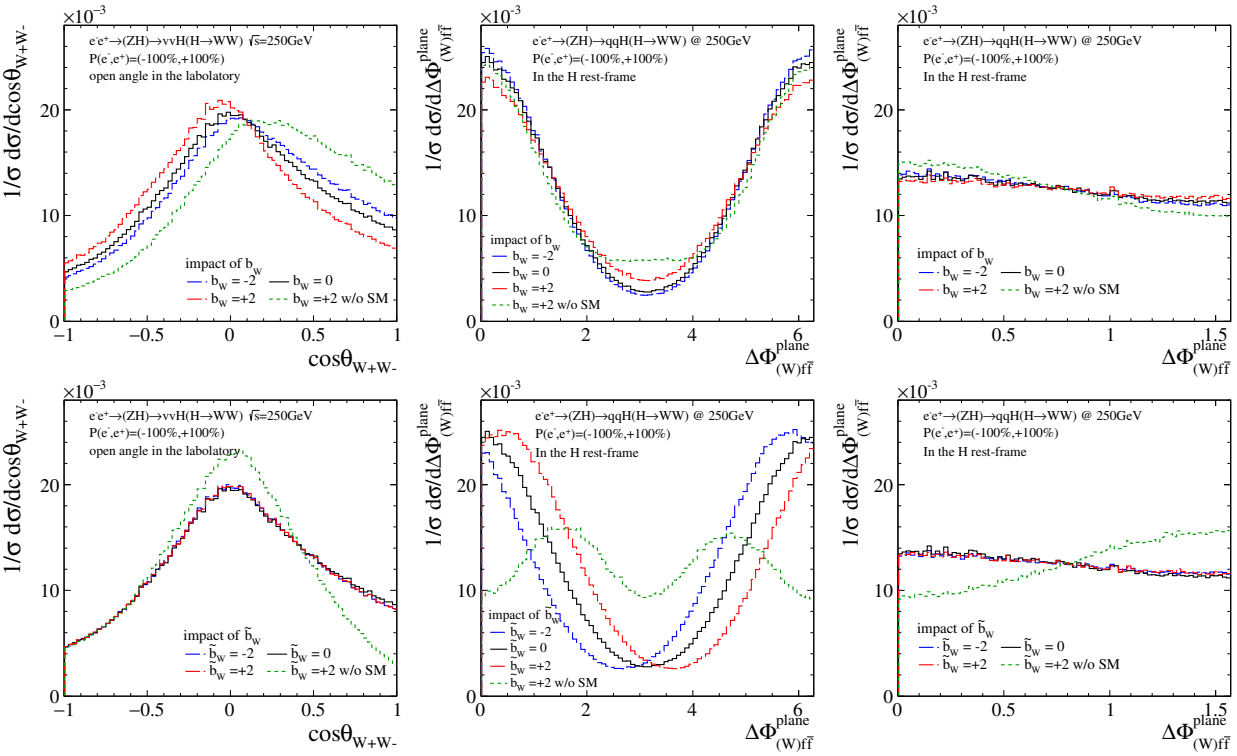

Figure 37: Distributions of the opening angle of the W bosons in the laboratory frame, and the angle between decay planes $\Delta\Phi$ in the Higgs rest-frame in the Higgs decay $H \to WW$ process. The other explanations are same as the above.

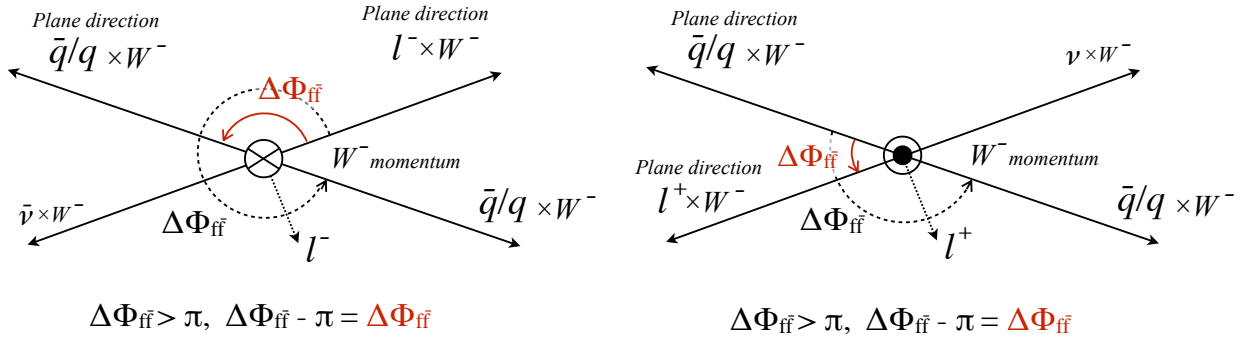

Figure 38: A view shows an illustration of $\Delta\Phi$ in the process of $WW \to qql^+\nu$ in which another fermion decaying from another W boson is not identified. $\Delta\Phi$ must be folded with $\Delta\Phi = \Delta\Phi - \pi$ if $\Delta\Phi$ exceeds π.

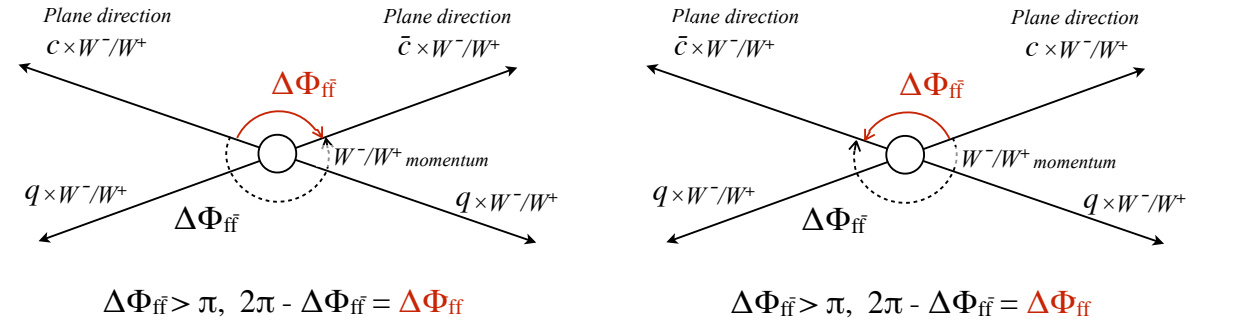

Figure 39: A view shows an illustration of $\Delta\Phi$ in the process of $WW \to c\bar{q}q\bar{c}$ in which a direction of an axis given by a specific W boson and consequently clockwise rotation can not be determined. $\Delta\Phi$ must be folded with $\Delta\Phi = 2\pi - \Delta\Phi$ when $\Delta\Phi$ exceeds π.

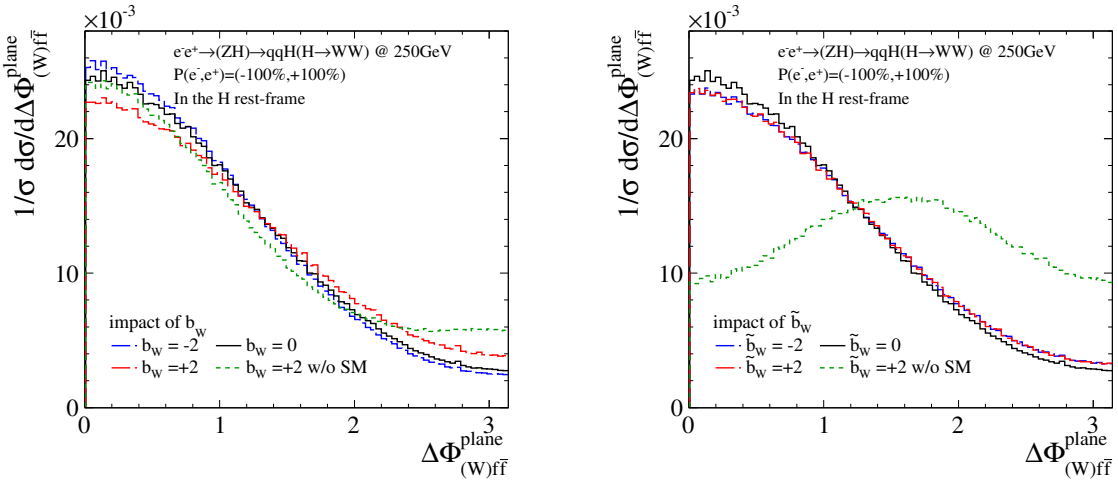

Figure 40: Distributions of $\Delta\Phi$ with range of [0–π] in the $WW \to c\bar{q}q\bar{c}$ process, assuming that complete c-flavor identification and no jet charge identification are imposed. Black and green lines show the exactly SM Higgs boson and completely the pseudo-scalar state, and blue and red lines are mixed states corresponding to $b_W = \pm 2$ and $\tilde{b}_W = \pm 2$.

4.2.3 The Higgs decay $H \to WW^*$ via the WW-fusion at $\sqrt{s}$ =500 GeV

At 500 GeV the $H \to WW^*$ decay through generation of the WW-fusion process might be useful. Since two WWH exist in the process, the W boson in the final state might be largely affected by these vertex. If the Higgs rest-frame is selected, the variation of the W momentum affected by the first vertex will be canceled when boosting decay products to the Higgs frame. Thus, the laboratory frame is selected to observe the W momentum, which is illustrated in Fig. 42.

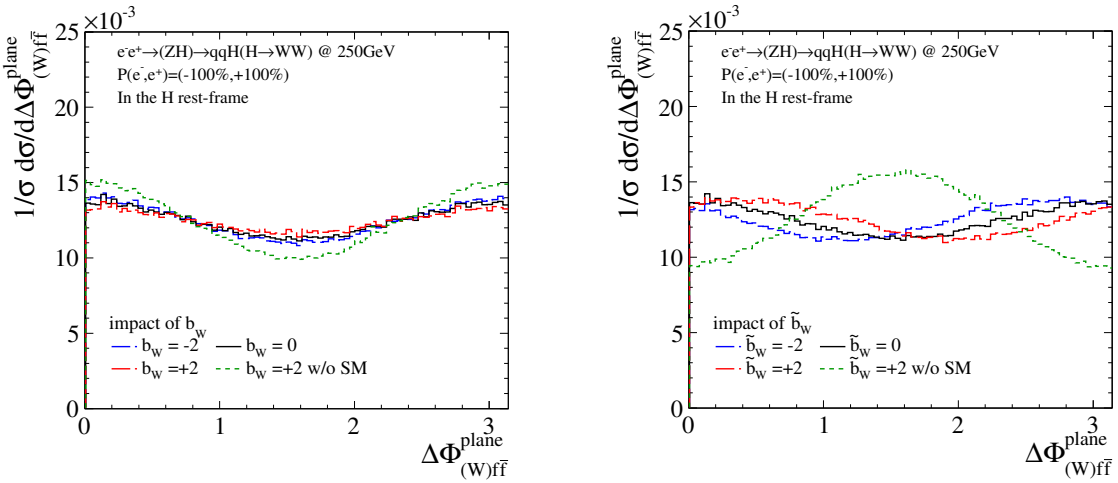

Figure 41: Distributions of $\Delta\Phi$ with range of $[0\text{–}\pi]$ in the $WW \to qql^+\nu$ process where no jet charge identification is assumed. The color definitions are same with above.

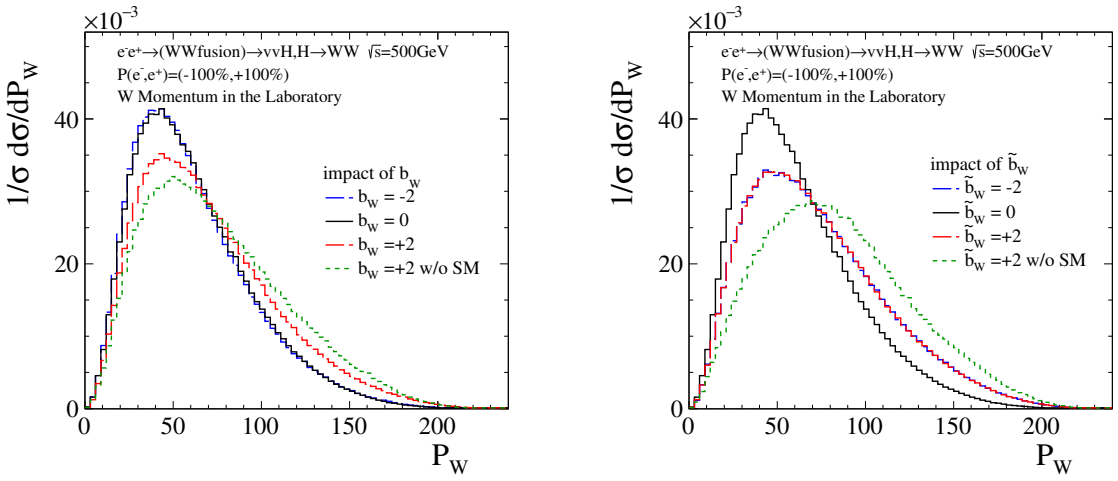

Figure 42: Distributions of the on-shell W boson momentum P_W in the laboratory-frame, which decays from the Higgs boson which is generated via WW-fusion. Black and green lines show the exactly SM Higgs boson and completely the pseudo-scalar state, and blue and red lines are mixed states corresponding to $b_W = \pm 2$ and $\tilde{b}_W = \pm 2$.

4.3 Production cross-sections due to anomalous ZZH and WWH couplings

The variation of the production cross-section on the Higgs-strahlung process and the vector boson fusion process is important information for the anomalous couplings studies. Particularly, the identification of the parameter a_V completely depends on this information. Plots in Fig. 43, Fig. 44, and Fig. 45 show relative variation of the production cross-section of the Higgs-strahlung, the ZZ-fusion, and WW-fusion processes at both center-of-mass energies $\sqrt{s} = 250$ and 500 GeV respectively. Since the SM-like depending on a_V does not have momentum dependence, a degree of variation of the cross-section due to a_V does not change at all compared to 500 GeV. In contrast, a degree of variation due to b_V and $\tilde{b}_V$ get sizably large at 500 GeV processes. Because the matrix element given in Eq. (14) and Eq. (15) in the Higgs-strahlung process have same sign which is negative, contributions from both structure have same tendency: the differences are positively vary when making the parameters increase, and vice versa. On the other hand, the matrix element of the b_Z term in the ZZ-fusion process given in Eq. (17) has different sign from the a_Z term, which is positive. Therefore, the tendency of the variation can be opposite compared to the a_Z term: the positive variation happens when making the parameters decrease, and vice versa.

The contribution derived from the $\tilde{b}_Z$ is always positive and symmetry. Because the structure of the $\tilde{b}_Z$ term can be calculated as Eq. (18), the contribution is always positive. Furthermore, when integrating the differential cross-section which is given by a charged particle, asymmetric information is completely gone. Thus, the cross-section is a CP-even observable. Because of these reason the contribution of the $\tilde{b}_Z$ is always positive and symmetry.

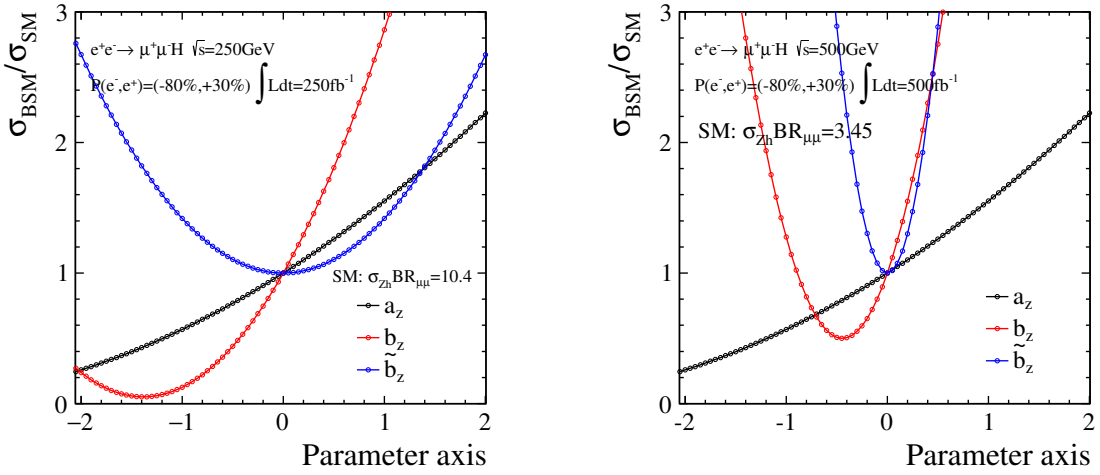

Figure 43: Plots show the relative variation of the production cross-section in the Higgs-strahlung process. The variation is described for one parameter dependence a_Z, b_Z, or $\tilde{b}_Z$. Left and right plot correspond to $\sqrt{s} = 250$ and 500 GeV respectively.

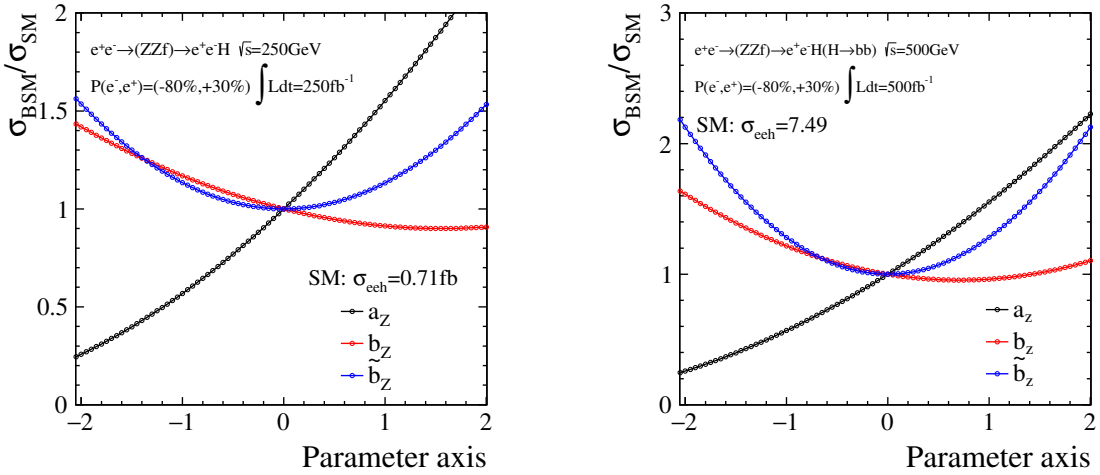

Figure 44: Plots show the relative variation of the production cross-section in the ZZ-fusion process. The variation is described for one parameter dependence a_Z, b_Z, or $\tilde{b}_Z$. Left and right plot correspond to $\sqrt{s} = 250$ and 500 GeV respectively.

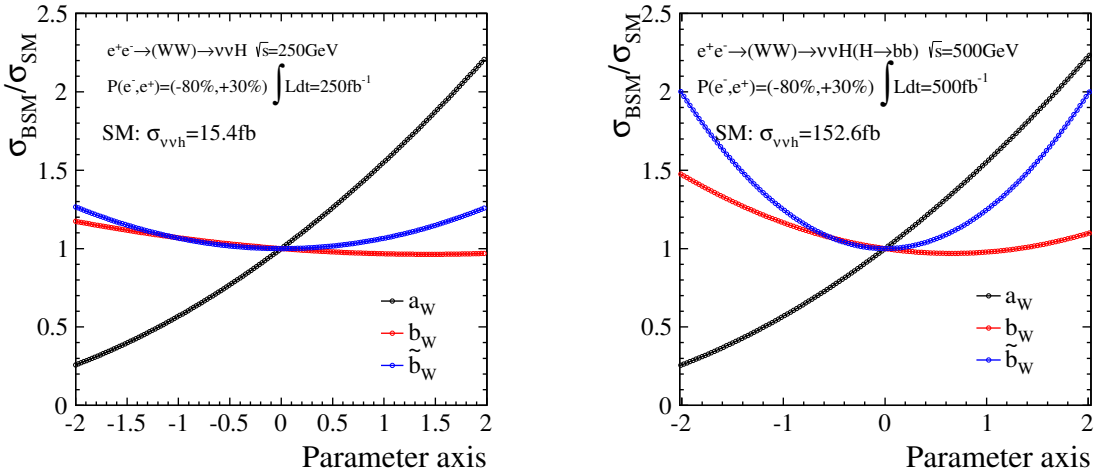

Figure 45: Plots show the relative variation of the production cross-section in the WW-fusion process. The variation is described for one parameter dependence a_Z, b_Z, or $\tilde{b}_Z$. Left and right plot correspond to $\sqrt{s} = 250$ and 500 GeV respectively.

4.4 A general strategy for evaluating the anomalous couplings

From this subsection a strategy of the analysis for detecting the anomalous VVH (ZZH and WWH) couplings is described. The strategy we took in this thesis is a general chi-squared test that is employed to distinguish whether one theoretical model is statistically reasonable or not based on stochastic basis. This method or a further extended method have been usually used in a high energy physics field to discard theoretical models beyond the SM.

As shown in the previous section, differential cross-sections showing kinematical distributions are possible to calculate for particles interacting with the Higgs boson using the SM parameters. In the case the anomalous couplings exist, it is also possible to calculate and predict the kinematical distributions that must be affected by the anomalous couplings, and construct one-, two- or n-dimensional distributions for any explicit anomalous parameters. In the analysis we performed, which is mentioned in the later section, each kinematical distributions are binned and those histograms are prepared in data-manipulation. Therefore, we perform the least squared minimization fitting, which is one of the technique in chi-squared test, and try to detect the anomalous couplings.

4.4.1 Constructing differential cross-section $\frac{d\sigma}{dx}(a_V, b_V, \tilde{b}_V)$

The differential-cross sections for angles and momenta of each particle based on the SM parameters, even with the parameters being affected by the anomalous parameters, can be obtained analytically by calculation of a scattering amplitude. The effective Lagrangian $\mathcal{L}_{eff}$ which includes the anomalous couplings can be decomposed as $\mathcal{L}_{eff} = \mathcal{L}_{SM} + a_V\mathcal{L}_{a_V} + b_V\mathcal{L}_{b_V} + \tilde{b}_V\mathcal{L}_{\tilde{b}_V}$. The scattering amplitude $\mathcal{A}_0$ that denotes the interaction with the SM parameters is also given with $|\langle f|\mathcal{L}_{SM}|i\rangle|^2 \propto |\mathcal{A}_0|^2$, where f and i show a final state and an initial state of certain process. Thus, a function of the differential cross-section which has the anomalous couplings can be described as follows,

$$\frac{d\sigma}{dx}(a_V, b_V, \tilde{b}_V) = \left|\mathcal{A}_0 + a_V\mathcal{A}_{a_V} + b_V\mathcal{A}_{b_V} + \tilde{b}_V\mathcal{A}_{\tilde{b}_V}\right|^2$$

where $\mathcal{A}_0$ corresponds to the scattering amplitude calculated with the SM parameters, and $\mathcal{A}_{a_V}$, $\mathcal{A}_{b_V}$, and $\mathcal{A}_{\tilde{b}_V}$ correspond to the scattering amplitude that are affected by the anomalous couplings derived from the parameters a_V, b_V, and $\tilde{b}_V$ ($V = Z$ or W). Since the parameter a_V does not change any kinematical distribution, which, in fact, affects only normalization of a corresponding process, the first term and the second term, which is normalized with the SM contribution $1/v$, can be grouped, which is as follows,

$$\begin{aligned}
\frac{d\sigma}{dx}(a_V, b_V, \tilde{b}_V) &= \left|\frac{(C+a_V)}{C}\mathcal{A}_0 + b_V\mathcal{A}_{b_V} + \tilde{b}_V\mathcal{A}_{\tilde{b}_V}\right|^2 \\
&= \frac{(C+a_V)^2}{C^2}|\mathcal{A}_0|^2 + b_V^2|\mathcal{A}_{b_V}|^2 + \tilde{b}_V^2|\mathcal{A}_{\tilde{b}_V}|^2 \\
&\quad + \left(\frac{C+a_V}{C}\right)b_V\ (\mathcal{A}_0\mathcal{A}_{b_V}^* + \mathcal{A}_{b_V}\mathcal{A}_0^*) + \left(\frac{C+a_V}{C}\right)\tilde{b}_V\ (\mathcal{A}_0\mathcal{A}_{\tilde{b}_V}^* + \mathcal{A}_{\tilde{b}_V}\mathcal{A}_0^*) \\
&\quad + b_V\tilde{b}_V(\mathcal{A}_{b_V}\mathcal{A}_{\tilde{b}_V}^* + \mathcal{A}_{\tilde{b}_V}\mathcal{A}_{b_V}^*) \\
&= \frac{(C+a_V)^2}{C^2}\ \frac{d\sigma}{dx}\bigg|_{SM} + b_V^2\ \frac{d\sigma}{dx}\bigg|_{b_V}^{pure} + \tilde{b}_V^2\ \frac{d\sigma}{dx}\bigg|_{\tilde{b}_V}^{pure} \\
&\quad + \frac{(C+a_V)b_V}{C}\ \frac{d\sigma}{dx}\bigg|_{a_V b_V}^{inter} + \frac{(C+a_V)\tilde{b}_V}{C}\ \frac{d\sigma}{dx}\bigg|_{a_V\tilde{b}_V}^{inter} + b_V\tilde{b}_V\ \frac{d\sigma}{dx}\bigg|_{b_V\tilde{b}_V}^{inter} .
\end{aligned}$$

where C is a constant value originating from the settings of the analysis, which is $C = \Lambda/v$ by assuming $\Lambda = 1$ TeV and $v = 246$ GeV. The second and third terms denoting *pure* in the last line give pure contributions from the anomalous parameters b_V and $\tilde{b}_V$ whereas last three terms

denoting *inter* in the last line give interfered contributions from each anomalous parameter a_V, b_V, and $\tilde{b}_V$.

When one wants to construct each differential cross-section showing the kinematical distributions analytically using the different anomalous parameters, each six term, which are like vectors showing distributions, are necessary. By setting the anomalous parameters $a_V = -C$ and $b_V = 1$, the pure terms depending on the anomalous parameter b_V can be constructed. The pure term of $\tilde{b}_V$ is given as well. Once the pure terms are prepared, it is also possible to construct the remaining three interference terms of the differential cross-section. The interference term between the parameters a_V and b_V, for instance, can be constructed by setting the parameters $a_V = 0$, $b_V = 1$ and $\tilde{b}_V = 0$. In this settings the given distribution has the contributions of both SM and b_V as follows,

$$\frac{d\sigma}{dx}(0,1,0) = \left.\frac{d\sigma}{dx}\right|_{SM} + \left.\frac{d\sigma}{dx}\right|_{b_V}^{pure} + \left.\frac{d\sigma}{dx}\right|_{a_V b_V}^{inter}$$

Therefore, the interfered distributions are constructed by subtracting the two distributions which are the SM distribution $d\sigma/dx|_{SM}$ and the pure b_V distribution $d\sigma/dx|_{b_V}^{pure}$.

Construction of the differential cross-section with basis vectors :

In the case there exist two vertices in a process, which are possible to take the anomalous couplings, for instance $e^+e^- \to (WW\text{-fusion})\nu\bar{\nu}h,\ h \to WW^*$ where two anomalous WWH couplings can be considered, the function of the differential cross-section would be

$$\begin{aligned}\frac{d\sigma}{dx}(a_W, b_W, \tilde{b}_W) &= \Big|\Big((1+a_{W_c})\mathcal{A}_{01} + b_W\mathcal{A}_{b1} + \tilde{b}_W\mathcal{A}_{\tilde{b}1}\Big) \\ &\qquad \Big((1+a_{W_c})\mathcal{A}_{02} + b_W\mathcal{A}_{b2} + \tilde{b}_W\mathcal{A}_{\tilde{b}2}\Big)\Big|^2\end{aligned}$$

where a_{W_c} is a_W/C. Indices of subscripts, for instance $\mathcal{A}_{01}, \mathcal{A}_{02}$ represent the amplitude with the parameter a in the production(1) and decay(2) vertices. This squared formula gives many terms, and it is impossible to extract properly the interference terms between each amplitude as described just above. Therefore, alternative way is considered, which is to exploit the fact that each arbitrary differential cross-section of certain process is constructed based on corresponding basis vectors of each term in linear expression of the function. The above function describing the differential cross-section gives 35 independent terms. The description of the formula would be

$$\frac{d\sigma}{dx}(a_W, b_W, \tilde{b}_W) = (\quad 35 \text{ independent terms} \quad \cdots \quad) \begin{pmatrix} \frac{\hat{d\sigma}}{dx} \\ 35 \text{ basis vectors} \\ \vdots \end{pmatrix}$$

where $\hat{d\sigma/dx}$ gives "an unit" vector of certain term. When preparing 35 independent combinations of (a, b, $\tilde{b}$), the formula would be described with the matrix of the independent terms, which is

$$\begin{pmatrix} \frac{d\sigma}{dx} \\ 35 \text{ combinations} \\ \vdots \end{pmatrix} = \boldsymbol{M} \begin{pmatrix} \frac{\hat{d\sigma}}{dx} \\ 35 \text{ basis vectors} \\ \vdots \end{pmatrix}$$

where $\boldsymbol{M}$ is a matrix composed of 35×35 independent terms. When multiplying above description by an inverse matrix $\boldsymbol{M}^{-1}$, each basis vector for constructing the differential cross-section can be given.

4.4.2 Constructing event acceptance η and migration matrix $\bar{f}$ functions

Required kinematical angular distributions for the evaluation of the sensitivity to the anomalous couplings are "detector-level" distributions which would be observed with the detectors in reality. Because reconstructed observables are subject to migration effects derived from detector finite resolutions and undetectable particles such as neutrinos, the distributions get smeared and shifted from the predicted models of the SM. Since the distributions being possible for us to generate with the anomalous parameters are pure "generator-level" distributions, the "generator-level" distributions have to be made transfer to the "detector-level" distributions by including all those kinds of migration effects, which will be realistic distributions given in the real experiment.

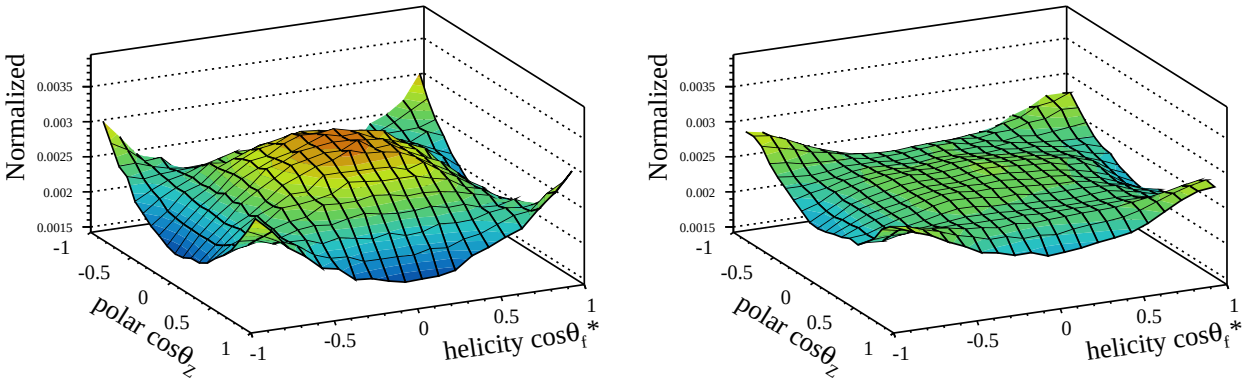

Figure 46: Plots show the two-dimensional distribution of $x(\cos\theta_Z, \cos\theta_f^*)$ of a full hadronic channel in the Higgs-strahlung $e^+e^- \to ZH \to q\bar{q}b\bar{b}$ at $\sqrt{s}$ =250 GeV for illustrating the migration effects, where the left shows a generator distribution and the right shows a distribution that would be observed in the ILD detector in reality.

To transfer the "generator-level" distributions, two effects are considered as components of a detector response function denoted with f. The first effect is an event acceptance represented with η_i that gives the meaning that events generated at i-th bin are successfully accepted (or not) after event reconstruction and background suppression, which can be simply defined for i-th bin using Monte Carlo (MC) truth information as $\eta_i = N_i^{accept}/N_i^{gene}$, where N_i^{accept} and N_i^{gene} mean the number of accepted and generated events.

The second effect is a so-called migration effect. The reconstructed observables affected by the detector finite resolutions and physical phenomena migrates from a generated bin (a truth bin) to the other bin through reconstruction chain and data-manipulation. Thus, special care must be taken for the consideration of these migration effects, which is important to predict the kinematical distributions observed in reality. In order to include these migration effects into the"generator-level" distributions, a migration matrix denoted with $\bar{f}_{ji}$ is constructed, that gives probability of the migration of bin-to-bin for the reconstruction of j-th bin. Reflecting the event acceptance η_i to the migration matrix $\bar{f}_{ji}$, the overall detector response function f is given as follows,

$$
\begin{aligned}
N^{Rec}(x_j^{Rec}) &= \sum_i f(x_j^{Rec}, x_i^{Gen}) \cdot N^{Gen}(x_i^{Gen}) \\
N^{Rec}(x_j^{Rec}) &= \sum_i f_{ji} \cdot N_i^{Gen} = \sum_i \bar{f}_{ji} \cdot \eta_i \cdot N_i^{Gen} \\
\eta_i &\equiv \frac{N_i^{Accept}}{N_i^{Gene}} \quad \text{(Event acceptance)} \\
\bar{f}_{ji} &\equiv \frac{N_{ji}^{Accept}}{N_i^{Accept}} \quad \text{(Migration matrix)}
\end{aligned}
\tag{19}
$$

where x_j^{Rec} and x_i^{Gen} correspond to the number of reconstructed and generated events on j-th and i-th bin. The generated distribution receives the event acceptance η_i and the migrations through the probability migration matrix $\bar{f}_{ji}$, in which events are transferred from the i-th bin to the j-th bin, and the reconstructed distribution on the j-th bin is given by summing events along i. Above equation can be applied for a one-dimensional distribution. The event acceptance and the migration matrix for a multi-dimensional distribution are easily expanded based on the above equation of the one-dimensional distribution, for instance, for the two-dimensional distribution:

$$
\begin{aligned}
N^{Reco}(x_{j\beta}^{Reco}) &= \sum_i \sum_\alpha f(x_{j\beta}^{Reco}, x_{i\alpha}^{Gene}) \cdot N^{Gene}(x_{i\alpha}^{Gene}) = \sum_i \sum_\alpha f_{j\beta i\alpha} \cdot N_{i\alpha}^{Gene} \\
N^{Reco}(x_{j\beta}^{Reco}) &= \sum_i \sum_\alpha \bar{f}_{j\beta i\alpha} \cdot \eta_{i\alpha} \cdot N_{i\alpha}^{Gene} \\
\eta_{i\alpha} &\equiv \frac{N_{i\alpha}^{Accept}}{N_{i\alpha}^{Gene}} \quad \text{(Event Acceptance)} \\
\bar{f}_{j\beta i\alpha} &\equiv \frac{N_{j\beta i\alpha}^{Accept}}{N_{i\alpha}^{Accept}} \quad \text{(Migration Matrix)} \\
&\vdots
\end{aligned}
$$

4.4.3 Constructing a chi-squared function for shape: χ^2_{shape}

The chi-squared formula defined as follows is used for extracting an impact derived from the variation of the kinematical distributions only. A formula for extracting an impact coming form the variation of the production cross-section is constructed later.

$$
\chi^2_{shape} = \sum_{j=1}^{n} \left[\frac{N_{SM} \sum_{i=1}^{n} \left(\frac{1}{\sigma}\frac{d\sigma}{dx}(x_i) \cdot f_{ji} - \frac{1}{\sigma}\frac{d\sigma}{dx}(x_i; a_V, b_V, \tilde{b}_V) \cdot f_{ji} \right)}{\Delta n_{SM}^{obs}(x_j)} \right]^2 \tag{20}
$$

where $\frac{1}{\sigma}\frac{d\sigma}{dx}(x_i)$ and $\frac{1}{\sigma}\frac{d\sigma}{dx}(x_i; a_V, b_V, \tilde{b}_V)$ are the normalized theoretical kinematical distributions for the SM and for the non-zero anomalous parameters, respectively, and x is a kinamatical variable. The kinematical distributions are renormalized to the number of expected events of the SM N_{SM} to extract the variation of the kinematical distributions depending on the parameters from the predictions of the SM.

n and j denote the total number of bins and certain bin number in an kinematical distribution. f is the detector response function for reconstructing the j-th bin including the detector acceptance, the detector resolutions, and the migration effects, which is composed of the event acceptance η and the probability matrix of the migration effectsx $\bar{f}$ which are defined and given in the previous section. $\Delta n_{SM}^{obs}(x_j)$ represents an observed statistical error for the j-th bin, where a simple standard statistical error based on Poisson probability ($=\sqrt{n^{sig}(x_j) + n^{bkg}(x_j)}$) is considered with full detector simulation. It is also possible to estimate the error by constructing probability density functions for the signal and the backgrounds distributions at each bin. However, a tons of background MC samples are necessary for constructing them because the kinematical distributions are divided into many bins. Thus it does not apply in this thesis. In the case multi-dimensional distributions are used for the chi-squared test, the above function can be easily expanded as follows,

$$
\chi^2_{shape} = \sum_{\beta=1}^{n} \sum_{j=1}^{n} \left[\frac{N_{SM} \sum_{\alpha=1}^{n} \sum_{i=1}^{n} \left(\frac{1}{\sigma}\frac{d\sigma}{dx}(x_{i\alpha}) \cdot f_{j\beta i\alpha} - \frac{1}{\sigma}\frac{d\sigma}{dx}(x_{i\alpha}; a_V, b_V, \tilde{b}_V) \cdot f_{j\beta i\alpha} \right)}{\Delta n_{SM}^{obs}(x_{\beta j})} \right]^2
$$

$$
\vdots
$$

4.4.4 Constructing a chi-squared function for cross-section: χ^2_{norm}

Another chi-squared formula is defined in order to include the impact of variation of the (production) cross-section separately, which is also affected by existence of the anomalous couplings.

In the processes of the Higgs-strahlung $e^+e^- \to ZH$ and the ZZ-fusion :
The given equation is

$$\chi^2_{norm} = \left[\frac{N_{SM} - N_{BSM}(a_V, b_V, \tilde{b}_V)}{\delta\sigma_{Zh}(\delta\sigma_{eeh}) \cdot N_{SM}} \right]^2 \tag{21}$$

where $\delta\sigma_{Zh}$ and $\delta\sigma_{eeh}$ show relative error of the production cross-section for the Zh and the ZZ-fusion processes, and N_{BSM} is the number of expected events for BSM models determined with the anomalous parameters. The relative error of the production cross-section for the Zh process is referred from the full simulation based studies, in which 2.0% and 3.0% for $\sqrt{s}$ =250 GeV and 500 GeV have been evaluated under the assumption of the accumulated luminosities of 250 fb^{-1} and 500 fb^{-1} [45, 46], respectively.

In the case of the ZZ-fusion process, the decay channel of the Higgs boson $H \to b\bar{b}$ is selected, which will be shown in the analysis part later. The Higgs branching fraction BR_{hbb} must vary depending on the anomalous ZZH and WWH couplings because of variation of the widths and it is not clear to handle properly. To cancel out the variation of BR_{hbb}, a relative error $\delta\sigma_{eeh}$ only is considered[11], which can be calculated by propagating errors using two independent measurements $\sigma_{eeh} \cdot BR_{hbb}$ and BR_{hbb}:

$$\sigma_{eeh} = \frac{(\sigma_{eeh} \cdot BR_{hbb})}{BR_{hbb}}.$$

The measurement of the relative error $\delta(\sigma_{eeh} \cdot BR_{hbb})$ have been evaluated for $\sqrt{s}$ =250 GeV with 250 fb^{-1} and 500 GeV with 500 fb^{-1} based on the full simulation studies, which are 27.0% and 4.0% [50, 51], respectively. Since the relative error of the branching fraction δBR_{hbb} are also given under the model independent measurements as 2.9 % and 3.5 % for $\sqrt{s}$ =250 GeV and 500 GeV with the same condition [32], the input values to $\delta\sigma_{eeh}$ are 27.16 % and 5.32 % for the settings of $\sqrt{s}$ =250 GeV with 250 fb^{-1} and 500 GeV with 500 fb^{-1}, respectively. To produce the combined results which are given based on the combination of 250 GeV and 500 GeV, the relative error δBR_{hbb} which is measured at 250 GeV is possible to be propagated, where 2.2 % is inputted as the error of a weighted average of the branching fraction of δBR_{hbb}.

To calculate the number of expected events with the anomalous parameters $N_{BSM}(a_V, b_V, \tilde{b}_V)$ the cross section with the different anomalous parameters $\sigma_{BSM}(a_V, b_V, \tilde{b}_V)$ is necessary. The

[11] Because of the same reason, we use the relative error $\delta\sigma_{\nu\nu h}$ in WW-fusion process.

$$\sigma_{\nu\nu h} = \frac{(\sigma_{\nu\nu h} \cdot BR_{hbb})}{BR_{hbb}}.$$

The relative errors of $\delta(\sigma_{\nu\nu h} \cdot BR_{hbb})$ has been evaluated for $\sqrt{s}$ =250 GeV with 250 fb^{-1} and 500 GeV with 500 fb^{-1}, which are respectively 8.1% and 1.0% [47–49].

$\sigma_{BSM}(a_V, b_V, \tilde{b}_V)$ is also possible to calculate analytically.

$$\begin{aligned}
\sigma(a_V, b_V, \tilde{b}_V) &= |\mathcal{A}_0 + a_V\mathcal{A}_{a_V} + b_V\mathcal{A}_{b_V} + \tilde{b}_V\mathcal{A}_{\tilde{b}_V}|^2 \\
&= |\mathcal{A}_0|^2 + a_V^2|\mathcal{A}_{a_V}|^2 + b_V^2|\mathcal{A}_{b_V}|^2 + \tilde{b}_V^2|\mathcal{A}_{\tilde{b}_V}|^2 \\
&\quad + 2a_V\,\mathrm{Re}(\mathcal{A}_0\mathcal{A}_{a_V}) + 2b_V\,\mathrm{Re}(\mathcal{A}_0\mathcal{A}_{b_V}) + 2\tilde{b}_V\,\mathrm{Re}(\mathcal{A}_0\mathcal{A}_{\tilde{b}_V}) \\
&\quad + 2a_Vb_V\,\mathrm{Re}(\mathcal{A}_{a_V}\mathcal{A}_{b_V}) + 2a_V\tilde{b}_V\,\mathrm{Re}(\mathcal{A}_{a_V}\mathcal{A}_{\tilde{b}_V}) + 2b_V\tilde{b}_V\,\mathrm{Re}(\mathcal{A}_{b_V}\mathcal{A}_{\tilde{b}_V}) \qquad (22) \\
&= \sigma_{SM} + a_V^2\sigma_{a_V} + b_V^2\sigma_{b_V} + \tilde{b}_V^2\sigma_{\tilde{b}_V} \\
&\quad + 2a_V\mathcal{I}_{0a_V} + 2b_V\mathcal{I}_{0b_V} + 2\tilde{b}_V\mathcal{I}_{0\tilde{b}_V} \\
&\quad + 2a_Vb_V\mathcal{I}_{a_Vb_V} + 2a_V\tilde{b}_V\mathcal{I}_{a_V\tilde{b}_V} + 2b_V\tilde{b}_V\mathcal{I}_{b_V\tilde{b}_V}
\end{aligned}$$

When considering amplitude of a wave function, a real part gives physical meaning and an imaginary part does not. By the above equation each value of the interference terms can be given by making the other parameters cancel with C which is the specific constant value. For example, in the case of $\sigma(1,0,0)$ which gives interference with the SM and a_V, the contribution would be

$$\begin{aligned}
\sigma(1,0,0) &= \sigma_{SM} + \sigma_{a_V} + 2\mathcal{I}_{0a_V} \quad , \\
\text{where } \mathcal{I}_{0a_V} &= \frac{1}{2}\Big[\sigma(1,0,0) - \sigma_{SM}(0,0,0) - \sigma_{a_V}(-C+1,0,0)\Big] \ ,
\end{aligned}$$

and likewise, the other values of the interference terms can be given as,

$$\begin{aligned}
\mathcal{I}_{0b_V} &= \frac{1}{2}\Big[\sigma(0,1,0) - \sigma_{SM}(0,0,0) - \sigma_{b_V}(-C,1,0)\Big] \\
\mathcal{I}_{0\tilde{b}_V} &= \frac{1}{2}\Big[\sigma(0,0,1) - \sigma_{SM}(0,0,0) - \sigma_{\tilde{b}_V}(-C,0,1)\Big] \\
\mathcal{I}_{a_Vb_V} &= \frac{1}{2}\Big[\sigma_{a_Vb_V}(-C+1,1,0) - \sigma_{a_V}(-C+1,0,0) - \sigma_{b_V}(-C,1,0)\Big] \\
\mathcal{I}_{a_V\tilde{b}_V} &= \frac{1}{2}\Big[\sigma_{a_V\tilde{b}_V}(-C+1,0,1) - \sigma_{a_V}(-C+1,0,0) - \sigma_{\tilde{b}_V}(-C,0,1)\Big] \\
\mathcal{I}_{b_V\tilde{b}_V} &= \frac{1}{2}\Big[\sigma_{b_V\tilde{b}_V}(-C,\quad 1,\quad 1) - \sigma_{b_V}(-C,\quad 1,\quad 0) - \sigma_{\tilde{b}_V}(-C,0,1)\Big]
\end{aligned}$$

4.4.5 Pseudo-experiment and correlation coefficients

Not only errors of each parameter but also correlated errors between parameters are important in the case that these parameter are used as input values to other evaluations or measurement: when a statistical parameter is given with a linear combination of two parameters like $c = ma_V + nb_V$, its error can be given as, $\sigma_c = \sqrt{m^2\sigma_{a_V}^2 + n^2\sigma_{b_V}^2 + 2mn\mathrm{Cov}(a_V, b_V)}$. Thus, showing correlations between parameters is required. To extract the correlations, pseudo-experiment is performed where statistical fluctuation is taken into account. The signal distribution, which is reflected with the detector response function shown in Eq. (19), is fluctuated according to the Poisson probability.

$$N_{SM}\sum_{i=1}^{n}\frac{1}{\sigma}\frac{d\sigma}{dx}(x_i)\cdot f_{ji} \equiv S_{SM}(x_j) \quad \text{, which is a shape of the SM.}$$

$$S'_{SM}(x_j) = \frac{\mathrm{Poiss}(S_{SM}(x_j) + B(x_j))}{\sum_{j=1}^{n}\Big[\mathrm{Poiss}(S_{SM}(x_j) + B(x_j)) - B(x_j)\Big]}\cdot N_{SM}$$

where "Poiss" in the equation denotes the Poisson probability, and $B(x_j)$ is a background distribution on j-th bin.

A relation between a least squared method and pseudo-experiment :

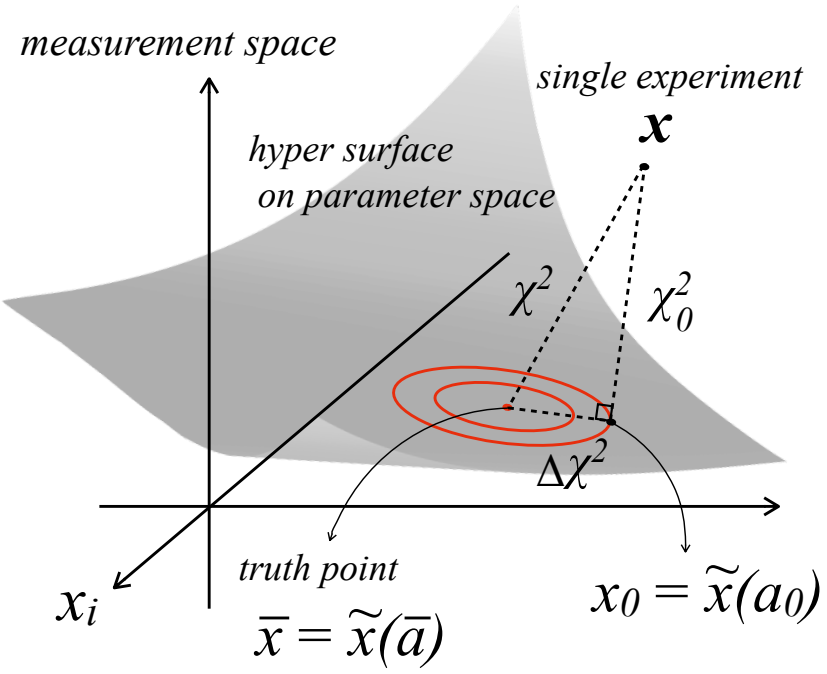

Figure 47: A schematic view shows a measurement space defined with basis vectors $\boldsymbol{x}$ which corresponds to observables on i-th bin. There exists a hyper surface parametrized by parameters $\boldsymbol{a}$ in the same coordinate system with the measurement space.

The number of events in each bin, where i-th bin is denoted with n_i, is statistically independent from the other bins. The averaged number of events on i-th bin can be represented as,

$$\bar{n}_i = L \int_{\boldsymbol{x}\in bin\ i} d\boldsymbol{x} \int d\boldsymbol{x}' f(\boldsymbol{x}, \boldsymbol{x}') \frac{d\sigma}{d\boldsymbol{x}'} \tag{23}$$

where L and f show luminosity and a detector response function. In the case that $\bar{n}_i$ is sufficiently large, its statistical fluctuation is given with the Poisson distribution of a gaussian shape. When the defined number of bins is m: $\boldsymbol{n} = (n_1,\ ...,\ n_m)$, a probability density function for a single experiment is defined as follows,

$$P(\boldsymbol{n}) = \prod_i^m \left(\frac{1}{\sqrt{2\pi\bar{n}_i}}\right) \exp\left(-\frac{1}{2}\left[\frac{(n_i - \bar{n}_i)}{\sqrt{\bar{n}_i}}\right]^2\right) dn_i \tag{24}$$

When $\bar{n}_i$ is normalized with Poisson error $\sqrt{\bar{n}_i}$ and $x_i = \bar{n}_i/\sqrt{\bar{n}_i}$ is defined, the above probability function becomes

$$P(\boldsymbol{x}) = \prod_i^m \left(\frac{1}{\sqrt{2\pi}}\right) \exp\left(-\frac{1}{2}\left[(x_i - \bar{x}_i)\right]^2\right) dx_i \quad . \tag{25}$$

Assuming that the current measurement space is represented as $\boldsymbol{x} = (x_1,\ ...,\ x_m)$, and the modeled hyper surface parametrized with parameters $\boldsymbol{a} = (a_V, b_V, \tilde{b}_V)$ forms a hyper surface in a curvilinear coordinate system which is defined with $\boldsymbol{x}$. Since a reference sample we used in the analysis is the SM, the corresponding true point on the hyper surface is $(a_V, b_V, \tilde{b}_V) = (0, 0, 0)$, that also gives

the true point in the measurement space:

$$\bar{\boldsymbol{x}} = (\bar{x}_l,\ ...,\ \bar{x}_m) \tag{26}$$

The defined chi-squared can represent the squared distance between the measured vector given with $\boldsymbol{x}$ and the true point $\bar{\boldsymbol{x}}$. Under this situation, minimization fitting with the given chi-squared function means that a minimum distance point from the measured vector $\boldsymbol{x}$ to the hyper surface is tried to find, that gives a line passing through $\boldsymbol{x}$ and being vertical to the hyper surface at $\boldsymbol{x}_0$. All points along the line give the same fitting results, and the probability of getting $\boldsymbol{x}$ for a single experiment is controlled by the total χ^2 which gives the distance squared between $\boldsymbol{x}$ and the true point $\bar{\boldsymbol{x}}$, and it can be decomposed into two components,

$$\chi^2 \cong (\boldsymbol{x} - \boldsymbol{x}_0)^2 + (\boldsymbol{x}_0 - \bar{\boldsymbol{x}})^2 = \chi_0^2 + \Delta\chi^2 \tag{27}$$

where χ_0^2 corresponds to the distance squared between $\boldsymbol{x}$ and the minimum distance point $\boldsymbol{x}_0$, and $\Delta\chi^2$ corresponds to the distance squared between $\boldsymbol{x}_0$ and the true point $\bar{\boldsymbol{x}}$. This decomposition must be realized under the assumption that the hyper surface is locally defined by a flat plain within an expected range of statistical fluctuations. Additionally, since there exists one-to-one correspondence between $\boldsymbol{x}_0$ and the point in the hyper surface described with the parameters $(a_V, b_V, \tilde{b}_V)$, $\boldsymbol{x}_0$ can be denoted as $\tilde{\boldsymbol{x}}(\boldsymbol{a}_0)$ at the hyper surface parametrized with the parameters. $\bar{\boldsymbol{x}}$ is similarly given with $\tilde{\boldsymbol{x}}(\bar{\boldsymbol{a}})$ in the hyper surface. When $\tilde{\boldsymbol{x}}(\boldsymbol{a}_0)$, which is the multivariable function of $\boldsymbol{a}$, is expanded in the vicinity of $\bar{\boldsymbol{a}}$, a given expansion in the first order and $\Delta\chi^2$ can be written as,

$$\tilde{\boldsymbol{x}}(\boldsymbol{a}_0) = \tilde{\boldsymbol{x}}(\bar{\boldsymbol{a}}) + \left(\frac{\partial\tilde{\boldsymbol{x}}}{\partial\boldsymbol{a}_0}(\bar{\boldsymbol{a}})\right)\cdot(\boldsymbol{a}_0 - \bar{\boldsymbol{a}})\ \text{, and} \tag{28}$$

$$\Delta\chi^2 = (\boldsymbol{x}_0 - \bar{\boldsymbol{x}})^2 = (\tilde{\boldsymbol{x}}(\boldsymbol{a}_0) - \tilde{\boldsymbol{x}}(\bar{\boldsymbol{a}}))^2 \tag{29}$$

$$= \Delta\boldsymbol{a}_0^T \left(\frac{\partial\tilde{\boldsymbol{x}}}{\partial\boldsymbol{a}_0}(\bar{\boldsymbol{a}})\right)^T \left(\frac{\partial\tilde{\boldsymbol{x}}}{\partial\boldsymbol{a}_0}(\bar{\boldsymbol{a}})\right) \Delta\boldsymbol{a}_0 \tag{30}$$

where the third line corresponds to diagonal elements of the second line. The probability of getting $(a_V, b_V, \tilde{b}_V)$ as a best fit point is given by integrating Eq. (25) along the minimum distance line, which shows the probability for getting the best fit point $\boldsymbol{x}_0$ on the hyper surface in the measurement space. The resultant probability density function for $\boldsymbol{x}_0$ is decided with the number of parameters, which is given by

$$\begin{aligned} P_{\parallel}(\boldsymbol{x}_0) &= \int d(\boldsymbol{x} - \boldsymbol{x}_0) P(\boldsymbol{x}) \\ &= \prod_i^3 \left(\frac{1}{\sqrt{2\pi}}\right) \exp\left(-\frac{1}{2}\left[(\boldsymbol{x}_0 - \bar{\boldsymbol{x}})\right]^2\right) \end{aligned} \tag{31}$$

On the other hand, the probability taking $P_{\parallel}(\boldsymbol{x}_0)$ can be also represented in the coordinate system

on the parameter hyper surface, which is given by

$$
\begin{aligned}
P(\boldsymbol{a}) &= \int_{\parallel} P(\boldsymbol{x}_0) d\boldsymbol{x} && (32)\\
&= \int_{\parallel} P(\tilde{\boldsymbol{x}}(\boldsymbol{a}_0)) \left| \frac{\partial \tilde{\boldsymbol{x}}}{\partial \boldsymbol{a}_0}(\bar{\boldsymbol{a}}) \right| d\boldsymbol{a} \quad (x_0 \to \tilde{\boldsymbol{x}}(\boldsymbol{a}_0)) && (33)\\
&= \prod_i^3 \left(\frac{1}{\sqrt{2\pi}} \right) \left| \frac{\partial \tilde{\boldsymbol{x}}}{\partial \boldsymbol{a}_0}(\bar{\boldsymbol{a}}) \right| \exp\left(-\frac{1}{2} \Delta \boldsymbol{a}_0^T \left(\frac{\partial \tilde{\boldsymbol{x}}}{\partial \boldsymbol{a}_0} \right)^T \left(\frac{\partial \tilde{\boldsymbol{x}}}{\partial \boldsymbol{a}_0} \right) \Delta \boldsymbol{a}_0 \right) && (34)\\
&= \prod_i^3 \left(\frac{1}{\sqrt{2\pi}} \right) \left| \frac{\partial \tilde{\boldsymbol{x}}}{\partial \boldsymbol{a}_0}(\bar{\boldsymbol{a}}) \right| \exp\left(-\frac{1}{2} \Delta \boldsymbol{a}_0^T E_{\boldsymbol{a}_0}^{-1} \Delta \boldsymbol{a}_0 \right) && (35)
\end{aligned}
$$

$E_{\boldsymbol{a}_0}^{-1}$ gives a variance-covariance matrix which includes statistical fluctuations and correlation coefficients for the parameter $\boldsymbol{a}$. These two equations showing $P_{\parallel}(\boldsymbol{x}_0)$ and $P(\boldsymbol{a})$ are equivalent, that mean χ_0^2 calculated as the minimum distance squared between $\boldsymbol{x}_0$ and $\bar{\boldsymbol{x}}$ give same results with $\Delta\chi^2$ calculated in the hyper surface defined with the parameters $\boldsymbol{a}$.

5 A framework and standard tools for analysis and reconstruction

For various physics studies, a full detector Montecarlo simulation package called ILCSoft [52] is prepared where the ILD detector for the future ILC experiment is available. The ILD detector model is described based on GEANT4 [53], which is called MOKKA [54] (Modellierung mit Objekten eines Kompakten Kalorimeters [55]). Realistic reconstruction chain is implemented by a framework called MARLIN [56] (Modular Analysis and Reconstruction for the LINear collider). All SM samples including Higgs processes, even for BSM processes, are commonly prepared for ILC and ILD related physics studies.

5.1 Montecarlo samples

Event generation of Montecarlo samples was performed with frameworks called WHIZARD [57] and PHYSSIM [58], (the latter one is used for several specific Higgs related signal processes), where both of the frameworks can handle electron and positron beam parameters and physical processes of the beams such as beam polarization, beam-strahlung, initial state radiation, and bremsstrahlung. Hadronization and parton-showering are implemented by PYTHIA [59] in both frameworks. After generating seed event samples, they are fed into the detector model, where the detector model used for the physics study is explicitly MOKKA-ILD_o1_v05, which is designed based on the descriptions mentioned in a detailed baseline design called DBD [38].

The generated particles are tracked inside the detectors while interacting with materials which configure the sub-detectors and depositing energy due to the interactions until it reaches certain cut-off energy. The deposited energies in the sub-detectors are stored as analogs of measured energy by the sub-detectors and used for the following reconstruction chain as inputs. The events are reconstructed in MARLIN. A tracking algorithm such as Kalman filter [60] is implemented to reconstruct each charged track, and these are stored as track objects eventually. Hits in the calorimeters are also clustered into calorimeter objects by an algorithm installed in the software package, which is called PandoraPFA [41]. After completing clustering of the objects, a pattern recognition is performed for all reconstructed objects, and all objects are identified as: charged tracks with fragments in the calorimeters, neutral particles without charged tracks, and so on, which are, in the end, handled as Particle Flow Objects (PFO) for physics studies.

The physics processes and the number of Montecarlo samples used for the analysis mentioned in this thesis are given in the flowing Table 1 and Table 2 for both of the center-of-mass energies which are 250 and 500 GeV. In all event samples a $\gamma\gamma \rightarrow$hadrons process caused by the radiated photons due to beam-beam interactions in the initial state is overlaid on the main processes. The number of expected overlaid $\gamma\gamma \rightarrow$hadrons events per bunch crossing are respectively estimated as $< N >$=0.33 and 1.7 for both 250 and 500 GeV [49, 61], which are inputted in the reconstruction step.

The MC samples are produced with complete polarized electron and positron beams with four combinations which are $\mathrm{P}(e^-, e^+) = (-100\%, +100\%)$, $(+100\%, -100\%)$, $(-100\%, -100\%)$, and $(+100\%, +100\%)$. Any beam polarization states and also corresponding cross-sections are possible to calculate by mixing up each polarization sample. When describing each beam polarization state as the total number of left- and right handed polarized electors or positrons inside the beam, it can be normalized by the sum of them. Therefore, each coefficient for mixing the samples are given as polarization factors for both right- $P^R_{e^-}$ and left-handed $P^L_{e^-}$ as

$$\begin{aligned} P_{e^-} &= \frac{N^R_{e^-} - N^L_{e^-}}{N^R_{e^-} + N^L_{e^-}} = \frac{N^R_{e^-}}{N^R_{e^-} + N^L_{e^-}} - \frac{N^L_{e^-}}{N^R_{e^-} + N^L_{e^-}} \\ &\equiv P^R_{e^-} - P^L_{e^-} \quad , \\ \text{and} \quad & \text{the sum is given as} \quad P^R_{e^-} + P^L_{e^-} = 1 \end{aligned}$$

where $N^{R/L}_{e^-}$ denotes the number of right- and left-handed polarized electrons. The given polar-

Table 1: Generated MC events of the Higgs production processes as additions of the common ILD samples. The MC samples are generated with fully beam polarization states: P(e^-, e^+)= $P^L_{e^-} P^R_{e^+} = (-100\%, +100\%)$ and the reconstructed performed using the MOKKA-ILD_o1_v05 with the overlayed $\gamma\gamma \rightarrow$hadrons.

process		fully polarization			
Energy	Process	$P^L_{e^-} P^R_{e^+}$	$P^R_{e^-} P^L_{e^+}$	$P^L_{e^-} P^L_{e^+}$	$P^R_{e^-} P^R_{e^+}$
250 GeV	$Zh \rightarrow l^+l^-h$	$4.0 \cdot 10^4$	$1.0 \cdot 10^4$	0	0
500 GeV	$Zh \rightarrow l^+l^-h$	$4.0 \cdot 10^4$	$1.0 \cdot 10^4$	0	0
250 GeV	$Zh \rightarrow q\bar{q}b\bar{b}$	$4.0 \cdot 10^5$	$2.0 \cdot 10^5$	0	0
500 GeV	$Zh \rightarrow q\bar{q}b\bar{b}$	$2.5 \cdot 10^5$	$1.0 \cdot 10^5$	0	0
250 GeV	$(t)e^+e^-h \rightarrow e^+e^-b\bar{b}$	$1.0 \cdot 10^4$	$1.0 \cdot 10^4$	3992	3992
500 GeV	$(t)e^+e^-h \rightarrow e^+e^-b\bar{b}$	$3.8 \cdot 10^4$	$0.8 \cdot 10^4$	$4.8 \cdot 10^4$	$4.4 \cdot 10^4$
250 GeV	$(t)\nu\bar{\nu}h$	$1.0 \cdot 10^5$	0	0	0
250 GeV	$(s)\nu\bar{\nu}h$	$1.0 \cdot 10^5$	$1.0 \cdot 10^5$	0	0
500 GeV	$(t)\nu\bar{\nu}h$	$4.4 \cdot 10^5$	0	0	0
500 GeV	$(s)\nu\bar{\nu}h$	$3.4 \cdot 10^4$	$2.2 \cdot 10^4$	0	0
250 GeV	$Zh \rightarrow q\bar{q}WW^* \rightarrow 2q2ql\nu$	$6.0 \cdot 10^4$	$3.0 \cdot 10^5$	0	0
250 GeV	$Zh \rightarrow q\bar{q}WW^* \rightarrow 2q4q$	$1.3 \cdot 10^5$	$8.0 \cdot 10^4$	0	0
250 GeV	$Zh \rightarrow \nu\bar{\nu}WW^* \rightarrow 2\nu4q$	$1.3 \cdot 10^5$	$1.3 \cdot 10^5$	0	0
500 GeV	$(t)\nu\bar{\nu}h \rightarrow \nu\bar{\nu}WW^* \rightarrow 2\nu4q$	$2.0 \cdot 10^5$	0	0	0

ization factors for the right- and left-handed electron beam are described as,

$$P^R_{e^-} = \frac{1 + P_{e^-}}{2}, \quad P^L_{e^-} = \frac{1 - P_{e^-}}{2}$$

The cross sections of each process with any beam polarization states, for instance, can be calculated by using these polarization factors and taking all polarization combinations, which can be described as

$$\sigma_{\mathrm{P(e^-,e^+)}} = P^L_{e^-} P^R_{e^+} \cdot \sigma_{LR} + P^R_{e^-} P^L_{e^+} \cdot \sigma_{RL} + P^L_{e^-} P^L_{e^+} \cdot \sigma_{LL} + P^R_{e^-} P^R_{e^+} \cdot \sigma_{RR} \ ,$$

where $P^L_{e^-}$, $P^R_{e^+}$, and σ_{LR} respectively represent the polarization factors for the electron and positron beams and the cross-section calculated with the fully polarized beam.

Table 2: Cross-sections and number of generated MC samples on the Higgs production processes and the major SM background processes for both $\sqrt{s} = 250$ and 500 GeV. The cross-sections given in the table are set to be each operation beam polarization states: $P(e^-, e^+) = (-80\%, +30\%)$ and $P(e^-, e^+) = (+80\%, -30\%)$, whereas the number of MC samples are given with fully beam polarization states: $P(e^-, e^+) = P^L_{e^-} P^R_{e^+} = (-100\%, +100\%)$. The eeH(s) and eeH(t) denote the s-channel ZH process and the t-channel ZZ-fusion processes. $2f\_l$ and $2f\_h$ in the table indicate that the final state has a lepton pair such as charged leptons or neutrinos, and a quark pair like $u\bar{u}$, $d\bar{d}$ except $t\bar{t}$. $4f\_l$ and $4f\_h$ are the same indication with $2f\_l$ or $2f\_h$, that means a final state has two lepton pairs or two quark pairs. $4f\_sl$ shows that a final state has a lepton pair and a quark pair. At $\sqrt{s} = 500$ GeV $6f$ is included in the SM backgrounds, where possible diagrams of 6 fermions in a final state are considered such as $t\bar{t}$ and a fermion pair with two W bosons and two fermion pairs with the Z boson.

$\sqrt{s}$=250 GeV operation polarization			fully polarization			
	Cross-section (fb)		MC sample			
$P(e^-, e^+)$	$(-80\%, +30\%)$	$(+80\%, -30\%)$	$P^L_{e^-} P^R_{e^+}$	$P^R_{e^-} P^L_{e^+}$	$P^L_{e^-} P^L_{e^+}$	$P^R_{e^-} P^R_{e^+}$
eeH(s)	10.7	7.14	$4.00 \cdot 10^4$	$1.00 \cdot 10^4$	0	0
eeH(t)	0.71	0.52	$1.00 \cdot 10^4$	$1.00 \cdot 10^4$	3992	3992
$\mu\mu H$	10.4	7.03	$4.00 \cdot 10^4$	$1.00 \cdot 10^4$	0	0
qqH	210.2	141.9	$5.45 \cdot 10^5$	$2.94 \cdot 10^5$	0	0
$\nu\nu H$ (s)	61.6	41.6	$12.8 \cdot 10^4$	$6.50 \cdot 10^4$	0	0
$\nu\nu H$ (t)	15.4	0.93	$12.8 \cdot 10^4$	$6.50 \cdot 10^4$	0	0
$2f\_l$	$3.82 \cdot 10^4$	$3.49 \cdot 10^4$	$2.63 \cdot 10^6$	$2.13 \cdot 10^6$	$5.03 \cdot 10^5$	$5.03 \cdot 10^5$
$2f\_h$	$7.80 \cdot 10^4$	$4.62 \cdot 10^4$	$1.75 \cdot 10^6$	$1.43 \cdot 10^6$	0	0
$4f\_l$	$6.03 \cdot 10^3$	$1.47 \cdot 10^3$	$2.25 \cdot 10^6$	$9.80 \cdot 10^4$	$2.73 \cdot 10^5$	$2.73 \cdot 10^5$
$4f\_sl$	$1.84 \cdot 10^4$	$2.06 \cdot 10^3$	$4.04 \cdot 10^6$	$3.56 \cdot 10^5$	$9.78 \cdot 10^4$	$9.78 \cdot 10^4$
$4f\_h$	$1.68 \cdot 10^4$	$1.57 \cdot 10^3$	$2.38 \cdot 10^6$	$2.42 \cdot 10^5$	0	0

$\sqrt{s}$=500 GeV operation polarization			fully polarization			
	Cross-section (fb)		MC sample			
$P(e^-, e^+)$	$(-80\%, +30\%)$	$(+80\%, -30\%)$	$P^L_{e^-} P^R_{e^+}$	$P^R_{e^-} P^L_{e^+}$	$P^L_{e^-} P^L_{e^+}$	$P^R_{e^-} P^R_{e^+}$
eeH(s)	3.44	2.32	$4.00 \cdot 10^4$	$1.00 \cdot 10^4$	0	0
eeH(t)	7.49	4.64	$3.79 \cdot 10^4$	$0.80 \cdot 10^4$	$4.84 \cdot 10^4$	$4.41 \cdot 10^4$
$\mu\mu H$	3.45	2.33	$4.00 \cdot 10^4$	$1.00 \cdot 10^4$	0	0
qqH	69.7	46.9	$3.00 \cdot 10^5$	$1.20 \cdot 10^5$	0	0
$\nu\nu H$(s)	20.5	13.8	$18.7 \cdot 10^4$	$2.15 \cdot 10^4$	0	0
$\nu\nu H$(t)	152.5	9.1	$18.7 \cdot 10^4$	0	0	0
$2f\_l$	$6.77 \cdot 10^3$	$5.96 \cdot 10^3$	$4.54 \cdot 10^5$	$3.59 \cdot 10^5$	$8.41 \cdot 10^4$	$8.41 \cdot 10^4$
$2f\_h$	$1.96 \cdot 10^4$	$1.16 \cdot 10^4$	$1.51 \cdot 10^6$	$8.37 \cdot 10^5$	0	0
$4f\_l$	$1.06 \cdot 10^3$	$7.48 \cdot 10^3$	$3.57 \cdot 10^6$	$1.40 \cdot 10^6$	$1.07 \cdot 10^6$	$1.07 \cdot 10^6$
$4f\_sl$	$1.32 \cdot 10^4$	$2.94 \cdot 10^3$	$9.70 \cdot 10^5$	$9.99 \cdot 10^4$	$7.18 \cdot 10^4$	$7.18 \cdot 10^4$
$4f\_h$	$8.65 \cdot 10^3$	$7.41 \cdot 10^2$	$6.87 \cdot 10^5$	$1.77 \cdot 10^4$	0	0
$6f$	$8.08 \cdot 10^2$	$3.31 \cdot 10^2$	$5.06 \cdot 10^5$	$5.05 \cdot 10^5$	$9.54 \cdot 10^4$	$9.54 \cdot 10^4$

5.2 Isolated lepton identification

A few isolated leptons are expected to exist in the final state of many Higgs related production and decay processes. Identification of these isolated leptons is efficiently a key point for the Higgs related physics studies, and on discrimination of certain signal process and background processes as well.

Classical method for the isolated lepton identification:

Leptons such as an electron and a muon can be generally extracted by using information of deposited energies in calorimeters. The electron basically deposits almost all of its energy in the ECAL through electro-magnetic (EM-) shower (which is caused by interactions with heavy materials, and brings emissions of bremsstrahlung photons and their pair productions). Since mass of the muon is about two hundred times heavier than that of the electron, it is much less likely to cause the EM-shower due to the interactions with the materials. Thus, the muon can easily passes through the materials and deposits a small fraction of its energy in the both calorimeters, the ECAL and the HCAL. On the other hand, a charged hadron can induces hadron shower caused by a strong interaction with nucleus in the HCAL. Therefore, large energy deposit can be seen in the HCAL for the charged hadron. In addition, it is possible that a charged pion drops own energy in the ECAL, or an unstable charged kaon can decay into an electron by emitting a neutral pion (π_0). These particles can make the EM-shower in the ECAL and resemble in electrons. This can sometimes cause misidentification of electrons. Because a high energy charged pion which is a stable particle, at least within a detector, can sometimes pass through the both calorimeters without making the shower, this pion also resembles in muons, and causes the misidentification.

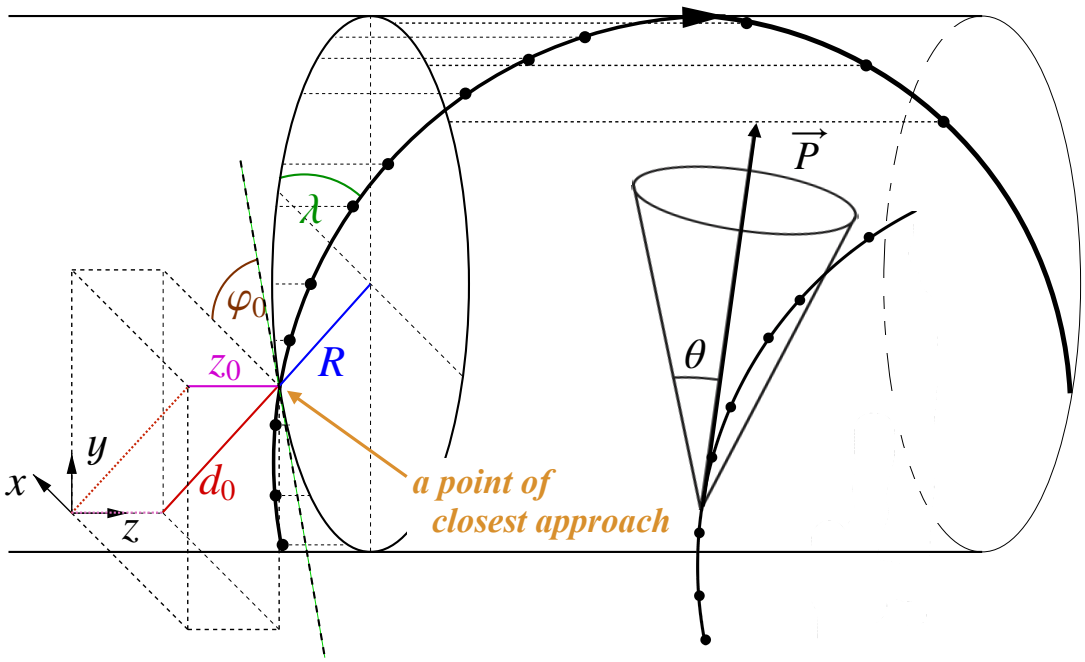

Figure 48: A schematic view of general track parameters and given cone along a momentum direction of a track[13]. The view is referred from [49, 62].

[13]The definitions of the track parameters are as follows by referring a point of closest approach (POCA),

- d_0: Distance between a reference point and POCA in the XY-plane.
- Z_0: Distance between a reference point and POCA along the Z-axis (beam-axis).
- ϕ_0: An angle between a momentum direction of a track at POCA and the positive X-axis.
- $\tan\lambda$: A slope of the straight line in the YZ-plane (radius of curvature).

A tau leptons is also possible to be misidentified as an electron or a muon. However, since the tau has clearly heavy mass and is unstable, the tau flies short length ($C\tau \sim 240\mu m$) and decays into leptons (or hadrons). To observe the flight length, impact parameters are generally exploited, which are defined as distances between an extrapolated track and the interaction point (IP) as shown in Fig. 48. Because the impact parameters, especially d_0 and Z_0 which are defined in a r-ϕ plane (XY-plane) and a Z-axis, tend to be larger for leptons originating from the tau, and these parameters are useful for the discrimination of the tau.

When requiring the isolation, a cone energy method has been classically applied. A cone is defined along the momentum direction of a charged particle (a lepton). After giving a parameter θ, which is an angle between the charged particle and other particles, and energies of particles inside the cone are checked and summed. By checking the cone energy, the isolation is judged. Other discriminations for both lepton identification and the isolation are considered by looking momentum of the charged particle measured with the tracker and comparing the momentum and the energies in the calorimeters.

Multivariate Analysis (MVA) method for the isolated lepton identification:

For physics studies on the Higgs boson at the ILC, a new idea for the isolated lepton identification was proposed based on Multivariate Analysis (MVA) method [63] and it has been developed and applied to the studies. ROOT [64] is supporting softwares for manipulation of MVA, which is known as The Toolkit for Multivariate Data Analysis with ROOT (TMVA) [65], and several classifiers are available inside the TMVA: Likelihood, Neural Nets (MLP), Boosted Decisions Tree (BDT). In this thesis the isolated lepton identification with the MVA base is implemented for the analysis of each channel which require extracting isolated leptons. Because one of the classifier methods, MLP, can provide better performance among several classifiers, MLP is used for the identification of the isolated leptons.

In order to train and construct neural nets of MLP, several observables must be given, which are extracted from each signal and background event samples. Several weight files are currently available for the physics studies at each center-of-mass energy $\sqrt{s}$ = 250, 350, and 500 GeV, whose neural nets are separately trained for each energy using full hadronic background processes together with certain process which has isolated leptons in the final state. The trained neural nets are respectively prepared for an isolated electron and an isolated muon. The input observables used for the training of the neural nets are described below for both electron and muon, and they are illustrated in Fig. 49 and Fig. 50,

- **Cone energy**:
  This is a classical observable mentioned in the previous subsection. It is expected to be larger for misidentified isolated leptons which come from hadronic processes. If a charged (or a neutral) particle is considered, it will be labeled as charged (or neutral) cone energy. in a plot.

- **Momentum**:
  A misidentified isolated lepton basically has smaller momentum compared with a *real* isolated lepton. The total momentum should be pay attention to require the isolation.

- **An energy ratio** $E_{lep}/(E_{lep} + E_{cone})$:
  A cone around the momentum direction of certain charged particle is defined and the sum of energies of particles inside the cone is taken. An isolated lepton should have small cone energy, so the energy ratio of the isolated lepton should be close to 1. If final state radiations happens, the ratio will be shifted slightly.

- **Cone angle** $\cos\theta_{cone}^{large}$:
  $\cos\theta_{cone}$ is defined as an angle between a charged particle and certain PFO, and $\cos\theta_{cone}$ =

- ω: A curvature of the circle in the XY-plane. A sign of the curvature represents the sign of the track (geometrical curvature).

0.95 is taken as a reference of a size of a jet. $\cos\theta_{cone}$ is calculated for all particles with respect to the charged particle, and $\cos\theta_{cone}^{large}$ is taken as the largest value. Because a misidentified isolated lepton can be a part of a jet, the largest value of $\cos\theta_{cone}$ can be larger compared to the *real* isolated leptons.

- **A ratio** $ECAL/CAL$:
  CAL denotes the sum of energies deposited in calorimeters. The ratio of the deposited energy in the $ECAL$ to the CAL should be close to 1 for the electron, which is a clear feature for the electron.

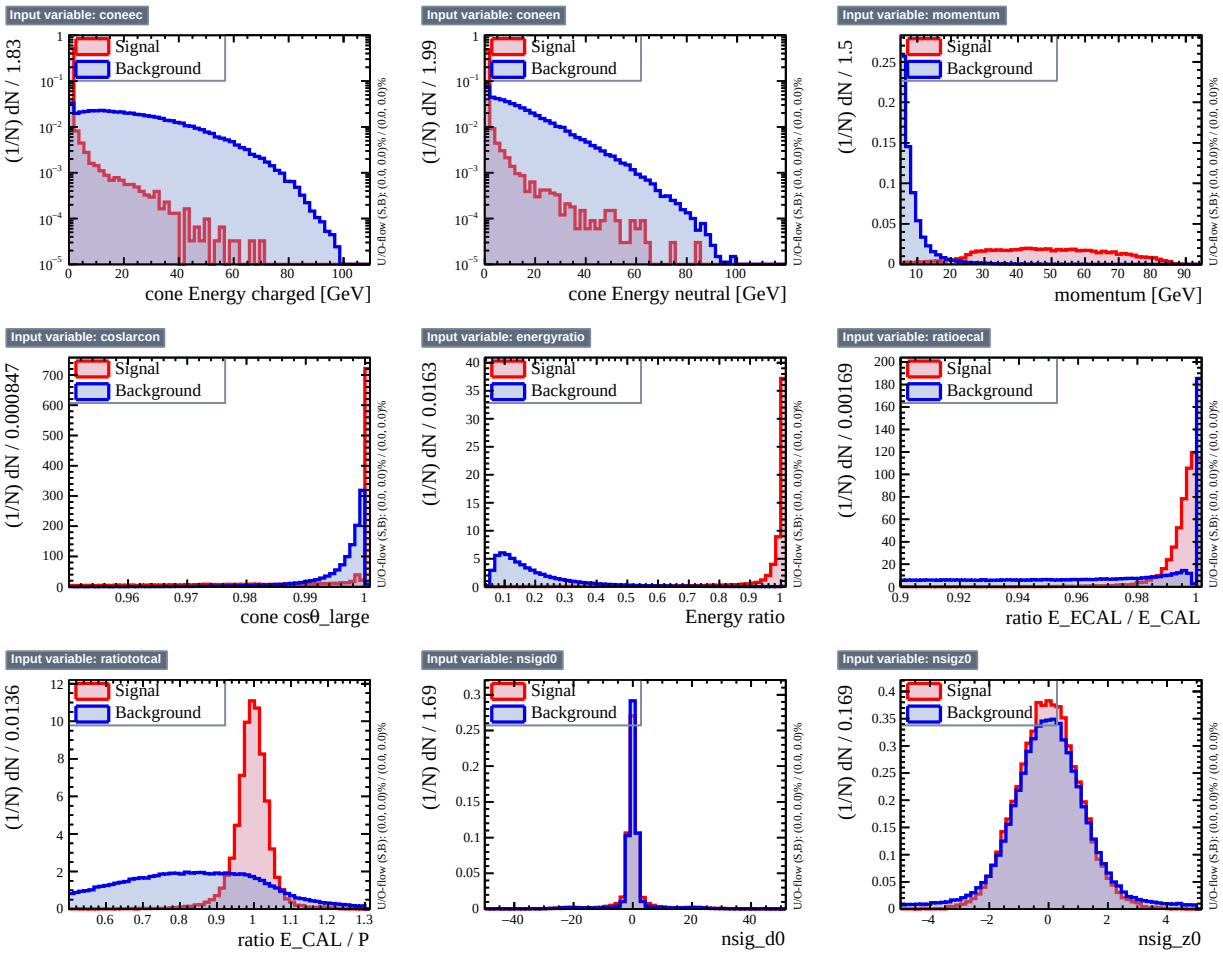

Figure 49: The plots show input variables for training neural nets, where $\sqrt{s}$=250 GeV $e^+e^- \to e^+e^-h$ process and $e^+e^- \to bbbb$ full hadronic process are given as the signal and background samples.

- **A ratio** CAL/P:
  P denotes momentum of certain charged particle. The ratio of the deposited energy in the CAL to the momentum P measured with the racker should be close to 1 for the electron, which is also a clear feature for the electron.

- **Yoke energy**:
  The yoke energy is expected to be larger for isolated muons compared to other charged particles.

- d_0 **and** Z_0:
  The impact parameters as distances between extrapolated tracks and the interaction point

in a r-ϕ plane (XY-plane) and a Z-axis. These values are expected to be useful for the discrimination of the tau leptons as described in the text.

The training of the neural nets are performed for charged particles which satisfy several requirements. For a electron and a muon, the momentum must be greater than 5 GeV, then, additional energy and momentum requirements for the electron are $0.5 < E_{CAL}/P < 1.3$ and $0.9 < E_{ECAL}/E_{CAL}$, and ones for the muon are $E_{CAL}/P < 0.3$ and 1.2 GeV$< E_{yoke}$. Furthermore, primary vertex constraints using impact parameters, d0 and z0, are also given, which are $|d_0/\delta d_0| < 50$ and $|z_0/\delta z_0| < 5$ for the electron, and also $|d_0/\delta d_0| < 5$ and $|z_0/\delta z_0| < 5$ for the muon. The output responses for both of the leptons and non-leptons are shown in Fig. 51.

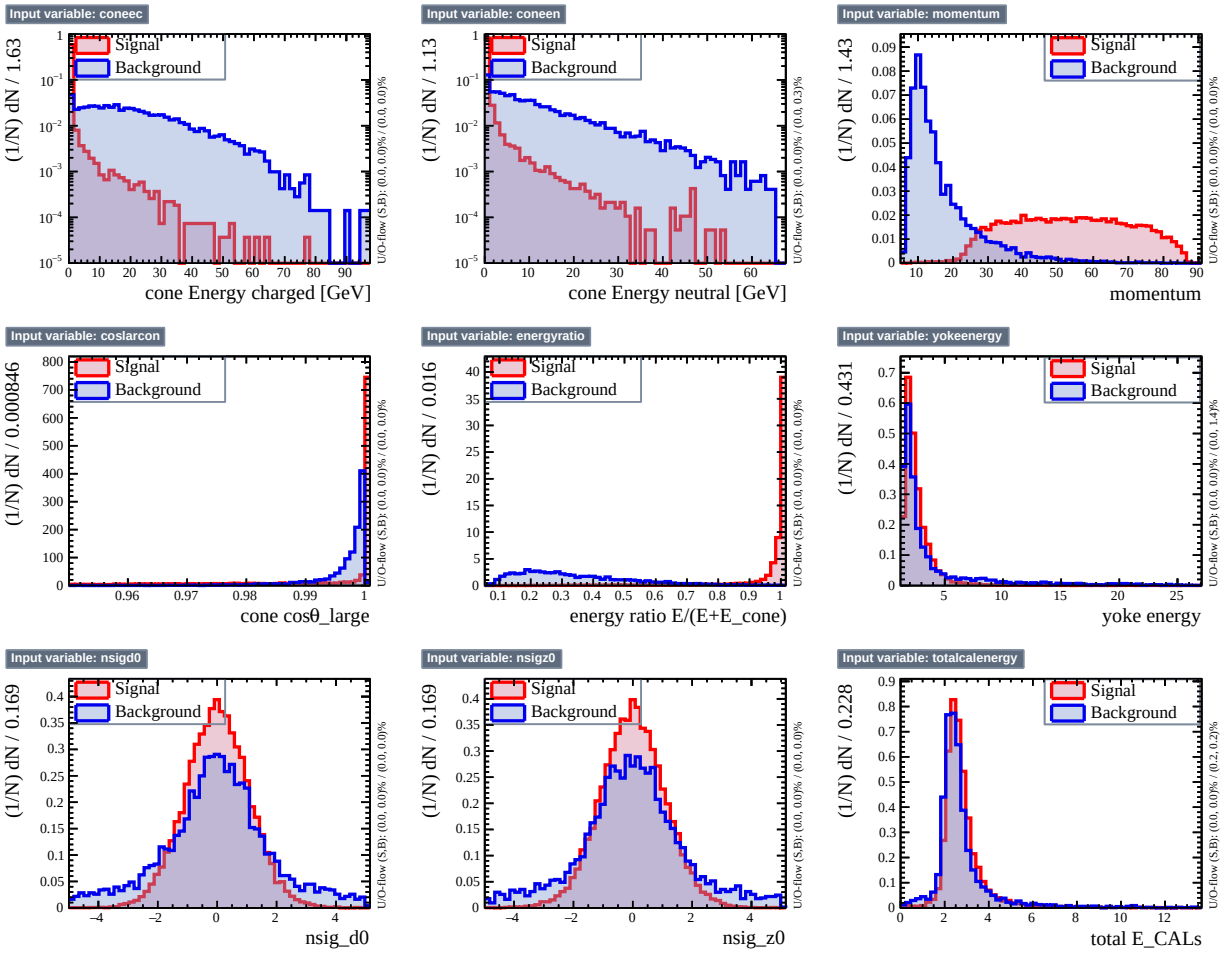

Figure 50: The plots show input variables for training neural nets, where $\sqrt{s}$=250 GeV $e^+e^- \to \mu^+\mu^- h$ process and $e^+e^- \to bbbb$ full hadronic process are given as the signal and background samples.

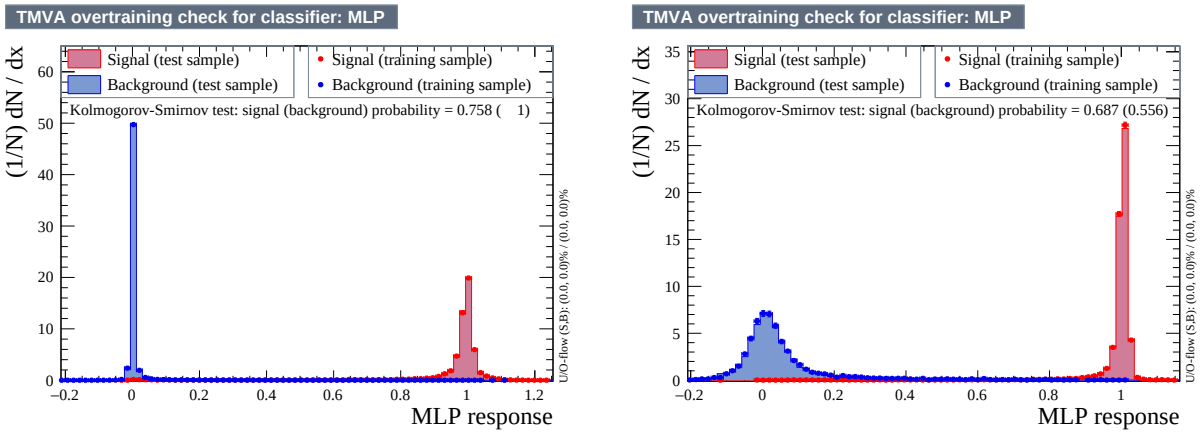

Figure 51: The MLP outputs for the muon versus backgrounds (Left) and electron versus backgrounds (Right).

5.3 Jet clustering algorithms

Quarks such as u, d and so on can not be seen alone in nature because of the color confinement in the QCD. Generated quarks through reactions originating from the electron and the positron can not be observed alone as well. Since single quarks have a so-called color charge, the state these quarks can take a stable state in nature is a colorless state in total, which is understood in the SM. When trying to tear off the quarks each other in high energy reaction of collider experiments, a pair of new quarks, which is also colorless, is generated between the quarks which are teared off and new colorless particles are generated. In the high energy reaction this process continuously happen, and the generated colorless particles which are often unstable particles can decay into other stable particles before reaching detectors. Eventually, particle jets called hadron jets which are composed of many colorless particles of mesons and baryons are observed as remnants of the initial quarks inside the detectors.

As with the case that an electron can emit a photon due to the initial state radiation or the bremsstrahlung, a quark can also emit a gluon when the quark is bended by a field formed by the color charges of nuclei. Based on knowledge of QCD, because the gluon, which can mediate the strong interaction, is equal to the colorless state which is same with the sate composed of quark and anti-quark, the gluon can form a gluon jet like the hadron jet. Fig. 52 gives such reactions.

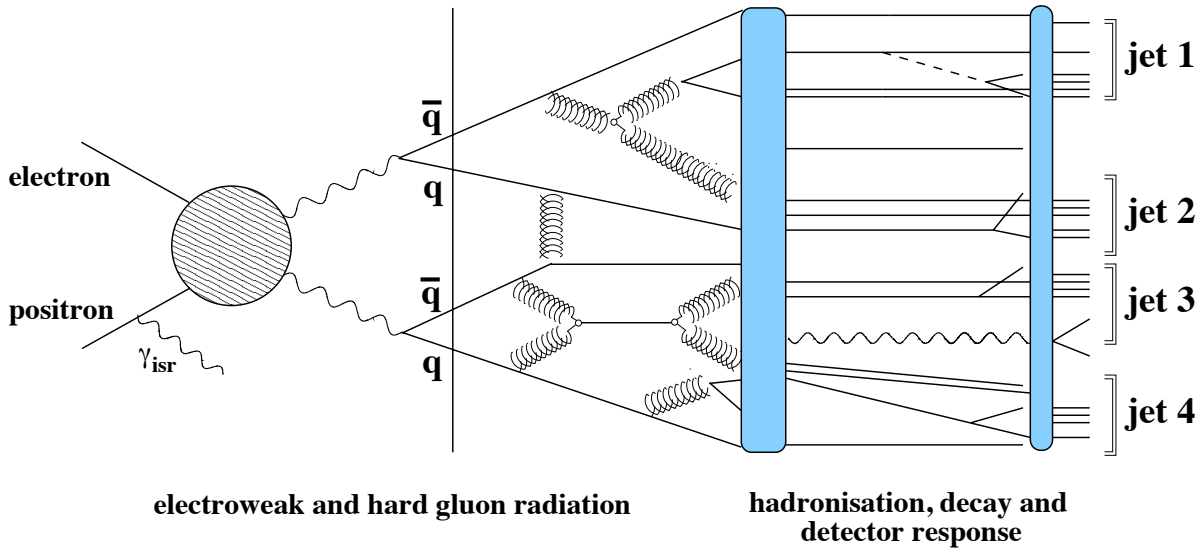

Figure 52: The schematic view is referred from [16]. The view illustrates interactions of an electron and a positron to a process of a four jets final state.

As explained above, the initial quarks and gluons which are generated through the interactions are observed as groups of many particles inside the detectors. Thus, if one wants to know dynamics of initial interactions, it's necessary to reconstruct the dynamics of parton-level using observed information, and extract information of the parton-level to evaluate the dynamics of the interactions. In generally, clustering algorithms are used to reconstruct the parton-level using particle energy and momentum, which try to cluster all particles originating from the partons into the corresponding partons. It is so-called jet clustering. Here, two general methods of the jet clustering algorithms, the Durham jet clustering and the k_T jet clustering which were widely used in the LEP2 experiment for the jet clustering, are briefly described. These jet clustering are also commonly used in the analysis of this thesis.

General jet clustering algorithms:

There are several general criteria for building up jets, which are :

- **Distance between particles (y_{ij})**:
  This parameter defines how much two particles i and j are a part from each other. This value becomes a criterion to decide which two particles should be combined at first.
- **Maximum distance ($y_{\rm cut}$)**:
  This parameter defines maximum distance to consider which two particles should be combined. This value becomes a criterion when the clustering should be ended.
- **A recombination scheme**:
  A rule of how four-momentum of particles are combined when two particles are merged.

Many jet clustering algorithms to cluster particles into jets take a similar way basically: Iterative procedures are implemented for each event using all particles. Taking two particles (i,j) in the final state, and calculate the distance between them based on certain definition of the algorithm. If a pair of the two particles (i,j) has the smallest value of y_{ij} compared to the other pairs, the particles (i,j) are combined by merging four-momentum of both particles and providing new four-momentum $P^\mu(i,j) = P^\mu(i) + P^\mu(j)$, which is based on the first definition of the recombination scheme. When the maximum distance parameter $y_{\rm cut}$ is set as a restriction criterion, the clustering is performed only for the condition that y_{ij} is smaller than the $y_{\rm cut}$ when the jets are built up. After the clustering is performed for two particles i and j, the event has $n-1$ particles and the distance between each pair are calculated agin. The procedure is repeated until all pairs of particles have y_{ij} ¿, $y_{\rm cut}$ and the number of remaining particles is equal to the number of requested jets which one gives.

The Durham jet clustering algorithm: [66]:

The Durham jet clustering algorithm is the most general jet clustering algorithm for the lepton collider experiments. In the Durham clustering, the distance between two particles y_{ij} is defined as follows, and a pair of two particles i and j, which has a minimum value of y_{ij} compared to the other, is combined. Based on the Lorentz invariant E scheme, which is one of the definition for the recombination procedure, jets called pseudo-jets are built up.

$$\begin{aligned} y_{ij} &= \frac{2\min(E_i^2, E_j^2)(1-\cos\theta_{ij})}{E_{vis}^2} \\ p_{ij}^\mu &= p_i^\mu + p_j^\mu \quad \text{(E-scheme)} \end{aligned}$$

where E_i and E_j show energy of particles i and j, and θ_{ij} shows an angle between two particles i and j. The distance y_{ij} is converted into a dimensionless value by normalizing to total squared visible energy in the event. When the number of merged pseudo-jets reaches to the number of requested jets one gives, the iteration of the Durham algorithm ends. The Durham clustering makes all particles forcibly involve into the requested number of jets. This algorithm can provide two kinds of output information $y_{m,m+1}$ and $y_{m-1,m}$, where m denotes the number of requested jets. When starting with n particles, the iterative procedure gives $n-1$, $n-2$, $n-3$, $\cdots$ and m pseudo-jets until the requested number of jets (m) is provided. These values $y_{m,m+1}$ and $y_{m-1,m}$ indicate a kind of transition of the number of jets in the final state, and are useful for discrimination of the signal and backgrounds which have different the number of jets in the final state.

The k_T jet clustering algorithms: [67, 68]

The k_T jet clustering algorithm is generally used in hadron collider experiments such as the LHC experiment. Particles which are derived from interactions of $\gamma\gamma$ →hadrons (called overlaid) induced by beam backgrounds have to be eliminated from reconstruction of events because these particles have nothing to do with the interaction one wants to focus on at all. The overlaid $\gamma\gamma$ →hadrons events have small transverse momenta. Since they tend to fly along beam line

(beam jet), these objects could be removed efficiently using the k_T jet clustering with the exclusive procedure.

The exclusive k_T jet clustering can judge whether a particle is a part of the beam jet or not, using an additional observable which is defined as distance between a position of the particle and the beam axis. In the case that the particle is regarded as a part of the beam jet, the particle is excluded from a particle list when pseudo-jets are built up. In the exclusive k_T jet clustering, all particles in the final state are not clustered, which is a different point with the Durham jet clustering. Firstly, one has to give a distance d_{ij} between particles i and j for usage of the k_T jet clustering, which are defined as,

$$\begin{aligned} d_{ij} &= \min(k_{Ti}^2, k_{Tj}^2)\frac{\Delta R_{ij}^2}{R^2} \\ \Delta R_{ij}^2 &= (\eta_i - \eta_j)^2 + (\phi_i - \phi_j)^2 \\ d_{iB}^2 &= k_{Ti}^2 \end{aligned}$$

where k_{Ti} shows transverse momentum of a particle i against the beam axis, and R is a parameter called jet-radius, which is necessary to set to adjust easiness of combine of particles into the beam jet depending on the situation. ΔR_{ij} is defined from two angles η_i and ϕ_i which show a psudo-rapidity and azimuthal angle, respectively. It is also required to define a distance d_{iB} between a position of particle and the beam axis in order to judge if the particle is originated from the interaction of the $\gamma\gamma$ overlay process or not.

In the exclusive k_T jet algorithm the values of d_{iB} and d_{ij} are calculated for every particle and every pair of (i,j). If $d_{ij} < d_{iB}$, particle i and j are paired as a pseudo-jet by combining their four-momenta $P^\mu(i,j) = P^\mu(i) + P^\mu(j)$. If $d_{iB} < d_{ij}$, the origin of the particle i is regards as the interaction of the $\gamma\gamma$ process and the particle i is removed from the particle list. This procedure is iterated until the number of pseudo-jet reaches to the number of requested jets.

After this jet-clustering procedure two beam jets and the requested number of jets are left. In the process of the exclusive k_T jet clustering, almost all of the overlaid $\gamma\gamma \rightarrow$hadrons process is expected to be excluded. The analysis described in the thesis uses the exclusive k_T jet clustering only for this purpose. The jets clustered with the k_T clustering are decomposed back into original single particles and these particles are used again with the latter analysis.

5.4 Heavy-flavor tagging

As mentioned above, the jets observed in the final state are originally quarks. Therefore, heavy quarks, particularly b-quark and c-quark, are possible to perform identification by exploiting its lifetime and corresponding travel distance until they decay, which is known as the heavy flavor tagging and a important technique for the Higgs and top quark physics since many b-quarks appear in the final state of the related processes. B-hadrons have relatively longer life times compared to other C-hadrons or S-hadrons. Currently the interactions between quarks through the weak force and its mixing are understood and described by the Cabibbo-Kobayashi-Maskawa (CKM) matrix [69].

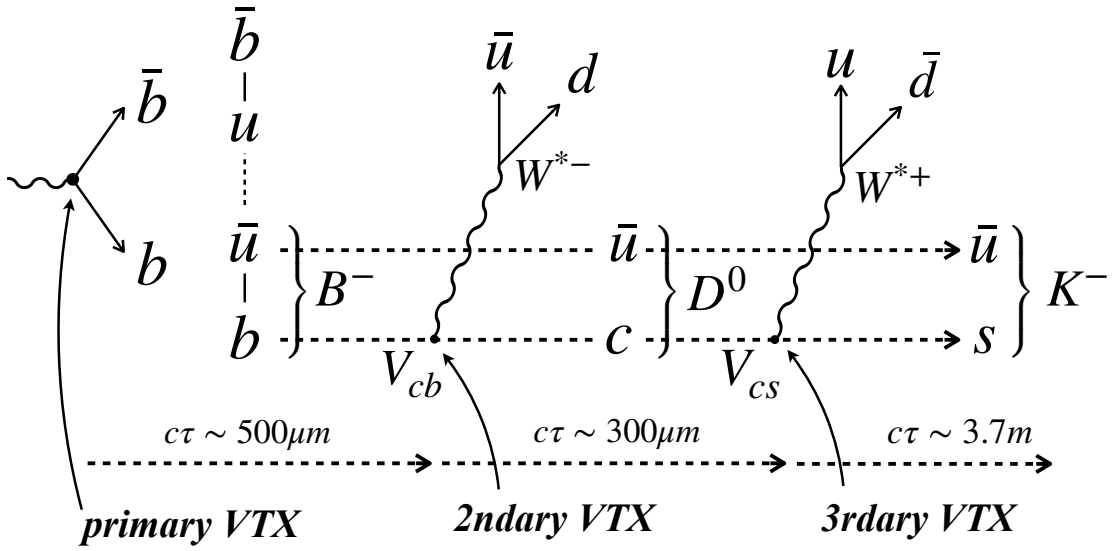

Figure 53: A schematic view of cascaded decay of a b-hadron, and the heavy-flavour tagging using secondary and thirdly vertices.

u- and d-quarks in the first generation can not decay themselves, and c- and s-quarks in the second generation can decay into light quarks such as the u- and d-quarks, whose tendencies or factors are given as elements of the CKM matrix[14]. In contrast, b-quark has much larger factors with its partner t-quark, and it has very small factors for different flavors, which are $|V_{tb}| = 0.999$ for t-quark and $|V_{cb}| = 0.041$ for c-quark (and physical phenomena are given with square of the factors). Furthermore, since t-quark has huge mass compared with the b-quark, the decay from b- to t-quark is not allowed. The possible decay of b-quark is from b- to c-quark by emitting (virtual) W boson through the weak force. And this decay is not very likely, but happen in the last. Thus, B-hadrons can have the longer lifetime and travel several millimeters in the detector before they decay. In higher energy particles receive Lorentz boost, and the lifetime could be expanded more. Because of similar reason, C-hadrons also have relatively longer lifetime. The identification of c-quark is possible, the b-quark as well. Fig. 53 gives such reactions.

In the ILCSoft framework, the heavy flavor identification is implemented in a software package called LCFIPlus [72]. The LCFIPlus performs the flavor identification based on Boosted Decision Trees (BDTs) inside TMVA framework with several input observables of clustered jets and found

[14]The matrix elements of the CKM matrix [70, 71] which are currently evaluated based on each measurement are given like,

$$\begin{bmatrix} |V_{ud}| & |V_{us}| & |V_{ub}| \\ |V_{cd}| & |V_{cs}| & |V_{cb}| \\ |V_{td}| & |V_{ts}| & |V_{tb}| \end{bmatrix} = \begin{bmatrix} 0.97428 & 0.2253 & 0.00347 \\ 0.2252 & 0.97345 & 0.0410 \\ 0.00862 & 0.0403 & 0.99915 \end{bmatrix}.$$

secondary vertices: the impact parameters d_0 and z_0, direction and energy of jet. The output is given as b-likeness and c-likeness and added for each jet.

5.5 Event shape observables

Each physical process have different event shapes [73] and these shapes become useful observables to discriminate the signal process against background processes. The jet clustering parameters $y_{n,n+1}$ described in the previous section are also one of the event shape observables. In the analysis of this thesis, the several event shape observables are used for the discrimination of the signal process, which are listed below,

- **Thrust T, Thrust-major T_{maj}, and Thrust-minor T_{min} :** [74, 75]
  Thrust values are respectively defined as,

$$\begin{aligned} T &= \max_{\vec{n}_T}\left(\frac{\sum_i |\vec{P}_i \cdot \vec{n}_T|}{\sum_i |\vec{P}_i|}\right), \\ T_{maj} &= \max_{\vec{n}\perp\vec{n}_T}\left(\frac{\sum_i |\vec{P}_i \cdot \vec{n}|}{\sum_i |\vec{P}_i|}\right), \\ T_{min} &= \frac{\sum_i |\vec{P}_i \cdot \vec{n}_{T_{min}}|}{\sum_i |\vec{P}_i|}, \quad \text{with} \quad \vec{n}_{T_{min}} = \vec{n}_T \times \vec{n}_{T_{maj}} \end{aligned}$$

  In the definition of Thrust a thrust axis $\vec{n}_T$ is chosen to make the expression maximize. The value can indicate that $T = 1$ gives narrower two-jet event and $T = 1/2$ gives spherical event. To define the Thrust-major T_{maj}, the axis is taken for maximizing the expression and to be orthogonal to the thrust axis $\vec{n}_T$, where $T_{maj} = 0$ and $=1/2$ indicate two-jet-like and spherical-like event shape. For the Thrust-minor T_{min}, the axis is taken as a direction perpendicular for both $\vec{n}_T$ and $\vec{n}_{T_{maj}}$. T_{min}=0 and 1/2 indicate that the event is two- or three-jet event and spherical-like event, respectively.

- **Oblateness O :** [76]
  The Oblateness is defined with the difference between Thrust-major T_{maj} and Thrust-minor T_{min} as $O = T_{maj} - T_{min}$, which indicates that $O = 0$ and $= T_{maj}$ give two-jet or spherical-like event, and three-jet event.

- **Sphericity S :** [77, 78]
  The Sphericity is defined as

$$S^{\alpha\beta} = \frac{\sum_i \vec{P}_i^{\alpha} \vec{P}_i^{\beta}}{\sum_i |\vec{P}_i|^2} \quad (\alpha, \beta = \text{components of } x, y, z)$$

  where the calculation runs over all particles. This observable indicates how a reaction is spherical-like event. $S = 0$ indicates the event is straight-like whereas $S = 1$ indicates the event is spherical-like.

Other useful observables have been defined and used for the LEP and LEP2 experiments, where certain standard set of event shape observables were defined. Although they are not used in this thesis, it would be worth knowing these ideas and results from [79–81].

6 Analysis on the anomalous ZZH couplings

The analysis we performed for evaluation of the sensitivity to the anomalous ZZH couplings that the ILC experiment can reach is described from this section. Since the ILC experiment is currently planned to operate from the center-of-mass energy $\sqrt{s}$ =250 GeV, Higgs production events coming from the Higgs-strahlung process $e^+e^- \to ZH$ will be observed. The large number of SM background events which contaminates with the Higgs process is also observed. To remove the SM background processes and extract the signal process, background suppression need to be performed using various kinematical or topological observables and characteristics that the signal and the background processes have. When applying the background suppression to the events using these observables, signal significance S_{sig}, defined as flows, is calculated for each observable while scanning given regions of the observables and minimizing the regions gradually, and then, certain region which gives a maximum S_{sig} is taken as the optimized point.

$$S_{sig} \equiv \frac{N_{sig}}{\sqrt{N_{sig} + N_{bkg}}}$$

where N_{sig} and N_{bkg} denote the number of remaining signal and backgrounds events. Above signal significance S_{sig} is, in fact, established by considering Poisson distribution. Events that are discretely and independently given one another in certain given interval are generally described by Poisson distribution that can give a probability for finding the number of events of N, which would be.

$$f(N;\lambda) = \frac{\lambda^N}{N!}e^{-\lambda}$$

where $\lambda = \overline{N}$ is the average number of events, and variance σ^2 showing how large a value fluctuates from its mean value is also given by $\sigma^2 = \bar{N}$. In a real experiment, a probability distribution when the number of observed events in certain given interval is $\overline{N}_{obs}$ is also given by Poisson distribution. $\overline{N}_{obs}$ is usually given as $\overline{N}_{obs} = N_{sig} + N_{bkg}$, and N_{sig} and N_{bkg} denote the number of signal and background events.

On a cross-section measurement of certain unclear process, for instance, the number of expected signal events is $\overline{N}_{sig} = \sigma_{sig} \cdot L$, whereas the number of expected background events coming from well-known background processes is given as $\overline{N}_{bkg} = \sigma_{bkg} \cdot L$, where L denotes an integrated luminosity. When the sum of observed events N_{obs} is given, the measured cross-section for the signal process is given as $\sigma_{meas} = (\overline{N}_{obs} - N_{bkg})/L$, and its statistical error is also given as $\Delta\sigma_{meas} = (\Delta N_{obs})/L = \sqrt{\overline{N}_{obs}}/L$ based on Poisson distribution. In the case better measurement is required, which means extraction of a better error is necessary, the situation that a statistical error is kept at a minimum value against the fluctuation of the background processes is recommended. Statistical precision for the measured cross-section is described as follows,

$$\frac{\Delta\sigma_{meas}}{\sigma_{meas}} = \frac{\sqrt{\overline{N}_{obs}}/L}{(\overline{N}_{obs} - N_{bkg})/L} = \frac{\sqrt{N_{sig} + N_{bkg}}}{N_{sig}} = \frac{1}{S_{sig}}$$

Therefore, the fact that making the statistical error minimize is identical with the situation that making the signal significance S_{sig} maximize.

General criteria on background suppression :

The most useful and effective observables for verifying the existence of the anomalous couplings are each kinematical angular distribution. In that case that these angular information are used for the background suppression, the corresponding regions of angular distributions which are suppressed also become completely insensible for the signal process as well. It will cause a bias to the sensitivity of the anomalous couplings, consequently. To avoid such situation the background

suppression is implemented without the angular information and observables which are correlated with the angular distribution as much as possible although these angular information are very useful for the suppression of several background processes.

Processes for evaluating the anomalous ZZH couplings :

To evaluate the sensitivity to the anomalous ZZH couplings, the following 8 channels of the two kinds of Higgs production processes at both center-of-mass energies $\sqrt{s} = 250$ and 500 GeV are used in this thesis. The analysis of each process for evaluating the anomalous couplings is mentioned from the next subsection.

$$\begin{cases} \sqrt{s} = 250 \text{ GeV} & e^+e^- \to Zh \to \mu^+\mu^- h & \text{(Higgs-strahlung)} \\ \cdots & e^+e^- \to Zh \to e^+e^- h & (\quad \cdots \quad) \\ \cdots & e^+e^- \to Zh \to q\bar{q}h, \quad h \to b\bar{b} & (\quad \cdots \quad) \\ \cdots & e^+e^- \to e^+e^- h, \quad h \to b\bar{b} & (ZZ\text{-fusion}) \\ \sqrt{s} = 500 \text{ GeV} & e^+e^- \to Zh \to \mu^+\mu^- h & \text{(Higgs-strahlung)} \\ \cdots & e^+e^- \to Zh \to e^+e^- h & (\quad \cdots \quad) \\ \cdots & e^+e^- \to Zh \to q\bar{q}h, \quad h \to b\bar{b} & (\quad \cdots \quad) \\ \cdots & e^+e^- \to e^+e^- h, \quad h \to b\bar{b} & (ZZ\text{-fusion}) \end{cases}$$

In the analysis both of the variations which are extracted from the kinematical shape distribution of each process and the production cross-section of the Higgs-strahlung and ZZ-fusion process are used for the estimation of the sensitive to the anomalous ZZH couplings. The analysis of two main channels, which are muon and hadronic channels of the Higgs-strahlung, are mentioned in the main text as examples. The other channels are summarized in the appendix.

6.1 $e^+e^- \to Zh \to \mu^+\mu^- h$ at $\sqrt{s} = 250$ GeV

In the process that the Z boson decays into a stable lepton pair, here an electron or a muon pair is assumed, it is expected that four-momentum of the final state leptons are precisely measured using the tracking detectors. Thus, the reconstructed Z boson from the lepton pair can also give the precise information on itself. Since the Higgs-strahlung Zh process is a simple two- body decay, the reaction related to the Higgs boson can be fully reconstructed by kinematical calculation using four-momenta of the initial state and the final state Z boson without looking at the Higgs boson, which is a so-called recoil mass technique described as follows,

$$M^2_{higgs} = M^2_{rec} = (\sqrt{2} - E_Z)^2 - |\boldsymbol{P}_Z|^2$$

where E_Z and $\boldsymbol{P}_Z$ show energy and absolute momentum of the Z boson reconstructed by the lepton pair. What is necessary to maximize the information that the Higgs-strahlung Zh process has is to identify these isolated leptons decaying from the Z boson efficiently.

6.1.1 Reconstruction and background suppression

Isolated lepton finding and radiation recovering :

The MVA based lepton finding is implemented for the selection of the isolated leptons, which is explained in the previous section. The MVA lepton finder can give likeness for each charged track based on input observables such as the measured momentum, the deposited energy in each calorimeter, impact parameters, and so on. To extract candidates of the isolated lepton, the electron-likeness of > 0.5 is applied to find the isolated electron, and the muon-likeness of > 0.7 is applied to find the isolated muon in the analysis.

After the MVA selection of the isolated leptons, it's necessary to identify which lepton pair is derived from the Z boson. The invariant mass of the Z boson M_Z must be 91.187 GeV [70] when the invariant mass is calculated using the lepton pair, which is well-known precisely. A requirement $|M_{ll} - M_Z| < 40(60)$ GeV, where M_{ll} denotes the invariant mass of the lepton pair, is also given for the $\mu(e)$ channels as an additional criterion to identify the proper lepton pair decaying from the Z boson. In the case of the electron, a trajectory of the electron is bended by a magnetic field or electrostatic force from molecules of gas inside the TPC while the electron is flying in the detectors. Therefore, the electron tends to radiate photons, and its probability is larger than that of the muon because of smallness of mass. The momenta of the final state electrons are often observed relatively lower than that of original one which are given shortly after the decay of the Z boson due to the radiated photons Thus, the reconstructed invariant mass of the Z boson are shifted compared with the muon pair without any recoveries of the final state radiation. Because of this reason the requirement for the invariant mass for the electron pair is set to be relatively loose. In the case the invariant mass of the lepton pare M_{ll} calculated by leptons from other semi-leptonic or full hadronic processes is largely deviated from the invariant mass of the Z boson. The above requirement is effective for the suppression of semi-leptonic or full hadronic background processes.

The reconstructed recoil mass M_{rec} distribution has broader tail due to several effects such as beam-strahlung, initial state radiations (ISR), bremsstrahlung, final state radiations (FSR), and finite resolution of the detectors. Since the beam-strahlung and ISR happen before interactions, and emitted photons fly along a direction of the beam axis, it is impossible to detect them and estimate the effects. These effects can be seen in the right tail of the recoil mass distribution in Fig. 54. In contrast the bremsstrahlung and FSR can be recovered because the emitted photons are possible to detect with the detectors.

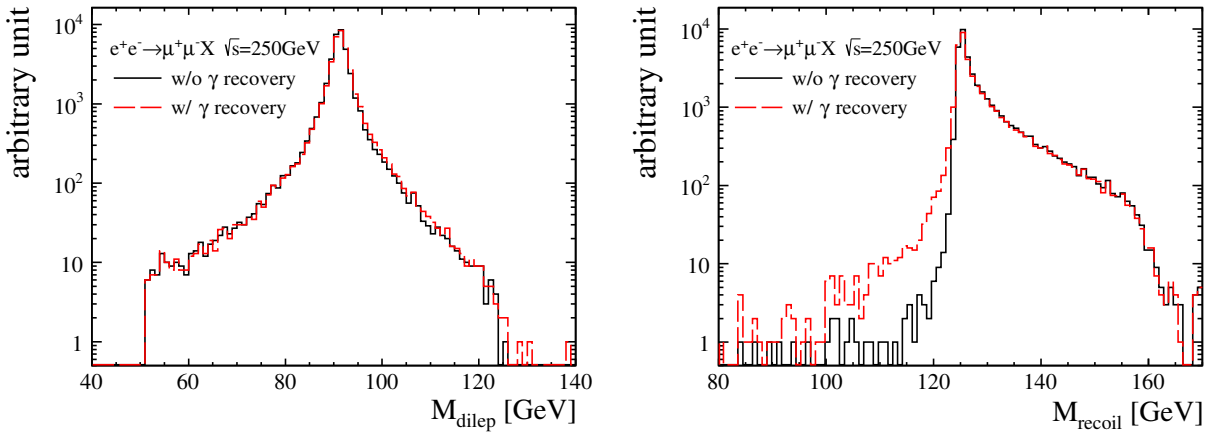

Figure 54: Distributions of the invariant mass of the muon pair M_{ll} (left) and the recoil mass M_{reco} (right) in $Zh \to \mu^+\mu^- h$ of the Higgs-strahlung process at $\sqrt{s}$=250 GeV. Black and red lines on both plots correspond to without and with recovering photons, respectively.

As a basic idea for recovering such photons, a cone is constructed along a momentum axis of the isolated leptons. A polar angle is calculated between the cone axis and momentum direction of all neutral particles which become a candidate of the bremsstrahlung and FSR photon. If $\cos\theta$ of the polar angle exceeds 0.995, these neutral particles are regarded as the bremsstrahlung or FSR photons, and its four-momentum are combined into that of the isolated leptons. This method for recovering the bremsstrahlung and FSR photons is implemented for both μ and e channels. Fig. 54 show comparison of the reconstructed invariant mass of the lepton pair M_{ll} and the recoil mass M_{reco} distributions at $\sqrt{s} = 250$ GeV with and without recovering the bremsstrahlung and FSR.

Reconstructed angular observables :

Fig. 55 show two important angular distributions which are sensitive to the anomalous couplings after reconstructing events with the ILD model through the realistic reconstruction chain of the framework of the ILC soft, MC truth and reconstructed distributions of $\cos\theta_Z$ and $\Delta\Phi$ are plotted, which are the polar angle of the Z boson and the the angle between production planes that are composed of momenta of the initial state electron and the final state anti-fermion (μ^+) with a momentum direction of the Z boson as an axis in the laboratory frame. Since the Higgs boson almost rests in the Higgs-strahlung process at 250 Gev, the laboratory frame can give the same observation on $\Delta\Phi$.

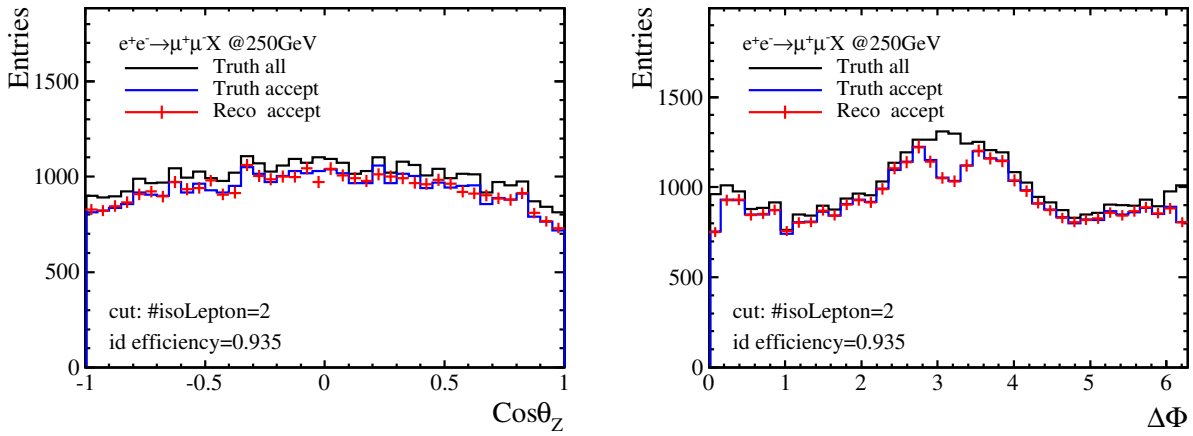

Figure 55: Plots show the MC truth and reconstructed distributions of both $\cos\theta_Z$ and $\Delta\Phi$ in $Zh \to \mu^+\mu^- h$ of the Higgs-strahlung process at $\sqrt{s}$=250 GeV. These observables give the sensitivities to the anomalous ZZH couplings. The clear dips at 0, π, and 2π on $\Delta\Phi$ is due to the missing final state muons.

In the plot of the reconstructed $\Delta\Phi$ distribution, clear dips can be seen at 0, π, and 2π. This is because one or both of the final state muons are missing when those muons fly along a beam pipe. At 0 and 2π the muon flies to the opposite (beam) direction of the initial electron, and the muon flies to the same direction with the initial electron. Except this unavoidable fact, it can be seen that each angle is precisely reconstructed.

Background suppression :

Since the channels of the Higgs-strahlung process with the leptonic decays of the Z boson have a very clear signature, the signals can be easily distinguished from the backgrounds with several kinematical and topological observables. Cut values for each observable are given by maximizing the signal significance S_{sig} as explained in the first part of this section. The following observables and values given in parentheses are imposed for the background suppressions, where the values are for the left-handed polarization state, which is P(e^-, e^+)= (-80%,+30%).

- Two leptons having opposite sign with the same flavor must exist exactly in one event (muon and anti-muon), which is given as a pre-selection.
- $N_{tracks} \in [6,\ 60]$
  The number of charged tracks, which is useful to remove huge two-fermion backgrounds.
- $E_Z \in [104.6,\ 111.7]$ GeV
  Since energy of the di-lepton system derived from one of the dominant background processes $e^+e^- \to llqq$ (ZZ-fusion) has a peak at 125 GeV, this observable is useful to separate it.
- $M_Z \in [83.0,\ 96.4]$ GeV
  The invariant mass of di-lepton $M_{\mu^+\mu^-}$ must be close to the mass of the Z boson.

- $E_{vis} - E_Z(\equiv E_{sub}) \in [60.0,\ 170.0]$ GeV
  Visible energy shows measured energy in the detectors. The subtracted value by the energy of the Z boson is close to 0 for the two-fermion process, which is still useful to distinguish the Higgs boson from other dispersed backgrounds.
- $M_{rec} \in [120,\ 137]$ GeV
  Recoil mass against the di-lepton system, which becomes a conclusive mass window to determine a Poisson error calculated by the remaining number of events on each bin on kinematical histograms.

Table 3: Tables show the expected number of remaining signal and background events after each cut for the $Zh \to \mu^+\mu^- h$ at $\sqrt{s}$=250 GeV, with both of the beam polarization states: P(e^-, e^+)= (-80%,+30%) and (+80%,-30%). The integrated luminosity of 250 fb^{-1} is assumed. The signal efficiency ϵ and significance S_{sig} are also given in the table.

$\sqrt{s}$=250 GeV P(e^-, e^+)= (-80%,+30%)

Cut variables	$\mu\mu H$	ϵ	eeH	$\tau\tau H$	$2f$	$4f$	S_{sig}
No cut	2603	100	2671	2598	$2.91 \cdot 10^7$	$1.02 \cdot 10^7$	-
ID of a di-lepton pair	2433	93.46	3	6	$4.30 \cdot 10^5$	$8.34 \cdot 10^4$	3.38
$N_{tracks} \in [6,\ 60]$	2246	86.28	1	4	6771	$2.43 \cdot 10^4$	12.3
$E_Z \in [104.6,\ 111.7]$ GeV	1740	66.84	0	0	156	1470	30.0
$M_Z \in [83.0,\ 96.4]$ GeV	1673	64.27	0	0	104	995	31.6
$E_{sub} \in [60.0,\ 170.0]$ GeV	1628	62.54	0	0	34	954	31.7
$M_{reco} \in [120,\ 137]$ GeV	1624	62.39	0	0	34	923	31.8

$\sqrt{s}$=250 GeV P(e^-, e^+)= (+80%,-30%)

Cut variables	$\mu\mu H$	ϵ	eeH	$\tau\tau H$	$2f$	$4f$	S_{sig}
No cut	1756	100	1786	1752	$2.03 \cdot 10^7$	$1.27 \cdot 10^6$	-
ID of a di-lepton pair	1641	93.45	2	4	$3.44 \cdot 10^5$	$2.61 \cdot 10^4$	2.69
$N_{tracks} \in [6,\ 60]$	1515	86.27	1	3	5294	$1.31 \cdot 10^4$	10.7
$E_Z \in [102.9,\ 112.0]$ GeV	1265	72.04	0	0	173	982	25.7
$M_Z \in [83.0,\ 98.2]$ GeV	1219	69.42	0	0	123	703	27.0
$E_{sub} \in [60.0,\ 170.0]$ GeV	1187	67.59	0	0	45	684	27.1
$M_{reco} \in [120,\ 137]$ GeV	1154	65.72	0	0	35	598	27.3

The distributions of each observable for suppressing the backgrounds and the recoil mass of the Z boson are plotted in Fig. 56, and the Table 3 shows the number of remaining signal and background events after each cut, where the integrated luminosity of 250 fb^{-1} with both of the beam polarization states: P(e^-, e^+)= (-80%,+30%) and (+80%,-30%) are assumed. The signal efficiency and the signal significance are also given for each cut.

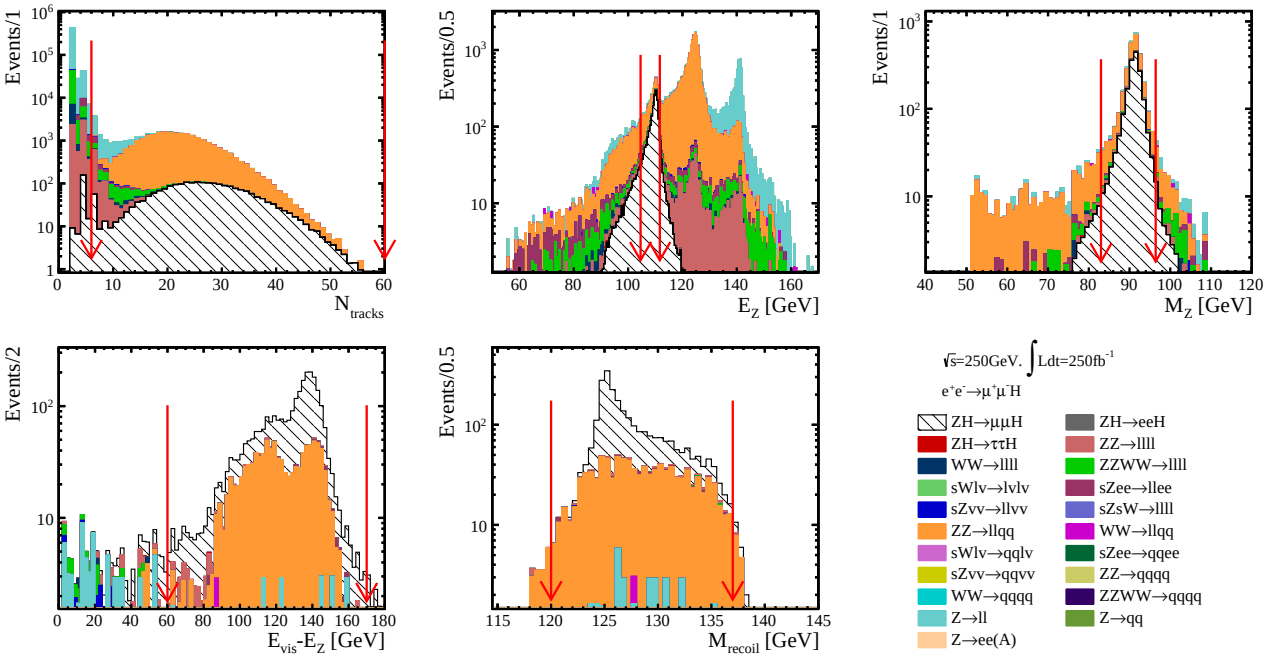

Figure 56: The distributions show each observable used for the background suppression assuming 250 fb^{-1} with P(e^-, e^+)= (-80%,+30%). The explanation of the observables are given in the text. Red arrows on each plot indicate the cut values applied to each observable as the background suppression.

6.1.2 Acceptance and migration on observables

Each sensitive observable is binned for the χ^2 test, and the statistical errors of each bin on each observable are given as the standard deviation of the Poisson probability using the remaining signal and background events, which is specifically given as: $Error = \sqrt{N_{sig} + N_{bkg}}$. Each observable are respectively binned in 30, 10, and 5 for the one-dimensional, two-dimensional, and three-dimensional distributions. As discussed in the section of the analysis strategy of the anomalous couplings, the most important key information to evaluate the sensitivity when the angular distributions are used is the detector response function which is composed of the event acceptance η and the probability of the migration effects $\bar{f}$. Fig. 57 and Fig. 58 show summary plots on the one-dimensional angular distributions of $\cos\theta_Z$ and $\Delta\Phi$ binned in 30, respectively. Since any angular cuts are not applied, the event acceptance η of $\cos\theta_Z$ maintains flatness, and one for $\Delta\Phi$ also maintains flatness except for the dips at 0, π, and 2π.

The probabilities of the migration effects are also very clear as given in the plots. In the case that certain bin of a realistic distribution x_j^{Rec}, for instance the 0-th bin x_0^{Rec}, is tried to construct from a theoretical distribution x_i^{Gen}, things to do is just to multiply the theoretical distribution x_i^{Gen} by the event acceptance η_i and the probability of the migration $\bar{f}_{0i}$. In this manner over the number of bins, theoretical angular distribution can be transferred to the realistic angular distribution which would be observed in the real detectors.

Summary plots of the two-dimensional angular distribution of $x(\cos\theta_Z, \Delta\Phi_{f\bar{f}})$ binned in 10×10 is also plotted instead of the three-dimensional distribution (because the illustration of the three-dimensional distribution is too difficult) as demonstration of a multi-dimensional distribution, which is given in Fig. 59. Similarly for the reconstruction of certain bin of a realistic distribution x_{jb}^{Rec}, for instance the (0,0)-th bin x_{00}^{Rec}, things to do is to multiply the theoretical distribution x_{ia}^{Gen} by the acceptance η_{ia} and the probability of the migration $\bar{f}_{00ia}$.

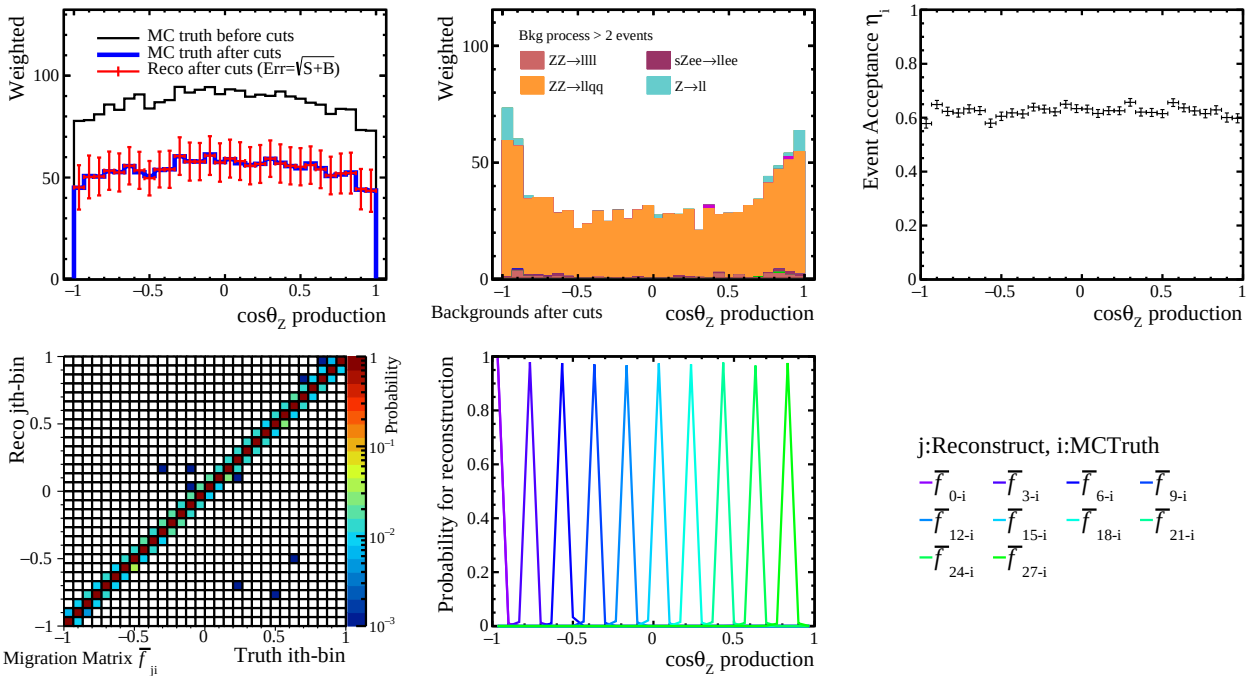

Figure 57: The distributions show the summary of the polar angle of the Z boson ($\cos\theta_Z$) after the background suppression. (Top left and middle): the remaining signal and the background distribution, which are given with the MC truth and the reconstructed, where the statistical error is given as the standard deviation of the Poisson probability. (Top right): the event acceptance function η_i. (Bottom left and middle): the distribution shows the probability matrix of the migration ($\bar{f}_{ji}$) that is applied for the reconstruction of the realistic distribution of $\cos\theta_Z$, and the cross-sections of $\bar{f}_{ji}$ as 1-dim plots.

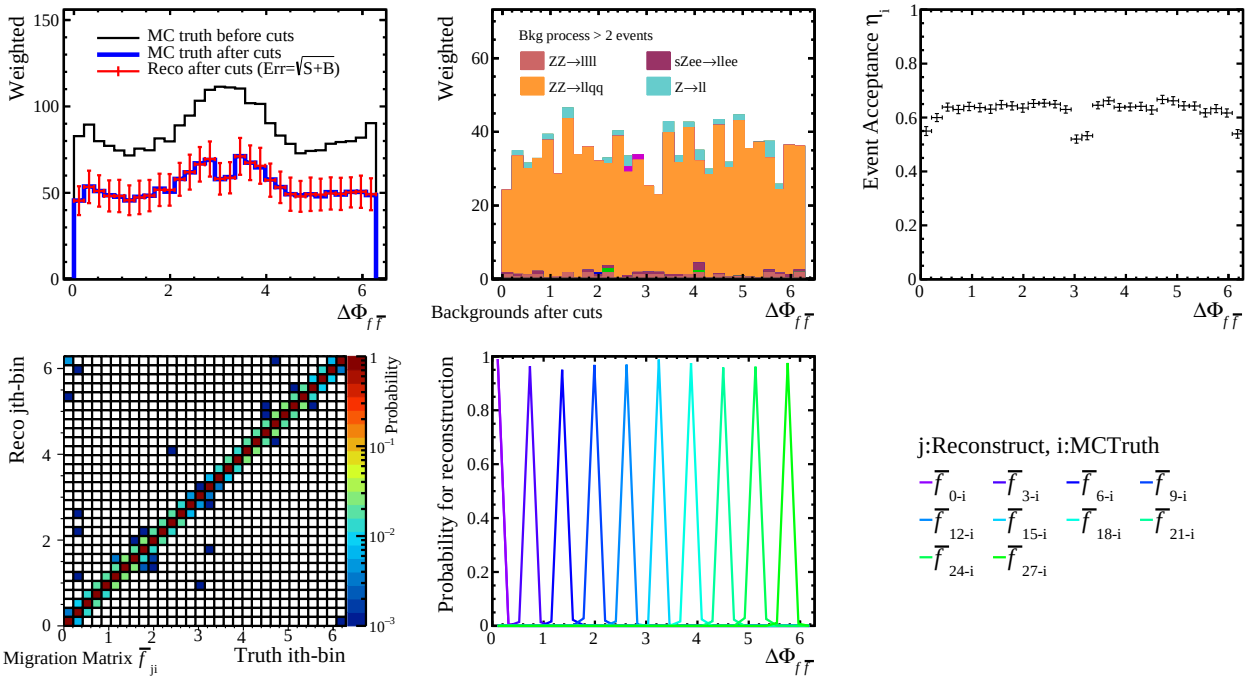

Figure 58: The distributions show the summary of the angle between production planes in the laboratory frame ($\Delta\Phi$) after the background suppression. (Top left and middle): the remaining signal and the background distribution, which are given with the MC truth and the reconstructed. (Top right): the event acceptance function η_i. (Bottom left and middle): the probability matrix of the migration ($\bar{f}_{ji}$) that is applied for the reconstruction of $\Delta\Phi$, and the cross-sections of $\bar{f}_{ji}$ as 1-dim plots.

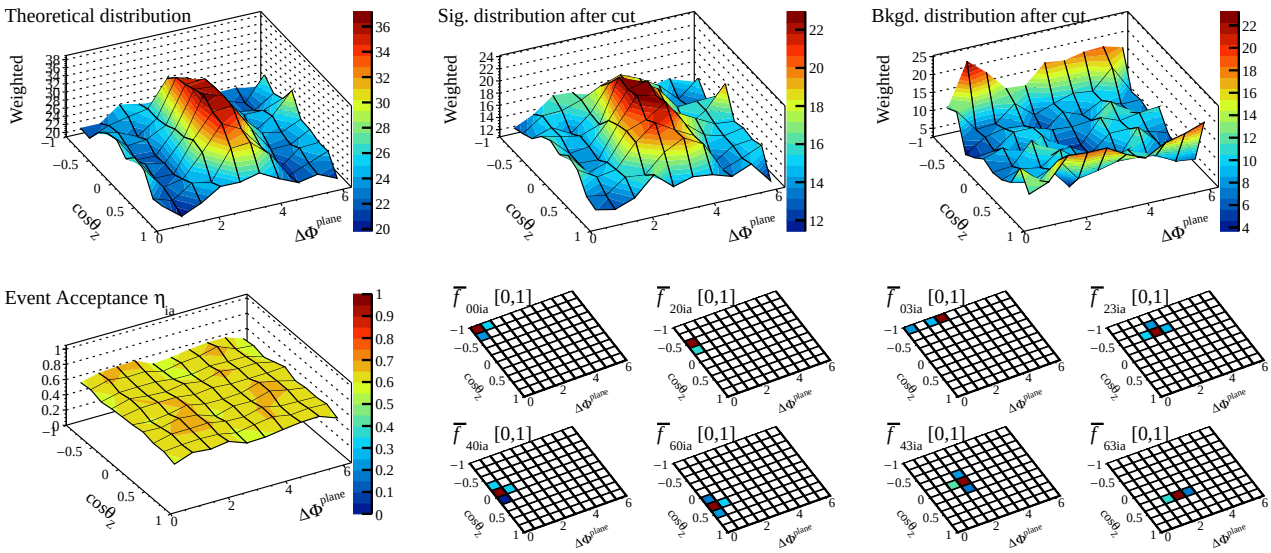

Figure 59: The distributions show the summary of the two-dimensional distribution consisted of the production angle of the Z boson $\cos\theta_Z$ and the angle between production planes in the laboratory frame ($\Delta\Phi$) after the background suppression. (Top left, middle, and right): The remaining MC truth and the reconstructed signal distribution, and the background distribution, respectively. (Bottom left): The event acceptance function η_{ia} shows whether each signal event on each bin is accepted or not after the suppression. (Bottom middle and right): Several examples on the probability matrix of the migration where the 2-dim plots give the cross-sections of $\bar{f}_{jbia}$ since the illustration of the migration is too difficult which is a 4-dimension distribution.

6.1.3 Impact of angular distributions

Using the event acceptance η and the probability of the migration effects $\bar{f}$ that are evaluated through the full simulation by the last section, the χ^2 test is performed, which is described in the section Sec. 4.4.3. Fig. 60 show the sensitivity to the anomalous ZZH couplings with one-parameter space of a_Z, b_Z, and $\tilde{b}_Z$, where $\Delta\chi^2$ is given as $\Delta\chi^2 = \chi^2 - \chi^2_{min}$ and χ^2_{min} is exactly 0 in the current settings since 0 values for each parameter can exactly recover the SM distributions. The evaluations are performed using the one-dimensional distributions of $x(\cos\theta_Z)$ and $x(\Delta\Phi_{f\bar{f}})$ as the demonstration, which are binned in 20, and the three-dimensional distribution of $x(\cos\theta^*_f, \cos\theta_Z, \Delta\Phi_{f\bar{f}})$ binned in $5\times5\times5$ is also used to confirm the impact of the multi-dimensional distribution. Since the parameter a_Z, which is the SM-like one, does not change any angular distributions at all, the values of $\Delta\chi^2$ of a_Z is uniformly 0 over the parameter space whereas the existence of the parameter b_Z or $\tilde{b}_Z$ would be detectable because both parameters b_Z and $\tilde{b}_Z$ can change the angular distribution largely from the SM predictions. It is also seen that both beam polarization states P(e^-, e^+)= (-80%,+30%) and (+80%,-30%) have similar impact on the sensitivity to the anomalous ZZH couplings.

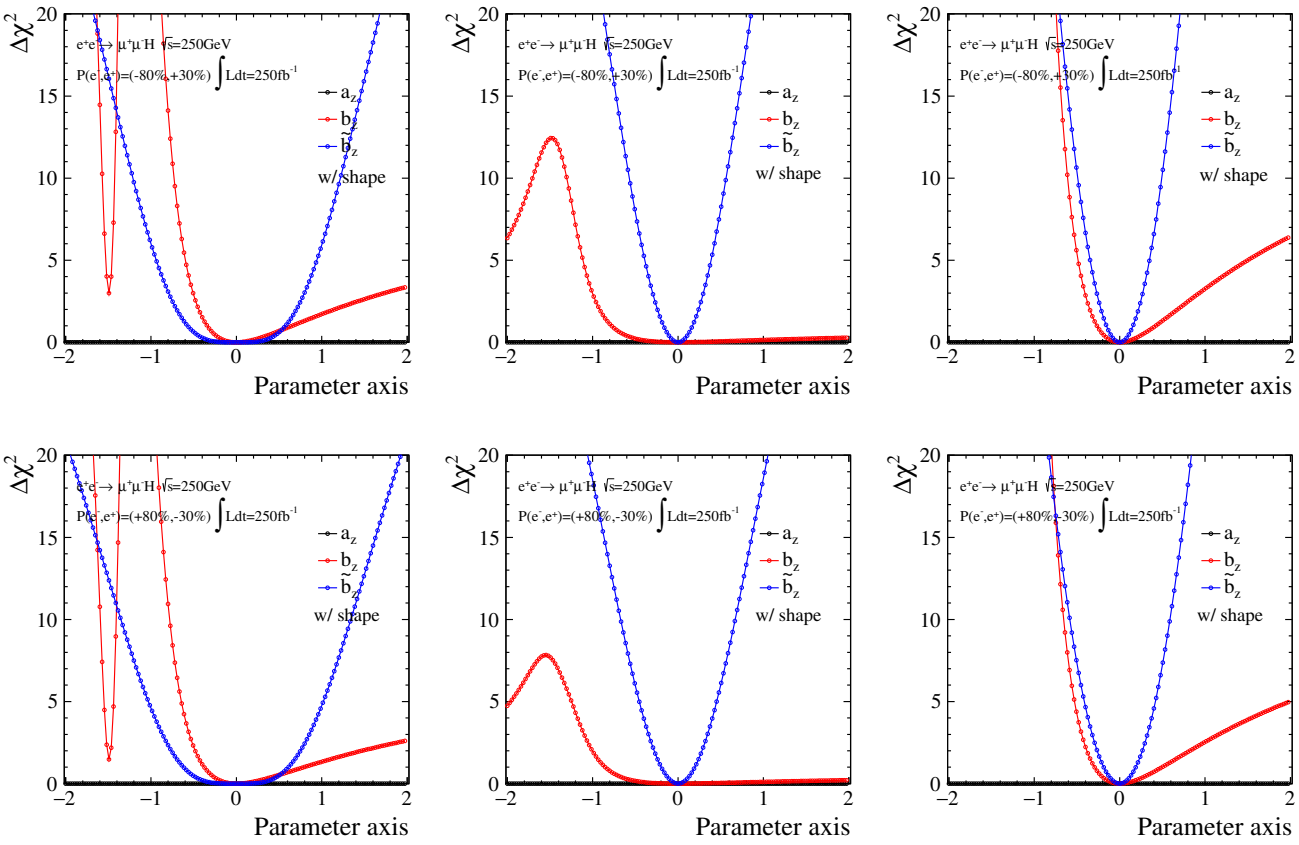

Figure 60: The distributions show $\Delta\chi^2$ as a function of each parameter of the anomalous ZZH couplings, and the evaluation is done in the one-parameter space. Black, red, and blue lines on the plots correspond to the parameters a_Z, b_Z, and $\tilde{b}_Z$. Since only the angular information is considered here, the χ^2 values of a_Z is exactly 0 over the given range. In upper and lower plots, the different beam polarizations are assumed with the integrated luminosity of 250 fb^{-1}: P(e^-, e^+)= (-80%,+30%) and (+80%,-30%), respectively. Difference of each column is the angular distributions used for the evaluation: (left) $x(\cos\theta_{Z)}$ binned in 20, (middle) $x(\Delta\Phi_{f\bar{f}})$ binned in 20, and (right) $x(\cos\theta^*_f, \cos\theta_Z, \Delta\Phi_{f\bar{f}})$ binned $5\times5\times5$ are used respectively.

Fig. 61 also show color plots of $\Delta\chi^2$ where the evaluations are done for each two-parameter space of a_Z-b_Z, a_Z-$\tilde{b}_Z$, and b_Z-$\tilde{b}_Z$. The one-dimensional distributions of $x(\cos\theta_Z)$ and $x(\Delta\Phi_{f\bar{f}})$, which are binned in 20, and three-dimensional distribution of $x(\cos\theta^*_f, \cos\theta_Z, \Delta\Phi_{f\bar{f}})$ binned in $5\times5\times5$ are used as the demonstrations. As well as the evaluation in the one-parameter space, the sensitivity for any a_Z when the parameter b_Z or $\tilde{b}_Z$ is 0 is nothing. The impact of difference of the angular distributions can be observed especially for the b_Z-$\tilde{b}_Z$ parameter space, and the three-dimensional distribution has both power.

6.1.4 Impact of production cross-section

The total production cross-section of the Higgs-strahlung process $e^+e^- \to ZH$ is also the strong observable for verifying the anomalous ZZH couplings. The relative variation of the production cross-section of the muon channel due to the anomalous couplings is illustrated in Fig. 43. Based on this variation of the production cross-section, the χ^2 test is performed. A clear different point compared to the impact of the angular distributions is the impact on the parameter a_Z, in which the sensitivity is quickly rising. Furthermore, compared with the impact of the angular distributions on the parameters b_Z and $\tilde{b}_Z$, the impact of the cross-section is considerably powerful for the parameter b_Z and equivalently for the parameter $\tilde{b}_Z$. These situation can be seen in Fig. 62. However, the parameter space of a_Z-b_Z has a strong correlation as shown in Fig. 62 where the same cross-section with he SM expectation is taken by tuning the parameters and the sensitivities

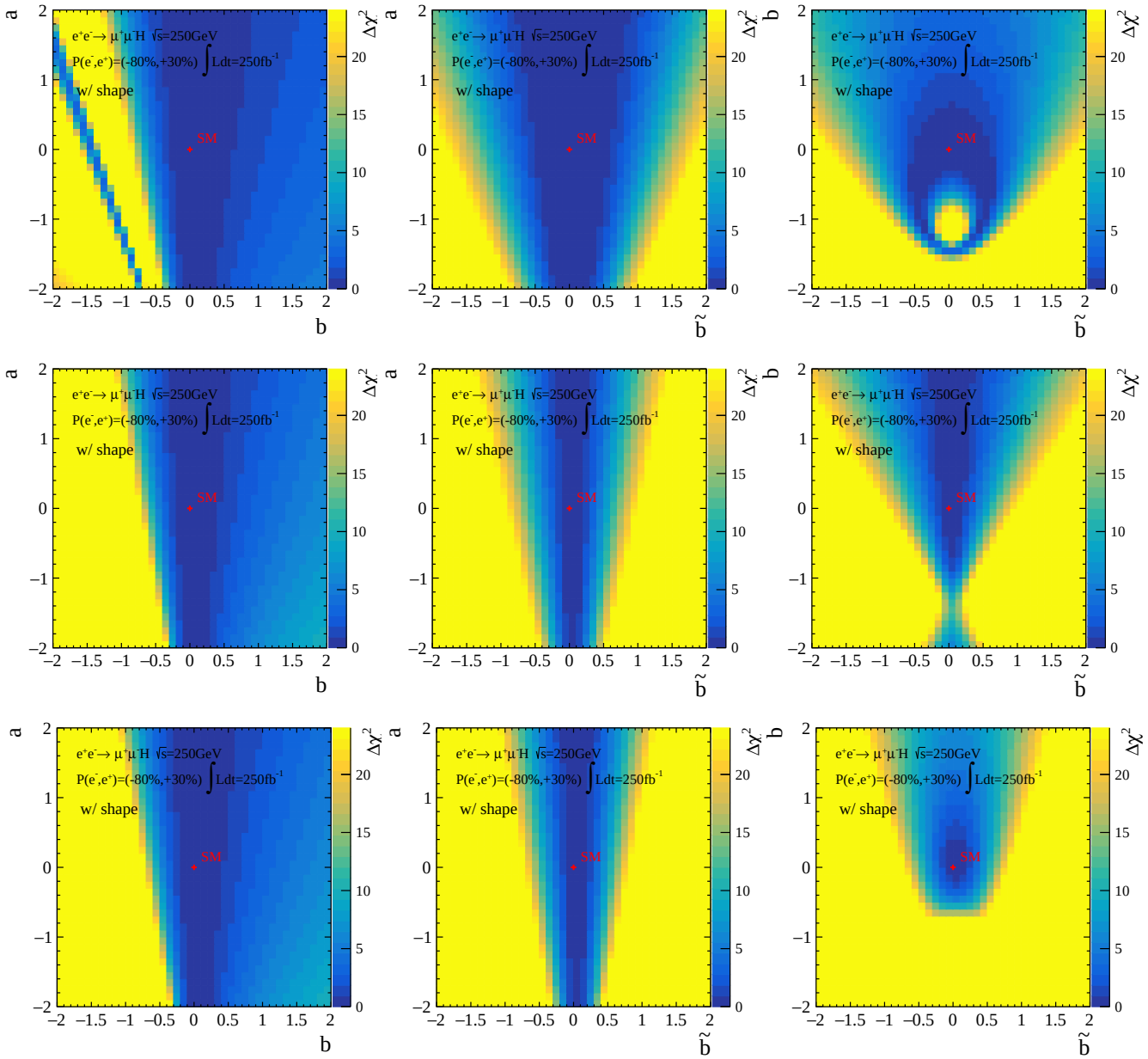

Figure 61: The distributions show $\Delta\chi^2$ in the two-dimensional parameter space a_Z-b_Z, a_Z-$\tilde{b}_Z$, and b_Z-$\tilde{b}_Z$. Only each angular distribution is used for the evaluations: (top) $x(\cos\theta_{Z)}$ binned in 20, (middle) $x(\Delta\Phi_{f\bar{f}})$ binned in 20, and (bottom) $x(\cos\theta^*_f, \cos\theta_Z, \Delta\Phi_{f\bar{f}})$ binned 5×5×5 are used respectively. The results are given only for the beam polarization of P(e^-, e^+)= (-80%,+30%). The sensitivity is 0.0 for the any a_z when b_Z or $\tilde{b}_Z$ is 0.0.

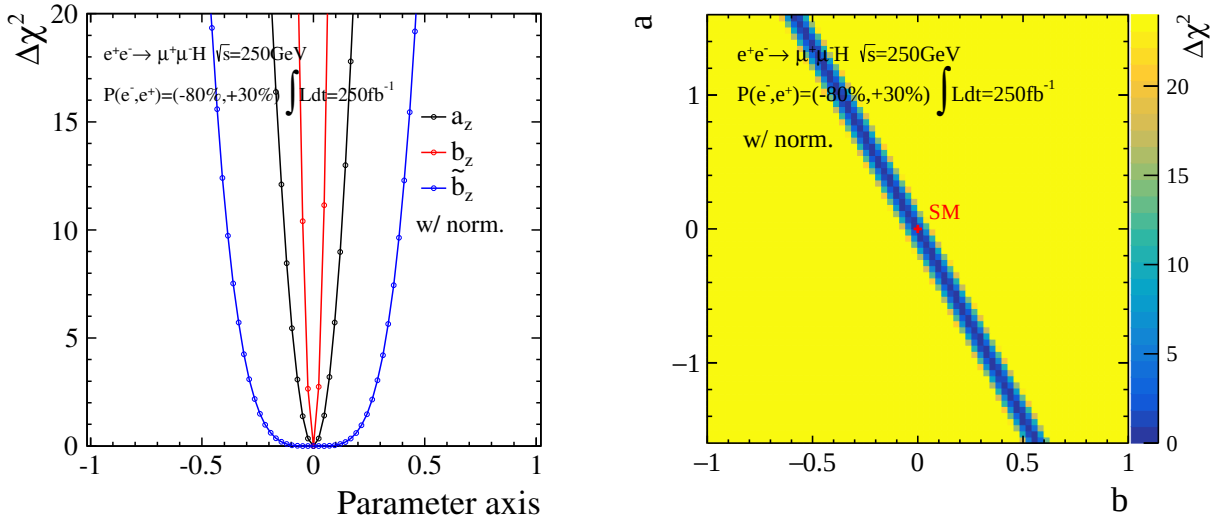

Figure 62: (Left) The distribution shows $\Delta\chi^2$ as a function of each parameter in the one parameter space, where the normalization information only is used for the evaluation. (Right) The distributions show $\Delta\chi^2$ in the two-dimensional parameter space of a_Z-b_Z.

are cancelled eventually. Thus, It is not definitely sufficient to make use of information of the cross-section only, and it is clearly necessary to use the angular distribution to disentangle the observed strong correlation between a_Z-b_Z.

6.1.5 Sensitivity in three parameter space

To get the full sensitivity to the anomalous ZZH couplings with the muon channel only, evaluation by fitting is performed assuming the integrated luminosity of 250 fb^{-1} with both of the beam polarization states P(e^-, e^+)= (-80%,+30%) and (+80%,-30%). Both of the angular information of the three-dimensional distributions $x(\cos\theta^*_f, \cos\theta_Z, \Delta\Phi_{f\bar{f}})$ binned 5×5×5 and the information of the production cross-section are combined. The fitting for extracting the sensitivity to each anomalous parameter is done by minimizing the two χ^2 functions defined in Sec. 4.4.3 and Sec. 4.4.4, where the three anomalous parameters a_Z, b_Z, and $\tilde{b}_Z$ are set to be completely free. A simultaneous minimization procedure for minimizing the χ^2 value is carried out by the TMunit package [82] implemented in the ROOT.

In the previous section, it seems that the variation of the cross-section is the strong information to verify the anomalous VVH couplings. However, once the information is applied to the three parameter space a_Z-b_Z-$\tilde{b}_Z$, the parameter bounds can not be restricted because of adjustment of the cross-section by the third parameter, which is shown in the left figure of Fig. 63. Since the amplitude of the parameters, which is $|\mathcal{A}_0 + a_Z\mathcal{A}_{a_Z} + b_Z\mathcal{A}_{b_Z}|^2$ when focusing on a_Z and b_Z, is analytical given as a formula of a general ellipse. When using the information of the cross-section, such behavior can be seen in the plot. Explanations of each direction of the color map are,

1. Both a_Z and b_Z can adjust each other by making the corse-section increase or decrease.

2. Both a_Z and b_Z can make the cross-section increase. However, any $\tilde{b}_Z$ can not adjust it as the third parameter since any $\tilde{b}_Z$ must increase the cross-section, whose tendency can be seen in Fig. 43. Thus, the bound is quickly restricted in this direction.

3. Both a_Z and b_Z can make the cross-section decrease. The third parameter $\tilde{b}_Z$ has huge room to recover the SM value by increasing the cross-section.

Once the shape information is included in the analysis, the bound is strongly constrained as illustrated with contours plotted in the right figure of Fig. 63.

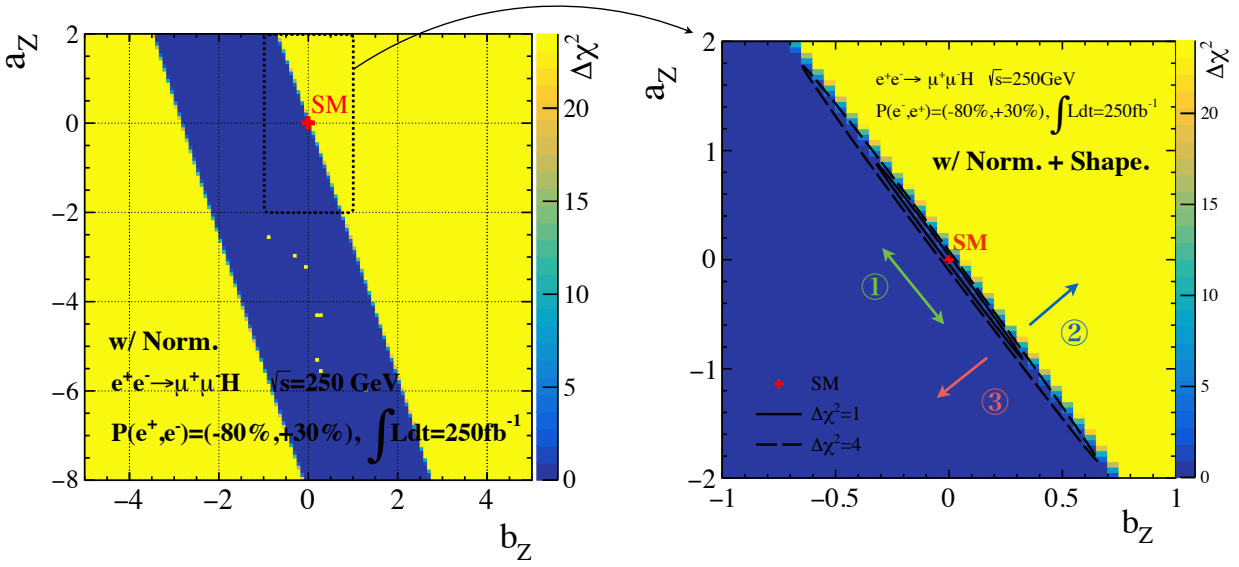

Figure 63: (Left) The plot shows the color map of the $\Delta\chi^2$ distribution in the three parameter space, where only the cross-section information is used to calculate $\Delta\chi^2$. The physical parameter limits are set to be < 8. (Right) when adding the shape information into the cross-section information, the sensitive bounds are strongly constrained. The 1σ and 2σ contours can be seen.

Upper plots in Fig. 64 illustrate the contours showing 1σ and 2σ bounds, where the simultaneous minimization fitting is performed in the three parameter space and the contours are projected onto the corresponding two-dimensional parameter space a_Z-b_Z, a_Z-$\tilde{b}_Z$, and b_Z-$\tilde{b}_Z$. Middle plots in Fig. 64 give $\Delta\chi^2$ distributions as a function of each anomalous parameter a_Z, b_Z, and $\tilde{b}_Z$. The evaluation is performed by scanning $\Delta\chi^2$ along one parameter axis while setting the other two parameters free, which corresponds to the simultaneous minimization in the three parameter space.

The results are evaluated using both of the angular and the cross-section information of the muon channel only. Explicit values corresponding to the 1σ bounds for each anomalous parameter a_Z, b_Z, and $\tilde{b}_Z$ and correlation matrix ρ which indicates correlation coefficients between the parameters are given in the last line of Fig. 64. Both beam polarization states P(e^-, e^+)= (-80%,+30%) and (+80%,-30%) with the benchmark integrated luminosity of 250 fb^{-1} are assumed. The correlation coefficients of the correlation matrix ρ are extracted from the pseudo-experiment which is described in Sec. 4.4.5.

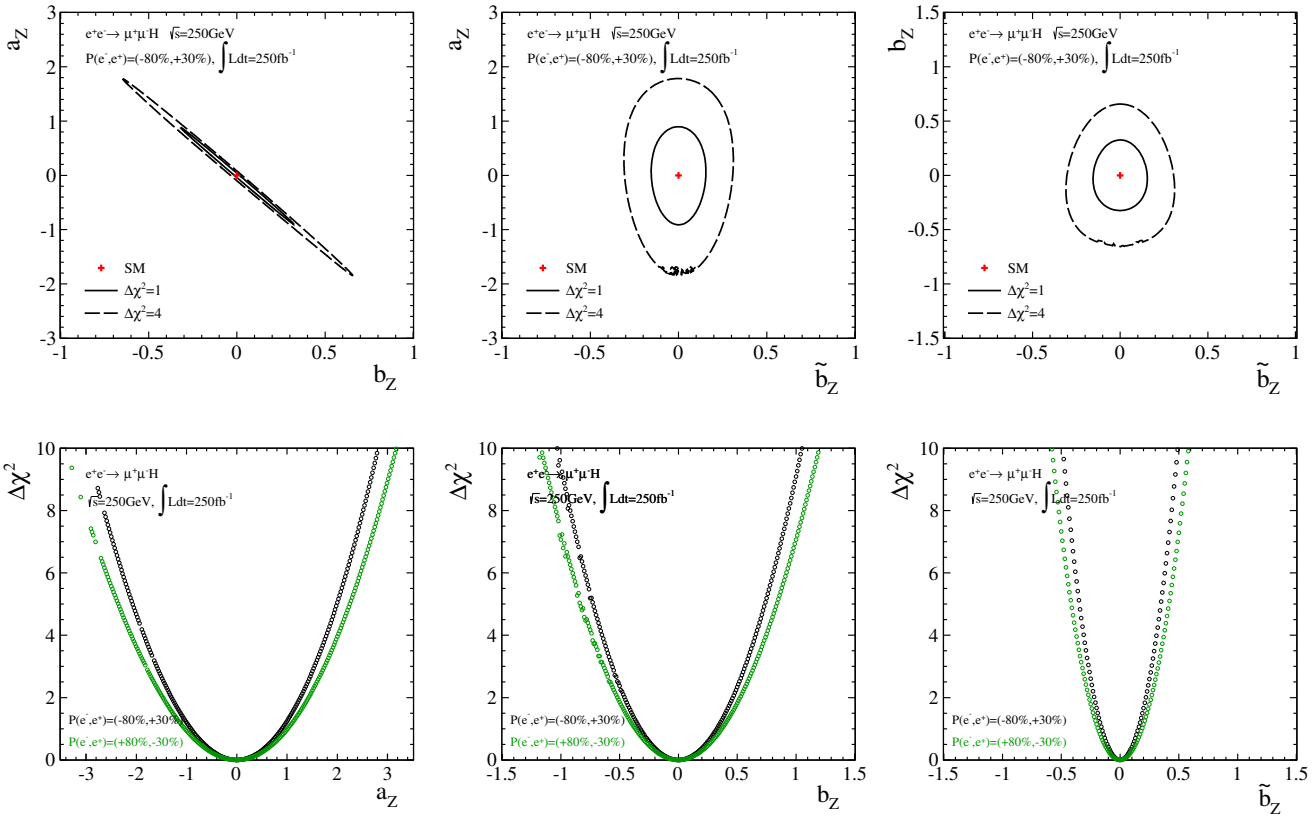

$$\sqrt{s} = 250 \text{ GeV with } \int \text{Ldt} = 250 \text{ fb}^{-1} \text{ and } \text{P}(e^-, e^+) = (-80\%, +30\%)$$

$$\begin{cases} a_Z = [-0.912, \quad 0.896] \\ b_Z = [-0.324, \quad 0.326] \\ \tilde{b}_Z = [-0.155, \quad 0.155] \end{cases}, \quad \rho = \begin{pmatrix} 1 & -0.9992 & -0.0176 \\ - & 1 & 0.0158 \\ - & - & 1 \end{pmatrix}$$

$$\sqrt{s} = 250 \text{ GeV with } \int \text{Ldt} = 250 \text{ fb}^{-1} \text{ and } \text{P}(e^-, e^+) = (+80\%, -30\%)$$

$$\begin{cases} a_Z = [-1.034, \quad 1.012] \\ b_Z = [-0.367, \quad 0.370] \\ \tilde{b}_Z = [-0.187, \quad 0.187] \end{cases}, \quad \rho = \begin{pmatrix} 1 & -0.9984 & 0.0155 \\ - & 1 & -0.0144 \\ - & - & 1 \end{pmatrix}$$

Figure 64: (Upper): The plots show contours corresponding to the 1σ and 2σ sensitivities to the anomalous ZZH couplings. The fitting is performed with the muon channel only under the three free parameter space. The integrated luminosity of 250 fb^{-1} with the beam polarization state P(e^-, e^+)= (-80%,+30%) is assumed. The results are projected onto the two-dimensional parameter spaces a_Z-b_Z, a_Z-$\tilde{b}_Z$, and b_Z-$\tilde{b}_Z$. Both of the information, which are the three-dimensional distributions $x(\cos\theta^*_f, \cos\theta_Z, \Delta\Phi_{f\bar{f}})$ binned 5×5×5 and the production cross-section are combined. (Middle): The plots show $\Delta\chi^2$ distributions as a function of each parameter space of the anomalous couplings a_Z, b_Z, and $\tilde{b}_Z$. The distributions are obtained by using both information (the angles and the cross-section) and scanning one parameter while setting the other two parameters to be completely free. (Lower): The explicit values corresponding to the 1σ bounds for each anomalous parameter a_Z, b_Z, and $\tilde{b}_Z$ and the correlation matrix indicating correlation coefficients between the parameters.

6.2 $e^+e^- \to Zh \to q\bar{q}H,\ h \to b\bar{b}$ at $\sqrt{s} = 250$ GeV

Since a branching fraction of the Z boson decaying into lepton pairs is a sum of approximately 10 %, as far as the pairs of electrons and muons are concerned, it is respectively about 3.4 %, the sensitivity is, therefore, statistically limited. In contrast, because the branching fraction of the Z boson decaying into a pair of quarks is about 70 %, usage of the quark channels has a big advantage statistically. It is expected that the sensitivity to the anomalous ZZH couplings is sizably improved by adding results of the analysis of the $Z \to q\bar{q}$ hadronic channels.

6.2.1 Reconstruction and background suppression

Jet clustering and pairing :

In the analysis with the $Z \to q\bar{q}$ hadronic channel the $h \to b\bar{b}$ channel is selected because the branching fraction of $h \to b\bar{b}$ is the largest, and performance of the heavy flavor tagging of b-quarks is expected to be superior, which is implemented by LCFIPlus in the ILCSoft framework. After removing isolated leptons from a event, remaining final state particles in each event are clustered into four jets by employing a Durham jet algorithm. The Durham algorithm can also provide one of the useful topological observables y_{ij} which is distance between pseudo-clustered jets. This observable is effective for discrimination of certain processes which have the different number of jets from the signal process. Since the final state of the signal process has a signature of four jets, combinations of a few pairs are possible to take. Proper jet pairs which come from the Z and the Higgs boson are chosen by minimizing the following χ^2 function,

$$\chi^2 = \left(\frac{M_{ij} - M_h}{\sigma_h}\right)^2 + \left(\frac{M_{kl} - M_Z}{\sigma_Z}\right)^2 \tag{36}$$

where i–l denote jets, and M_Z and M_h denote the mass of the Z boson and the Higgs boson. σ_Z is set to be 5.2 GeV and σ_h is set to be 7.0 GeV, which represent the Z mass and the Higgs mass resolutions, respectively.

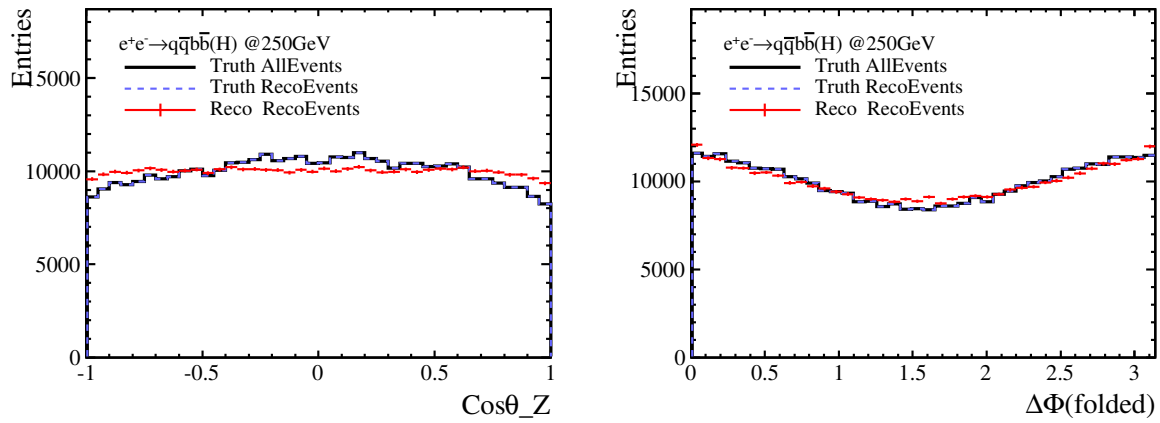

Figure 65: Plots show the MC truth and reconstructed distributions of the polar angle of the Z boson $\cos\theta_Z$ and the angle between production planes $\Delta\Phi$ in the $q\bar{q}h(h \to b\bar{b})$ channel of the Higgs-strahlung process at $\sqrt{s}$=250 GeV. These observables give the sensitivities to the anomalous ZZH couplings. Unless jet charge identification is applied, full sensitivity of $\Delta\Phi$ [0–2π] is not available, and it becomes [0–π] by folding back the distribution if $\Delta\Phi$ exceeds π.

Reconstructed angular observables :

Fig. 65 show the reconstructed angular distributions of the polar angle of the Z boson ($\cos\theta_Z$) and the difference of the angle between production planes ($\Delta\Phi$) in the laboratory frame, which are

important observables for detecting the anomalous ZZH couplings. Since jet charges identification for both b-jets decaying from the Higgs boson is not implemented for the current analysis technic, $\Delta\Phi$ can not be fully reconstructed in $[0–2\pi]$ range which is explained in Sec. 4.1.2. When the calculated value of $\Delta\Phi$ is exceeded in π, $\Delta\Phi$ is folded as $\Delta\Phi - \pi$. Thus, the available sensitivity of the $\Delta\Phi$ distribution is $[0–\pi]$ which is shown right side of Fig. 65.

Background suppression :

The following observables and values are imposed for the background suppressions. The distributions of each observable for the suppression and the invariant mass of the Higgs boson are shown in Fig. 66, and the reduction tables showing the number of remaining signal and background events in each cut is given in Table 11, where the integrated luminosity of 250 fb^{-1} with both of the beam polarization states P(e^-, e^+)= (-80%,+30%) and (+80%,-30%) are assumed. The signal efficiency and the signal significance are also given for each cut.

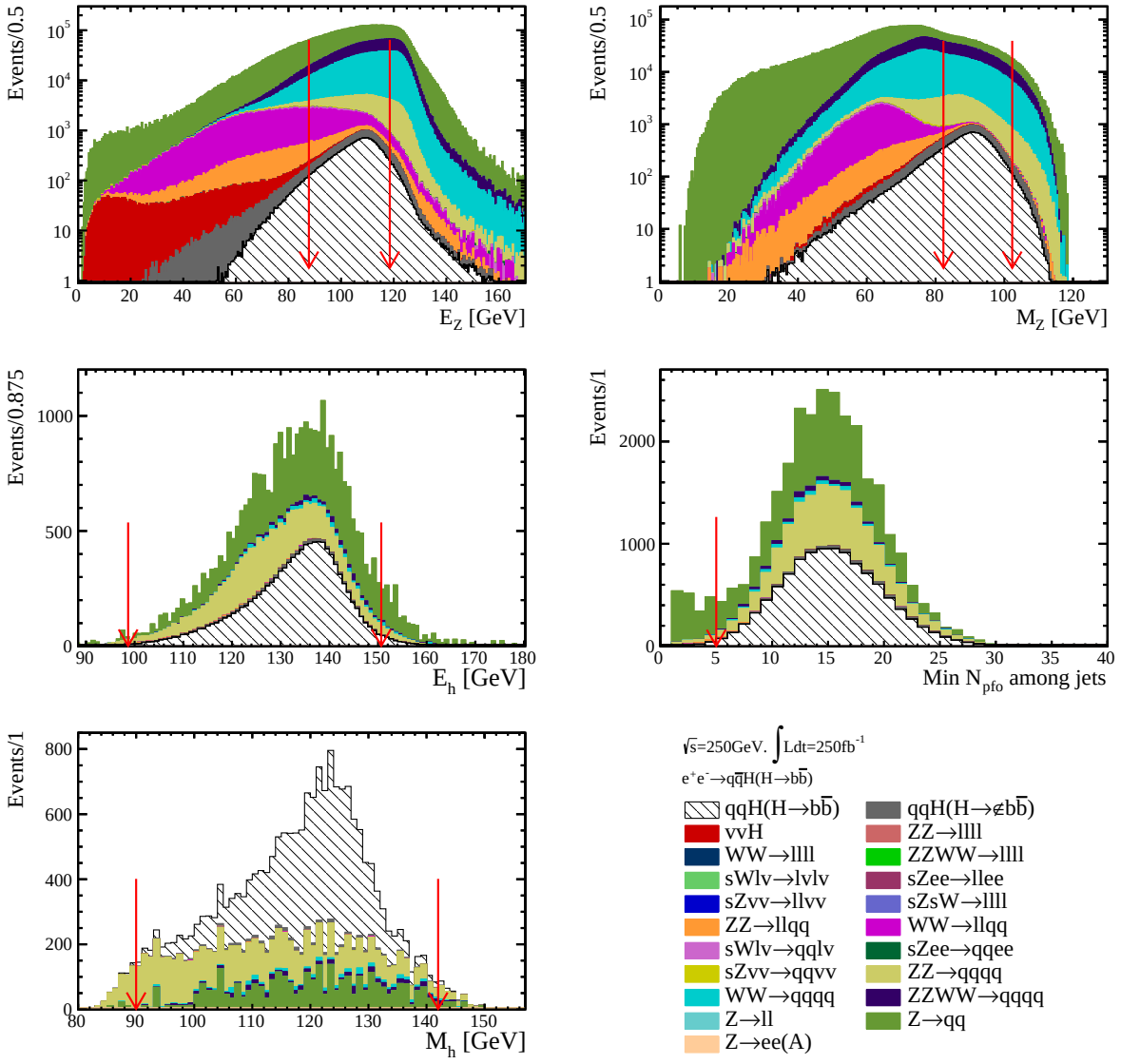

Figure 66: The distributions show each observable used for the background suppression assuming 250 fb^{-1} with P(e^-, e^+)= (-80%,+30%). The explanation of the observables are given in the text. Red arrows on each plot indicate the cut values applied to each observable as the background suppression.

- $N_{jet} = 4$ and $N_{isolep} = 0$
  Properly four jets are clustered and exist in a event, additionally the number of isolated leptons must be 0 since the final state of the signal process is full hadronic environment.
- $N_{pfo} \in [55,\ 170]$
  The number of Particle Flow Objects (PFOs). Two fermion processes and four fermion semi-leptonic decay processes can be almost suppressed with this observable.
- $E_Z \in [87.8,\ 118.5]$ GeV and $M_Z \in [82.3,\ 102.3]$ GeV
  The energy of the Z boson calculated with the paired two jets. The invariant mass of the Z boson calculated with the paired two jets, which should be close to the mass of the Z boson.
- The sum of b-tag $\in [1.25,\ 2.0]$
  Both of the jets originating from the Higgs boson have higher b-likeness since the $h \to b\bar{b}$ channel is selected as the signal process.
- $E_H \in [98.7,\ 150.7]$ GeV
  The energy of the Higgs boson.
- The number of minimum PFOs $N_{pfo} \in [5,\ 40]$ among jet objects, and the jet clustering parameters $-\log y_{32} \in [0.5,\ 3.62]$ and $-\log y_{43} \in [1.8,\ 5.52]$
  y_{32} show the minimum distance when the pseudo-jets are merged from 3 to 2. This is useful to discriminate topology of two jets environment from that of multiple jets. y_{43} also show the minimum distance when the pseudo-jets are merged from 4 to 3.
- The thrust value $T \in [0.5,\ 0.89]$
  T denotes the *thrust* value explained in Sec. 5.5. When T is close to 1, an event topology could be a pair of narrow jets generated linearly. If T gets close to 1/2, the topology will be multiple jets which spread to all directions in the detector.
- $M_H \in [90,\ 142]$ GeV
  The invariant mass of the Higgs boson calculated with the paired two jets, which is the mass window to determine a Poisson error calculated by the remaining number of events on each bin on kinematical histograms.

6.2.2 Acceptance and migration on observables

Fig. 67 and Fig. 68 show the summary plots on the one-dimensional angular distributions of $\cos\theta_Z$ and $\Delta\Phi$ binned in 30. The error of the remaining signal and background distributions is given with the standard error of the Poisson probability. Similarly, summary plots of the two-dimensional distribution of $x(\cos\theta_Z, \Delta\Phi_{f\bar{f}})$ is also given in Fig. 69 which is binned in 10×10.

A big difference of this hadronic channel $q\bar{q}b\bar{b}(h)$ compared to the lepton channel of the Zh process is the probability of the migration effects. Since the full hadronic $q\bar{q}b\bar{b}(h)$ channel has the multiple jet environment, the number of observed particles in the final state, which have various energy, is large. An effect of missing neutrinos will make observed distributions shift from the generated distributions. Finite detector resolutions will also smear the observed information. Thus, the larger migration can be given, which are clearly seen in the observables.

Table 4: The expected number of remaining signal and background events after each cut for the $Zh \to q\bar{q}b\bar{b}$ at $\sqrt{s}$=250 GeV, with with both of the beam polarization states: P(e^-, e^+)= (-80%,+30%) and (+80%,-30%). The integrated luminosity of 250 fb^{-1} is assumed. The signal efficiency ϵ and significance S_{sig} are also given in the table.

$\sqrt{s}$=250 GeV P(e^-, e^+)= (-80%,+30%)

Cut variables	$q\bar{q}b\bar{b}$	ϵ	$q\bar{q}H(H \notin b\bar{b})$	$2f$	$4f$	S_{sig}
No cut	30372	100	22175	$2.9 \cdot 10^7$	$1.02 \cdot 10^7$	-
$N_{isolep} = 0$	30314	99.8	17492	$2.6 \cdot 10^7$	$6.9 \cdot 10^6$	5.28
$N_{pfo} \in [55,\ 170]$	30218	99.5	15141	$6.0 \cdot 10^6$	$4.4 \cdot 10^6$	9.37
$E_Z \in [87.75,\ 118.50]$ GeV	25712	84.7	11365	$3.3 \cdot 10^6$	$2.8 \cdot 10^6$	10.35
$M_Z \in [82.29,\ 102.29]$ GeV	18658	61.4	7572	$3.8 \cdot 10^5$	$1.0 \cdot 10^6$	15.62
b-$tag \in [1.25,\ 2.0]$	11203	36.9	381	9364	8454	65.76
$E_H \in [98.67,\ 150.67]$ GeV	10909	35.9	368	8242	7998	66.21
Min $N_{pfo} \in [5,\ 40]$	10841	35.7	358	6932	7792	67.81
$-\log y_{32} \in [0.5, 3.62]$	10409	34.3	349	3917	7453	70.53
$-\log y_{43} \in [1.8, 5.52]$	10065	33.2	346	2921	7027	71.15
thrust $T \in [0.5,\ 0.89]$	9966	32.8	345	2520	7004	71.39
$M_H \in [90,\ 142]$ GeV	9907	32.6	335	2419	6382	72.43

$\sqrt{s}$=250 GeV P(e^-, e^+)= (+80%,-30%)

Cut variables	$q\bar{q}b\bar{b}$	ϵ	$q\bar{q}H(H \notin b\bar{b})$	$2f$	$4f$	S_{sig}
No cut	20512	100	14976	$2.03 \cdot 10^7$	$1.27 \cdot 10^6$	-
$N_{isolep} = 0$	20473	99.8	11813	$1.76 \cdot 10^7$	$8.21 \cdot 10^5$	4.77
$N_{pfo} \in [55,\ 170]$	20408	99.5	10226	$3.55 \cdot 10^6$	$4.20 \cdot 10^5$	10.20
$E_Z \in [91.5,\ 119.25]$ GeV	16830	82.0	7435	$1.82 \cdot 10^6$	$2.63 \cdot 10^5$	11.60
$M_Z \in [82.3,\ 102.86]$ GeV	12670	61.8	5182	$2.30 \cdot 10^5$	$1.06 \cdot 10^5$	21.28
b-$tag \in [1.15,\ 2.0]$	8240	40.2	317	6784	4244	58.87
$E_H \in [97.33,\ 154.00]$ GeV	8127	39.6	312	6350	4144	59.06
Min $N_{pfo} \in [4,\ 40]$	8107	39.5	307	5615	4068	60.26
$-\log y_{32} \in [0.5, 3.80]$	7888	38.5	303	3581	3929	62.95
$-\log y_{43} \in [1.8, 6.00]$	7796	38.0	302	3002	3814	63.84
thrust $T \in [0.5,\ 0.89]$	7674	37.4	301	2442	3792	64.38
$M_H \in [90,\ 142]$ GeV	7608	37.1	291	2279	3404	65.28

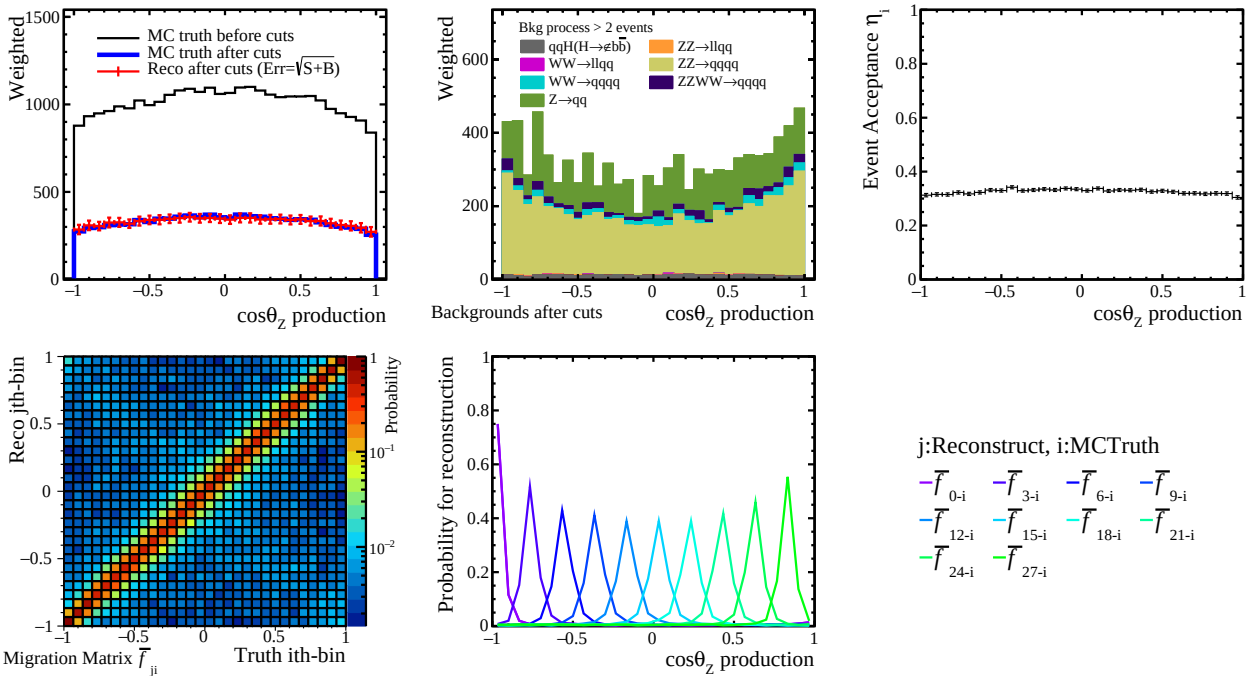

Figure 67: The distributions show the summary of the polar angle of the Z boson ($\cos\theta_Z$) after the background suppression. (Top left and middle): the remaining signal and the background distribution, which are given with the MC truth and the reconstructed, where the statistical error is given as the standard deviation of the Poisson probability. (Top right): the event acceptance function η_i. (Bottom left and middle): the distribution shows the probability matrix of the migration ($\bar{f}_{ji}$) that is applied for the reconstruction of the realistic distribution of $\cos\theta_Z$, and the cross-sections of $\bar{f}_{ji}$ as 1-dim plots.

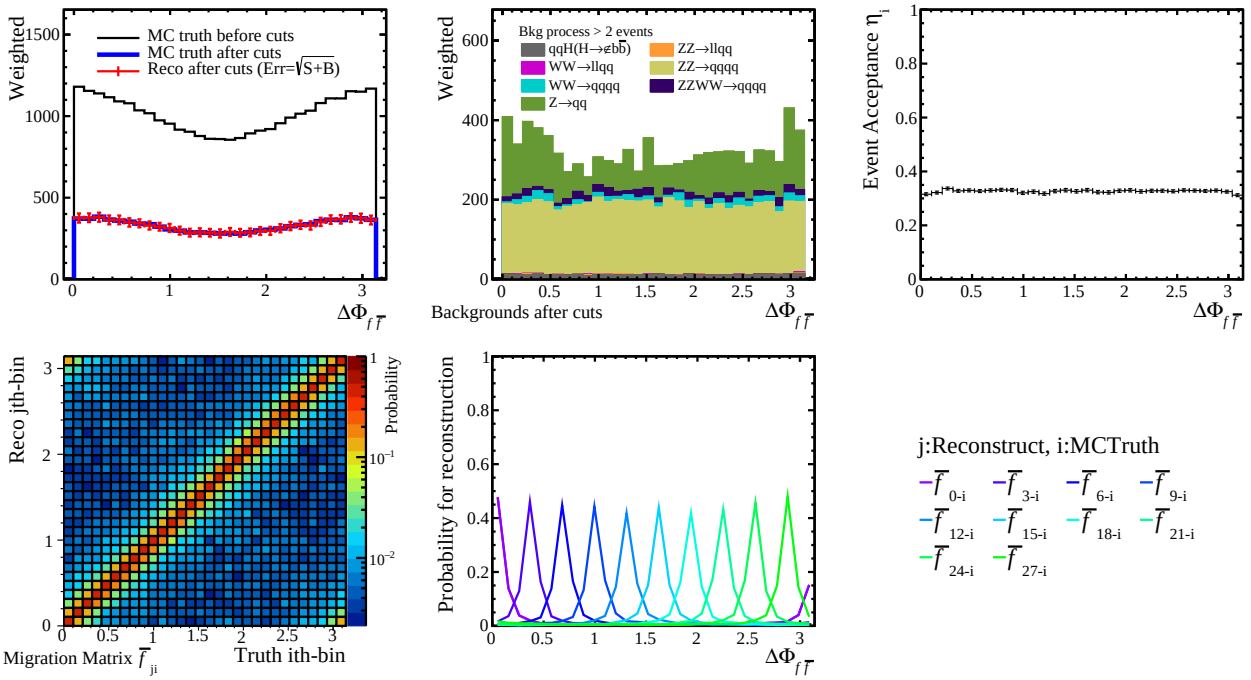

Figure 68: The distributions show the summary of the angle between production planes in the laboratory frame ($\Delta\Phi$) after the background suppression. (Top left and middle): the remaining signal and the background distribution, which are given with the MC truth and the reconstructed. (Top right): the event acceptance function η_i. (Bottom left and middle): the probability matrix of the migration ($\bar{f}_{ji}$) that is applied for the reconstruction of $\Delta\Phi$, and the cross-sections of $\bar{f}_{ji}$ as 1-dim plots.

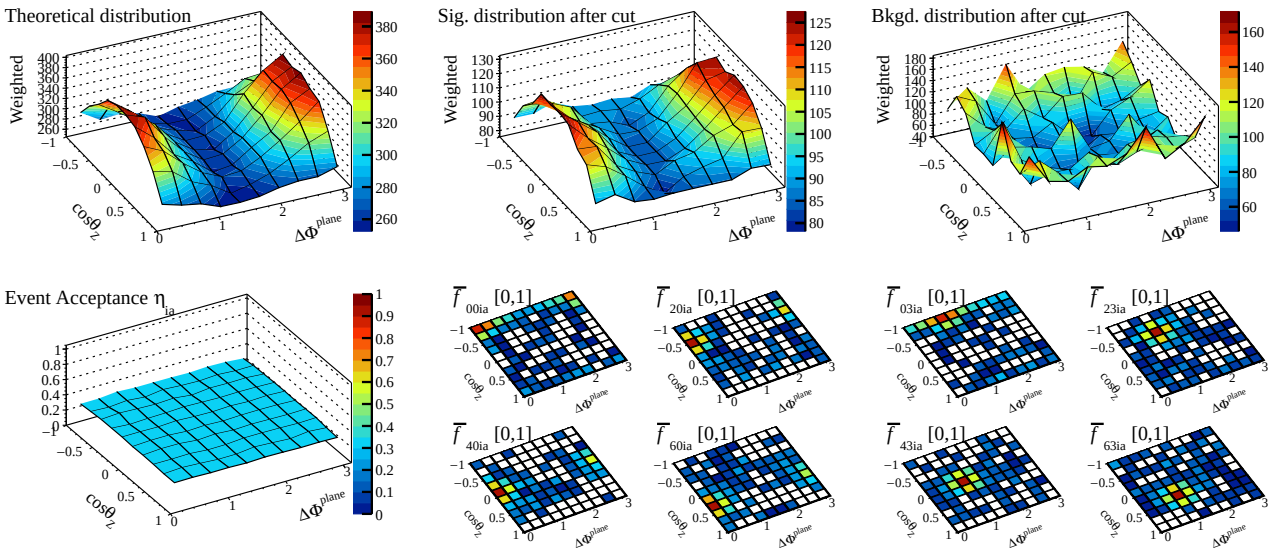

Figure 69: The distributions show the summary of the two-dimensional distribution consisted of the production angle of the Z boson $\cos\theta_Z$ and the angle between production planes in the laboratory frame ($\Delta\Phi$) after the background suppression. (Top left, middle, and right): The remaining MC truth and the reconstructed signal distribution, and the background distribution, respectively. (Bottom left): The event acceptance function η_{ia} shows whether each signal event on each bin is accepted or not after the suppression. (Bottom middle and right): Several examples on the probability matrix of the migration where the 2-dim plots give the cross-sections of $\bar{f}_{jbia}$ since the illustration of the migration is too difficult which is a 4-dimension distribution.

6.2.3 Impact of angular distribution

Fig. 70 show the $\Delta\chi^2$ distributions as the sensitivities to the anomalous ZZH couplings in the one-parameter space of a_Z, b_Z, and $\tilde{b}_Z$, where the one-dimensional distributions of $x(\cos\theta_Z)$ and $x(\Delta\Phi_{f\bar{f}})$ binned in 20 are used as the demonstrations, and the three-dimensional distribution of $x(\cos\theta^*_f, \cos\theta_Z, \Delta\Phi_{f\bar{f}})$ binned in $5\times5\times5$ is also used to compare the impact of the multi-dimensional distribution. The evaluations are given for both beam polarization states P(e^-, e^+)= (-80%,+30%) and (+80%,-30%) with the integrated luminosities of $\int L$ =250 fb^{-1}. Fig. 71 give the color maps showing the $\Delta\chi^2$ value in each two-parameter space of a_Z-b_Z, a_Z-$\tilde{b}_Z$, and b_Z-$\tilde{b}_Z$.

Although the probability of the migration effects are significantly larger, and furthermore the sensitivity given by the $\Delta\Phi$ distribution is half compared to the muon channel, the impact of the angular information is sizably larger than that of the muon channels. This is simply the benefit of the statistics of the hadronic $q\bar{q}b\bar{b}(h)$ channel, which is roughly six times better than the lepton channel.

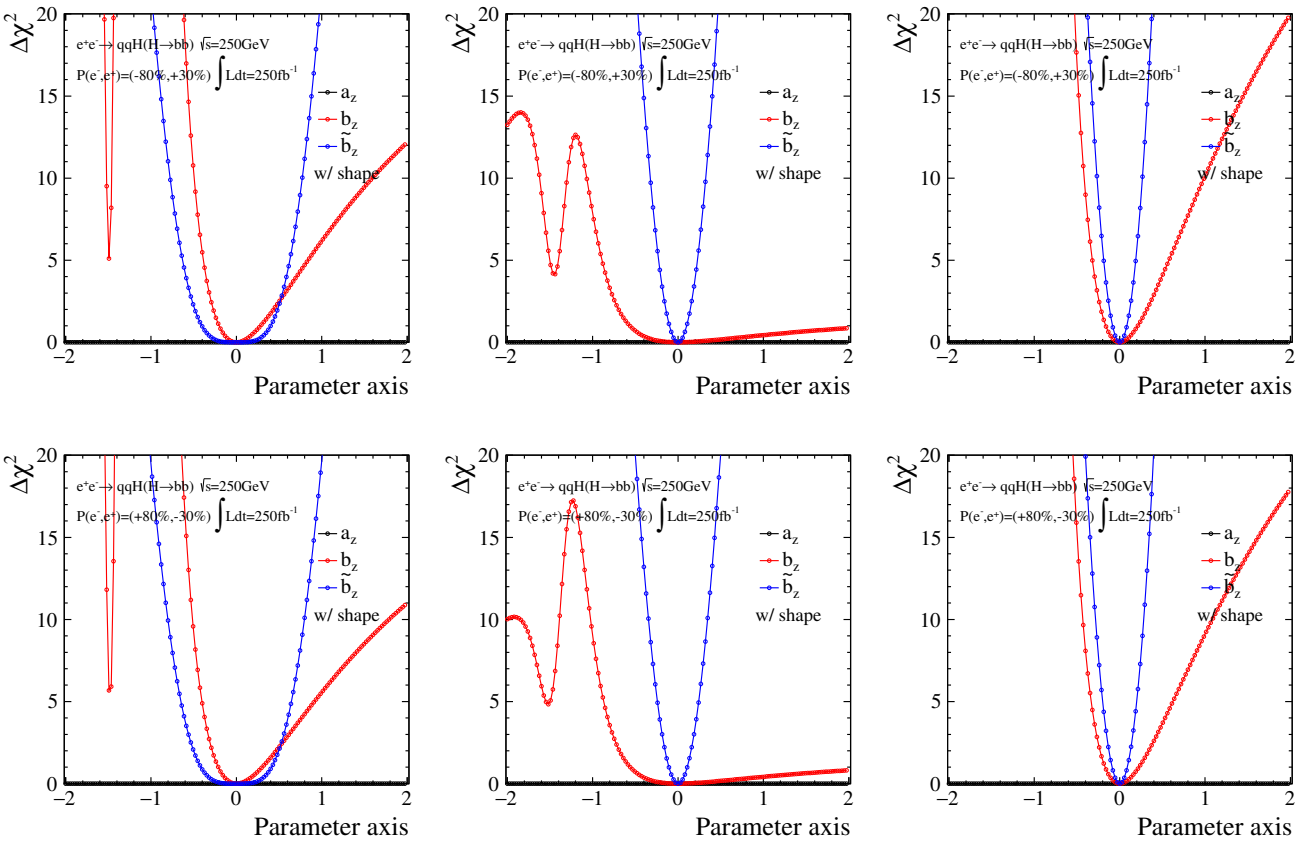

Figure 70: Distributions show $\Delta\chi^2$ as a function of each parameter which gives anomalous ZZH couplings, and the evaluation is done in the one-parameter axis. Black, red, and blue line on the plots correspond to the parameters a_Z, b_Z, and $\tilde{b}_Z$. Since only the angular information is considered here, the χ^2 values of a_Z is 0.0 over the given range. In upper and lower plots the different beam polarizations are assumed with the integrated luminosity of 250 fb^{-1}: P(e^-, e^+)= (-80%,+30%) and (+80%,-30%), respectively. Difference of each column is the angular distributions used for the evaluation: (left) $x(\cos\theta_Z)$ binned in 20, (middle) $x(\Delta\Phi_{f\bar{f}})$ binned in 20, and (right) $x(\cos\theta^*_f, \cos\theta_Z, \Delta\Phi_{f\bar{f}})$ binned $5\times5\times5$ are used respectively.

6.2.4 Sensitivity in three parameter space

The sensitivity to the anomalous ZZH couplings with the Higgs hadronic $q\bar{q}H(b\bar{b})$ channel only is evaluated assuming the integrated luminosity of 250 fb^{-1} with both of the beam polarization states P(e^-, e^+)= (-80%,+30%) and (+80%,-30%). The angular information of the three-dimensional distributions $x(\cos\theta^*_f, \cos\theta_Z, \Delta\Phi_{f\bar{f}})$ binned $5\times5\times5$, and the information of the production cross-section is combined. The minimization fitting is done in the three anomalous parameter space.

Upper plots in Fig. 72 give contours showing 1σ and 2σ bounds for each parameter, which are projected onto the corresponding two-dimensional parameter space a_Z-b_Z, a_Z-$\tilde{b}_Z$, and b_Z-$\tilde{b}_Z$. The strong correlation between the a_Z and b_Z parameters is also seen same as the lepton channels. Middle plots in Fig. 72 give $\Delta\chi^2$ distributions as a function for each anomalous parameter a_Z, b_Z, and $\tilde{b}_Z$. The evaluation is performed by scanning $\Delta\chi^2$ along one parameter axis while setting the other two parameters free, which corresponds to the simultaneous minimization in the three parameter space. The results are given using both of the angular and the cross-section information of the electron channel only. Explicit values corresponding to the 1σ bounds for each anomalous parameter a_Z, b_Z, and $\tilde{b}_Z$ and correlation matrix ρ indicating correlation coefficients between the parameters are given in the last line of Fig. 72. Both beam polarization states P(e^-, e^+)= (-80%,+30%) and (+80%,-30%) with the benchmark integrated luminosity of 250 fb^{-1} are assumed.

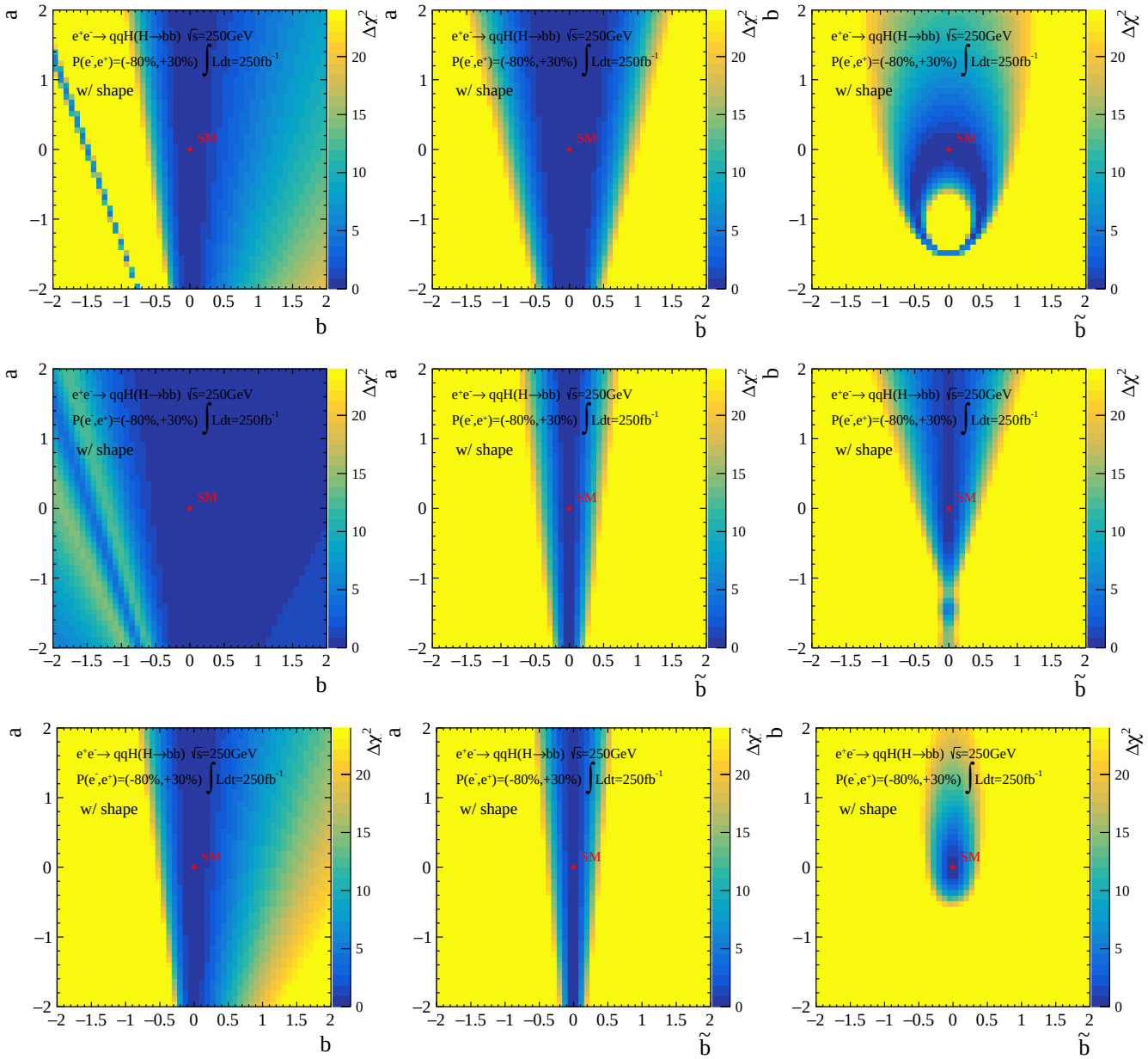

Figure 71: The distributions show $\Delta\chi^2$ in the two-dimensional parameter space a_Z-b_Z, a_Z-$\tilde{b}_Z$, and b_Z-$\tilde{b}_Z$. Only each angular distribution is used for the evaluations: (top) $x(\cos\theta_{Z)}$ binned in 20, (middle) $x(\Delta\Phi_{f\bar{f}})$ binned in 20, and (bottom) $x(\cos\theta^*_f, \cos\theta_Z, \Delta\Phi_{f\bar{f}})$ binned 5×5×5 are used respectively. The results are given only for the beam polarization of P(e^-, e^+)= (-80%,+30%). The sensitivity is 0.0 for the any a_z when b_Z or $\tilde{b}_Z$ is 0.0.

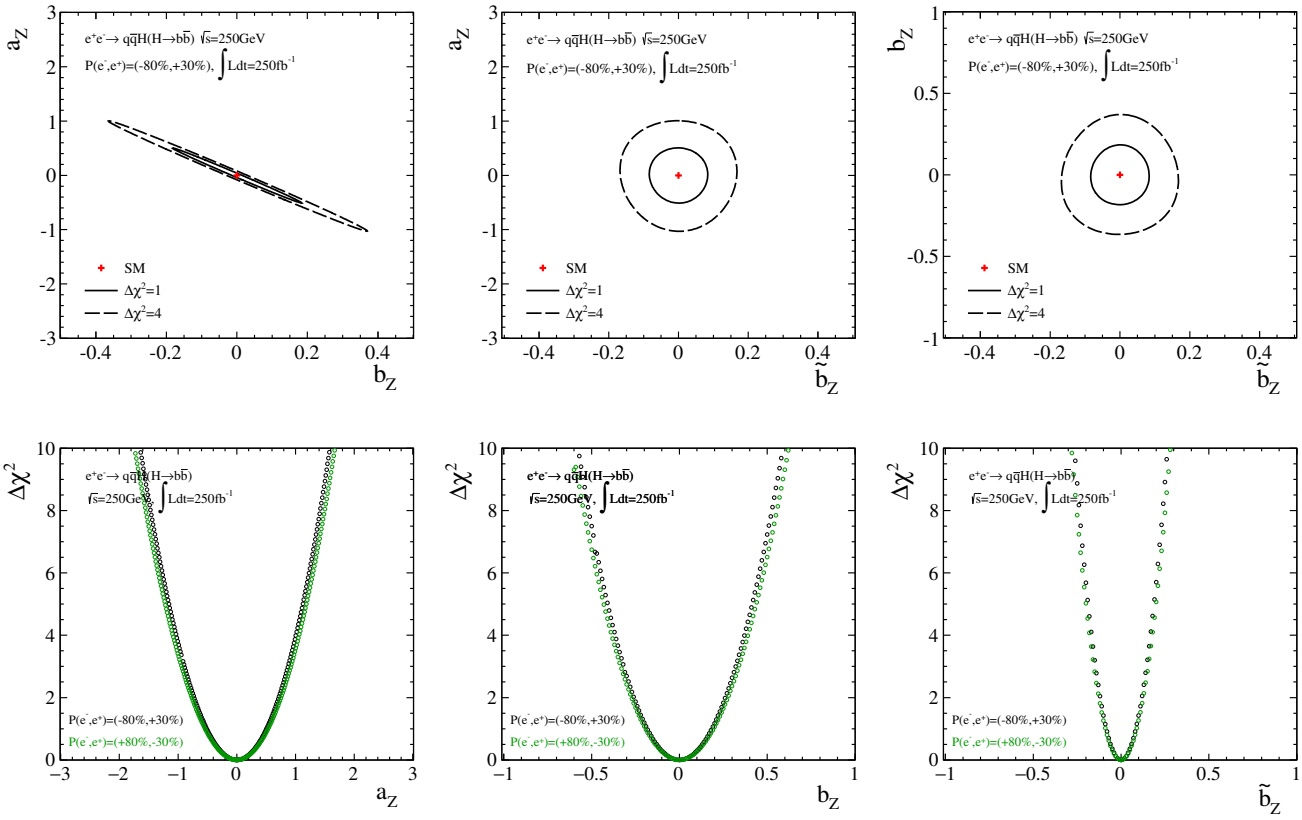

$$\sqrt{s} = 250 \text{ GeV with } \int \text{Ldt} = 250 \text{ fb}^{-1} \text{ and } \text{P}(e^-, e^+) = (-80\%, +30\%)$$

$$\begin{cases} a_Z = [-0.512, \quad 0.506] \\ b_Z = [-0.183, \quad 0.184] \\ \tilde{b}_Z = [-0.0837, \quad 0.0837] \end{cases}, \quad \rho = \begin{pmatrix} 1 & -0.9998 & -0.0757 \\ - & 1 & 0.0796 \\ - & - & 1 \end{pmatrix}$$

$$\sqrt{s} = 250 \text{ GeV with } \int \text{Ldt} = 250 \text{ fb}^{-1} \text{ and } \text{P}(e^-, e^+) = (+80\%, -30\%)$$

$$\begin{cases} a_Z = [-0.540, \quad 0.533] \\ b_Z = [-0.193, \quad 0.195] \\ \tilde{b}_Z = [-0.0891, \quad 0.0889] \end{cases}, \quad \rho = \begin{pmatrix} 1 & -0.9997 & -0.0012 \\ - & 1 & 0.0048 \\ - & - & 1 \end{pmatrix}$$

Figure 72: (Upper): The plots show contours corresponding to the 1σ and 2σ sensitivities to the anomalous ZZH couplings. The fitting is performed with the hadronic channel only under the three free parameter space. The integrated luminosity of 250 fb^{-1} with the beam polarization state P(e^-, e^+)= (-80%,+30%) is assumed. The results are projected onto the two-dimensional parameter spaces a_Z-b_Z, a_Z-$\tilde{b}_Z$, and b_Z-$\tilde{b}_Z$. Both of the information, which are the three-dimensional distributions $x(\cos\theta^*_f, \cos\theta_Z, \Delta\Phi_{f\bar{f}})$ binned 5×5×5 and the production cross-section are combined. (Middle): The plots show $\Delta\chi^2$ distributions as a function of each parameter space of the anomalous couplings a_Z, b_Z, and $\tilde{b}_Z$. The distributions are obtained by using both information (the angles and the cross-section) and scanning one parameter while setting the other two parameters to be completely free. (Lower): The explicit values corresponding to the 1σ bounds for each anomalous parameter a_Z, b_Z, and $\tilde{b}_Z$ and the correlation matrix indicating correlation coefficients between the parameters.

6.3 Combined results on the sensitivity to the anomalous ZZH couplings

All information evaluated using each channel of the two leading Higgs production processes must be combined to give the achievable sensitivities in the ILC. The available information which sutisfy statistically independent are the kinematical distributions derived from each channel, which are three-dimensional distributions from the Higgs-strahlung process and one-dimensional distribution from the ZZ-fusion, respectively. The variation of the production cross-section of both of the process are also strong information to constraint the anomalous couplings.

6.3.1 Results in parameter space of (a_Z, b_Z, $\tilde{b}_Z$)

With the benchmarking luminosity at $\sqrt{s} = 250$ GeV :

Plots in Fig. 73 give 1σ and 2σ bounds as the prospective sensitivities to the anomalous ZZH couplings, where the sensitivities coming from both of the ZH and ZZ processes are separately plotted onto each parameter space. The 1σ bound in the ZZ process which can be seen in the a_Z-b_Z space is actually extending to the left side of the plot. Thus, the lower bound along a_Z is hidden in the a_Z-b_Z space,

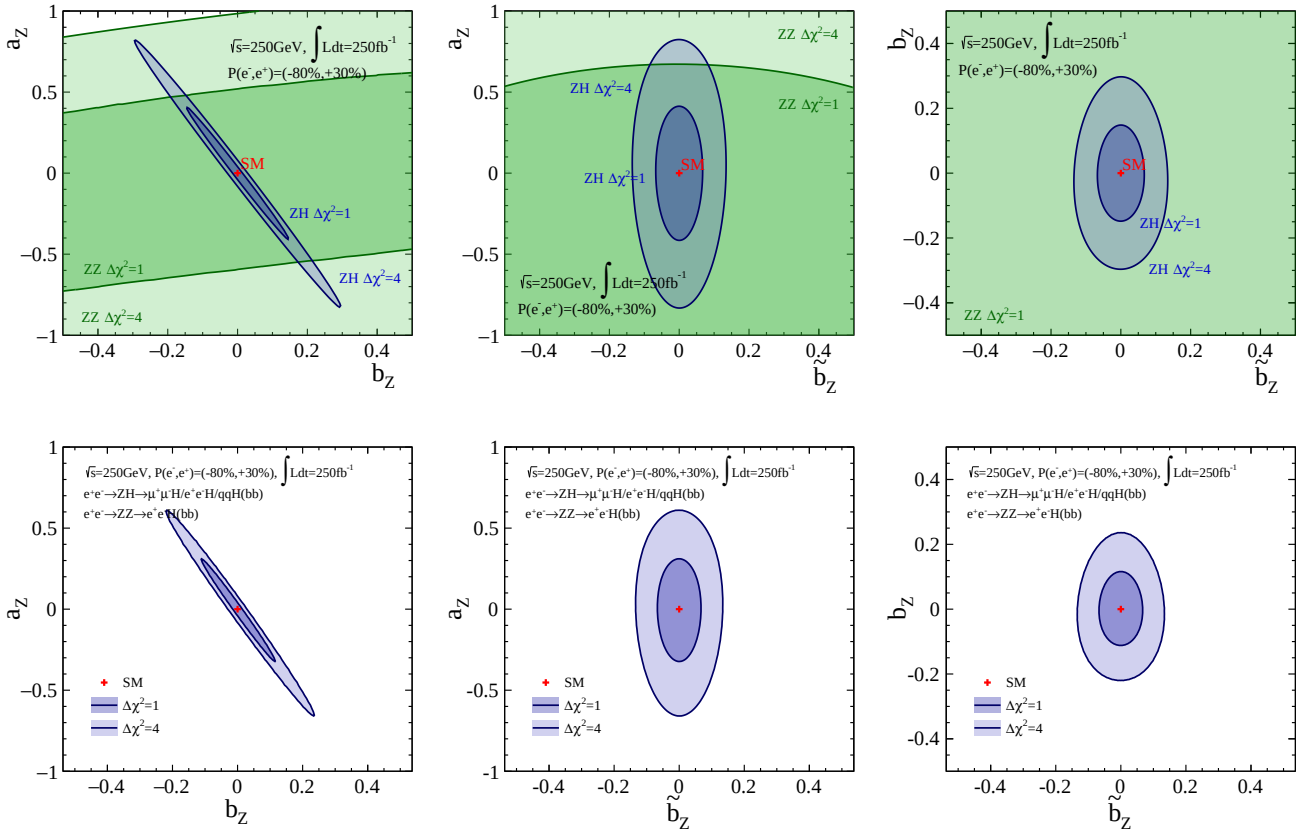

Figure 73: The Plots show contours corresponding to the 1σ and 2σ sensitivity to the anomalous ZZH couplings at $\sqrt{s} = 250$ GeV with the assumption of the integrated luminosity of 250 fb^{-1} and the beam polarization state P(e^-, e^+)= (-80%,+30%). Both of the information are considered: the three-dimensional distributions $x(\cos\theta_Z, \cos\theta^*_f, \Delta\Phi_{f\bar{f}})$ binned in 5×5×5 and the one-dimensional distribution $x(\Delta\Phi_{f\bar{f}})$ binned in 5 respectively for three channels of the Zh and one channel of the ZZ processes. After the simultaneous fitting the results are projected onto the two-dimensional parameter spaces a_Z-b_Z, a_Z-$\tilde{b}_Z$, and b_Z-$\tilde{b}_Z$. (Upper): The results are separately given, which are the Higgs-strahlung and the ZZ-fusion process. The sensitive region of the 1σ bound in the ZZ process is extending to the left side to some extent. (Lower): The results are combined into one. The physical parameter limits are set to be < 8 for all case.

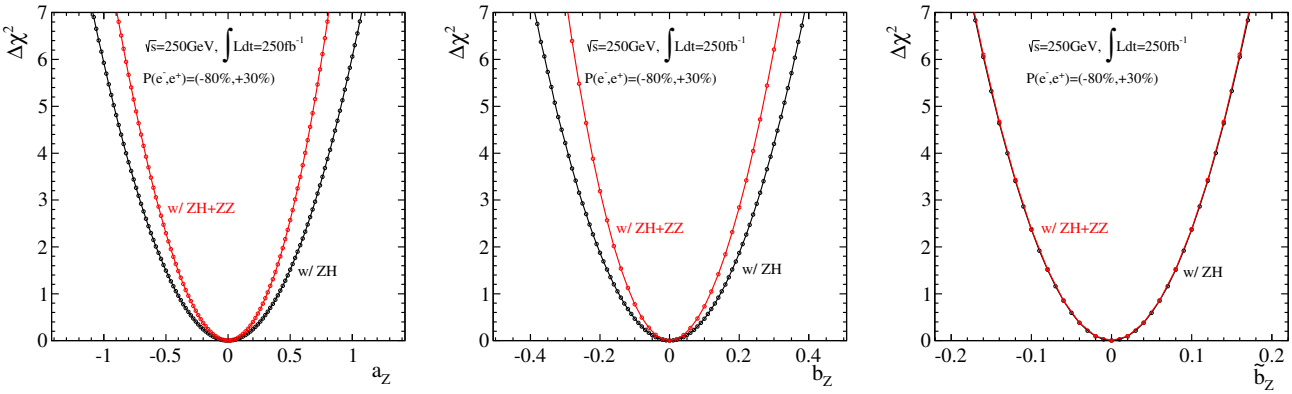

Figure 74: Plots show $\Delta\chi^2$ distributions as a function of each parameter space of the anomalous couplings a_Z, b_Z, and $\tilde{b}_Z$ at $\sqrt{s} = 250$ GeV with 250 fb^{-1}, where the four channels of the Zh (black) and the ZZ-fusion (red) processes are plotted. The distributions are obtained by using both information and scanning one parameter while setting the other two parameters to be completely free. The three-dimensional distributions $x(\cos\theta_Z, \cos\theta^*_f, \Delta\Phi_{f\bar{f}})$ binned in $5\times5\times5$ are used for the three channels of the Zh process and the one-dimensional distribution $x(\Delta\Phi_{f\bar{f}})$ binned in 5 is used for the ZZ-fusion process. (The physical parameter limits are set to be < 8 for all case, which is sufficiently large compared to the area we focus.)

$$Zh \text{ at } \sqrt{s} = 250 \text{ GeV with } \int \text{Ldt} = 250 \text{ fb}^{-1} \text{ and } \text{P}(e^-, e^+) = (-80\%, +30\%)$$

$$\begin{cases} a_Z = [-0.409,\ \ 0.407] \\ b_Z = [-0.146,\ \ 0.146] \\ \tilde{b}_Z = [-0.0648,\ \ 0.0648] \end{cases}, \quad \rho = \begin{pmatrix} 1 & -0.9998 & 0.0062 \\ - & 1 & -0.0062 \\ - & - & 1 \end{pmatrix}$$

$$Zh \text{ at } \sqrt{s} = 250 \text{ GeV with } \int \text{Ldt} = 250 \text{ fb}^{-1} \text{ and } \text{P}(e^-, e^+) = (+80\%, -30\%)$$

$$\begin{cases} a_Z = [-0.439,\ \ 0.436] \\ b_Z = [-0.157,\ \ 0.157] \\ \tilde{b}_Z = [-0.0717,\ \ 0.0716] \end{cases}, \quad \rho = \begin{pmatrix} 1 & -0.9998 & -0.0061 \\ - & 1 & 0.0062 \\ - & - & 1 \end{pmatrix}$$

$$Zh + ZZ \text{ at } \sqrt{s} = 250 \text{ GeV with } \int \text{Ldt} = 250 \text{ fb}^{-1} \text{ and } \text{P}(e^-, e^+) = (-80\%, +30\%)$$

$$\begin{cases} a_Z = [-0.323,\ \ 0.311] \\ b_Z = [-0.112,\ \ 0.116] \\ \tilde{b}_Z = [-0.0646,\ \ 0.0646] \end{cases}, \quad \rho = \begin{pmatrix} 1 & -0.9924 & -0.0036 \\ - & 1 & 0.0035 \\ - & - & 1 \end{pmatrix}$$

$$Zh + ZZ \text{ at } \sqrt{s} = 250 \text{ GeV with } \int \text{Ldt} = 250 \text{ fb}^{-1} \text{ and } \text{P}(e^-, e^+) = (+80\%, -30\%)$$

$$\begin{cases} a_Z = [-0.335,\ \ 0.321] \\ b_Z = [-0.115,\ \ 0.120] \\ \tilde{b}_Z = [-0.0717,\ \ 0.0716] \end{cases}, \quad \rho = \begin{pmatrix} 1 & -0.9927 & -0.0019 \\ - & 1 & 0.0018 \\ - & - & 1 \end{pmatrix}$$

Fig. 74 give the $\Delta\chi^2$ distributions as a function of each parameter space for the benchmark performance, where the left-handed polarization state P(e^-, e^+)= (-80%,+30%) is elected as the illustration. The impact of the Zh and the ZZ-fusion process are separately plotted in each parameter. Because the impact of the kinematical distribution derived from the ZZ-fusion process is too less to increase the sensitivity to the parameter due to the lack of statistics, at least for the benchmark luminosity of 250 fb^{-1}, it can not give any improvement for the parameter $\tilde{b}$. However, the correlation between parameters a_Z and b_Z in the ZZ-fusion process is the opposite diagonal compared to the direction of the correlation with the Zh process as shown in the plots. The information of the ZZ-fusion process can constrain the parameters and squeeze the parameter space which is allowed to move in the a_Z-b_Z plane. The summary of the sensitivities to the anomalous ZZH couplings corresponding to 1σ bounds as the prospective results at $\sqrt{s} = 250$ GeV with the benchmark integrated luminosities of 250 fb^{-1} is given for both beam polarization states P(e^-, e^+)= (-80%,+30%) and (+80%,-30%) in the Fig. 74.

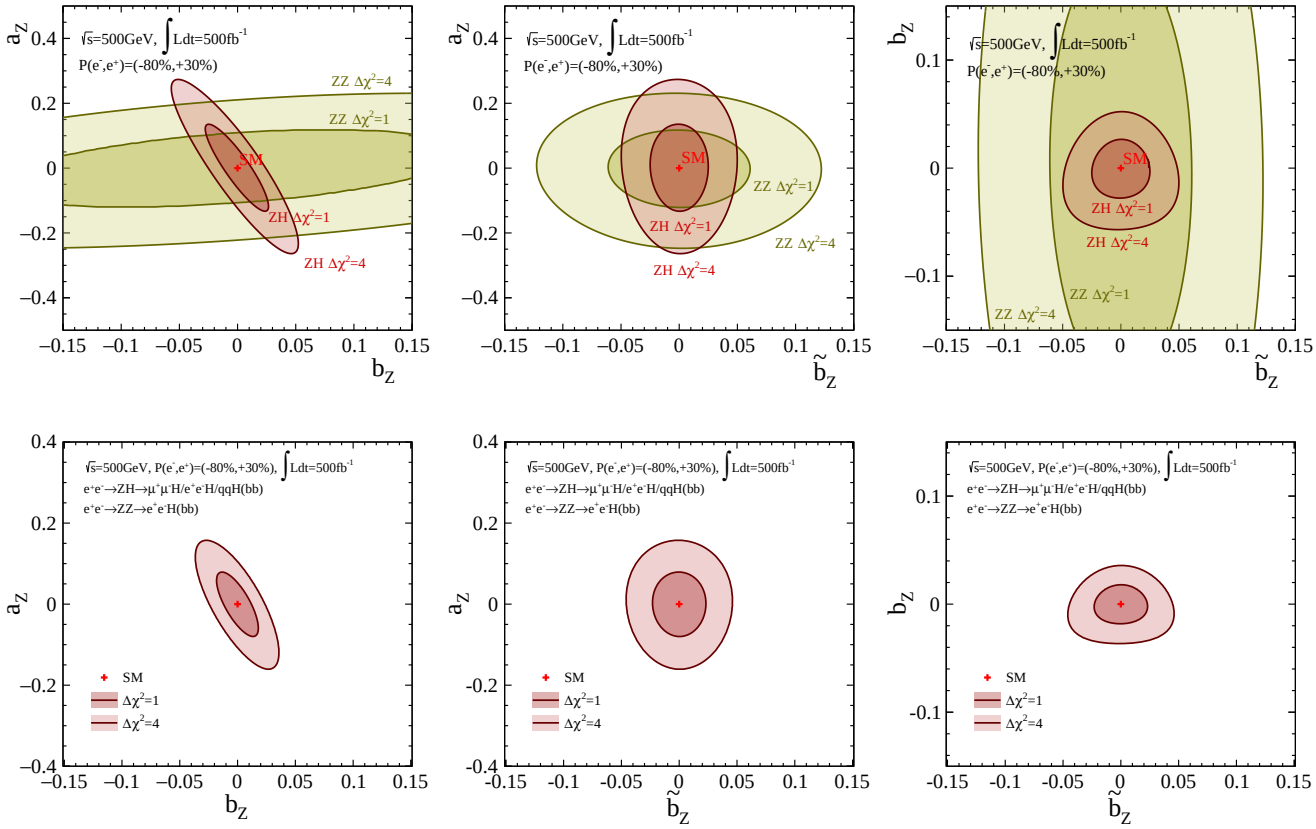

Figure 75: Plots show contours corresponding to the 1σ and 2σ sensitivity to the anomalous ZZH couplings at $\sqrt{s} = 500$ GeV. Fitting is performed with the three free parameters under the assumption of the integrated luminosity of 500 fb^{-1} with the beam polarization state P(e^-, e^+)= (-80%,+30%). The results are projected onto the two-dimensional parameter spaces a_Z-b_Z, a_Z-$\tilde{b}_Z$, and b_Z-$\tilde{b}_Z$. (Upper) The results are separately given, which are the Higgs-strahlung Zh and the ZZ-fusion process and (lower) the results are combined into one. Both information are considered: the three-dimensional distributions $x(\cos\theta_Z, \cos\theta^*_f, \Delta\Phi_{f\bar{f}})$ binned in $5\times5\times5$ and the two-dimensional distribution $x(\cos\theta_{higgs}, \Delta\Phi_{f\bar{f}})$ binned in 10×10 for three channels of the Zh and one channel of the ZZ processes.

The strong correlation in the a_Z-b_Z plane :

As discussed in Sec. 4.1, the matrix elements contributing from both of the Zh and the ZZ-fusion process are described as,

$$\begin{cases} \mathcal{M}_{a_Z}^{Zh} = -(\boldsymbol{\epsilon}_1 \cdot \boldsymbol{\epsilon}_2) \\ \mathcal{M}_{b_Z}^{Zh} = -2E_2\sqrt{s}(\boldsymbol{\epsilon}_1 \cdot \boldsymbol{\epsilon}_2) \end{cases}$$

$$\begin{cases} \mathcal{M}_{a_Z}^{ZZf} = -(\boldsymbol{\epsilon}_1 \cdot \boldsymbol{\epsilon}_2) \\ \mathcal{M}_{b_Z}^{ZZf} = (q_h^2 - 2q_1^2 - 2q_2^2)(\boldsymbol{\epsilon}_1 \cdot \boldsymbol{\epsilon}_2) + 2(\boldsymbol{q}_1 \cdot \boldsymbol{\epsilon}_2)(\boldsymbol{q}_2 \cdot \boldsymbol{\epsilon}_1) \end{cases}$$

$\mathcal{M}_{a_Z}^{Zh}$ and $\mathcal{M}_{a_Z}^{ZZf}$ have the same structure because the Z bosons have energy and the Lorentz condition is imposed in any case. Although the actual contributions are given with squared of the both matrix elements, the tendency is understandable from the elements. The signs of the matrix elements for Zh are same while the signs for the ZZ-fusion are different each other. Therefore, the opposite correlation will be appear in both Zh and ZZ-fusion process in the a_Z-b_Z plane.

With the benchmarking luminosity at $\sqrt{s} = 500$ GeV :

Plots in Fig. 75 give 1σ and 2σ bounds as the prospective sensitivities to the anomalous ZZH couplings and in Fig. 76 give $\Delta\chi^2$ distributions as a function of each parameter space at $\sqrt{s} =$ 500 GeV with a benchmark integrated luminosities of 500 fb^{-1}, assuming the left-handed polarization state P(e^-, e^+)= (-80%,+30%). The impact of the Zh process and the ZZ-fusion process are separately plotted.

Thanks to the higher energy and higher momentum of the Z bosons, which can lead quick variation of the kinematical distributions of the process, the strong correlation appears in a_Z-b_Z plane at 250 GeV is well squeezed compared. The impact of the ZZ-fusion that can give the opposite diagonal correlation is additionally sizable to improve the sensitivity to the anomalous ZZH couplings. The summary of the sensitivities to the anomalous ZZH couplings corresponding to 1σ bounds as the prospective results at $\sqrt{s} = 500$ GeV with the benchmark integrated luminosities of 500 fb^{-1} is given for both beam polarization states P(e^-, e^+)= (-80%,+30%) and (+80%,-30%) in the Fig. 76.

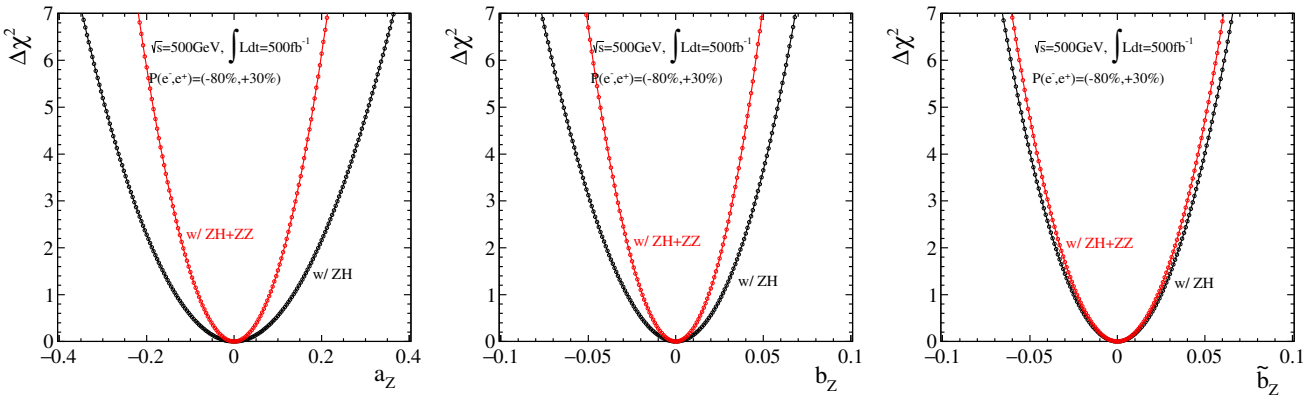

Figure 76: Plots show $\Delta\chi^2$ distributions as a function of each parameter space of the anomalous couplings a_Z, b_Z, and $\tilde{b}_Z$ at $\sqrt{s} = 500$ GeV with 500 fb^{-1}, where the four channels of the Zh (black) and the ZZ-fusion (red) processes are plotted. The distributions are obtained by using both information and scanning one parameter while setting the other two parameters to be completely free. The three-dimensional distributions $x(\cos\theta_Z, \cos\theta^*_f, \Delta\Phi_{f\bar{f}})$ binned in 5×5×5 are used for the three channels of the Zh process and the one-dimensional distribution $x(\cos\theta_{higgs}, \Delta\Phi_{f\bar{f}})$ binned in 10 is used for the ZZ-fusion process.

$$Zh \text{ at } \sqrt{s} = 500 \text{ GeV with } \int \text{Ldt} = 500 \text{ fb}^{-1} \text{ and } \text{P}(e^-, e^+) = (-80\%, +30\%)$$

$$\begin{cases} a_Z = [-0.133, \quad 0.136] \\ b_Z = [-0.0278, \quad 0.0266] \\ \tilde{b}_Z = [-0.0250, \quad 0.0250] \end{cases}, \quad \rho = \begin{pmatrix} 1 & -0.9910 & -0.0198 \\ - & 1 & 0.0148 \\ - & - & 1 \end{pmatrix}$$

$$Zh \text{ at } \sqrt{s} = 500 \text{ GeV with } \int \text{Ldt} = 500 \text{ fb}^{-1} \text{ and } \text{P}(e^-, e^+) = (+80\%, -30\%)$$

$$\begin{cases} a_Z = [-0.133, \quad 0.136] \\ b_Z = [-0.0278, \quad 0.0267] \\ \tilde{b}_Z = [-0.0255, \quad 0.0255] \end{cases}, \quad \rho = \begin{pmatrix} 1 & -0.9892 & 0.0037 \\ - & 1 & -0.0037 \\ - & - & 1 \end{pmatrix}$$

$$Zh + ZZ \text{ at } \sqrt{s} = 500 \text{ GeV with } \int \text{Ldt} = 500 \text{ fb}^{-1} \text{ and } \text{P}(e^-, e^+) = (-80\%, +30\%)$$

$$\begin{cases} a_Z = [-0.0821, \quad 0.0813] \\ b_Z = [-0.0191, \quad 0.0188] \\ \tilde{b}_Z = [-0.0231, \quad 0.0231] \end{cases}, \quad \rho = \begin{pmatrix} 1 & -0.7605 & -0.0146 \\ - & 1 & 0.0146 \\ - & - & 1 \end{pmatrix}$$

$$Zh + ZZ \text{ at } \sqrt{s} = 500 \text{ GeV with } \int \text{Ldt} = 500 \text{ fb}^{-1} \text{ and } \text{P}(e^-, e^+) = (+80\%, -30\%)$$

$$\begin{cases} a_Z = [-0.0818, \quad 0.0809] \\ b_Z = [-0.0190, \quad 0.0188] \\ \tilde{b}_Z = [-0.0240, \quad 0.0240] \end{cases}, \quad \rho = \begin{pmatrix} 1 & -0.7579 & 0.00784 \\ - & 1 & -0.0167 \\ - & - & 1 \end{pmatrix}$$

6.3.2 Results in parameter space of (η_Z, ζ_{ZZ}, $\tilde{\zeta}_{ZZ}$, ζ_{AZ}, $\tilde{\zeta}_{AZ}$)

In this section the effective Lagrangian describing the ZZH couplings defined in Eq. (12) is expanded to include the anomalous γZH couplings in the evaluation of the sensitivities.

The $e^+e^- \to ZH$ process is conducted by a s-channel exchange of the Z boson. The ZH diagram conducted by a photon exchange and existence of the direct γZH couplings can be naively assumed although it is completely forbidden at tree level because of no interaction of the Higgs boson via an electric charge and allowed to include as loop corrections caused with charged massive particles. In the SM framework, fields of the photon A^μ and the Z boson Z^μ are mixing through the gauge fields B^μ and W_3^μ which are generated by the $SU(2)_L \otimes U(1)_Y$ gauge symmetry. Once the anomalous ZZH couplings are assumed to exist as the loop corrections of the SM, the anomalous γZH couplings must be possible to exist as anomalies which are automatically generated by the higher dimension field operators as discussed in Sec. 2.3.2. Thus, one must consider these contributions in the effective Lagrangian.

The sensitivity to the anomalous γZH couplings that the ILC experiment will reach can be also evaluated by exploiting two different beam polarization states: namely left-handed and right-handed states. As mentioned above, because of the mixing of the gauge fields B^μ and W_3^μ, interference of both fields can not be disentangled with only one beam polarization state. However, utilizing the two beam polarization states and the fact that the gauge field B^μ couples to both left-handed and right-handed fermions in the same way through the $U(1)_Y$ gauge symmetry and the field W_3^μ couples to the left-handed fermions only through the $SU(2)_L$ gauge symmetry, the interference must be disentangled.

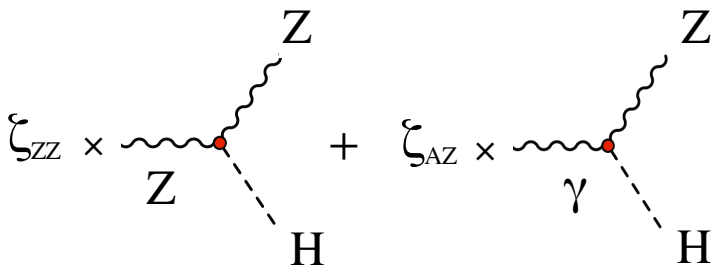

Figure 77: A view illustrates vertices of the ZZH and the γZH on the ZH process. The given parameters ζ_{ZZ} and ζ_{AZ} are describing both contributions.

To include the anomalous γZH couplings into the effective Lagrangian, the defined parameterization of the anomalous ZZH couplings in Eq. (12) is replaced with new parameterization which is composed of both of the anomalous ZZH and γZH couplings. The parameters b_Z and $\tilde{b}_Z$ are replaced by introducing dimensionless parameters ζ_{ZZ} and $\tilde{\zeta}_{ZZ}$, which are defined in Eq. (37). In addition, new dimensionless parameters ζ_{AZ} and $\tilde{\zeta}_{AZ}$ which describe the anomalous γZH couplings, as illustrated in Fig. 77, are also introduced into the effective Lagrangian.

$$\eta_Z = \frac{v}{\Lambda} a_Z \ , \quad \zeta_{ZZ} = \frac{v}{\Lambda} b_Z \ , \quad \text{and} \quad \tilde{\zeta}_{ZZ} = \frac{v}{\Lambda} \tilde{b}_Z \tag{37}$$

$$\begin{aligned} \mathcal{L}_{ZZH+\gamma ZH} \ = \ & M_Z^2 \frac{1}{v}\Big(1+\eta_Z\Big) Z_\mu Z^\mu h \\ & + \frac{\zeta_{ZZ}}{2v} Z_{\mu\nu} Z^{\mu\nu} h + \frac{\zeta_{AZ}}{v} A_{\mu\nu} Z^{\mu\nu} h \\ & + \frac{\tilde{\zeta}_{ZZ}}{2v} Z_{\mu\nu} \tilde{Z}^{\mu\nu} h + \frac{\tilde{\zeta}_{AZ}}{v} A_{\mu\nu} \tilde{Z}^{\mu\nu} h \end{aligned} \tag{38}$$

where v and Λ denote the vacuum expectation value and the new physics scale, which are 246 GeV and 1 TeV. The new effective Lagrangian describing both of the anomalous ZZH and γZH

couplings redefined in Eq. (38) are recovering Eq. (11) except the anomalous WWH and $\gamma\gamma H$ couplings.

Contributions of each structure derived from both ZZH and γZH couplings can be evaluated by connecting the first parameterization with the new one and considering the two different beam polarization states. To clarify the connection of both of the parameterizations, theoretical calculation was performed with the PHYSSIM generator to put the coefficients giving the contributions, which are calculated in terms of relative difference of the production cross-section of σ_{BSM}/σ_{SM}. The given relation between the two parameterizations for the $\sqrt{s}$=250 GeV are as follows, in the case of b_Z,

$$\begin{cases} e_L^- e_R^+ : 1 + 5.70\ \zeta_{ZZ} + 7.70\ \zeta_{AZ} = 1 + 5.70\ b_Z^{e_L^- e_R^+} \\ e_R^- e_L^+ : 1 + 5.70\ \zeta_{ZZ} - 9.05\ \zeta_{AZ} = 1 + 5.70\ b_Z^{e_R^- e_L^+} \end{cases} \tag{39}$$

$$\begin{cases} \zeta_{ZZ} = 0.54\ b_Z^{e_L^- e_R^+} + 0.46\ b_Z^{e_R^- e_L^+} \\ \zeta_{AZ} = 0.34\ b_Z^{e_L^- e_R^+} - 0.34\ b_Z^{e_R^- e_L^+} \end{cases} \tag{40}$$

and as for $\tilde{b}_Z$,

$$\begin{cases} e_L^- e_R^+ : \ 1 - \frac{1.14}{10^3}\ \tilde{\zeta}_{ZZ} - \frac{1.80}{10^3}\ \tilde{\zeta}_{AZ} = 1 - \frac{1.14}{10^3}\ \tilde{b}_Z^{e_L^- e_R^+} \\ e_R^- e_L^+ : \ 1 + \frac{2.40}{10^3}\ \tilde{\zeta}_{ZZ} + \frac{1.18}{10^3}\ \tilde{\zeta}_{AZ} = 1 + \frac{2.40}{10^3}\ \tilde{b}_Z^{e_R^- e_L^+} \end{cases} \tag{41}$$

$$\begin{cases} \tilde{\zeta}_{ZZ} = -0.46\ \tilde{b}_Z^{e_L^- e_R^+} + 1.46\ \tilde{b}_Z^{e_R^- e_L^+} \\ \tilde{\zeta}_{AZ} = \ \ 0.93\ \tilde{b}_Z^{e_L^- e_R^+} - 0.93\ \tilde{b}_Z^{e_R^- e_L^+} \end{cases} \tag{42}$$

where $b_Z^{e_L^- e_R^+}$ and $b_Z^{e_R^- e_L^+}$ given in the relations denote the anomalous parameters corresponding to the nominal beam polarizations: $\mathrm{P}(e^-, e^+) = (-80\%, +30\%)$ and $(+80\%, -30\%)$, respectively. In the equations of Eq. (39) and Eq. (41), for instance, the left side show the variation of the normalization described with the new parameters ζ_{ZZ} and ζ_{AZ}, while the right side show the variation described with b_Z. The same relation can be established for the parameter $\tilde{b}_Z$, and similarly for the higher energy $\sqrt{s}$ =500 GeV.

With the benchmarking luminosity at $\sqrt{s} = 250$ GeV :

Under this connection the fitting was performed to give the sensitivities to both of the ZZH and γZH couplings simultaneously assuming the benchmark luminosity of 250 fb^{-1}. Fig. 78 show summaries of the evaluation for each parameter. Notice that the relations Eq. (40) and Eq. (42) are directly using to translate to the ζ parameters. Thus, the given values must be multiplied by $\Lambda/v = 4.065$.

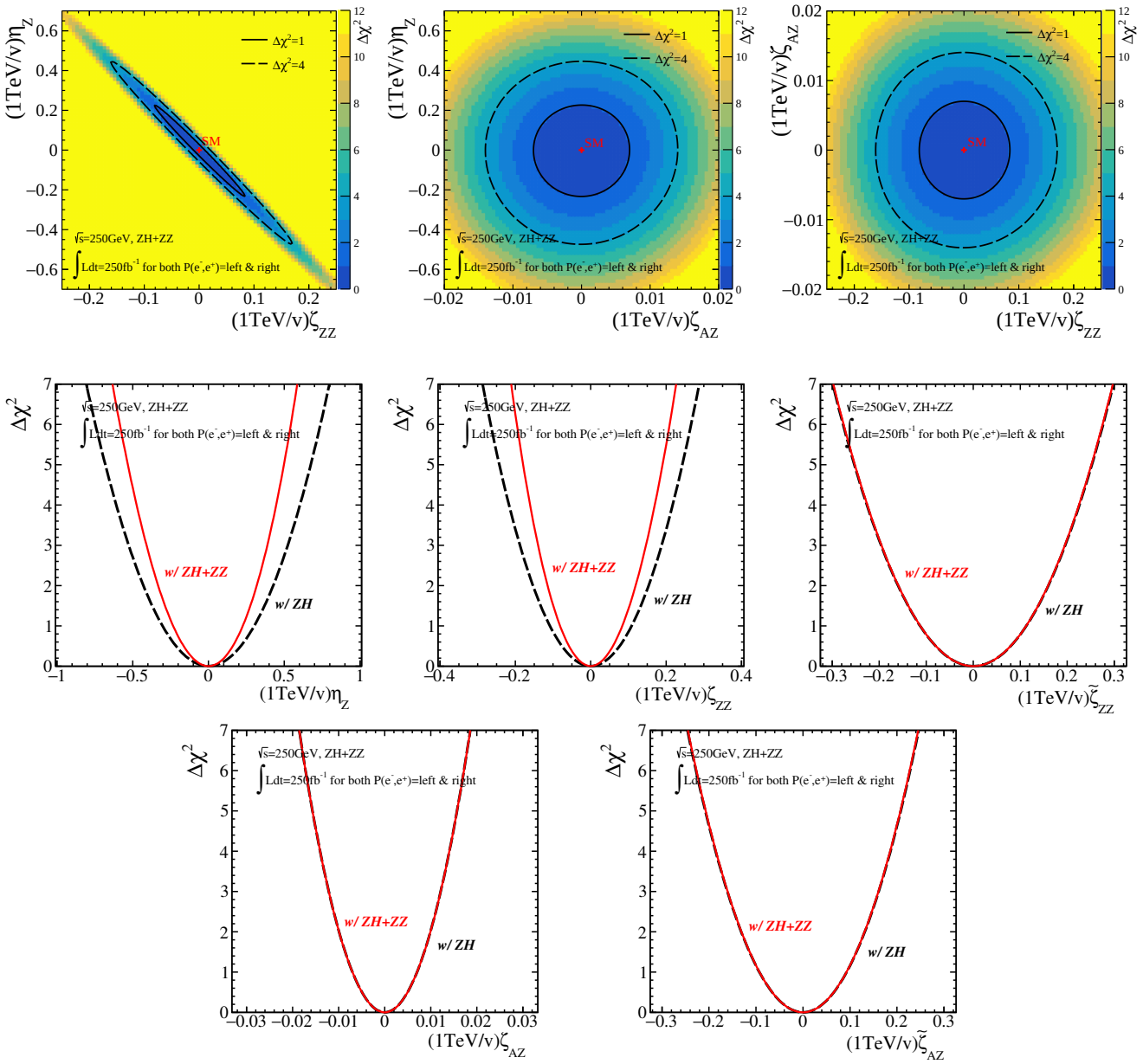

$$\sqrt{s} = 250 \text{ GeV with } \int \text{Ldt} = 250 \text{ fb}^{-1} \text{ for both P}(e^-, e^+) = \text{left- and right-poralization}$$

$$\begin{cases} \eta_Z &= \pm 0.0569 \\ \zeta_{ZZ} &= \pm 0.0204 \\ \zeta_{AZ} &= \pm 0.0034 \\ \tilde{\zeta}_{ZZ} &= \pm 0.0267 \\ \tilde{\zeta}_{AZ} &= \pm 0.0440 \end{cases}, \quad \rho = \begin{pmatrix} 1 & -.992 & .006 & -.0002 & -.001 \\ - & 1 & .004 & .0003 & .0009 \\ - & - & 1 & .0015 & -.0014 \\ - & - & - & 1 & -.896 \\ - & - & - & - & 1 \end{pmatrix}$$

Figure 78: (Upper): The color maps give the $\Delta\chi^2$ after 5 parameters fit, which are projected onto several parameter spaces as examples. (Middle) The distributions show the $\Delta\chi^2$ distributions projected onto each parameter axis. The variation of the cross-section and the three-dimensional distributions $x(\cos\theta_Z, \cos\theta^*_f, \Delta\Phi_{f\bar{f}})$ binned in 5×5×5 and the one-dimensional distribution $x(\Delta\Phi_{f\bar{f}})$ binned in 5 respectively for three channels of the Zh and one channel of the ZZ processes are used. (Lower) The given values correspond 1σ bounds as the sensitivities to each anomalous ZZH and γZH couplings. Since the a_Z, b_Z, and $\tilde{b}_Z$ parameters directly used, it is necessary to convert them by a factor of $\Lambda/v = 4.065$.

With the benchmarking luminosity at $\sqrt{s} = 500$ GeV :

The following relations are calculated at $\sqrt{s}$=500 GeV as the coefficients of the contributions, which are respectively for b_Z

$$\begin{cases} e_L^- e_R^+ : \ 1 + 9.77\ \zeta_{ZZ} + 14.73\ \zeta_{AZ} = 1 + 9.77\ b_Z^{e_L^- e_R^+} \\ e_R^- e_L^+ : \ 1 + 9.75\ \zeta_{ZZ} - 17.22\ \zeta_{AZ} = 1 + 9.75\ b_Z^{e_R^- e_L^+} \end{cases} \tag{43}$$

$$\begin{cases} \zeta_{ZZ} = 0.54\ \ b_Z^{e_L^- e_R^+} + 0.46\ \ \ b_Z^{e_R^- e_L^+} \\ \zeta_{AZ} = 0.306\ b_Z^{e_L^- e_R^+} - 0.306\ b_Z^{e_R^- e_L^+} \end{cases} \tag{44}$$

and for $\tilde{b}_Z$

$$\begin{cases} e_L^- e_R^+ : \ 1 - \frac{6.72}{10^3}\ \tilde{\zeta}_{ZZ} - \frac{9.71}{10^3}\ \tilde{\zeta}_{AZ} = 1 - \frac{6.72}{10^3}\ \tilde{b}_Z^{e_L^- e_R^+} \\ e_R^- e_L^+ : \ 1 + \frac{2.42}{10^3}\ \tilde{\zeta}_{ZZ} - \frac{6.47}{10^2}\ \tilde{\zeta}_{AZ} = 1 + \frac{2.42}{10^3}\ \tilde{b}_Z^{e_R^- e_L^+} \end{cases} \tag{45}$$

$$\begin{cases} \tilde{\zeta}_{ZZ} = 0.950\ \ \tilde{b}_Z^{e_L^- e_R^+} + 0.051\ \ \ \tilde{b}_Z^{e_R^- e_L^+} \\ \tilde{\zeta}_{AZ} = 0.0355\ \tilde{b}_Z^{e_L^- e_R^+} - 0.0355\ \tilde{b}_Z^{e_R^- e_L^+} \end{cases} \tag{46}$$

The sensitivities to both of the ZZH and γZH couplings assuming the benchmark luminosity of 500 fb^{-1} are given in Fig. 79. Again, notice that the relations Eq. (44) and Eq. (46) are directly using to translate to the ζ parameters. Thus, the given values must be multiplied by $\Lambda/v = 4.065$.

With ILC full operation :

The achievable sensitivities to the anomalous couplings assuming ILC full operation are also evaluated. One of the scenarios among the operation proposals of the ILC [46] is known as H20, where total luminosities of 2 ab^{-1} and 4 ab^{-1} are planned to be accumulated for $\sqrt{s}$ =250 and 500 GeV, respectively. Approximately 67.5 % and 22.5 % out of the integrated luminosity of 2 ab^{-1} are planed to be assigned for both of the beam polarization states of $\mathrm{P}(e^-, e^+) = (-80\%, +30\%)$ and $(+80\%, -30\%)$ at $\sqrt{s}$=250 GeV, whereas 40 % out of the 4 ab^{-1} are also planned to be assigned for both polarization states at $\sqrt{s}$=500 GeV. Fig. 80 illustrate $\Delta\chi^2$ distributions showing the prospective sensitivities to the anomalous ZZH and γZH couplings which are evaluated under the assumption of the H20 scenario, where all information evaluated up to here are combined. Notice again that the given values must be multiplied by $\Lambda/v = 4.065$.

The sensitivity to η_Z, which is the SM-like parameter, can reach 0.55 %, and the sensitivities to the other new structures describing anomalous ZZH couplings can also respectively reach 0.2 % and 0.3 %. The sensitivities to the new structures describing anomalous γZH couplings can reach less than 0.1 % as well.

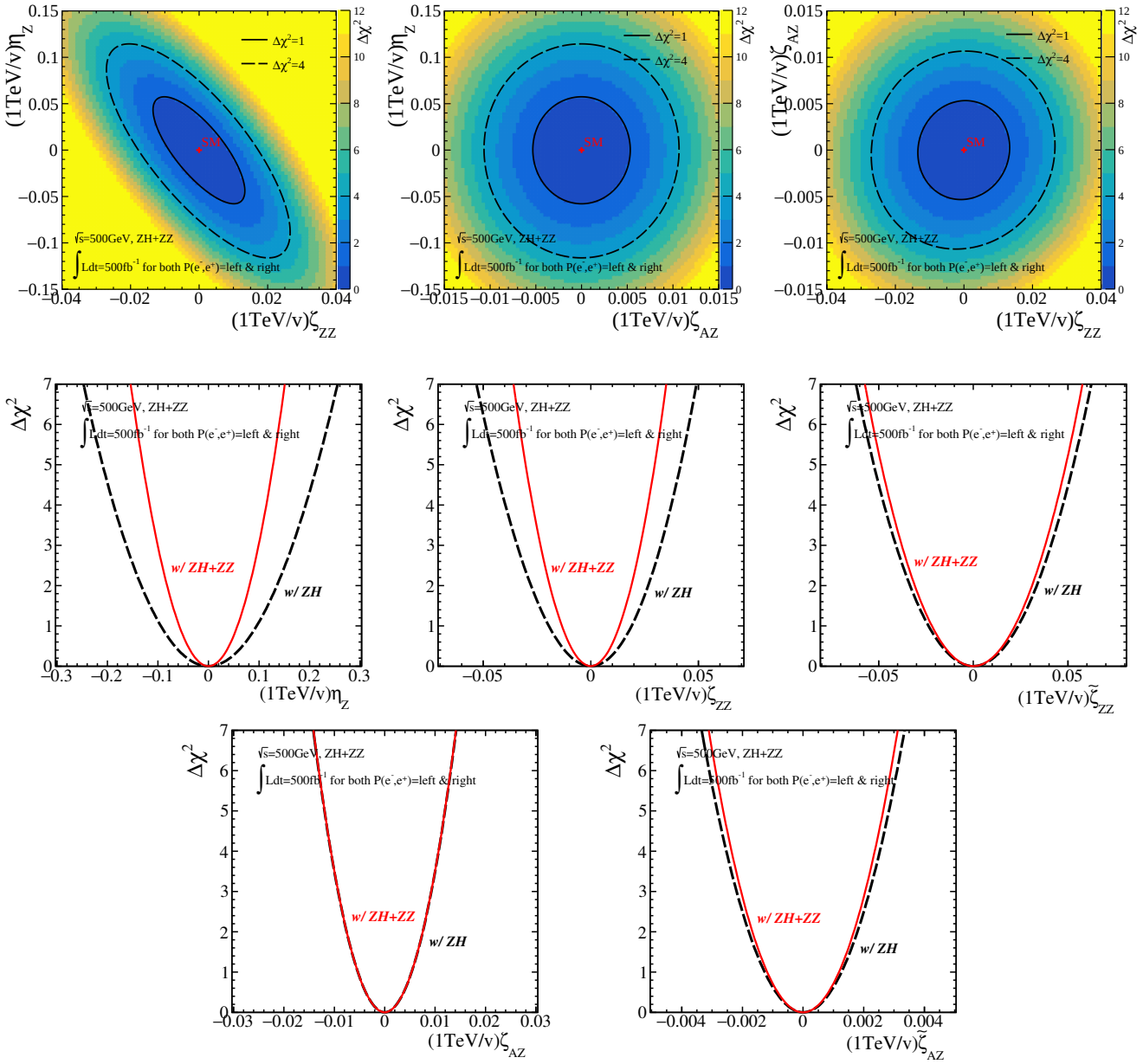

$$\sqrt{s} = 500 \text{ GeV with } \int \text{Ldt} = 500 \text{ fb}^{-1} \text{ for both P}(e^-, e^+) = \text{left- and right-poralization}$$

$$\begin{cases} \eta_Z &= \pm 0.0142 \\ \zeta_{ZZ} &= \pm 0.0033 \\ \zeta_{AZ} &= \pm 0.0026 \\ \tilde{\zeta}_{ZZ} &= \pm 0.0541 \\ \tilde{\zeta}_{AZ} &= \pm 0.0060 \end{cases}, \quad \rho = \begin{pmatrix} 1 & -.758 & -.002 & -.0.010 & -.001 \\ - & 1 & .051 & .008 & .012 \\ - & - & 1 & .0076 & -.0006 \\ - & - & - & 1 & .652 \\ - & - & - & - & 1 \end{pmatrix}$$

Figure 79: (Upper): The color maps give the $\Delta\chi^2$ after 5 parameters fit, which are projected onto several parameter spaces as examples. (Middle) The distributions show the $\Delta\chi^2$ distributions projected onto each parameter axis. The variation of the cross-section and the three-dimensional distributions $x(\cos\theta_Z, \cos\theta^*_f, \Delta\Phi_{f\bar{f}})$ binned in 5×5×5 and the one-dimensional distribution $x(\Delta\Phi_{f\bar{f}})$ binned in 5 respectively for three channels of the Zh and one channel of the ZZ processes are used. (Lower) The given values correspond 1σ bounds as the sensitivities to each anomalous ZZH and γZH couplings. Since the a_Z, b_Z, and $\tilde{b}_Z$ parameters directly used, it is necessary to convert them by a factor of $\Lambda/v = 4.065$.

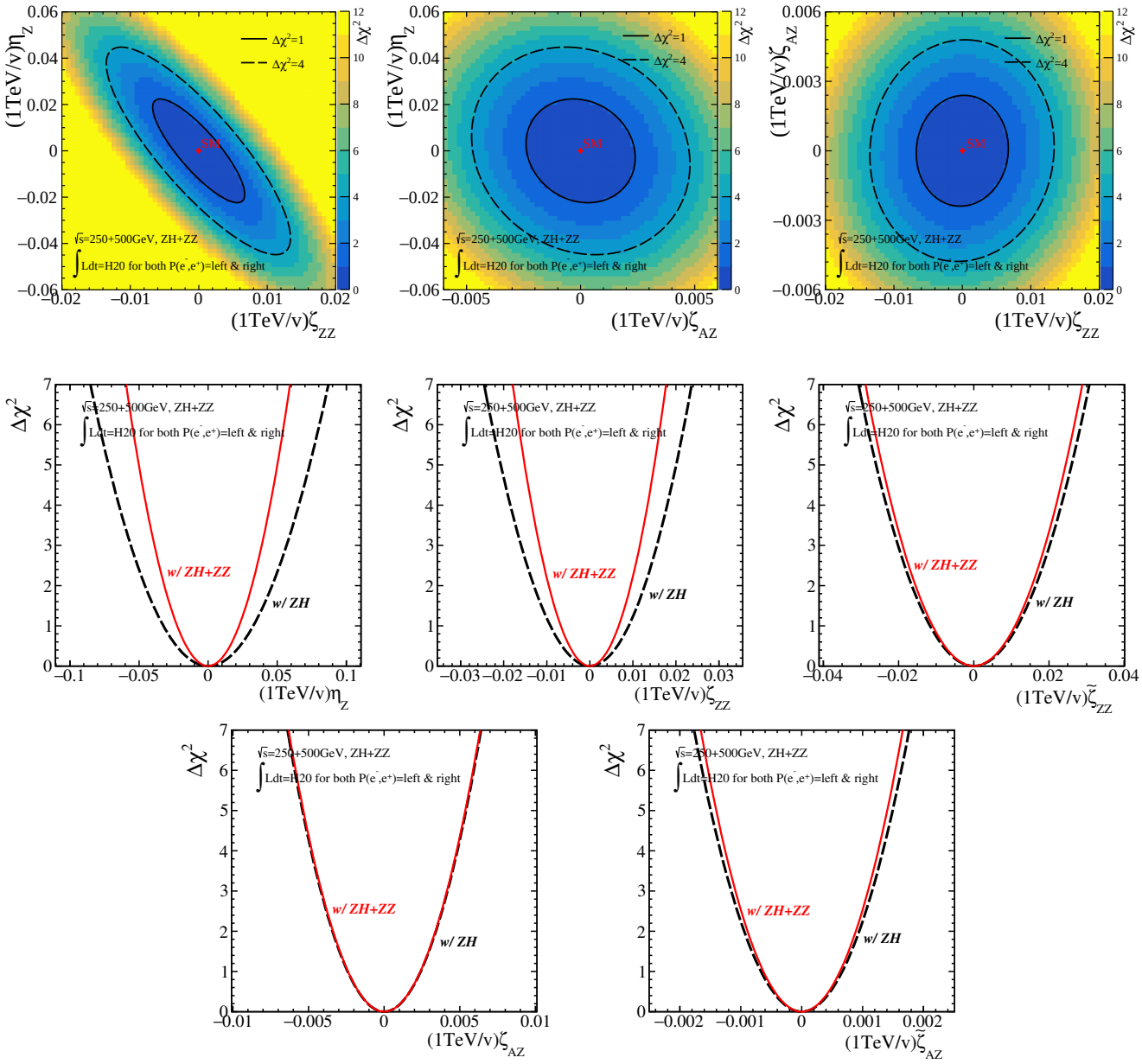

$$\sqrt{s} = 250 + 500 \text{ GeV with } \int \text{Ldt} = \text{H20}$$

$$\begin{cases} \eta_Z &= \pm 0.0055 \\ \zeta_{ZZ} &= \pm 0.0017 \\ \zeta_{AZ} &= \pm 0.0012 \\ \tilde{\zeta}_{ZZ} &= \pm 0.0027 \\ \tilde{\zeta}_{AZ} &= \pm 0.0003 \end{cases}, \quad \rho = \begin{pmatrix} 1 & -.837 & -.134 & -.009 & -.010 \\ - & 1 & .040 & .008 & .013 \\ - & - & 1 & .006 & -.0012 \\ - & - & - & 1 & .600 \\ - & - & - & - & 1 \end{pmatrix}$$

Figure 80: (Upper): The color maps give the $\Delta\chi^2$ after 5 parameters fit, which are projected onto several parameter spaces as examples. (Middle) The distributions show the $\Delta\chi^2$ distributions projected onto each parameter axis. The variation of the cross-section and the three-dimensional distributions $x(\cos\theta_Z, \cos\theta^*_f, \Delta\Phi_{f\bar{f}})$ binned in 5×5×5 and the one-dimensional distribution $x(\Delta\Phi_{f\bar{f}})$ binned in 5 respectively for three channels of the Zh and one channel of the ZZ processes are used. (Lower) The given values correspond 1σ bounds as the sensitivities to each anomalous ZZH and γZH couplings. Since the a_Z, b_Z, and $\tilde{b}_Z$ parameters directly used, it is necessary to convert them by a factor of $\Lambda/v = 4.065$.

7 Analysis on the anomalous WWH couplings

In the framework of the EFT, the field operators being the gauge invariant can generate not only the anomalous ZZH and γZH couplings but also the anomalous WWH couplings as well because of the $SU(2)$ symmetry, which are included in the effective Lagrangian given in Eq. (13) as the η_W, ζ_W, and $\tilde{\zeta}_W$ parameters. The effect derived from the anomalous WWH couplings is assumed to appear in the variation of cross-section and kinematical distributions which are strongly originating from the new Lorentz structures. The anomalous WWH couplings originally have a relation with the anomalous ZZH couplings by requiring the $SU(2) \times U(1)$ invariance which are ensured by the field operators of the EFT. Therefore, on the study exploiting the EFT framework in the ILC [32], η_W and ζ_W are considered as the parameters which are constrained with measurement accuracies of the cross-section, and a part of the global fitting to evaluate all parameter precisions simultaneously.

However, as with the estimation of the sensitivity to the anomalous ZZH, there exists sufficient capability that both sensitivities to η_W and ζ_W are improved by using the kinematical distribution derived from the structures of the anomalous WWH couplings. But this consideration has not been given in the EFT framework discussed in [32] for the moment. The purpose of this section is to evaluate how much the sensitivities to WWH couplings which are independently evaluated from the anomalous ZZH studies by exploiting the kinematical distribution can reach, compared to the results given by the ZZH studies alone, and to estimate whether the sensitivities to WWH couplings can improve the results of the anomalous VVH couplings or not.

Processes for evaluating the anomalous WWH couplings :

To evaluate the sensitivity to the anomalous WWH couplings, the following 6 channels of both of the Higgs production process through the WW-fusion and Higgs decay processes through the Higgs-strahlung at both center-of-mass energies $\sqrt{s} = 250$ and 500 GeV are considered:

$$
\begin{cases}
\sqrt{s} = 250 \text{ GeV} & e^+e^- \to \nu_e\bar{\nu}_e h, \quad h \to b\bar{b} & (WW\text{-fusion process}) \\
\cdots & e^+e^- \to Zh \to q\bar{q}h, \quad h \to WW^* \to q\bar{q}l\bar{\nu} & (\text{Higgs-strahlung}) \\
\cdots & e^+e^- \to Zh \to q\bar{q}h, \quad h \to WW^* \to q\bar{q}q\bar{q} & (\quad \cdots \quad) \\
\cdots & e^+e^- \to Zh \to \nu\bar{\nu}h, \quad h \to WW^* \to q\bar{q}q\bar{q} & (\quad \cdots \quad) \\
\sqrt{s} = 500 \text{ GeV} & e^+e^- \to \nu_e\bar{\nu}_e h, \quad h \to b\bar{b} & (WW\text{-fusion process}) \\
\cdots & e^+e^- \to \nu_e\bar{\nu}_e h, \quad h \to WW^* \to q\bar{q}q\bar{q} & (\quad \cdots \quad)
\end{cases}
$$

The WW-fusion at 250 GeV listed in the first line can give both information: variation of the production cross-section in the production vertex and the kinematical distribution derived from the vertex, which is expected to have small migration effects because of a clear feature of the final state. However, the process $Zh \to \nu\bar{\nu}b\bar{b}$ of the Higgs-strahlung has same final state and is possible for the shape to vary depending on the anomalous ZZH couplings. which must be care in the analysis. The analysis of two main channels, which are the WW-fusion process with the $h \to b\bar{b}$ decay and the Higgs-strahlung process with the $h \to W^+W^- \to q\bar{q}l\nu$ are mentioned in the main text as examples. The other channels are summarized in the appendix.

A full hadronic channel $Zh \to q\bar{q}h$, $h \to WW^* \to q\bar{q}q\bar{q}$ of the Higgs-strahlung seems to have advantage in terms of the statistics. However, the shape information of kinematical distributions of this channel receives the huge migration effects due to multi jet environment. Therefore, most of the shape information is lost and can not be extracted at all, which is discussed in Sec. B.1. The Z decaying to neutrino channel $Zh \to \nu\bar{\nu}h$, $h \to WW^* \to q\bar{q}q\bar{q}$ is tried to categorize to maximize the sensitivity to the parameter $\tilde{b}_W$ that is given from the angle between decay planes $\Delta\Phi$. The key performance is the heavy flavor tagging to identify c-quarks. This will be also discussed in Sec. B.2.

7.1 $e^+e^- \to \nu_e\bar{\nu}_e h,\ h \to b\bar{b}$ at $\sqrt{s} = 250$ GeV

7.1.1 Reconstruction and background suppression

The event reconstruction was done by clustering inclusively all PFOs into two jets with the Durham jet algorithm and the heavy flavor tagging was implemented with LCFIPlust software package. When extracting the shape information at $\sqrt{s}$=250 GeV using the t-channel $\nu\bar{\nu}h$ reaction of the WW-fusion process, one problem is interference with the s-channel Higgs-strahlung process that has the same final state of $\nu\bar{\nu}h$ and a larger cross-section of 61.6 fb with the left-handed polarization: P(e^-, e^+)= (-80%,+30%), which is a few times larger than that of the signal whose cross-section is 15.4 fb. This s-channel process completely overlaps with the signal process and it is almost irreducible. A two-fermion SM process of hadronic reaction $e^+e^- \to q\bar{q} + (\gamma)$, where γ denotes a radiative return to the Z boson, has more than 1000 times large cross-section and it is also possible source as the background suppression.

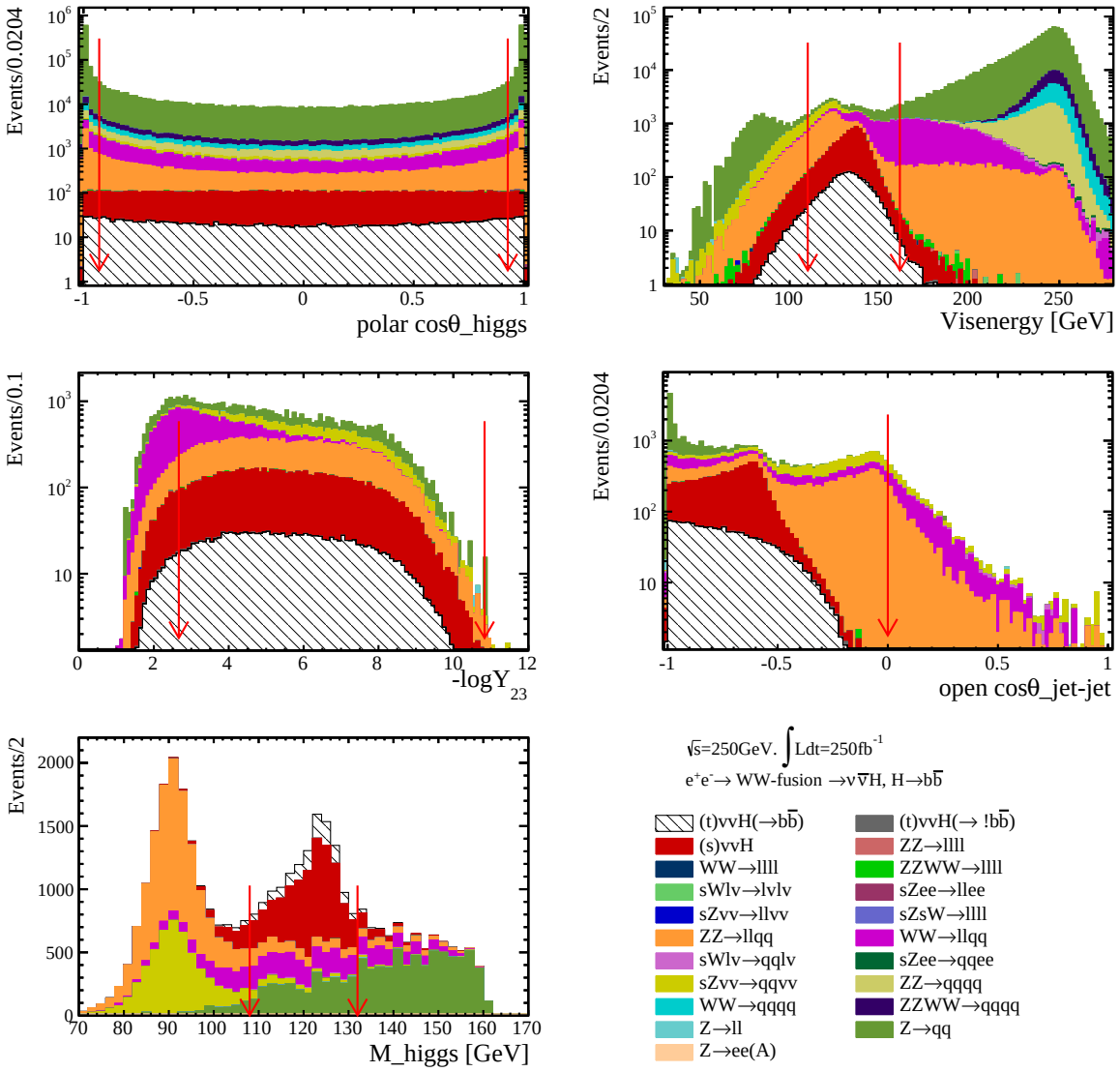

Figure 81: The distributions show each observable used for the background suppression assuming 250 fb^{-1} with P(e^-, e^+)= (-80%,+30%). The explanation of the observables are given in the text. Red arrows on each plot indicate the cut values applied to each observable as the background suppression.

Available observables which are sensitive to the anomalous WWH couplings in the WW-fusion process are the momentum P_h and the polar angle $\cos\theta_h$ distribution of the Higgs boson as illustrated in Sec. 4.2. However, a lot of two-fermion backgrounds, for instance, are possible to cover the sensitive area of the polar angle of the Higgs boson after the background suppression as illustrated in the first plot of Fig. 81. The most strong observable among the shape information for testing the anomalous couplings seems to be the momentum distribution of the Higgs according to the variation of the shape listed in Sec. 4.2. For the purpose of making the sensitivity coming from the momentum distribution of the Higgs boson maximize and the signal significance increase, the polar angle cut was imposed together with the other cuts to suppress the huge two-fermion background. All cut observables for the suppression are as follows, and Table 5 shows reduction table of the signal and backgrounds.

Table 5: The expected number of remaining signal and background events after each cut on the t-channel $\nu\bar{\nu}h,\ h \to b\bar{b}$ at $\sqrt{s}$=250 GeV. The integrated luminosity of 250 fb^{-1} is assumed. ϵ and S_{sig} denote the signal efficiency and significance respectively.

Cut variables $\sqrt{s}$=250 GeV P(e^-, e^+)= (-80%,+30%)

	$\nu\bar{\nu}h$			SM backgrounds			
process	$(t)h \to b\bar{b}$	ϵ	$h \to$others	$(s)\nu\bar{\nu}h$	$2f$	$4f$	S_{sig}
cross-section (fb)	9.12	-	6.28	61.60	-	-	-
Expected	2279	100	1571	15177	$2.91 \cdot 10^7$	$1.02 \cdot 10^7$	-
$N_{isoLeps} = 0$	2273	99.74	1213	13923	$2.15 \cdot 10^7$	$9.69 \cdot 10^6$	0.43
$N_{\mathrm{PFOs}} \in [30,\ 90]$	2210	96.97	892	12379	$1.72 \cdot 10^7$	$6.11 \cdot 10^6$	0.47
sum of b-tag > 1.0	2062	90.47	18	8302	$2.97 \cdot 10^6$	$4.64 \cdot 10^6$	1.15
$\cos\theta_h \in [-0.928,\ 0.927]$	1862	81.70	16	7751	$7.25 \cdot 10^6$	$1.80 \cdot 10^5$	1.95
$E_{vis} \in [110.0,\ 161.25]$	1687	74.02	14	7190	$1.04 \cdot 10^4$	$3.14 \cdot 10^4$	7.50
$-\log y_{23} \in [2.67, 10.83]$	1574	69.06	14	6721	7980	$2.58 \cdot 10^4$	7.68
min $N_{\mathrm{PFOs}} > 10$	1556	68.27	11	6647	7624	$2.31 \cdot 10^4$	7.88
$\cos\theta_{jets}^{open} < 0.0$	1555	68.23	11	6645	7602	$1.98 \cdot 10^4$	8.24
$M_h \in [108,\ 132]$	1319	57.87	9	5526	2370	3684	11.6

- $N_{isoLeps} = 0$, $N_{\mathrm{PFOs}} \in [30,\ 90]$, and sum of b-tag for both jets > 1.0
  Since an isolated lepton is expected not to be exist in the final state and it is not a multiple jet environment, the number of isolated leptons and PFOs are useful observable to distinguish the signal from the background. Additionally two clustered jet have larger b-likeness.
- $\cos\theta_h \in [-0.928,\ 0.927]$
  The polar angle of the di-jet is useful to suppress the 2-fermion events originating from the radiative return to the Z. The radiated γ flies along the beam axis and becomes missing, and the Z boson generated in the reaction also flies back-to-back to the γ. Thus it has the very small polar angle.
- $E_{vis} \in [110.0,\ 161.25]$ GeV,
  the jet clustering parameter $-\log y_{23} \in [2.67, 10.83]$, and min $N_{\mathrm{PFOs}} > 10$
  The visible energy in the reaction, the parameter for giving jet transition from 2 to 3 jets, and the number of minimum PFOs among jets in the reaction. These values are useful to suppress full hadronic process and processes which has the different number of jets in the reaction.
- $\cos\theta_{jets}^{open} < 0.0$
  A clear difference can been seen between t-channel and s-channel processes because products through t-channel reactions fly to very forward and backward area kinematically.

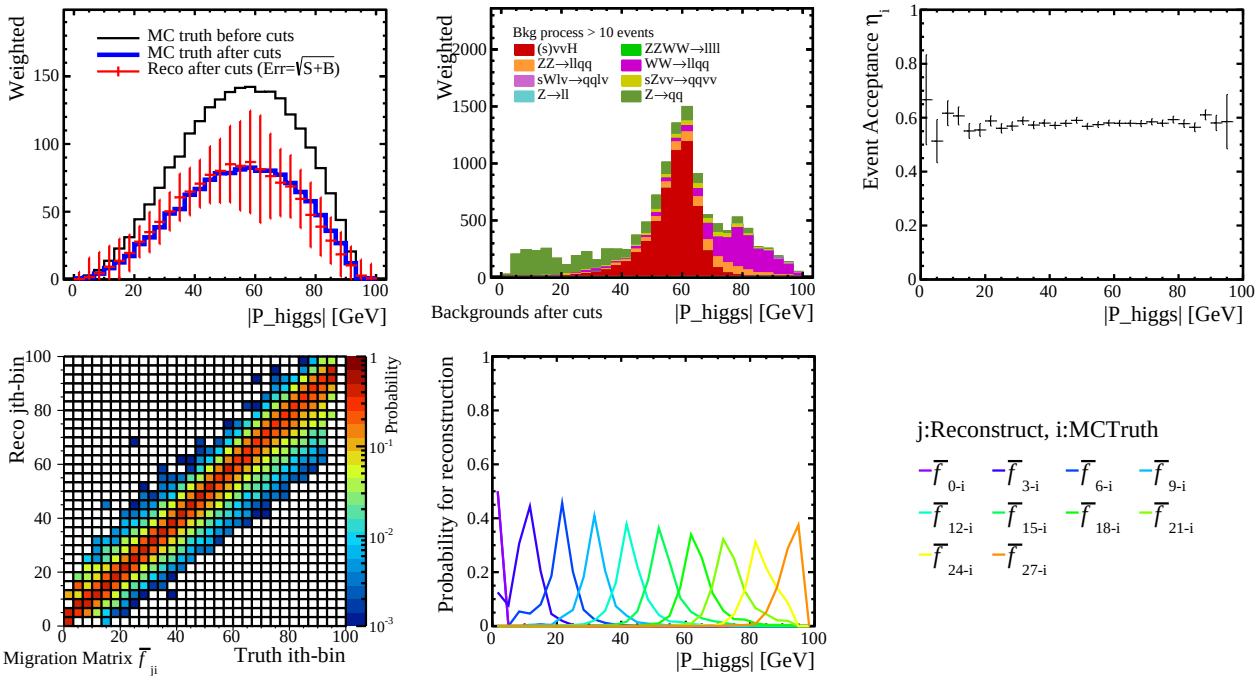

Figure 82: The distributions show the summary of the Higgs momentum P_h distribution after the background suppression. (Top left and middle): the remaining signal and the background distribution, which are given with the MC truth and the reconstructed, where the statistical error is given as the standard deviation of the Poisson probability. Notice that the s-channel $\nu\bar{\nu}h$ process overlaps in the sensitive area of the t-channel $\nu\bar{\nu}h$ process. (Top right): the event acceptance function η_i. (Bottom left and middle): the distribution shows the probability matrix of the migration ($\bar{f}_{ji}$) that is applied for the reconstruction of the realistic distribution of $\cos\theta_Z$, and the cross-sections of $\bar{f}_{ji}$ as 1-dim plots.

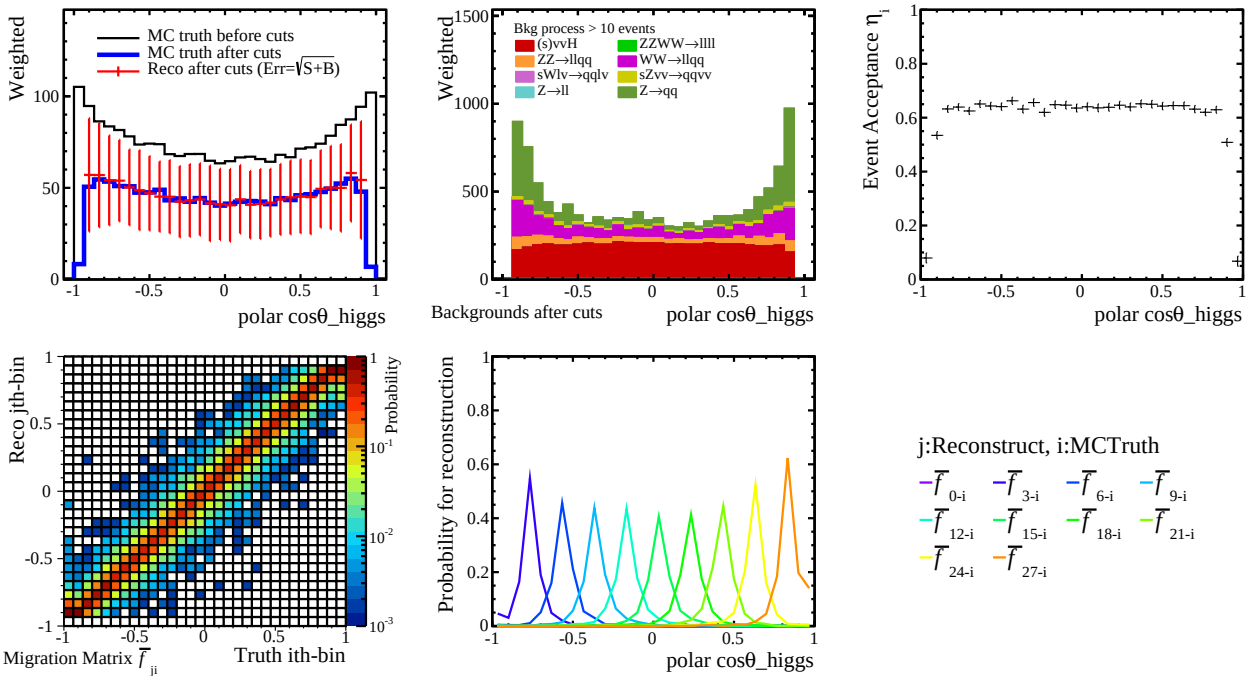

Figure 83: The distributions show the summary of the Higgs polar angle $\cos\theta_{higgs}$ after the background suppression. (Top left and middle): the remaining signal and the background distribution, which are given with the MC truth and the reconstructed. (Top right): the event acceptance function η_i. (Bottom left and middle): the probability matrix of the migration ($\bar{f}_{ji}$) that is applied for the reconstruction of $\cos\theta_{higgs}$, and the cross-sections of $\bar{f}_{ji}$ as 1-dim plots.

- $M_h \in [108,\ 132]$ GeV
  The invariant mass of the di-jet system, which becomes a conclusive mass window to determine the statistical error on each bin of kinematical histograms.

The momentum and polar angle distributions of the Higgs boson after all cuts are given in Fig. 82 and Fig. 83, where the 2-fermion background is sufficiently suppressed while a lot of s-channel $\nu\bar{\nu}h$ events still remain, which completely cover the signal region of the t-channel $\nu\bar{\nu}h$ process as shown in Fig. 82. Since there are only clear two jets in the final state and the jets can be separated because of the less boost, it can be seen that the migration effects is very small.

7.1.2 Impact of kinematical distribution

To evaluate the impact of the shape information, χ^2 test was performed using P_h, $\cos\theta_h$, and the three-dimensional distribution composed of $(P_h, \cos\theta_h, \cos\phi_h)$, where $\cos\phi_h$ denotes the azimuth angle. Fig. 84 give the $\Delta\chi^2$ for each anomalous WWH parameter. The results in which the polar angle cut is not imposed are also given to consider the effect of the polar angle cut.

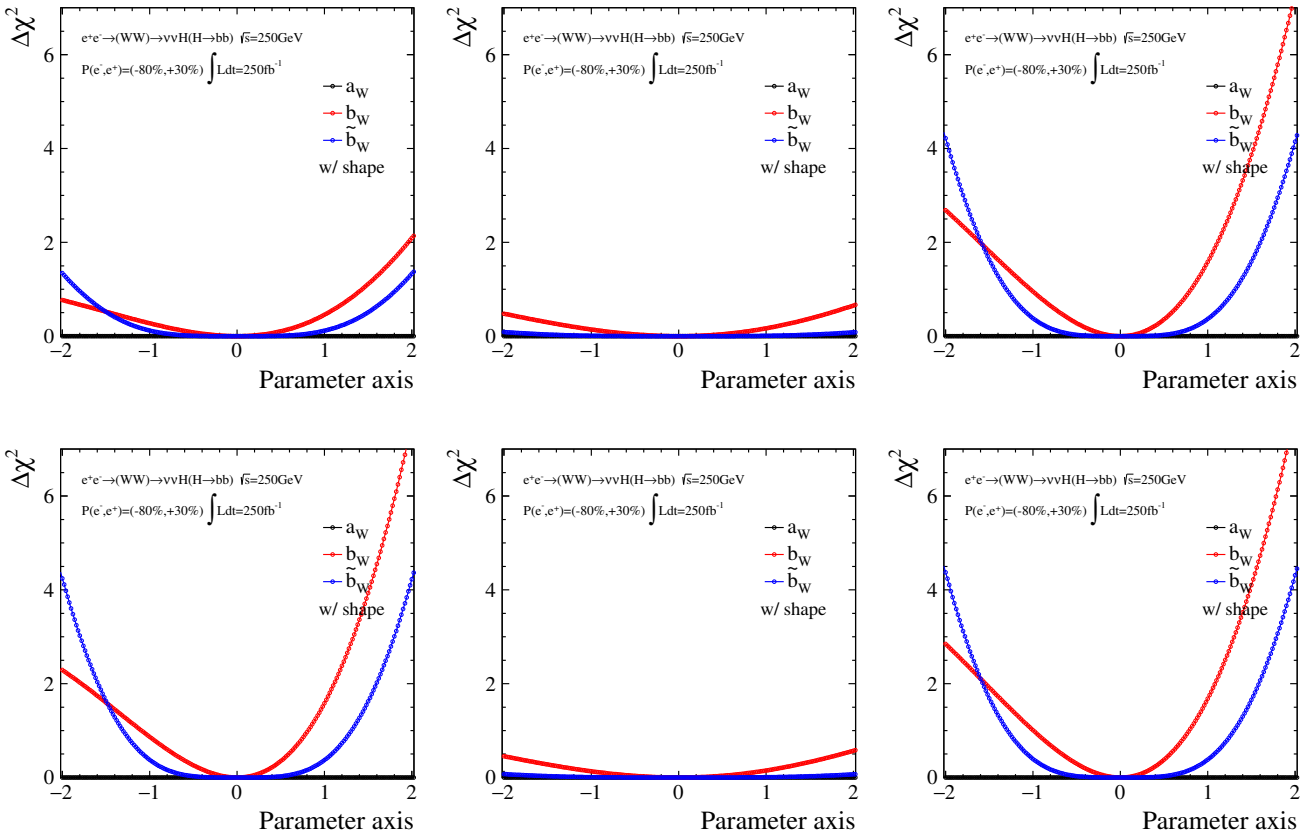

Figure 84: Distributions show $\Delta\chi^2$ as a function of each anomalous WWH parameter a_W, b_W, and $\tilde{b}_W$. The evaluation is done in the one-parameter axis. Black, red, and blue line on the plots correspond to the parameters a_Z, b_Z, and $\tilde{b}_Z$. Since only the angular information is considered here, the χ^2 values of a_W is 0.0 over the given range. (Upper) the polar angle cut is not imposed. (Lower) the polar angle cut is imposed to maximize the sensitivity given by P_h of the Higgs boson. Each distribution are used: respectively (left) $x(P_h)$, (middle) $x(\cos\theta_h)$ which are binned in 20, and (right) $x(P_h, \cos\theta_h, \cos\phi_h)$ binned $5\times5\times5$. The integrated luminosity of 250 fb^{-1} and the beam polarization of P(e^-, e^+)= (-80%,+30%) are assumed.

It is seen that the sensitivity coming from the P_h is significantly improved and one of $\cos\phi_h$ is slightly worse because of respectively the less background and the lost of the acceptance in the edge of the distribution. However, it is also observed that the impact of the three-dimensional distribution does not change with and without the polar angle cut. This is because, when the multi-dimension, for instance $x(P_h, \cos\theta_h)$ is focused on as given in Fig. 85, the 2-fermion backgrounds distribute around especially the edge of $\cos\theta_h = \pm 1$ and do not exist in the center area whereas the signal process distributes uniformly over the area and the variation of the shape depending on the parameter can also happen over the given area. Therefore, even if a lot of 2-fermion backgrounds remain, it does not strongly affect the sensitivity that the momentum distribution can give as far as the multi-dimensional distribution is used. Nevertheless, because the results with the polar angle cut give the slightly better sensitivity for both parameters, these results are used for extracting the shape information.

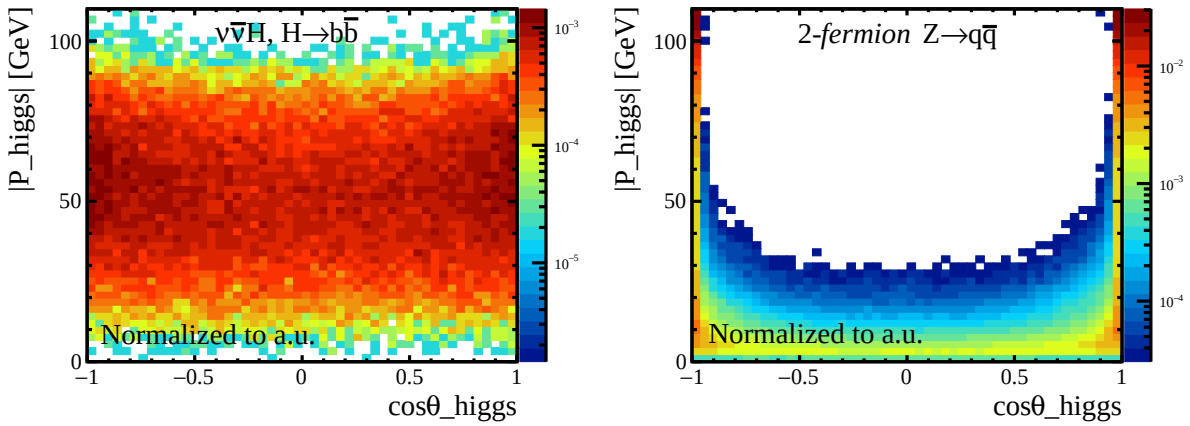

Figure 85: The scatter plots show $x(P_h, \cos\theta_h)$ for both of the t-channel $\nu\bar{\nu}h$ and the two-fermion SM background processes, where the index h denotes the di-jets system.

7.1.3 Impact of production cross-section

The branching fraction of the Higgs boson to b-quark would possible to vary because of the variation of the partial width of $h \to ZZ$ and $h \to WW$ and its Higgs total width due to the anomalous couplings. Therefore, only the variation coming from the $h \to WW$ production vertex is considered, whose explanation is given in Sec. 4.4.4. According to the distributions showing the relative difference of the production cross-section of the WW-fusion $\sigma_{\nu\nu h}$ illustrated in Fig. 45, each variation given by each parameter of the anomalous WWH couplings are slightly small compared to the variation of the production cross-section of the ZZ-fusion. Nevertheless, the variation of the cross-section depending on the parameter a_W is still strong and powerful to find out the anomalous structures whereas ones depending on the parameters b_W and $\tilde{b}_W$ might be relatively weak.

A left plot in Fig. 86 gives $\Delta\chi^2$ distribution as a function of each anomalous parameter using only the variation of the cross-section. The error of the production cross-section $\delta\sigma_{\nu\nu h}$ is given through error propagation to cancel out the variation of the branching fraction of the b-quark, which has already discussed in Sec. 4.4.4. A right plot in Fig. 86 also gives color map of $\Delta\chi^2$ in two-parameter space of a_W-b_W.

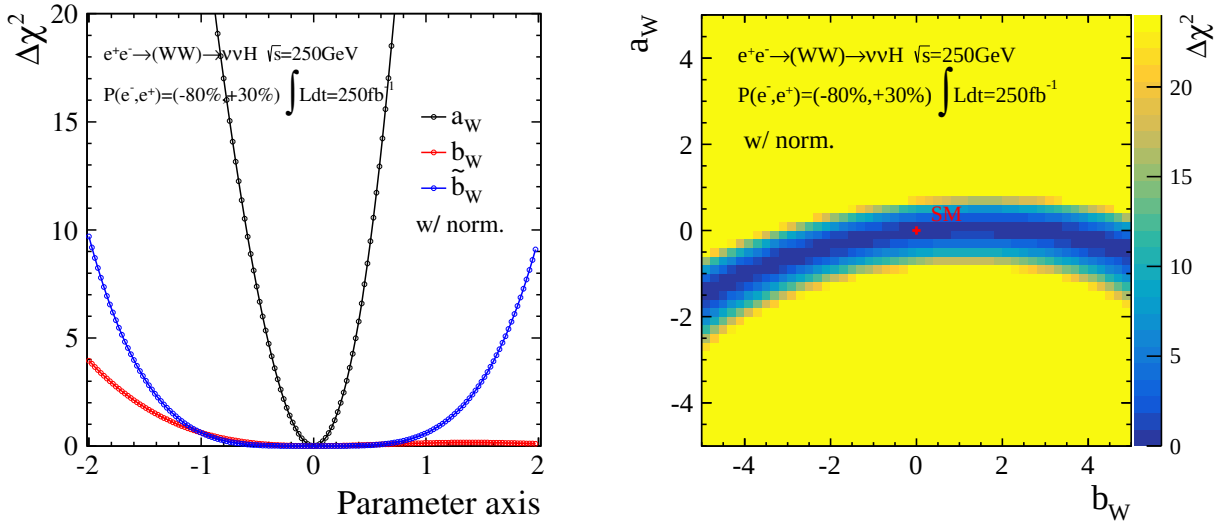

Figure 86: (Left) The distribution shows $\Delta\chi^2$ as a function of each parameter in the one parameter space, where the normalization information only is used for the evaluation. (Right) The distributions show $\Delta\chi^2$ in the two-dimensional parameter space of a_W-b_W.

7.1.4 Consideration on contribution of the anomalous ZZH couplings

As clearly shown in Fig. 82, the large number of s-channel $\nu\bar{\nu}h$ events is remaining. Since the s-channel $\nu\bar{\nu}h$ is the interaction through the ZZH vertex, the kinematical distributions and the normalization of the s-channel process can vary depending on the existence of the anomalous ZZH couplings. To consider the contributions of the variation of the anomalous ZZH couplings, the chi-squared formula is expanded to include such variation effects which is originating from the ZZH couplings as follows,

$$\begin{aligned}\chi^2_{total} &= \sum_j^n \left(\frac{S^{t\text{-}\nu\nu h}_{SM}(x_j) - S^{t\text{-}\nu\nu h}_{BSM}(x_j;\vec{a}_W) + S^{s\text{-}\nu\nu h}_{SM}(x_j) - S^{s\text{-}\nu\nu h}_{BSM}(x_j;\vec{a}_Z)}{\Delta n^{obs}_{SM}(x_j)} \right)^2 \\ &+ \left(\frac{N^{t\text{-}\nu\nu h}_{SM} - N^{t\text{-}\nu\nu h}_{BSM}(\vec{a}_W) + N^{s\text{-}\nu\nu h}_{SM} - N^{s\text{-}\nu\nu h}_{BSM}(\vec{a}_Z)}{\delta\sigma_{\nu\nu h}\cdot N^{t\text{-}\nu\nu h}_{SM}} \right)^2 \\ &+ \vec{a}_Z{}^{\mathrm{T}}\ (\boldsymbol{C}^{250\mathrm{GeV}}_{ZZH})^{-1}\ \vec{a}_Z \quad ,\end{aligned}$$

where the shape denoted with S is given by applying each f_{ji} and normalizing as,

$$S^{t/s\text{-}\nu\nu h}(x_j) = N^{t/s\text{-}\nu\nu h}_{SM} \sum_{i=1}^{n} \frac{1}{\sigma}\frac{d\sigma}{dx}(x_i;\vec{a}_V)\Big|_{t/s\text{-}\nu\nu h} \cdot f^{t/s\text{-}\nu\nu h}_{ji}$$

The column vectors $\vec{a}_V$ and the variance-covariance matrix $\boldsymbol{C}_{ZZH}$ are respectively given as,

$$\vec{a}_V = \begin{pmatrix} a_V \\ b_V \\ \tilde{b}_V \end{pmatrix}, \quad \boldsymbol{C}_{ZZH} = \begin{pmatrix} \sigma^2_{a_Z} & \rho_{a_Z b_Z}\sigma_{a_Z}\sigma_{b_Z} & \rho_{a_Z \tilde{b}_Z}\sigma_{a_Z}\sigma_{\tilde{b}_Z} \\ \rho_{a_Z b_Z}\sigma_{a_Z}\sigma_{b_Z} & \sigma^2_{b_Z} & \rho_{b_Z \tilde{b}_Z}\sigma_{b_Z}\sigma_{\tilde{b}_Z} \\ \rho_{a_Z \tilde{b}_Z}\sigma_{a_Z}\sigma_{\tilde{b}_Z} & \rho_{b_Z \tilde{b}_Z}\sigma_{b_Z}\sigma_{\tilde{b}_Z} & \sigma^2_{\tilde{b}_Z} \end{pmatrix}$$

The first and the second terms are including the variation of the production cross-section and the kinematical distributions derived from the t-channel $\nu\bar{\nu}h$ and s-channel $\nu\bar{\nu}h$ processes, which depend on the anomalous WWH and anomalous ZZH couplings represented with the indication of t-$\nu\bar{\nu}h$ and s-$\nu\bar{\nu}h$ in the formula. The variation and the correlations of the anomalous ZZH

parameters derived from the ZZH vertex in the s-channel $\nu\bar{\nu}h$ is constrained and are given with a variance-covariance matrix denoted by $\boldsymbol{C}_{ZZH}^{250\text{GeV}}$ which is evaluated through the anomalous ZZH studies described in the previous section, where the index of 250GeV means the results with 250 GeV.

7.1.5 Sensitivity in three parameter space

Once expanding the parameter space from the two to three, the third parameter start to adjust to recover the SM situations. Thus the cross-section information only is not sufficient to constrain the parameter space. A left plot in Fig. 87 show the color map of $\Delta\chi^2$ distribution in the a_W-b_W plane after performing the simultaneous fitting with three parameters using the cross-section information only. It is obvious that the huge ellipse apperas including the SM point where there exit no constraints for the anomalous WWH couplings. When adding the shape information to the cross-section, the sensitive bounds are given around the SM, which is shown in the right plot.

1. In this direction, a_W makes the cross-section decrease, and both of the permeates b_Z and $\tilde{b}_W$ have huge room to adjust the value and recover the SM condition by increasing and decreasing the cross-section.

2. a_W can make the cross-section increase, but b_W can not change it largely by moving the positive direction since the positive direction also makes the cross-section increase. Furthermore, any $\tilde{b}_W$ can not adjust it since any $\tilde{b}_Z$ make the cross-section increase. Thus, the bound is quickly restricted in this direction.

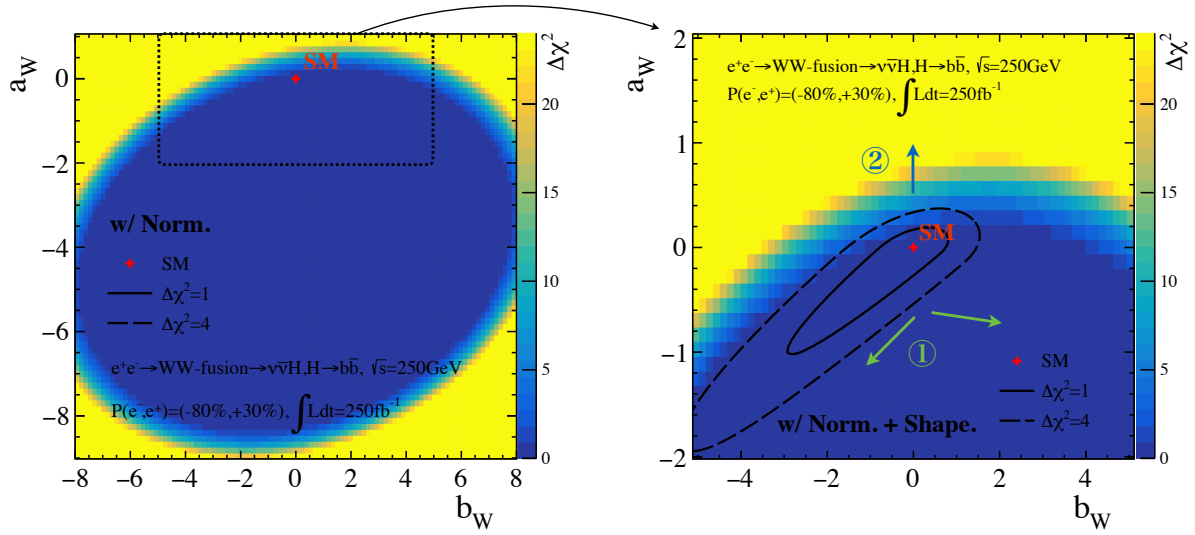

Figure 87: (Left) The plot shows the color map of the $\Delta\chi^2$ distribution in the three parameter space, where only the cross-section information is used to calculate $\Delta\chi^2$. The physical parameter limits are set to be < 10. (Right) when adding the shape information into the cross-section information, the sensitive bounds are strongly constrained. The 1σ and 2σ contours can be seen.

Fig. 88 give the sensitivity to the anomalous WWH couplings after performing simultaneous fitting in the three parameter space of a_W, b_W, and $\tilde{b}_W$, where the benchmark luminosity of 250 fb^{-1} is assumed. Compared to the results which do not include the contributions of the anomalous ZZH couplings, the results with the ZZH contributions get slightly worse, which is a few percent level for b_W. The parameters between a_Z and b_Z of the anomalous ZZH couplings have the strong negative correlation. Because of this reason the sensitivity of $\vec{a}_W$ does not affect strongly by ZZH couplings. Nevertheless, because there is a small room that the parameters $\vec{a}_Z$ can take values along positive diagonal, the variation of $\vec{a}_Z$ can make $\vec{a}_W$ get slightly worse.

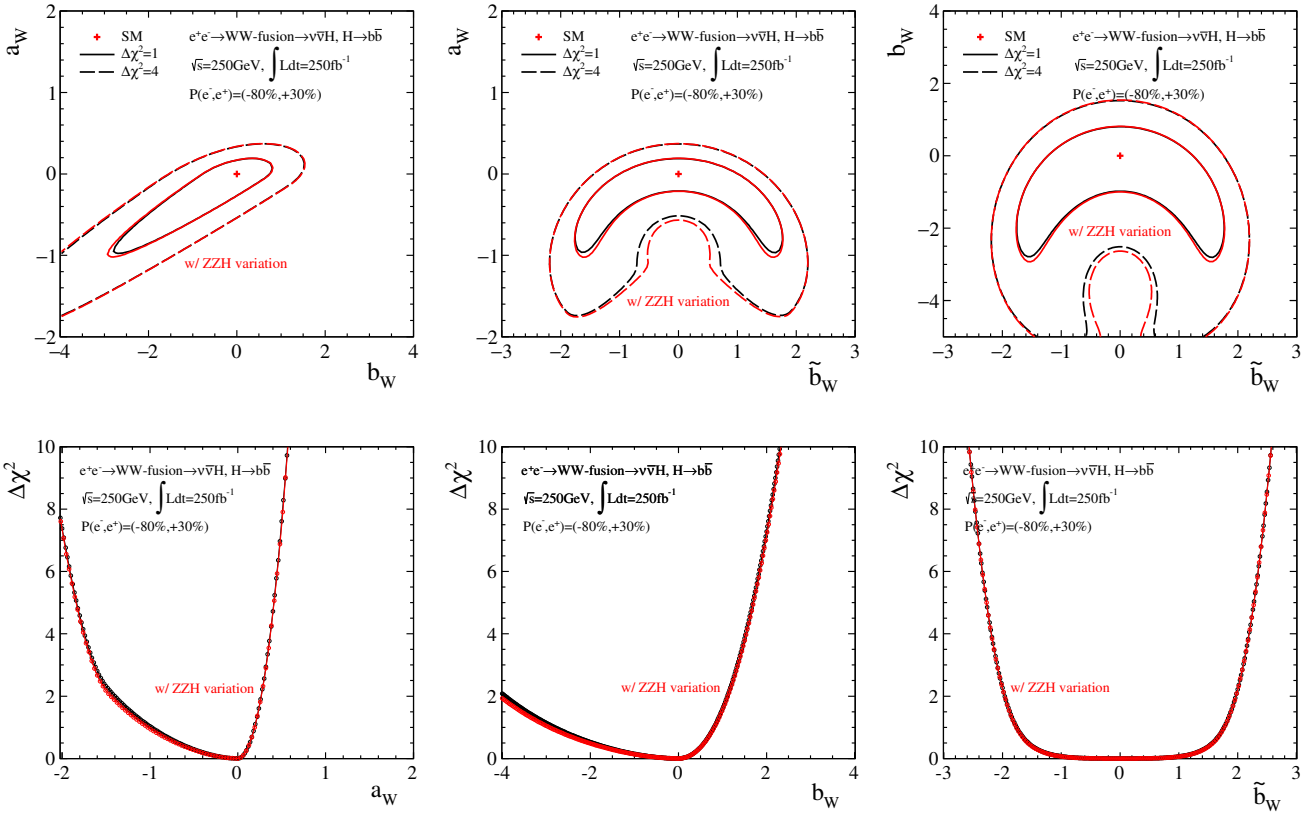

$$\sqrt{s} = 250 \text{ GeV with } \int \text{Ldt} = 250 \text{ fb}^{-1} \text{ and } \text{P}(e^-, e^+) = (-80\%, +30\%)$$

$$\begin{cases} a_W = [-0.983, \quad 0.191] \\ b_W = [-2.808, \quad 0.805] \\ \tilde{b}_W = [-1.759, \quad 1.768] \end{cases}, \quad \rho = \begin{pmatrix} 1 & 0.6365 & -0.6687 \\ - & 1 & -0.4940 \\ - & - & 1 \end{pmatrix}$$

$$\sqrt{s} = 250 \text{ GeV with } \int \text{Ldt} = 250 \text{ fb}^{-1} \text{ and } \text{P}(e^-, e^+) = (-80\%, +30\%)$$

w/ ZZH contributions

$$\begin{cases} a_W = [-1.025, \quad 0.192] \\ b_W = [-2.929, \quad 0.815] \\ \tilde{b}_W = [-1.766, \quad 1.774] \\ a_Z = [-0.363, \quad 0.376] \\ b_Z = [-0.134, \quad 0.130] \\ \tilde{b}_Z = [-0.065, \quad 0.065] \end{cases}, \quad \rho = \begin{pmatrix} 1 & .6355 & -.6652 & -.0568 & -.0552 & -.0430 \\ - & 1 & -.4873 & -.1397 & .1398 & .0039 \\ - & - & 1 & -.0129 & .0130 & .0009 \\ - & - & - & 1 & -.9997 & -.0154 \\ - & - & - & - & 1 & .0293 \\ - & - & - & - & - & 1 \end{pmatrix}$$

Figure 88: Upper plots show contours projected onto the two-dimensional parameter spaces a_W-b_W, a_W-$\tilde{b}_W$, and b_W-$\tilde{b}_W$ with the simultaneous minimization, which correspond to the 1σ and 2σ sensitivity to the anomalous WWH couplings at $\sqrt{s}$ =250 GeV with L_{int} =250 fb^{-1} and beam polarization of $\text{P}(e^-, e^+)$= (-80%,+30%) . Middle plots are $\Delta\chi^2$ distributions as a function of each parameter space of the anomalous couplings a_W, b_W, and $\tilde{b}_W$. Both of the information: the shape of the three-dimensional distribution of $x(\cos\theta_h, P_h, \cos\phi_h)$ binned $5\times5\times5$ and the production cross-section are combined. Lower values give the 1σ bounds for each anomalous parameter a_W, b_W, and $\tilde{b}_W$and correlation matrix indicating correlation coefficients between the parameters.

7.2 $e^+e^- \to Zh \to q\bar{q}h,\ h \to WW^* \to q\bar{q}l\bar{\nu}$ at $\sqrt{s} = 250$ GeV

Through the LEP and LEP2 experiment the W boson was well studied and fractions of a pair of the W bosons to a fully hadronic state, a semi-leptonic state, and a fully leptonic state have been well measured, which are respectively 45.7 %, 43.8%, and 10.5% [70].

In the first analysis of the Higgs decay $h \to WW^*$ of the Higgs-strahlung process, the hadronic decay channel of the Z boson $Z \to q\bar{q}$ is selected, which gives larger cross-section. Nevertheless, the fully leptonic channel of the W bosons of the Higgs decay process has less statistics, furthermore, there are two neutrinos in the final state generating from the decay of the W bosons, which are undetectable. Thus, most of the information of the shape which can give connection to the anomalous WWH coupling will be missing. In contrast, the fully hadronic of Z and the semi-leptonic channel of the W pair will have sufficient statistics for extracting the shape information of the kinematics of reactions.

The semi-leptonic channel would be much clear information than the fully hadronic channel since the final state has one isolated lepton and a missing neutrino which can be recovered based on the momentum conservation between the initial and the final state. Additionally, since a charge of the lepton can be identified, the distribution of $\Delta\Phi$ is possible to reconstruct with the range of [0–π] and it is expected that it can give better sensitivity to the parameter $\tilde{b}_W$.

7.2.1 Reconstruction and background suppression

To extract the isolated lepton in the final state, the MVA based isolated lepton finding is firstly applied to a event, where only an electron and a muon which should have momentum of more than 5 GeV are considered while a tau is ignored completely. After applying the lepton finding and extracting the isolated leptons, the rest of remaining particles are forcibly clustered into four jets with the Durham jet algorithm. The four jets are tried to pair each other based on the chi-squared mass constraint[15]. A neutrino in the final state decaying from one W boson is also reconstructed by imposing the constraint of the momentum conservation and assuming it is a massless particle[16]. The on-shell W boson is also identified by comparing the invariant mass of the W boson, which is $m_W = 80.385$ GeV [70], after the missing neutrino was reconstructed.

Background supression :

The observables used for the background suppression are listed below, and Table 6 gives the number of remaining signal and background events after the background suppression using each cut, where the integrated luminosity of 250 fb^{-1} with the both beam polarization states are assumed. The several distributions of the observables used for reduction of the backgrounds are illustrated in Fig. 89.

- Require that an isolated electron or muon having momentum of more then 5 GeV exists in a event. (Notice that the reconstruction of a tau is not taken into account here.)

[15]The mass constraint among four jets in the final state, which are derived from the Z and the Higgs boson, is given with the equation,

$$\chi^2 = \left(\frac{M_{ij} - M_Z}{\sigma_Z}\right)^2$$

where i and j denote the each jet and the mass resolution σ_Z is set to be 5.2 GeV.

[16]In the final state it is assumed to exist the Z boson, and the W boson and the isolated lepton which are coming from the Higgs boson. Thus, the equations imposing the conservation is

$$\begin{aligned} (\sqrt{s}\sin(0.007),\ 0,\ 0) &= \vec{P}_Z + \vec{P}_W + \vec{P}_l + \vec{P}_\nu \quad \text{(momentum conservation)} \\ E_\nu^2 &= |\vec{P}_\nu|^2 \quad \text{(for massless particle)} \end{aligned}$$

where 0.007 with a unit of rad gives correction of a crossing angle of the initial state. Since a ISR photon emitted along the beam pipe sometimes exist, which has four-momentum of ($|\vec{P}_\gamma|$, $\vec{P}_\gamma$). Although this might have to be considered, it is not given here.

- $N_{\mathrm{PFOs}} \in [45,\ 150]$ and $E_{vis} \in [140,\ 250]$
  The number of Particle Flow Objects and the observed energy in the reaction are useful to suppress hadronic decay processes which have relatively the number of larger particles.
- $M_Z \in [85.5,\ 102.0]$ GeV, $E_Z\ \in [89.33,\ 118.67]$ GeV,
  $M_W \in [46.67,\ 90.0]$ GeV, and $E_W \in [49.0,\ 102.25]$ GeV
  The final state of the signal process has the Z boson and one on-shell W boson decaying from the Higgs boson. Therefore, clear peaks at the M_Z and M_W can be seen.

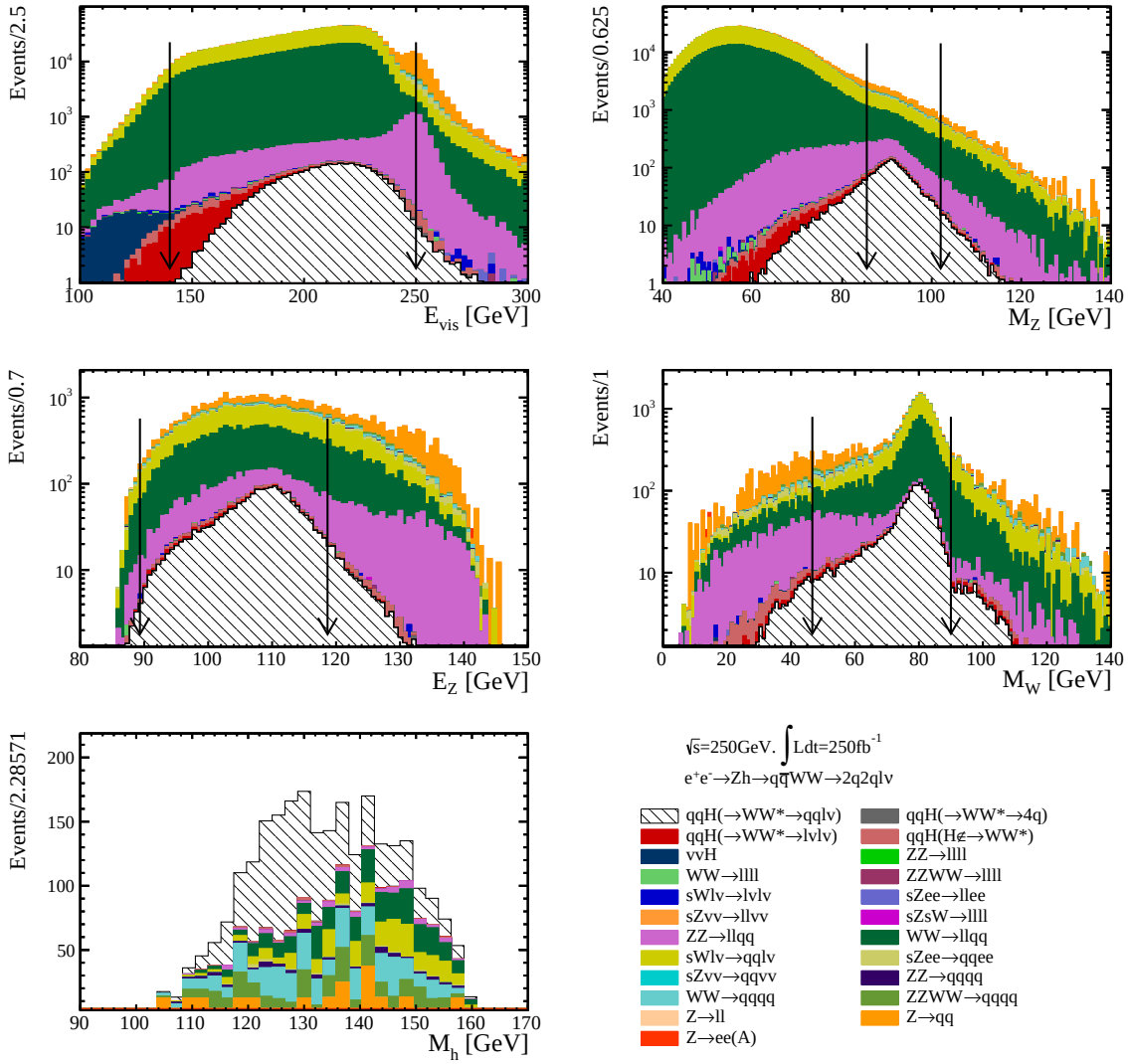

Figure 89: The distributions show each observable used for the background suppression assuming 250 fb^{-1} with P(e^-, e^+)= (-80%,+30%). The explanation of the observables are given in the text. Black arrows on each plot indicate the cut values applied to each observable as the background suppression. The signal process is $Zh \to q\bar{q}h,\ h \to WW^* \to q\bar{q}l\bar{\nu}$.

- $-\log y_{23} \in [0.92, 4.04]$, $-\log y_{34} \in [1.50, 5.18]$,
  min thrust$\in$ [0.12 0.55], and min $N_{\mathrm{PFOs}} \in [7,\ 27]$
  There are still the large number of 4-fermion hadronic processes that include one W and Z boson and 2-fermion $Z \to q\bar{q}$ SM backgrounds would remain, which generate the different number of jets in the final state. Thus, the parameter of the jet clustering which shows the jet transition and the minimum number of PFOs among jets are useful to suppress them.
- $M_h\ \in [100,\ 160]$ GeV

Table 6: The expected number of remaining signal and background events after the suppression using each cut for the $Zh \to q\bar{q}h,\ h \to WW^* \to q\bar{q}l\bar{\nu}$ channel at $\sqrt{s}$=250 GeV, with both beam polarization states: P(e^-, e^+)= (-80%,+30%) and (+80%,-30%). The integrated luminosity of 250 fb^{-1} is assumed. The signal efficiency ϵ and significance S_{sig} are also given in the table.

Cut variables $\sqrt{s}$=250 GeV P(e^-, e^+)= (-80%,+30%)

	$Zh \to q\bar{q}WW^* \to q\bar{q}+$			SM backgrounds			
process	$q\bar{q}l\nu$	ϵ	other	$h \notin WW^*$	$2f$	$4f$	S_{sig}
cross-section (fb)	19.87	-	25.52	164.79	-	-	-
Expected	4969	100	6382	41196	$2.91 \cdot 10^7$	$1.02 \cdot 10^7$	-
ID an iso-lepton (e/μ)	2933	59.02	572	644	$1.36 \cdot 10^6$	$3.14 \cdot 10^6$	1.38
$N_{\mathrm{PFOs}} \in [45,\ 150]$	2882	57.99	572	422	$8.79 \cdot 10^4$	$1.17 \cdot 10^6$	2.56
$E_{vis} \in [140,\ 250]$	2834	57.03	290	380	$5.57 \cdot 10^4$	$1.12 \cdot 10^6$	2.61
$M_Z \in [85.5,\ 102.0]$	1983	39.90	64	159	9967	$3.30e \cdot 10^4$	9.20
$E_Z \in [89.33,\ 118.67]$	1832	36.86	58	134	5284	$2.46e \cdot 10^4$	10.14
$M_W \in [46.67,\ 90.0]$	1642	33.04	36	63	2193	$1.93e \cdot 10^4$	10.66
$E_W \in [49.0,\ 102.25]$	1473	29.64	33	57	1975	$1.21e \cdot 10^4$	11.62
$-\log y_{23} \in [0.92, 4.04]$	1370	27.57	25	52	1510	9360	12.14
$-\log y_{34} \in [1.50, 5.18]$	1119	22.51	9	33	678.2	4126	14.08
min thrust$\in$ [0.12 0.55]	1082	21.77	8	21	526.8	3724	14.31
min $N_{\mathrm{PFOs}} \in [7,\ 27]$	966	19.44	3	21	177.8	1087	19.06
$M_h \in [100,\ 160]$	966	19.44	3	21	177.8	1087	19.06

Cut variables $\sqrt{s}$=250 GeV P(e^-, e^+)= (+80%,-30%)

	$Zh \to q\bar{q}WW^* \to q\bar{q}+$			SM backgrounds			
process	$q\bar{q}l\nu$	ϵ	other	$h \notin WW^*$	$2f$	$4f$	S_{sig}
cross-section (fb)	13.42	-	17.24	111.29	-	-	-
Expected	3356	100	4310	27823	$1.23 \cdot 10^7$	$1.27 \cdot 10^6$	-
ID an iso-lepton (e/μ)	1981	59.03	387	435	$1.23 \cdot 10^6$	$3.12 \cdot 10^6$	1.59
$N_{\mathrm{PFOs}} \in [45,\ 150]$	1946	57.99	223	285	$5.23 \cdot 10^4$	$9.79 \cdot 10^4$	4.98
$E_{vis} \in [140,\ 250]$	1914	57.03	195	256	$3.30 \cdot 10^4$	$9.04 \cdot 10^4$	5.39
$M_Z \in [85.0,\ 104.0]$	1403	41.81	47	115	6542	5565	11.96
$E_Z \in [89.33,\ 118.0]$	1272	37.90	17	95	3286	3579	13.92
$M_W \in [63.33,\ 89.17]$	993	29.59	15	20	519.1	1650	17.47
$E_W \in [67.0,\ 106.75]$	949	28.28	12	18	456.7	1269	18.16
$-\log y_{23} \in [0.62, 4.28]$	894	26.64	12	17	355.5	993.3	18.66
$-\log y_{34} \in [1.50, 5.76]$	811	24.17	6	13	206.6	578.2	20.04
min thrust$\in$ [0.10, 0.55]	796	23.72	6	13	179.4	534.2	20.21
min $N_{\mathrm{PFOs}} \in [4,\ 29]$	782	23.30	4	11	105.3	267.2	22.66
$M_h \in [100,\ 160]$	782	23.30	4	11	105.3	267.2	22.66

The invariant mass of the Higgs boson reconstructed two W bosons. This is a mass window to determine the statistical error.

7.2.2 Impact of kinematical distribution

To demonstrate the acceptance and the migration of observables which are sensitive to the WWH, P_W and $\Delta\Phi$ are shown in Fig. 90 and Fig. 91, which are the momentum distribution of the W boson in the Higgs rest-frame and the the difference of the angle between both decay planes calculated in the Higgs rest-frame. Thanks to the unique signature of the reaction of $h \to WW^* \to q\bar{q}l\nu$, as expected, it can be seen that the migration effects for each sensitive observable for testing the WWH couplings are relatively small.

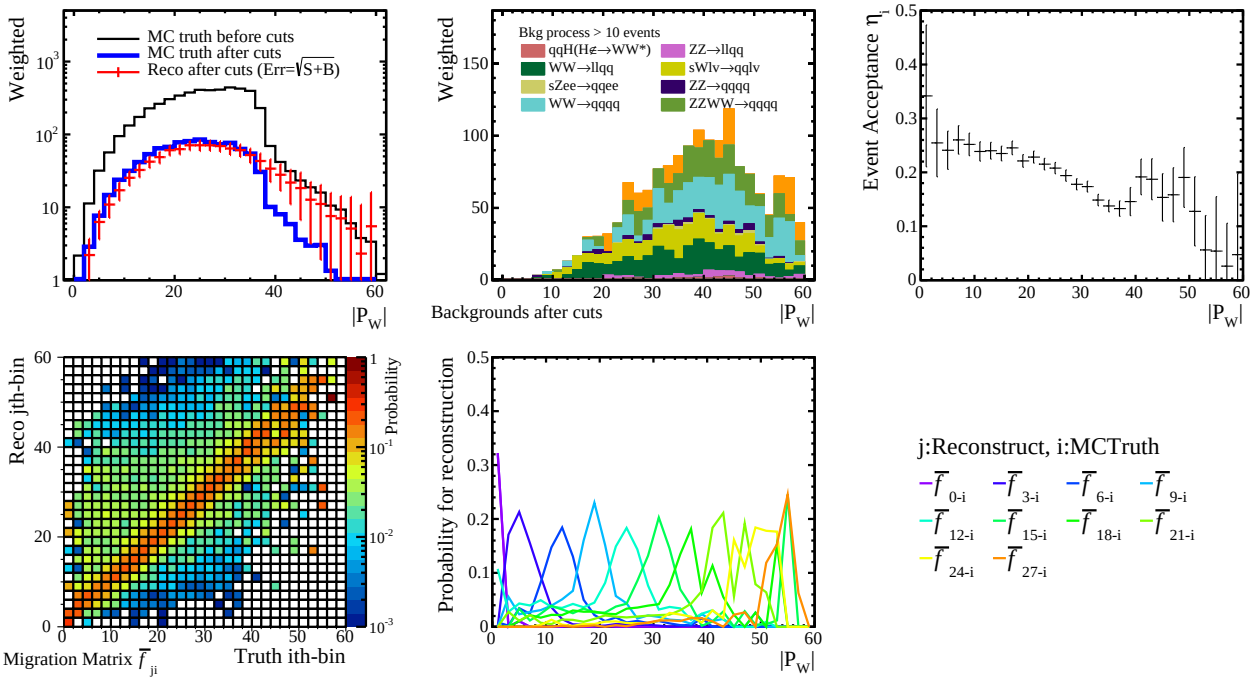

Figure 90: The distributions show the summary of the momentum distribution of the W boson (P_W) calculated in the Higgs rest-frame after the background suppression. (Top left and middle): the remaining signal and the background distributions which are given with the MC truth and the reconstructed, where the statistical error is given as the standard deviation of the Poisson probability. (Top right): the event acceptance function η_i. (Bottom left and middle): the distribution shows the probability matrix of the migration ($\bar{f}_{ji}$) that is applied for the reconstruction of the realistic distribution of P_W, and the cross-sections of $\bar{f}_{ji}$ as 1-dim plots.

Event acceptance and off-shell W bosons :

The event acceptance for the $\Delta\Phi$ distribution is maintaining flatness well over the given region. In contrast, the event acceptance on the P_W distribution drops around 35 GeV, which corresponds to the transition of the P_W distribution. In the higher region >50 GeV the acceptance gets worse. However, both of the W bosons which are came from the Higgs boson and have the momentum of >50 GeV in the Higgs rest-frame are off-shell W boson as shown in Fig. 92. Because it can not be identified whether certain event is given by the Higgs reaction or not if both of the W bosons are off-shell, these events should be removed from the evaluation of the anomalous couplings. Therefore, the degradation of the event acceptance at higher region does not care. (Although the acceptance is slightly given in the plot, the contribution summed to be negligible because of the less remaining events.)

To extract the sensitivity of the kinematical shape information to the anomalous WWH couplings, the chi-squared test was performed using the one-dimensional distributions of the momen-

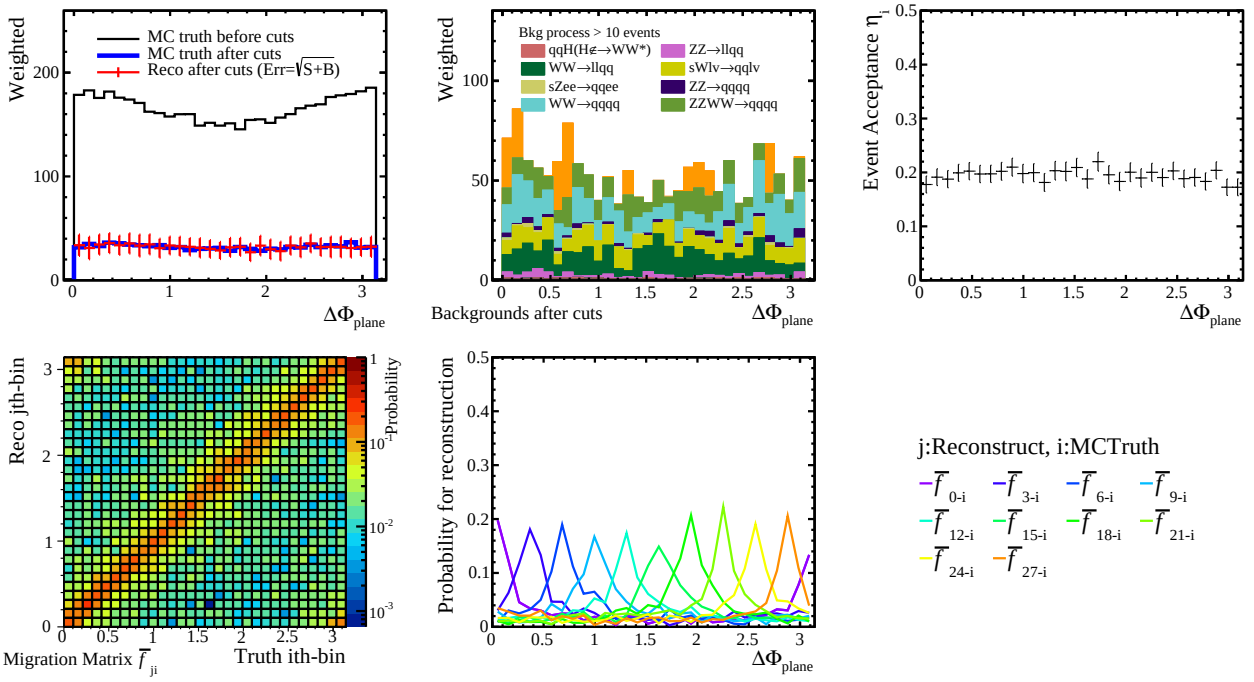

Figure 91: The distributions show the summary of the angle between decay planes in the Higgs rest-frame ($\Delta\Phi$) after the background suppression. (Top left and middle): the remaining signal and the background distribution, which are given with the MC truth and the reconstructed. (Top right): the event acceptance function η_i. (Bottom left and middle): the probability matrix of the migration ($\bar{f}_{ji}$) that is applied for the reconstruction of $\Delta\Phi$, and the cross-sections of $\bar{f}_{ji}$ as 1-dim plots.

tum of the W boson $x(P_W)$ binned in 20, the angle between decay planes $x(\Delta\Phi)$ binned in 20, and the three-dimensional distribution of $x(\cos\theta^*_{Wl}, P_W, \Delta\Phi)$ by adding the helicity angle of the daughter lepton originating from the W boson, which is binned in 5×5×5 . Fig. 93 give the results for both beam polarization states under the assumption of the integrated luminosity of 250 fb^{-1}. It can be seen that:

- The main sensitivity to the b_W parameter is given by the W momentum distribution, which can be clearly seen in the results which are evaluated by using the three-dimensional distribution and the one-dimensional distribution of $x(P_W)$.
- In contrast, the impact of $\Delta\Phi$ to both b_W and $\tilde{b}_W$ is very small compared to the results with $x(P_W)$. However, when focusing on the results evaluated by the three-dimensional distribution, there is a little sensitivity to $\tilde{b}_W$, which is derived from $\Delta\Phi$ and its combination with P_W. The variation of P_W depending on $\tilde{b}_W$ is quite small, but one of $\Delta\Phi$ is large, which can be seen in the plots of Sec. 4.2.2 illustrating the variations of the kinematical shape.

7.2.3 Sensitivity in three parameter space

Because the available information is the kinematical distribution and the information of the cross-section is missing, the large are of the parameter space will not be constrained. Therefore, we skip the fitting in three parameter space here.

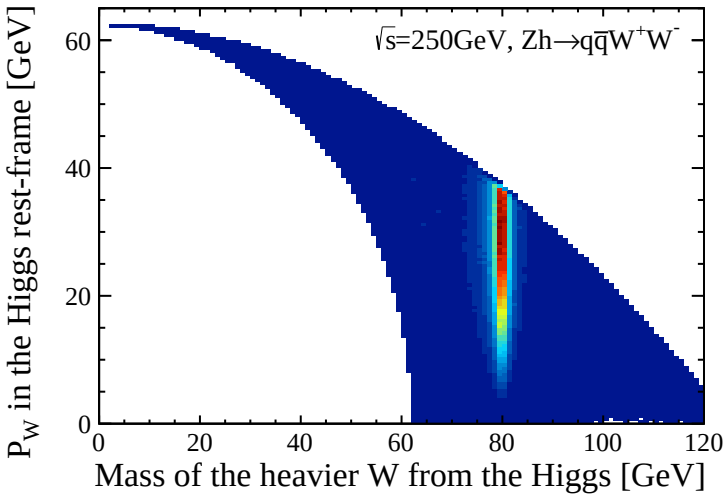

Figure 92: The distribution, given with the log scale, shows the momentum of the W boson in the Higgs rest-frame versus the mass of the heavier W boson in two W bosons which come from the Higgs boson. The W boson which has the momentum of > 50 GeV in the Higgs frame is a off-shell particle.

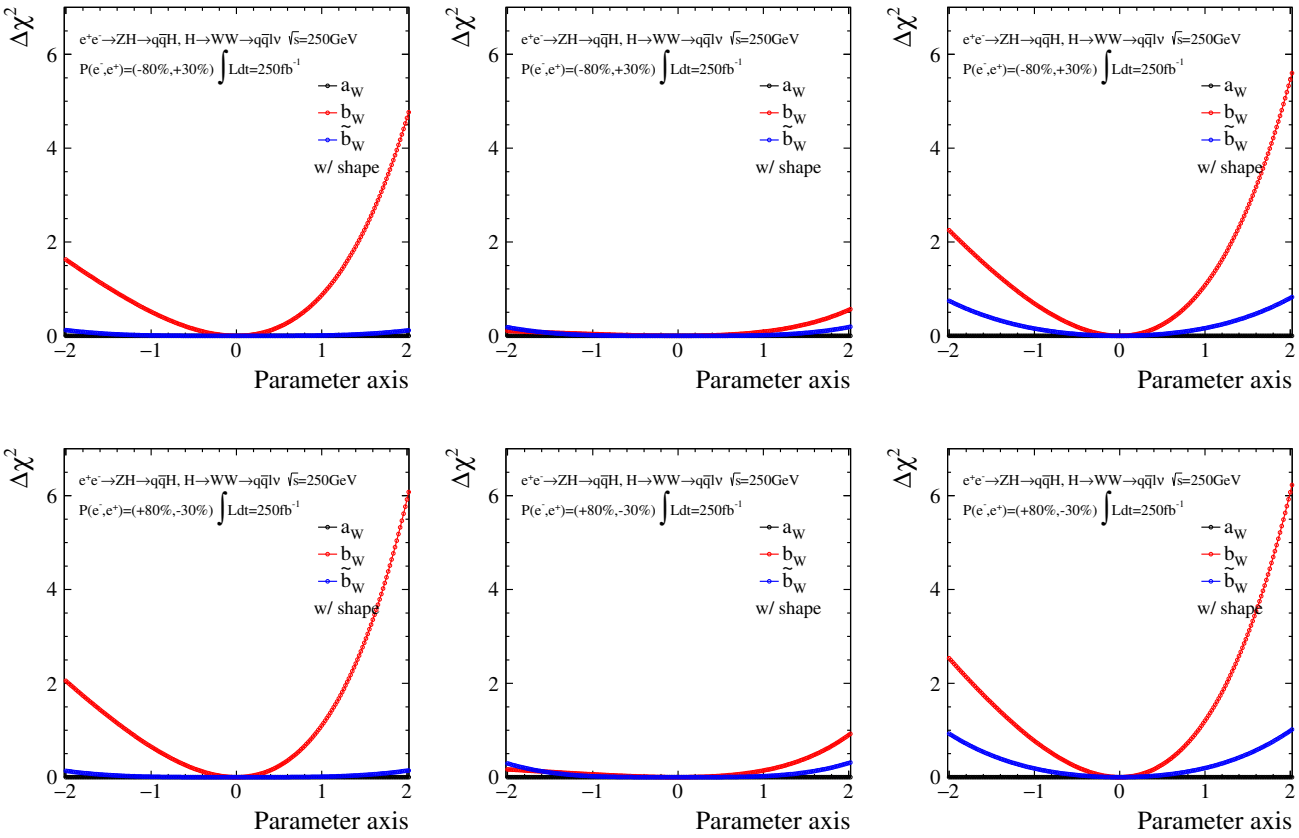

Figure 93: The distributions show $\Delta\chi^2$ as a function of each parameter a_W, b_W, and $\tilde{b}_W$, where both of the beam polarizations: P(e^-, e^+)= (-80%,+30%) and (+80%,-30%), and the integrated luminosity of 250 fb^{-1} are assumed. The one-dimensional distributions of $x(P_W)$ (left) and $x(\Delta\Phi)$ (middle) binned in 20, and the three-dimensional distribution of $x(\cos\theta^*_{Wl}, P_W, \Delta\Phi)$ binned $5\times 5\times 5$ (right) are used respectively.

7.3 Combined results on the sensitivity to the anomalous WWH couplings

In this subsection combined results showing the sensitivity to the anomalous WWH couplings are given for $\sqrt{s}$ =250 and 500 GeV using each information evaluated up to here. Results with the assumption of the ILC full operation based on the scenario of H20 are also given.

7.3.1 Results in parameter space of (a_W, b_W, $\tilde{b}_W$)

The results of the sensitivities of each anomalous parameter at $\sqrt{s}$ = 250 GeV are given for left-handed beam condition of P(e^-, e^+)= (-80%,+30%) as examples. The results with the right-handed beam condition can not give good constraints on the parameters because the available information is the shape information of the Higgs-strahlung process only. Therefore, the right-handed results are omitted for $\sqrt{s}$ = 250 GeV.

With the benchmarking luminosity at $\sqrt{s}$ = 250 GeV :

For benchmarking of the performance of the sensitivity to WWH couplings under the condition of $\sqrt{s}$ = 250 GeV and the integrated luminosity of $\int Ldt$ = 250 fb^{-1}, the information used for the evaluation are as follows,

- The variation of the production cross-section of the t-channel WW-fusion process $\sigma_{\nu\bar{\nu}h}$ is included, where the relative error of the production cross-section is used. The error is $\delta\sigma_{\nu\bar{\nu}h}$ = 8.20% through the error propagation of $\delta(\sigma_{\nu\bar{\nu}h}BR_{h\bar{b}\bar{b}})$ = 8.1% and $\delta(BR_{h\bar{b}\bar{b}})$ = 2.9%. The $\sigma \times BR$ would change depending on the Higgs width which will be affected by the anomalous couplings of ZZH and WWH if they exist. To retain model independent estimation, we avoid such situation and remove the unclear variation of the Higgs widths.

- The variation of the kinematical shape distribution of the t-channel WW-fusion process is included, where the channel $h \to b\bar{b}$ is selected and the three-dimensional distribution of $x(\cos\theta_h, P_h, \cos\phi_h)$ binned in 5×5×5 is used.

- In the above consideration, the variation of the production cross-section and the kinematical shape distribution of the t-channel WW-fusion process are possible to be affected by the variation derived from the anomalous ZZH couplings in the s-channel $\nu\bar{\nu}h$ of the Higgs-strahlung process. Thus, these contributions have to be taken into account, which is realized to include the variance-covariance matrix that must be evaluated using the 250 GeV process with left-handed polarization, which is given in third line under Fig. 74.

- The variation of the kinematical shape distribution of the Higgs decay $h \to WW^* \to q\bar{q}l\nu$ of the Higgs-strahlung process is included in the evaluation. The three-dimensional distribution of $x(\cos\theta^*_{Wl}, P_W, \Delta\phi[0\text{-}\pi])$ binned in 5×5×5 is used.

- The variation of the kinematical shape distribution of the Higgs decay $h \to WW^* \to q\bar{q}q\bar{q}$ of the Higgs-strahlung process is also included in the evaluation. The final states of the channel are categorized by appling the flavor tagging into $q\bar{q}q\bar{q}$ and $c\bar{x}x\bar{c}$ to extract the sensitivity to $\tilde{b}_W$. The three-dimensional distribution of $x(\cos\theta^*_{Wl}, P_W, \Delta\phi[0\text{-}\frac{1}{2}\pi])$ binned in 5×5×5 is used for the channel of $q\bar{q}q\bar{q}$ and the one-dimensional distribution of $x(\Delta\phi[0\text{-}\pi])$ binned in 5 is used for the channel of $c\bar{x}x\bar{c}$.

Fig. 94 give the sensitivity to each anomalous parameter. The sensitivity to each parameter using the t-channel WW-fusion process only can not be strongly given due to less information because of the missing neutrinos, insufficient cross-section measurement compared to the Zh process, and the correlation between the parameters a_W-b_W. However, the inclusion of the Higgs decay process $h \to WW^*$ to extract the shape information can significantly improve the sensitivity, especially for the disentangling of the correlation, where the dominant process contributing the improvement is the $WW^* \to q\bar{q}l\nu$ semi-leptonic decay process. Unfortunately, because the fully reconstruction of the observable $\Delta\Phi$ which is very sensitive to $\tilde{b}_W$ can not be performed with any

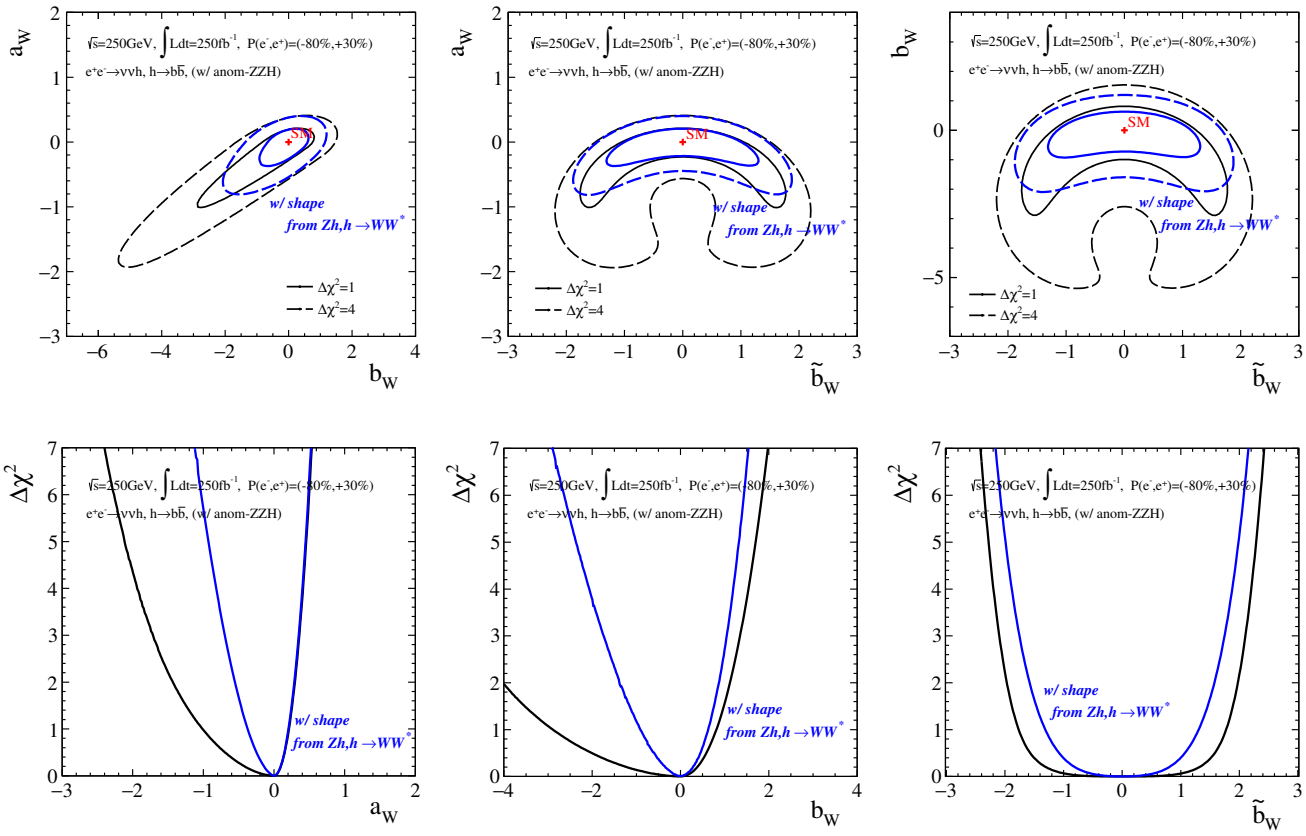

$\sqrt{s} = 250$ GeV with $\int \mathrm{Ldt} = 250$ fb^{-1} and $\mathrm{P}(e^-, e^+) = (-80\%, +30\%)$

the shapes from the Higgs-strahlung and the ZZH variation are included.

$$\begin{cases} a_W = [-0.373, \quad 0.206] \\ b_W = [-0.929, \quad 0.630] \\ \tilde{b}_W = [-1.312, \quad 1.305] \\ a_Z \ = \pm 0.298 \\ b_Z \ = \pm 0.107 \\ \tilde{b}_Z \ = \pm 0.065 \end{cases}, \quad \rho = \begin{pmatrix} 1 & .3399 & .0076 & -.0577 & -.0011 & -.0028 \\ - & 1 & .0156 & -.1070 & .1079 & -.0048 \\ - & - & 1 & -.0153 & .0154 & -.0006 \\ - & - & - & 1 & -.9912 & .0429 \\ - & - & - & - & 1 & -.0424 \\ - & - & - & - & - & 1 \end{pmatrix}$$

Figure 94: (Upper) The plots show contours projected onto the two-dimensional parameter spaces a_W-b_W, a_W-$\tilde{b}_W$, and b_W-$\tilde{b}_W$ after the simultaneous fitting in the three-parameter spaces. Each contour correspond to the 1σ and 2σ sensitivity to the anomalous WWH parameters. (Middle) The plots are $\Delta\chi^2$ distributions as a function of each parameter of the anomalous couplings of a_W, b_W, and $\tilde{b}_W$. The informations used for the evaluation are listed in the main text. (Lower) The values give the 1σ bounds for each anomalous parameter of a_W, b_W, and $\tilde{b}_W$. The values which make the variation of the ZZH are also given as the results of the simultaneous fitting, which includes the correlations between each parameter.

Higgs reactions for the WWH couplings, the sensitive to $\tilde{b}_W$ is relatively worse compared to the ZZH studies.

With the benchmarking luminosity at $\sqrt{s} = 500$ GeV :

The achievable sensitivity to anomalous WWH couplings at $\sqrt{s} = 500$ GeV is also evaluated. The main difference is that the Higgs-strahlung process is not considered to extract the shape information since the production cross-section is very small compared to the WW-fusion process at 500 GeV. The impact on the sensitivity is completely dominated by the WW-fusion process at 500 GeV, and there will be no expectation that the small Higgs-strahlung contribution can improve the sensitivity over the impact coming from the WW-fusion process. However, the Higgs-strahlung process is considered as the background which would vary depending on the existence of the anomalous ZZH couplings. Since the WW-fusion process has large production cross-section at 500 GeV, the Higgs decay $h \to WW^*$ gives sufficient the number of events to extract the shape information, where two WWH vertices are contributing the reaction. Therefore, the Higgs decay $h \to WW^*$ in the t-channel WW-fusion process is considered in the simultaneous fitting.

- The variation of the production cross-section of the t-channel WW-fusion process $\sigma_{\nu\bar{\nu}h}$ is included, where the relative error of the production cross-section only is considered which is $\delta\sigma_{\nu\bar{\nu}h} = 1.59\%$ through the error propagation of $\delta(\sigma_{\nu\bar{\nu}h}BR_{hb\bar{b}}) = 1.0\%$ and $\delta(BR_{hb\bar{b}})$. This is because the variation of the branching fraction would change depending on the existence of the anomalous couplings of ZZH and WWH which affect the Higgs width and it should avoid the unpredictable variation.

- The variation of the kinematical shape distribution of the t-channel WW-fusion process is included, where the channel $h \to b\bar{b}$ is selected and the three-dimensional distribution of $x(\cos\theta_h, P_h, \cos\phi_h)$ binned in $5\times5\times5$ is used.

- In the above consideration, the variation of the production cross-section and the kinematical shape distribution of the t-channel WW-fusion process are possible to be affected by the variation derived from the anomalous ZZH couplings in the s-channel $\nu\bar{\nu}h$ of the Higgs-strahlung process. Thus, these contributions have to be taken into account, which is realized to include the variance-covariance matrix that must be evaluated using the 500 GeV process with left-handed polarization, which is given in third line under Fig. 76.

- The variation of the kinematical shape information of the Higgs decay $h \to WW^* \to q\bar{q}q\bar{q}$ in the t-channel WW-fusion process is also included in the evaluation. The final states of the channel are not categorized as it is done at 250 GeV because the variation of the momentum distribution is stronger as illustrated in Fig. 42. The three-dimensional distribution of $x(\cos\theta^*_{Wl}, P_W, \Delta\phi[0\text{-}\frac{1}{2}\pi])$ binned in $5\times5\times5$ is used for this channel. The observable P_W is measured in the laboratory frame.

Fig. 95 give a summery of the sensitivity to each anomalous parameter at 500 GeV with the benchmark luminosity. It was already mentioned in the Sec. B.3 that the variation coming from the anomalous ZZH couplings through the Higgs-strahlung process does not affect the sensitivity to the anomalous WWH couplings because the anomalous ZZH couplings are clearly identified at 500 GeV. Additionally it can be also seen that the Higgs decay $h \to WW^*$ can not improve the sensitivity at 500 GeV. Since the variation of the information, the cross-section and the shape, is really strong at 500 GeV and the statistics of the event of the WW-fusion process with the $h \to b\bar{b}$ channel is sufficiently provided to give the strong constraints to the anomalous parameters. Although two HWW vertices contribute to the chain reaction of $W^-W^+ \to h, h \to W^-W^+$ and make the kinematical distribution change, the statistics of this channel is insufficient to improve the sensitivities over the impact given by the $h \to b\bar{b}$ channel only.

7.3.2 Results in parameter space of (η_W, ζ_{WW}, $\tilde{\zeta}_{WW}$)

To evaluate the sensitivities to the general parametrization of η and ζ as given in Eq. (11), both of the beam polarization states are combined, where each parameter a_W, b_W, and $\tilde{b}_W$ are replaced

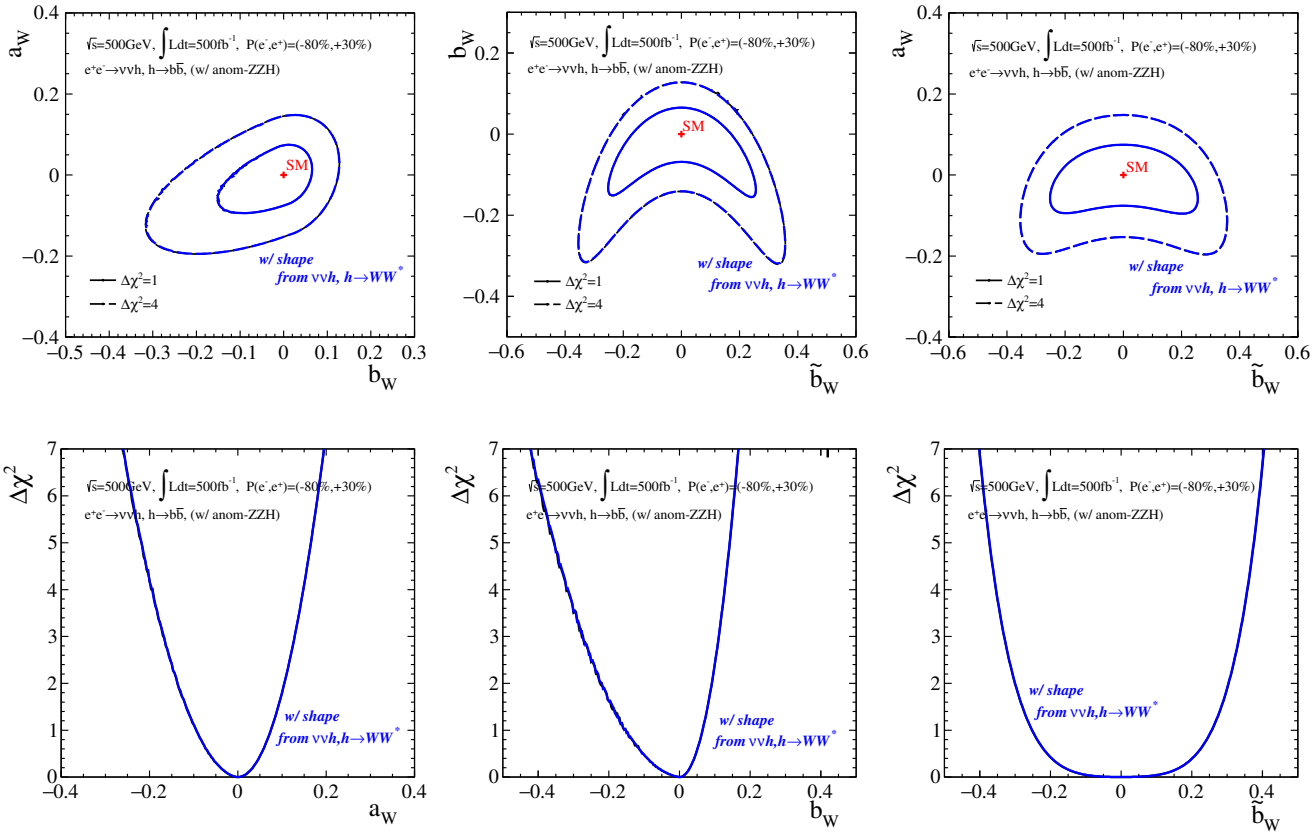

$\sqrt{s} = 500$ GeV with $\int \mathrm{Ldt} = 500$ fb^{-1} and $\mathrm{P}(e^-, e^+) = (-80\%, +30\%)$

the shapes from the $h \to WW \to q\bar{q}q\bar{q}$ decay in the WW-fusion and the ZZH variation are included.

$$\begin{cases} a_W = [-0.094, \quad 0.075] \\ b_W = [-0.153, \quad 0.065] \\ \tilde{b}_W = [-0.253, \quad 0.256] \\ a_Z = \pm 0.0800 \\ b_Z = \pm 0.0182 \\ \tilde{b}_Z = \pm 0.0231 \end{cases}, \quad \rho = \begin{pmatrix} 1 & .1831 & .0141 & -.0142 & -.0152 & -4.2 \cdot 10^{-5} \\ - & 1 & .0117 & .0015 & -.0020 & -.0004 \\ - & - & 1 & -.0124 & .0168 & 5.5 \cdot 10^{-5} \\ - & - & - & 1 & -.7382 & -.0144 \\ - & - & - & - & 1 & .0146 \\ - & - & - & - & - & 1 \end{pmatrix}$$

Figure 95: (Upper) The plots show contours projected onto the two-dimensional parameter spaces a_W-b_W, a_W-$\tilde{b}_W$, and b_W-$\tilde{b}_W$ after the simultaneous fitting in the three-parameter spaces. Each contour correspond to the 1σ and 2σ sensitivity to the anomalous WWH parameters. (Middle) The plots are $\Delta\chi^2$ distributions as a function of each parameter of the anomalous couplings of a_W, b_W, and $\tilde{b}_W$. The informations used for the evaluation are listed in the main text. (Lower) The values give the 1σ bounds for each anomalous parameter of a_W, b_W, and $\tilde{b}_W$. The values which make the variation of the ZZH are also given as the results of the simultaneous fitting, which includes the correlations between each parameter.

with η_W, ζ_{WW}, and $\tilde{\zeta}_{WW}$ by multiplying the factor of $\Lambda/v = 4.065$.

With the benchmarking luminosity at $\sqrt{s} = 250$ GeV :

Assuming the benchmarking luminosity of 250 fb^{-1} for both of the beam polarizations and considering the contribution of the variation coming from the anomalous ZZH and γZH couplings, the evaluated sensitivities are given as follows,

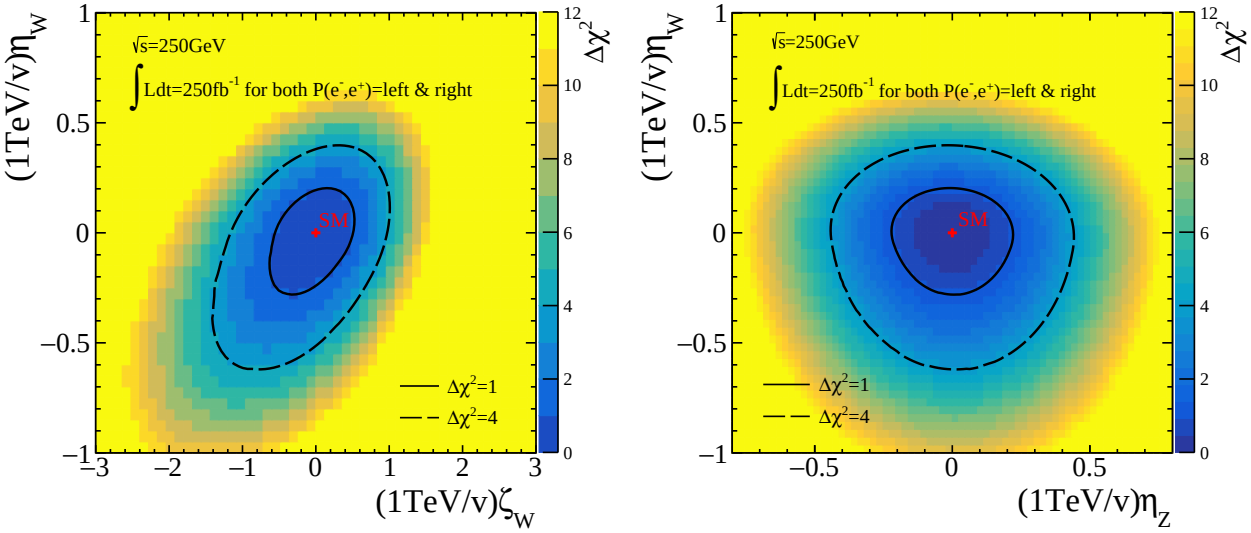

Figure 96: The plots show contours corresponding to the 1σ and 2σ bounds in the η_Z-η_W parameter space and the ζ_Z-ζ_W parameter space assuming the ILC benchmark operation, where the accumulated luminosities for both beam polarization are 250 fb^{-1}.

$$\begin{cases} \eta_W &= [-0.0691, 0.0499] \\ \zeta_{WW} &= [-0.1553, 0.1297] \\ \tilde{\zeta}_{WW} &= [-0.2783, 0.2793] \\ \eta_Z &= \pm 0.0544 \\ \zeta_{ZZ} &= \pm 0.0195 \\ \zeta_{AZ} &= \pm 0.0034 \\ \tilde{\zeta}_{ZZ} &= \pm 0.0267 \\ \tilde{\zeta}_{AZ} &= \pm 0.0440 \end{cases}, \tag{47}$$

$$\rho = \begin{pmatrix} 1 & 0.2852 & -0.0123 & -0.0381 & -0.0083 & -0.3217 & -0.0006 & 0.0008 \\ - & 1 & -0.0207 & -0.0657 & 0.0663 & 0.0071 & 0.0002 & 0.0003 \\ - & - & 1 & -0.0061 & 0.0061 & 0.0006 & 3.0 \cdot 10^{-5} & 3.1 \cdot 10^{-5} \\ - & - & - & 1 & -0.9913 & 0.0170 & -0.0040 & -0.0048 \\ - & - & - & - & 1 & -0.0067 & 0.0040 & 0.0140 \\ - & - & - & - & - & 1 & 0.0066 & 0.0047 \\ - & - & - & - & - & - & 1 & -0.8967 \\ - & - & - & - & - & - & - & 1 \end{pmatrix}$$

With the benchmarking luminosity at $\sqrt{s} = 500$ GeV :

Assuming the benchmarking luminosity of 500 fb^{-1} for both of the beam polarizations, the achievable sensitivities are given as follows,

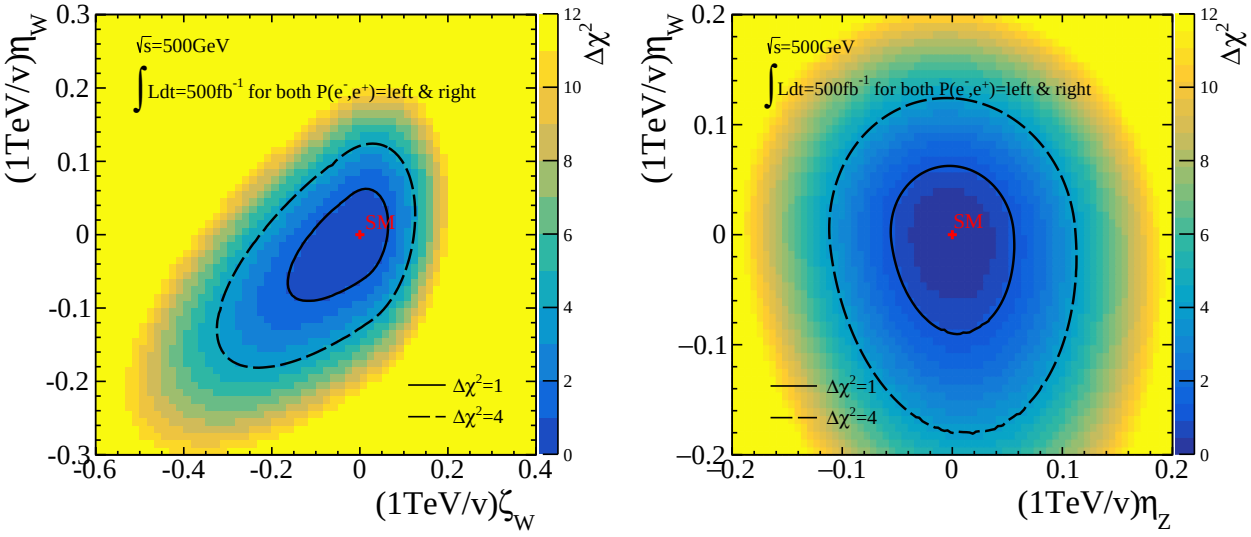

Figure 97: The plots show contours corresponding to the 1σ and 2σ bounds in the η_Z-η_W parameter space and the ζ_Z-ζ_W parameter space assuming the ILC benchmark operation, where the accumulated luminosities for both beam polarization are 500 fb^{-1}.

$$\begin{cases} \eta_W = [-0.0211, 0.0154] \\ \zeta_{WW} = [-0.0345, 0.0158] \\ \tilde{\zeta}_{WW} = [-0.0616, 0.0625] \\ \eta_Z = \pm 0.0137 \\ \zeta_{ZZ} = \pm 0.0031 \\ \zeta_{AZ} = \pm 0.0026 \\ \tilde{\zeta}_{ZZ} = \pm 0.0054 \\ \tilde{\zeta}_{AZ} = \pm 0.0006 \end{cases}, \tag{48}$$

$$\rho = \begin{pmatrix} 1 & 0.2150 & 0.0152 & -0.0454 & -0.0537 & 0.0923 & 0.0009 & -0.00281 \\ - & 1 & 0.0172 & 8.9 \cdot 10^{-5} & -0.0003 & -0.0022 & -0.0004 & -0.0003 \\ - & - & 1 & -0.0038 & 0.0053 & 0.0013 & -0.0002 & -0.0002 \\ - & - & - & 1 & -0.7465 & 0.0089 & -0.0102 & -0.0003 \\ - & - & - & - & 1 & 0.0636 & 0.0085 & 0.0113 \\ - & - & - & - & - & 1 & 0.0079 & 0.0008 \\ - & - & - & - & - & - & 1 & 0.6520 \\ - & - & - & - & - & - & - & 1 \end{pmatrix}$$

With ILC full operation :

Assuming the ILC full operation, where the total luminosities of 2 ab^{-1} and 4 ab^{-1} are accumulated for $\sqrt{s}$ =250 and 500 GeV, respectively. Approximately 67.5 % and 22.5 % out of the integrated luminosity of 2 ab^{-1} are assigned for both of the beam polarization at $\sqrt{s}$=250 GeV, whereas 40 % out of the 4 ab^{-1} are assigned for both polarization at $\sqrt{s}$=500 GeV. The achievable sensitivities are given below.

$$\begin{cases} \eta_W = [-0.0080, 0.0045] \\ \zeta_{WW} = [-0.0172, 0.0088] \\ \tilde{\zeta}_{WW} = [-0.0429, 0.0438] \\ \eta_Z = \pm 0.0054 \\ \zeta_{ZZ} = \pm 0.0016 \\ \zeta_{AZ} = \pm 0.0010 \\ \tilde{\zeta}_{ZZ} = \pm 0.0027 \\ \tilde{\zeta}_{AZ} = \pm 0.0003 \end{cases}, \tag{49}$$

$$\rho = \begin{pmatrix} 1 & 0.4071 & -0.0546 & -0.0148 & -0.0773 & 0.006 & -0.0004 & -0.0016 \\ - & 1 & -0.0833 & -0.0076 & 0.0005 & 0.010 & -3.6 \cdot 10^{-6} & 4.8 \cdot 10^{-7} \\ - & - & 1 & 0.0024 & -0.0010 & 0.0007 & 3.4 \cdot 10^{-5} & 6.8 \cdot 10^{-6} \\ - & - & - & 1 & -0.8523 & -0.1888 & -0.0115 & -0.0115 \\ - & - & - & - & 1 & 0.0829 & 0.0103 & 0.0140 \\ - & - & - & - & - & 1 & 0.0066 & -0.0001 \\ - & - & - & - & - & - & 1 & 0.6000 \\ - & - & - & - & - & - & - & 1 \end{pmatrix}$$

8 Discussions and conclusion

Systematic uncertainties on the study :

In the analysis discussed up to here, the results include the statistical error only and the systematic uncertainties have not been considered. Since the systematic uncertainties must be taken into account in measurements, several uncertainties related to the study are shortly discussed below.

- Uncertainty on center-of-mass energies including beamstrahlung
  To distinguish the Higgs process $Zh \to e^+e^-h/\mu^+\mu^-h$ from the SM backgrounds, the recoil mass technique was used, which strongly depends on the initial information. The uncertainties of the center-of-mass energies and the beamstrahlung directly propagate to measurements realized by the recoil mass technique. This consideration has been discussed, for instance, in [83, 84]. According to the documents, the ZZ-final state process can be available. We know the mass of the Z boson with precision of a few MeV level [70]. By applying the same technique to the ZZ-final state process, the measured values as the center-of-mass energies are precisely controlled. Through measurements using beam calorimeter, which is installed in just outside of the beam pipe and called BeamCal, the beam parameters will be understood well.

- Uncertainty on beam polarization and luminosity
  The uncertainty on the beam polarization is also discussed in [84]. Since the beam polarization affect cross-section of the BhaBha scattering process and the WW-final state process which is one of the sensitive processes to the polarization, these processes are available for the evaluation of the beam polarization. The uncertainty of the beam polarization was estimated as 10^{-3} [84]. This uncertainty is negligible compared to the statistical errors of the several cross-section measurements, which are inputs of the anomalous VVH couplings study. The luminosity will be precisely measured using the BhaBha process and luminosity calorimeter called LumiCal. The beam calorimeter is also useful to measure bunch-by-bunch luminosity. The relative precision will be reach to 10^{-3} [85] which includes several systematic uncertainties such as the beam polarization, cross-section of the BhaBha and resolution of the calorimeters.

- Uncertainty on momentum, lepton identification, and flavor tagging
  Measured momenta are also possible causes of the uncertainty, which is derived from misalignment of tracking system, non uniformity of magnetic and electric field, bremsstrahlung and so on. Using 2-fermion process $Z \to l^+l^-$ and measuring the invariant mass of the Z boson, the tracking system can be precisely calibrated and the uncertainty strongly constrained. The uncertainty of flavor tagging will be also well evaluated by using the large number of $Z \to q\bar{q}$ samples and comparing the samples with real data.

- Uncertainty on method of background suppression
  Cut variables applied for the background suppression are basic observables. The uncertainties can be small. In fact, the MVA method, which is almost blackbox and difficult to evaluate the uncertainty, was applied for the ZZ-fusion process of $\sqrt{s}$ =250 GeV. However, the statistical error is completely dominant in this process since the cross-section is small.

- Uncertainty on event acceptance and detector response functions
  To evaluate both of the functions, the large number of MC samples are used. Therefore, the uncertainties for both functions are assumed to be negligible.

- Uncertainty on theoretical Higgs properties
  The theoretical uncertainties for the Higgs couplings and production cross-sections related to the Higgs are less than 1% level, which are negligible compared to expected experimental statistical errors, at least, up to $\sqrt{s}$ =500 GeV [86]. However, the document concluded that some considerations are necessary when the energy goes to 1 TeV.

- Uncertainty on event generator, parton showering, geometries of the detector and so on
  Every event samples used in the study was generated with PYTHIA. It might be useful to use different event generators and compare differences among them. Inconsistency between the detector geometry and the real detector will be also source of the uncertainty. These kinds of estimations will be future tasks, but we assume that it is negligible.

Precisions of the Higgs couplings with full ILC-EFT fit :

The remarkable point we revealed through the anomalous VVH studies is that, if the available information is the cross-section only, we can not give any constraints to the anomalous parameters due to the adjustment of the third parameter. Therefore, the inclusion of the shape information is definitely indispensable to give the constraints to the parameters of EFT. Fig. 98 shows the precisions of the Higgs couplings to the other SM particles with the EFT framework, where the evaluation was performed including the correlation of the ZZH couplings which we provided from the study. Even with the ILC-250 GeV physics program, which was proposed as a new ILC Higgs physics program at 2016 [87], the precisions for the vector bosons, up-type, and down-type fermions can reach 1 % level.

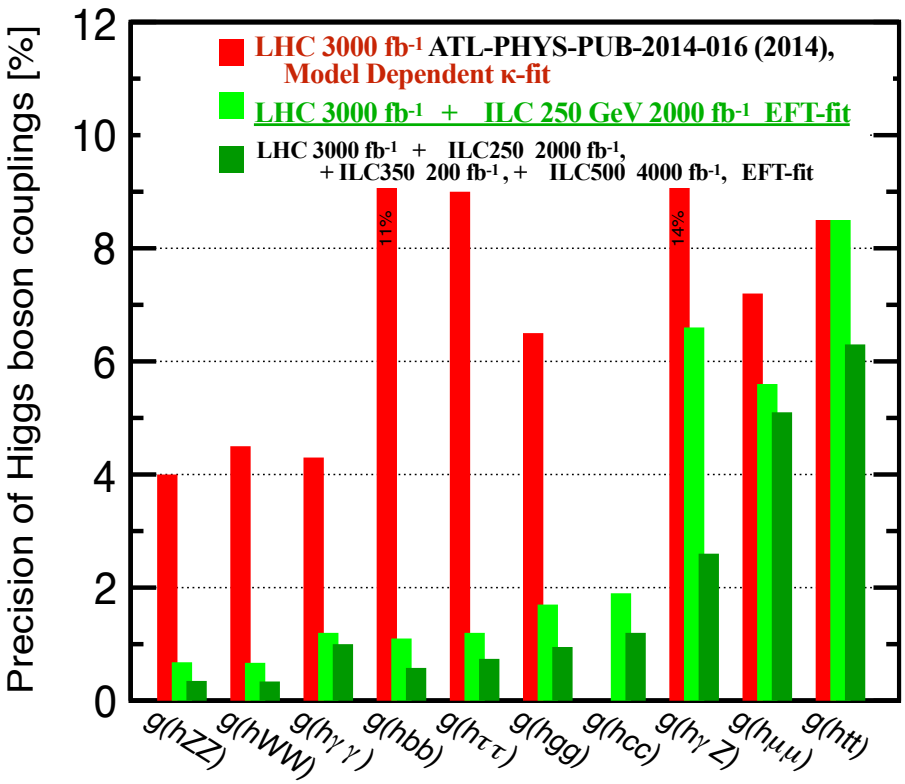

Figure 98: The plot is referred from [87]. Precision of the Higgs boson coupling to the SM particles under the EFT framework. Comparison with the results of the model-dependent estimation of the HL-LHC is also presented.

Impact of the anomalous WWH couplings study :

In fact, the precisions with the full ILC-EFT fit shown above does not include the results of the anomalous WWH study although the result of the cross-section measurement of the WW-fusion process is included. It is supposedly expected that the information of the differential cross-section given by the WW-fusion process and the Higgs decay process $h \to W^+W^-$ can further more improve the sensitivities to the EFT parameters, and consequently the precisions to the other SM

particles can be also improved. Therefore, it is worth mentioning the improvement of the precisions to some extent. However, because the discussion has not sufficiently done for the moment, the concrete values are not shown here. Since the evaluated errors for the anomalous WWH are asymmetric errors, the better bound is taken as the sensitivities to the parameters η_W and ζ_W, and also the correlation between them. The evaluated precisions under this condition give a few % relative improvement for the ZZH and WWH couplings compared to the precisions with the full ILC-EFT fit shown above. This improvement can also improve the other precisions of the Higgs couplings.

Comparison with the expectation of LHC :

The ATLAS group of the LHC collaboration is also studying the Lorentz structures of the Higgs couplings to the SM gauge bosons under the framework of EFT using real data [88]. According to the report they published using accumulated 36 fb^{-1}, the precisions for κ_{HVV} and κ_{AVV} are not good, which correspond to roughly (-30%, 200%) and (-200%, 200%) when interpreting to our b_V and $\tilde{b}_V$. The final precisions they will reach when assuming 3000 fb^{-1} can be (-3%, 20%) and (-20%, 20%), which are roughly 10 times larger compared to the precisions of ζ_{ZZ} and $\tilde{\zeta}_{ZZ}$ in the ILC-250 program.

Conclusion :

Analysis on the anomalous VVH couplings at the future International Linear Collider was presented by employing the framework of the Effective Filed Theory with the lowest dimension-6 filed operators. The evaluations of the sensitivities to the anomalous VVH couplings were done using full detector simulation of the International Large Detector model where the SM backgrounds are also included. To include the shape information (differential cross-section) of the processes, the event acceptance and detector response functions were constructed, which are applied for the construction of the shape with the different anomalous parameters.

The anomalous ZZH and γZH couplings were evaluated by using 8 channels of the major Higgs production processes, the Higgs-strahlung and the ZZ-fusion, and the left- and right-handed beam polarizations were considered to disentangle the mixing of the Z boson and γ, which is the advantage of the linear collider. Under the general parametrization of (η_Z, ζ_{ZZ}, ζ_{AZ}, $\tilde{\zeta}_{ZZ}$, $\tilde{\zeta}_{AZ}$), the evaluated sensitivities to each anomalous coupling with the ILC full operation following the H20 scenario are given in Fig. 80. The sensitivity of 0.55 % is possible to achieve for the SM-like coupling of η_Z, and the sensitivities to the other anomalous couplings relevant to the ZZH couplings are also less than 0.30 % for both of the CP-even and -odd structures. The sensitivities to the anomalous γZH couplings are more strongly constrained, which reach to less than 0.10 %.

The anomalous WWH couplings were also evaluated as well, where the WW-fusion Higgs production and the decay of the Higgs boson in the Higgs-strahlung process are considered for the evaluation of the couplings of WWH. In the WW-fusion process, the contamination of the Higgs-strahlung process, which has the same final state of s-channel $\nu\bar{\nu}h$, was considered because it is possible that the kinematical distribution and the normalization of the s-channel vary depending on the existence of the anomalous ZZH couplings. The evaluated sensitivities to the anomalous coupling of the general parametrization of (η_W, ζ_{WW}, $\tilde{\zeta}_{WW}$) with the ILC full operation following the H20 scenario are given in Eq. (49), where the contribution of the parameters (η_Z, ζ_{ZZ}, ζ_{AZ}, $\tilde{\zeta}_{ZZ}$, $\tilde{\zeta}_{AZ}$) is considered.

The sensitivity to the SM-like coupling of η_W in the anomalous WWH couplings reach 0.45 %–0.80 %, which is similarly sensitivity with η_Z of the ZZH couplings. The sensitivity to the CP-even structure was evaluated as 0.88 %–1.72 %. Unfortunately, the sensitivity to the CP-odd structure will reach approximately 4.40 %, which is a bit weaker sensitivity compared to the ZZH couplings. This is because it is difficult to perform fully reconstruction of the observable sensitive to the CP-odd structure like $\Delta\Phi$ due to the missing neutrinos and less performance of c-quark flavor tagging implemented with the LCFIPlus package. However, if the c-quark tagging is specially tuned with new information such as existence of a K meson in a hadron jet, the performance will improve

and the sensitivity be improved. In fact, it can be also true that the CP-odd structure will be complete identified through the anomalous ZZH couplings. It is also observed that η_W and ζ_{WW} have the correlation by the adjustment of the cross-sections, and here, notable thing is that, when assuming the ILC-250 GeV physics program, the achievable sensitivity to η_W is $[-3.5\ \%- + 2.5\ \%]$ whereas the one to η_Z is ± 2.9 %. This is because of the magnitude of the correlation between a-b (or η-ζ) are different. Therefore, η_W gives roughly 15 % better sensitivity, and potentially it might be possible to improve the results of the global fitting shown in Fig. 98.

This study indicated that the future ILC experiment has sufficient capability to decide the structure of the VVH couplings precisely, which is one of the important information to reveal the Higgs sector completely.

9 Prospects

In the end of the thesis it is worth mentioning prospect of further improvement of the sensitivities to the anomalous VVH couplings. One of the advanced analysis methods utilized in high energy physics is the Matrix Element method, which can directory link observed events to a theory in terms of observed momenta of particles. The ME method was originally developed for top quark physic by D0 and CDF collaboration at the Tevatron experiment [89–92], and became widely used after that to compare real data and theories and verify theoretical parameters describing physics processes. Usually, in order to verify the theory and the real data, we construct distributions directly: one is based on observed events and another is generated one according to the theory, which detector simulation is applied to later. In contrast, the ME method gives likelihood based on the events we observed, which is completely based on the theory in terms of differential cross-section of certain process and calculation in terms of the specific parameters describing the theory. When one wants to have a multi-dimensional distribution to increase the available information, the construction of such distribution is sometimes difficult because of lack of the statistics. However, the ME method can provide a single observable in which all kinematical information are encoded by exporting the fact that any kinematical information are calculated based on the observed momenta. Therefore, the usage of the ME method corresponds to the usage of the multi-dimensional distribution, which gives us complete information.

Application to $e^+e^- \to \mu^+\mu^- h$ process at $\sqrt{s}$=250 GeV as a trial :

To discuss prospective sensitivity to the anomalous couplings with the ME method, we apply the method to the $Zh \to \mu^+\mu^- h$ which is the simplest process in the e^+e^- reaction relevant to the Higgs boson. However, the method in the ILC analysis framework has been still beginning of development, which is called MarlinPhyssim [50], and we will take long time to implement it. In fact, through the analysis of the application to the $\mu^+\mu^- h$, it turns out that handling of the initial state radiation and bremsstrahlung, which are the Next Leading Order (NLO) contribution, is critical toward the evaluation when would like to discuss less than 1 % sensitivity to the anomalous couplings.

The implementation of the ISR and the bremsstrahlung in the ME calculator is not easy within a short period of time. Therefore, we try to compare the sensitivities which are evaluated with the signal process only, preparing two results: one is evaluated based on the traditional analysis, where the shape, the cross-section information and the ISR and bremsstrahlung are considered, another one is evaluated based on the ME method, where the ISR and bremsstrahlung are temporary ignored.

Constructing a probability density function for given theoretical assumption :

A probability density function to each event, which has a parameter α, would be given in terms of observed momenta of particles as

$$P(\bar{\boldsymbol{p}}^\mu;\alpha) = \frac{1}{\sigma(\alpha)} \int d\Phi_f |\mathcal{M}(\bar{\boldsymbol{p}}^\mu;\alpha)|^2$$

where $|\mathcal{M}(\bar{\boldsymbol{p}}^\mu;\alpha)|^2$ is the squared matrix element for given $\bar{\boldsymbol{p}}^\mu$ in the final state f particles and the theoretical parameter α, and $d\Phi_f$ shows a phase space term in the f-body phase space that must be integrated over the possible four-momentum space based on the four-momentum conservation, which is generally given as $d\Phi_f = \prod_f \left[\int \frac{d^3\bar{\boldsymbol{p}}_f}{(2\pi)^3 2E_f} \right] (2\pi)^4 \delta^4(\Sigma_f \bar{p}^\mu_f - \bar{p}^\mu_{e^-} - \bar{p}^\mu_{e^+})$. The integrated value is normalized with $\sigma(\alpha)$ to guarantee $P(\bar{\boldsymbol{p}}^\mu;\alpha)$ gives likelihood.

However, this probability based on the theory and does not include any physical effects such as detector resolution as input from experiment [93, 94]. Thus, the function is expanded as

$$P(\bar{\boldsymbol{p}}^{\mu};\boldsymbol{a}_Z) = \frac{1}{A(\boldsymbol{a}_Z)\sigma(\boldsymbol{a}_Z)} \int d\Phi_f |\mathcal{M}(\bar{\boldsymbol{p}}^{\mu};\boldsymbol{a}_Z)|^2 \; T(\boldsymbol{p}^{\mu},\bar{\boldsymbol{p}}^{\mu}) \; \epsilon(\boldsymbol{p}^{\mu})$$

where $\bar{\boldsymbol{p}}^{\mu}$ and $\boldsymbol{p}^{\mu}$ respectively stand for the true momentum and observed momentum, and the theoretical parameter is replaced $\boldsymbol{a}_Z$ which shows the anomalous ZZH couplings. The transfer function $T(\boldsymbol{p}^{\mu},\bar{\boldsymbol{p}}^{\mu})$ gives the probability which gives a connection between observed momentum and theoretical momentum of certain particle. The acceptance of an event in which particles have momenta of $\boldsymbol{p}^{\mu}$ is described with $\epsilon(\boldsymbol{p}^{\mu})$. The denominator of the probability $A(\boldsymbol{a}_Z)\sigma(\boldsymbol{a}_Z)$ includes the cross-section of the process with the parameter $\boldsymbol{a}_Z$, which is affected by the overall acceptance $A(\boldsymbol{a}_Z)$ of the process.

As far as the momenta of the particles are extremely well measured, the transfer function can be assumed to be a delta function: $T(\boldsymbol{p}^{\mu},\bar{\boldsymbol{p}}^{\mu}) \simeq \delta(\boldsymbol{p}^{\mu} - \bar{\boldsymbol{p}}^{\mu})$. In that case the probability function can be simplified like

$$P(\boldsymbol{p}^{\mu};\boldsymbol{a}_Z) = \frac{|\mathcal{M}(\boldsymbol{p}^{\mu};\boldsymbol{a}_Z)|^2 \; \epsilon(\boldsymbol{p}^{\mu})}{A(\boldsymbol{a}_Z)\sigma(\boldsymbol{a}_Z)} \tag{50}$$

Calculation of the denominator :

Independent calculation of $\sigma(\boldsymbol{a}_Z)$ is easily performed using the physics generator, in our case PHYSSIM. To evaluate the overall acceptance $A(\boldsymbol{a}_Z)$, it is necessary to integrate over all possible momentum configurations where the momentum acceptance $\epsilon(\boldsymbol{p}^{\mu})$ must be included for each momentum same time. To calculate the cross-section which includes the over all acceptance for any configuration of the anomalous couplings, each contribution from pure and interference terms are calculated, which is discussed in Sec. 22, while including the momentum acceptance $\epsilon(\boldsymbol{p}^{\mu})$ which is set by putting the one-dimensional distribution of $\Delta\Phi$ as shown in Fig. 58 after applying smoothing to realize a continuous function. Fig. 99 show the smoothed $\Delta\Phi$ distribution to apply the momentum acceptance and the analytic distribution showing $A(\boldsymbol{a}_Z)\sigma(\boldsymbol{a}_Z)$, where the process is $e^+e^- \to \mu^+\mu^- h$ process at $\sqrt{s}$=250 GeV and fully left- and right-handed polarization for the electron and the positron beams are assumed.

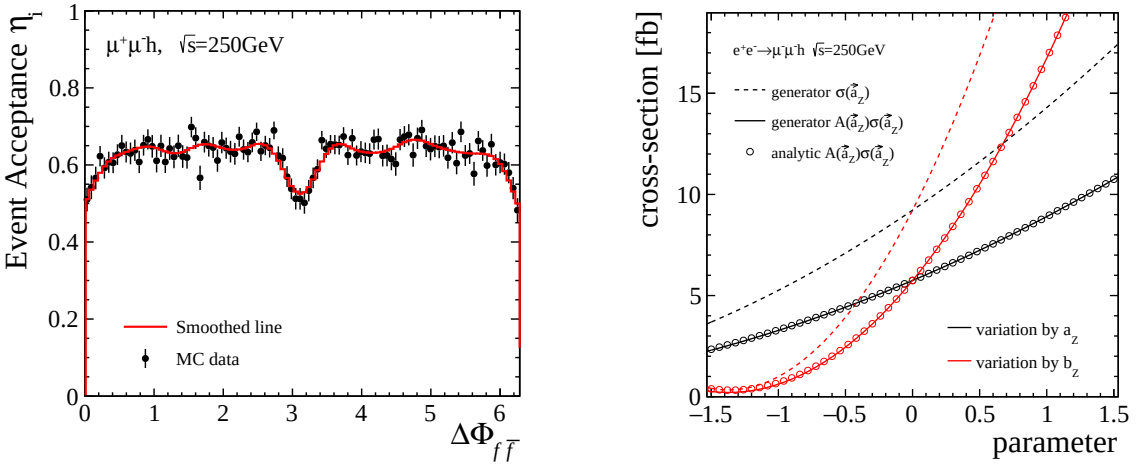

Figure 99: The plots show the smoothed acceptance function of $\Delta\Phi$ to input to the phase space integration for the cross-section calculation (left) and the calculated cross-section of $e^+e^- \to \mu^+\mu^- h$ process at $\sqrt{s}$=250 GeV with fully left- and right-handed polarization for the electron and the positron beams.

Likelihood ratio test :

To estimate the parameters of a theoretical mode, one of the analysis techniques is Maximum Likelihood (ML) where we test the parameters to find which parameters can explain the data more suitably based on the observed information. Using the maximum Likelihood, two theoretical models can be also compared.

$$\chi^2 = -2\log\Delta L = -2w_{\rm pol}\Big(\log L(\boldsymbol{a}_Z) - \log L_{SM}\Big)$$

where $w_{\rm pol}$ is a factor for scaling the MC events to the number of expected real events. $L(\boldsymbol{a}_Z)$ denotes the likelihood function depending on the anomalous ZZH couplings, which is defined with

$$\begin{aligned} L(\boldsymbol{a}_Z) &= L_{\rm shape}(\boldsymbol{a}_Z)\cdot L_{\rm norm}(\boldsymbol{a}_Z) \\ &= \prod_{i=1}^{\rm MCevents} P_{\rm shape}(\boldsymbol{p}_i^{\mu};\boldsymbol{a}_Z)\cdot P_{\rm norm}(\boldsymbol{a}_Z) \end{aligned}$$

where $P_{\rm shape}(\boldsymbol{p}_i^{\mu};\boldsymbol{a}_Z)$ corresponds to Eq. (50). Because, for the moment, we have interested in the development of the first probably, so the second probably coming from the normalization information is ignored.

Prospects :

To compare the "intrinsic" performance which the ME method provides us, a χ^2 value is extracted over the parameter space of b_Z-$\tilde{b}_Z$ using the signal sample only, which is generated with ISR, bremsstrahlung, and FSR, and without them. Notice that the ME calculator can handle LO order only.

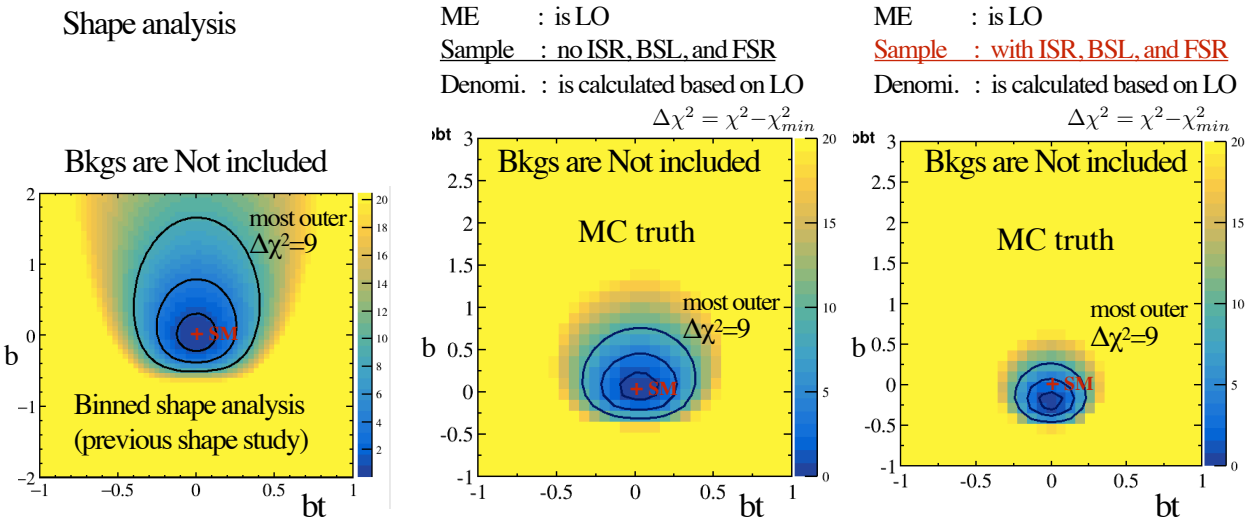

Figure 100: The distributions show the $\Delta\chi^2$ distributions with the different conditions using the $e^+e^- \to \mu^+\mu^- h$ process at 250 GeV: (left) the traditional shape analysis, (middle) the ME method assuming the LO contributions, and (right) the ME method assuming the LO contributions but the sample includes the NLO contributions.

Fig. 100 show the $\Delta\chi^2$ distributions for each condition, where the result based on the standard method with the shape information is plotted for the comparison. The second plot gives presum-

ably "intrinsic" sensitivity to the parameters, where the suitable condition is considered, which means the ME calculator handles LO and there exists LO process of $e^+e^- \to \mu^+\mu^- h$. Once ISR and bremsstrahlung and considered in the process, ME with LO can not perform proper estimation since the momenta of final state particles are slightly vary, which is shown in the third plot. Therefore, when implementing the handling of NLO in ME, it is expected that the sensitivity will get better to the extent of the second plot.

References

[1] S. L. Glashow, M. Gell-Mann, Gauge theories of vector particles, Annals of Physics 15 (3) (1961) 437 – 460. doi:https://doi.org/10.1016/0003-4916(61)90193-2.
URL http://www.sciencedirect.com/science/article/pii/0003491661901932

[2] F. Englert, R. Brout, Broken symmetry and the mass of gauge vector mesons, Phys. Rev. Lett. 13 (1964) 321–323. doi:10.1103/PhysRevLett.13.321.
URL https://link.aps.org/doi/10.1103/PhysRevLett.13.321

[3] P. W. Higgs, Broken symmetries and the masses of gauge bosons, Phys. Rev. Lett. 13 (1964) 508–509. doi:10.1103/PhysRevLett.13.508.
URL https://link.aps.org/doi/10.1103/PhysRevLett.13.508

[4] S. Weinberg, A model of leptons, Phys. Rev. Lett. 19 (1967) 1264–1266. doi:10.1103/PhysRevLett.19.1264.
URL https://link.aps.org/doi/10.1103/PhysRevLett.19.1264

[5] Example: Standard model of physics.
URL http://www.texample.net/tikz/examples/model-physics/

[6] A. Airapetian *et al.*, ATLAS: Detector and physics performance technical design report. Volume 1.

[7] A. Airapetian *et al.*, ATLAS detector and physics performance: Technical Design Report, 2, Technical Design Report ATLAS, CERN, Geneva, 1999.
URL https://cds.cern.ch/record/391177

[8] S. Chatrchyan *et al.*, The CMS Experiment at the CERN LHC, JINST 3 (2008) S08004. doi:10.1088/1748-0221/3/08/S08004.

[9] G. Aad *et al.*, Observation of a new particle in the search for the standard model higgs boson with the atlas detector at the LHC, Physics Letters B 716 (1) (2012) 1 – 29. doi:https://doi.org/10.1016/j.physletb.2012.08.020.
URL http://www.sciencedirect.com/science/article/pii/S037026931200857X

[10] S. Chatrchyan *et al.*, Observation of a new boson at a mass of 125 GeV with the cms experiment at the LHC, Physics Letters B 716 (1) (2012) 30 – 61. doi:https://doi.org/10.1016/j.physletb.2012.08.021.
URL http://www.sciencedirect.com/science/article/pii/S0370269312008581

[11] L. Evans, P. Bryant, Lhc machine, Journal of Instrumentation 3 (08) (2008) S08001.
URL http://stacks.iop.org/1748-0221/3/i=08/a=S08001

[12] Event display of a H→ 4e candidate event, general Photo (Jul 2012).
URL http://cds.cern.ch/record/1459495

[13] S. Dawson *et al.*, Higgs working group report of the snowmass 2013 community planning study (2013). arXiv:arXiv:1310.8361.

[14] W. N. Cottingham, D. A. Greenwood, An introduction to the standard model of particle physics, Cambridge University Press, 2007.

[15] F. Halzen, A. D. Martin, QUARKS AND LEPTONS: AN INTRODUCTORY COURSE IN MODERN PARTICLE PHYSICS, 1984.

[16] I. B. van Vulpen, Measurement of Z boson pair production and a search for the Higgs boson in e^+e^- collisions at LEP, Ph.D. thesis, NIKHEF, Amsterdam (2002).
URL http://inspirehep.net/record/585652/files/cer-002704727.pdf

[17] A. Kopp, Search for higgs bosons using the l3 detector at lep, Ph.D. thesis.

[18] M. Dam, Tests of the electroweak theory with the delphi detector atlep, Ph.D. thesis.

[19] S. Weinberg, Baryon- and lepton-nonconserving processes, Phys. Rev. Lett. 43 (1979) 1566–1570. doi:10.1103/PhysRevLett.43.1566.
URL https://link.aps.org/doi/10.1103/PhysRevLett.43.1566

[20] K. Fujii *et al.*, Physics Case for the International Linear ColliderarXiv:1506.05992.

[21] R. S. Gupta, H. Rzehak, J. D. Wells, How well do we need to measure higgs boson couplings?, Phys. Rev. D 86 (2012) 095001. doi:10.1103/PhysRevD.86.095001.
URL https://link.aps.org/doi/10.1103/PhysRevD.86.095001

[22] H. Baer *et al.*, The International Linear Collider Technical Design Report - volume 2: Physics (2013). arXiv:arXiv:1306.6352.

[23] H. E. Haber, Challenges for nonminimal Higgs searches at future colliders, in: Perspectives for electroweak interactions in e^+e^- collisions. Proceedings, Ringberg Workshop, Tegernsee, Germany, February 5-8, 1995, 1996, pp. 219–232, [,151(1995)]. arXiv:hep-ph/9505240.
URL http://preprints.cern.ch/cgi-bin/setlink?base=preprint&categ=cern&id=th95-109

[24] M. Carena *et al.*, Distinguishing a minimal supersymmetric standard model higgs boson from the sm higgs boson at a linear collider, Phys. Rev. D 65 (2002) 055005. doi:10.1103/PhysRevD.65.055005.
URL https://link.aps.org/doi/10.1103/PhysRevD.65.055005

[25] K. Agashe, R. Contino, A. Pomarol, The minimal composite higgs model, Nuclear Physics B 719 (1) (2005) 165 – 187. doi:https://doi.org/10.1016/j.nuclphysb.2005.04.035.
URL http://www.sciencedirect.com/science/article/pii/S0550321305003445

[26] R. Contino, L. Da Rold, A. Pomarol, Light custodians in natural composite higgs models, Phys. Rev. D 75 (2007) 055014. doi:10.1103/PhysRevD.75.055014.
URL https://link.aps.org/doi/10.1103/PhysRevD.75.055014

[27] A. David *et al.*, LHC hxswg interim recommendations to explore the coupling structure of a higgs-like particle (2012). arXiv:arXiv:1209.0040.

[28] S. Heinemeyer *et al.*, Handbook of LHC higgs cross sections: 3. higgs propertiesarXiv:arXiv:1307.1347, doi:10.5170/CERN-2013-004.

[29] D. Zeppenfeld *et al.*, Measuring higgs boson couplings at the cern LHC, Phys. Rev. D 62 (2000) 013009. doi:10.1103/PhysRevD.62.013009.
URL https://link.aps.org/doi/10.1103/PhysRevD.62.013009

[30] S. Bock, Higgs physics at the LHC (fakultat fur physik und astronomie ruprecht-karls-universitat heidelberg), Ph.D. thesis.
URL https://www.thphys.uni-heidelberg.de/~plehn/includes/theses/bock_m.pdf

[31] K. Fujii *et al.*, Physics case for the international linear collider (2015). arXiv:arXiv:1506.05992.

[32] T. Barklow *et al.*, Improved formalism for precision higgs coupling fits, Phys. Rev. D 97 (2018) 053003. doi:10.1103/PhysRevD.97.053003.
URL https://link.aps.org/doi/10.1103/PhysRevD.97.053003

[33] W. Buchmuller, D. Wyler, Effective Lagrangian Analysis of New Interactions and Flavor Conservation, Nucl. Phys. B268 (1986) 621–653. doi:10.1016/0550-3213(86)90262-2.

[34] B. Grzadkowski *et al.*, Dimension-six terms in the standard model lagrangianarXiv:arXiv:1008.4884, doi:10.1007/JHEP10(2010)085.

[35] T. Barklow *et al.*, Model-independent determination of the triple higgs coupling at e^+e^- colliders, Phys. Rev. D 97 (2018) 053004. doi:10.1103/PhysRevD.97.053004.
URL https://link.aps.org/doi/10.1103/PhysRevD.97.053004

[36] T. Behnke *et al.*, The International Linear Collider Technical Design Report - volume 1: Executive summary (2013). arXiv:arXiv:1306.6327.

[37] C. Adolphsen *et al.*, The International Linear Collider Technical Design Report - volume 3: Accelerator R&D in the technical design phase (2013). arXiv:arXiv:1306.6353.

[38] T. Behnke *et al.*, The International Linear Collider Technical Design Report - volume 4: Detectors (2013). arXiv:arXiv:1306.6329.

[39] Particle-Flow Event Reconstruction in CMS and Performance for Jets, Taus, and MET, Tech. Rep. CMS-PAS-PFT-09-001, CERN, Geneva (Apr 2009).
URL https://cds.cern.ch/record/1194487

[40] M. A. Thomson, Particle flow calorimetry at the international linear collider, Pramana 69 (6) (2007) 1101–1107. doi:10.1007/s12043-007-0236-9.
URL https://doi.org/10.1007/s12043-007-0236-9

[41] M. Thomson, Particle flow calorimetry and the pandoraPFA algorithm, Nucl. Instrum. Meth. A 611 (1) (2009) 25 – 40. doi:https://doi.org/10.1016/j.nima.2009.09.009.
URL http://www.sciencedirect.com/science/article/pii/S0168900209017264

[42] T. Abe *et al.*, The International Large Detector: Letter of Intent arXiv:1006.3396, doi:10.2172/975166.

[43] J. S. Marshall, M. A. Thomson, Pandora Particle Flow Algorithm, in: Proceedings, International Conference on Calorimetry for the High Energy Frontier (CHEF 2013): Paris, France, April 22-25, 2013, 2013, pp. 305–315. arXiv:1308.4537.
URL http://inspirehep.net/record/1250003/files/arXiv:1308.4537.pdf

[44] M. G. Green, S. L. Lloyd, P. N. Ratoff, Electron positron physics at the Z, Studies in high energy physics, cosmology and gravitation, IOP, Bristol, 1998.
URL http://cds.cern.ch/record/357258

[45] D. M. Asner *et al.*, ILC higgs white paper (2013). arXiv:arXiv:1310.0763.

[46] T. Barklow *et al.*, ILC operating scenarios (2015). arXiv:arXiv:1506.07830.

[47] H. Ono, A. Miyamoto, A study of measurement precision of the higgs boson branching ratios at the international linear collider, The European Physical Journal C 73 (3) (2013) 2343. doi:10.1140/epjc/s10052-013-2343-8.
URL https://doi.org/10.1140/epjc/s10052-013-2343-8

[48] C. Durig *et al.*, Model independent determination of HWW coupling and higgs total width at ILC (2014). arXiv:arXiv:1403.7734.

[49] F. J. Mueller, Development of a Triple GEM Readout Module for a Time Projection Chamber & Measurement Accuracies of Hadronic Higgs Branching Fractions in $\nu\nu$H at a 350 GeV ILC, Ph.D. thesis, DESY, Hamburg (2016). doi:10.3204/PUBDB-2016-02659.
URL http://bib-pubdb1.desy.de/search?cc=Publication+Database&of=hd&p=reportnumber:DESY-THESIS-2016-018

[50] J. Tian, Matrix Element Method for ILC Physics Analysis.
URL https://agenda.linearcollider.org/event/6301/contributions/29469/attachments/24440/37804/MatrixElement_AWLC14.pdf

[51] Internal note: The ZZ-fusion process at the International Linear Collider is under preparation.

[52] Common software packages developed for the International Linear Collider ILC.
URL http://ilcsoft.desy.de/portal

[53] S. Agostinelli, GEANT4: A Simulation toolkit, Nucl. Instrum. Meth. A506 (2003) 250–303. doi:10.1016/S0168-9002(03)01368-8.

[54] P. M. de Freitas, H. Videau, Detector simulation with MOKKA / GEANT4: Present and future, lc-tool-2003-010.
URL http://flc.desy.de/lcnotes/notes/localfsExplorer_read?currentPath=/afs/desy.de/group/flc/lcnotes/LC-TOOL-2003-010.ps.gz

[55] Laboratory leprince-ringuet (llr).
URL https://indico.ihep.ac.cn/event/4287/contribution/3/material/slides/0.pdf

[56] Marlin [modular analysis and reconstruction for the linear collider].
URL http://ilcsoft.desy.de/Marlin/current/doc/html/index.html

[57] J. R. W. Kilian, T. Ohl, The whizard event generator, Eur. Phys. J. C 71 (2011) 1742.
URL https://whizard.hepforge.org

[58] Physics study libraries. physsim.
URL http://www-jlc.kek.jp/subg/offl/physsim/

[59] High-energy-physics event generation with PYTHIA.
URL http://home.thep.lu.se/~torbjorn/Pythia.html

[60] F. Gaede *et al.*, Track reconstruction at the ilc: the ild tracking software, Journal of Physics: Conference Series 513 (2) (2014) 022011.
URL http://stacks.iop.org/1742-6596/513/i=2/a=022011

[61] C. F. Durig, Measuring the Higgs Self-coupling at the International Linear Collider, Ph.D. thesis, Hamburg U., Hamburg (2016).
URL http://bib-pubdb1.desy.de/search?cc=Publication+Database&of=hd&p=reportnumber:DESY-THESIS-2016-027

[62] T. Kramer, Track parameters in LCIO.
URL http://flc.desy.de/lcnotes/notes/localfsExplorer_read?currentPath=/afs/desy.de/group/flc/lcnotes/LC-DET-2006-004.pdf

[63] J. Tian, Isolated lepton tagging and new jet clustering.
URL https://agenda.linearcollider.org/event/6869/contributions/33771/attachments/27825/42160/IsoLep_JetClustering_20150905.pdf

[64] R. Brun, F. Rademakers, ROOT: An object oriented data analysis framework, Nucl. Instrum. Meth. A389 (1997) 81–86. doi:10.1016/S0168-9002(97)00048-X.

[65] A. Hocker *et al.*, TMVA - Toolkit for Multivariate Data Analysis, PoS ACAT (2007) 040. arXiv:physics/0703039.

[66] S. Catani *et al.*, New clustering algorithm for multijet cross sections in e+e − annihilation, Physics Letters B 269 (3) (1991) 432 – 438. doi:https://doi.org/10.1016/0370-2693(91)90196-W.

[67] S. Catani *et al.*, Longitudinally-invariant k ⊥ -clustering algorithms for hadron-hadron collisions, Nuclear Physics B 406 (1) (1993) 187 – 224. doi:https://doi.org/10.1016/0550-3213(93)90166-M.
URL http://www.sciencedirect.com/science/article/pii/055032139390166M

[68] S. D. Ellis, D. E. Soper, Successive combination jet algorithm for hadron collisions, Phys. Rev. D 48 (1993) 3160–3166. doi:10.1103/PhysRevD.48.3160.
URL https://link.aps.org/doi/10.1103/PhysRevD.48.3160

[69] M. Kobayashi, T. Maskawa, CP-Violation in the Renormalizable Theory of Weak Interaction, Progress of Theoretical Physics 49 (1973) 652–657. doi:10.1143/PTP.49.652.

[70] C. Patrignani *et al.*, Review of Particle Physics, Chin. Phys. C40 (10) (2016) 100001. doi:10.1088/1674-1137/40/10/100001.

[71] C. Patrignani *et al.*, Ckm quark-mixing matrix.
URL http://pdg.lbl.gov/2017/reviews/rpp2017-rev-ckm-matrix.pdf

[72] T. Suehara, T. Tanabe, LCFIPlus: A Framework for Jet Analysis in Linear Collider Studies, Nucl. Instrum. Meth. A808 (2016) 109–116. arXiv:1506.08371, doi:10.1016/j.nima.2015.11.054.

[73] G. Abbiendi *et al.*, Measurement of event shape distributions and moments in $e^+e^- \to$ hadrons at 91-209 gev and a determination of α_s.

[74] S. Brandt *et al.*, The Principal axis of jets. An Attempt to analyze high-energy collisions as two-body processes, Phys. Lett. 12 (1964) 57–61. doi:10.1016/0031-9163(64)91176-X.

[75] E. Farhi, Quantum chromodynamics test for jets, Phys. Rev. Lett. 39 (1977) 1587–1588. doi:10.1103/PhysRevLett.39.1587.
URL https://link.aps.org/doi/10.1103/PhysRevLett.39.1587

[76] D. P. Barber *et al.*, Discovery of three-jet events and a test of quantum chromodynamics at petra, Phys. Rev. Lett. 43 (1979) 830–833. doi:10.1103/PhysRevLett.43.830.
URL https://link.aps.org/doi/10.1103/PhysRevLett.43.830

[77] J. D. Bjorken, S. J. Brodsky, Statistical model for electron-positron annihilation into hadrons, Phys. Rev. D 1 (1970) 1416–1420. doi:10.1103/PhysRevD.1.1416.
URL https://link.aps.org/doi/10.1103/PhysRevD.1.1416

[78] G. Hanson *et al.*, Evidence for jet structure in hadron production by e^+e^- annihilation, Phys. Rev. Lett. 35 (1975) 1609–1612. doi:10.1103/PhysRevLett.35.1609.
URL https://link.aps.org/doi/10.1103/PhysRevLett.35.1609

[79] A. Heister *et al.*, Studies of QCD at e^+e^- centre-of-mass energies between 91-GeV and 209-GeV, Eur. Phys. J. C35 (2004) 457–486. doi:10.1140/epjc/s2004-01891-4.

[80] J. Abdallah *et al.*, The Measurement of alpha(s) from event shapes with the DELPHI detector at the highest LEP energies, Eur. Phys. J. C37 (2004) 1–23. arXiv:hep-ex/0406011, doi:10.1140/epjc/s2004-01889-x.

[81] P. Achard *et al.*, Studies of hadronic event structure in e+e- annihilation from 30 to 209gev with the l3 detector, Physics Reports 399 (2) (2004) 71 – 174. doi:https://doi.org/10.1016/j.physrep.2004.07.002.
URL http://www.sciencedirect.com/science/article/pii/S0370157304002753

[82] F. James, MINUIT Function Minimization and Error Analysis: Reference Manual Version 94.1.

[83] H. Li, Higgs Recoil Mass and Cross-Section Analysis at ILC AND Calibration of the CALICE SiW ECAL Prototype, Ph.D. thesis, Orsay (2009-09).
URL https://tel.archives-ouvertes.fr/tel-00430432/fr/

[84] H. Abramowicz *et al.*, Forward Instrumentation for ILC Detectors, JINST 5 (2010) P12002. arXiv:1009.2433, doi:10.1088/1748-0221/5/12/P12002.

[85] T. Abe *et al.*, The International Large Detector: Letter of IntentarXiv:1006.3396, doi:10.2172/975166.

[86] A. Droll, H. E. Logan, Physics impact of ilc higgs coupling measurements: The effect of theory uncertainties, Phys. Rev. D 76 (2007) 015001. doi:10.1103/PhysRevD.76.015001.
URL https://link.aps.org/doi/10.1103/PhysRevD.76.015001

[87] K. Fujii *et al.*, Physics Case for the 250 GeV Stage of the International Linear ColliderarXiv:1710.07621.

[88] M. Aaboud *et al.*, Measurement of the Higgs boson coupling properties in the $H \to ZZ^* \to 4\ell$ decay channel at $\sqrt{s} = 13$ TeV with the ATLAS detector, JHEP 03 (2018) 095. arXiv:1712.02304, doi:10.1007/JHEP03(2018)095.

[89] K. Kondo, Dynamical likelihood method for reconstruction of events with missing momentum. i. method and toy models, Journal of the Physical Society of Japan 57 (12) (1988) 4126–4140. doi:10.1143/JPSJ.57.4126.
URL https://doi.org/10.1143/JPSJ.57.4126

[90] K. Kondo, Dynamical likelihood method for reconstruction of events with missing momentum. ii. mass spectra for $2 \to 2$ processes, Journal of the Physical Society of Japan 60 (3) (1991) 836–844. doi:10.1143/JPSJ.60.836.
URL https://doi.org/10.1143/JPSJ.60.836

[91] K. Kondo, T. Chikamatsu, S.-H. Kim, Dynamical likelihood method for reconstruction of events with missing momentum. iii. analysis of a cdf high pt eμ event as $t\bar{t}$ production, Journal of the Physical Society of Japan 62 (4) (1993) 1177–1182. doi:10.1143/JPSJ.62.1177.
URL https://doi.org/10.1143/JPSJ.62.1177

[92] V. M. Abazov *et al.*, A precision measurement of the mass of the top quark, Nature 429 (2004) 638–642. arXiv:hep-ex/0406031, doi:10.1038/nature02589.

[93] V. M. Abazov *et al.*, Measurement of the top quark mass in the lepton+jets final state with the matrix element method, Phys. Rev. D 74 (2006) 092005. doi:10.1103/PhysRevD.74.092005.
URL https://link.aps.org/doi/10.1103/PhysRevD.74.092005

[94] F. Fiedler *et al.*, The matrix element method and its application to measurements of the top quark mass, Nuclear Instruments and Methods in Physics Research Section A: Accelerators, Spectrometers, Detectors and Associated Equipment 624 (1) (2010) 203 – 218. doi:https://doi.org/10.1016/j.nima.2010.09.024.
URL http://www.sciencedirect.com/science/article/pii/S0168900210020176

[95] Y. Takubo *et al.*, Measuring anomalous couplings in $h \to WW^*$ decays at the international linear collider, Phys. Rev. D 88 (2013) 013010. doi:10.1103/PhysRevD.88.013010.
URL https://link.aps.org/doi/10.1103/PhysRevD.88.013010

Acknowledgement

The author would like to thank Keisuke Fujii and Junping Tian for their strong support, advises, corrections, and teaching on the physics study, and also Daniel Jeans for teaching me English. In the end, the author would also like to really thank Toru Takeshita and Katsushige Kotera on their many guidance in this field and attitude toward a study. I continued to work hard during this more than 5 years, maybe because of you, Kotera-san, and I will keep it! ... Oh, no, I almost forgot! thank Makoto Kobayashi (not a laureate of Nobel prize) for your lectures on TPC experiments over night, over night, and over night :).

A The other channels for the anomalous ZZH couplings

A.1 $e^+e^- \to Zh \to e^+e^-h$ at $\sqrt{s} = 250$ GeV

The electron channel of the Higgs-strahlung Zh process has a similar signature with the muon channel, thus this channel is also expected to give the similar sensitivity to the anomalous ZZH couplings as with the muon channel although the effect of the photon radiations could be larger compared with the muon channel. The strategy of the analysis of the electron channel is basically same as the muon channel.

A.1.1 Reconstruction and background suppression

Isolated lepton finding and radiation recovering :

Finding the final state electrons and recovering the photon radiations in the electron channel is performed as with the muon channel using the MVA based lepton finding algorithm.

- charged particle has momentum of more than 5 GeV.
- MLP response for the electron candidate must be larger than 0.5.
- Neutral particles which are identified as a photon are merged into the charged particle if the polar angle between both exceeds 0.99.

Charged tracks that the algorithm gives electron-likeness of > 0.5 are regarded as the isolated electron, and the candidates of the electron decaying from the Z boson are paired to find the proper electrons as the daughter particles of the Z boson. After finding the proper electron-positron pair, the algorithm for receiving the radiated photons is implemented, which is the once based technique mentioned in the section of the muon channel.

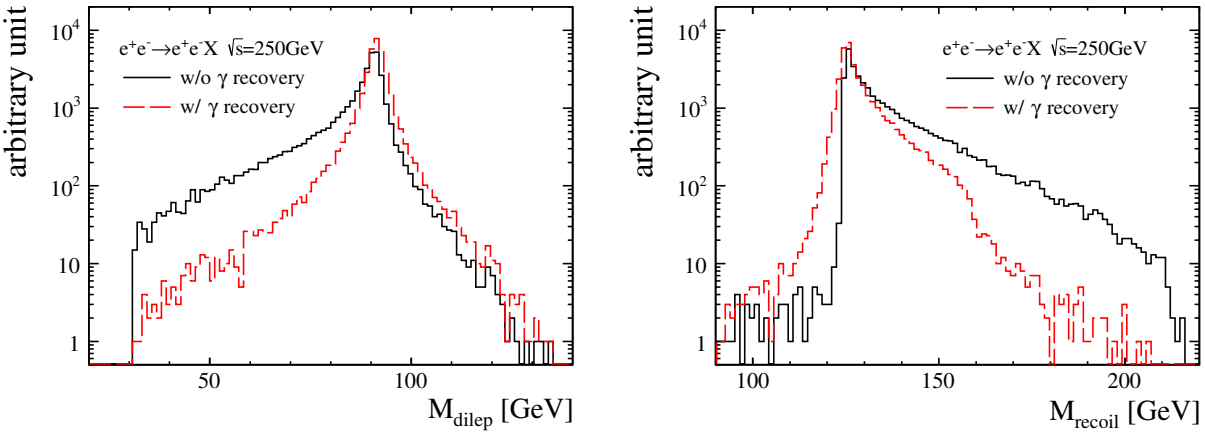

Figure 101: Distributions of the invariant mass of the electron pair M_{ll} (left) and the recoil mass M_{reco} (right) of the electron channel in the Higgs-strahlung Zh process at $\sqrt{s}$=250 GeV. Black and red lines on both plots correspond to without and with recovering photons, respectively.

Fig. 101 show the comparison of the reconstructed invariant mass of the electron pair M_{ll} and the recoil mass distributions of the electron channel with and without recovering the bremsstrahlung and FSR. Since the electron tends to emit the photons, it is clearly seen that the algorithm for recovering the radiated photons is more effective compared to the muon channel.

Reconstructed angular observables :

Plots in Fig. 102 show the reconstructed observables on the polar angle of the Z boson $\cos\theta_Z$ and the angle between production planes $\Delta\Phi$, which are sensitive to the anomalous ZZH couplings. The distribution of $\Delta\Phi$ has clear dips at 0, π, and 2π, which is the same situation with the muon

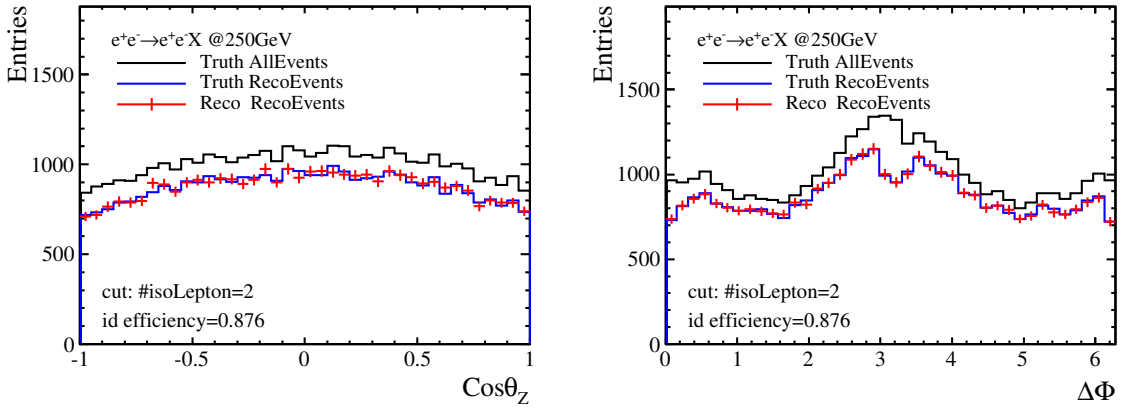

Figure 102: Plots show the MC truth and reconstructed distributions (left), the migration effects (middle), and resolutions (right) of $\cos\theta_Z$, $\cos\theta^*_f$, and $\Delta\Phi$ of the electron channel in the Higgs-strahlung Zh process at $\sqrt{s}$=250 GeV. Those observables give the sensitivities to the anomalous ZZH couplings. The clear dips at 0, π, and 2π on $\Delta\Phi$ is due to the missing final state electrons.

channel as shown in Fig. 55, which is due to the missing one or both final state fermions coming from Z. The overall acceptance is bit worse compared to the muon channel, which is shown in the plots between Fig. 102 and Fig. 55 or a table in Table 7. This is probably because the invariant mass of the di-lepton system, which should be close to the mass of the Z boson, is rather shifted from the constraints because of radiated photons due to the bremsstrahlung of the final state electron and positron.

Background suppression :

The observables used for the background suppression are same ones with the muon channel although detailed values are optimized for the electron channel. The following observables and values given in parentheses are imposed for the background suppressions in the electron channel, where the values are for the left-handed polarization state: P(e^-, e^+)= (-80%,+30%). The distributions of the each observable for suppressing the backgrounds and the recoil mass of the Z boson are plotted in Fig. 103, and the Table 7 shows the number of remaining signal and background events after each cut, where the integrated luminosity of 250 fb^{-1} with both of the beam polarization states: P(e^-, e^+)= (-80%,+30%) and (+80%,-30%) are assumed. The signal efficiency and the signal significance are also given for each cut.

- Two leptons having opposite sign with the same flavor must exist exactly in one event (electron and anti-electron), which is given as a pre-selection.
- $N_{tracks} \in [6,\ 60]$
  The number of charged tracks, which is useful to remove huge two-fermion backgrounds.
- $E_Z \in [103.1,\ 112.5]$ GeV
  Since energy of the di-lepton system derived from one of the dominant background process $e^+e^- \to ZZ \to$ semi-leptonic decay has a peak at 125 GeV, this observable is useful to separate it.
- $M_Z \in [86.0,\ 97.3]$ GeV
  The invariant mass of di-lepton $M_{e^+e^-}$ must be close to the mass of the Z boson.
- $E_{vis} - E_Z(\equiv E_{sub}) \in [50.0,\ 165.0]$ GeV
  Visible energy shows measured energy in the detectors. The subtracted value by the energy of the Z boson is close to 0 for the two-fermion process, which is still useful to distinguish the Higgs boson from other dispersed backgrounds.
- $M_{rec} \in [119,\ 138]$ GeV
  Recoil mass against the di-lepton system, which becomes a conclusive mass window to deter-

mine a Poisson error calculated by the remaining number of events on each bin on kinematical histograms.

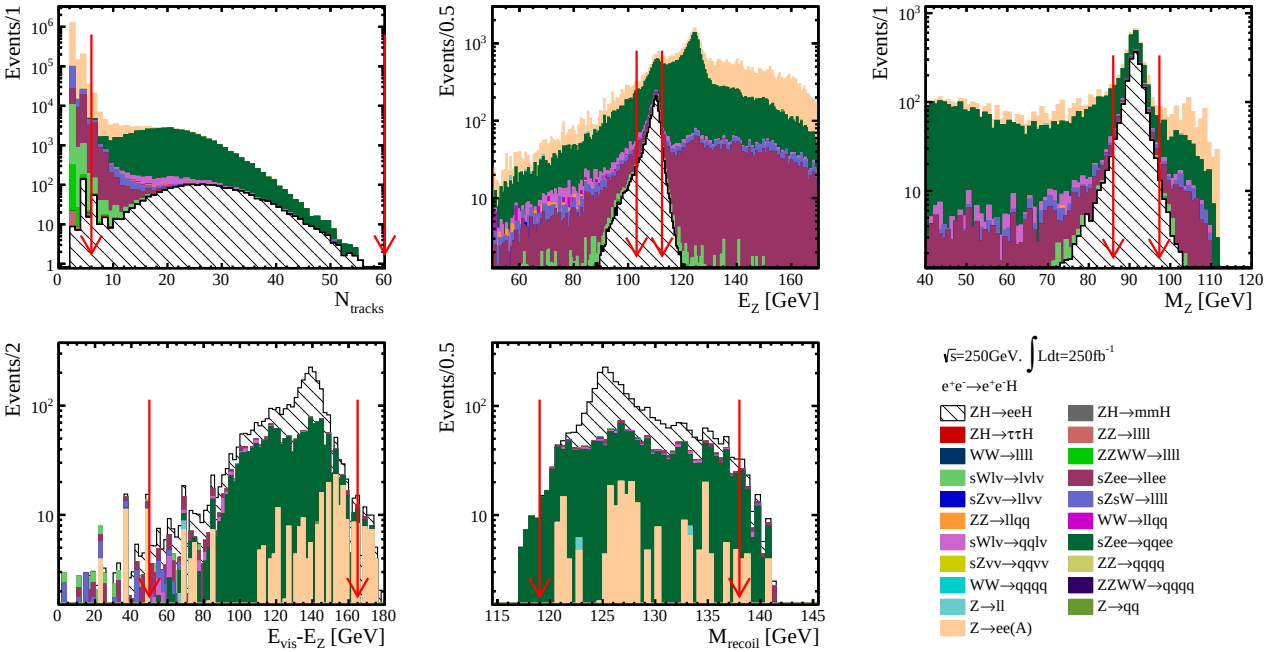

Figure 103: The distributions show each observable used for the background suppression assuming 250 fb^{-1} with P(e^-, e^+)= (-80%,+30%). The explanation of the observables are given in the text. Red arrows on each plot indicate the cut values applied to each observable as the background suppression.

A.1.2 Acceptance and migration on observables

Fig. 104 and Fig. 105 illustrate summary plots showing the remaining signal and background distributions, event acceptance η, and the probability of the migration effects $\bar{f}$ on the one-dimensional angular distribution of $\cos\theta_Z$ and $\Delta\Phi_{f\bar{f}}$ binned in 30. Similarly, Fig. 106 show summary plots on the two-dimensional distribution of $x(\cos\theta_Z, \Delta\Phi_{f\bar{f}})$ binned in 10×10. The event acceptance for each angular distribution retain flatness over the given range except the ineluctable dips in $\Delta\Phi_{f\bar{f}}$. However, he probabilities of the migration effects slightly worse compared to the muon channel as shown in Fig. 57 although it is still great clear compared to the hadronic channel as shown in Fig. 67. This is because the recovery of the radiated photons is not complete. Since the radiated photons carry away moment from the electron, the measured moment of di-lepton will be shifted as if the radiated photons are not complete combined.

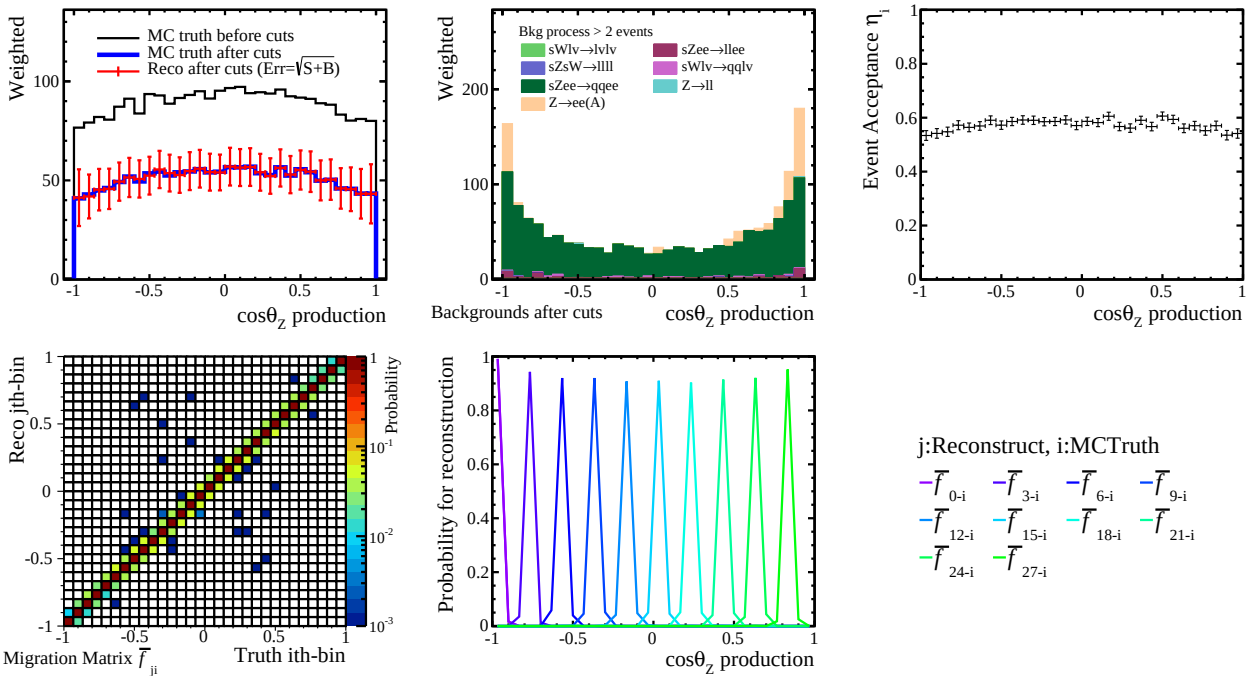

Figure 104: The distributions show the summary of the polar angle of the Z boson ($\cos\theta_Z$) after the background suppression. (Top left and middle): the remaining signal and the background distribution, which are given with the MC truth and the reconstructed, where the statistical error is given as the standard deviation of the Poisson probability. (Top right): the event acceptance function η_i. (Bottom left and middle): the distribution shows the probability matrix of the migration ($\bar{f}_{ji}$) that is applied for the reconstruction of the realistic distribution of $\cos\theta_Z$, and the cross-sections of $\bar{f}_{ji}$ as 1-dim plots.

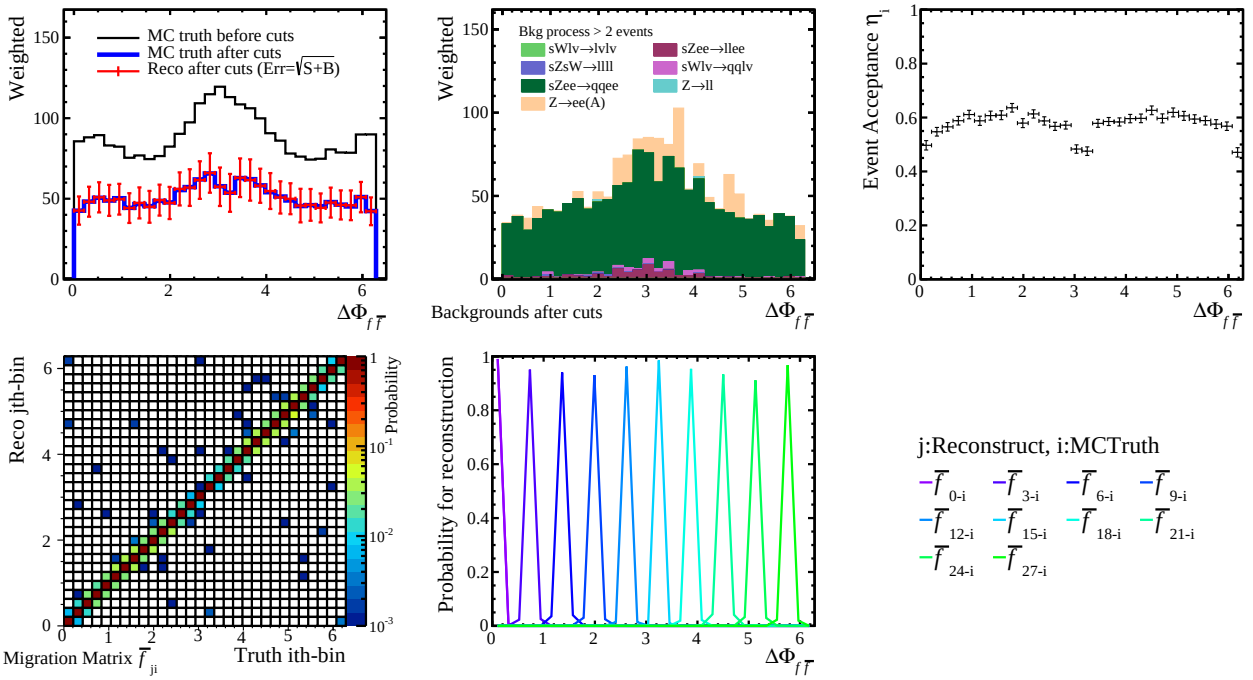

Figure 105: The distributions show the summary of the angle between production planes in the laboratory frame ($\Delta\Phi$) after the background suppression. (Top left and middle): the remaining signal and the background distribution, which are given with the MC truth and the reconstructed. (Top right): the event acceptance function η_i. (Bottom left and middle): the probability matrix of the migration ($\bar{f}_{ji}$) that is applied for the reconstruction of $\Delta\Phi$, and the cross-sections of $\bar{f}_{ji}$ as 1-dim plots.

Table 7: Tables show the expected number of remaining signal and background events after each cut for the $Zh \to e^+e^-h$ at $\sqrt{s}$=250 GeV, with both of the beam polarization states: P(e^-, e^+)= (-80%,+30%) and (+80%,-30%). The integrated luminosity of 250 fb^{-1} is assumed. The signal efficiency ϵ and significance S_{sig} are also given in the table.

$\sqrt{s}$=250 GeV P(e^-, e^+)= (-80%,+30%)

Cut variables	$(s)eeh$	ϵ	$\mu\mu h$	$\tau\tau h$	$2f$	$4f$	S_{sig}
No cut	2671	100	2603	2598	$2.91 \cdot 10^7$	$1.02 \cdot 10^7$	-
ID of a di-lepton pair	2343	87.72	1	12	$1.54 \cdot 10^6$	$1.87 \cdot 10^5$	1.78
$N_{tracks} \in [6,\ 60]$	2171	81.28	0	9	$3.46 \cdot 10^4$	$4.83 \cdot 10^4$	7.44
$E_Z \in [103.1,\ 112.5]$ GeV	1721	64.43	0	1	1641	5706	18.1
$M_Z \in [86.0,\ 97.3]$ GeV	1588	59.45	0	1	337	1179	28.5
$E_{sub} \in [50.0,\ 165.0]$ GeV	1551	58.07	0	1	270	1120	28.6
$M_{reco} \in [119,\ 138]$ GeV	1532	57.36	0	1	254	1036	28.8

$\sqrt{s}$=250 GeV P(e^-, e^+)= (+80%,-30%)

Cut variables	$(s)eeh$	ϵ	$\mu\mu h$	$\tau\tau h$	$2f$	$4f$	S_{sig}
No cut	1786	100	1756	1752	$2.03 \cdot 10^7$	$1.27 \cdot 10^6$	-
ID of a di-lepton pair	1566	87.68	0	8	$1.51 \cdot 10^6$	$8.95 \cdot 10^4$	1.24
$N_{tracks} \in [6,\ 60]$	1452	81.30	0	6	$3.37 \cdot 10^4$	$3.75 \cdot 10^4$	5.38
$E_Z \in [103.8,\ 112.5]$ GeV	1128	63.16	0	0	1516	4218	13.6
$M_Z \in [86.0,\ 96.0]$ GeV	1026	57.44	0	0	268	811	22.4
$E_{sub} \in [50.0,\ 165.0]$ GeV	1002	56.10	0	0	205	787	22.4
$M_{reco} \in [119,\ 138]$ GeV	998	55.88	0	0	201	750	22.6

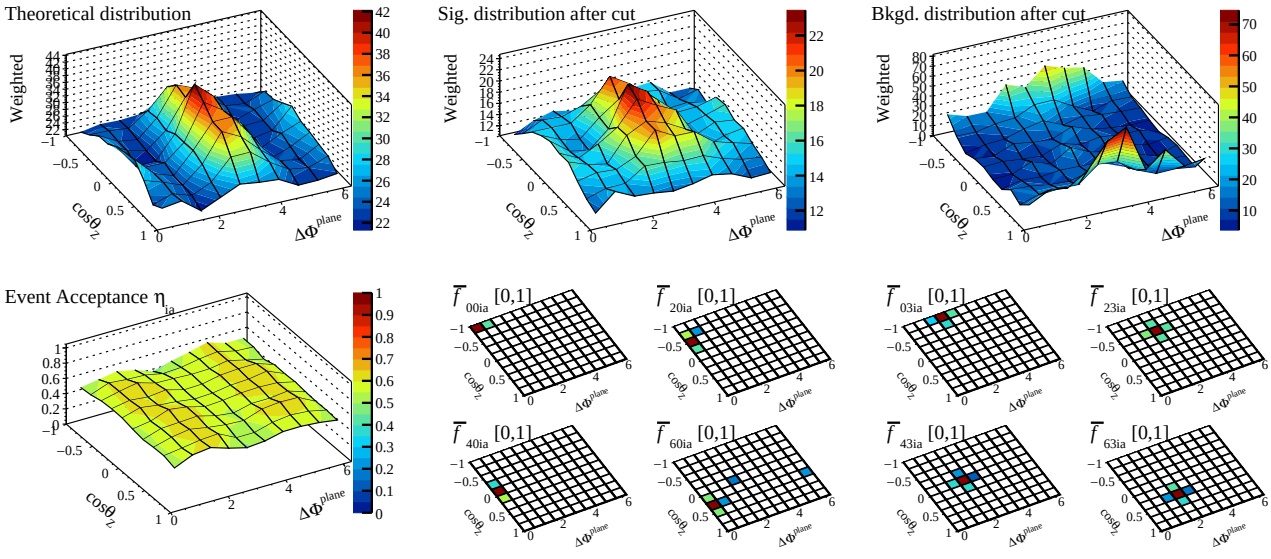

Figure 106: The distributions show the summary of the two-dimensional distribution consisted of the production angle of the Z boson $\cos\theta_Z$ and the angle between production planes in the laboratory frame ($\Delta\Phi$) after the background suppression. (Top left, middle, and right): The remaining MC truth and the reconstructed signal distribution, and the background distribution, respectively. (Bottom left): The event acceptance function η_{ia} shows whether each signal event on each bin is accepted or not after the suppression. (Bottom middle and right): Several examples on the probability matrix of the migration where the 2-dim plots give the cross-sections of $\bar{f}_{jbia}$ since the illustration of the migration is too difficult which is a 4-dimension distribution.

A.1.3 Impact of angular distribution

The χ^2 test is performed for the electron channel only, using the evaluated event acceptance η, the probability of the migration effects $\bar{f}$, and statistical error. Fig. 107 show the $\Delta\chi^2$ distributions in the one parameter axis of the anomalous couplings a_Z, b_Z, and $\tilde{b}_Z$. The sensitivities are individually evaluated using the one-dimensional distributions of $\cos\theta_Z$ and $\Delta\Phi$ are binned 20, and the three-dimensional distribution of $x(\cos\theta^*_f, \cos\theta_Z, \Delta\Phi_{f\bar{f}})$ binned in $5\times5\times5$ respectively for both of the beam polarization states. The overall power from the angular information of the electron channel is slightly worse than that of the muon channel because the remaining SM backgrounds are more compared to the muon channel. Especially, two-fermion events remain in the very forward and backward region, which are the sensitive area to the anomalous couplings, and it makes statistical error increase and the impact of the angular information degrade, which is clearly seen in the plot of Fig. 104 showing the $\cos\theta_Z$ distribution. It also remains around π of the $\Delta\Phi$ distribution as well, which is also shown in Fig. 105 (π in $\Delta\Phi$ corresponds to the very forward and backward directions).

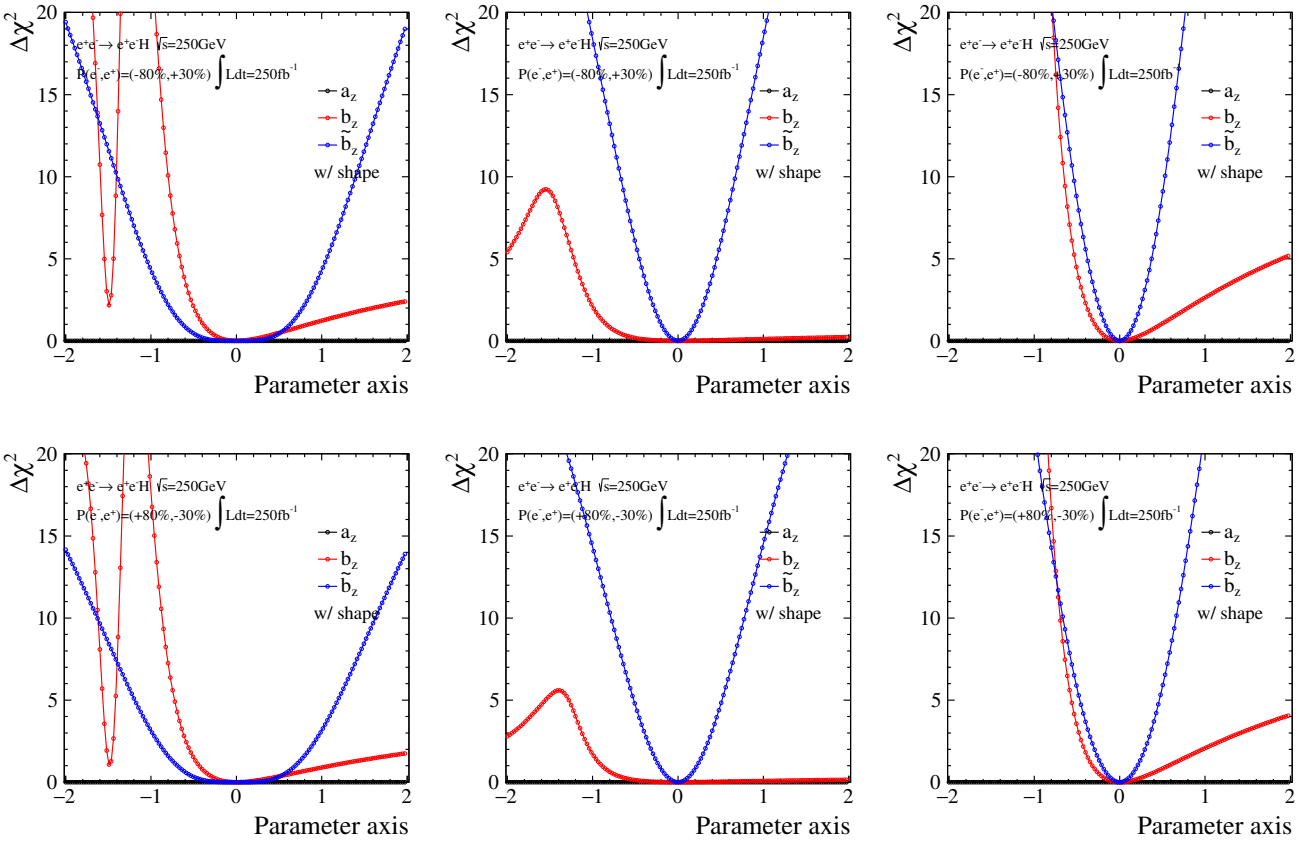

Figure 107: The distributions show $\Delta\chi^2$ as a function of each parameter of the anomalous ZZH couplings, and the evaluation is done in the one-parameter space. Black, red, and blue lines on the plots correspond to the parameters a_Z, b_Z, and $\tilde{b}_Z$. Since only the angular information is considered here, the χ^2 values of a_Z is exactly 0 over the given range. In upper and lower plots, the different beam polarizations are assumed with the integrated luminosity of 250 fb^{-1}: P(e^-, e^+)= (-80%,+30%) and (+80%,-30%), respectively. Difference of each column is the angular distributions used for the evaluation: (left) $x(\cos\theta_{Z)}$ binned in 20, (middle) $x(\Delta\Phi_{f\bar{f}})$ binned in 20, and (right) $x(\cos\theta^*_f, \cos\theta_Z, \Delta\Phi_{f\bar{f}})$ binned in $5\times5\times5$ are used respectively.

A.1.4 Sensitivity in three parameter space

The sensitivity to the anomalous ZZH couplings with the electron channel only is evaluated assuming the integrated luminosity of 250 fb^{-1} with both of the beam polarization states: P(e^-, e^+)= (-80%,+30%) and (+80%,-30%). The variation of the angular distribution of the three-dimensional distribution $x(\cos\theta^*_f, \cos\theta_Z, \Delta\Phi_{f\bar{f}})$ binned in 5×5×5 , and the variation of the production cross-section are combined. The minimization fitting is done in the three-parameter space of the anomalous couplings.

Upper plots in Fig. 108 give contours corresponding to 1σ and 2σ bounds, which are projected onto each two-dimensional parameter space a_Z-b_Z, a_Z-$\tilde{b}_Z$, and b_Z-$\tilde{b}_Z$ after the simultaneous fitting in the three-parameter space. The strong correlation can be seen between a_Z and b_Z as shown in the muon channel. Middle plots in Fig. 108 give $\Delta\chi^2$ distributions as a function of each anomalous parameter a_Z, b_Z, and $\tilde{b}_Z$. The evaluation is performed by scanning $\Delta\chi^2$ along the parameter axis while setting the other two parameters free, which corresponds to the simultaneous minimization in the three parameter space. The results are given using both of the angular and the cross-section information of the electron channel only. Explicit values corresponding to the 1σ bounds for each anomalous parameter a_Z, b_Z, and $\tilde{b}_Z$ and a correlation matrix ρ indicating correlation coefficients between the parameters are given in the last line of Fig. 108. Both beam polarization states P(e^-, e^+)= (-80%,+30%) and (+80%,-30%) with the benchmark integrated luminosity of 250 fb^{-1} are assumed.

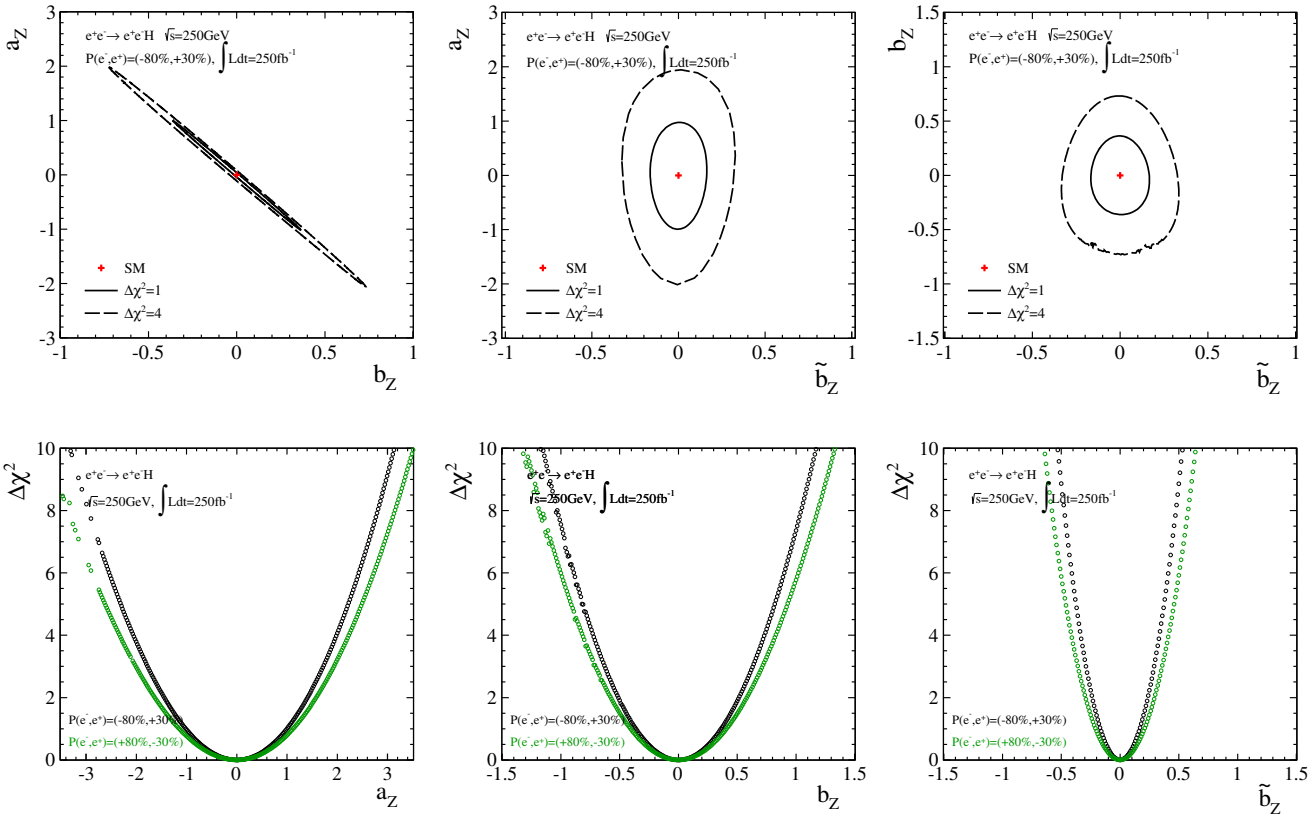

$$\sqrt{s} = 250 \text{ GeV with } \int \text{Ldt} = 250 \text{ fb}^{-1} \text{ and } \text{P}(e^-, e^+) = (-80\%, +30\%)$$

$$\begin{cases} a_Z = [-1.015, \quad 0.997] \\ b_Z = [-0.362, \quad 0.363] \\ \tilde{b}_Z = [-0.167, \quad 0.167] \end{cases}, \quad \rho = \begin{pmatrix} 1 & -0.9989 & 0.0316 \\ - & 1 & -0.0339 \\ - & - & 1 \end{pmatrix}$$

$$\sqrt{s} = 250 \text{ GeV with } \int \text{Ldt} = 250 \text{ fb}^{-1} \text{ and } \text{P}(e^-, e^+) = (+80\%, -30\%)$$

$$\begin{cases} a_Z = [-1.146, \quad 1.121] \\ b_Z = [-0.407, \quad 0.410] \\ \tilde{b}_Z = [-0.208, \quad 0.208] \end{cases}, \quad \rho = \begin{pmatrix} 1 & -0.9981 & -0.0747 \\ - & 1 & 0.0715 \\ - & - & 1 \end{pmatrix}$$

Figure 108: (Upper): The plots show contours corresponding to the 1σ and 2σ sensitivities to the anomalous ZZH couplings. The fitting is performed with the muon channel only under the three free parameter space. The integrated luminosity of 250 fb^{-1} with the beam polarization state P(e^-, e^+)= (-80%,+30%) is assumed. The results are projected onto the two-dimensional parameter spaces a_Z-b_Z, a_Z-$\tilde{b}_Z$, and b_Z-$\tilde{b}_Z$. Both of the information, which are the three-dimensional distributions $x(\cos\theta^*_f, \cos\theta_Z, \Delta\Phi_{f\bar{f}})$ binned in $5\times5\times5$ and the production cross-section are combined. (Middle): The plots show $\Delta\chi^2$ distributions as a function of each parameter space of the anomalous couplings a_Z, b_Z, and $\tilde{b}_Z$. The distributions are obtained by using both information (the angles and the cross-section) and scanning one parameter while setting the other two parameters to be completely free. (Lower): The explicit values corresponding to the 1σ bounds for each anomalous parameter a_Z, b_Z, and $\tilde{b}_Z$ and the correlation matrix indicating correlation coefficients between the parameters.

A.2 $e^+e^- \to e^+e^-h,\ h \to b\bar{b}$ at $\sqrt{s} = 250$ GeV

At the center-of-mass energy $\sqrt{s}$ =250 GeV the cross section of the ZZ-fusion process $e^+e^- \to e^+e^-h$ predicted with the SM parameters is very small, which is approximately 0.71 fb, and it is be 0.41 fb when the $h \to bb$ decay is considered. Nevertheless, the variation of both of the production cross-section and the angular distribution depending on the anomalous ZZH couplings is expected to give good information and improvement of the sensitivity to these couplings. In the case that events are accumulated through the ILC full operation, the ZZ-fusion process would give sizable impact for the sensitivity, even at $\sqrt{s}$ =250 GeV.

A.2.1 Reconstruction and background suppression

The production cross-section of the ZZ-fusion process at 250 GeV is

Isolated lepton finding and radiation recovering :

Concerning the selection of the final state electron pair, MVA based selection is implemented as with the analysis of the Higgs-strahlung process. However, the identification that the isolated leptons are derived from the Z boson is not implemented in this channel.

- A charged particle must have momentum of greater than 5 GeV.
- MLP response for the electron candidate must be larger than 0.5.
- A neutral particle which is identified as a photon based on the criterion that the polar angle along the charged particle exceeds 0.999 is merged into the charged particle as a radiated photon because of bremsstrahlung.

The comparison with and without the recovering is given in Fig. 109.

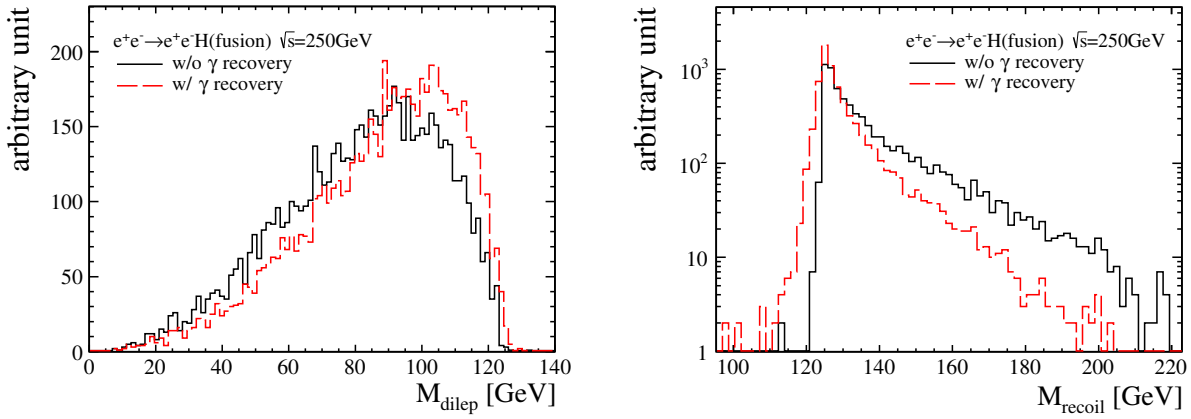

Figure 109: Distributions of the invariant mass of the electron pair M_{dilep} (left) and the recoil mass M_{reco} (right) of the ZZ-fusion process at $\sqrt{s}$=250 GeV. Black and red lines on both plots correspond to without and with recovering photons, respectively.

Suppression with MVA method :

A problem of the t-channel ZZ-fusion process at $\sqrt{s}$ =250 GeV is irreducible dominant backgrounds that are the s-channel Higgs-strahlung Zh process and processes being consisting of single Z boson and a pair of an electron and a positron (single Zee). Both of the processes are quite large production cross-sections, compared with the ZZ-fusion process at $\sqrt{s}$ =250 GeV. Furthermore, these dominant backgrounds make a peak at the invariant mass of the Z boson in which the signal process also makes a broader peak. Because these dominant backgrounds are

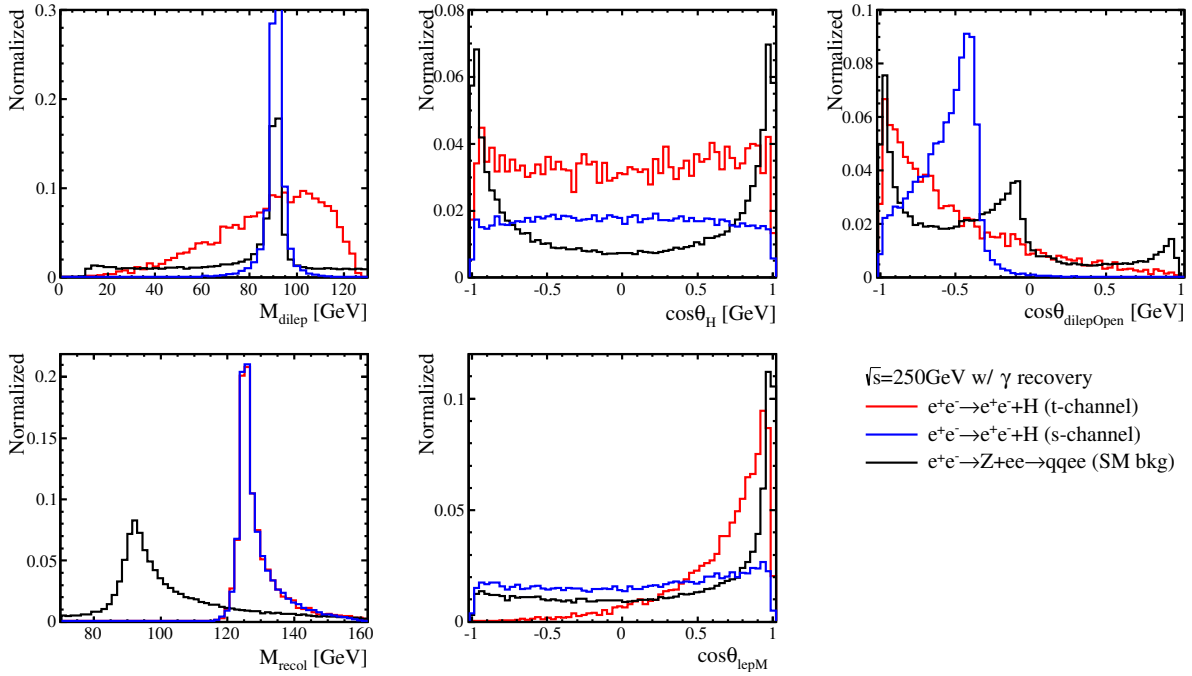

Figure 110: The distributions show the several observables in the signal and the dominant backgrounds processes at 500 GeV: the di-lepton mass M_{dilep}, the polar angle of the Higgs boson $\cos\theta_h$, the opening angle in the di-lepton system $\cos\theta_{ep}^{open}$, the recoil mass against the di-lepton system M_{reco}, and the polar angle of the final state electron $\cos\theta_e$. Red line is the signal process of the ZZ-fusion.

completely overlapped as given in Fig. 110, it makes difficult to separate the signal and the backgrounds. Therefore, multivariate analysis implemented in a TMVA package is employed to exploit combination of kinematical observables and extract the signal process.

Although the original strategy of the analysis is that any angular observables and corresponding information should not be used for the background suppression in order to avoid insensitive regions which become bias against the sensitivity to the anomalous couplings, distributions such as the production angles of the Higgs boson $\cos\theta_h$ and the final state electron $\cos\theta_e$ and positron $\cos\theta_p$ are input into MVA training as variables. The observables input into the MVA are: $\cos\theta_h$, $\cos\theta_e$, $\cos\theta_p$, M_{dilep} which is the invariant mass of the di-lepton system, and M_{higgs} which is calculated with two b-jets decaying from the Higgs boson. Fig. 111 gives performance showing rejection-efficiency on several main MVA classifiers, and response of BDT classifier which gives the best performance among the MVA classifiers.

The following observables and values are imposed for the background suppressions. The distributions of each observable for the suppression, the BDT output, and the invariant mass of the Higgs boson are shown in Fig. 112, and the reduction tables showing the number of remaining signal and background events in each cut is given in Table 8, where the integrated luminosity of 250 fb^{-1} with the beam polarization states P(e^-, e^+)= (-80%,+30%) and (+80%,-30%) are assumed. The signal efficiency and the signal significance are also given for each cut.

- There must exist one electron and one positron exactly in one event.
- $E_{tracks} \in [15,\ 55]$

  Since the final state of the signal process has multi jet environment, the number of charged tracks are larger than that of leptonic processes. This observable is applied as a pre-cut before MVA training.
- Sum of b-tag for di-jets coming from the Higgs boson > 1.004

  Sum of the b-likeness of di-jet decaying from the Higgs boson has a large value. This observable is applied as a pre-cut before MVA training.

- $\cos\theta_h \in [-0.920,\ 0.920]$

  There is no preferable production direction since spin of the Higgs boson is 0 while a Z boson has a specific direction. Thus this observable is useful for supreeing several processes such as a single $Z+$ electron pair process. This observable is inputted into the MVA training.

- $\cos\theta_e \in [-0.200,\ 0.986]$ and $\cos\theta_p \in [-0.986,\ 0.204]$

  Since the signal process is the t-channel interaction, the final state electron and positron flies towards the very forward and backward regions. This observable is useful to remove the s-channel Higgs production which has the same final state. This observable is inputted into the MVA training.

- $M_{dilep} \in [25.17,\ 124.83]$

  Since the dominant backgrounds make a peak at the invariant mass of the Z boson and these are completely overlapped with the signal process, this is not powerful for the particular processes. Nevertheless the other broader backgrounds can be suppressed with this observable. This observable is inputted into the MVA training.

- $M_{reco} \in [119.95,\ 146.35]$

  This observable is useful to remove one of the dominant backgrounds which is a single Z with an electron pair process and it makes a peak at M_Z.

- BDT > 0.14

  BDT response after training and testing using the inputted five observables, which are explained in the above text.

- $M_{dijet} \in [90,\ 160]$

  The invariant mass of the Higgs boson calculated with the di-jet system, which is a mass window to determine a statistical error calculated using the remaining number of events on each bin of the distribution

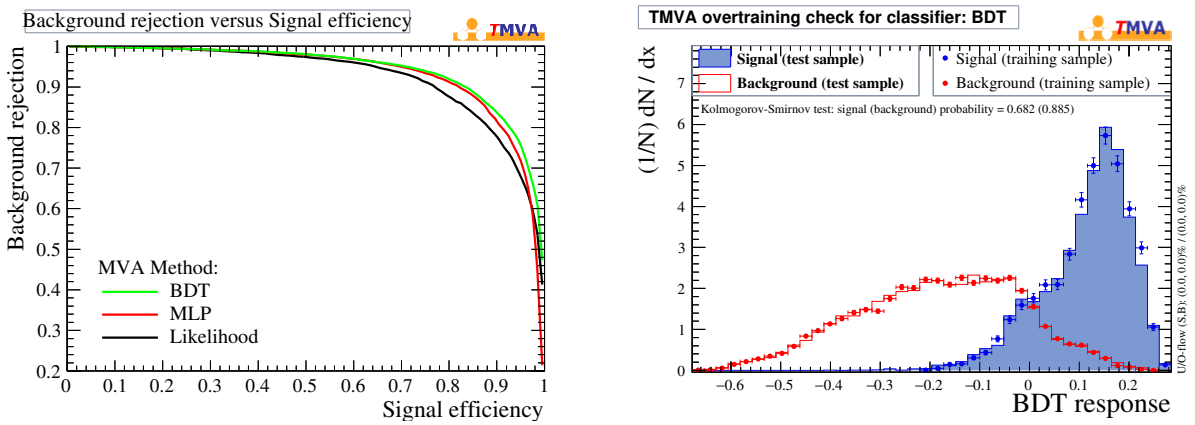

Figure 111: (Left) A plot shows Receiver Operating Characteristic (ROC) curves for each MVA classifiers, which gives the performance of the classifiers. (Right) Response of the BDT classifier for the signal and background processes.

A.2.2 Acceptance and migration on observables

Fig. 113 and Fig. 114 are the summary plots showing the Higgs momentum P_h and the angle between production planes $\Delta\Phi$ in the Higgs rest-frame. Since the number of remaining events is too less because of the small production cross-section, an available distribution would be the one-dimensional distribution only at $\sqrt{s}$ =250 GeV.

The event acceptance of the $\Delta\Phi$ distribution can maintain the fatness. However, one of the momentum P_h distribution seems to be slightly dropped at higher edge. This is because the

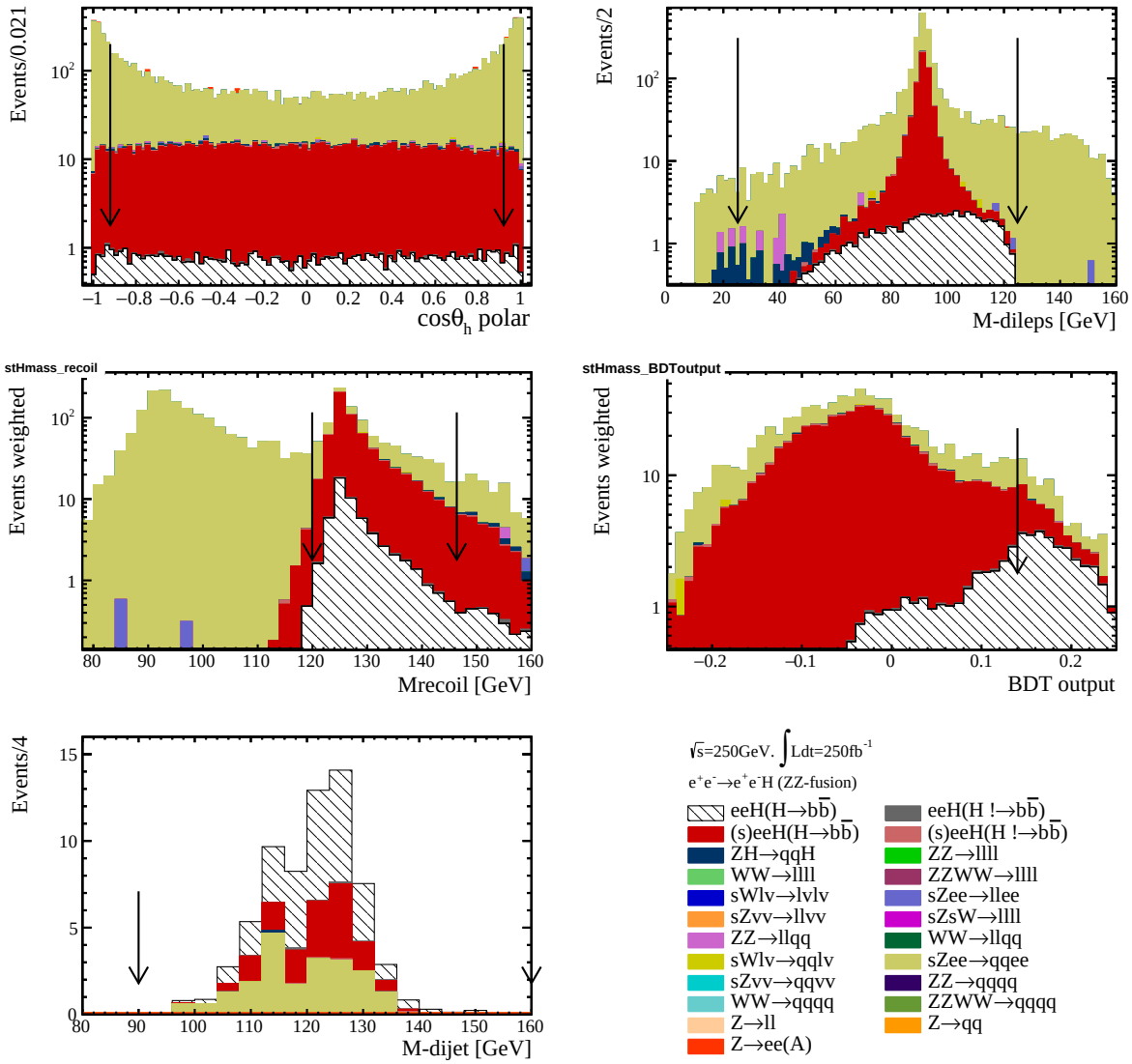

Figure 112: Distributions show each observable used for the background suppression. Explanation of the observables are given in the text. Black arrows on the plots indicate the cut values applied to each observable.

Table 8: The expected number of remaining signal and background events after each cut for the $ZZ \to e^+e^-h,\ h \to b\bar{b}$ at $\sqrt{s}$=250 GeV, with with both of the beam polarization states: P(e^-, e^+)= (-80%,+30%) and (+80%,-30%). The integrated luminosity of 250 fb^{-1} is assumed. The signal efficiency ϵ and significance S_{sig} are also given in the table. (t) and (s) in the table denote t-channel and s-channel Higgs production.

$\sqrt{s}$=250 GeV P(e^-, e^+)= (-80%,+30%)

Cut variables	$(t)eeh(b\bar{b})$	ϵ	$(t)eeh(h \notin b\bar{b})$	$(s)eeh$	$2f$	$4f$	S_{sig}
No cut	103	100	75	2671	$2.91 \cdot 10^7$	$1.02 \cdot 10^7$	-
ID of a ep pair	82	79.61	46	2070	$2.66 \cdot 10^6$	$1.60 \cdot 10^5$	0.05
$N_{tracks} \in [15,\ 55]$	80	77.67	34	1840	4877	$3.64 \cdot 10^4$	0.38
Sum b-tag> 1.004	75	72.81	2	1242	54	6450	0.84
$\cos\theta_h \in [-0.920,\ 0.920]$	68	66.02	1	1153	19	4108	0.93
$\cos\theta_e \in [-0.200,\ 0.986]$	64	62.13	1	711	19	2787	1.07
$\cos\theta_p \in [-0.986,\ 0.204]$	61	59.22	1	580	19	1919	1.19
$M_{dilep} \in [25.17,\ 124.83]$	60	58.25	1	580	6	1569	1.28
$M_{reco} \in [119.95,\ 146.35]$	56	54.39	1	547	0	192	1.98
BDT> 0.14	31	30.10	1	16	0	24	3.68
$M_{reco} \in [90,\ 160]$	31	30.10	1	16	0	24	3.68

$\sqrt{s}$=250 GeV P(e^-, e^+)= (+80%,-30%)

Cut variables	$(t)eeh(b\bar{b})$	ϵ	$(t)eeh(h \notin b\bar{b})$	$(s)eeh$	$2f$	$4f$	S_{sig}
No cut	74	100	54	1786	$2.02 \cdot 10^7$	$1.27 \cdot 10^6$	-
ID of a ep pair	59	79.39	33	1384	$2.60 \cdot 10^6$	$1.20 \cdot 10^5$	0.04
$N_{tracks} \in [15,\ 55]$	58	78.38	24	1231	4743	$2.82 \cdot 10^4$	0.31
Sum b-tag> 1.004	54	72.98	1	830	52	5105	0.69
$\cos\theta_h \in [-0.884,\ 0.884]$	47	63.51	1	746	18	2889	0.77
$\cos\theta_e \in [+0.272,\ 0.986]$	39	52.70	1	302	18	1459	0.92
$\cos\theta_p \in [-0.986,\ 0.153]$	35	47.30	1	232	18	875	1.04
$M_{dilep} \in [31.67,\ 123.83]$	35	47.30	1	232	6	639	1.16
$M_{reco} \in [119.4,\ 147.45]$	33	44.60	1	221	0	83	1.79
BDT> 0.10	23	31.08	0	18	0	19	2.99
$M_{reco} \in [90,\ 160]$	23	31.08	0	18	0	18	2.99

absolute momentum of the Higgs boson is correlated with the invariant mass of the di-lepton system (the electron and the position in the final state) and the opening angle calculated between them as well to a certain extent. These observables are used for the background suppression to remove the huge dominant single Z with a pair of an electron and a positron process. When the final state particles boosted into the very forward and backward area with smaller angles along the beam axis, uncertainty of momentum measurement of a charged track gets worse due to the number of measured points, and also a photon as the bremsstrahlung sometimes become missing. Consequently the momentum of the Higgs boson and both of the opening angle and the invariant mass of the di-lepton system have correlation each other to some extent [17] This tendency is also clearly seen in analysis of 500 GeV process discussed in latter A.6.

The migration effects of both of the observables are not large since the signal reaction has a pair of the electron and the positron, which is clearly seen, and two jets in back-to-back only.

A.2.3 Impact of angular distribution

Fig. 115 show the $\Delta\chi^2$ distributions in the one-parameter space of a_Z, b_Z, and $\tilde{b}_Z$. The one-dimensional kinematical distributions of $x(P_{higgs})$ and $x(\Delta\Phi_{f\bar{f}})$ binned in 5 are only used for demonstrating the sensitivity. The evolution are given for both beam polarization states P(e^-, e^+)= (-80%,+30%) and (+80%,-30%) with the integrated luminosities of L_{int} =250 fb^{-1}. Fig. **??** also show $\Delta\chi^2$ each two-parameter space of a_Z-b_Z, a_Z-$\tilde{b}_Z$, and b_Z-$\tilde{b}_Z$. Since the remaining signal events are too less to extract the sensitivity to the anomalous couplings by using kinematical distributions. the results are not good in this channel.

A.2.4 Impact of production cross-section

Effect of the variation of the production cross-section of the ZZ-fusion process $e^+e^- \to e^+e^-h$ is also included in the evaluation, whose variations as a function of each anomalous parameter are illustrated in Fig. 44. As discussed in Sec. 4.4.4, the error of the production cross-section is given through the error propagation. The left plot in Fig. 116 give $\Delta\chi^2$ in one-dimensional parameter space, where the information of the cross-section is used for the evaluation. The impact on the sensitivity coming from the variation of the cross-section looks large even though the cross-section itself is small at $\sqrt{s}$ =250 GeV. A remarkable thing is that the correlation between the parameters a_Z and b_Z given in the ZZ-fusion process is oppositely correlated compared with that of the Higgs-strahlung process, which can partially squeeze the sensitivity to the anomalous ZZH couplings in

[17] Thinking a simple two-body decay in the laboratory frame, where an initial electron decays into a positron and a vector boson, which have four momentum as follows,

$$\begin{aligned} q_{e^-} &= (E_i,\ 0,\ 0,\ E_i\ ) \\ q_{e^+} &= (E_f,\ 0,\ |\boldsymbol{p}_{e^+}|\sin\phi,\ |\boldsymbol{p}_{e^+}|\cos\phi) \\ q_V &= (E_V,\ 0,\ |\boldsymbol{p}_V|\sin\theta,\ |\boldsymbol{p}_V|\cos\theta) \end{aligned}$$

where $m_{e^-} << E$ is assumed, and ϕ and θ are defined for angles along the beam axis, which give polar angles. When imposing the four-momentum conservation, a relation would be given as,

$$\begin{aligned} q_{e^+}^2 &= (q_{e^-} - q_V)^2 = q_{e^-}^2 - 2q_{e^-}q_V + q_V^2 \\ 0 &= -2E_iE_V + 2E_i|\boldsymbol{p}_V|\cos\theta + M_V^2 \\ \cos\theta &= \frac{E_V}{|\boldsymbol{p}_V|} - \frac{M_V^2}{2E_i|\boldsymbol{p}_V|} \end{aligned}$$

where the mass of positron is assumed to be $m_{e^+} << E_f$. If assuming the vector boson is highly boosted, $M_V << |\boldsymbol{p}_V|$, and ignoring the second term, the equation will be

$$\cos\theta \sim \frac{E_V}{|\boldsymbol{p}_V|} \sim 1 \quad \text{in the limit.}$$

where ϕ has similarly small angle. Therefore, when a high momentum Higgs boson is produced through the ZZ-fusion, the final state positron has small angle, which brings the large opening angle for the e^--e^+ system and relatively larger measurement error for $M_{e^-e^+}$, consequently it becomes correlations.

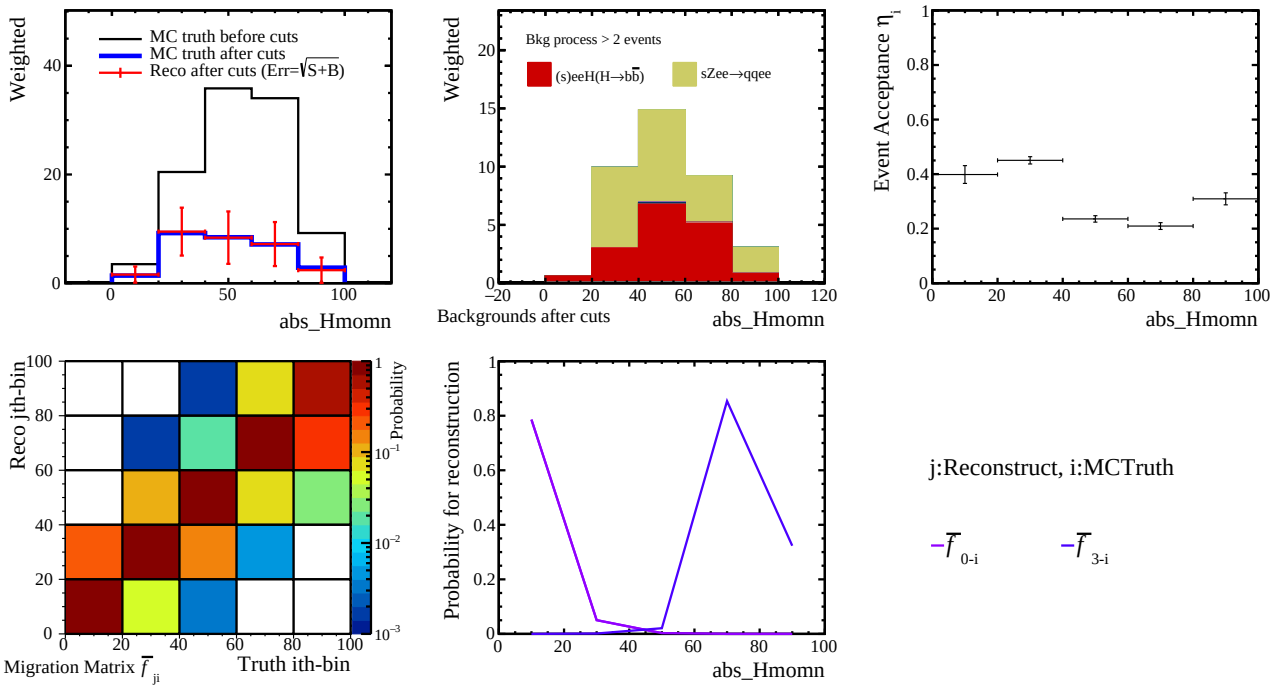

Figure 113: Distributions show the summary on the absolute momentum of the Higgs boson (P_h) after the background suppression. (Top left and middle) The remaining signal (which are given with the MC truth and the reconstructed) and the background distribution, in which the statistical error is given as the standard deviation of the Poisson probability. (Top right) The event acceptance function η_i shows whether each signal event on each bin is accepted or not after the suppression. (Bottom left and middle) The distribution shows the probability matrix of the migration that is applied for reconstructing a realistic distribution of P_h, and several plots of 1d.

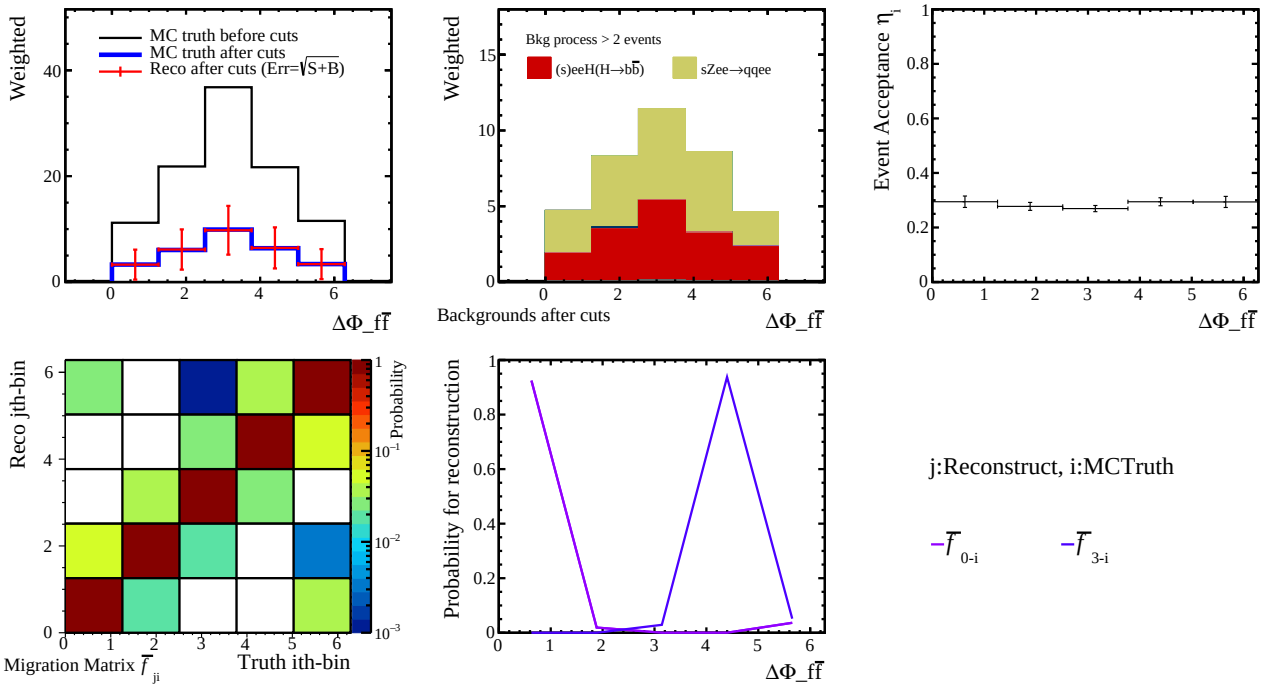

Figure 114: Distributions show the summary on the angle between production planes in the Higgs rest frame ($\Delta\Phi$) after the background suppression. (Top left and middle) The remaining signal and the background distribution. (Top right) The event acceptance function η_i. (Bottom left and middle) The distribution shows the probability matrix of the migration, and several plots of 1d.

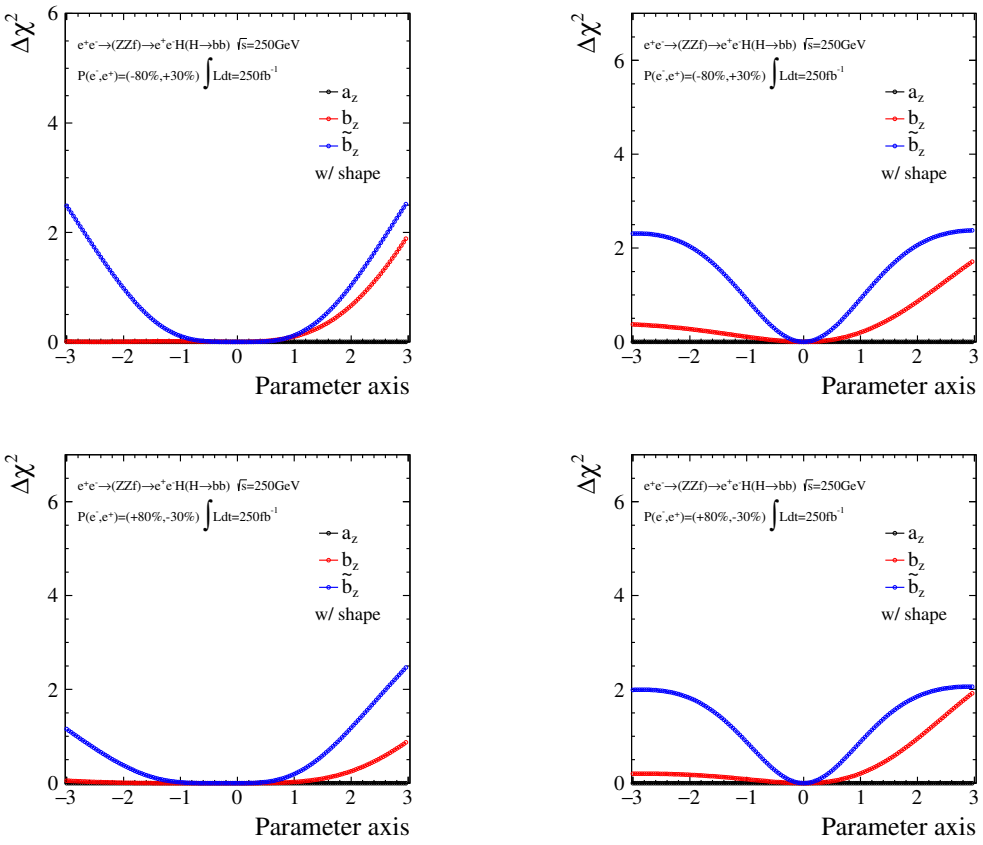

Figure 115: Distributions show $\Delta\chi^2$ as a function of each parameter. The evaluations are done in the one-parameter axis. Each color corresponds to the parameters a_Z, b_Z, and $\tilde{b}_Z$. Since only the angular information is considered, the χ^2 values of a_Z is 0.0 over the given range. In upper and lower plots the different beam polarizations are assumed with the integrated luminosity of 250 fb^{-1}: P(e^-, e^+)= (-80%,+30%) and (+80%,-30%), respectively. Difference of each column is the knematical distributions used for the evaluation: (left) $x(P_{higgs})$ binned in 5, (right) $x(\Delta\Phi_{f\bar{f}})$ binned in 5.

the three parameter space. This behavior was discussed in Sec. 6.3.

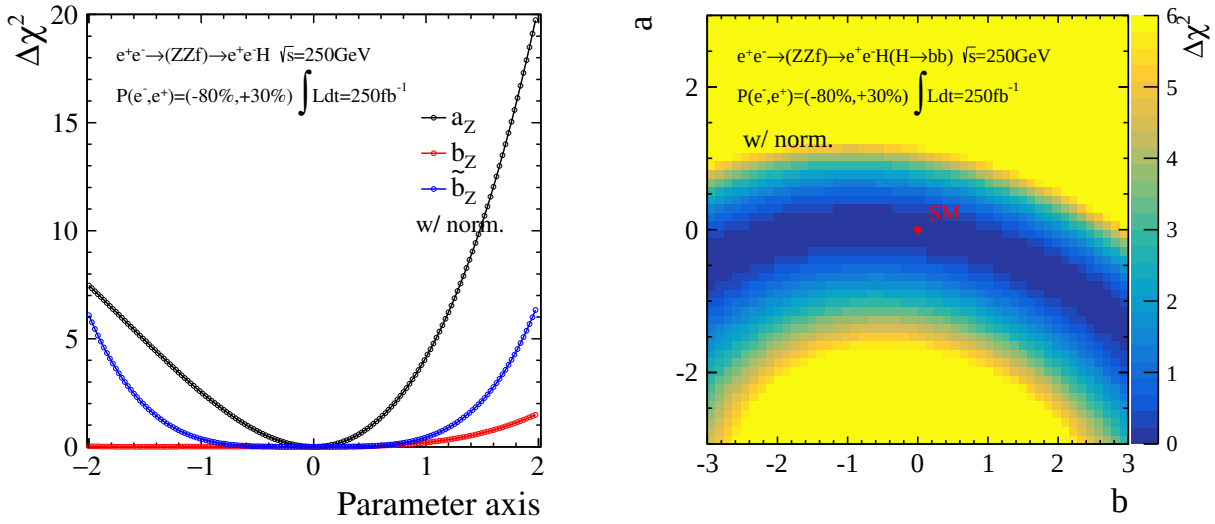

Figure 116: (Left) The distribution shows $\Delta\chi^2$ as a function of each parameter in the one parameter space, where the normalization information only is used for the evaluation. (Right) The distributions show $\Delta\chi^2$ in the two-dimensional parameter space of a_Z-b_Z.

A.3 $e^+e^- \to Zh \to \mu^+\mu^- h$ at $\sqrt{s} = 500$ GeV

Although the production cross-section of the Higgs-strahlung Zh process becomes less than half at $\sqrt{s}$=500 GeV compared to that of 250 GeV, the increase of momentum of the Z boson in the reaction can lead the strong anomalous couplings and give quick and clear variations of the kinematical distribution. Therefore, inclusion of results at 500 GeV processes could give sizable impacts on the improvement of the sensitivity to the anomalous ZZH couplings.

A.3.1 Reconstruction and background suppression

The strategy of the analysis is almost same as the analysis of the case at 250 GeV.

Isolated lepton finding and radiation recovering :

The finding of the isolated muons derived from the Z boson and the recovering of the radiated photons in the final state are implemented as with the analysis of 250 GeV processes. The requirements for extracting the isolated muons are

- A charged particle has momentum of more than 5 GeV.
- MLP response for the muon candidate must be larger than 0.7.
- Neutral particles which are identified as a photon are merged into the charged particle if the polar angle between both exceeds 0.99.

After pairing isolated muons by referring the invariant mass of the Z boson, the daughters decaying from the Z boson are identified. Plots in Fig. 117 give the invariant mass of the Z boson and its recoil mass, and the effect of the photon recovery.

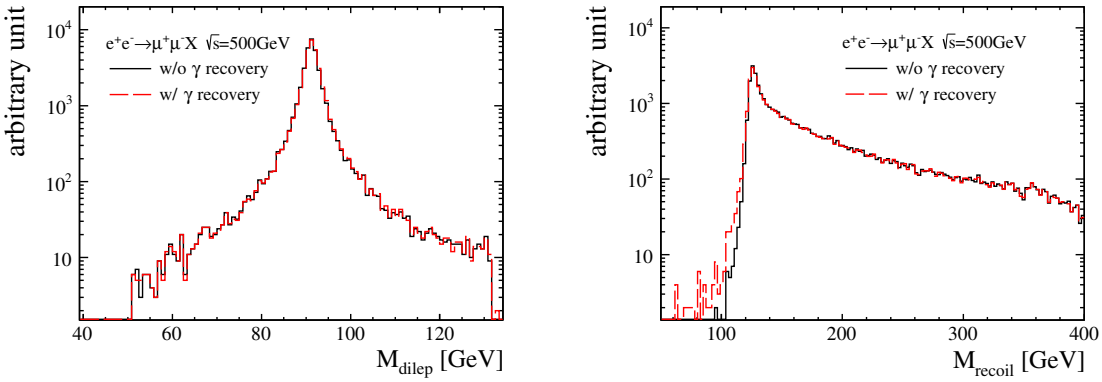

Figure 117: Distributions of the invariant mass of the muon pair M_{ll} (left) and the recoil mass M_{reco} (right) of the muon channel in the Higgs-strahlung Zh process at $\sqrt{s}$=500 GeV. Black and red lines on both plots correspond to without and with recovering photons, respectively.

Reconstructed angular observables :

The reconstructed observables being sensitive to the anomalous couplings are illustrated in Fig. 118, where the production angle of the Z boson $\cos\theta_Z$ and the angle between production planes $\Delta\Phi$ are given. Due to the fact that the one or both muons fly to the beam direction, which is same reason with the case at 250 GeV, dips at 0, π, and 2π appear, and it is irreducible reactions.

Background suppression :

The background suppression was performed by using the same observables which are used for the $\mu^+\mu^- H$ study at 250 GeV. Each observable implemented for the suppression is illustrated

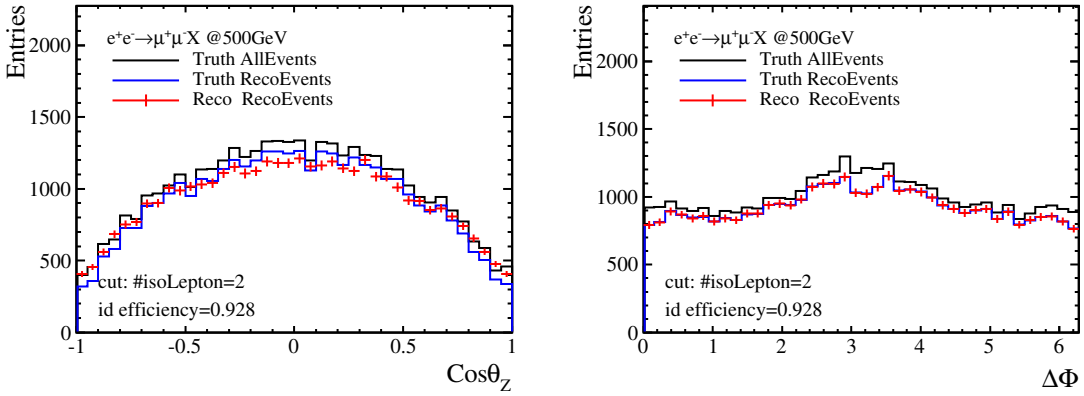

Figure 118: Plots show the MC truth and reconstructed distributions (left), the migration effects (middle), and resolutions (right) of $\cos\theta_Z$, $\cos\theta^*_f$, and $\Delta\Phi$ of the muon channel in the Higgs-strahlung Zh process at $\sqrt{s}$=500 GeV. Those observables give the sensitivities to the anomalous ZZH couplings. The clear dips at 0, π, and 2π on $\Delta\Phi$ is due to the missing final state muons.

in Fig. 119. The explicit values for each observable are optimized by calculating the signal significance and its detail is given in Table 9, where the left-handed polarization state: P(e^-, e^+)= (-80%,+30%) with the integrated luminosity of 500 fb^{-1} are assumed.

- Two leptons having opposite sign with the same flavor must exist exactly in one event (muon and anti-muon), which is given as a pre-selection.
- $N_{tracks} \in [13,\ 70]$
  The number of charged tracks, which is useful to remove huge two-fermion backgrounds.

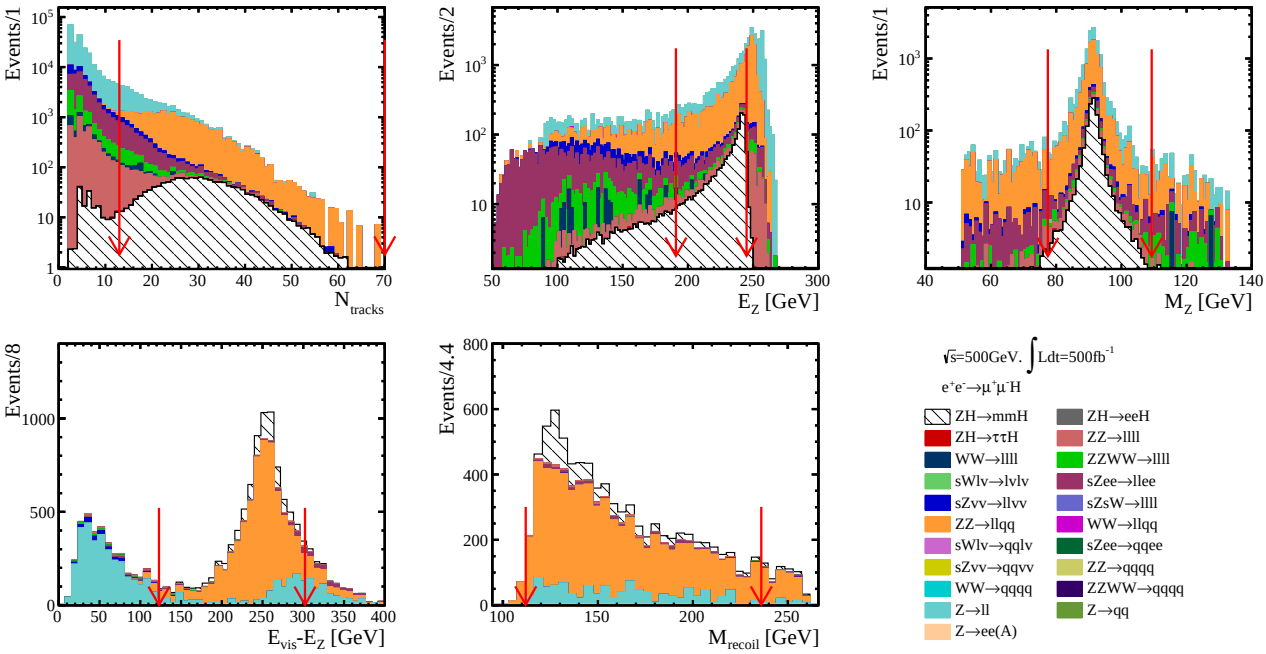

Figure 119: The distributions show each observable used for the background suppression assuming 500 fb^{-1} with P(e^-, e^+)= (-80%,+30%). The explanation of the observables are given in the text. Red arrows on each plot indicate the cut values applied to each observable as the background suppression.

- $E_Z \in [190.8,\ 245.0]$ GeV, and $M_Z \in [77.45,\ 109.30]$ GeV
  Since energy of the di-lepton system derived from one of the dominant background process

$e^+e^- \to ZZ \to$ semi-leptonic decay has a peak at 125 GeV, this observable is useful to separate it. The invariant mass of di-lepton $M_{e^+e^-}$ must be close to the mass of the Z boson.

- $E_{vis} - E_Z (\equiv E_{sub}) \in [122.92,\ 302.08]$ GeV
  Visible energy shows measured energy in the detectors. The subtracted value by the energy of the Z boson is close to 0 for the two-fermion process, which is still useful to distinguish the Higgs boson from other dispersed backgrounds.
- $M_{rec} \in [112,\ 236]$ GeV
  Recoil mass against the di-lepton system, which becomes a conclusive mass window to determine a Poisson error calculated by the remaining number of events on each bin on kinematical histograms.

Table 9: The expected number of remaining signal and background events after each cut for the $Zh \to \mu^+\mu^- h$ at $\sqrt{s}$=500 GeV, with with both of the beam polarization states: P(e^-, e^+)= (-80%,+30%) and (+80%,-30%). The integrated luminosity of 500 fb^{-1} is assumed. The signal efficiency ϵ and significance S_{sig} are also given in the table. 6_f SM background processes are not considered here, which would give no contamination to the clear $\mu^+\mu^- h$ signal channel.

$\sqrt{s}$=500 GeV P(e^-, e^+)= (-80%,+30%)

Cut variables	$\mu\mu h$	ϵ	eeh	$\tau\tau h$	$2f$	$4f$	S_{sig}
No cut	1725	100	1720	1720	$1.32 \cdot 10^7$	$1.62 \cdot 10^7$	-
ID of a di-lepton pair	1602	92.87	3	3	$1.81 \cdot 10^5$	$7.45 \cdot 10^4$	3.16
$N_{tracks} \in [13,\ 70]$	1432	83.02	1	1	$1.69 \cdot 10^4$	$2.30 \cdot 10^4$	7.04
$E_Z \in [190.8,\ 245.0]$ GeV	1209	70.09	0	1	5180	8719	9.84
$M_Z \in [77.45,\ 109.30]$ GeV	1179	68.35	0	0	4634	7519	10.2
$E_{sub} \in [122.92,\ 302.08]$ GeV	1094	63.42	0	0	1058	6273	11.9
$M_{reco} \in [112,\ 236]$ GeV	1039	60.23	0	0	987	5748	11.8

$\sqrt{s}$=500 GeV P(e^-, e^+)= (+80%,-30%)

Cut variables	$\mu\mu h$	ϵ	eeh	$\tau\tau h$	$2f$	$4f$	S_{sig}
No cut	1163	100	1162	1162	$8.81 \cdot 10^6$	$5.58 \cdot 10^6$	-
ID of a di-lepton pair	1080	92.86	2	2	$1.46 \cdot 10^5$	$4.43 \cdot 10^4$	2.47
$N_{tracks} \in [13,\ 70]$	965	82.98	1	1	$1.36 \cdot 10^4$	$1.26 \cdot 10^4$	5.86
$E_Z \in [168.33,\ 245.0]$ GeV	866	74.46	0	0	4695	5269	8.32
$M_Z \in [84.80,\ 104.40]$ GeV	811	69.73	0	0	3861	4113	8.65
$E_{sub} \in [133.33,\ 304.17]$ GeV	746	64.14	0	0	891	3324	10.6
$M_{reco} \in [112,\ 236]$ GeV	673	57.87	0	0	738	2851	10.3

A.3.2 Acceptance and migration on observables

Fig. 120, and Fig. 121 show summary plots on the one-dimensional angular distributions of $\cos\theta_Z$, and $\Delta\Phi$ binned in 30, which include the remaining signal and background distributions, event acceptance η, and the probability of the migration effects $\bar{f}$ after the background suppression. Summary plots of the two-dimensional distribution of $x(\cos\theta_Z, \Delta\Phi_{f\bar{f}})$ are also given in Fig. 122 which are binned in 10×10. The event acceptance of $\Delta\Phi$ distribution maintains flatness well, but drops appear in the $\cos\theta_Z$ distribution. The probabilities of the migration effects of each distribution are also extremely clear.

Main difference compared to the 250 GeV process is that the event acceptance of the $\cos\theta_Z$ drops at the edge of the distribution (-1 and +1) although any observables which are correlated to

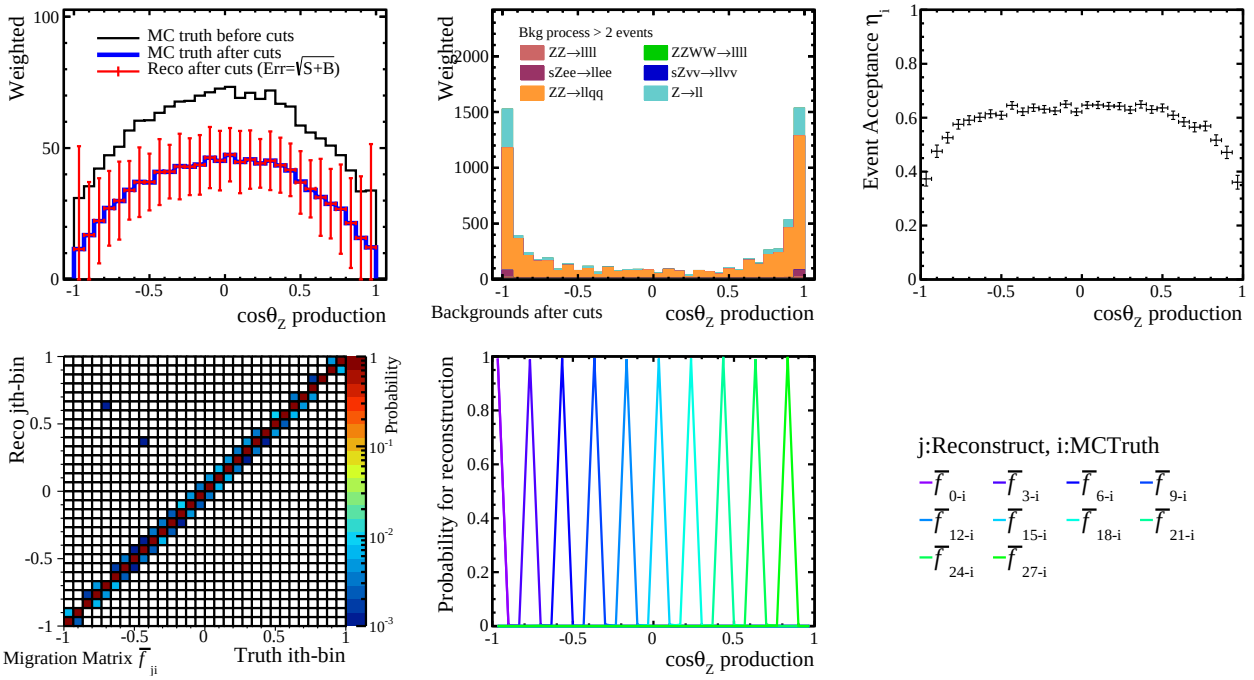

Figure 120: The distributions show the summary of the polar angle of the Z boson ($\cos\theta_Z$) after the background suppression. (Top left and middle): the remaining signal and the background distribution, which are given with the MC truth and the reconstructed, where the statistical error is given as the standard deviation of the Poisson probability. (Top right): the event acceptance function η_i. (Bottom left and middle): the distribution shows the probability matrix of the migration ($\bar{f}_{ji}$) that is applied for the reconstruction of the realistic distribution of $\cos\theta_Z$, and the cross-sections of $\bar{f}_{ji}$ as 1-dim plots.

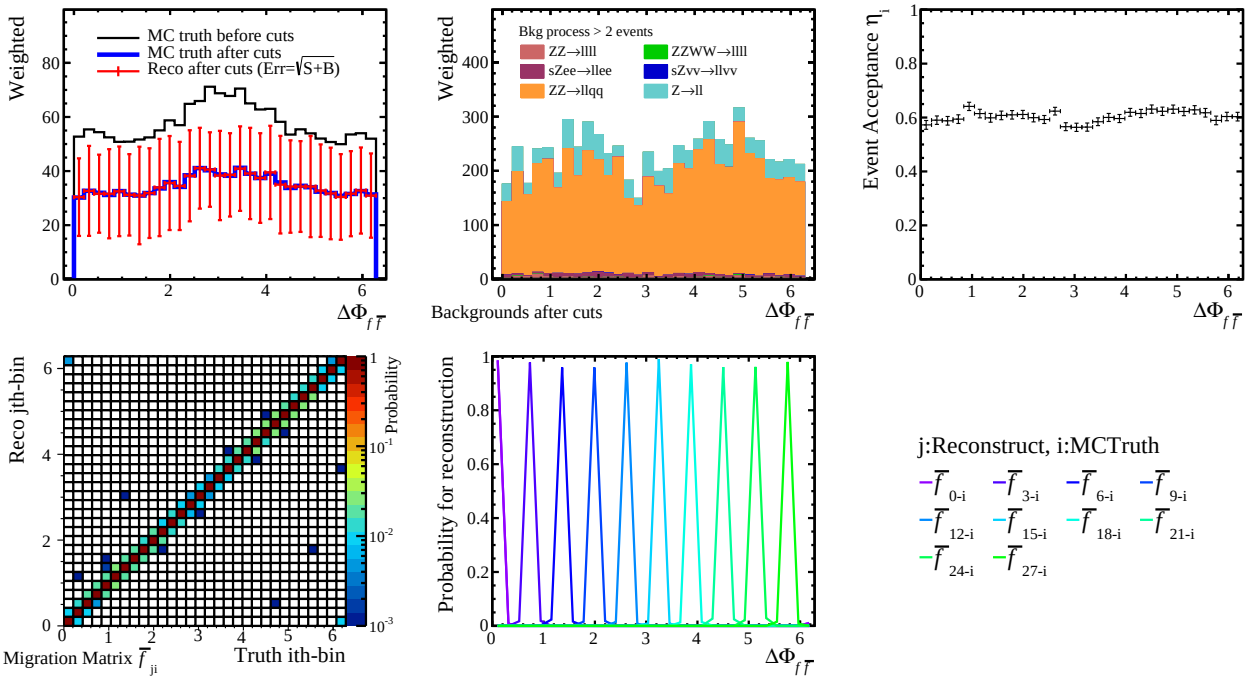

Figure 121: The distributions show the summary of the angle between production planes in the laboratory frame ($\Delta\Phi$) after the background suppression. (Top left and middle): the remaining signal and the background distribution, which are given with the MC truth and the reconstructed. (Top right): the event acceptance function η_i. (Bottom left and middle): the probability matrix of the migration ($\bar{f}_{ji}$) that is applied for the reconstruction of $\Delta\Phi$, and the cross-sections of $\bar{f}_{ji}$ as 1-dim plots.

the angle $\cos\theta_Z$ are not used. Since the leptons decaying form the Z boson have larger energy and corresponding momenta, they are highly boosted, and one or both leptons tend to fly along the momentum direction of the Z boson. When the high momentum Z boson is generated toward the beam direction, its daughters could fly toward the beam direction, and eventually they become missing particles. If looking a plot showing $\Delta\Phi$ vs $\cos\theta_Z$ with missing events, the correlation between $\Delta\Phi$ and $\cos\theta_Z$ can be clearly seen for 500 GeV and not for 250 GeV. Thus, the drops at (-1 and +1) in $\cos\theta_Z$ distribution are also irreducible.

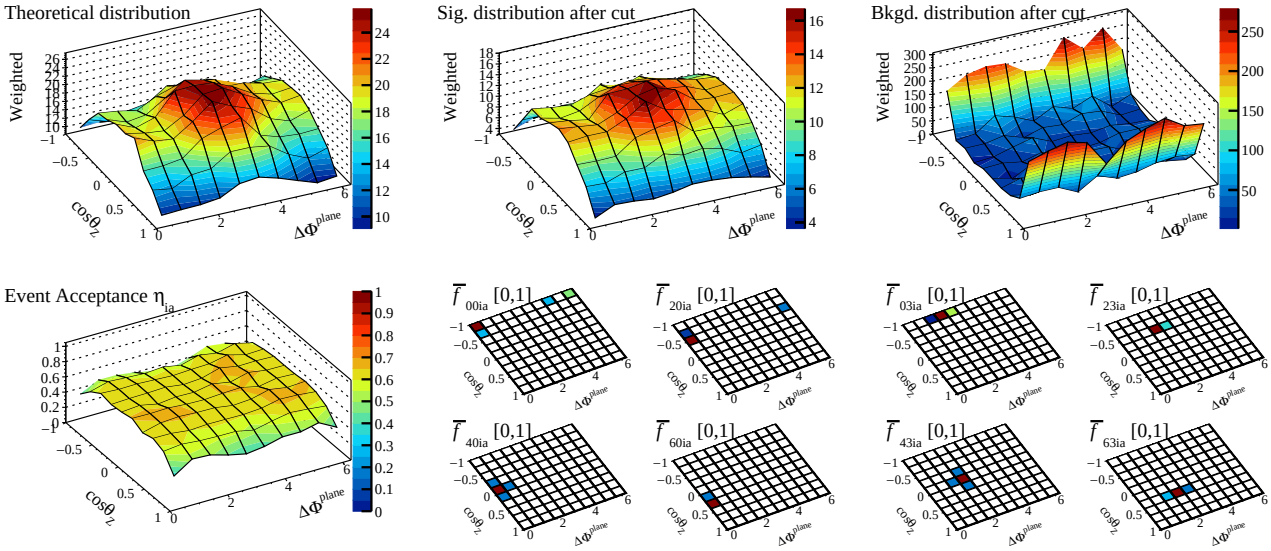

Figure 122: The distributions show the summary of the two-dimensional distribution consisted of the production angle of the Z boson $\cos\theta_Z$ and the angle between production planes in the laboratory frame ($\Delta\Phi$) after the background suppression. (Top left, middle, and right): The remaining MC truth and the reconstructed signal distribution, and the background distribution, respectively. (Bottom left): The event acceptance function η_{ia} shows whether each signal event on each bin is accepted or not after the suppression. (Bottom middle and right): Several examples on the probability matrix of the migration where the 2-dim plots give the cross-sections of $\bar{f}_{jbia}$ since the illustration of the migration is too difficult which is a 4-dimension distribution.

A.3.3 Impact of angular distributions

Fig. 123 give $\Delta\chi^2$ distributions for each one-dimensional parameter axis, where one-dimensional distributions of $x(\cos\theta_Z)$ and $x(\Delta\Phi)$ binned in 20, and the three-dimensional distribution of $x(\cos\theta^*_f, \cos\theta_Z, \Delta\Phi_{f\bar{f}})$ binned in $5\times5\times5$ are used for the evaluation. Each of one-dimensional distribution has different power, and there dimensional distribution can give the improvement of the sensitivity.

Notable things is that, because it seem that there exist certain area that can negate the variation of the kinematical distribution and recover the SM distribution, the minimum point, where $\Delta\chi^2$ is close to 0, appear for b_Z with the $\cos\theta_Z$ distribution only. However, by adding the information of the $\Delta\Phi$, it can be identified. It also observed that the sensitivity given by the $\Delta\Phi$ distribution is limited because of statistical error although the variation of the $\Delta\Phi$ distribution is strong and quickly reach maximum. Since the cross-section with right-handed beam polarization is less compared to the left-handed due to the conservation of angular momentum, the sensitivity gets slightly worse.

Fig. 124 give $\Delta\chi^2$ distributions for each two-dimensional parameter space with each kinematical information. The similar behavior with the one-dimensional $\Delta\chi^2$ distribution can be seen. With $\cos\theta_Z$ the area that can negate the variation appear except the direction along a_Z

for a_Z-b_Z and b_Z-$\tilde{b}_Z$ parameter space. And these are clearly identified with the three-dimensional distribution.

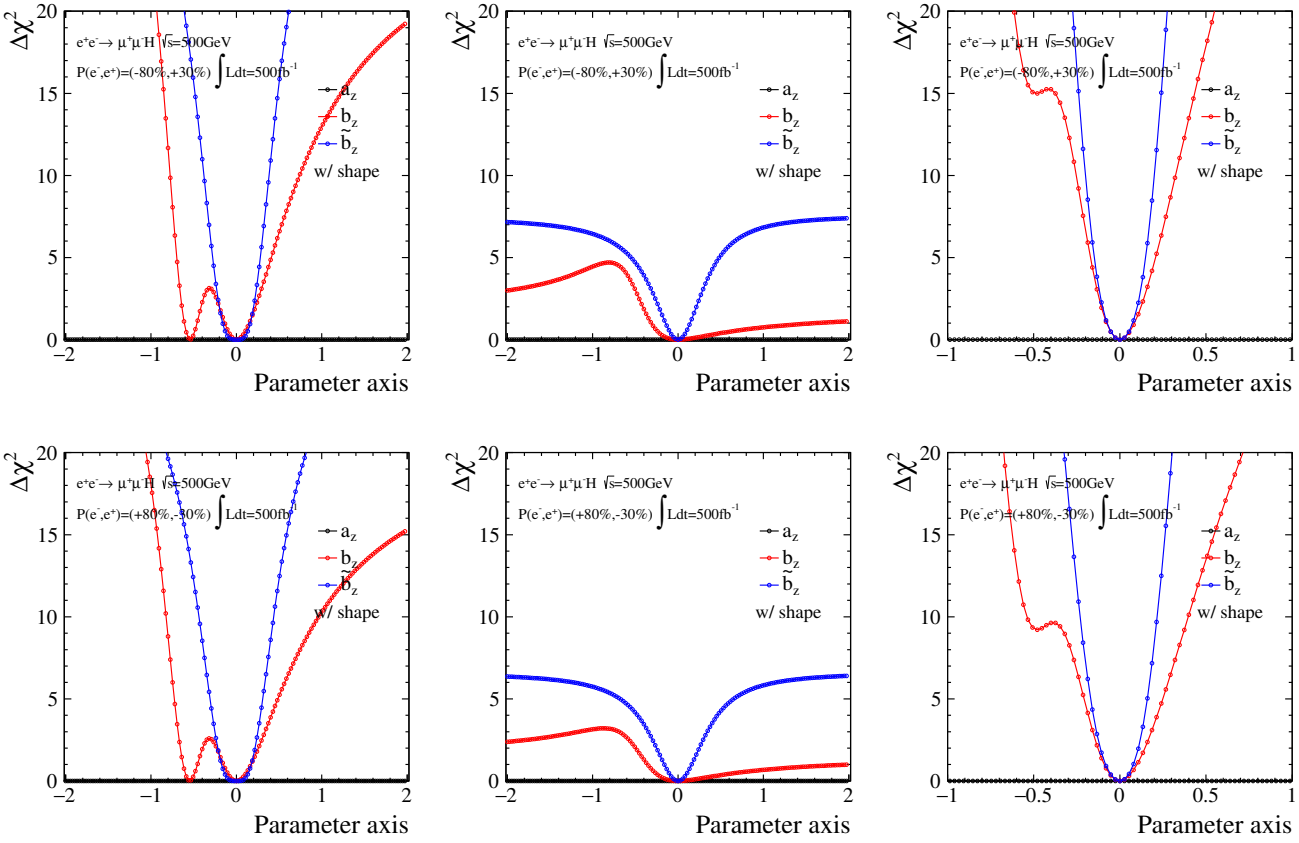

Figure 123: The distributions show $\Delta\chi^2$ as a function of each parameter of the anomalous ZZH couplings, and the evaluation is done in the one-parameter space. Black, red, and blue lines on the plots correspond to the parameters a_Z, b_Z, and $\tilde{b}_Z$. Since only the angular information is considered here, the χ^2 values of a_Z is exactly 0 over the given range. In upper and lower plots, the different beam polarizations are assumed with the integrated luminosity of 500 fb^{-1}: P(e^-, e^+)= (-80%,+30%) and (+80%,-30%), respectively. Difference of each column is the angular distributions used for the evaluation: (left) $x(\cos\theta_{Z)}$ binned in 20, (middle) $x(\Delta\Phi_{f\bar{f}})$ binned in 20, and (right) $x(\cos\theta^*_f, \cos\theta_Z, \Delta\Phi_{f\bar{f}})$ binned in $5\times5\times5$ are used respectively.

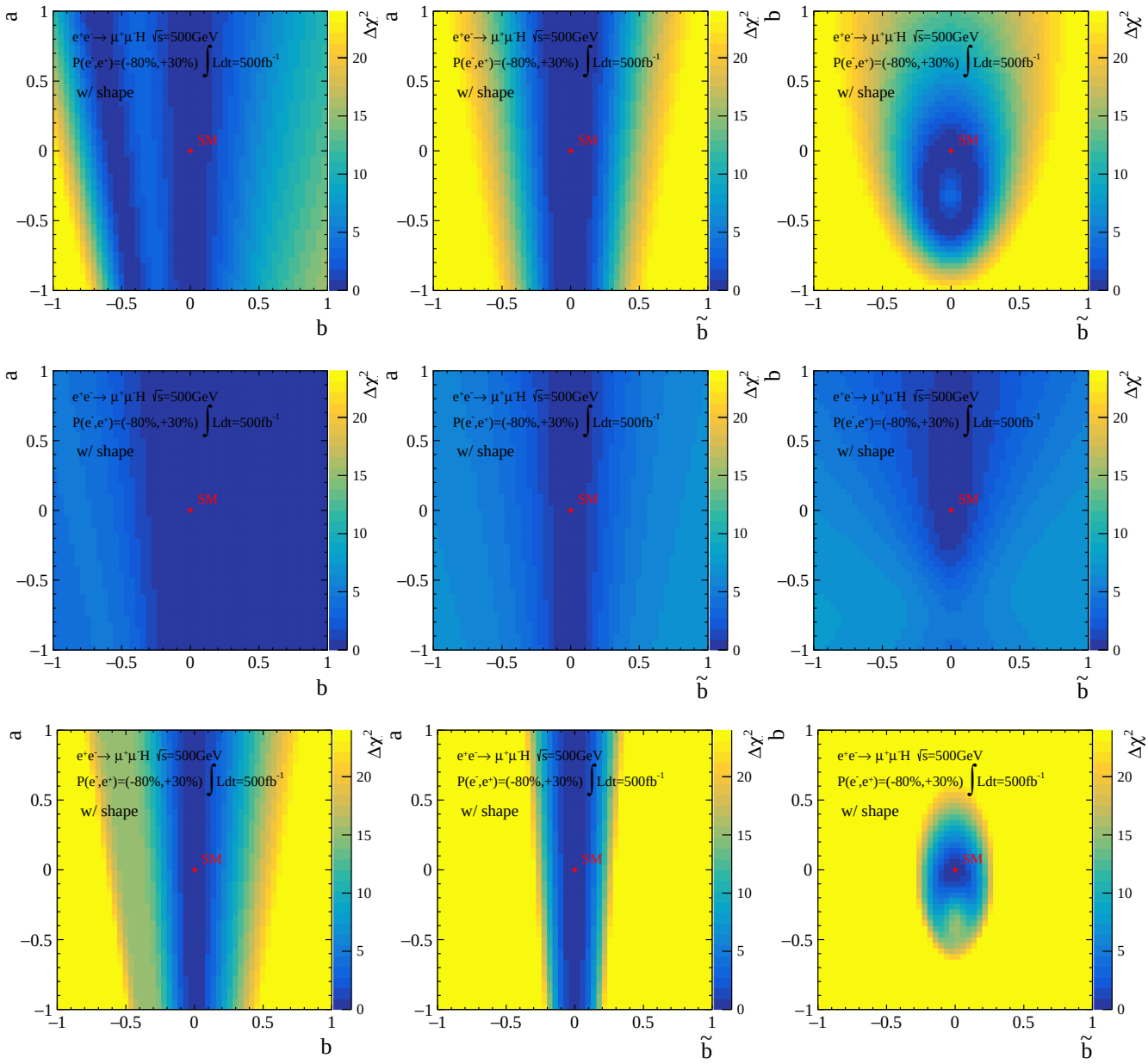

Figure 124: The distributions show $\Delta\chi^2$ in the two-dimensional parameter space a_Z-b_Z, a_Z-$\tilde{b}_Z$, and b_Z-$\tilde{b}_Z$. Only each angular distribution is used for the evaluations: (top) $x(\cos\theta_{Z)}$ binned in 20, (middle) $x(\Delta\Phi_{f\bar{f}})$ binned in 20, and (bottom) $x(\cos\theta^*_f, \cos\theta_Z, \Delta\Phi_{f\bar{f}})$ binned in 5×5×5 are used respectively. The results are given only for the beam polarization of P(e^-, e^+)= (-80%,+30%). The sensitivity is 0.0 for the any a_z when b_Z or $\tilde{b}_Z$ is 0.0.

A.3.4 Impact of production cross-section

The variation of the production cross-section which depends on the anomalous parameters is also useful observable. At 500 GeV, the variation of the cross-section rather quickly change compared to the case of 250 GeV, which is illustrated in Fig. 125. In this information the are that can cancel out the variation of the cross-section appears, and it is necessary to use the variation of the kinematical distribution to disclose the canceled area. Both of the informations are complementary each other.

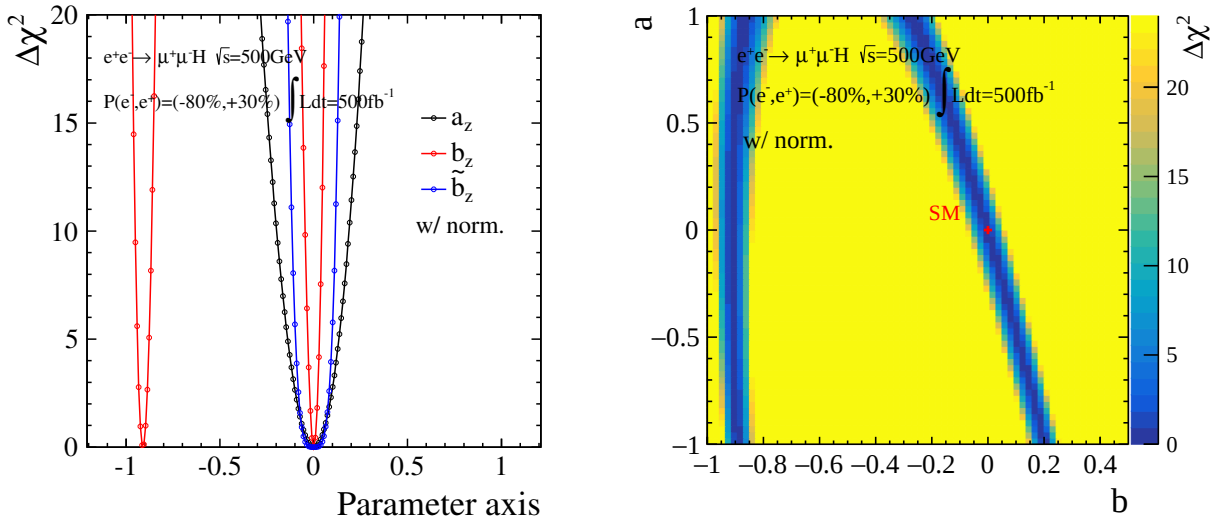

Figure 125: (Left) The distribution shows $\Delta\chi^2$ as a function of each parameter in the one parameter space, where the normalization information only is used for the evaluation. (Right) The distributions show $\Delta\chi^2$ in the two-dimensional parameter space of a_Z-b_Z.

A.3.5 Sensitivity in three parameter space

The sensitivities to the anomalous ZZH couplings with the muon channel only are given in Fig. 126, where the variation of the three-dimensional distribution $x(\cos\theta^*_f, \cos\theta_Z, \Delta\Phi_{f\bar{f}})$ binned in $5\times5\times5$ and the variation of the production cross-section are considered.

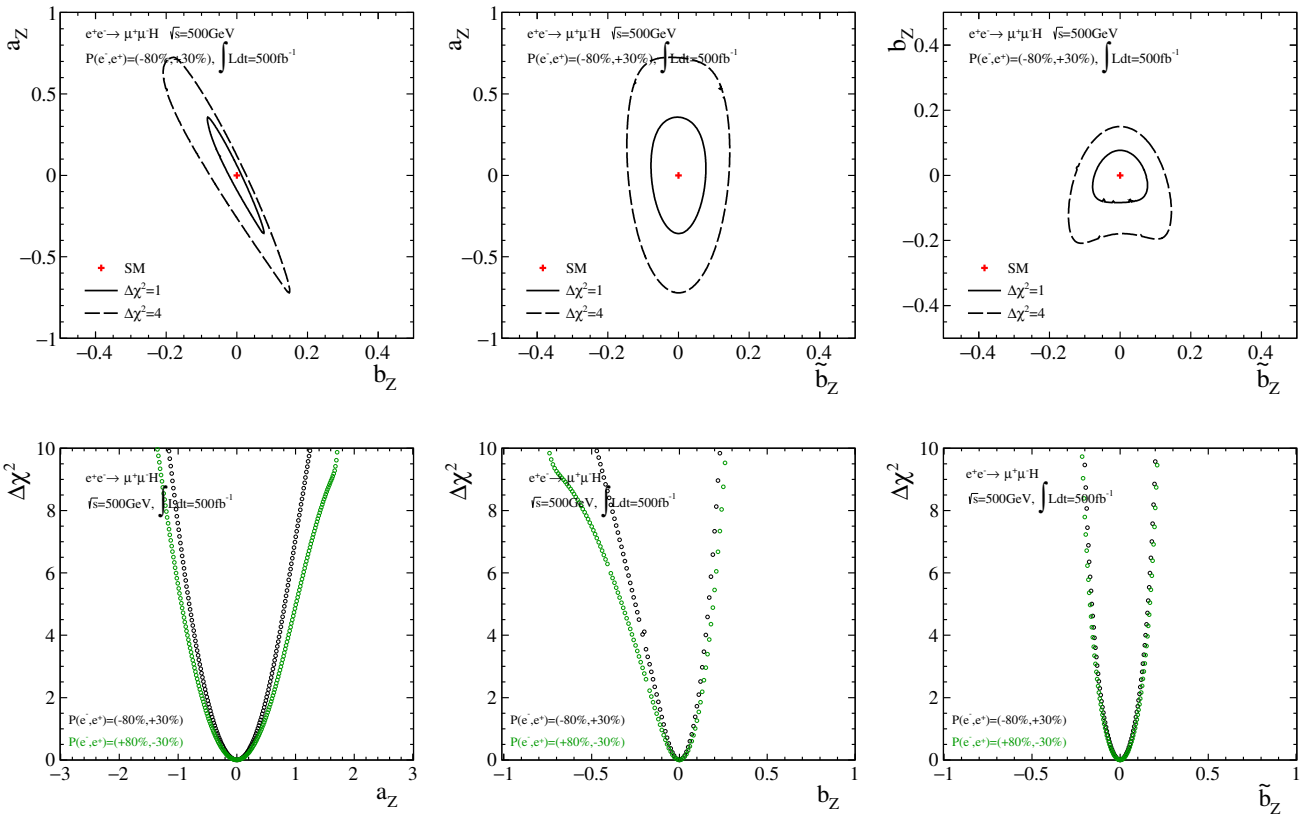

$$\sqrt{s} = 500 \text{ GeV with } \int \text{Ldt} = 500 \text{ fb}^{-1} \text{ and } \text{P}(e^-, e^+) = (-80\%, +30\%)$$

$$\begin{cases} a_Z = [-0.358, \quad 0.357] \\ b_Z = [-0.0837, \quad 0.0768] \\ \tilde{b}_Z = [-0.0779, \quad 0.0774] \end{cases}, \quad \rho = \begin{pmatrix} 1 & -0.9882 & 0.0176 \\ - & 1 & -0.0184 \\ - & - & 1 \end{pmatrix}$$

$$\sqrt{s} = 500 \text{ GeV with } \int \text{Ldt} = 500 \text{ fb}^{-1} \text{ and } \text{P}(e^-, e^+) = (+80\%, -30\%)$$

$$\begin{cases} a_Z = [-0.417, \quad 0.423] \\ b_Z = [-0.1024, \quad 0.0894] \\ \tilde{b}_Z = [-0.0841, \quad 0.0841] \end{cases}, \quad \rho = \begin{pmatrix} 1 & -0.9912 & 0.0973 \\ - & 1 & -0.1044 \\ - & - & 1 \end{pmatrix}$$

Figure 126: (Upper): The plots show contours corresponding to the 1σ and 2σ sensitivities to the anomalous ZZH couplings. The fitting is performed with the muon channel only under the three free parameter space. The integrated luminosity of 500 fb^{-1} with the beam polarization state P(e^-, e^+)= (-80%,+30%) is assumed. The results are projected onto the two-dimensional parameter spaces a_Z-b_Z, a_Z-$\tilde{b}_Z$, and b_Z-$\tilde{b}_Z$. Both of the information, which are the three-dimensional distributions $x(\cos\theta^*_f, \cos\theta_Z, \Delta\Phi_{f\bar{f}})$ binned in 5×5×5 and the production cross-section are combined. (Middle): The plots show $\Delta\chi^2$ distributions as a function of each parameter space of the anomalous couplings a_Z, b_Z, and $\tilde{b}_Z$. The distributions are obtained by using both information (the angles and the cross-section) and scanning one parameter while setting the other two parameters to be completely free. (Lower): The explicit values corresponding to the 1σ bounds for each anomalous parameter a_Z, b_Z, and $\tilde{b}_Z$ and the correlation matrix indicating correlation coefficients between the parameters.

A.4 $e^+e^- \to Zh \to e^+e^-h$ at $\sqrt{s} = 500$ GeV

The electron channel, which is another clear lepton channel, is expected to give similar sensitivity with the muon channel discussed in the previous section.

A.4.1 Reconstruction and background suppression

The flow of the analysis is same as the analysis of the muon channel.

Isolated lepton finding and radiation recovering :

The finding of the isolated electrons and the recovering of the radiated photons are implemented by IsoLeptonFinder as with the analysis of 250 GeV. The requirements for extracting the isolated electrons are,

- charged particle has momentum of more than 5 GeV.
- MLP response for the electron candidate must be larger than 0.5.
- Neutral particles which are identified as a photon are merged into the charged particle if the polar angle between both exceeds 0.99.

After pairing isolated electrons by referring the invariant mass of the Z boson, the daughters decaying from the Z boson are identified. Plots in Fig. 127 give the invariant mass of the Z boson and its recoil mass, and the effect of the photon recovery.

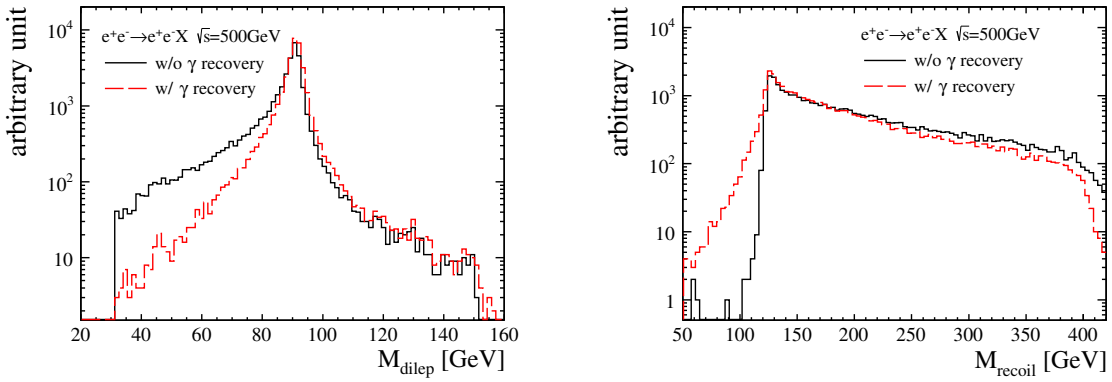

Figure 127: Distributions of the invariant mass of the muon pair M_{ll} (left) and the recoil mass M_{reco} (right) of the electron channel in the Higgs-strahlung Zh process at $\sqrt{s}$=500 GeV. Black and red lines on both plots correspond to without and with recovering photons, respectively.

Reconstructed angular observables :

The reconstructed observables for verifying the anomalous couplings are illustrated in Fig. 128, where the production angle of the Z boson $\cos\theta_Z$ and the angle between production planes $\Delta\Phi$ are given as with the muon channel. The dips can be seen at 0, π, and 2π.

Background suppression :

The background suppression was performed by using the same observables which are used for the e^+e^-h study at 250 GeV. Each observable implemented for the suppression is illustrated in Fig. 129. The explicit values for each observable are optimized by calculating the signal significance and its detail is given in Table 10, where the left-handed polarization state: P(e^-, e^+)= (-80%,+30%) with the integrated luminosity of 500 fb^{-1} are assumed.

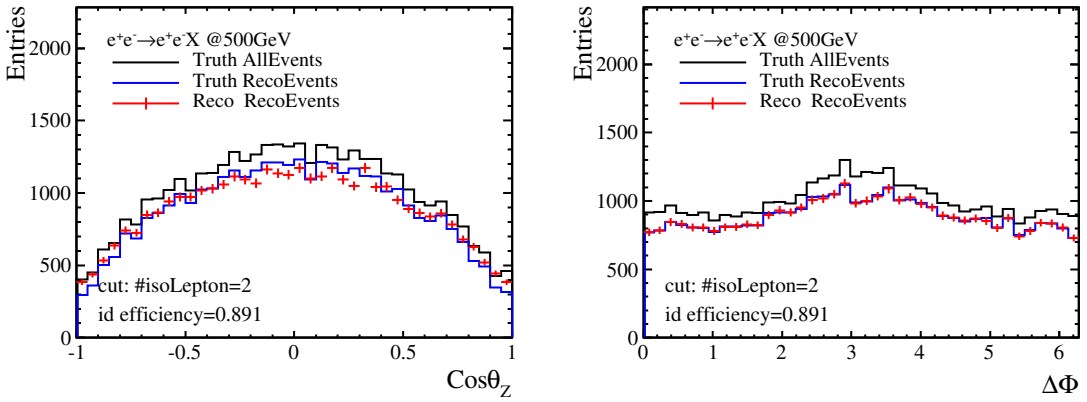

Figure 128: Plots show the MC truth and reconstructed distributions (left), the migration effects (middle), and resolutions (right) of $\cos\theta_Z$, $\cos\theta^*_f$, and $\Delta\Phi$ of the electron channel in the Higgs-strahlung Zh process at $\sqrt{s}$=500 GeV. Those observables give the sensitivities to the anomalous ZZH couplings. The clear dips at 0, π, and 2π on $\Delta\Phi$ is due to the missing final state muons.

- Two isolated leptons, which have opposite signs: electron and positron, must exist exactly in one event. The reaction that does not have two isolated leptons is suppressed.
- $N_{tracks} \in [13,\ 70]$
  This represents the number of charged tracks in each reaction, which is useful to remove huge two-fermion SM backgrounds.
- $E_Z \in [190.8,\ 245.0]$ GeV and $M_Z \in [77.45,\ 109.30]$ GeV
  Since energy of the di-lepton system derived from one of the dominant background process $e^+e^- \to ZZ \to$ semi-leptonic decay has a peak at 125 GeV, this observable is useful to separate it. The invariant mass of di-lepton $M_{e^+e^-}$ must be close to the mass of the Z boson.
- $E_{vis} - E_Z(\equiv E_{sub}) \in [122.92,\ 302.08]$ GeV
  Visible energy shows measured energy in the detectors. The subtracted value by the energy of the Z boson is close to 0 for the two-fermion process, which is still useful to distinguish the Higgs boson from other dispersed backgrounds.
- $M_{rec} \in [112,\ 236]$ GeV
  Recoil mass against the di-lepton system, which becomes a conclusive mass window to determine a Poisson error calculated by the remaining number of events on each bin on kinematical histograms.

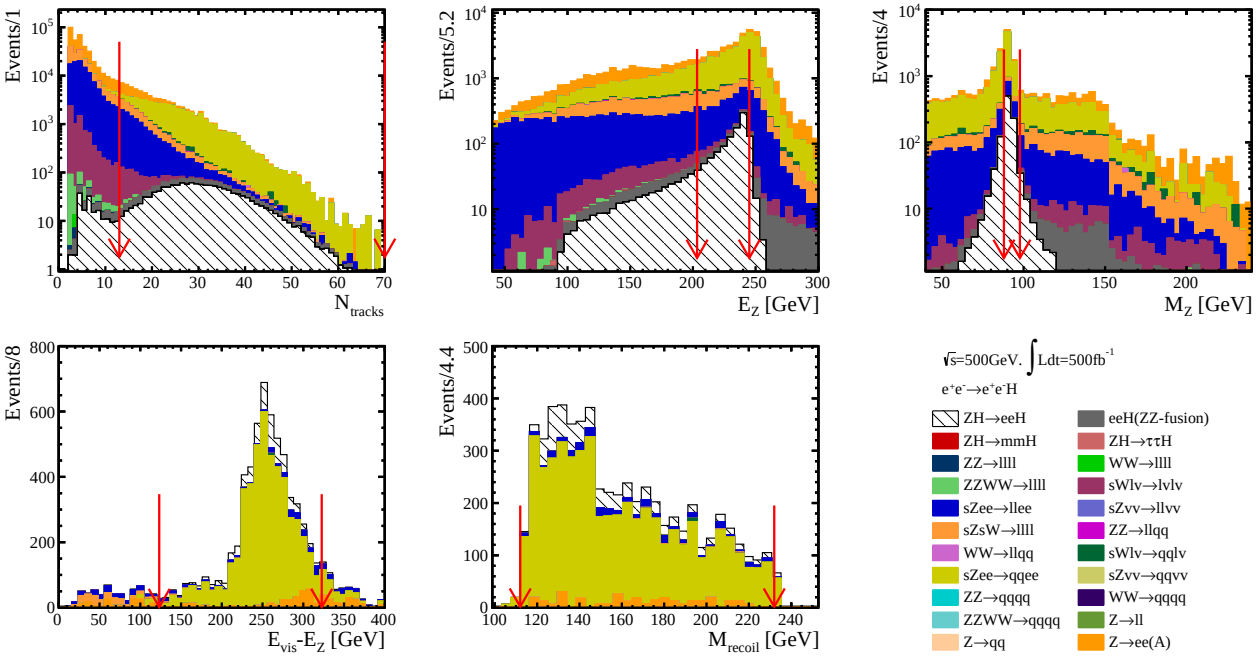

Figure 129: The distributions show each observable used for the background suppression assuming 500 fb^{-1} with P(e^-, e^+)= (-80%,+30%). The explanation of the observables are given in the text. Red arrows on each plot indicate the cut values applied to each observable as the background suppression.

Table 10: The expected number of remaining signal and background events after each cut for the $Zh \to e^+e^-h$ at $\sqrt{s}$=500 GeV, with with both of the beam polarization states: P(e^-, e^+)= (-80%,+30%) and (+80%,-30%). The integrated luminosity of 500 fb^{-1} is assumed. The signal efficiency ϵ and significance S_{sig} are also given in the table. 6_f SM background processes are not considered here, which would give no contamination to the clear $\mu^+\mu^-h$ signal channel.

$\sqrt{s}$=500 GeV P(e^-, e^+)= (-80%,+30%)

Cut variables	$(s)eeh$	ϵ	$(t)eeh$	$\mu\mu h$	$\tau\tau h$	$2f$	$4f$	S_{sig}
No cut	1720	100	3745	1725	1720	$1.32 \cdot 10^7$	$1.62 \cdot 10^7$	-
ID of a di-lepton pair	1536	89.30	400	0	6	$2.07 \cdot 10^5$	$2.20 \cdot 10^5$	2.34
$N_{tracks} \in [13,\ 70]$	1375	79.94	331	0	4	$1.86 \cdot 10^4$	$4.90 \cdot 10^4$	5.22
$E_Z \in [203.33,\ 245.0]$ GeV	998	58.02	91	0	0	4024	$1,76 \cdot 10^4$	6.62
$M_Z \in [87.95,\ 97.75]$ GeV	758	44.07	5	0	0	542	4490	9.96
$E_{sub} \in [123.23,\ 322.62]$ GeV	723	42.03	5	0	0	266	3823	10.4
$M_{reco} \in [112,\ 232]$ GeV	705	40.99	4	0	0	262	3688	10.3

$\sqrt{s}$=500 GeV P(e^-, e^+)= (-80%,+30%)

Cut variables	$(s)eeh$	ϵ	$(t)eeh$	$\mu\mu h$	$\tau\tau h$	$2f$	$4f$	S_{sig}
No cut	1162	100	2319	1163	1162	$8.81 \cdot 10^6$	$5.58 \cdot 10^6$	-
ID of a di-lepton pair	1037	90.96	247	0	4	$1.96 \cdot 10^5$	$1.49 \cdot 10^5$	1.76
$N_{tracks} \in [14,\ 70]$	920	79.17	201	0	3	$1.46 \cdot 10^4$	$3.71 \cdot 10^4$	4.00
$E_Z \in [190.83,\ 245.83]$ GeV	731	62.91	69	0	0	4039	$1.66 \cdot 10^4$	4.99
$M_Z \in [86.90,\ 98.10]$ GeV	583	50.17	4	0	0	583	5100	7.36
$E_{sub} \in [131.54,\ 308.08]$ GeV	538	46.30	4	0	0	195	4256	7.61
$M_{reco} \in [112,\ 232]$ GeV	494	42.51	3	0	0	166	3761	7.43

A.4.2 Acceptance and migration on observables

Fig. 130, and Fig. 131 show summary plots on the one-dimensional angular distributions of $\cos\theta_Z$, and $\Delta\Phi$ binned in 30, where the remaining signal and background distributions, event acceptance η, and the probability of the migration effects $\bar{f}$ after the background suppression are shown. Summary plots of the two-dimensional distribution of $x(\cos\theta_Z, \Delta\Phi_{f\bar{f}})$ are also given in Fig. 132 which are binned in 10×10. The event acceptance of $\Delta\Phi$ distribution maintains flatness, but drops appear in the $\cos\theta_Z$ distribution. The probabilities of the migration effects of each distribution are also extremely clear.

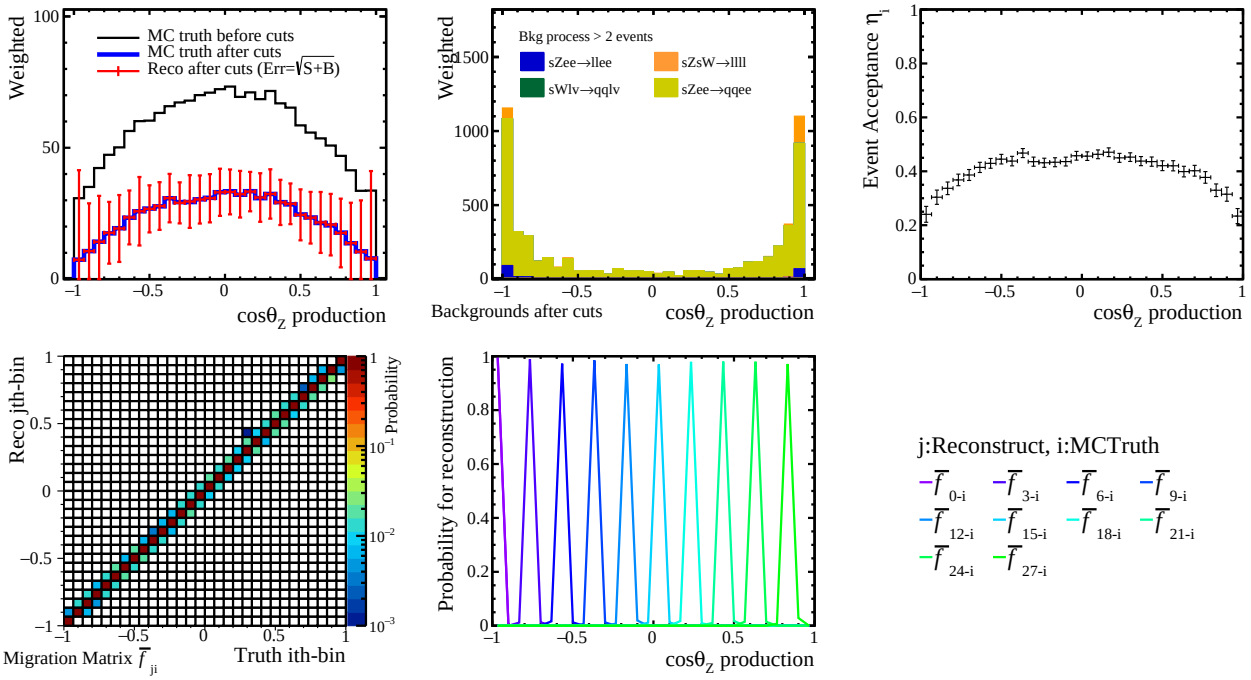

Figure 130: The distributions show the summary of the polar angle of the Z boson ($\cos\theta_Z$) after the background suppression. (Top left and middle): the remaining signal and the background distribution, which are given with the MC truth and the reconstructed, where the statistical error is given as the standard deviation of the Poisson probability. (Top right): the event acceptance function η_i. (Bottom left and middle): the distribution shows the probability matrix of the migration ($\bar{f}_{ji}$) that is applied for the reconstruction of the realistic distribution of $\cos\theta_Z$, and the cross-sections of $\bar{f}_{ji}$ as 1-dim plots.

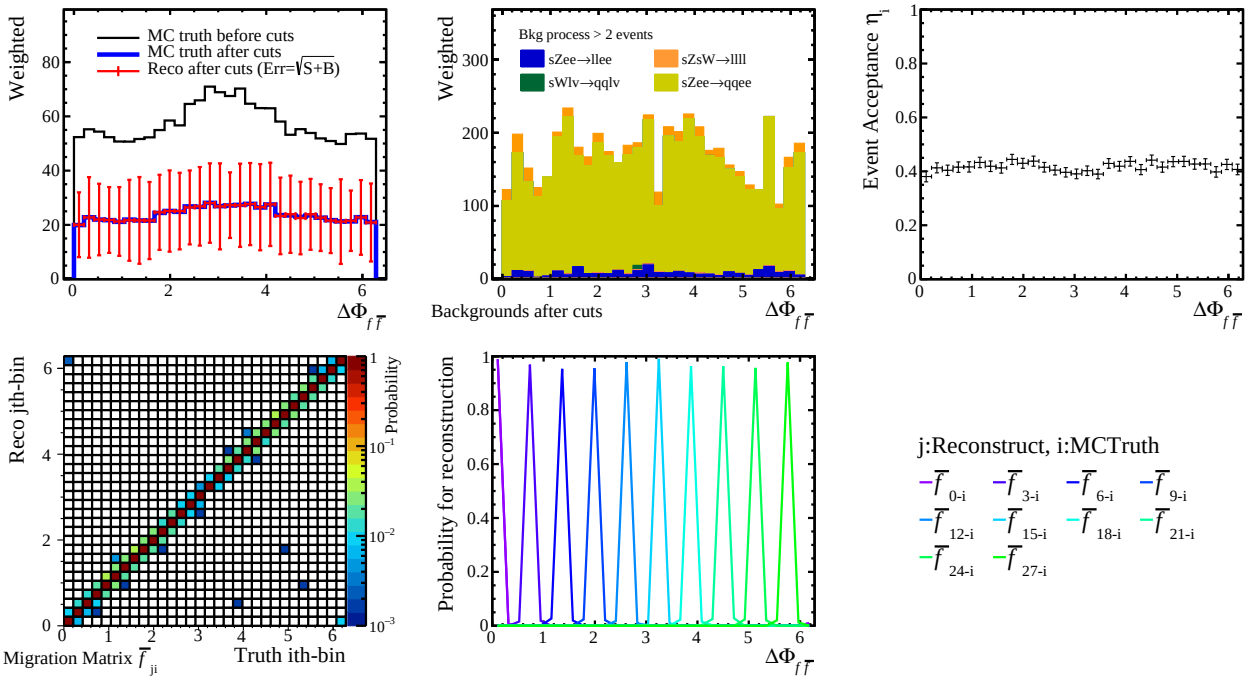

Figure 131: The distributions show the summary of the angle between production planes in the laboratory frame ($\Delta\Phi$) after the background suppression. (Top left and middle): the remaining signal and the background distribution, which are given with the MC truth and the reconstructed. (Top right): the event acceptance function η_i. (Bottom left and middle): the probability matrix of the migration ($\bar{f}_{ji}$) that is applied for the reconstruction of $\Delta\Phi$, and the cross-sections of $\bar{f}_{ji}$ as 1-dim plots.

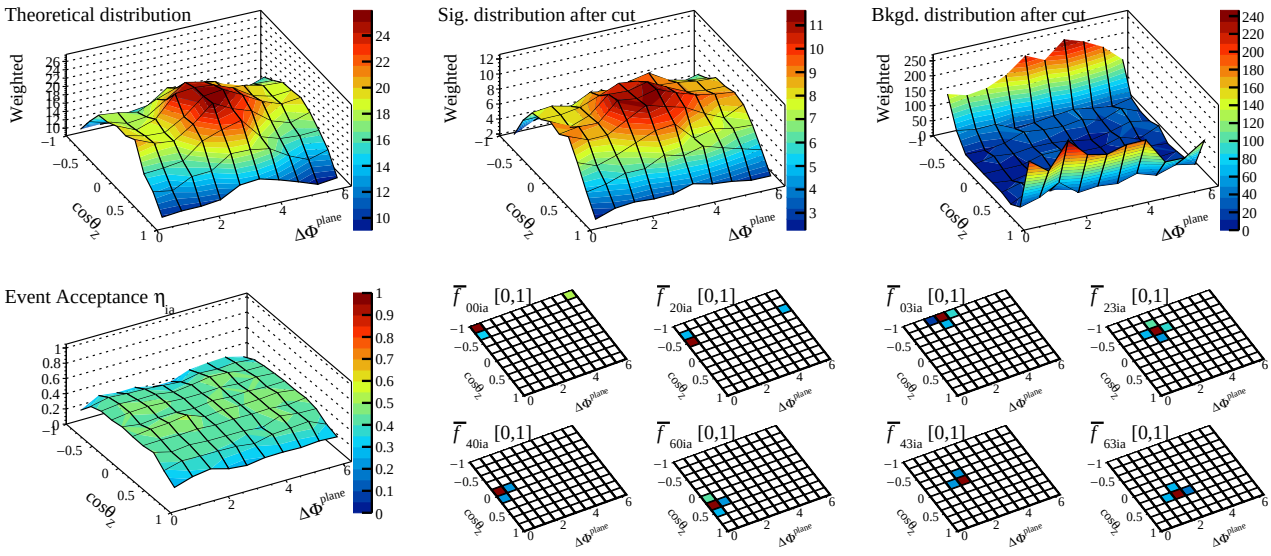

Figure 132: The distributions show the summary of the two-dimensional distribution consisted of the production angle of the Z boson $\cos\theta_Z$ and the angle between production planes in the laboratory frame ($\Delta\Phi$) after the background suppression. (Top left, middle, and right): The remaining MC truth and the reconstructed signal distribution, and the background distribution, respectively. (Bottom left): The event acceptance function η_{ia} shows whether each signal event on each bin is accepted or not after the suppression. (Bottom middle and right): Several examples on the probability matrix of the migration where the 2-dim plots give the cross-sections of $\bar{f}_{jbia}$ since the illustration of the migration is too difficult which is a 4-dimension distribution.

A.4.3 Impact of angular distributions

Fig. 133 give $\Delta\chi^2$ distributions for each one-dimensional parameter axis, where one-dimensional distributions of $x(\cos\theta_Z)$ and $x(\Delta\Phi)$ binned in 20, and the three-dimensional distribution of $x(\cos\theta^*_f, \cos\theta_Z, \Delta\Phi_{f\bar{f}})$ binned in $5\times5\times5$ are used for the evaluation.

Compared to the muon channel, the overall sensitivity that the electron channel can provide is little bit worse. This is simply because the remaining background is larger than that of the muon channel, and it cause the large statistical error and make the variation of the kinematical distribution unclear. The behaviors, like, the are that can negate the variation of the kinematical distribution appear, is same with the muon channel.

A.4.4 Sensitivity in three parameter space

The sensitivities to the anomalous ZZH couplings with the muon channel only are given in Fig. 134, where the variation of the three-dimensional distribution $x(\cos\theta^*_f, \cos\theta_Z, \Delta\Phi_{f\bar{f}})$ binned in $5\times5\times5$ and the variation of the production cross-section are considered.

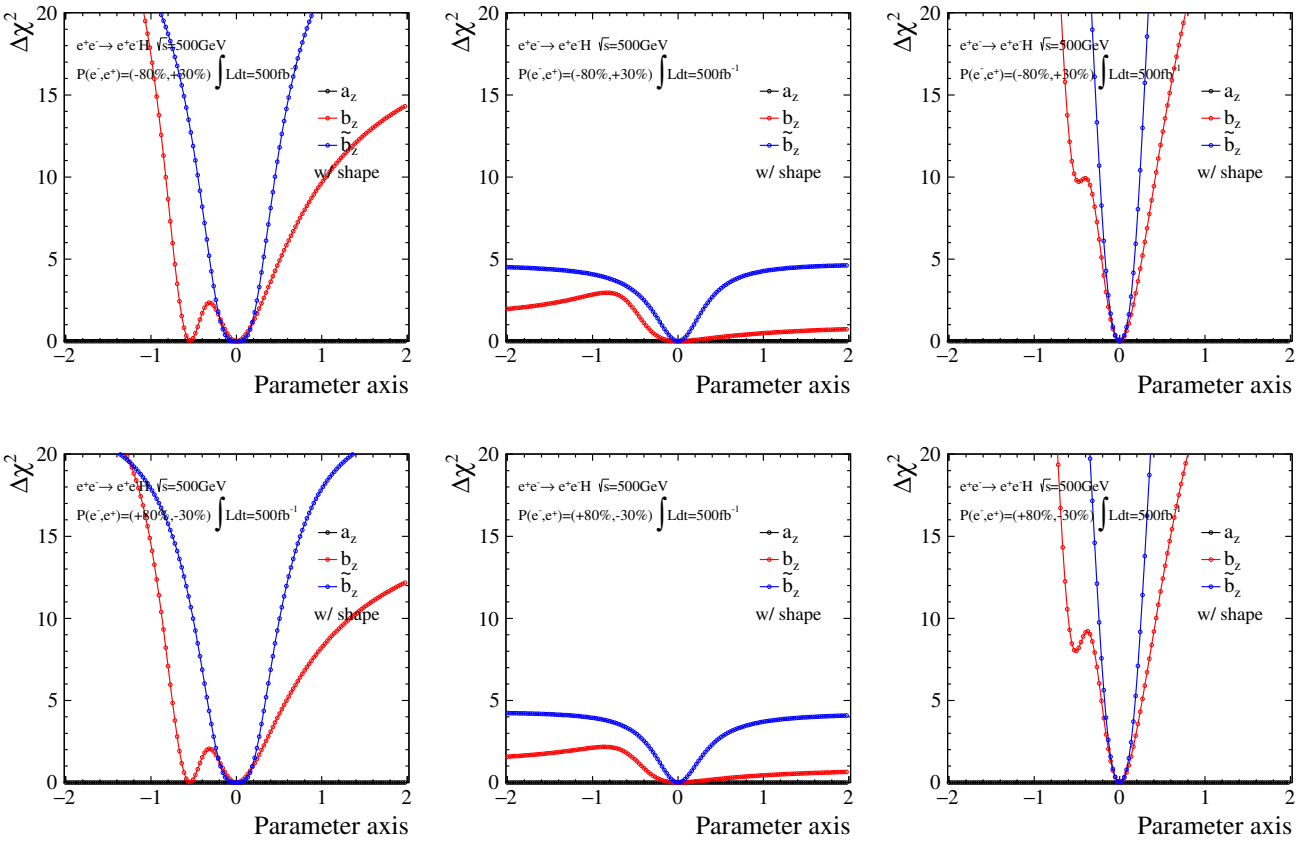

Figure 133: The distributions show $\Delta\chi^2$ as a function of each parameter of the anomalous ZZH couplings, and the evaluation is done in the one-parameter space. Black, red, and blue lines on the plots correspond to the parameters a_Z, b_Z, and $\tilde{b}_Z$. Since only the angular information is considered here, the χ^2 values of a_Z is exactly 0 over the given range. In upper and lower plots, the different beam polarizations are assumed with the integrated luminosity of 500 fb^{-1}: P(e^-, e^+)= (-80%,+30%) and (+80%,-30%), respectively. Difference of each column is the angular distributions used for the evaluation: (left) $x(\cos\theta_{Z)}$ binned in 20, (middle) $x(\Delta\Phi_{f\bar{f}})$ binned in 20, and (right) $x(\cos\theta^*_f, \cos\theta_Z, \Delta\Phi_{f\bar{f}})$ binned in $5\times5\times5$ are used respectively.

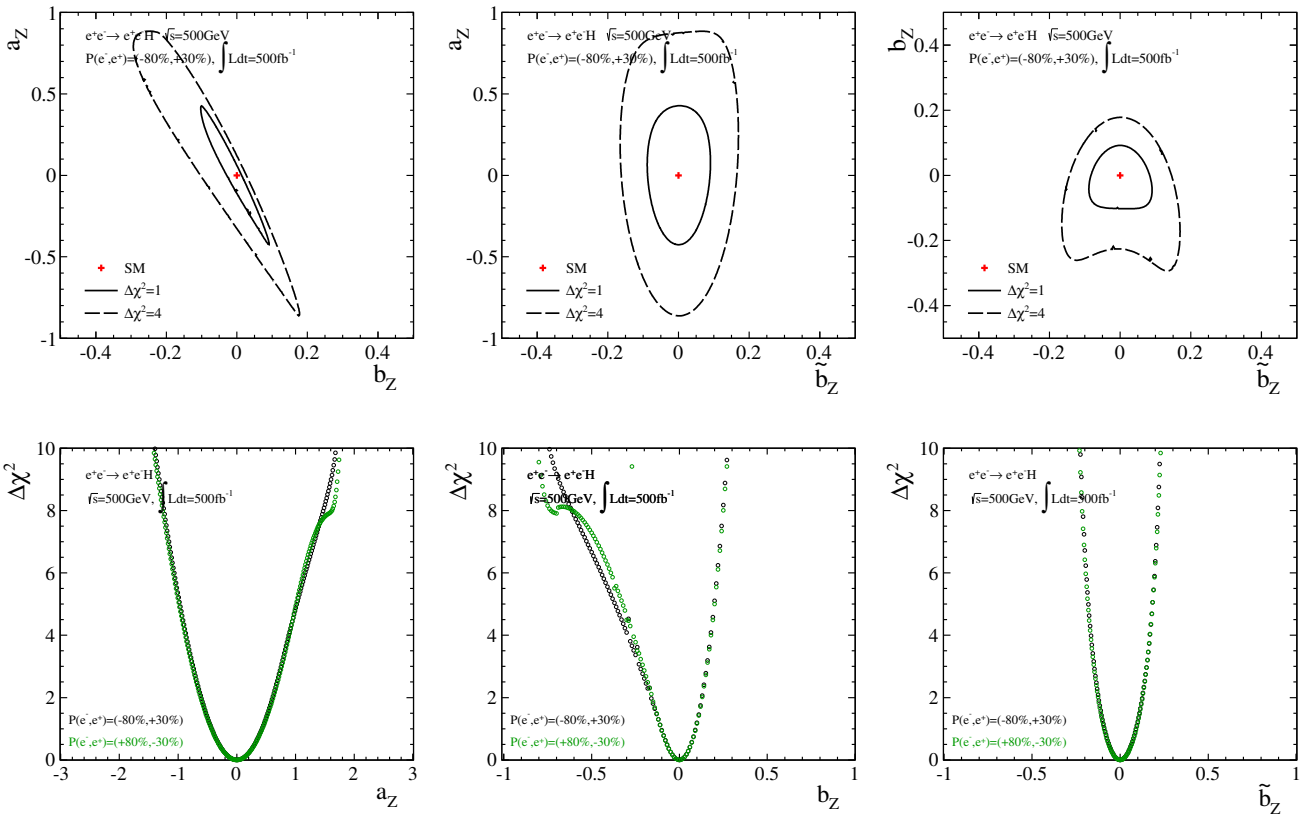

$$\sqrt{s} = 500 \text{ GeV with } \int \text{Ldt} = 500 \text{ fb}^{-1} \text{ and } \text{P}(e^-, e^+) = (-80\%, +30\%)$$

$$\begin{cases} a_Z = [-0.426, \quad 0.428] \\ b_Z = [-0.1026, \quad 0.0918] \\ \tilde{b}_Z = [-0.0886, \quad 0.0904] \end{cases}, \quad \rho = \begin{pmatrix} 1 & -0.9919 & -0.0241 \\ - & 1 & 0.0235 \\ - & - & 1 \end{pmatrix}$$

$$\sqrt{s} = 500 \text{ GeV with } \int \text{Ldt} = 500 \text{ fb}^{-1} \text{ and } \text{P}(e^-, e^+) = (+80\%, -30\%)$$

$$\begin{cases} a_Z = [-0.433, \quad 0.435] \\ b_Z = [-0.1035, \quad 0.0927] \\ \tilde{b}_Z = [-0.0906, \quad 0.0919] \end{cases}, \quad \rho = \begin{pmatrix} 1 & -0.9914 & -0.0103 \\ - & 1 & 0.00456 \\ - & - & 1 \end{pmatrix}$$

Figure 134: (Upper): The plots show contours corresponding to the 1σ and 2σ sensitivities to the anomalous ZZH couplings. The fitting is performed with the muon channel only under the three free parameter space. The integrated luminosity of 500 fb^{-1} with the beam polarization state P(e^-, e^+)= (-80%,+30%) is assumed. The results are projected onto the two-dimensional parameter spaces a_Z-b_Z, a_Z-$\tilde{b}_Z$, and b_Z-$\tilde{b}_Z$. Both of the information, which are the three-dimensional distributions $x(\cos\theta^*_f, \cos\theta_Z, \Delta\Phi_{f\bar{f}})$ binned in 5×5×5 and the production cross-section are combined. (Middle): The plots show $\Delta\chi^2$ distributions as a function of each parameter space of the anomalous couplings a_Z, b_Z, and $\tilde{b}_Z$. The distributions are obtained by using both information (the angles and the cross-section) and scanning one parameter while setting the other two parameters to be completely free. (Lower): The explicit values corresponding to the 1σ bounds for each anomalous parameter a_Z, b_Z, and $\tilde{b}_Z$ and the correlation matrix indicating correlation coefficients between the parameters.

A.5 $e^+e^- \to Zh \to q\bar{q}h,\ h \to b\bar{b}$ at $\sqrt{s} = 500$ GeV

Among the analysis using 250 GeV processes, the most powerful channel was the hadronic channel of the Zh although one of the useful observable $\Delta\Phi$ is not fully reconstructed with the sensitivity from 0 to 2π. At 500 GeV the production cross-section is actually less than that of 250 GeV, nevertheless, it is expected that better sensitivity to the anomalous couplings can be extracted with the hadronic channel, compared to the leptonic channels.

A.5.1 Reconstruction and background suppression

Contamination of the signal process due to the $\gamma\gamma$-hadrons which is derived from radiated photons from the initial electron-positron beam become serious at 500 GeV. The reaction $\gamma\gamma$-hadrons generate objects which have low transverse momenta and these objects fly parallel to beam direction. These objects are mixed with the signal process and pollute it.

Removing overlay and jet pairing :

The k_T jet clustering which is described in the previous section is often implemented to remove these overlaid objects frying along the beam direction. Fig. 135 show the invariant mass of the Higgs and the Z boson in the process $e^+e^- \to Zh \to qqh$ at 500 GeV. Events are generated and reconstructed with and without the overlaid objects and all PFOs are inclusively clustered into four pseudo jets with the Durham jet clustering and paired by constraining with $\chi^2 = ((M_{ij} - M_h)/\sigma_h)^2 + ((M_{kl} - M_Z)/\sigma_Z)^2$, where $i,\ j,\ k$, and l give indices for each pseudo jet.

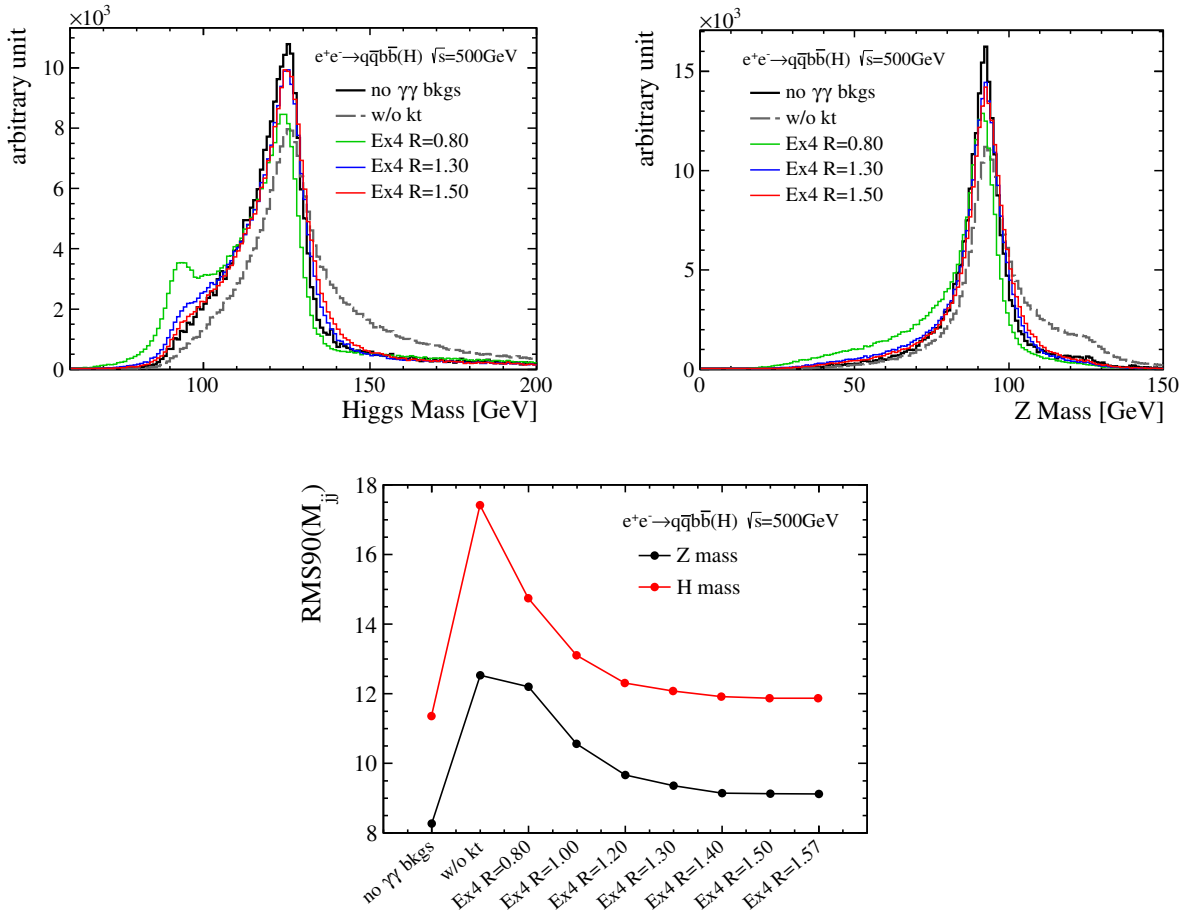

Figure 135:

If the Durham jet clustering is applied directly without the exclusive k_T jet clustering, the mass distributions are clearly broader. When the exclusive k_T jet clustering is applied with the

parameter R, the mass distribution of the Higgs boson become gradually shaper. To quantify the effect of the overlaid objects and optimize the parameter R, the RMS90 is defined, which is defined as RMS ($=\sqrt{\sum_i^n x_i^2/n}$) in the smallest range of the mass distribution containing 90 % of the events *** reference***. The value of RMS90 gets plateau at R of more than 1.5.

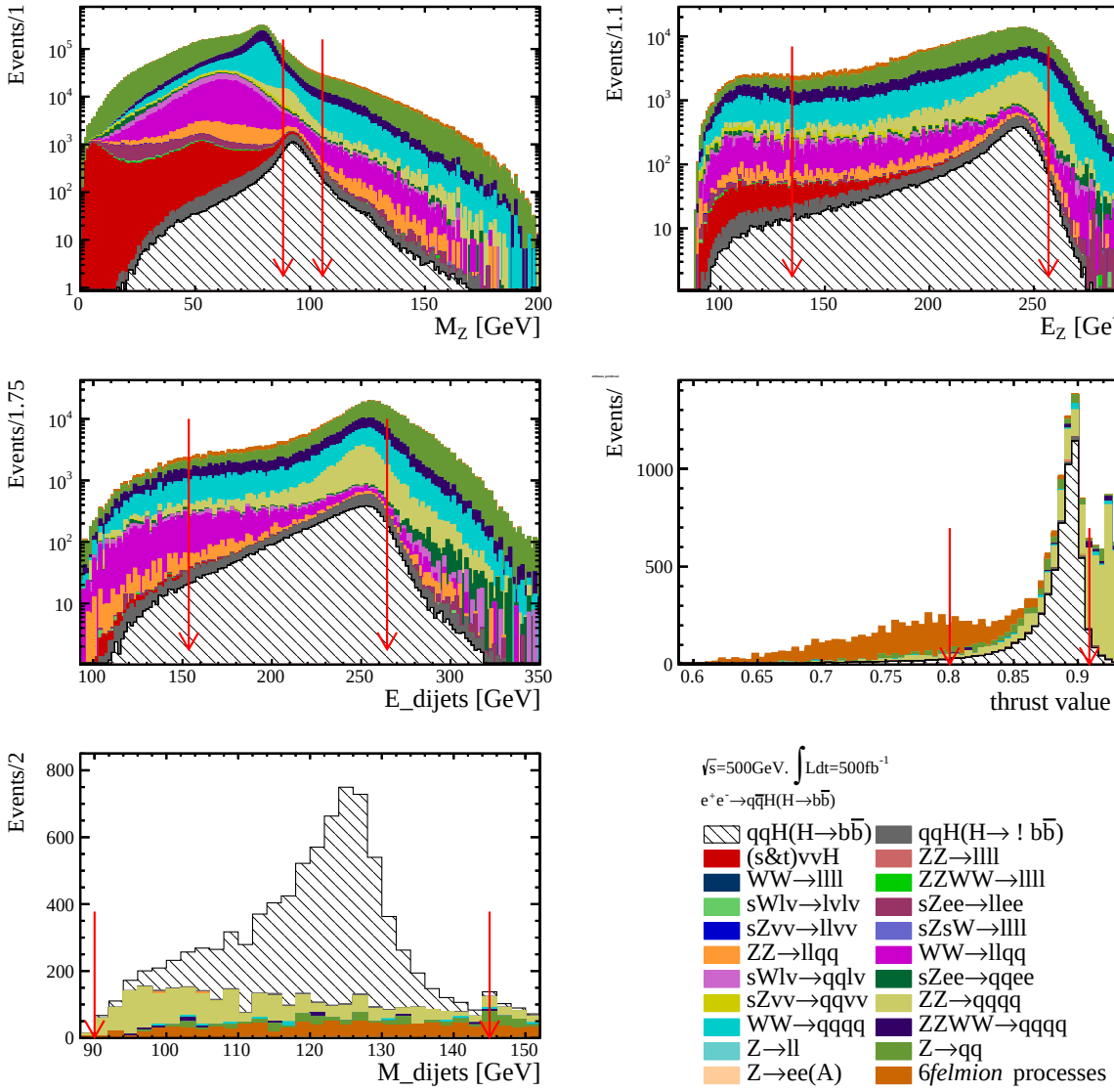

Figure 136: The distributions show each observable used for the background suppression assuming 500 fb^{-1} with P(e^-, e^+)= (-80%,+30%). The explanation of the observables are given in the text. Red arrows on each plot indicate the cut values applied to each observable as the background suppression.

Background suppression :

The background suppression was performed by using the same observables which are used for the e^+e^-h study at 250 GeV. Each observable implemented for the suppression is illustrated in Fig. 129. The explicit values for each observable are optimized by calculating the signal significance and its detail is given in Table 10, where the left-handed polarization state: P(e^-, e^+)= (-80%,+30%) with the integrated luminosity of 500 fb^{-1} are assumed.

- $N_{jet} = 4$ and $N_{isolep} = 0$

Properly four jets are clustered and exist in a event, additional the number of isolated leptons must be 0 since the final state of the signal process is full hadronic environment.

- $N_{pfo} \in [55,\ 170]$
  The number of Particle Flow Objects (PFOs). Two fermion processes and four fermion semi-leptonic decay processes can be almost suppressed with this observable.
- $E_Z \in [87.8,\ 118.5]$ GeV and $M_Z \in [82.3,\ 102.3]$ GeV
  The energy of the Z boson calculated with the paired two jets. The invariant mass of the Z boson calculated with the paired two jets, which should be close to the mass of the Z boson.
- The sum of $b\text{-}tag \in [1.25,\ 2.0]$
  Both of the jets originating from the Higgs boson have higher b-likeness since the $h \to b\bar{b}$ channel is selected as the signal process.
- $E_h \in [98.7,\ 150.7]$ GeV
  The energy of the Higgs boson.
- Minimum $N_{pfo} \in [5,\ 40]$ among jets and
  The jet clustering parameter $-\log y_{32} \in [0.5,\ 3.62]$ and $-\log y_{43} \in [1.8,\ 5.52]$
  The minimum number of PFOs among each jet. y_{32} show the minimum distance when the pseudo-jets are merged from 3 to 2. This is useful to discriminate topology of two jets environment from that of multiple jets. y_{43} show the minimum distance when the pseudo-jets are merged from 4 to 3.
- The thrust value $T \in [0.5,\ 0.89]$
  T denotes the *thrust* value explained in Sec. 5.5. When T is close to 1, an event topology could be a pair of narrow jets generated linearly. If T gets close to $1/2$, the topology will be multiple jets which spread to all directions in the detector.
- $M_h \in [90,\ 142]$ GeV
  The invariant mass of the Higgs boson calculated with the paired two jets, which is the mass window to determine a Poisson error calculated by the remaining number of events on each bin on kinematical histograms.

Table 11: The expected number of remaining signal and background events after each cut for the $Zh \to q\bar{q}b\bar{b}(h)$ at $\sqrt{s}$=250 GeV, with with both of the beam polarization states: P(e^-, e^+)= (-80%,+30%) and (+80%,-30%). The integrated luminosity of 250 fb^{-1} is assumed. The signal efficiency ϵ and significance S_{sig} are also given in the table.

$\sqrt{s}$=500 GeV P(e^-, e^+)= (-80%,+30%) L_{int}=500 fb^{-1}

	$Zh \to$		SM backgrounds				
Cut variables	$q\bar{q}b\bar{b}$	ϵ	$q\bar{q}$+others	$2f$	$4f$	$6f$	S_{sig}
No cut	20134	100	14700	$1.32 \cdot 10^7$	$1.62 \cdot 10^7$	$4.04 \cdot 10^5$	-
$N_{isolep} = 0$	20094	99.80	11974	$1.11 \cdot 10^7$	$1.06 \cdot 10^7$	$2.15 \cdot 10^5$	4.28
$N_{pfo} \in [55,\ 190]$	20041	99.53	11021	$5.41 \cdot 10^6$	$5.50 \cdot 10^6$	$2.05 \cdot 10^5$	5.99
$M_Z \in [88.29,\ 105.4]$ GeV	11660	57.91	5109	$3.90 \cdot 10^5$	$4.25 \cdot 10^5$	$5.10 \cdot 10^4$	12.4
$E_Z \in [134.3,\ 257.0]$ GeV	11062	54.94	4761	$3.36 \cdot 10^5$	$3.31 \cdot 10^5$	$4.12 \cdot 10^4$	13.0
$E_h \in [153.5,\ 264.5]$ GeV	9980	49.56	4174	$1.64 \cdot 10^5$	$2.42 \cdot 10^5$	$3.14 \cdot 10^4$	14.9
b-$tag \in [1.46,\ 2.0]$	6911	34.32	140	3210	6760	5334	46.2
Min $N_{pfo} \in [5,\ 40]$	6857	34.05	131	2248	6636	5040	47.4
$-\log y_{23} \in [0.22, 4.33]$	6526	32.41	120	1538	5130	5003	48.2
$-\log y_{34} \in [2.27, 6.23]$	6330	31.43	118	794	4774	4953	48.6
thrust $T \in [0.8,\ 0.91]$	5731	28.46	93	466	1837	1466	58.5
$M_h \in [90,\ 145]$ GeV	5670	28.16	90	240	1608	882	61.5

$\sqrt{s}$=500 GeV P(e^-, e^+)= (+80%,-30%) L_{int}=500 fb^{-1}

	$Zh \to$		SM backgrounds				
Cut variables	$q\bar{q}b\bar{b}$	ϵ	$q\bar{q}$+others	$2f$	$4f$	$6f$	S_{sig}
No cut	13574	100	9910	$8.81 \cdot 10^6$	$5.58 \cdot 10^6$	$1.65 \cdot 10^5$	-
$N_{isolep} = 0$	13547	99.80	8072	$6.97 \cdot 10^7$	$3.67 \cdot 10^6$	$8.78 \cdot 10^4$	4.13
$N_{pfo} \in [55,\ 190]$	13511	99.53	7430	$3.22 \cdot 10^6$	$6.00 \cdot 10^5$	$8.42 \cdot 10^4$	6.81
$M_Z \in [88.29,\ 108.0]$ GeV	8139	59.96	3603	$2.50 \cdot 10^5$	$6.47 \cdot 10^4$	$2.38 \cdot 10^4$	13.8
$E_Z \in [115.7,\ 255.7]$ GeV	7771	57.24	3415	$2.19 \cdot 10^5$	$5.49 \cdot 10^4$	$2.21 \cdot 10^4$	14.0
$E_h \in [141.5,\ 264.5]$ GeV	7086	52.20	3035	$1.13 \cdot 10^5$	$4.18 \cdot 10^4$	$1.83 \cdot 10^4$	16.5
b-$tag \in [1.30,\ 2.0]$	5275	38.86	134	2928	3411	4058	42.0
Min $N_{pfo} \in [5,\ 40]$	5233	38.55	121	2231	3299	3751	43.3
$-\log y_{23} \in [0.27, 4.55]$	5108	37.63	115	1593	2854	3735	44.1
$-\log y_{34} \in [2.27, 6.49]$	4991	36.76	113	897	2695	3709	44.8
thrust $T \in [0.80,\ 0.909]$	4403	32.43	90	522	1027	983	52.5
$M_h \in [90,\ 145]$ GeV	4351	32.05	86	282	887	598	55.2

A.5.2 Acceptance and migration on observables

Fig. 137, and Fig. 138 show summary plots on the one-dimensional angular distributions of $\cos\theta_Z$, and $\Delta\Phi$ binned in 30, where the remaining signal and background distributions, event acceptance η, and the probability of the migration effects $\bar{f}$ after the background suppression are shown. Summary plots of the two-dimensional distribution of $x(\cos\theta_Z, \Delta\Phi_{f\bar{f}})$ are also given in Fig. 139 which are binned in 10×10.

The event acceptance of $\Delta\Phi$ distribution maintains flatness well, but drops as well appear in the $\cos\theta_Z$ distribution. Theses drops in both edges are not seen in the hadronic channel at 250 GeV. This could be come from the situation of the boosted final state objects and the usage of the k_T jet algorithm. Since the final state objects decaying from the high momentum Z boson are boosted and could fly rather along the direction of the Z boson, and become missing if the objects fly along the beam pipe. Furthermore, the objects which are located in a close area could be removed because of the usage of the k_T jet algorithm. Therefore, the reconstructed Z bosons in such reactions have incomplete information as the Z boson, and those events are removes when applying the cuts using the information of the Z boson. This situation is also irreducible. The migration effects are slightly observed for both observables, which is mainly derived from the miss pairing of the pseudo-jets.

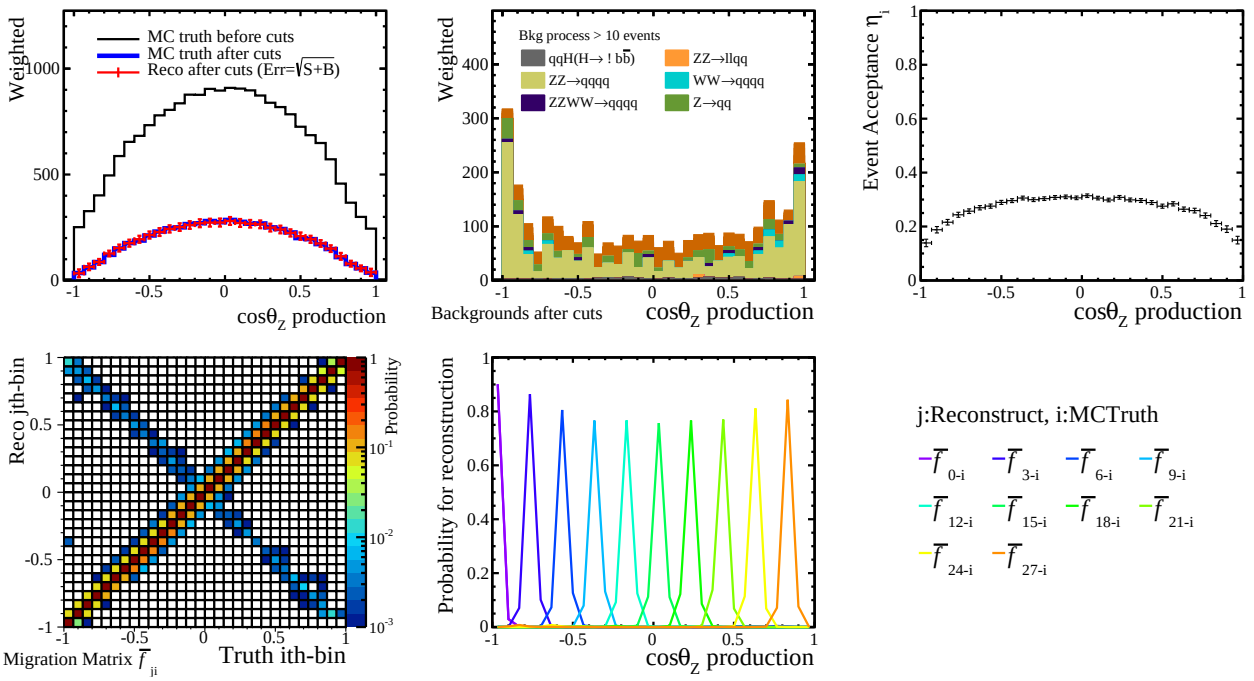

Figure 137: The distributions show the summary of the polar angle of the Z boson ($\cos\theta_Z$) after the background suppression. (Top left and middle): the remaining signal and the background distribution, which are given with the MC truth and the reconstructed, where the statistical error is given as the standard deviation of the Poisson probability. (Top right): the event acceptance function η_i. (Bottom left and middle): the distribution shows the probability matrix of the migration ($\bar{f}_{ji}$) that is applied for the reconstruction of the realistic distribution of $\cos\theta_Z$, and the cross-sections of $\bar{f}_{ji}$ as 1-dim plots.

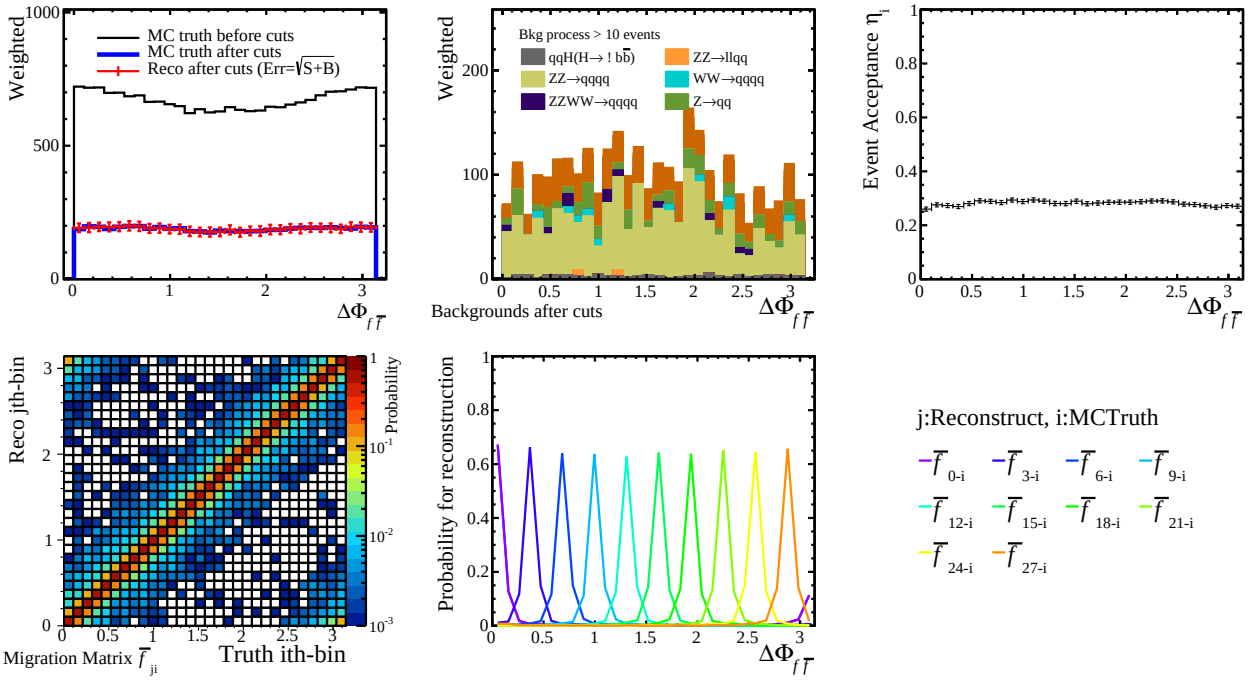

Figure 138: The distributions show the summary of the angle between production planes in the laboratory frame ($\Delta\Phi$) after the background suppression. (Top left and middle): the remaining signal and the background distribution, which are given with the MC truth and the reconstructed. (Top right): the event acceptance function η_i. (Bottom left and middle): the probability matrix of the migration ($\bar{f}_{ji}$) that is applied for the reconstruction of $\Delta\Phi$, and the cross-sections of $\bar{f}_{ji}$ as 1-dim plots.

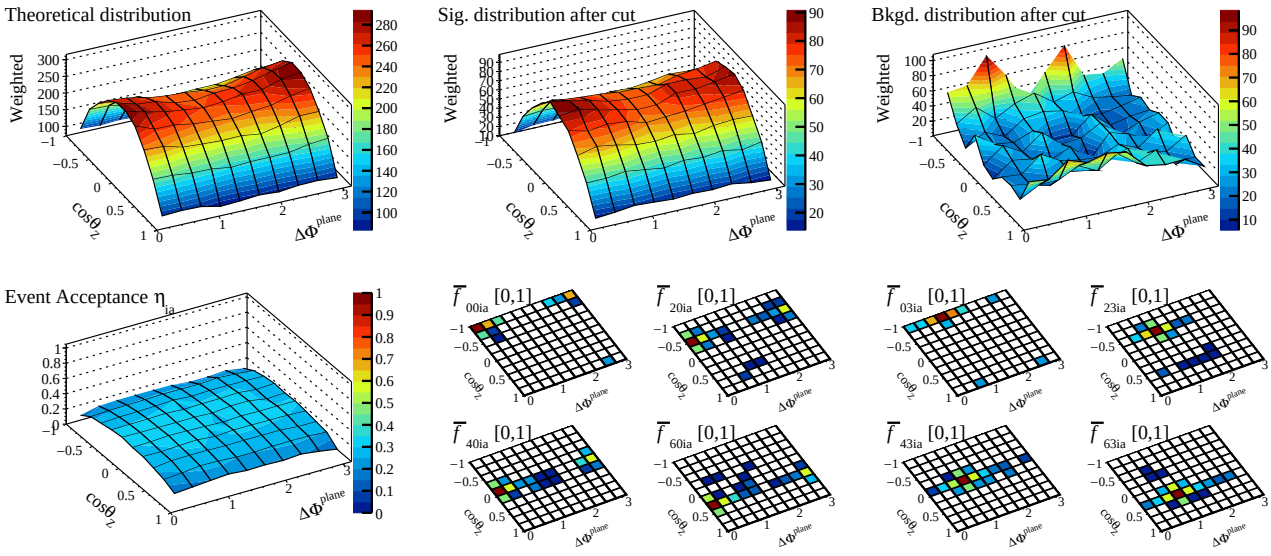

Figure 139: The distributions show the summary of the two-dimensional distribution consisted of the production angle of the Z boson $\cos\theta_Z$ and the angle between production planes in the laboratory frame ($\Delta\Phi$) after the background suppression. (Top left, middle, and right): The remaining MC truth and the reconstructed signal distribution, and the background distribution, respectively. (Bottom left): The event acceptance function η_{ia} shows whether each signal event on each bin is accepted or not after the suppression. (Bottom middle and right): Several examples on the probability matrix of the migration where the 2-dim plots give the cross-sections of $\bar{f}_{jbia}$ since the illustration of the migration is too difficult which is a 4-dimension distribution.

A.5.3 Impact of angular distributions

Fig. 140 give $\Delta\chi^2$ distributions for each one-dimensional parameter axis, where one-dimensional distributions of $x(\cos\theta_Z)$ and $x(\Delta\Phi)$ binned in 20, and the three-dimensional distribution of $x(\cos\theta^*_f, \cos\theta_Z, \Delta\Phi_{f\bar{f}})$ binned in $5\times5\times5$ are used for the evaluation. Also, Fig. 141 give $\Delta\chi^2$ distributions for each two-dimensional parameter space with each kinematical information. The $\Delta\Phi$ distribution actually gives the half sensitivity [0–π], compared to the lepton channel. However, because the large number of signal events remain, significantly better sensitivity is achievable. The plots indicate that the different shape information have different power against the anomalous parameters.

A.5.4 Sensitivity in three parameter space

The sensitivities to the anomalous ZZH couplings with the hadronic channel only are given in Fig. 142, where the variation of the three-dimensional distribution $x(\cos\theta^*_f, \cos\theta_Z, \Delta\Phi_{f\bar{f}})$ binned in $5\times5\times5$ and the variation of the production cross-section are considered.

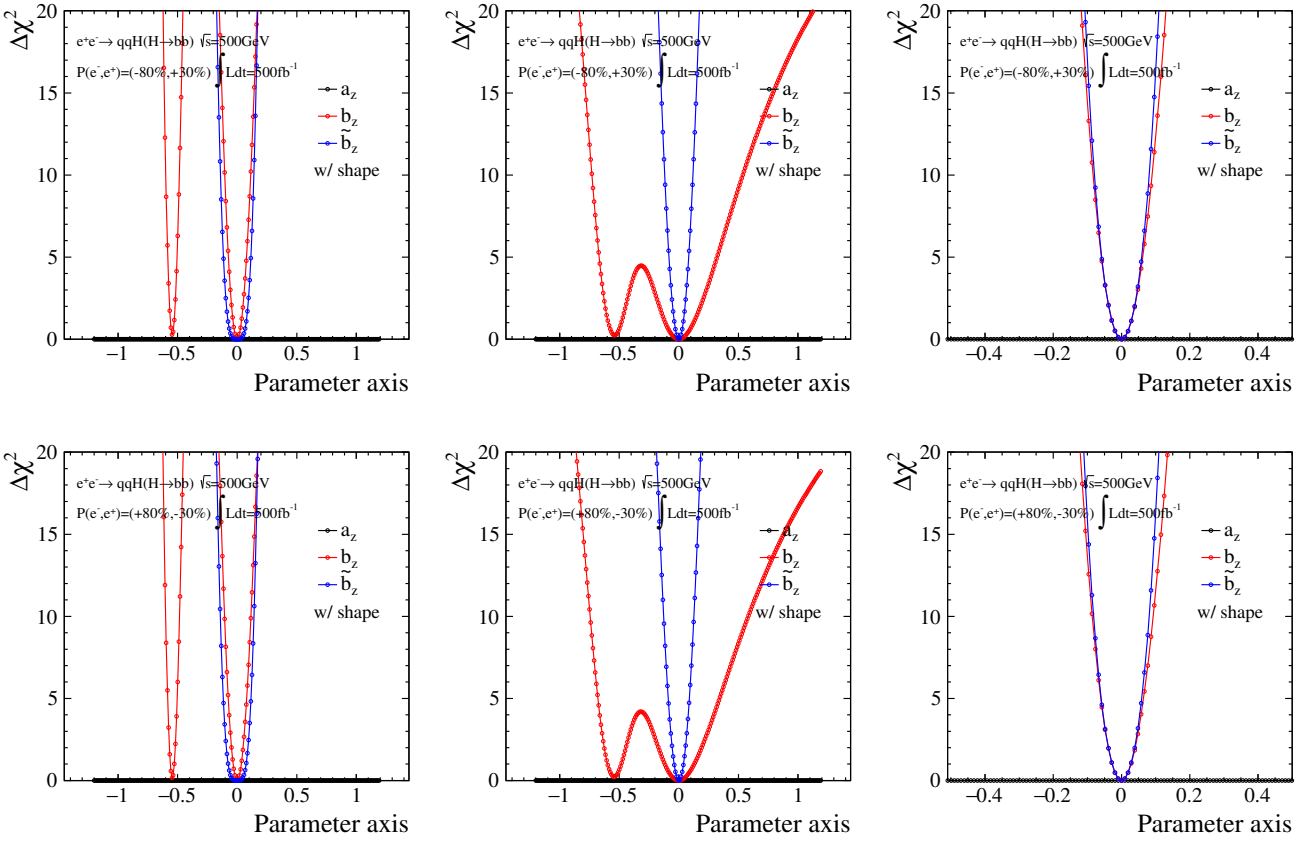

Figure 140: Distributions show $\Delta\chi^2$ as a function of each parameter which gives anomalous ZZH couplings, and the evaluation is done in the one-parameter axis. Black, red, and blue line on the plots correspond to the parameters a_Z, b_Z, and $\tilde{b}_Z$. Since only the angular information is considered here, the χ^2 values of a_Z is 0.0 over the given range. In upper and lower plots the different beam polarizations are assumed with the integrated luminosity of 250 fb^{-1}: P(e^-, e^+)= (-80%,+30%) and (+80%,-30%), respectively. Difference of each column is the angular distributions used for the evaluation: (left) $x(\cos\theta_{Z)}$ binned in 20, (middle) $x(\Delta\Phi_{f\bar{f}})$ binned in 20, and (right) $x(\cos\theta^*_f, \cos\theta_Z, \Delta\Phi_{f\bar{f}})$ binned in $5\times5\times5$ are used respectively.

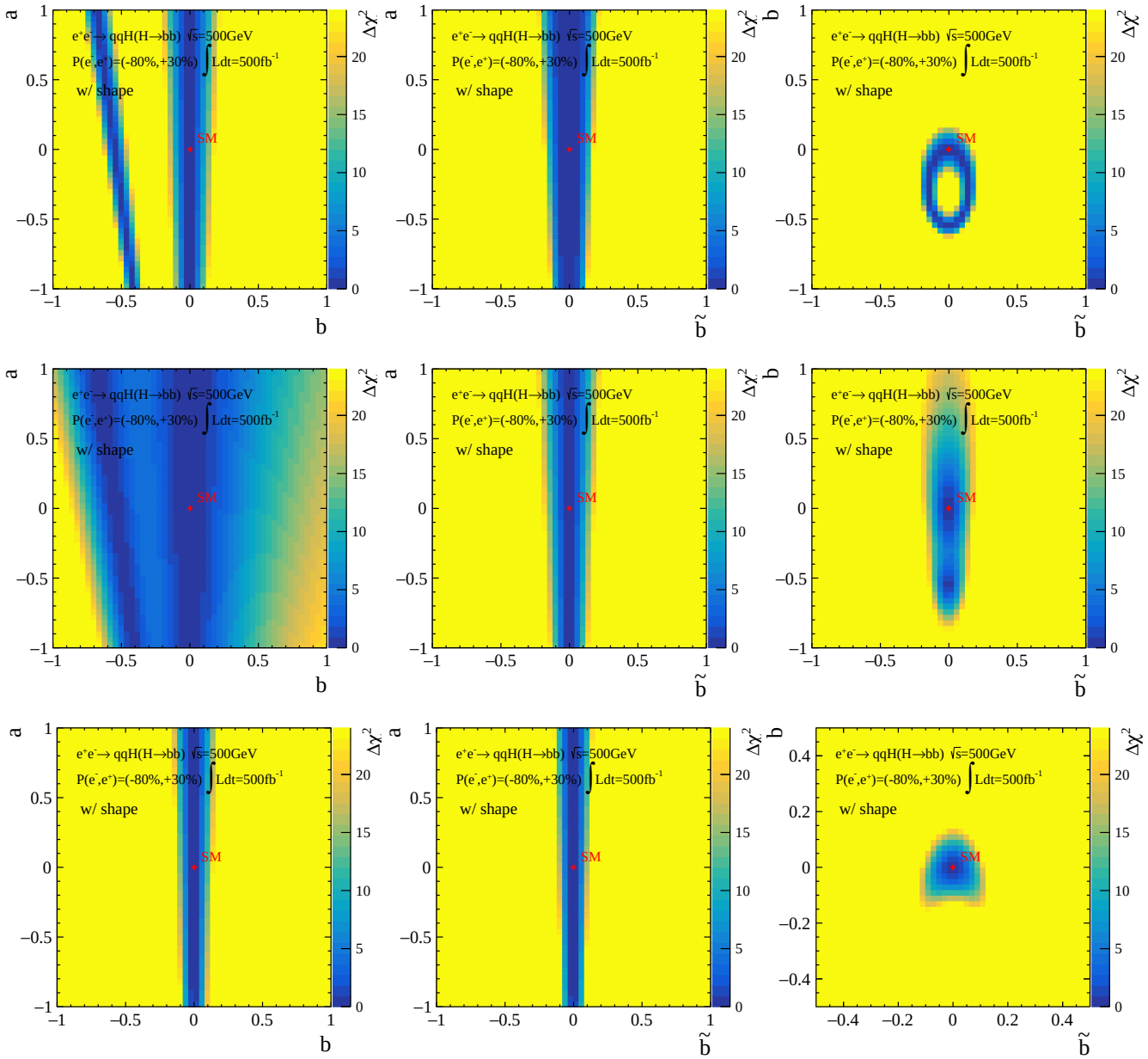

Figure 141: The distributions show $\Delta\chi^2$ in the two-dimensional parameter space a_Z-b_Z, a_Z-$\tilde{b}_Z$, and b_Z-$\tilde{b}_Z$. Only each angular distribution is used for the evaluations: (top) $x(\cos\theta_{Z)}$ binned in 20, (middle) $x(\Delta\Phi_{f\bar{f}})$ binned in 20, and (bottom) $x(\cos\theta^*_f, \cos\theta_Z, \Delta\Phi_{f\bar{f}})$ binned in 5×5×5 are used respectively. The results are given only for the beam polarization of P(e^-, e^+)= (-80%,+30%). The sensitivity is 0.0 for the any a_z when b_Z or $\tilde{b}_Z$ is 0.0.

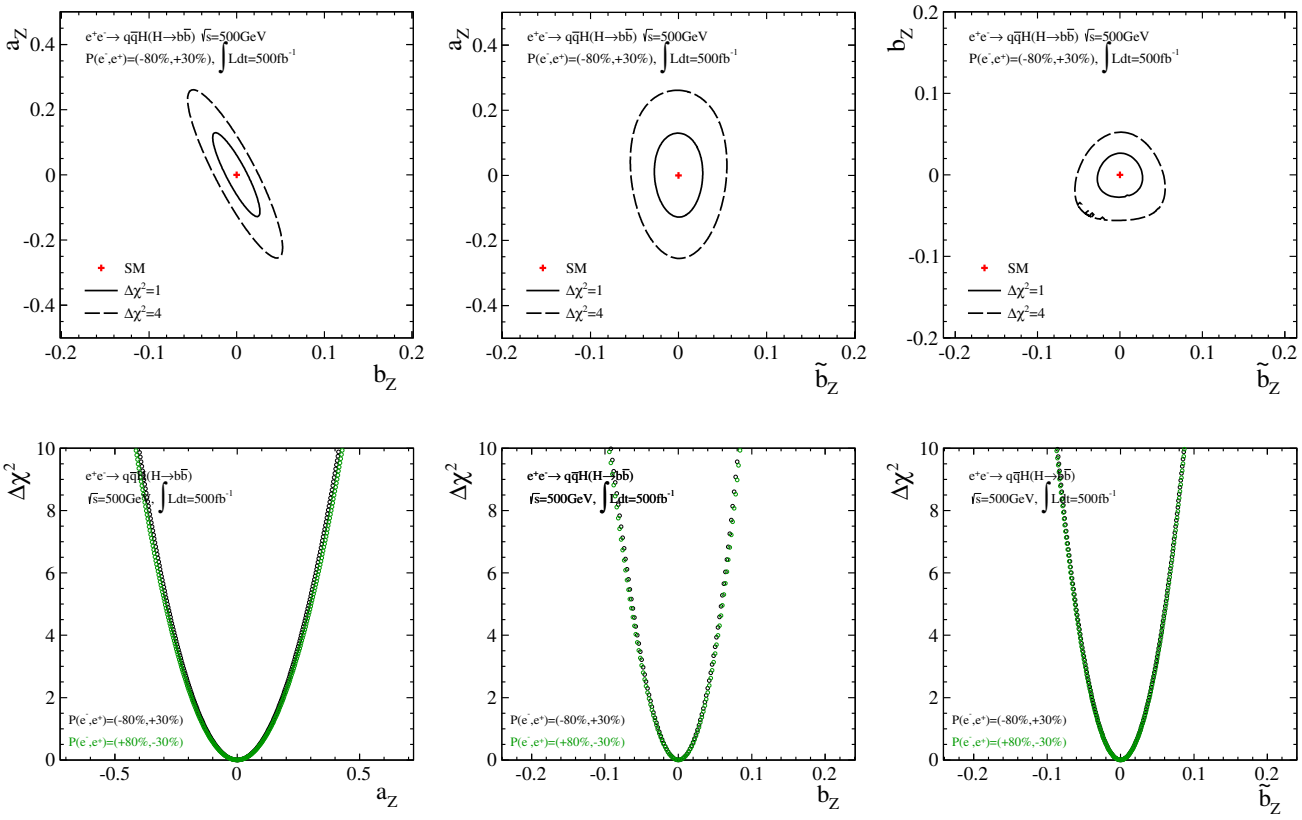

$$\sqrt{s} = 500 \text{ GeV with } \int \text{Ldt} = 500 \text{ fb}^{-1} \text{ and } \text{P}(e^-, e^+) = (-80\%, +30\%)$$

$$\begin{cases} a_Z = [-0.128, \quad 0.130] \\ b_Z = [-0.0274, \quad 0.0266] \\ \tilde{b}_Z = [-0.0275, \quad 0.0275] \end{cases}, \quad \rho = \begin{pmatrix} 1 & -0.9855 & 0.0165 \\ - & 1 & -0.0457 \\ - & - & 1 \end{pmatrix}$$

$$\sqrt{s} = 500 \text{ GeV with } \int \text{Ldt} = 500 \text{ fb}^{-1} \text{ and } \text{P}(e^-, e^+) = (+80\%, -30\%)$$

$$\begin{cases} a_Z = [-0.133, \quad 0.134] \\ b_Z = [-0.0283, \quad 0.0274] \\ \tilde{b}_Z = [-0.0279, \quad 0.0278] \end{cases}, \quad \rho = \begin{pmatrix} 1 & -0.9853 & -0.0797 \\ - & 1 & 0.1128 \\ - & - & 1 \end{pmatrix}$$

Figure 142: (Upper): The plots show contours corresponding to the 1σ and 2σ sensitivities to the anomalous ZZH couplings. The fitting is performed with the muon channel only under the three free parameter space. The integrated luminosity of 500 fb^{-1} with the beam polarization state P(e^-, e^+)= (-80%,+30%) is assumed. The results are projected onto the two-dimensional parameter spaces a_Z-b_Z, a_Z-$\tilde{b}_Z$, and b_Z-$\tilde{b}_Z$. Both of the information, which are the three-dimensional distributions $x(\cos\theta^*_f, \cos\theta_Z, \Delta\Phi_{f\bar{f}})$ binned in $5\times5\times5$ and the production cross-section are combined. (Middle): The plots show $\Delta\chi^2$ distributions as a function of each parameter space of the anomalous couplings a_Z, b_Z, and $\tilde{b}_Z$. The distributions are obtained by using both information (the angles and the cross-section) and scanning one parameter while setting the other two parameters to be completely free. (Lower): The explicit values corresponding to the 1σ bounds for each anomalous parameter a_Z, b_Z, and $\tilde{b}_Z$ and the correlation matrix indicating correlation coefficients between the parameters.

A.6 $e^+e^- \to e^+e^-h,\ h \to b\bar{b}$ at $\sqrt{s} = 500$ GeV

At $\sqrt{s}$ =500 GeV the ZZ-fusion process opens and has large cross-section which is twice larger than the electron channel of the Higgs-strahlung process. Therefore, the ZZ-fusion process is expected to give sizable impact on the improvement of the sensitivity to the anomalous ZZH couplings because the a_Z and b_Z parameter relation has opposite correlation with the Higgs-strahlung process as discussed in Sec. 6.3. Furthermore, a reaction of the ZZ-fusion event has a very clear features such as, a pair of an electron and positron which have high momentum and fly to very forward and backward region, and there are clear Higgs decay objects in addition, especially when selecting the decay of $h \to b\bar{b}$. Thus, the identification of the signal reaction will be easier compared to other Higgs channels. It is also expected that SM backgrounds can be almost suppressed by exploiting there signal features, which is discussed in Sec. A.2 to some extent.

A.6.1 Reconstruction and background suppression

The flow of the analysis is basically similar with the selection of the other lepton channels of the Higgs-strahlung and the ZZ-fusion process at 250 GeV.

Isolated lepton finding and radiation recovering :

The finding of the isolated electrons and the recovering of the radiated photons are implemented by IsoLeptonFinder, which is explained in Sec. 5.2. The requirements for extracting the isolated electrons are as follows,

- A charged particle must have momentum of greater than 5 GeV.
- MLP response for the electron candidate must be larger than 0.5.
- A neutral particle which is identified as a photon based on the criterion that the polar angle along the charged particle exceeds 0.999 is merged into the charged particle as a radiated photon because of bremsstrahlung.

Plots in Fig. 143 illustrate the invariant mass of the pair of the electron and positron and the recoil mass against the pair, where the effect of the radiation recovering is separately plotted.

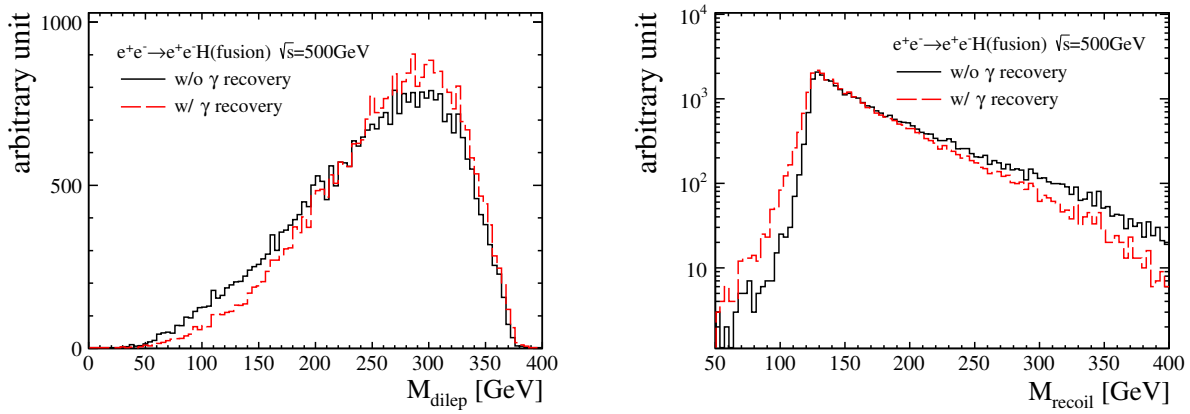

Figure 143: The distributions show (left) the invariant mass of the pair of the electron and positron M_{di-lep} in the ZZ-fusion process at $\sqrt{s}$=500 GeV and (right) the recoil mass against the pair M_{reco}. Black and red lines in both plots correspond to the situation which the radiation recovering is applied to or is not, respectively.

Removing overlay and jet clustering :

Since relatively large $\gamma\gamma$ →hadrons coming from the beam interactions are overlaid in events at

500 GeV, the k_T jet algorithm is exclusively implemented to remove them. After disentangling the pseudo jets, the Durham jet algorithm is applied to cluster the remaining objects inclusively into the expected jets. where the heavy flavor tagging is also implemented through LCFIPlus.

Reconstructed angular observables :

Fig. 144 show the reconstructed Higgs momentum P_{higgs} in the laboratory frame and the angle between production planes $\Delta\Phi$ in the Higgs rest-frame, which are sensitive to the anomalous couplings. The reconstructed $\Delta\Phi$ distribution has dips, which is the same reason with the other lepton channels of the Higgs-strahlung process (a missing final state positron which flies along the beam axis). The reconstructed P_{higgs} distribution is slightly shifted from the truth distribution because missing neutrinos are generated through decay chains of the b-quark like $b \to W(\to l\nu)+c$ and so on.

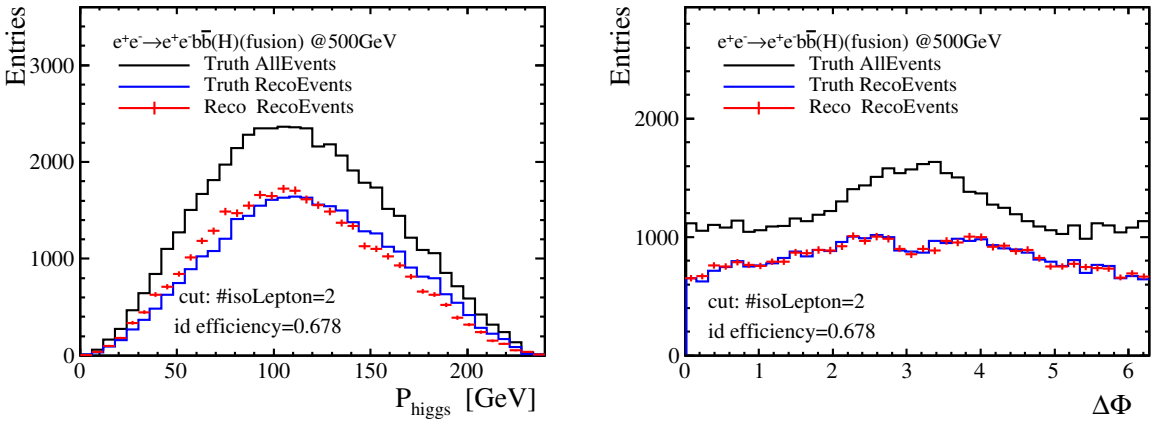

Figure 144: Plots show the MC truth and reconstructed distributions (left), the migration effects (middle), and resolutions (right) of $\cos\theta_h$, $\Delta\Phi$, and P_h in the ZZ-fusion process at $\sqrt{s}$=250 GeV. Those observables give the sensitivities to the anomalous ZZH couplings. The clear dip can be seen at π due to the missing final state positron.

Background suppression :

Unlike in the case of the ZZ-fusion analysis at 250 GeV, the SM backgrounds and the s-channel Higgs production processes which has the same final state but the different feature are easily removed from the signal reaction by using several observables. The only dominant background is a diagram which generates a single Z boson together with a pair of e^- and e^+. These background candidates are illustrated in Fig. 145.

The s-channel Higgs production with the decay of $Z \to e^-e^+$ has the same final state with the signal process, whose kinematics is possible to change depending on the existence of the anomalous couplings. Therefore, s-channel should be removed using the mass of the di-lepton system M_{di-lep}, which is close to M_Z for s-channel process. However, because the lower are of the M_{di-lep} is slightly correlated with higher area of the momentum of the Higgs boson as discussed in Sec. A.2.2, the usage of $M_{di\text{-}lep}$ slightly will affect the acceptance of the momentum distribution. The observables applied for the background suppression are listed as follows, and several ones are illustrated in Fig. 147. The detail numbers for each cut are given in Table 12.

- A pair of an electron and a positron must exist exactly in one event, in which MVA based lepton selection is used except the constraint of the mass of the Z boson.
- $N_{tracks} \in [13,\ 65]$
  This gives the number of charged tracks, which is useful to remove large two-fermion SM

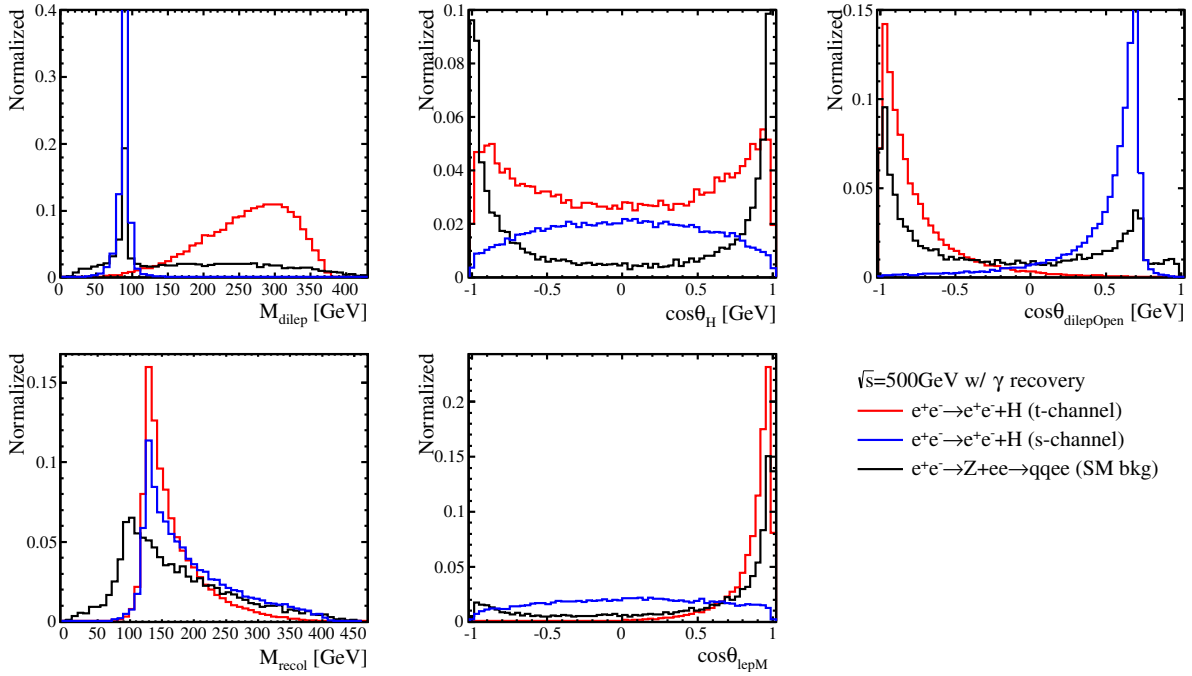

Figure 145: The distributions show the several observables in the signal and the dominant backgrounds processes at 500 GeV: the di-lepton mass M_{dilep}, the polar angle of the Higgs boson $\cos\theta_h$, the opening angle in the di-lepton system $\cos\theta_{ep}^{open}$, the recoil mass against the di-lepton system M_{reco}, and the polar angle of the final state electron $\cos\theta_e$. Red line is the signal process of the ZZ-fusion.

backgrounds.

- $M_{dilep} \in [126.0,\ 385.0]$ GeV
  The mass of the di-lepton system has a clear peak at the mass of the Z boson in s-channel process, so this observable can remove such events,
- Sum of b-tag > 1.16
  Both of the jets originating from the Higgs boson have higher b-likeness since the $h \to b\bar{b}$ channel is selected as the signal process.
- $M_{reco} > 114.3$
  This observable is useful to remove one of the dominant backgrounds which is a single Z with an electron pair process and it makes a peak at M_Z.
- $E_{dijet} \in [108.0,\ 255.4]$ GeV
  The visible energy of the di-jet system, which is used to remove scattered remaining SM backgrounds.
- $M_{dijet} \in [100,\ 150]$
  The invariant mass of the Higgs boson calculated with the di-jet system, which is a mass window to determine a statistical error calculated using the remaining number of events on each bin of the distribution

A.6.2 Acceptance and migration on observables

Fig. 147, and Fig. 148 show summary plots on the one-dimensional angular distributions of P_h, and $\Delta\Phi$ binned in 30 after the background suppression, where the remaining signal and background distributions, the event acceptance η, and the probability of the migration effects $\bar{f}$ are shown. A summary plot of the two-dimensional distribution of $x(\cos\theta_h, \Delta\Phi)$ binned in 10×10, where $\cos\theta_h$ denotes polar angle of the Higgs boson, is also given in Fig. 149.

Table 12: The expected number of remaining signal and background events after each cut for the $ZZ \to e^+e^-h,\ h \to b\bar{b}$ at $\sqrt{s}$=500 GeV, with with both of the beam polarization states: P(e^-, e^+)= (-80%,+30%) and (+80%,-30%). The integrated luminosity of 500 fb^{-1} is assumed. The signal efficiency ϵ and significance S_{sig} are also given in the table. (t) and (s) in the table denote t-channel and s-channel Higgs production. 6_f SM background processes are not considered here.

$\sqrt{s}$=500 GeV P(e^-, e^+)= (-80%,+30%)

	e^+e^-h			SM backgrounds			
Cut variables	$(t)h \to b\bar{b}$	ϵ	$h \to$others	$(s)e^+e^-h$	$2f$	$4f$	S_{sig}
No cut	2165	100	1580	1720	$1.32 \cdot 10^7$	$1.62 \cdot 10^7$	-
ID of a ep pair	1471	67.94	883	1395	$1.07 \cdot 10^6$	$4.05 \cdot 10^5$	1.21
$N_{tracks} \in [13,\ 65]$	1466	67.71	722	1301	$1.13 \cdot 10^5$	$1.01 \cdot 10^5$	3.14
$M_{dilep} \in [126.0,\ 385.0]$	1424	65.77	686	10	$8.16 \cdot 10^4$	$5.36 \cdot 10^4$	3.84
Sum of b-tag > 1.16	1160	53.61	24	8	166	4506	15.2
$M_{reco} > 114.3$	1127	52.06	23	8	100	2875	17.5
$E_{dijet} \in [108.0,\ 255.4]$	1091	50.39	17	7	28	2452	18.2
$M_{dijet} \in [100,\ 150]$	977	45.13	12	7	0	337	26.8

$\sqrt{s}$=500 GeV P(e^-, e^+)= (+80%,-30%)

	e^+e^-h			SM backgrounds			
Cut variables	$(t)h \to b\bar{b}$	ϵ	$h \to$others	$(s)e^+e^-h$	$2f$	$4f$	S_{sig}
No cut	1340	100	979	1161	$8.81 \cdot 10^6$	$5.56 \cdot 10^6$	-
ID of a ep pair	911	67.99	547	942	$1.02 \cdot 10^6$	$2.73 \cdot 10^5$	0.8
$N_{tracks} \in [13,\ 65]$	908	67.76	447	878	$1.08 \cdot 10^5$	$8.07 \cdot 10^4$	2.1
$M_{dilep} \in [126.0,\ 385.0]$	882	65.82	425	7	$7.79 \cdot 10^4$	$4.18 \cdot 10^4$	2.5
Sum of b-tag > 0.999	821	61.27	29	6	420	5422	10.0
$M_{reco} \in [118.6,\ 307.1]$	770	57.46	27	6	202	3190	11.9
$E_{higgs} \in [105.9,\ 245.5]$	738	55.07	22	5	58	2694	12.5
$M_{higgs} \in [90,\ 160]$	640	47.76	15	4	0	372	19.9

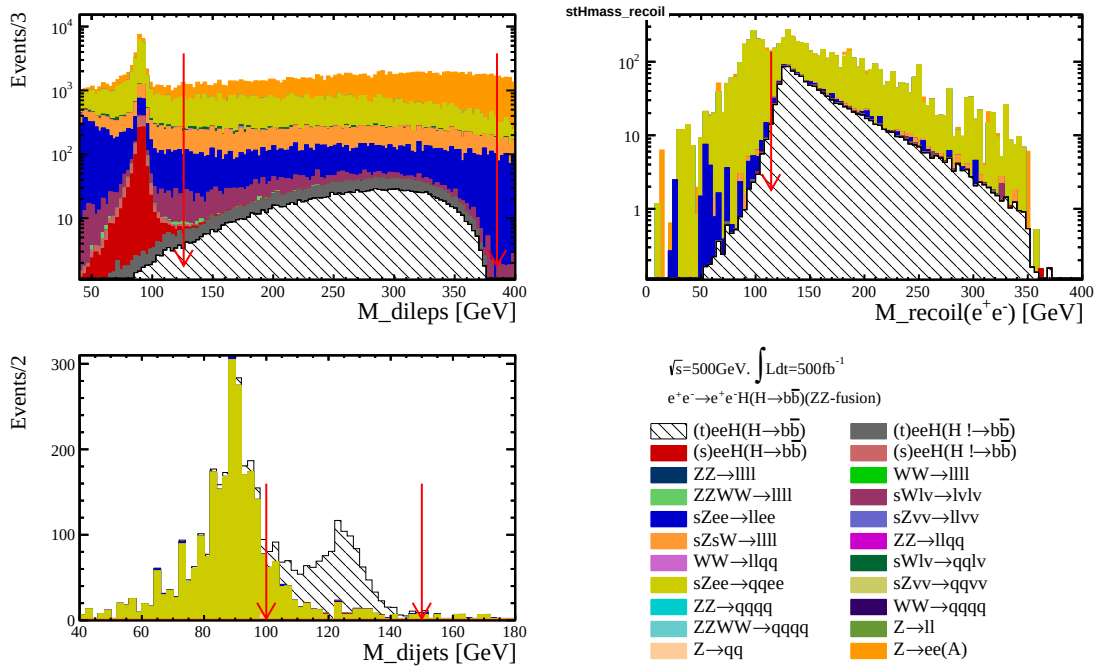

Figure 146: The distributions show several observable used for the background suppression. Explanation of the observables are given in the text. Red arrows on the plots indicate the cut values applied to each observable.

The event acceptance of P_h slightly goes down in the most higher area. Because the momentum of the Higgs boson and the invariant mass of the di-lepton system has correlation, which is discussed in the analysis of the 250 GeV process as shown in Sec. A.2.2. Nevertheless, the lower cut of the di-lepton mass is definitely necessary to remove s-channel Higgs production process. Thus, the lower cut is made lose as much as possible. The event acceptance of $\Delta\Phi$ at 0, π, and 2π also drops due to the same reason with the other lepton channels.

A.6.3 Impact of angular distributions

As illustrated in Fig. 148, the number of MC samples of the background processes is insufficient and the background distribution is not smooth. This might bring a problem that the error estimation in the evaluation is not properly done, especially the case that a kinematical distribution is binned into a two- or three-dimensional distribution.

A background distribution with reweighted statistics:

To avoid this situation, the background distribution was constructed separately with large statistics by removing one of the observables used for the background suppression in the analysis, such as the b-tag cut, whose performance is expected to have nothing to do with the angular information. If an observable is depending on the angular information, the large statistics background distribution will differ from the one which the full suppression is applied to. The constructed background distribution with the large statistics must be properly weighted by scaling to the number of background events with the full suppression. Fig. 150 illustrate the two-dimensional background distribution after applied the reweighted of the statistics. The statistics error of each bin is also calculated again using both of the signal and the reweighted background distributions, and these errors are used for the evaluation.

Fig. 151 give $\Delta\chi^2$ distributions for each one-dimensional parameter axis, where the one-dimensional distribution of $x(P_h)$ and $x(\Delta\Phi)$ binned in 20, and the two-dimensional distribution of $x(P_h,\ \cos\theta_h,\ \Delta\Phi_{f\bar{f}})$ binned in $5\times5\times5$ are respectively used for the evaluation. Compared the results between the one-dimensional distribution and the two-dimensional distribution, it can

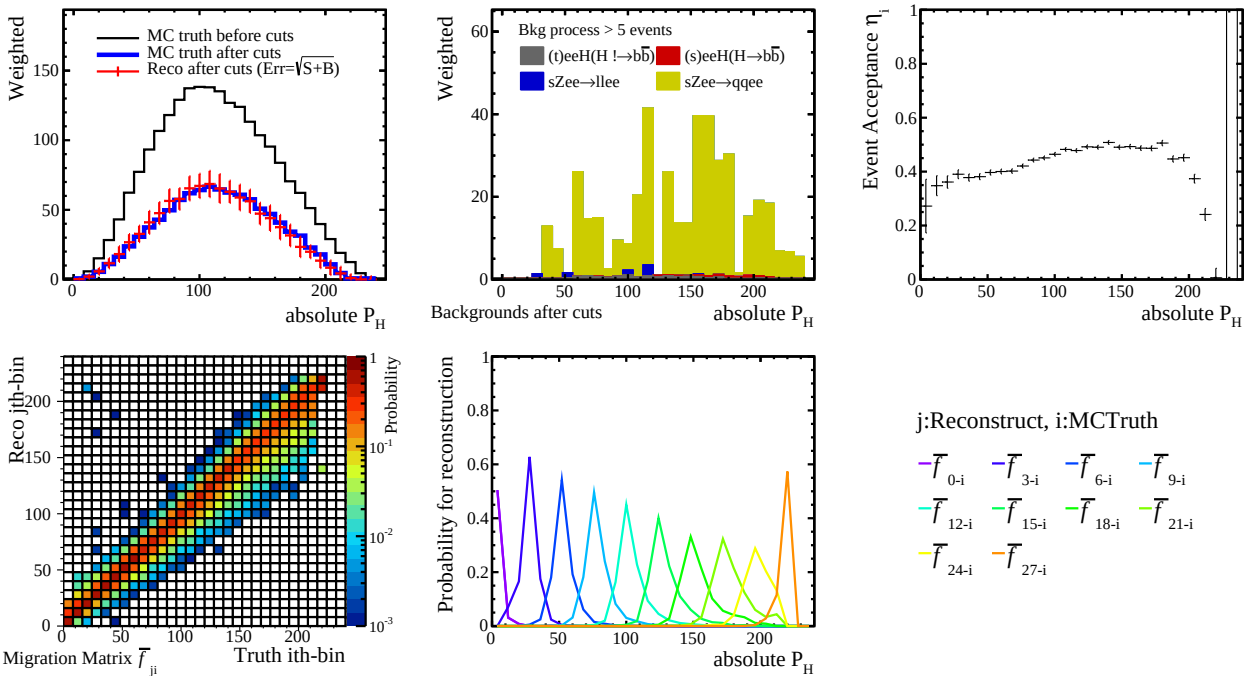

Figure 147: The distributions show the summary of the momentum of the Higgs boson (P_h) after the background suppression. (Top left and middle): the remaining signal and the background distribution, which are given with the MC truth and the reconstructed, where the statistical error is given as the standard deviation of the Poisson probability. (Top right): the event acceptance function η_i. (Bottom left and middle): the distribution shows the probability matrix of the migration ($\bar{f}_{ji}$) that is applied for the reconstruction of the realistic distribution of P_h, and the cross-sections of $\bar{f}_{ji}$ as 1-dim plots.

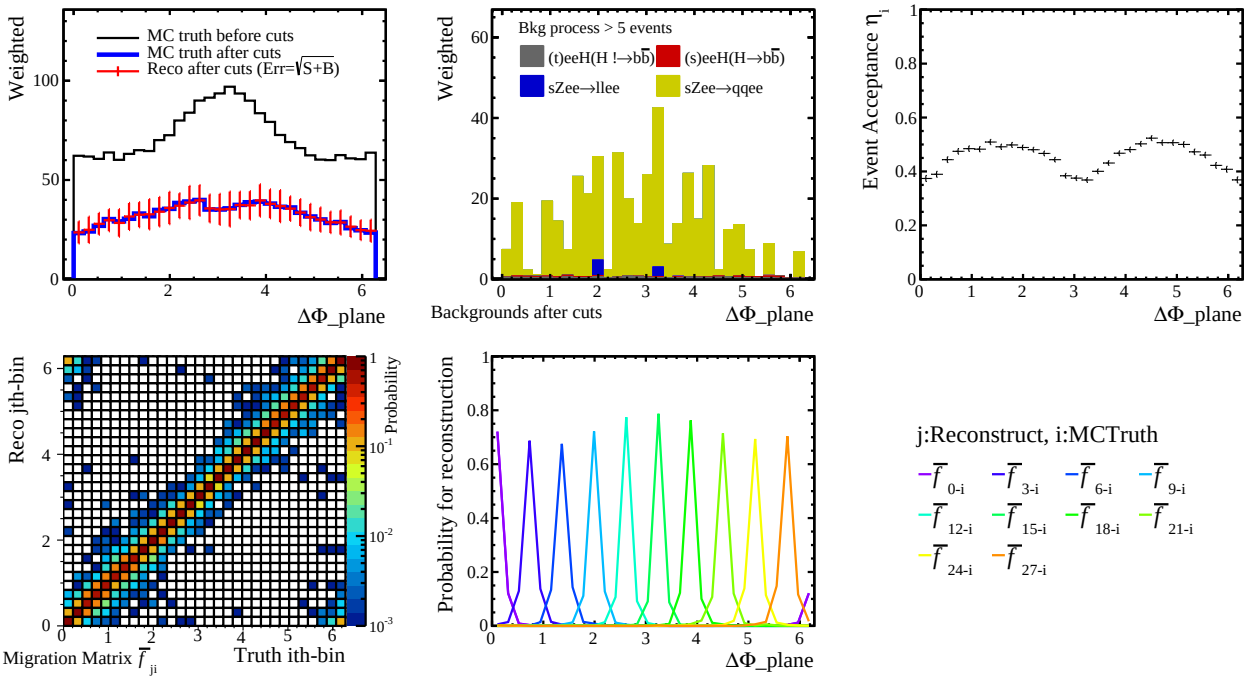

Figure 148: The distributions show the summary of the angle between production planes in the laboratory frame ($\Delta\Phi$) after the background suppression. (Top left and middle): the remaining signal and the background distribution, which are given with the MC truth and the reconstructed. (Top right): the event acceptance function η_i. (Bottom left and middle): the probability matrix of the migration ($\bar{f}_{ji}$) that is applied for the reconstruction of $\Delta\Phi$, and the cross-sections of $\bar{f}_{ji}$ as 1-dim plots.

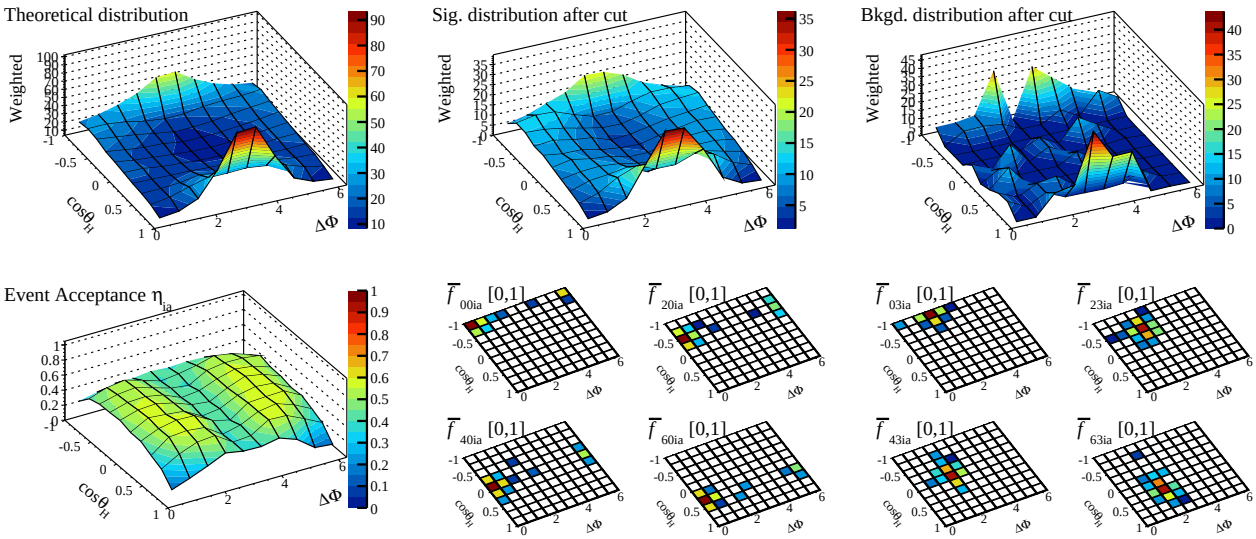

Figure 149: The distributions show the summary of the two-dimensional distribution consisted of the production angle of the Higgs boson $\cos\theta_h$ and the angle between production planes in the laboratory frame ($\Delta\Phi$) after the background suppression. (Top left, middle, and right): The remaining MC truth and the reconstructed signal distribution, and the background distribution, respectively. (Bottom left): The event acceptance function η_{ia} shows whether each signal event on each bin is accepted or not after the suppression. (Bottom middle and right): Several examples on the probability matrix of the migration where the 2-dim plots give the cross-sections of $\bar{f}_{jbia}$ since the illustration of the migration is too difficult which is a 4-dimension distribution.

be seen that the results with the two-dimensional distribution get slightly improved for especially both edges of the b_Z parameter. $\tilde{b}_Z$ is strongly constrained by the distribution of $\Delta\Phi$. Thus, the clear improvement can not be seen in the results with the two-dimensional distribution.

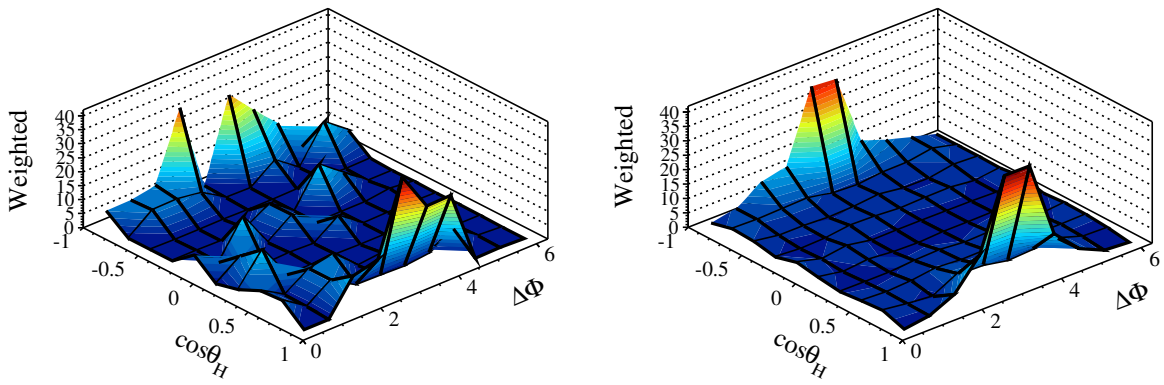

Figure 150: The plots show the two-dimensional background distribution of $x(\cos\theta_h, \Delta\Phi_{f\bar{f}})$. Because of insufficent MC events, the distribution is not smooth enough, which gets smooth after applying the reweighted statistics as shown in the right.

A.6.4 Impact of production cross-section

Effect of the variation of the production cross-section of the ZZ-fusion process $e^+e^- \to e^+e^-h$ is also included in the evaluation, whose variations as a function of each anomalous parameter are illustrated in Fig. 44. As discussed in Sec. 4.4.4, the error of the production cross-section is given

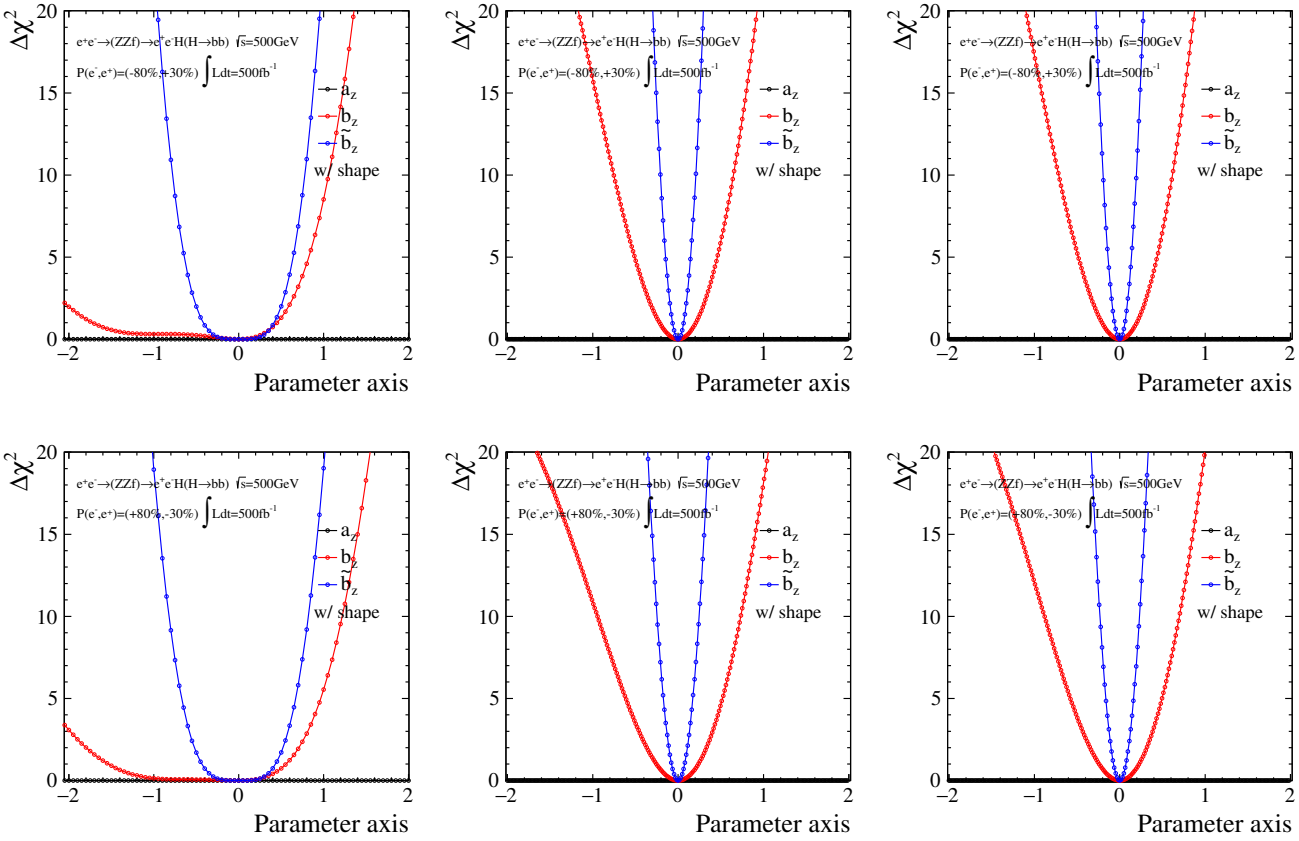

Figure 151: Distributions show $\Delta\chi^2$ as a function of each parameter which gives anomalous ZZH couplings, and the evaluation is done in the one-parameter axis. Black, red, and blue line on the plots correspond to the parameters a_Z, b_Z, and $\tilde{b}_Z$. Since only the angular information is considered here, the χ^2 values of a_Z is 0.0 over the given range. In upper and lower plots the different beam polarizations are assumed with the integrated luminosity of 500 fb^{-1}: P(e^-, e^+)= (-80%,+30%) and (+80%,-30%), respectively. Difference of each column is the angular distributions used for the evaluation: (left) $x(P_{higgs})$ binned in 20, (middle) $x(\Delta\Phi_{f\bar{f}})$ binned in 20, and (right) $x(P_{higgs}, \Delta\Phi_{f\bar{f}})$ binned in 10×10, respectively.

through the error propagation. The left plot in Fig. 151 give $\Delta\chi^2$ in one-dimensional parameter space, where the information of the cross-section is used for the evaluation. The impact on the sensitivity coming from the variation of the cross-section seems large and looks a band, so, to give constraints in the sensitivity the shape information is definitely necessary.

A.6.5 Sensitivity in three parameter space

The sensitivities to the anomalous ZZH couplings with the ZZ-fusion process at $\sqrt{s} = 500$ GeV only are given in Fig. 153, where the variation of the three-dimensional distribution $x(P_h, \cos\theta_h, \Delta\Phi_{f\bar{f}})$ binned in $5\times5\times5$ and the variation of the production cross-section are considered.

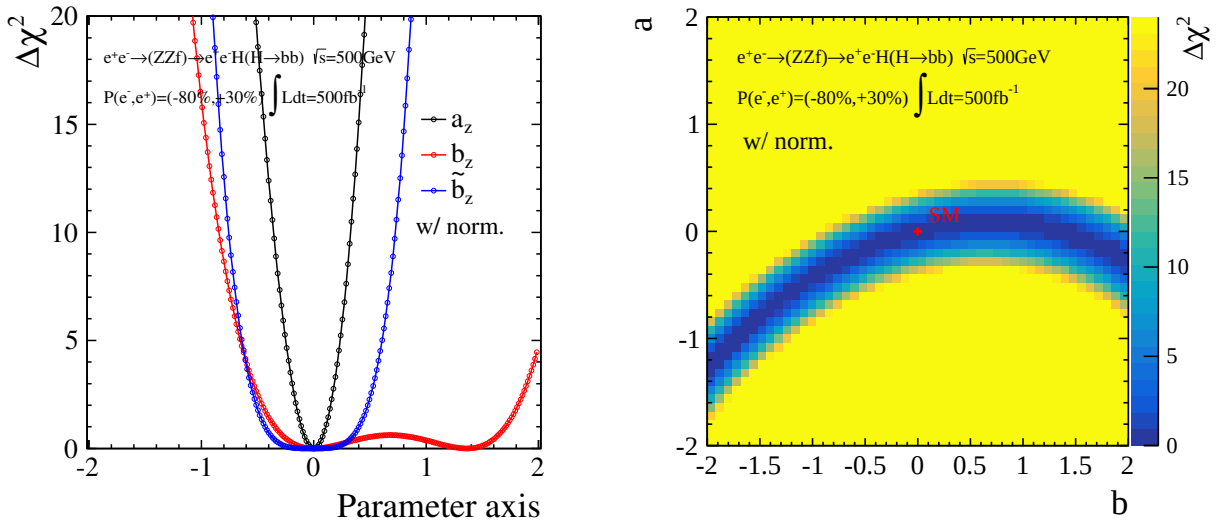

Figure 152: (Left) The distribution shows $\Delta\chi^2$ as a function of each parameter in the one parameter space, where the normalization information only is used for the evaluation. (Right) The distributions show $\Delta\chi^2$ in the two-dimensional parameter space of a_Z-b_Z.

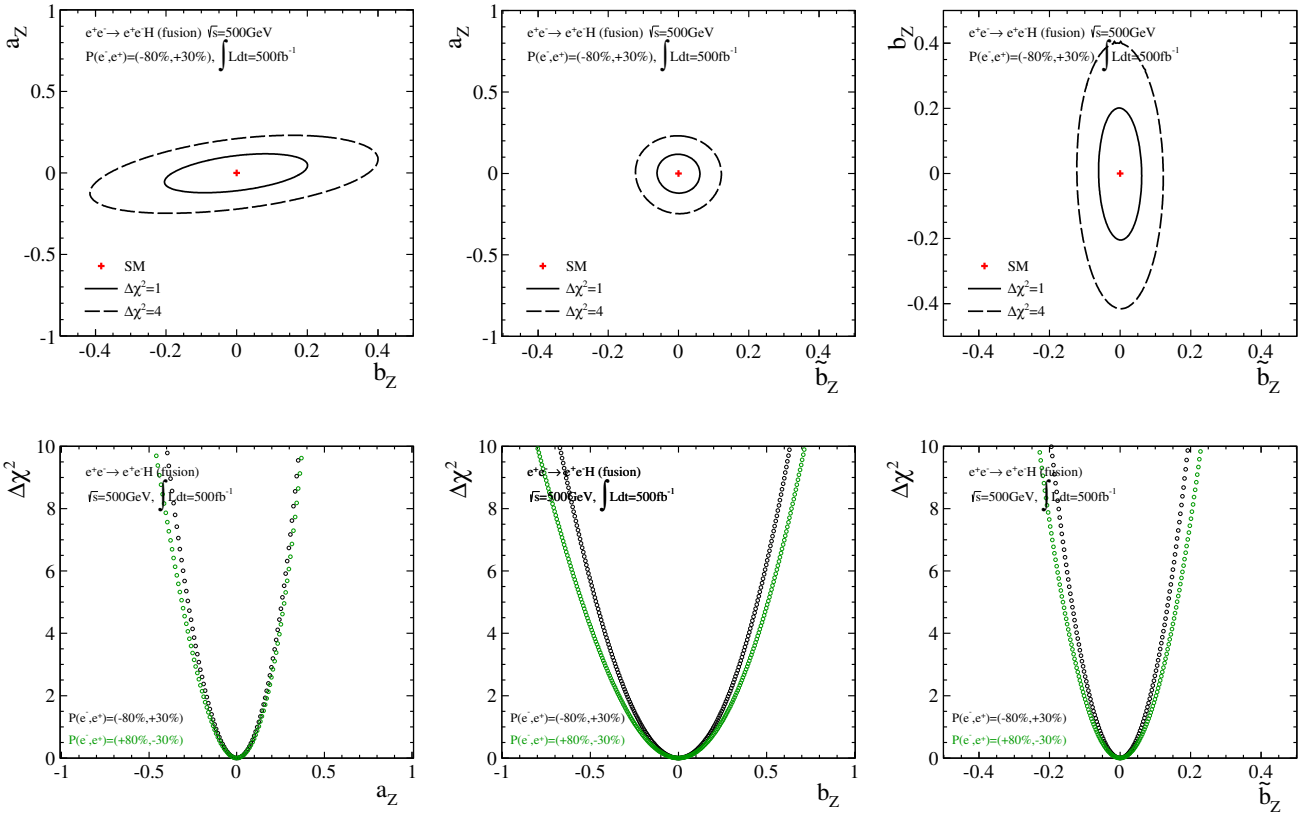

$$\sqrt{s} = 500 \text{ GeV with } \int \text{Ldt} = 500 \text{ fb}^{-1} \text{ and } \text{P}(e^-, e^+) = (-80\%, +30\%)$$

$$\begin{cases} a_Z = [-0.121, \quad 0.117] \\ b_Z = [-0.205, \quad 0.201] \\ \tilde{b}_Z = [-0.0611, \quad 0.0609] \end{cases}, \quad \rho = \begin{pmatrix} 1 & 0.4263 & -0.0281 \\ - & 1 & -0.0430 \\ - & - & 1 \end{pmatrix}$$

$$\sqrt{s} = 500 \text{ GeV with } \int \text{Ldt} = 500 \text{ fb}^{-1} \text{ and } \text{P}(e^-, e^+) = (+80\%, -30\%)$$

$$\begin{cases} a_Z = [-0.133, \quad 0.125] \\ b_Z = [-0.236, \quad 0.229] \\ \tilde{b}_Z = [-0.0722, \quad 0.0721] \end{cases}, \quad \rho = \begin{pmatrix} 1 & 0.5357 & -0.0087 \\ - & 1 & -0.0120 \\ - & - & 1 \end{pmatrix}$$

Figure 153: (Upper) Plots show contours corresponding to the 1σ and 2σ sensitivity to the anomalous ZZH couplings. Fitting is performed with the muon channel only under the three free parameter space. The integrated luminosity of 250 fb^{-1} with the beam polarization state $\text{P}(e^-, e^+)$= (-80%,+30%) is assumed. The results are projected onto the two-dimensional parameter spaces a_Z-b_Z, a_Z-$\tilde{b}_Z$, and b_Z-$\tilde{b}_Z$. Both information of the three-dimensional distributions $x(\cos\theta_f^*, \cos\theta_Z, \Delta\Phi_{f\bar{f}})$ binned in 5×5×5 and of the production cross-section are combined. (Middle) Plots show $\Delta\chi^2$ distributions as a function of each parameter space of the anomalous couplings a_Z, b_Z, and $\tilde{b}_Z$. The distributions are obtained by using both information (the angles and the cross-section) and scanning one parameter while setting the other two parameters to be completely free. (Lower) Explicit values corresponding to the 1σ bounds for each anomalous parameter a_Z, b_Z, and $\tilde{b}_Z$ and correlation matrix indicating correlation coefficients between the parameters.

B The other channels for the anomalous WWH couplings

B.1 $e^+e^- \to Zh \to q\bar{q}h,\ h \to WW^* \to q\bar{q}q\bar{q}$ at $\sqrt{s} = 250$ GeV

Because the fraction of a pair of W bosons to a fully hadronic state is 45.7 % and there exit no missing neutrinos in the final state. Therefore, it is possible to reconstruct reaction completely and it seems to be expected, thanks to the sufficient statistics, that the hadronic process gives good power to improve the sensitivities by using the information of the kinematical distribution. However, it turned out that the probability of the migration effect, which is coming from miss clustering presumably, is really enormous because of the multi six jets environment and these jets are relatively wider since they are coming from the decay chain of Zh process. And it can easily guess that all kinematical shape information will disappear.

In this section the analysis are roughly described to illustrate such situation, but the analysis is not used for the combined results to show the sensitivity to the anomalous WWH couplings since the improvement can not be almost expected.

Reconstruction of the reaction :

Firstly, the MVA based lepton finding is applied to a event to separate the signal from the backgrounds which look like a leptonic process later. After applying the lepton finding, all PFOs are forcibly clustered into six jets with the Durham jet algorithm together with the heavy flavor tagging using LCFIPlus. Then the jets are paired each of them based on the chi-squared mass constraint[18] to find proper pairs that correspond to the Z and W bosons and off-shell W boson.

Reconstruction of the reaction :

Using several observers, the SM backgrounds are suppressed although the values are not optimized well and listed here explicitly. The distributions of the momentum of the W boson in the Higgs rest-frame after the suppression are given in Fig. 154, where the evaluation of the signal significance S_{sig} is 7.5. A notable thing here is that huge migration is observed, and the similar migrations are also observed for the other observables such as the helicity angle and the angle between decay planes. Therefore, it can be concluded that all shape information being sensitive to the anomalous couplings will disappear and it is not useful to improve the sensitivity.

B.2 $e^+e^- \to Zh \to \nu\bar{\nu}h,\ h \to WW^* \to q\bar{q}q\bar{q}$ at $\sqrt{s} = 250$ GeV

Unfortunately, the fully hadronic state of the Higgs-strahlung $Zh \to q\bar{q}WW^*$ that was described in the previous part of Sec. B.1 does not seem to give the expectation that the shape information is provided for the improvement because of the huge migration effects coming from the multiplicity of the jets in the final state. Whereas, in the process with the $Z \to \nu\bar{\nu}$ decay: $Zh \to \nu\bar{\nu}h,\ h \to WW^* \to q\bar{q}q\bar{q}$, it can be possible to extract the shape information well since the final state has only four jets coming from the pair of the W bosons. The branching fraction of the W boson to a quark pair is understood through the CKM matrix in the SM where six parameters are given as matrix elements which describe phenomena related to each quark pair and these values have been measured experimentally Sec. 5.4. The CKM matrix is currently understood that the diagonal elements are dominant, which means the W boson mainly decays to a quark pair being in the same generation such as $u\bar{d}$ and $c\bar{s}$, except $t\bar{b}$ because of the mass constraint by the W boson.

[18] The chi-squared formula for giving the mass constraint is given with

$$\chi^2 = \left(\frac{M_{ij} - M_Z}{\sigma_Z}\right)^2 + \left(\frac{M_{kl} - M_W}{\sigma_W}\right)^2,$$

where k, l, m, and n denote each jet, and the mass resolution σ_Z and σ_W are respectively set to be 5.2 and 4.5 GeV.

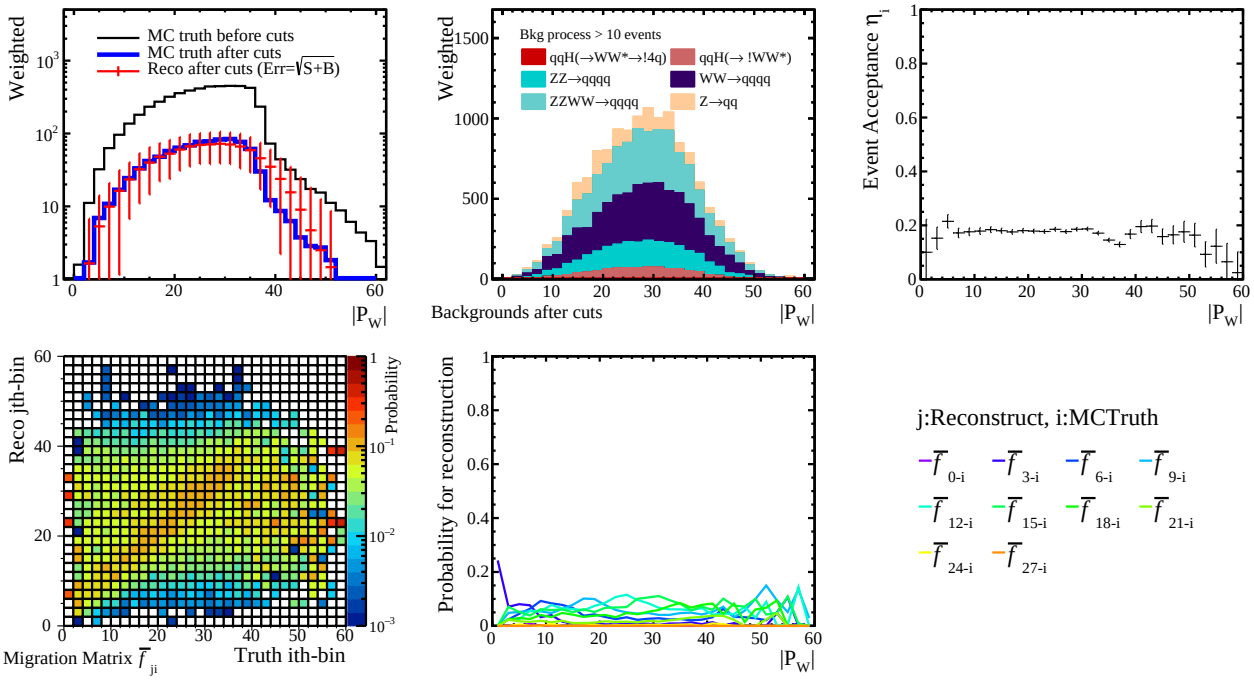

Figure 154: The distributions show the summary of the W boson momentum P_W in the Higgs rest-frame. (Top left and middle): the remaining signal and the background distribution, which are given with the MC truth and the reconstructed. (Top right): the event acceptance function η_i. (Bottom left and middle): the distribution shows the probability matrix of the migration ($\bar{f}_{ji}$) that is applied for the reconstruction of the realistic distribution of P_W, and the cross-sections of $\bar{f}_{ji}$ as 1-dim plots.

Additionally, there is the fact that c-hadrons such as a D-meson can fly about several hundred micro meter. If both c-jets coming from the pair of the W bosons decaying from the Higgs boson are successfully well identified by utilizing this reaction and finding secondary vertices created by a decay reaction of the c-hadrons, the reconstruction of $\Delta\Phi$, which is sensitive to the parameter $\tilde{b}_W$, is possible with the sensitivity of $[0–\pi]$. Of course, as far as a special algorithm like jet charge identification is not applied, it can not be really identified whether one c-jet is a fermion or an anti-fermion. Thus, the full sensitivity of $[0–2\pi]$ is not achievable, and $\Delta\Phi$ have to be folded as $\pi - \Delta\Phi$ if $\Delta\Phi$ exceed 2π as mentioned in the section Sec. 4.2.2. The ILD would be possible to attain both implementations in the future software development although the jet charge identification is not considered in this study.

B.2.1 Reconstruction and background suppression

For the purpose of the improvement of the sensitivity to the parameter $\tilde{b}_W$, the signal process $Zh \to \nu\bar{\nu}h,\ h \to WW^* \to q\bar{q}q\bar{q}$ is categorized into two categories: one is the full hadronic process of $WW^* \to q\bar{q}q\bar{q}$, and another is the process that c-tag identification is performed.

The procedure of the reconstruction and the background suppressions are common before categorizing events into two categories. The algorithm for finding an isolated lepton firstly apply to each event. After extracting the isolated leptons (if it exists), remaining PFOs are forcibly clustered into four jets with the Durham jet algorithm in which the flavor tag with LCFIPlus is also implemented. The clustered jets are paired each other with the mass constraint[19]. The

[19]The chi-squared formula for giving the constraint is given with

$$\chi^2 = \left(\frac{M_{ij} - M_W}{\sigma_W}\right)^2,$$

where i and j denote each jet, and the mass resolution σ_W are set to be 4.5 GeV.

background suppression was performed with the following observables, and several corresponding distributions are illustrated in Fig. 155. Table 15 gives the number of remaining signal and background events after each cut with the assumption of the integrated luminosity of 250 fb^{-1} and the both beam polarization states.

- Require that there is no isolated lepton in the final state of a reaction.
- $N_{\text{PFOs}} \in [45,\ 95]$, $E_{vis} \in [123.79,\ 144.36]$, and sum of b-tag < 0.926
  The number of Particle Flow Objects and the observed energy in the reaction, which can suppress large number of full-hadronic decay processes. Existing PFOs are also clustered into two jets in addition with the flavor tagging, and the sum of b-likeness from two jets is taken. This can be useful mainly to suppress the decay of the Higgs boson of $h \to b\bar{b}$.

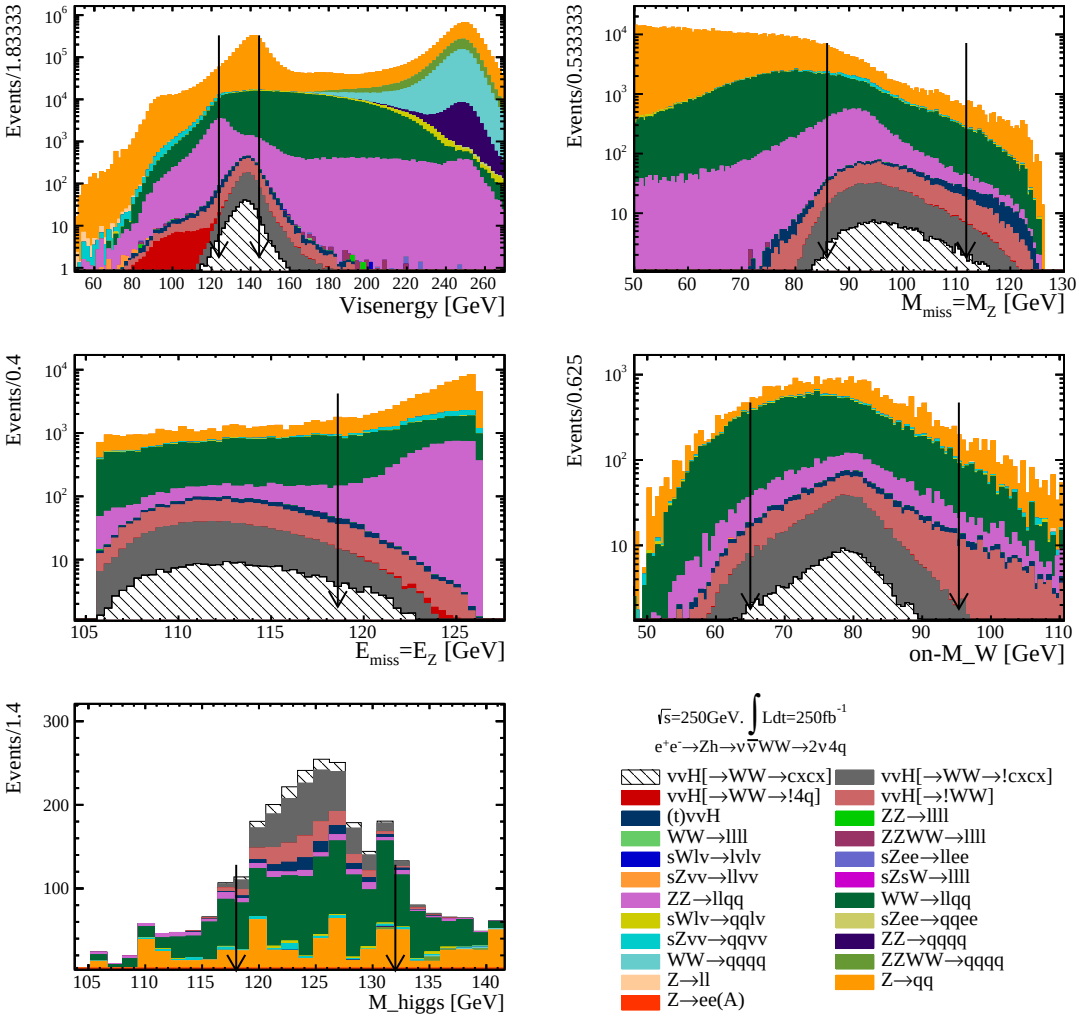

Figure 155: Distributions show the several observables used for the background suppression, where the signal process is $Zh \to \nu\bar{\nu}h,\ h \to WW^* \to q\bar{q}q\bar{q}$. The cut values are mentioned in the main text.

- $M_{miss} \in [85.9,\ 111.8]$ GeV, $E_{miss}\ < 118.6$ GeV, $M_W \in [65.0,\ 95.33]$ GeV
  The final state of the signal process has the Z boson which would appear as the missing mass derived form the neutrinos. The one on-shell W boson decaying from the Higgs boson exist.
- $-\log y_{23} \in [1.61, 3.92]$, $-\log y_{34} \in [2.72, 5.36]$
  min $N_{\text{PFOs}} > 6$, and thrust $\in [0.56\ 0.83]$

To suppress the remaining 2-fermion hadronic and 4-fermion semi-leptonic SM background processes, several event topology cuts are useful: the jet transition parameters of the jet clustering, the minimum number of PFOs among clustered jets, and thrust value.

- c-tag categorization: require that one c-jet for each W boson exist.

  To detect c-jet decaying from both W bosons and take an optimal point where c-tag performance is maximized, efficiency and purity are defined, which can give information how efficiently and purely c-jets are tagged,

$$\text{efficiency} = \frac{\text{ID } c\text{-jet} = 1 \cap \text{truth}(W \to c\bar{x})}{\text{truth}(W \to c\bar{x})}$$

$$\text{purity} = \frac{\text{ID } c\text{-jet} = 1 \cap \text{truth}(W \to c\bar{x})}{\text{ID } c\text{-jet} = 1}$$

  where the vale of "ID c-jet" is given by comparing tagged c-likeness for two jet each, which is $\sum_j^2 \text{tagged-}c_j > c$-likeness. Fig. 156 gives a plot showing the efficiency and the purity for both W bosons where the c-likenesses of each jet from both W bosons are scanned from 0 to 1. Optimal points which are respectively 0.75 for W and 0.66 for W^* are taken for the c-tag categorization.

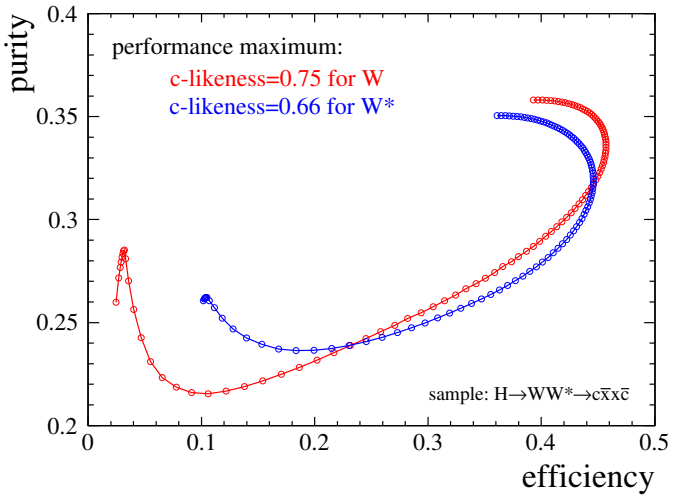

Figure 156: A plot shows the efficiency versus the purity for both W bosons. The optimal points are taken for the c-tag categorization.

After applying c-tag categorization, the remaining events for $c\bar{x}x\bar{c}$ are 144 $\to$ 21 with the P(e^-, e^+)= (-80%,+30%) state, consequently the overall efficiency for the $c\bar{x}x\bar{c}$ selection is approximately 15 %. The remaining events of 123 excluding 21 are included in the $q\bar{q}q\bar{q}$ category. The performance of the $c\bar{x}x\bar{c}$ selection of 15 % is significantly small compared to previous study [95], where the performance of the $c\bar{x}x\bar{c}$ selection is 80 %. An event ratio of finding the secondary vertices in the reaction of $h \to WW^* \to c\bar{x}x\bar{c}$ is given in Fig. 157. It can be seen that the event ration that two secondary vertices are correctly found in the reaction is about 5 %.

This is probably because c-hadrons derived from the chain reaction of $h \to WW^*$ decay into other particles with relatively short lifetime, and due to this unfoundness of the secondary vertices, the performance of c-identification cannot become better. This would be a point the performance should be improved[20].

[20]Common LCFIPlus package was used in the analysis, which is trained including b-hadrons for the b-jet identification. If the LCFIPlus is specially tuned under the assumption that there exists no b-jet in the final state, where there are only c-jet and other light jets (since this process does not include any b-jet in the final state), it can be expected that the performance of the c-jet identification will be improved to some extent.

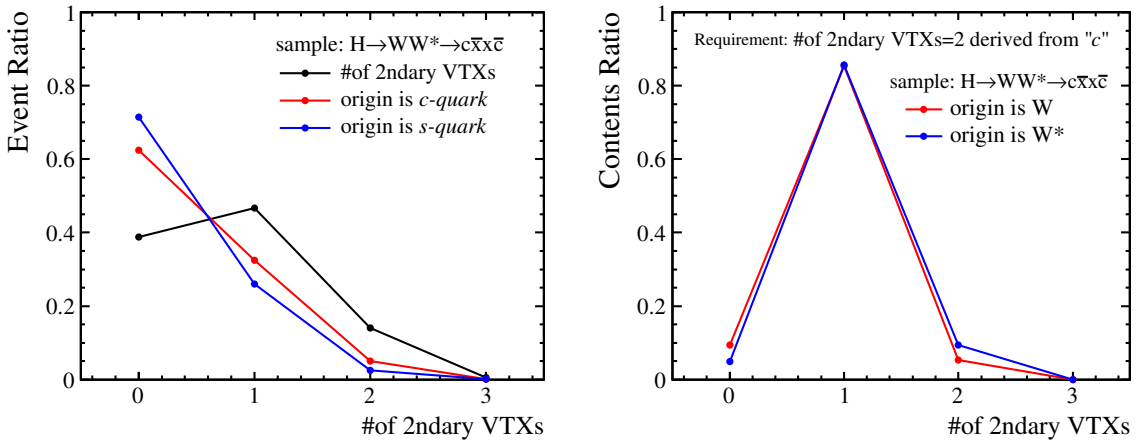

Figure 157: (Left) Plot shows the event ration of finding the secondary vertices in the reaction of $h \to WW^* \to c\bar{x}x\bar{c}$. The ratio that two secondary vertices are correctly found in the reaction of $c\bar{x}x\bar{c}$ is about 5 %. (Right) Plot shows the content ration of the origin of the secondary vertex in the reaction that two secondary vertices are correctly found. The ratio of the origin of the secondary vertex for W and W^* are the similar ratio.

- $M_h \in [100,\ 160]$ GeV
  The invariant mass of the Higgs boson reconstructed two W bosons. This is a mass window to deter- mine the statistical error.

B.2.2 Acceptance and migration on observables

Fig. 158 show the summary plots on the P_W distribution of the $q\bar{q}q\bar{q}$ category. The acceptance of the P_W distribution degrade at the higher edge, which is affected by the cut of the invariant mass of the on-shell W boson, where both W bosons are off-shell as discussed in the section Sec. 7.2.2. Since two W bosons are off-shell, it is unknown whether a parent generating two W bosons is originating from the Higgs boson or not. Thus, it should be removed, but special treatment is not applied here because the number of remaining evens is less. A clear dip at around 35 GeV is an edge of the transition of the distribution, which has component of the two off-shell W bosons and the acceptance drops luckily (in fact we do not want to have the acceptance in the highest region because two W bosons are off-shell). The migration effects are relatively large compared to the previous semi-leptonic decay process. Because the jets in the final state of this process come from the decay chain of $h \to WW^* \to q\bar{q}q\bar{q}$, energy of each jet get relatively small and can be wider than jets having larger energy, which are, for instance, jets derived from $Z \to q\bar{q}$ in the previous process.

The $\Delta\Phi$ distributions of the $c\bar{x}x\bar{c}$ category are also illustrated in Fig. 159. The remaining events of the signal are too less to extract the information and say something. However, the acceptance keeps flatness and the migration are relatively small within the accepted events.

B.2.3 Impact of angular distributions

Fig. 160 show $\Delta\chi^2$ distributions as impact of the angular distributions: the momentum of the W boson in the Higgs ret frame, $\Delta\Phi$ in the $q\bar{q}q\bar{q}$ category whose sensitivity is (0–π/2), and three-dimensional distribution distribution including the polar angle of the lepton decaying from the W boson. It is clearly shown that $\Delta\Phi$ does not contribute to the sensitivity to the anomlaous WWH couplings. All sensitivity is given with the momentum distribution of the W boson.

Fig. 161 also show $\Delta\chi^2$ as a function of each parameter a_W, b_W, and $\tilde{b}_W$with the $\Delta\Phi$ distribution in the $c\bar{x}x\bar{c}$ category whose sensitivity is (0–π). It is shown that the sensitivity given with $\Delta\Phi$ is less due to small number of remaing events. Even with the large integrated luminosity, the

Table 13: The expected number of remaining signal and background events after each cut for the $Zh \to \nu\bar{\nu}h,\ h \to WW^* \to q\bar{q}q\bar{q}$ channel at $\sqrt{s}$=250 GeV, with both beam polarization states: P(e^-, e^+)= (-80%,+30%) and (+80%,-30%). The integrated luminosity of 250 fb^{-1} is assumed. The index $q\bar{q}q\bar{q}$ in the table indicates $c\bar{x}x\bar{c}$ is excluded. The selection is for the $q\bar{q}q\bar{q}$ analysis.

Cut variables $\sqrt{s}$=250 GeV P(e^-, e^+)= (-80%,+30%)

$Zh \to \nu\bar{\nu}WW^* \to \nu\bar{\nu}+$				SM backgrounds			
process	$c\bar{x}x\bar{c}$	$q\bar{q}q\bar{q}$	ϵ	$h \notin WW^*$	$2f$	$4f$	S_{sig}
cross-section (fb)	1.52	4.57	-	48.30	-	-	-
Expected	479	1437	100	15196	$2.91 \cdot 10^7$	$1.02 \cdot 10^7$	-
Niso-leptons=0	478	1435	99.84	14670	$2.09 \cdot 10^7$	$5.98 \cdot 10^6$	0.37
$N_{\text{PFOs}} \in [45,\ 95]$	451	1334	93.16	11101	$1.09 \cdot 10^7$	$4.23 \cdot 10^6$	0.46
sum of b-tag < 0.926	419	1310	90.24	2402	$8.25 \cdot 10^6$	$3.89 \cdot 10^6$	0.50
$E_{vis} \in [123,79\ 144.36]$	345	1071	73.90	1855	$2.07 \cdot 10^6$	$1.68 \cdot 10^5$	0.95
$M_{miss} \in [85.9,\ 111.8]$	303	942	64.98	1566	$5.97 \cdot 10^4$	$5.11 \cdot 10^4$	3.69
$E_{miss}\ < 118.6$	260	863	58.61	1364	$1.31 \cdot 10^4$	$2.17 \cdot 10^4$	5.82
$M_W \in [65.0,\ 95.33]$	243	805	54.70	1058	$1.02 \cdot 10^4$	$1.74 \cdot 10^4$	6.08
min $N_{\text{PFOs}} > 6$	216	704	48.02	934	5925	5383	8.02
- $\log y_{23} \in [1.61, 3.92]$	195	640	43.58	487	2770	4012	9.27
- $\log y_{34} \in [2.72, 5.36]$	158	526	35.70	258	1351	1937	10.51
thrust $\in [0.56\ 0.83]$	144	481	32.62	221	863	1546	10.96
c-tag categorization	123	479	32.51	215	843	1494	10.71
$M_h\ \in [100,\ 160]$	123	479	32.52	215	843	1494	10.71

$\sqrt{s}$=250 GeV P(e^-, e^+)= (+80%,-30%)

$Zh \to q\bar{q}WW^* \to q\bar{q}+$				SM backgrounds			
Cut variables	$c\bar{x}x\bar{c}$	$q\bar{q}q\bar{q}$	ϵ	$h \notin WW^*$	$2f$	$4f$	S_{sig}
Expected	263	789	100	8347	$2.03 \cdot 10^7$	$1.27 \cdot 10^6$	-
Niso-leptons=0	263	788	99.90	8057	$1.28 \cdot 10^7$	$6.462e \cdot 10^5$	0.29
$N_{\text{PFOs}} \in [44,\ 95]$	248	733	93.25	6097	$6.48 \cdot 10^6$	$4.153e \cdot 10^5$	0.37
sum of b-tag < 0.909	228	718	89.93	1303	$4.86 \cdot 10^6$	$3.503e \cdot 10^5$	0.41
$E_{vis} \in [123.14,\ 145.0]$	193	603	75.67	1035	$1.29 \cdot 10^6$	$2.381e \cdot 10^4$	0.70
$M_{miss} \in [85.5,\ 115.0]$	175	542	68.16	902	$4.57 \cdot 10^4$	$1.068e \cdot 10^4$	2.98
$E_{miss}\ < 120.08$	156	510	63.31	813	$1.06 \cdot 10^4$	3200	5.38
$M_W \in [65.0,\ 95.33]$	145	475	58.94	631	8313	2557	5.63
min $N_{\text{PFOs}} > 6$	129	415	51.71	557	4728	974	6.59
- $\log y_{23} \in [1.54, 3.78]$	113	367	45.63	268	2008	547	8.35
- $\log y_{34} \in [2.80, 6.20]$	106	348	43.16	217	1433	396	9.08
thrust $\in [0.56\ 0.857]$	102	336	41.63	201	1096	352	9.59
c-tag categorization	87	335	40.11	197	1073	341	9.35
$M_h\ \in [100,\ 160]$	87	335	40.11	197	1073	341	9.35

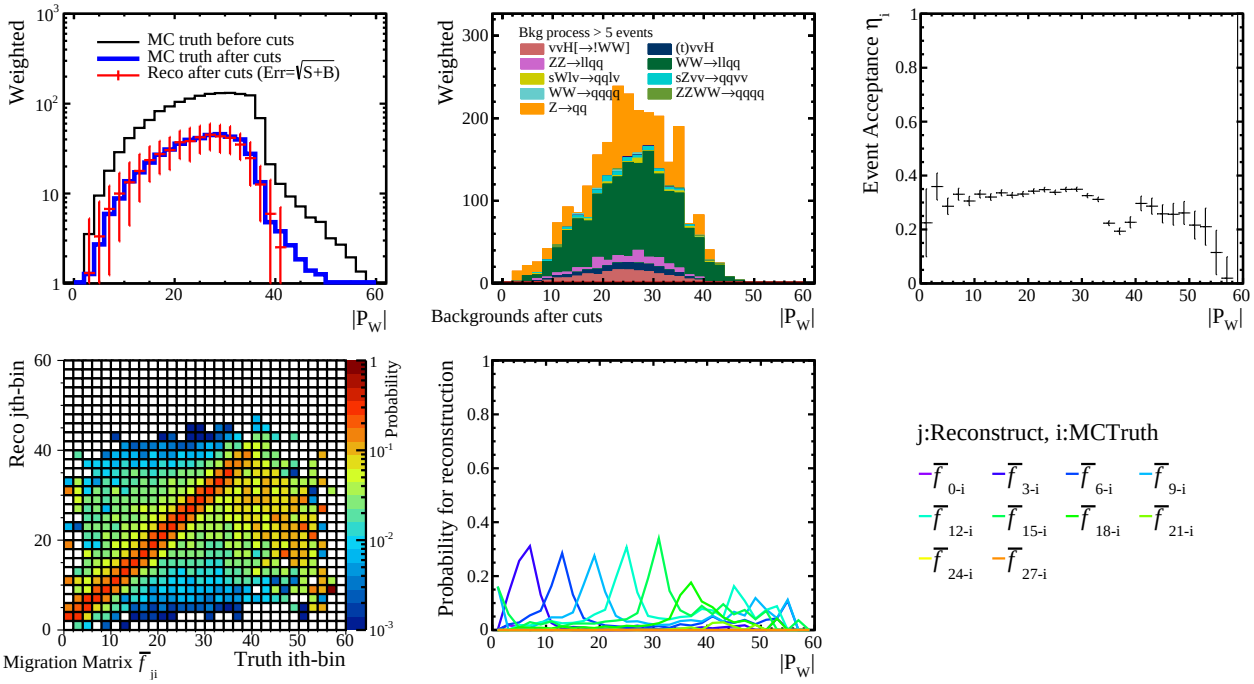

Figure 158: The distributions show the summary of the W momentum P_W distribution in the Higgs rest-frame after the background suppression. (Top left and middle): the remaining signal and the background distribution, which are given with the MC truth and the reconstructed. (Top right): the event acceptance function η_i. (Bottom left and middle): the distribution shows the probability matrix of the migration ($\bar{f}_{ji}$) that is applied for the reconstruction of the realistic distribution of P_W, and the cross-sections of $\bar{f}_{ji}$ as 1-dim plots.

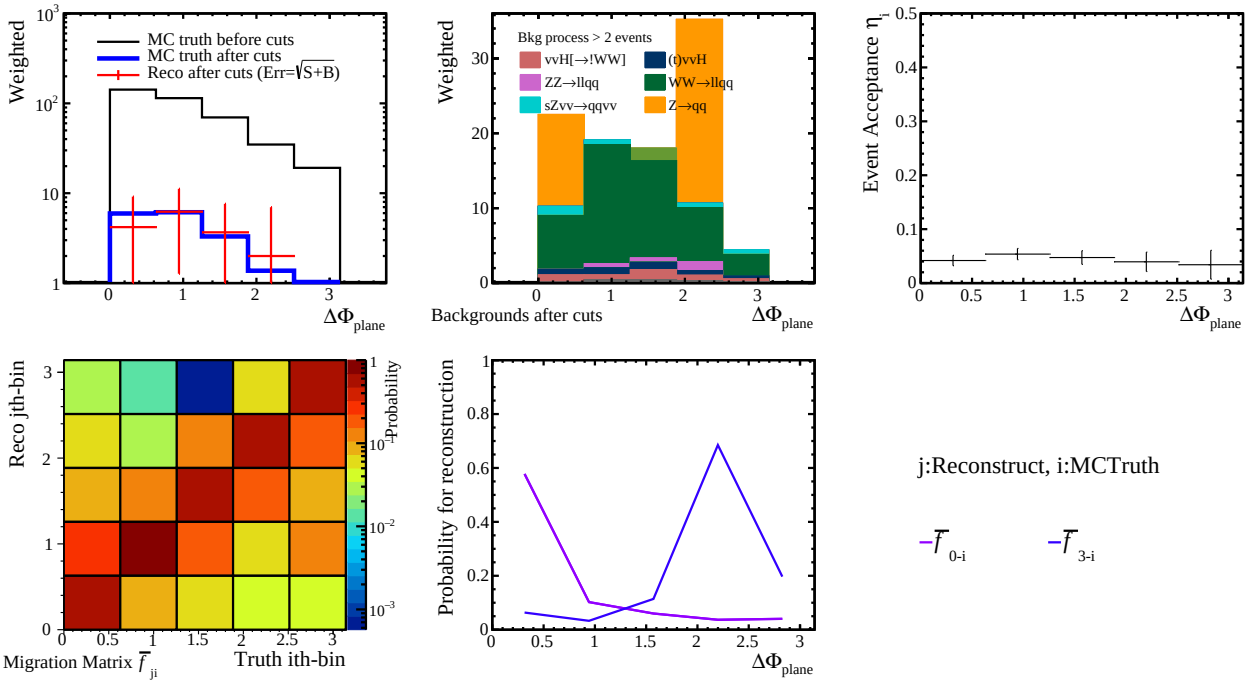

Figure 159: The distributions show the summary of the angle between decay planes $\Delta\Phi_{f\bar{f}}$ in the Higgs rest-frame after the background suppression. (Top left and middle): the remaining signal and the background distribution, which are given with the MC truth and the reconstructed. (Top right): the event acceptance function η_i. (Bottom left and middle): the probability matrix of the migration ($\bar{f}_{ji}$) that is applied for the reconstruction of $\Delta\Phi$, and the cross-sections of $\bar{f}_{ji}$ as 1-dim plots.

sensitivity to the anomalous WWH given with $\Delta\Phi$ is small. One expectation for the improvement is that, if the flavor tagging implemented in `LCFIPlus` is specially tuned focusing on finding c-quark in the condition that there is no b-quark, the performance might be improved.

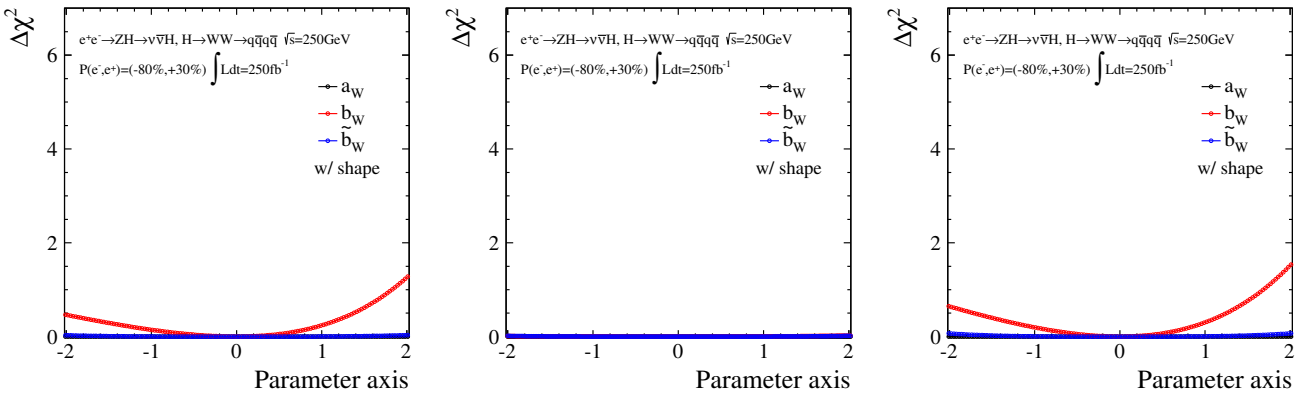

Figure 160: Distributions show $\Delta\chi^2$ as a function of each parameter a_W, b_W, and $\tilde{b}_W$, where the beam polarization of P(e^-, e^+)= (-80%,+30%) and the integrated luminosity of 250 fb^{-1} are assumed. The category of the analysis is $q\bar{q}q\bar{q}$. The one-dimensional distributions of $x(P_W)$ calculated in the Higgs rest frame (left) and $x(\Delta\Phi)$ whose sensitivity is [0–$\pi/2$] (middle) binned in 20, and the three-dimensional distribution of $x(\cos\theta^*_{Wl}, P_W, \Delta\Phi)$ binned $5\times5\times5$ (right) are used respectively. It is clear that $\Delta\Phi$ does not give the sensitivity and all sensitivity come from P_W.

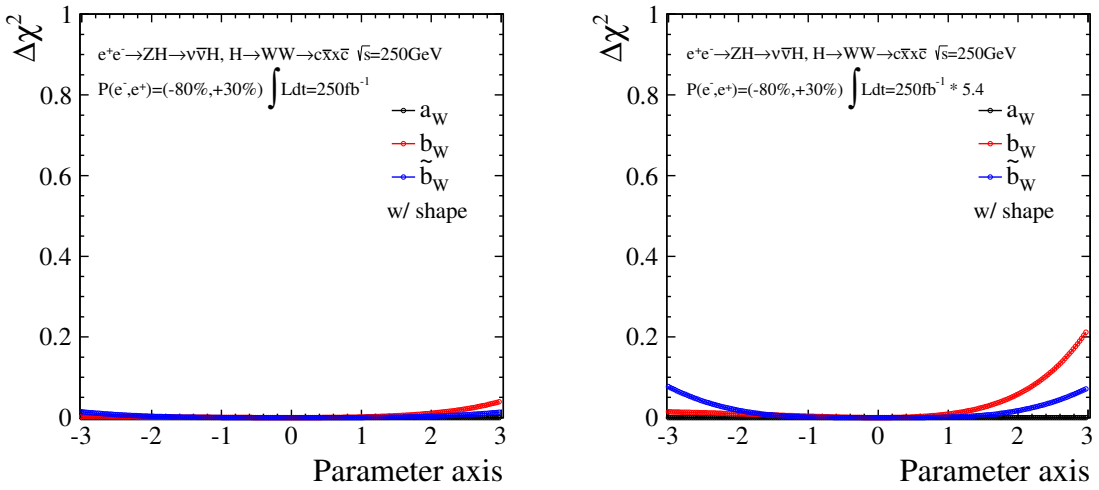

Figure 161: Distributions show $\Delta\chi^2$ as a function of each parameter a_W, b_W, and $\tilde{b}_W$, where the beam polarization of P(e^-, e^+)= (-80%,+30%) is assumed. The category of the analysis is $c\bar{x}x\bar{c}$ and the used distribution is $x(\Delta\Phi)$ whose sensitivity is [0–π]. The assumed integrated luminosities are 250 fb^{-1} (left) and H20 of 250 GeV which is 5.4 times larger luminosity. Even with the high luminosity the current result is not good.

B.3 $e^+e^- \to \nu_e\bar{\nu}_e h,\ h \to b\bar{b}$ at $\sqrt{s} = 500$ GeV

At $\sqrt{s}$ =500 GeV the WW-fusion Higgs production process sufficiently open and become leading, which has a roughly 1.5 times larger production cross-section compared to the Higgs-strahlung process. As already shown in the analysis at $\sqrt{s}$ =250 GeV, or when refering other physics studies using the WW-fusion process, it is expected that large sensitivity to the anomalous WWH couplings can be also obtained.

B.3.1 Reconstruction and background suppression

Firstly, the MVA based isolated lepton finding was applied for all reconstructed PFOs. Since electron and position beam that are highly accelerated tend to emit photons because of the bremsstrahlung or synchrotron radiation derived from electric and magnetic field created by each beam, the reaction of $\gamma\gamma \to$ hadrons become significant compared to the reaction at $\sqrt{s}$ =250 GeV. Thus, the exclusive k_t-jet clustering with R of 1.5 was implemented to remove these reactions, where two jets are required in the final state. After dispersing clustered jets to PFOs again, all PFOs are inclusively clustered again to two jets with the Durham jet clustering together with the implementation of the flavor tag. The background suppression was also performed using several observables as follows, and Table 14 shows reduction of the signal and backgrounds.

- $N_{isoLeps} = 0$, $N_{\mathrm{PFOs}} \in [40,\ 100]$, $E_{vis} \in [100.0,\ 320.0]$, and sum of b-tag > 1.0
  Since an isolated lepton is expected not to be exist in the final state and it is not a multiple jet environment, the number of isolated leptons and PFOs are useful observables to distinguish the signal from backgrounds which especially decay leptonically and hadronically. The two clustered jets coming from the Higgs boson expected to have larger b-likeness.

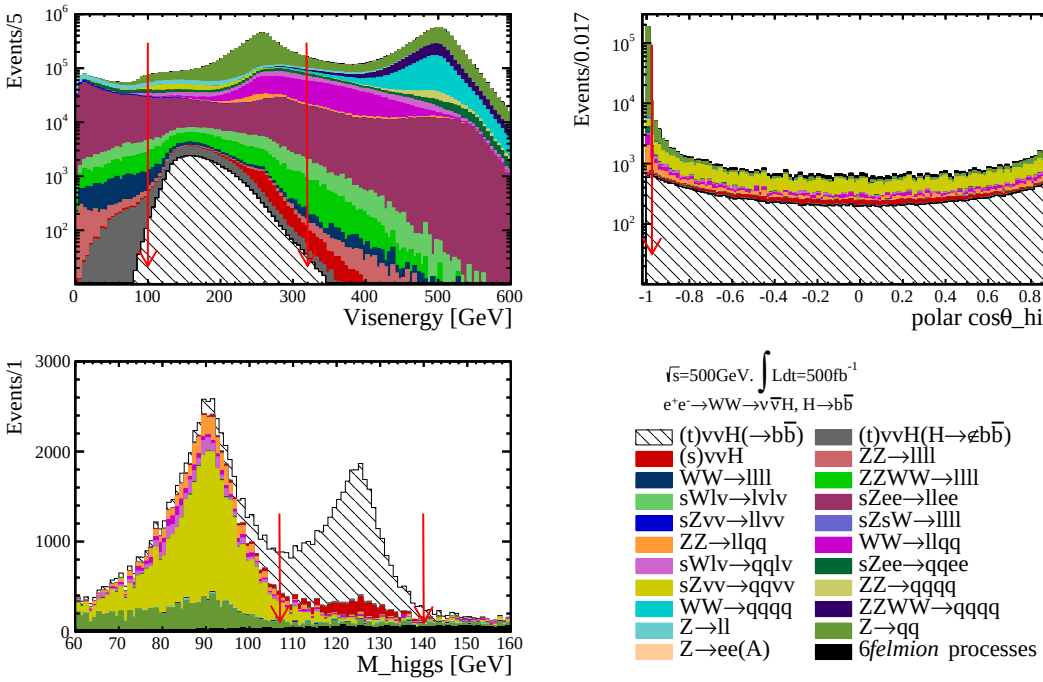

Figure 162: Distributions show the observables used for the background suppression. The cut values are mentioned in the main text.

Additionally the visible energy cut is added as shown in Fig. 162 to suppress mainly the large number of two fermion hadronic state. Because the visible energy and the absolute momentum of the Higgs boson are slightly correlated, the cut values for upper side is set to be relatively loose. Although the usage of this cut affect the flatness of the acceptance of the absolute momentum distribution, a benefit for reducing statistical uncertainty is larger compared to the slight loss of the acceptance when getting the final results.

- $-\log y_{12} < 2.875$, $-\log y_{23} \in [1.87,\ 10.38]$, $-\log y_{34} \in [4.00,\ 11.60]$
  min thrust$\in [0.03,\ 0.3]$, and min $N_{\mathrm{PFOs}} > 8$

  The parameter for giving jet transition from 1 to 2 jets, from 2 to 3 jets, and from 3 to 4 jets, which are useful topological observables. The minor thrust angle can suppress other backgrounds. the number of minimum PFOs among jets in the reaction can also suppress other backgrounds.

- $\cos\theta_h \in [-0.975,\ 0.975]$

  The polar angle of the di-jet is also given to suppress the 2-fermion events originating from the radiative return to the Z, which is also shown in Fig. 162. This observable also affect the flatness of the acceptance of the polar angle distribution of the Higgs boson. However, as discussed in the analysis at 250 GeV, the benefit for reducing statistical uncertainty is larger compared to the slight loss of the acceptance.

- $M_h \quad \in [107,\ 140]$ GeV

  The invariant mass of the di-jet system, which becomes a conclusive mass window to determine the statistical error on each bin of kinematical histograms.

B.3.2 Acceptance and migration on observables

Fig. 163 and Fig. 164 give summary plots on two observables P_{higgs} and $\cos\theta_{higgs}$. The event acceptance of the upper area of the P_{higgs} distribution and the edges of the $\cos\theta_{higgs}$ distribution are slightly affected because of the cut values whereas the probabilities of the migration for both observables are very clear.

B.3.3 Impact of kinematical distribution

Fig. 166 illustrate impacts of the shape information, where two situations, $\cos\theta_{higgs}$ cut is applied or not applied, are given. When focusing on one-dimensional distribution, because of better statistical unsertainties the sensitivities to each parameter with the $\cos\theta_{higgs}$ cut get larger although some acceptances of the observables are slightly lost. Even focusing on three-dimensional distribution can give better sensitivity, which is $\tilde{b}_W$=$\pm$0.614 for $\Delta\chi^2$=1 with the simultaneous three parameter fit whereas $\tilde{b}_W$= $\pm$0.615 without the $\cos\theta_{higgs}$ cut. Thus, the results with the $\cos\theta_{higgs}$ cut are used.

B.3.4 Impact of production cross-section

Since the anomalous tensor structures depend on the momentum of the W boson, the higher energy can also bring the large variation of the production cross-section. Fig. 166 gives the relative variation of the production cross-section and the impact to the each anomalous parameter.

B.3.5 Consideration on contribution of the anomalous ZZH couplings

Since a few number of s-channel $\nu\bar{\nu}h$ process remain in the upper area of the P_{higgs} distribution and cover over the $\cos\theta_{higgs}$ distribution, contributions of the variation of the anomalous ZZH couplings are also considered. The method is same with the analysis at 250 GeV process, where a variance-covariance matrix evaluated through the 500 GeV processes C^{500}_{ZZH} is used. The error of the production cross-section is given through the error propagation of the relation $\delta(\sigma_{\nu\bar{\nu}h}BR_{hb\bar{b}})/\delta(BR_{hb\bar{b}})$, where $\delta(\sigma_{\nu\bar{\nu}h}BR_{hb\bar{b}})$ and $\delta(BR_{hb\bar{b}})$ are respectively assumed to be 1.0 % and 3.5 % from references.

Fig. 167 give the sensitivity to each parameter of anomalous WWH couplings with the information that can be provided with the $\nu\bar{\nu}h$, $h \to b\bar{b}$ only. The results with the contributions of the variation coming from the s-channel $\nu\bar{\nu}h$ process are also given.

Table 14: The expected number of remaining signal and background events after each cut on the t-channel $\nu\bar{\nu}h,\ h \to b\bar{b}$ at $\sqrt{s}$=250 GeV. The integrated luminosity of 250 fb^{-1} is assumed. ϵ and S_{sig} denote the signal efficiency and significance respectively.

Cut variables $\sqrt{s}$=500 GeV P(e^-, e^+)= (-80%,+30%) L_{int}=500 fb^{-1}

	$(t)\nu\bar{\nu}h$, $h \to$			SM backgrounds				
process	$b\bar{b}$	ϵ	others	$(s)\nu\bar{\nu}h$	$2f$	$4f$	$6f$	S_{sig}
cross-section (fb)	90.3	-	62.2	20.5	-	-	-	-
Expected	45157	100	31122	10229	$1.32 \cdot 10^7$	$1.62 \cdot 10^7$	$4.04{\cdot}10^5$	-
$N_{isoLeps} = 0$	45125	99.93	24707	9396	$1.06 \cdot 10^7$	$1.01 \cdot 10^7$	$2.15{\cdot}10^5$	9.90
$E_{vis} \in [100.0,\ 320.0]$	44714	99.02	21625	8731	$5.54 \cdot 10^6$	$3.03 \cdot 10^6$	$2.56{\cdot}10^4$	15.21
$N_{\mathrm{PFOs}} \in [40,\ 100]$	40927	90.63	16805	7411	$3.90 \cdot 10^6$	$1.39 \cdot 10^6$	$1.88{\cdot}10^4$	17.69
sum of b-tag > 0.995	38047	84.25	1050	5008	$8.89 \cdot 10^5$	$1.18 \cdot 10^5$	$1.12{\cdot}10^4$	37.11
min $N_{\mathrm{PFOs}} > 8$	37755	83.61	1006	4944	$8.72 \cdot 10^5$	$1.02 \cdot 10^5$	$1.02{\cdot}10^4$	37.44
$-\log y_{12} < 2.875$	35950	79.61	930	3691	$4.61 \cdot 10^5$	$6.79 \cdot 10^4$	9936	47.66
$-\log y_{23} \in [1.87, 10.38]$	35664	78.98	929	3577	$4.31 \cdot 10^5$	$6.68 \cdot 10^4$	9845	48.61
$-\log y_{34} \in [4.00, 11.60]$	35497	78.61	908	3536	$4.18 \cdot 10^5$	$6.61 \cdot 10^4$	9379	49.02
min thrust$\in [0.03, 0.3]$	35279	78.13	883	3488	$4.04 \cdot 10^5$	$6.44 \cdot 10^4$	8847	49.50
$\cos\theta_h \in [-0.975, 0.975]$	33245	73.62	828	3440	$2.49 \cdot 10^4$	$5.05 \cdot 10^4$	8582	98.93
$M_h \in [107,\ 140]$	25192	55.79	465	2783	1174	3419	1619	138.6

Cut variables $\sqrt{s}$=500 GeV P(e^-, e^+)= (+80%,-30%) L_{int}=500 fb^{-1}

	$(t)\nu\bar{\nu}h$, $h \to$			SM backgrounds				
process	$b\bar{b}$	ϵ	others	$(s)\nu\bar{\nu}h$	$2f$	$4f$	$6f$	S_{sig}
cross-section (fb)	5.4	-	3.7	13.8	-	-	-	-
Expected	2702	100	1842	6891	$8.81 \cdot 10^6$	$5.58 \cdot 10^6$	$1.65{\cdot}10^5$	-
$N_{isoLeps} = 0$	2700	99.93	1478	6330	$6.50 \cdot 10^6$	$3.39 \cdot 10^6$	$8.77{\cdot}10^4$	0.85
$E_{vis} \in [100.0,\ 320.0]$	2675	99.02	1294	5882	$3.38 \cdot 10^6$	$1.33 \cdot 10^6$	9163	1.23
$N_{\mathrm{PFOs}} \in [40,\ 100]$	2449	90.63	1005	4993	$2.32 \cdot 10^6$	$2.75 \cdot 10^5$	6646	1.52
sum of b-tag > 0.995	2276	84.25	63	3374	$5.29 \cdot 10^5$	$2.74 \cdot 10^4$	4712	3.02
min $N_{\mathrm{PFOs}} > 8$	2259	83.61	60	3331	$5.19 \cdot 10^5$	$2.45 \cdot 10^4$	4270	3.04
$-\log y_{12} < 2.875$	2151	79.61	56	2487	$2.74 \cdot 10^5$	$1.48 \cdot 10^4$	4195	3.94
$-\log y_{23} \in [1.87, 10.38]$	2134	78.98	56	2410	$2.57 \cdot 10^5$	$1.44 \cdot 10^4$	4157	4.03
$-\log y_{34} \in [4.00, 11.60]$	2124	78.61	54	2382	$2.49 \cdot 10^5$	$1.42 \cdot 10^4$	3957	4.07
min thrust$\in [0.03, 0.3]$	2111	78.13	53	2350	$2.40 \cdot 10^5$	$1.38 \cdot 10^4$	3729	4.12
$\cos\theta_h \in [-0.975, 0.975]$	1989	73.62	50	2317	$1.50 \cdot 10^4$	8995	3622	11.1
$M_h \in [107,\ 140]$	1507	55.79	28	1875	725	578	685	20.5

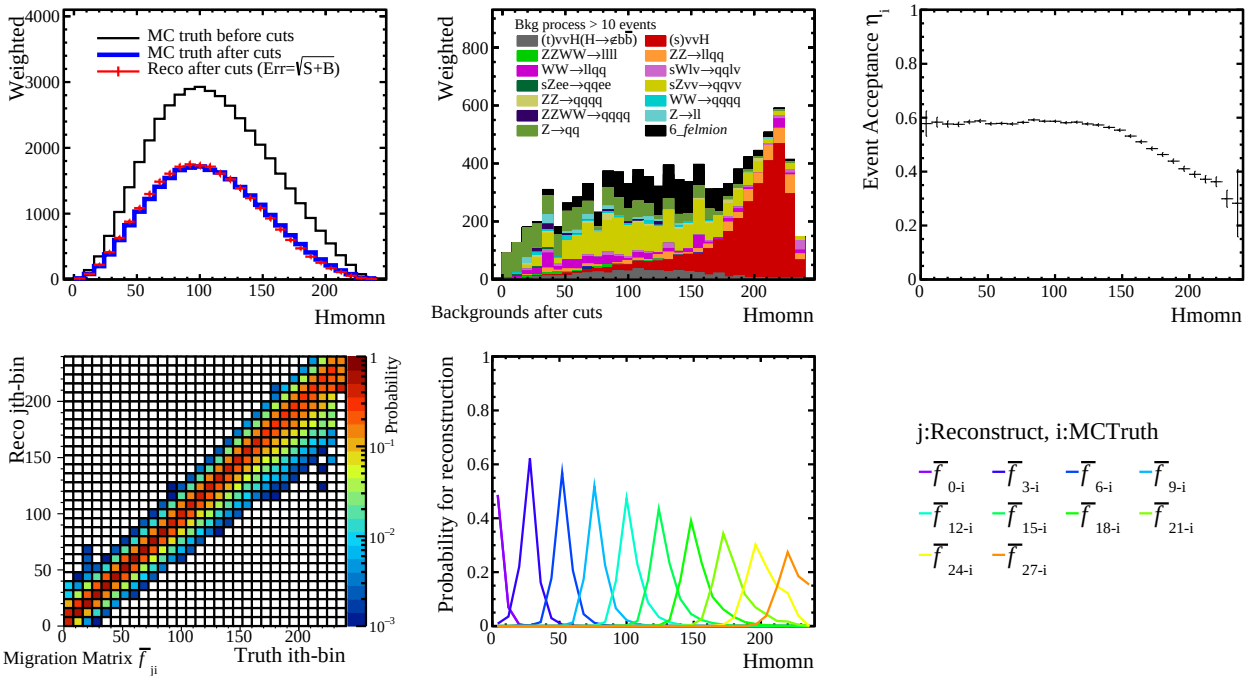

Figure 163: The distributions show the summary of the Higgs momentum P_h distribution after the background suppression. (Top left and middle): the remaining signal and the background distribution, which are given with the MC truth and the reconstructed, where the statistical error is given as the standard deviation of the Poisson probability. Notice that the s-channel $\nu\bar{\nu}h$ process overlaps in the sensitive area of the t-channel $\nu\bar{\nu}h$ process. (Top right): the event acceptance function η_i. (Bottom left and middle): the distribution shows the probability matrix of the migration ($\bar{f}_{ji}$) that is applied for the reconstruction of the realistic distribution of $\cos\theta_Z$, and the cross-sections of $\bar{f}_{ji}$ as 1-dim plots.

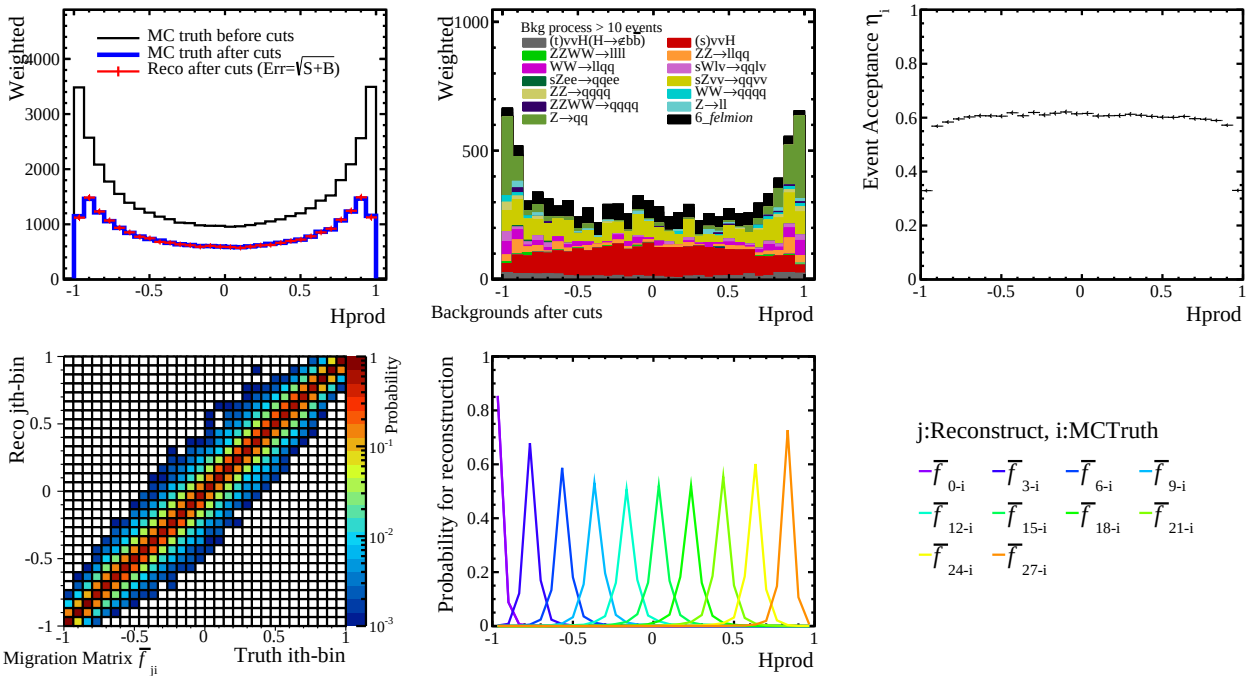

Figure 164: The distributions show the summary of the Higgs polar angle $\cos\theta_{higgs}$ after the background suppression. (Top left and middle): the remaining signal and the background distribution, which are given with the MC truth and the reconstructed. (Top right): the event acceptance function η_i. (Bottom left and middle): the probability matrix of the migration ($\bar{f}_{ji}$) that is applied for the reconstruction of $\cos\theta_{higgs}$, and the cross-sections of $\bar{f}_{ji}$ as 1-dim plots.

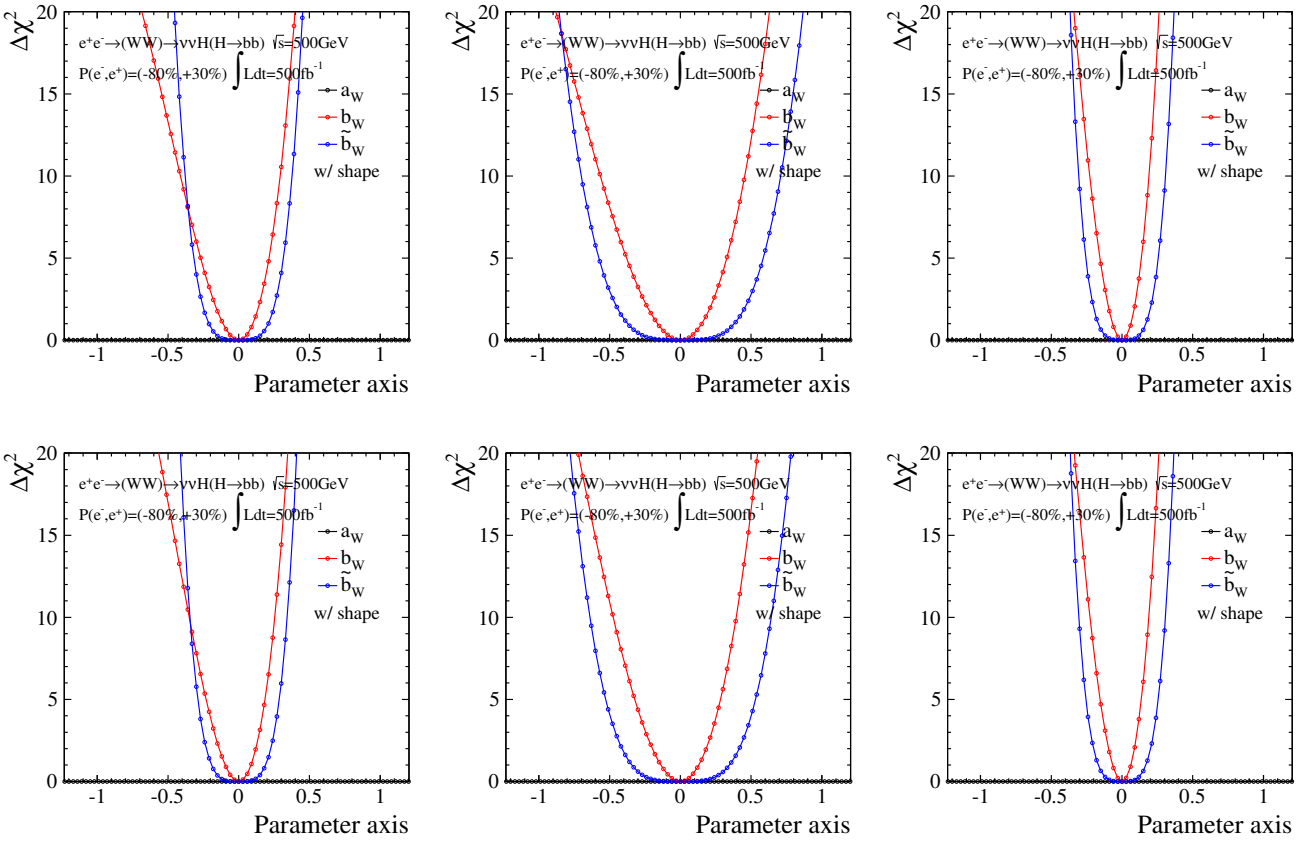

Figure 165: Distributions show $\Delta\chi^2$ as a function of each anomalous WWH parameter a_W, b_W, and $\tilde{b}_W$. The evaluation is done in the one-parameter axis. Since only the angular information is considered, the χ^2 values of a_W is 0 over the given range. (Upper) the polar angle cut is not imposed. (Lower) the polar angle cut is imposed to maximize the sensitivity of P_h of the Higgs boson. Each distribution are used: respectively (left) $x(P_h)$, (middle) $x(\cos\theta_h)$ which are binned in 20, and (right) $x(P_h, \cos\theta_h, \cos\phi_h)$ binned $5\times5\times5$.

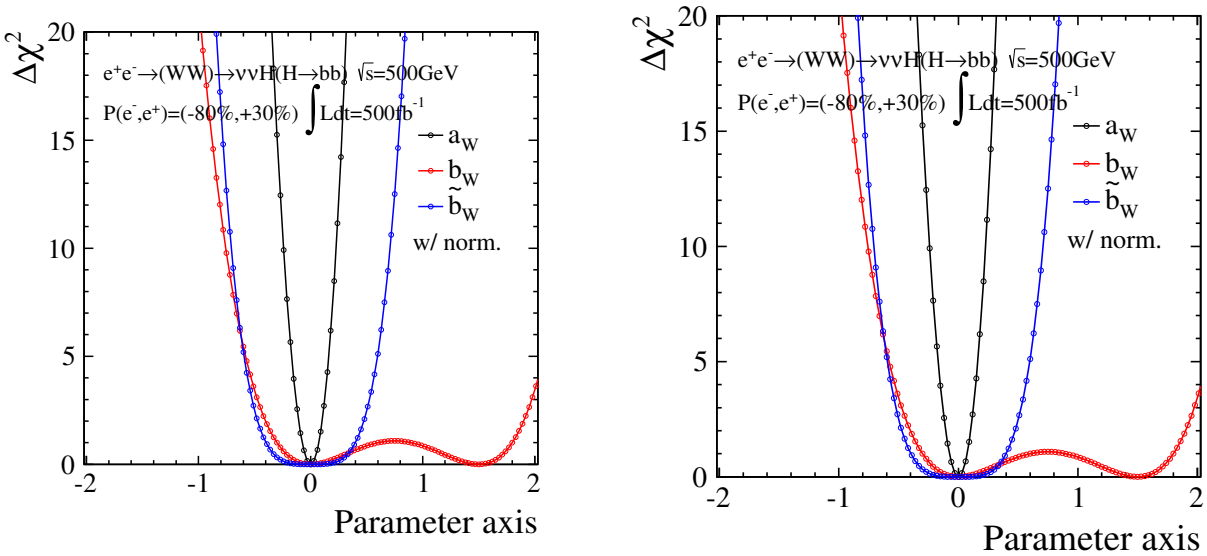

Figure 166: (Left) The distribution shows $\Delta\chi^2$ as a function of each parameter in the one parameter space, where the normalization information only is used for the evaluation. (Right) The distributions show $\Delta\chi^2$ in the two-dimensional parameter space of a_W-b_W.

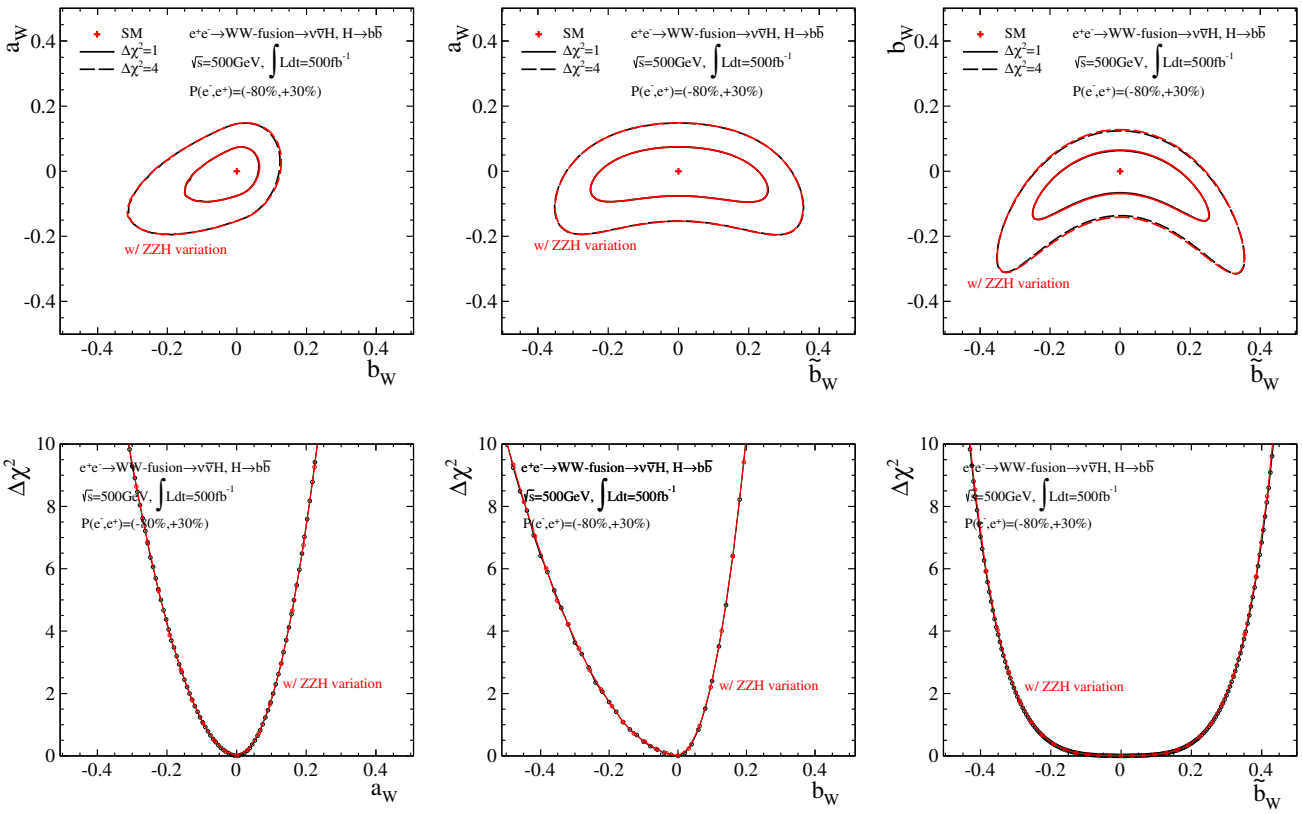

$\sqrt{s} = 250$ GeV with $\mathrm{L_{int}} = 250$ fb^{-1} and $\mathrm{P}(e^-, e^+) = (-80\%, +30\%)$

$$\begin{cases} a_W = [-0.078, \quad 0.051] \\ b_W = [-0.153, \quad 0.0648] \\ \tilde{b}_W = [-0.251, \quad 0.255] \end{cases}, \quad \rho = \begin{pmatrix} 1 & 0.1904 & -0.0604 \\ - & 1 & -0.1760 \\ - & - & 1 \end{pmatrix}$$

$\sqrt{s} = 250$ GeV with $\mathrm{L_{int}} = 250$ fb^{-1} and $\mathrm{P}(e^-, e^+) = (-80\%, +30\%)$

w/ ZZH contributions

$$\begin{cases} a_W = [-0.079, \quad 0.052] \\ b_W = [-0.153, \quad 0.0651] \\ \tilde{b}_W = [-0.249, \quad 0.254] \\ a_Z = [-0.136, \quad 0.136] \\ b_Z = [-0.028, \quad 0.028] \\ \tilde{b}_Z = [-0.025, \quad 0.025] \end{cases}, \quad \rho = \begin{pmatrix} 1 & .1888 & -.0637 & -.0463 & .0439 & .0009 \\ - & 1 & -.0.1731 & .0285 & -.0278 & -.0010 \\ - & - & 1 & .0779 & -.0769 & -.0013 \\ - & - & - & 1 & -.9875 & -.0163 \\ - & - & - & - & 1 & .0010 \\ - & - & - & - & - & 1 \end{pmatrix}$$

Figure 167: Upper plots show contours projected onto the two-dimensional parameter spaces a_W-b_W, a_W-$\tilde{b}_W$, and b_W-$\tilde{b}_W$ with the simultaneous minimization, which correspond to the 1σ and 2σ sensitivity to the anomalous WWH couplings at $\sqrt{s}$ =250 GeV with L_{int} =250 fb^{-1} and beam polarization of $\mathrm{P}(e^-, e^+)$= (-80%,+30%) . Middle plots are $\Delta\chi^2$ distributions as a function of each parameter space of the anomalous couplings a_W, b_W, and $\tilde{b}_W$. Both of the information: the shape of the three-dimensional distribution of $x(\cos\theta_h, P_h, \cos\phi_h)$ binned $5\times5\times5$ and the production cross-section are combined. Lower values give the 1σ bounds for each anomalous parameter a_W, b_W, and $\tilde{b}_W$and correlation matrix indicating correlation coefficients between the parameters.

B.4 $e^+e^- \to \nu_e\bar{\nu}_e h,\ h \to WW^* \to q\bar{q}q\bar{q}$ at $\sqrt{s} = 500$ GeV

In the decay process $h \to WW^*$ following the WW-fusion process, two WWH vertices exist. Since the anomalous couplings affect the momentum distribution of the W bosons, the Higgs boson interacting with those W bosons also gets some influence and the momentum distribution can vary. The influence that the Higgs boson is received could be also propagated to the W bosons appeared in the final state. Thus, it is expected that the W bosons decaying from the Higgs boson will give the momentum distribution which shows the stronger influence of the anomlaous couplings. If the Higgs rest-frame is used for the calculation of the momentum of the W boson, the variation derived from the production vertex will be removed. Because of this reason the momentum of the W boson should be observed in the laboratory frame. As for the other angles are observed in the Higgs rest-frame because the angular variation appear around the Higgs boson and the Higgs frame is the best frame to observe them.

B.4.1 Reconstruction and background suppression

The reconstruction of the events is implemented as follows,

- Try to find out isolated leptons for each reaction using `IsolatedLeptonFinder` which is based on the MVA method.
- PFOs after applying the lepton finding (if they exist) are clustered into four jets with the k_T jet algorithm which is done exclusively with the parameter R of 1.5. This jet algorithm is to remove the overlaid objects derived from the $\gamma\gamma \to$hadrons.
- The clustered pseudo-jet objects are disentangled and clustered again using the Durham jet algorithm into four jets with the flavor tagged information implemented with the `LCFIPlus` package.

Background suppression :

The background suppression was performed using the following observables, several of those are illustrated in Fig. 168. The explicit values for each observable are optimized by calculating the signal significance and its detail is given in Table **??**. Because several observables for suppressing the backgrounds are strongly correlated with the momentum of the W boson which is observed in the laboratory frame, those correlated observables are arbitrary made loosen to maintain the flatness of the acceptance function.

Through the analysis of the process $h \to WW^* \to q\bar{q}q\bar{q}$ at 250 GeV with the categorization into $q\bar{q}q\bar{q}$ and $c\bar{x}x\bar{c}$, it turned out that the flavor tag for c-quack does not give sufficient information with the current standard usage of `LCFIPlus` and the reconstructed $\Delta\Phi$ does not effectively improve the sensitivity to the anomlaous WWH couplings. Furthermore, as shown in the plots of the section [**?**], the momentum distribution of the W boson observed in the laboratory frame seems to observe the large variation against the parameter of $\tilde{b}_W$ in the $h \to WW^* \to q\bar{q}q\bar{q}$ of the WW-fusion at 500 GeV. Thus, the categorization used in 250 GeV analysis is not applied here. The signal is regarded as $q\bar{q}q\bar{q}$ to maximize the sensitivity which the momentum distribution can provide us.

- Require that there is no isolated leptons in the reaction. This can suppress large number of the leptonic processes.
- $N_{\mathrm{PFOs}} \in [45,\ 95]$, $E_{vis} \in [125.72\ 300]$, and sum of b-tag < 0.926
  The number of PFOs and the energy observed in the reaction, which can suppress large number of the full-hadronic decay processes. Because the observable E_{vis} is correlated with the momentum of the W boson, the upper bound of E_{vis} is loosen slightly. Since it is expected that there is no b-jet in the final state, the requirement of the b-likeness can effectively suppress $h \to b\bar{b}$ decay proess.

- $M_W \in [59.83,\ 94.83]$, $P_W\ < 55$,
  $M_{W^*} \in [22.5,\ 56.3]$, and $E_{W^*} \in [30.63,\ 103.54$
  It can be expected that the clustered jets are originating from the on-shell W and the off-shell W. Thus, these information on the W bosons are useful.

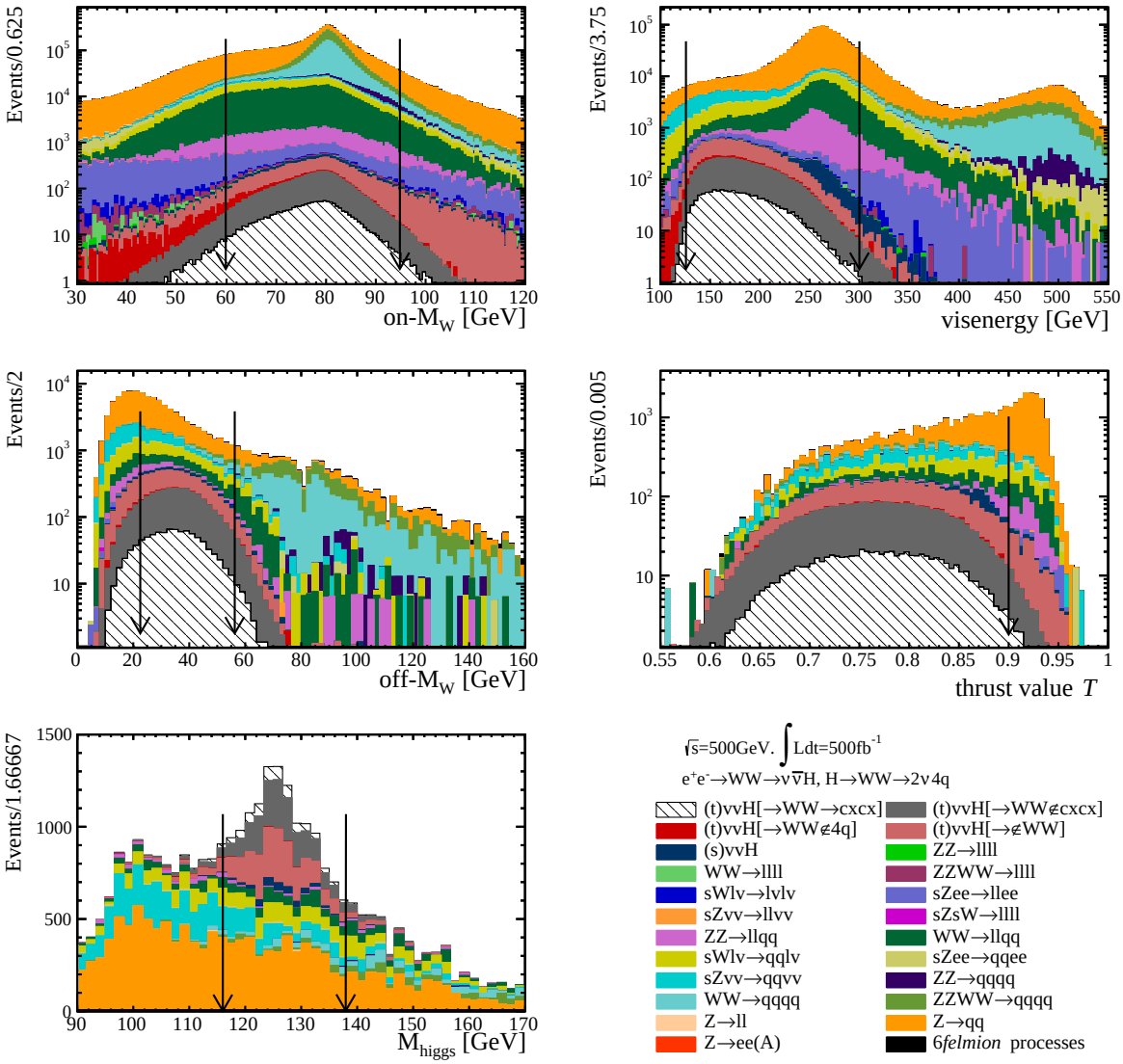

Figure 168: Distributions show the several observables used for the background suppression, where the signal process is $e^+e^- \to \nu_e\bar{\nu}_e h,\ h \to WW^* \to q\bar{q}q\bar{q}(c\bar{x}x\bar{c})$. The cut values are mentioned in the main text.

- min $N_{\mathrm{PFOs}} > 8$, $-\log y_{34} \in [2.64, 7.0]$,
  thrust min > 0.1, and thrust $\in [0.5\ 0.9]$
  The number of minimum PFOs among the clustered jets, transition parameter of the jet clustering, and thrust values. These topological information are also useful to discriminate the signal process from the SM backgrounds. Because these observables except N_{PFOs} are correlated with the momentum of the W boson, the values for both upper and lower bounds are slightly loosen from the optimal values.

- $M_h\ \in [116,\ 138]$
  The invariant mass of the Higgs boson calculated with the paired two jets, which is the mass window to determine Poisson error which is calculated by the remaining number of events of each bin of kinematical histograms.

B.4.2 Consideration on the shape

One concern is that the $h \to ZZ^*$ channel of about 185 events remains in the remaining backgrounds of 2190 in the t-channel $\nu_e\bar{\nu}_e h$ process, and also $h \to WW^*$ channel of about 202 events from the s-channel $\nu_e\bar{\nu}_e h$ process remains. These two channels coming through the ZZH vertex are possible to vary the shape of the background distribution. However, The anomalous ZZH couplings are sufficiently identified, which have been already shown in the ZZH analysis in [**?**], and also it has been shown in the previous section that the contaminations coming from the anomalous ZZH couplings at 500 GeV are almost negligible in the parameter space where the anomalous ZZH parameters can take. Therefore, it can be concluded that the effect due to the contamination by each roughly 200 events could be negligible since such small variations of the distribution depending on the anomalous ZZH couplings will be hidden in the statistical error of each bin. Because of this reason, special care is not taken for this point here[21].

Table 15: The expected number of remaining signal and background events after each cut for the $e^+e^- \to \nu_e\bar{\nu}_e h,\ h \to WW^* \to q\bar{q}q\bar{q}$ channel at $\sqrt{s}$=500 GeV, with the beam polarization state: P(e^-, e^+)= (-80%,+30%). The integrated luminosity of 500 fb^{-1} is assumed. The selection is for the $q\bar{q}q\bar{q}$ analysis and the index $q\bar{q}q\bar{q}$ in the table does not include the $c\bar{x}x\bar{c}$ channel (separately shown).

Cut variables $\sqrt{s}$=500 GeV P(e^-, e^+)= (-80%,+30%)

	$(t)\nu_e\bar{\nu}_e h,$	$h \to WW^* \to$			SM backgrounds				
process	$c\bar{x}x\bar{c}$	$q\bar{q}q\bar{q}$	ϵ	$h \notin WW^*$	$(s)\nu\bar{\nu}h$	$2f$	$4f$	$6f$	S_{sig}
cross-section (fb)	3.77	11.3	-	119.6	20.5		-		-
Expected	1884	5655	100	59803	10229	$1.3 \cdot 10^7$	$1.6 \cdot 10^7$	$4.0 \cdot 10^5$	-
Niso-leptons=0	1882	5646	99.8	58472	9352	$1.1 \cdot 10^7$	$9.9 \cdot 10^6$	$2.2 \cdot 10^4$	1.65
$N_{\rm PFOs} \in [48,\ 125]$	1799	5333	93.1	45581	7327	$6.5 \cdot 10^6$	$5.7 \cdot 10^6$	$1.1 \cdot 10^4$	2.02
sum of b-tag < 0.94	1564	5091	90.2	9599	2334	$4.8 \cdot 10^6$	$4.7 \cdot 10^6$	$2.3 \cdot 10^4$	2.16
$M_W \in [59.83,\ 94.83]$	1462	4795	54.7	7678	1961	$3.3 \cdot 10^6$	$4.2 \cdot 10^6$	$2.0 \cdot 10^4$	2.28
$P_W\ < 55$	1446	4736	73.9	7446	1813	$1.5 \cdot 10^6$	$5.1 \cdot 10^5$	3582	4.40
$E_{vis} \in [125.72\ 300]$	1420	4672	73.9	7264	1704	$1.2 \cdot 10^6$	$3.3 \cdot 10^5$	1953	4.88
min $N_{\rm PFOs} > 8$	1004	3237	48.0	5170	1141	$4.7 \cdot 10^5$	$9.6 \cdot 10^4$	948	5.56
- $\log y_{34} \in [2.64, 7.0]$	973	3154	35.7	4330	832	$1.2 \cdot 10^5$	$5.6 \cdot 10^4$	890	9.63
thrust min > 0.1	938	3043	32.6	3862	700	$6.3 \cdot 10^4$	$4.4 \cdot 10^4$	838	11.68
$M_{W^*} \in [22.5,\ 56.3]$	772	2522	64.9	2897	581	$3.2 \cdot 10^4$	$1.7 \cdot 10^4$	211	13.94
$E_{W^*} \in [30.63,\ 103.54$	738	2402	58.6	2779	416	$2.5 \cdot 10^4$	$1.4 \cdot 10^4$	171	14.70
thrust $\in [0.5\ 0.9]$	728	2368	32.6	2621	392	$1.3 \cdot 10^4$	$1.2 \cdot 10^4$	167	17.47
$M_h\ \in [116,\ 138]$	600	1994	32.5	2190	334	4072	3969	69	22.56

Fig. 169 give summary plots on the momentum distribution of the W boson P_W measured in the laboratory frame. Fig. 170 also give the momentum distribution of the W boson P_W measured in the Higgs rest-frame for the comparison, where the remaining signal and the signal significance are respectively 1794 and 22.6 with the optimal cut values although the detail is not described in the text. Both of the distributions are binned in 30 for visualization.

[21] Another technical reason in terms of constructing the shape distribution is that the amplitude with the combination of anomalous ZZH and WWH couplings can be described as,

$$\frac{d\sigma}{dx}(a_W, b_W, \tilde{b}_W, a_Z, b_Z, \tilde{b}_Z) = \left|\left((1+a_{W_c})\mathcal{A}_{0a_W} + b_W\mathcal{A}_{b_W} + \tilde{b}_W\mathcal{A}_{\tilde{b}_W}\right)\left((1+a_{Z_c})\mathcal{A}_{0a_Z} + b_Z\mathcal{A}_{b_Z} + \tilde{b}_Z\mathcal{A}_{\tilde{b}_Z}\right)\right|^2$$

where a_{W_c} and a_{Z_c} are respectively a_W/C and a_Z/C. This description will give 210 independent linear terms. To extract basis vectors for constructing the kinematical shape, it is necessary to give 210 independent combinations of $(a_W, b_W, \tilde{b}_W, a_Z, b_Z, \tilde{b}_Z)$. If the situation of the analysis seems that the variation depending on the ZZH parameters largely affect the results, it will have to make an effort for this contamination.

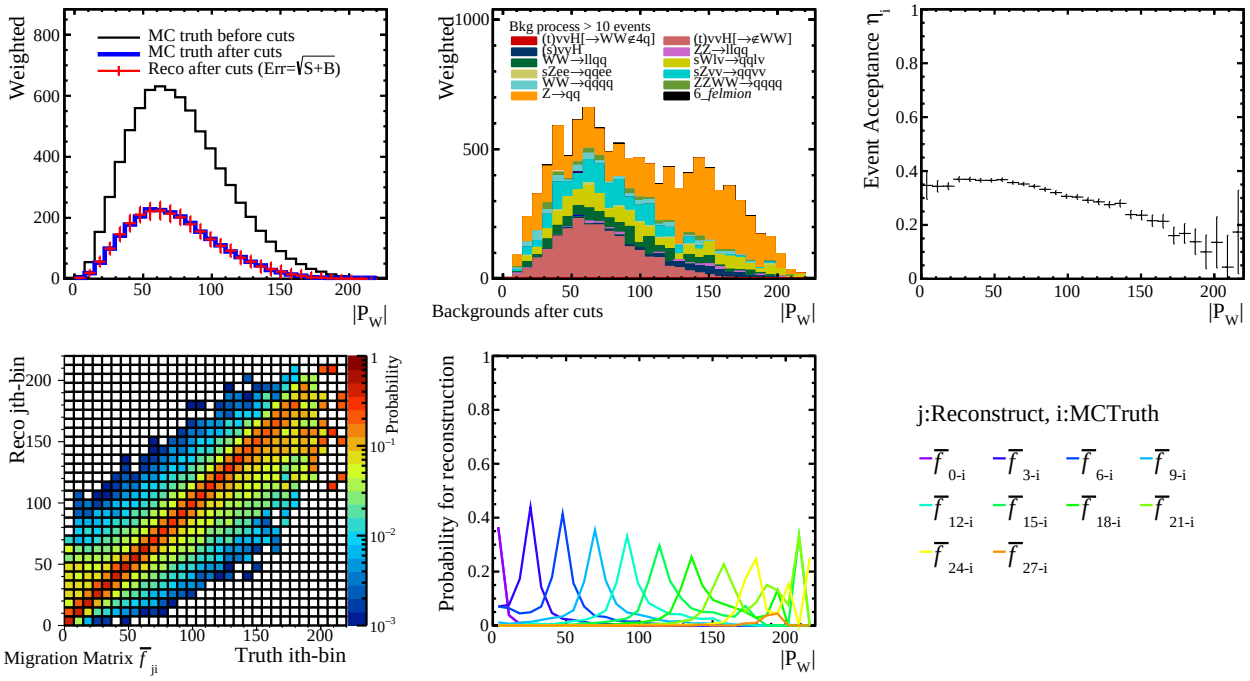

Figure 169: Distributions show the summary plots of the W boson momentum P_W distribution under the assumption of $\sqrt{s}$=500 GeV and L_{int}=500 fb^{-1}. P_W is calculated in the laboratory frame. The s-channel $\nu_e\bar{\nu}_e h$ process is slightly overlapping in the high momentum region of the t-channel $\nu_e\bar{\nu}_e h$ process, which is sensitive region to the anomalous couplings.

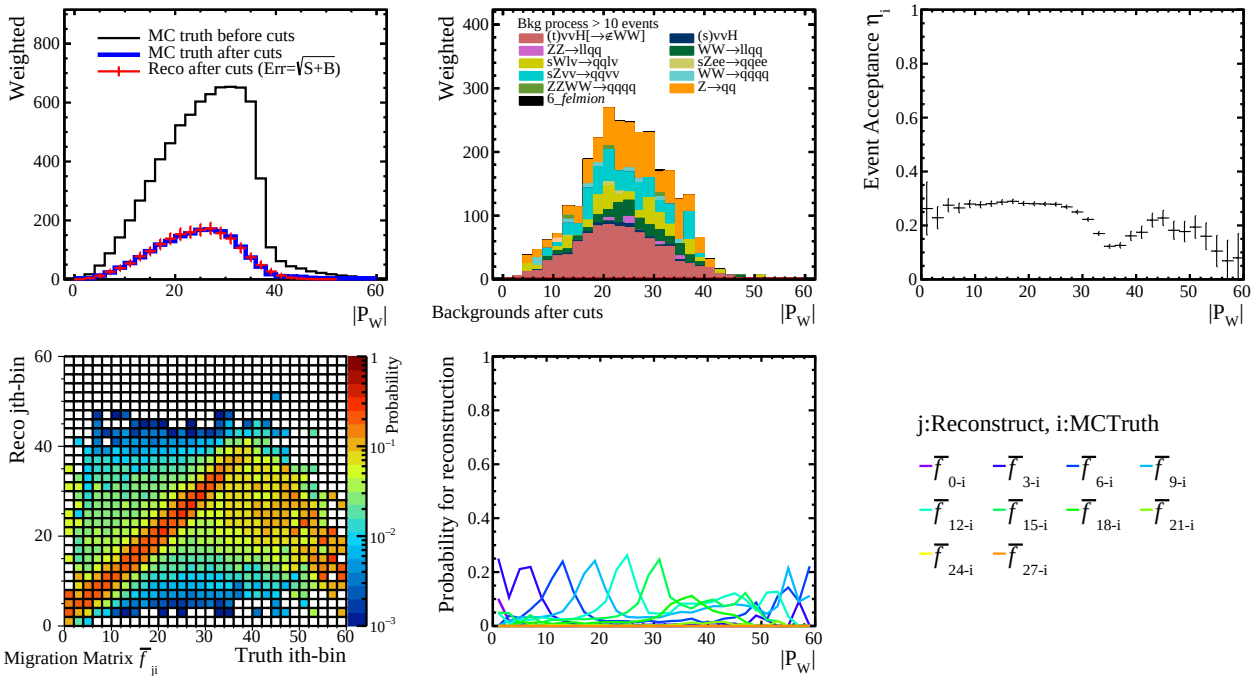

Figure 170: Distributions show the summary plots of the W boson momentum P_W distribution under the assumption of $\sqrt{s}$=500 GeV and L_{int}=500 fb^{-1}. P_W is calculated in the Higgs-rest frame.

B.4.3 Impact of the kinematical distribution

Plots in Fig. 171 show impact of the kinematical distribution, where the two kinds of plots of the W momentum which is calculated in the laboratory frame and the Higgs rest-frame are given. It is clearly shown that all sensitivity is given with the W momentum distribution when comparing the 1-dimension and 3-dimension distributions, and also shown that the W momentum calculated in the laboratory frame has more sensitivities to the anomalous WWH couplings.

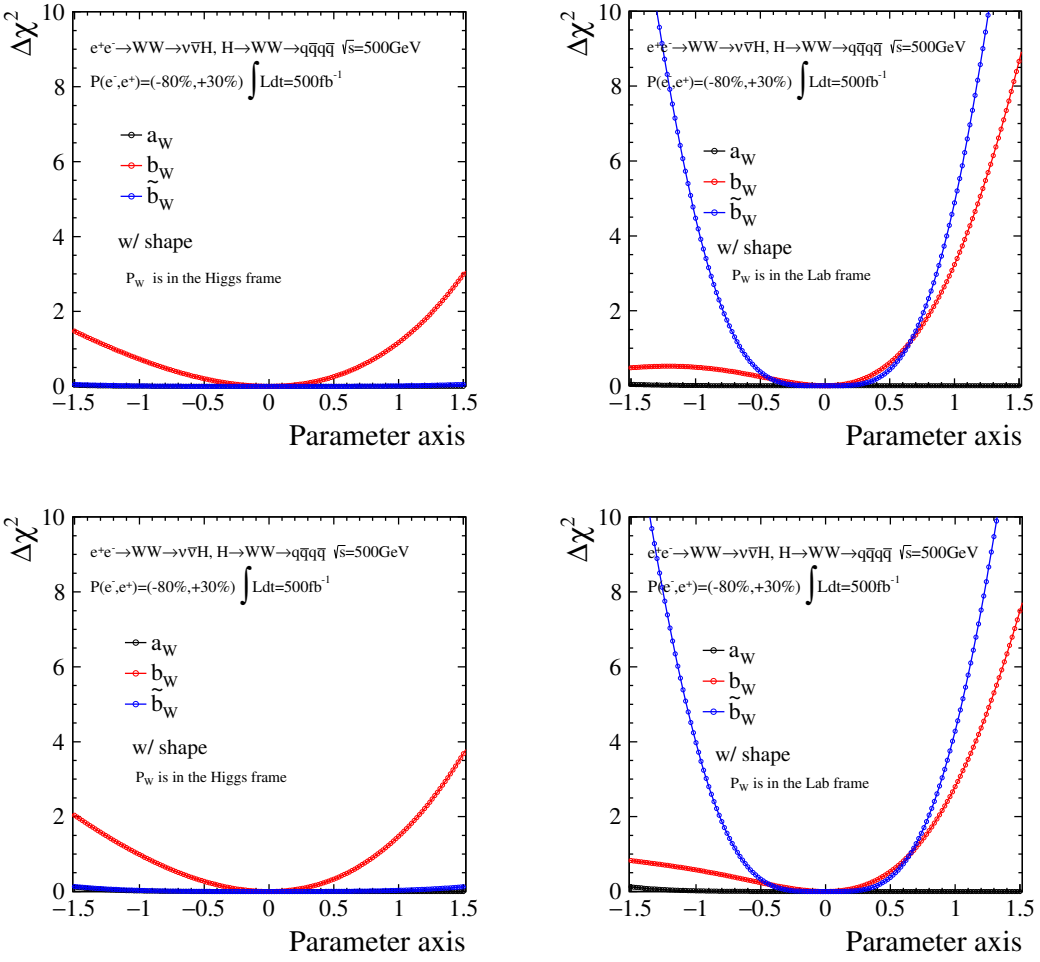

Figure 171: Distributions show $\Delta\chi^2$ as a function of each parameter a_W, b_W, and $\tilde{b}_W$, assuming the beam polarization of P(e^-, e^+)= (-80%,+30%) and the integrated luminosity of 500 fb^{-1}. In the left two plots the W momentum is calculated in the Higgs-rest frame. In the right two plots the W momentum is calculated in the laboratory frame. The difference between upper and lower plots are the distributions used for the evaluation: the one-dimensional distributions of the W boson momentum for the upper plots, and the three-dimensional distributions of $x(\cos\theta^*_{Wl}, P_W, \Delta\Phi[0 - -\pi/2])$ binned $5\times5\times5$ for the lower ones. The kinematical distributions only are used for the evaluation.